Relationship between Microstructure, Properties and HICC Resistance of HSLA steel weld metals

by

Adalberto Rosales Mendoza

Submitted in accordance with the
requirements for the degree of
Doctor of Philosophy
at
The University of Leeds

The candidate confirms that the content of this thesis is original, except where reference is made to the work of others. No part of this dissertation has been submitted for a degree at any other university.

March 2008

Institute for Materials Research,
School of Process, Environmental and Materials Engineering,
University of Leeds,
Leeds, England, UK,
LS29JT

ACKNOWLEDGMENTS

This research was carried out in the Institute for Materials Research at the University of Leeds, UK, under the sponsorship of Universidad Simón Bolívar and FONACIT, Fondo Nacional de Ciencia y Tecnología, both located in Caracas, Venezuela.

I would like to thank Prof. Robert C. Cochrane for offering me such complicated subject to study. The first day we met I did not understand what he was talking about otherwise I could have run away. Now, seriously, thanks to this offer I have learn a little about: ferrous and welding metallurgy, fractography, failure analysis, electron microscopy, relationship between microstructure and mechanical properties, the existence of MAC, hydrogen induced cracking, the many millions NMI's in a weld metal, how to treat complicated things to try to understand them and a very long etcetera. And I say little at the beginning of the list because there is a lot more about I do not know. Many thanks Bob, specially for the final push.

I would like to express my gratitude to Dr. Rik Brydson, Dr. Andy Brown and Mr John Harrington, from the Leeds Electron Microscopy and Spectroscopy Centre (LEMAS), for your invaluable contribution to my SEM and TEM training and practice, and, of course, for the utilisation of your excellent facilities. I will come back some day.

In my time at the university I attended various lectures by Prof. R. C. Cochrane, Prof. D. V. Edmonds, Dr. Chris Hammond, Dr. Rik Brydson, Dr. R. F. Cochrane, about ferrous and non ferrous metallurgy, deformation and fracture, failure analysis, structure of materials, characterisation of materials, phase transformations and materials selection. They do not know, but they gave me guidance during those dark ages when you do not know what to do and you are afraid to ask. Thanks. In the classroom I met a very good friend I has abandon Mr. Ruben del Amo, who I am going to contact again after this.

I would like to thank Mrs Joy Bielby, for her collaboration and cheerful disposition to help me to sort things out. And for answering almost all my e-mails when seemed that the communication were broken from this part of the planet. A million thanks. I think this page is getting smaller and smaller every minute I think back, so I will hurry up. I want to say thanks to: Mrs Diane Bavester, Dr. K He, Dr. Andy Watson, Dr. Shukru Talas, Xiong, Lee, Jan, Dee, Nene, Oi, Noi, Kee, Mr Don Doomore (Language Centre), and many more. A million thanks for all.

Adalberto Rosales-Mendoza
March 2008

DEDICATORY

DEDICATED
TO
AURORA AND OUR D.A.'S

AND

MY FAMILY,
SPECIALLY MY MOTHER, MARITZA,
WHO IS NOW AND ALWAYS PRAYING FOR ME,
MY FATHER, ADALBERTO,
MY BROTHER AND SISTER,
JOSE LUIS AND MARILBERTH,

MY NIECES:
GENESIS, ESTEFANIA, SAMANTA Y LUCIA
AND MY NEPHEW AND GODSON
JOSE LUIS JR.

AND GODDOUGHTER
DAMARIS

Relationship between Microstructure, Properties and HICC Resistance of HSLA steel weld metals

Adalberto Rosales Mendoza

Submitted in accordance with the
requirements for the degree of
Doctor of Philosophy

Abstract

The effects of microstructure, mechanical properties and hydrogen content on the hydrogen induced cold cracking (HICC) resistance of high strength low alloy (HSLA) steel weld metals were studied in this investigation. The weld metals were designed in a previous work. Their microstructures were characterised by optical and electron microscopy (FEG-SEM and TEM). Microphases, such as non metallic inclusions (NMI) and martensite-austenite-carbide constituent (MAC), were studied in some detail due to their hydrogen trapping capacity. Fractographic studies of hydrogen charged tensile samples were carried out to study the effect of microstructure and hydrogen content on the fracture micromechanisms. A critical hydrogen content (C_k) was estimated for each weld metal. The trapping capacity of each weld metal was studied using an electrochemical double pulse technique to measure the hydrogen trapping constant (k). The weld metals were classified based on composition, microstructure and micro-phase characteristics. NMI number density, size and spatial distribution were determined and thermodynamic calculations were proposed to identify their type. MAC morphology and distribution were qualitatively assessed. Retention of austenite was estimated, considering chemical and size stabilisation of remaining austenite. It was found that a continuous network of grain boundary ferrite (PF(G)), in combination with the presence of retained austenite in the MAC particle and certain NMI characteristics were beneficial to increase C_k. In weld metals without PF(G), retained austenite proportion and NMI distribution and size play a critical role in maintaining tolerance to hydrogen. From fractographic observations, it was proposed a phenomenological model that correlates microstructure, hydrogen content and the stress intensity factor, with the activation of different fracture micromechanisms: micro-void coalescence (MVC), quasicleavage (QC) and intergranular (IG). The trapping capacity of the weld metals was evaluated and results indicate that this capacity is the result of a complex combination of factors such a NMI inclusion size and distribution, presence of retained austenite and microstructure. The value of k takes into account these effects.

List of Contents

LIST OF TABLES AND ILLUSTRATIONS

LIST OF TABLES

LIST OF FIGURES

LIST OF ABBREVIATIONS

AF	acicular ferrite
α_{gb}	grain boundary ferrite, also PF(G)
B_f	bainite finish temperature
B_S	bainite start temperature
CCT	continuous cooling transformation diagrams
CEV	carbon equivalent number
$C\gamma$	carbon content in the last remaining untransformed austenite
C_K	critical hydrogen concentration
D	diffusion coeficient
D_a	apparent diffusion coefficient
D_L	lattice diffusion coefficient
E_A	initial cathodic potential (E_{corr} - 10mV)
E_C	charging cathodic potential
E_{corr}	corrosion potential
FATT	fracture appearance transition temperature
FCAW	flux cored arc welding process
FEG-SEM	field emission gun scanning electron microscope or microscopy
FS(A)	ferrite with aligned second phase
FS(B)	bainite
FS(NA)	ferrite with non aligned second phase
FS(SP)	ferrite side plates
GMAW	gas metal arc welding process
GTAW	gas tungsten arc welding process
HAZ	heat affected zone
H_D	diffusible hydrogen
HDT	hydrogen thermal desorption
HEI	hydrogen embrittlement index
HEI_{AR}	hydrogen embrittlement index based on area reduction loss
HEI_{EL}	hydrogen embrittlement index based on elongation loss
HICC	hydrogen induced cold cracking
HSLA steels	high strength low alloy steels
IG	intergranular fracture micromechanism
IIW	International Institute of Welding
LCLA steels	low carbon low alloy steels
M	martensite
MA or M/A	martensite austenite island or microphase
MAC	martensite austenite carbide aggregate or microphase
M_f	martensite finish temperature
MMAW	manual metal arc welding process
M_s	martensite start temperature
MVC	micro-voids coalescence fracture micromechanism
NMI	non metallic inclusions
N_v	NMI number density
PDP	double pulse technique
PF(G)	polygonal ferrite in grain boundary or grain boundary ferrite
QC	quasicleavage fracture micromechanism
SAW	submerged arc welding process
SCE	standard Calomel electrode (reference electrode)
S_f	true fracture stress
S_m	engineering maximum or tensile stress
SMAW	shielded metal arc welding process
S_y	engineering yield stress
TEM	transmision electron microscope or microscopy
TTT	temperature transformation time or isothermal diagrams

CHAPTER 1

INTRODUCTION

Economical welding of high strength, upto 890 MPa, low alloy (HSLA) steels requires the continuous research and development of consumables to produce weld metal deposits with mechanical properties and corrosion resistance equal or exceeding that of the base metal coupled with a need to reduce or eliminate the use of pre-heating before welding. The principal characteristics that provide the incentive to use HSLA steels are: higher strength, excellent toughness, ductility and formability, but especially the improved weldability that results from reduction of the carbon equivalent value (CEV) primarily by the use of lower carbon content (below 0.10% C) [1]. The utilisation for lightweight construction and minimum fabrication cost has made HSLA steels particularly attractive for the construction and offshore structure industries [2].

High-strength low alloy (HSLA) are a group of low carbon steels that utilise small amounts of alloying elements to obtain minimum yield strengths between 350 and 550 MPa in the as-rolled or normalised condition [1,3]. These steels have better mechanical properties and sometimes better corrosion resistance than as-rolled carbon steels. The ferrite in HSLA steels is typically strengthened by grain refinement, precipitation hardening and, in minor importance, solid solution strengthening. Grain refinement is the most desirable strengthening mechanism because it improves not only strength but also toughness [3]. This refinement of the ferrite grain size is produced by additions of microalloying elements such as aluminium, vanadium, niobium, and titanium in combination with various forms of thermomechanical processing. At the same time, this has made possible improvement of the resistance of steels to hydrogen assisted cold cracking, stress corrosion cracking, and brittle fracture initiation in the weld heat-affected zone (HAZ) region, without sacrificing base metal strength, ductility, or low-temperature toughness. Higher strengths can be obtained by the use of the quenching and tempering process, in excess of 890 MPa can be achieved with appropriate steel compositions. Whilst, lower strength HSLA steels can be welded economically without the use of pre-heating, in general the higher strength grades, such as those with yield strengths of 690 or 890 MPa, have traditionally required pre-heating before welding to prevent hydrogen induced

cold cracking (HICC) of the weld metal and HAZ. The former becomes a more serious problem as the CEV of the steel are progressively reduced to both reduce pre-heating requirements and prevent HICC in the weld HAZ. Currently, steels are available which do not crack when welding without pre-heating. However, a key problem is that, in such circumstances, the weld metal is then prone to cracking partially because of a different microstructure from the base metal and partially because to achieve the weld metal mechanical properties a higher CEV composition is often necessary.

In the welding of HSLA steels, hydrogen-induced cold cracking (HICC) is a severe problem and it occurs when the following four factors are present simultaneously: hydrogen in the weld metal and/or HAZ, a sufficiently high stress, a susceptible microstructure and relatively low temperature [4]. Cold cracks are weldment defects that form as the result of presence of certain amount of hydrogen in the weld microstructure. Hydrogen-induced cracking is usually a delayed phenomenon, occurring possibly hours, days, weeks or even months after the welding operation. The temperature at which these defects tend to appear ranges from -50 to 150 °C in steels. The fracture is either intergranular or transgranular cleavage and as with other forms of cracking, hydrogen-induced cracking involves both a particular microstructure and a threshold level of stress. It also involves a critical level of hydrogen, which is alloy and microstructure dependent [5].

The weldability and the resistance to HAZ HICC of HSLA steels have been mainly improved by reducing carbon contents and impurities and controlling the microstructure. Other remedies for the HICC are the control of the welding parameters (preheating, postweld heating, bed tempering, etc.) and the use of proper welding processes and materials (low hydrogen processes and consumables, low strength filler metals, etc.) [4, 6]. As was mentioned before, the thermomechanical control process used in the hot rolling of steel plates has further promoted this trend in the case of the HAZ [7], but problems have been continuously found in the weld metal. For this reason, new welding consumables to produce weld metal deposits with similar mechanical properties to the base metal and improved resistance to HICC have been developed in recent years. At first, this development has been concentrated on the achievement of a maximum toughness and ductility for a given strength level by control of the weld metal microstructure [1]. Recently, this development has included the improvement of the HICC resistance.

There seems to be general agreement that microstructures primarily consisting of acicular ferrite provide optimum weld metal mechanical properties, both from a strength and toughness point of view, compared with grain-boundary, polygonal, or Widmanstätten ferrite [1, 5]. This effect of the acicular ferrite is related with its small grain size (typically 1-3 μm) and high angle grain boundaries [1]. The formation of large proportions of upper bainite, ferrite side plates, or grain boundary ferrite, on the other hand, are considered detrimental to toughness, since these structures provide preferential crack propagation paths, especially when continuous films of carbides are present between the ferrite laths or plates. Attempts to control the weld metal acicular ferrite content have led to the introduction of welding consumables containing complex deoxidizers (Si, Mn, Al, and Ti) and balanced additions of various alloying elements (Nb, V, Cu, Ni, Cr, Mo, and B) [1]. Acicular ferrite is often nucleated on minor phase particles, such as specific oxides or borides [5].

Wildash [8] has shown that there are potentially several ways, based on microstructural changes, to improve the mechanical properties and the HICC resistance of HSLA steels weld metals. The weld metal produced with the modified consumables offered higher strength than that produced with commercial consumables. With respect to the HICC, Wildash and collaborators [8-10] suggested that a relationship existed between HICC susceptibility, diffusible hydrogen concentration (H_D), and the presence of microstructural constituents and phases in the weld metal, such as grain boundary ferrite, martensite/austenite islands, carbides, and non-metallic inclusions. For example, a reduction in the content of grain boundary ferrite was reported to be beneficial to the HICC resistance whilst an increase in the fraction of martensite-austenite-carbide (MAC) islands and non-metallic inclusion (NMI) produced improvements to the HICC resistance that depended on the quantity of H_D in the weld metal [8-10]: the increase of MAC was beneficial at low levels of H_D and for the case of NMI the beneficial effect was detected at high H_D contents. These results could indicate that the presence of NMI is more important than that of the MAC constituent in improving the HICC resistance. However, other factors not taken in account by Wildash[8], such as the NMI composition, size spatial distribution and the presence of different types of microconstituents (for example, retained austenite, martensite islands, and/or MAC) could be responsible for the oversetting of the benefits of each other to the HICC resistance. Another contradictory result reported by Wildash [8] was the effect of the grain boundary ferrite (α_{gb}), which

was claimed to be deleterious to the HICC resistance, although in some cases the presence of this microstructure seemed to increase the critical hydrogen content to produce a decrease in the ductility at low H_D. This was suggested to be the result of the presence of NMI and MAC, which outweighed the harmful effect of the α_{gb}, and not to a possible beneficial effect of this microstructural constituent at low H_D concentrations. This work intends to clarify the role of the α_{gb}, NMI and MAC on the HICC resistance, taking in account their influence on the mechanical properties, hydrogen transport and trapping behaviour of the HSLA steel weld metal designed by Wildash[8].

In the study of the weld metal HICC susceptibility it is important to measure the H_D content of the different steel weldments because this permits the determination of the hydrogen levels supported by the material. Several techniques have been used to determine the weld metal diffusible hydrogen (H_D) content and a considerable number of hydrogen assisted cracking tests have been proposed [6, 7]. To measure H_D a mercury displacement method (International Institute of Welding method) and a gas chromatography method are considered preferable because they can collect very small amounts of hydrogen. Hydrogen assisted cracking tests have been developed for investigation of the mechanism of hydrogen assisted cracking and for proper selection of welding materials and welding conditions to avoid hydrogen assisted cracking. These tests are divided into two groups: an external restraint type and a self-restraint type. The safe welding condition is, in general, determined from the result of a hydrogen cracking test and the advantages and disadvantages between them are reviewed by Yurioka and Suzuki elsewhere [7].

Other methods used in the study of HICC involve hydrogen charging of the steel to simulate the hydrogen quantity that could present in the weld metal and/or HAZ during the welding process. Many researchers have reported lower reproducibility than others, but in general, electrochemical charging has been used around the world to study the hydrogen damage. Wildash and collaborators [8, 11] analysed the various factors that should be taken into account when using and interpreting the results of hydrogen induced cracking through the utilisation of the cathodic hydrogen charging method. Although it was concluded in these studies that the cathodic method could be used to simulate the hydrogen induced cold cracking behaviour of different HSLA steels; the problem of low reproducibility was still present, and that was minimised by the ability of measure H_D concentrations after

precharging [11]. However, in several cases, the details of the method of charging did not permit a controlled increment of the H_D content, and this factor made difficult the comparison between the different weld metals. This low reproducibility and control over the hydrogen charging could be the consequence of the several experimental variables which intervene in an electrochemical process as for example: the sample microstructure and surface finishing, the corrosion behaviour of the samples, the variation of the electrolyte pH during the charging, the charging potential and current, the different corrosion inhibitors, the type of electrolyte, the temperature of the solution, the time of charging, etc.. The utilisation of controlled sample preparation and experimental procedures (controlled temperature, potentiostatic control of the polarisation), buffer electrolytes, and the same quantities of entry promoters (inhibitors and hydrogen entry promoters) could result in acceptable reproducibility levels. Nevertheless, Wildash was able to show a correlation between the results of hydrogen charging and the propensity for weld metal HICC and, subsequently, to use this technique to show that the weld metal HICC susceptibility could be improved empirically.

The general target of this investigation is to study in more detail the relationship between microstructure, hydrogen trapping behaviour and the hydrogen cracking response of HSLA weld metals of different strength levels obtained with different consumables. These consumables were selected and designed by Wildash [8] with the intention of varying the microstructure and study the effect of this variation on the hydrogen cracking resistance.

To gain knowledge of microstructure-hydrogen induced cracking relationships, the followings objectives were proposed:

1- To determine the effect of the consumable composition on the microstructure of the weld metal obtained: specifically phase proportions, size and distribution and relate this to their effect on mechanical properties and HICC resistance

2- Using Field Emission Gun Scanning Electron Microscopy (FEG-SEM) and Transmission Electron Microscopy (TEM) identify the potential hydrogen trapping features which could be found in different weld metal microstructures: martensite-austenite-carbides (MAC) constituents, non-metallic inclusions (NMI), retained austenite, ferrite/austenite or ferrite/martensite interfaces, dislocation arrangements and density, etc

3- To study the influence of microstructure, mechanical properties and hydrogen content of the weld metal on the fracture induced cracking and

propose a mechanism that relates these variables and the micromechanisms usually found in hydrogen induced fracture

4- Using an electrochemical technique, a potentiostatic double-step method, study the hydrogen diffusion and trapping processes for the different weldments and relate this with their microstructural components and their resistance to HICC

5- Elucidate the response of the studied weld metals to real welding situations based on the results obtained in this investigation in regard to their HICC resistance.

Chapter Two

High Strength Low Alloy Steels and their Welding

In this chapter, firstly, a brief description of the characteristics of HSLA steels is presented: mechanical properties, alloying elements and their weldability. Secondly, the metallurgy of the welding of the HSLA steels is briefly explained. In this section the evolution of the microstructure is described, including: the formation of non metallic inclusions, the solidification and its effect on the final microstructure, and the solid state transformation and the factors which control its development.

2.1 High Strength Low Alloy Steels

High strength low alloy (HSLA) steels provide an optimum combination of properties such as high strength, toughness, ductility, formability, weldability and atmospheric corrosion resistance. The high strength permits the construction of lightweight structures and the consequent low cost of fabrication. The potential weight reduction and the low cost of HSLA steels are compared with other materials in figure 2.1.

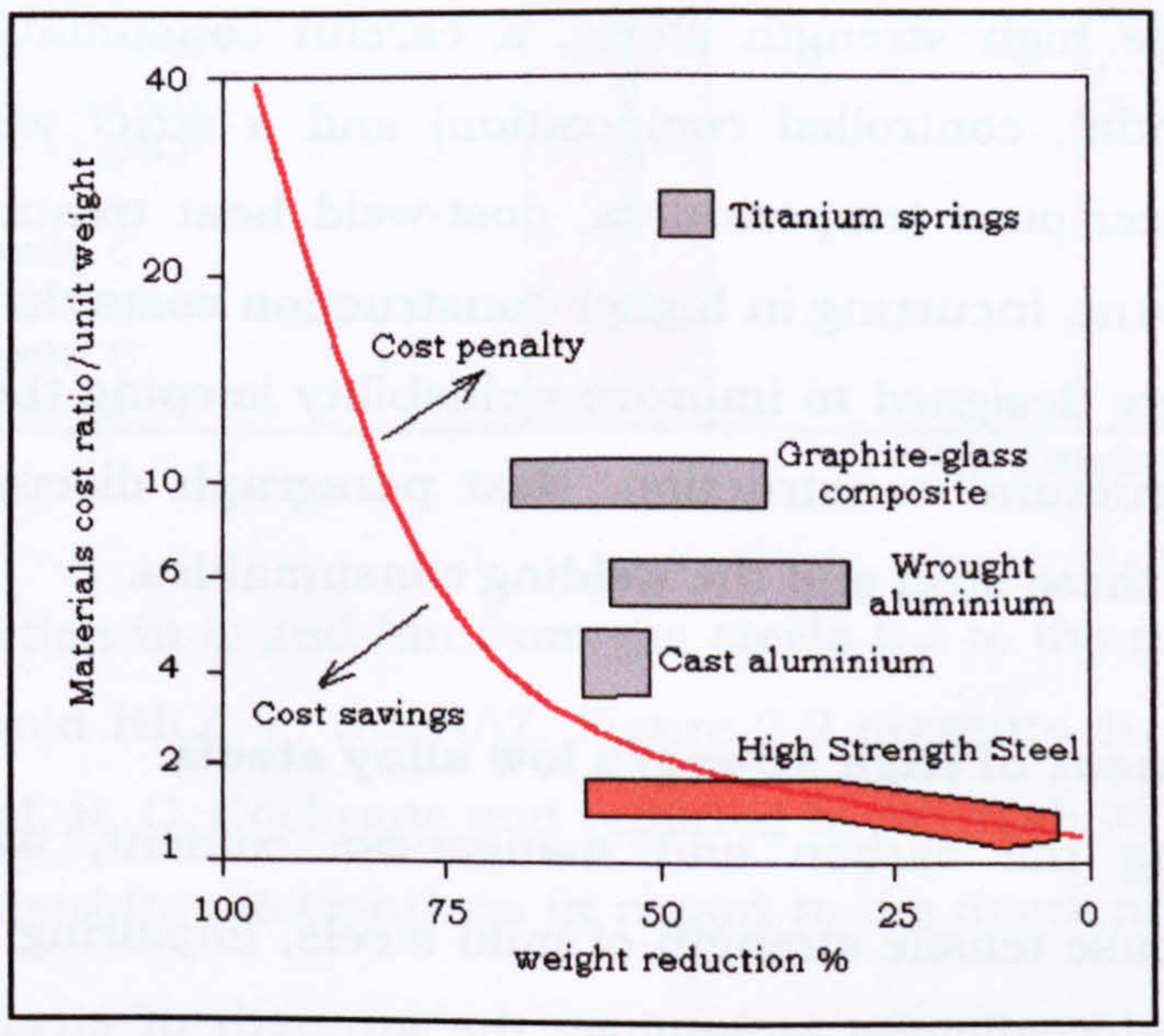

Figure 2.1 Material cost ratio as a function of weight reduction potential for various materials compared to mild steel as the base. Adapted from Wright[3].

Hot rolled HSLA steels (which are also called microalloyed steels) are a group of low carbon steels that utilise small amounts of alloying elements, such as Nb, V or Ti, to produce minimum yield strengths between 275 and 550 MPa and Charpy V-notch fracture appearance transition temperature

(FATT) about -60 °C. In general, the maximum carbon content is less than 0.2 wt%C and the total alloy content is less than 2 wt%. Apart from manganese (up to 1.5 wt%) and silicon (up to 0.7 wt%), as in carbon steels, HSLA steels often contain small amounts of niobium (up to approximately 0.05 wt%), vanadium (up to about 0.1 wt%), and titanium (up to about 0.07 wt%) to ensure both grain refinement and precipitation hardening, the two strengthening mechanisms more used compared with the solid solution strengthening, which is used in lesser extent [3, 4]. Niobium (Nb), vanadium (V) and titanium (Ti) are strong carbide and nitride formers, particles responsible for the reduction of the grain boundaries movement and in consequence the grain growth. Among the carbides and nitrides of Nb, V, and Ti, titanium nitride (TiN) is the most stable, making it the most effective in limiting the extent of grain growth during welding [4]. As discussed in the next chapter, grain size control is the key factor to produce high strength and excellent toughness for these low alloy steels.

Higher strength, in excess of 550 MPa, can be obtained by adding small amounts of Ni, Mo or Cr coupled with severe controlled rolling and/or accelerated cooling. Alternatively, re-austenitisation followed by quenching and tempering may be used to produce the highest grades of steel such as X100 to X120 or yield strengths in the order of 690 to 890 MPa. For the welding of these high strength steels, a careful consumable selection (low hydrogen potential, controlled composition) and a strict welding procedure (pre-heating, inter-pass temperatures, post-weld heat treatment) have to be taken into account, incurring in higher construction costs. In this respect, the HSLA steels were designed to improve weldability keeping the necessary high strength for structural construction. Next paragraph discusses the parallel development of these steel and the welding consumables.

2.1.1 Development of High strength low alloy steels

Increasing the carbon and manganese content, was a traditional method to increase tensile strength of mild steels, impairing weldability. With the arrival of microalloying technology the strength of steels was kept high while C and Mn quantities were reduced, hence improving weldability. Since then, the utilization of combined small amounts of Nb, V and Ti, in addition to Mn, Si, Cr, Mo, Ni, Cu and Al, and the application of thermo-mechanical treatments are used today for the production of weldable and tough high strength steels. Gladman[12] summarises the factors that led to initial

development of microalloyed steels: materials cost saving due to weight reductions of structures, a need for weldable high strength pipelines, the development in welding processes and the close interaction between metallurgy scientist and industry, leading to the production of high strength steels at low cost. Table 2.1 shows chronologically the discoveries and developments of these high strength steels.

Table 2.1 Discovery and development of microalloyed steels.
Adapted from Gladman[12]

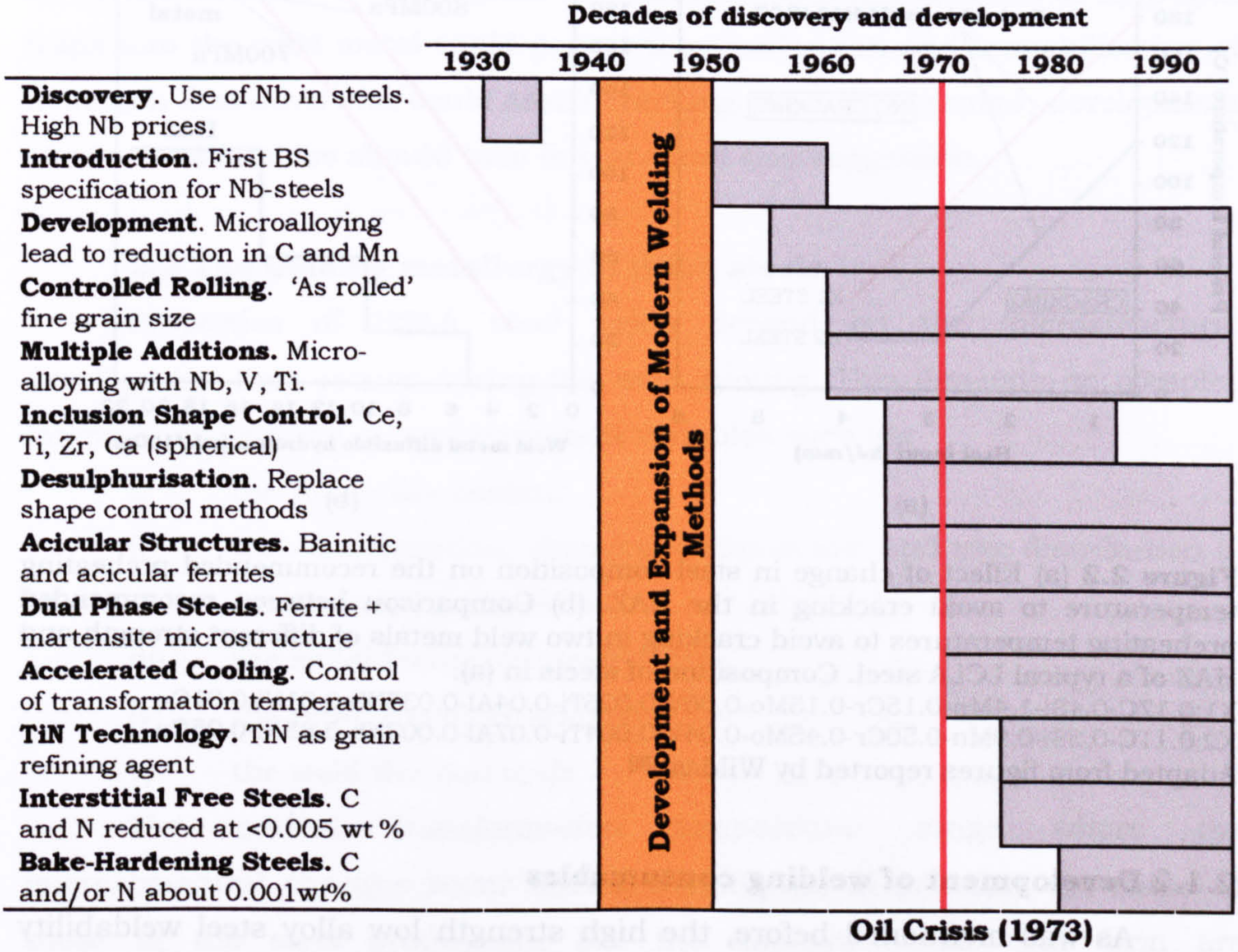

The reduction in C and Mn from the steels led to the reduction in heat treatments to avoid HICC in the HAZ. Figure 2.2 presents diagrams originally developed by Prof. R. C. Cochrane and reported by Wildash [8]. These diagrams highlight two important observations in regard to the development of weldable steels:

1- Reduction in C and Mn, in combination with small additions of Cr, Mo and Ni, decreases the preheat temperature, needed to avoid cracking in the HAZ of welded low carbon low alloy steels (LCLA) by approximately 60 °C, at low heat inputs (<3 kJ/mm). For the modified steel, room temperature (25 °C) was the minimum necessary preheating at heat inputs above 3 kJ/mm. Figure 2.2(a) presents the calculated preheating temperature for two steels.

2- Although improvement on the weldability was achieved with the modified LCLA steels using microalloying, weld metals of high strength needed a preheating in excess of that for LCLA steels HAZ. This preheating temperature depends on weld metal strength: the higher the strength the higher the preheating. These reduce the advantages offered by the designed steels, increasing production costs. Impulse to develop new consumables appeared.

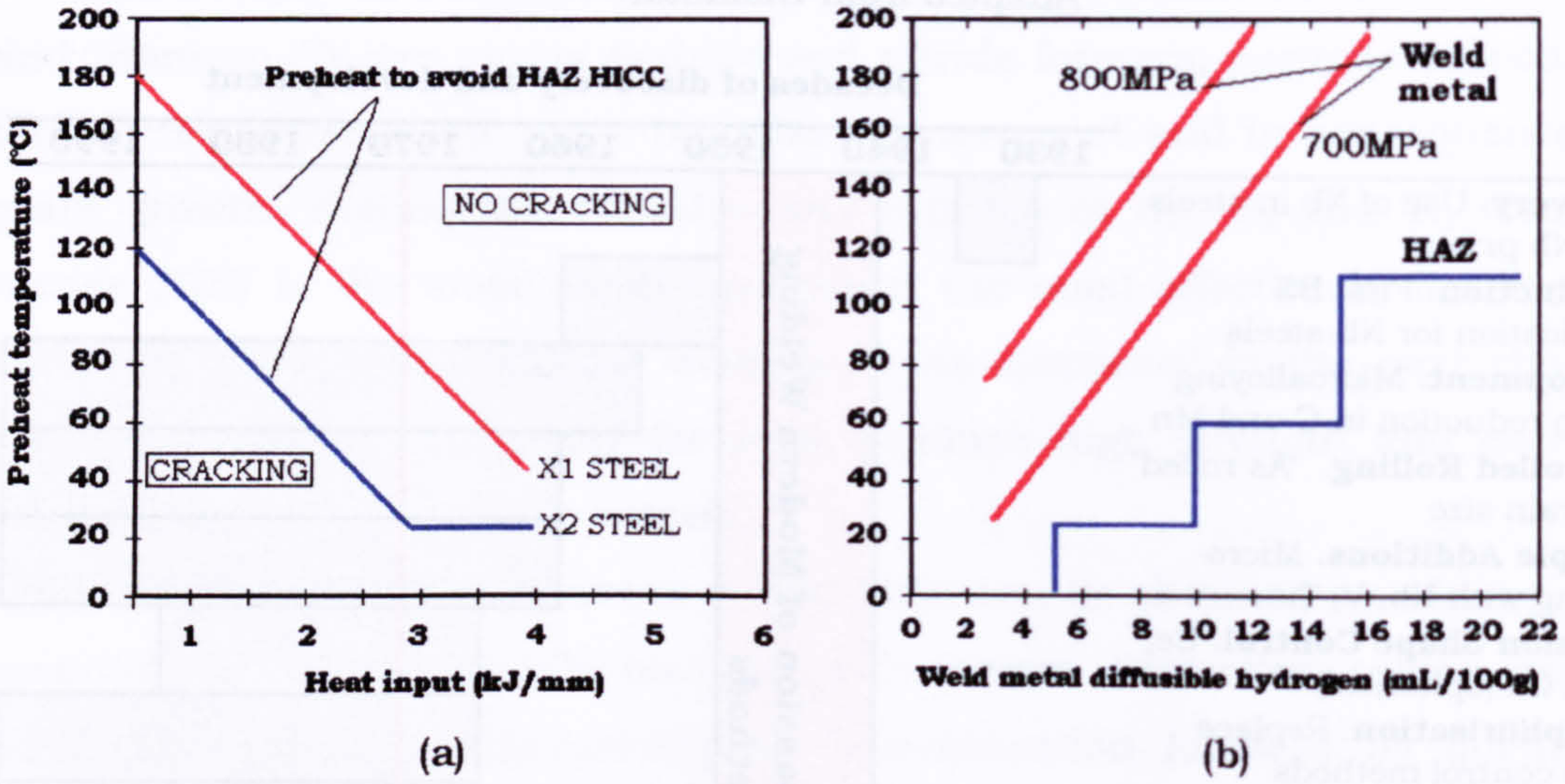

Figure 2.2 (a) Effect of change in steel composition on the recommended preheating temperature to avoid cracking in the HAZ. (b) Comparison between recommended preheating temperatures to avoid cracking in two weld metals of different strength and HAZ of a typical LCLA steel. Composition of steels in (a):
X1:0.17C-0.4Si-1.4Mn-0.15Cr-0.15Mo-0.06V-0.025Ti-0.04Al-0.035Nb-0.01Ni-0.01Cu
X2:0.11C-0.3Si-0.9Mn-0.50Cr-0.45Mo-0.04V-0.004Ti-0.07Al-0.003Nb-0.85Ni-0.25Cu
Adapted from figures reported by Wildash[8]

2.1.2 Development of welding consumables

As was mentioned before, the high strength low alloy steel weldability was improved throughout microalloying, but cracking appeared in the high strength weld metals. As consequence consumable development was aimed to:

1- Control microstructure and mechanical properties of the weld metal. This was achieved through the careful selection of consumable components to provide adequate transfer of alloying elements, protect the weldment from atmospheric gases and offer good arc properties. Wildash [8-10] and collaborators have demonstrated how to obtain yield strength between 400 and 900 MPa in the as welded condition. Chapter 3 deals with the effect of alloying elements on weld metal microstructure and properties.

2- Reduce the potential hydrogen which could be introduced to the weld pool. MMA consumables with basic coating and flux-cored

electrodes could introduce low hydrogen content to the weld. In chapter 4 the potential hydrogen content from different welding consumables is compared.

Hydrogen could be minimised in the weld metal by the use of correct welding procedures, consumables and protecting gases. This combination of factors will improve the soundness of the weld metal when matching the base metal mechanical properties. A recently hydrogen trapping theory, which is discussed in chapter 4, suggests that an adequate introduction of hydrogen traps into the weld metal could permit the distribution and immobilisation of hydrogen that otherwise could assist cracking. With this in mind, development of new consumables should take into account this suggestion.

2.2 The welding metallurgy of HSLA steels

Properties of HSLA steel welds depend on the microstructural development that occurs during the weld cooling. This depends on complex interactions between several important variables such as:

i) the total alloy content
ii) the concentration, chemical composition, and size distribution of non-metallic inclusions
iii) the solidification microstructure
iv) the prior austenite grain size
v) the weld thermal cycle

The critical transformation temperature range where the microstructural changes occur during welding are in principle the same as those in the steel production, but the microstructures that form are considerably different due to some particular effects resulting from the arc welding process:

(a) A high volume fraction of inclusions in the weld metal due to much higher amount of oxygen introduced during welding. The presence of these inclusions influences the austenite/ferrite transformation, restricting grain growth and offering alternative nucleation sites leading to acicular ferrite or ferrite side plate microstructures.

(b) Significant segregation. During weld metal solidification, alloying and impurity elements tend to segregate extensively to interdendritic or intercellular spaces under the conditions of rapid cooling. This affects the kinetic of the posterior solid-state transformation [1].

Figure 2.3 summarises the steps involved in the development of the weld metal microstructure. During the liquid state, chemical reactions occur in the liquid metal (weld pool) to form non-metallic inclusions (step I).These inclusions could form during solidification as well and then be trapped in the weld metal during this process (step II). The solidification process will determine the final microstructure of the weld metal. Steps from the step III to VII correspond to the solid-state transformation of the weld, which depend on the products of steps I and II, the composition of the alloy, the welding parameters, and the cooling rate. In this section the basis of the microstructural development of the weld metal will be described briefly.

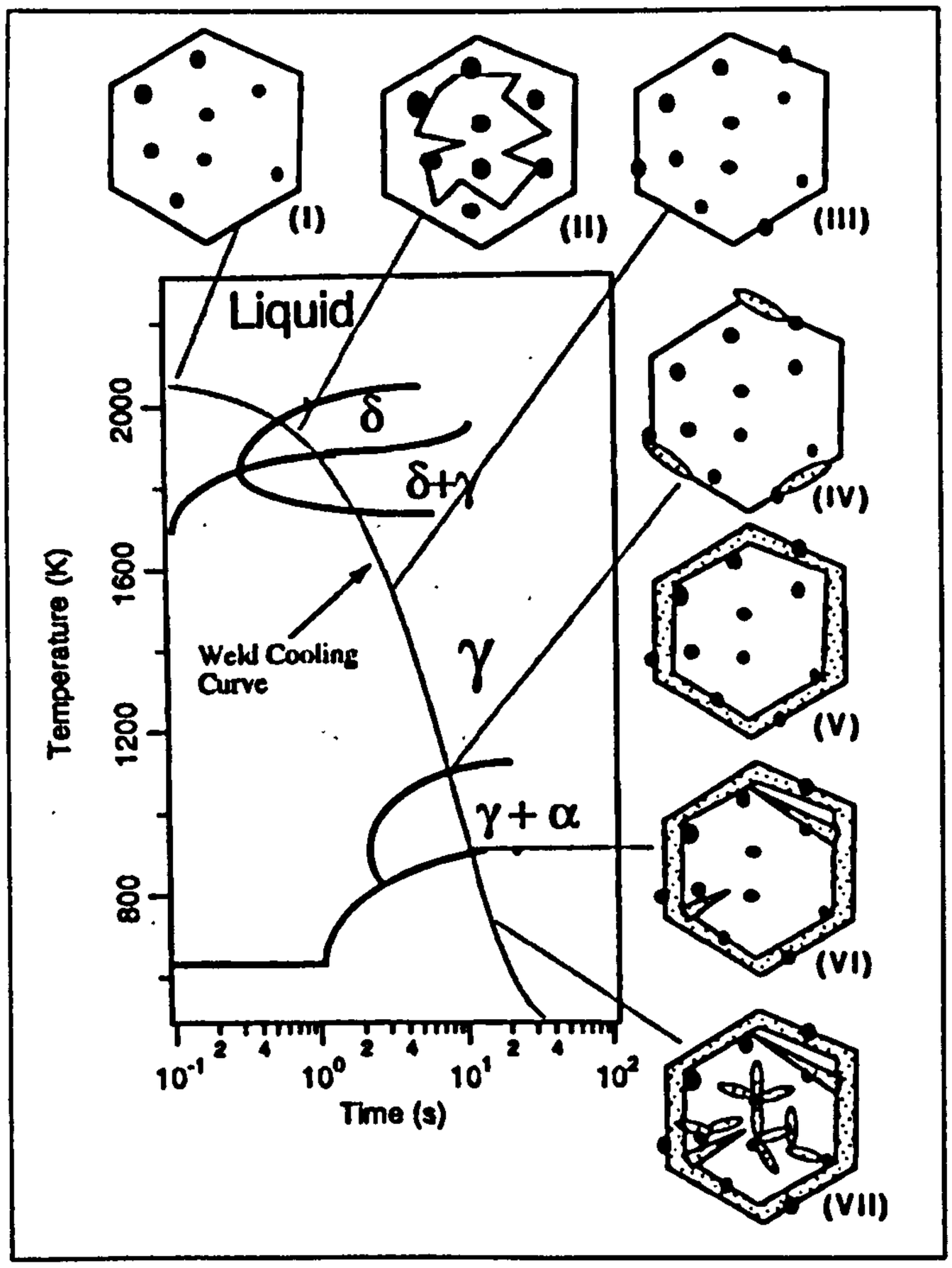

Figure 2.3 Schematic representation of a continuous cooling transformation diagram presenting the basic steps involved in the weld metal microstructure development. (I) inclusions formation, (II) solidification, (III) austenite phase, (IV) beginning of primary ferrite nucleation and growth, (V) Finishing of the primary ferrite growth, (VI) nucleation and growth of ferrite side plates, and (VII) acicular ferrite formation [13, 14].

2.2.1 Non-metallic inclusion formation in the weld metal

In the weld metal, the first reaction known to influence the final weld microstructure is inclusion formation. During the welding process, some of the products of the oxidation/de-oxidation reactions, which took place in the arc

and in the melt, are trapped as spherical non-metallic inclusions into the bulk of the weld metal. Microanalysis of such inclusions generally reveals the presence of manganese, silicon, aluminium, and titanium [15]. In table 2.2 is shown examples of non-metallic inclusions found in C-Mn and low-alloy steel weld metals. It has always been assumed that the oxides or inclusions will form in a fixed sequence Al_2O_3, Ti_2O_3, SiO_2, and MnO, regardless of the weld metal composition. This sequence is derived according to decreasing stability, or decreasing the absolute value of the standard free energy of formation. However, this does not necessarily represent the observed reaction processes, because the stability of the oxides depends on the reactant concentration in the weld, that is, segregation, and the formation of complex oxides [16].

Table 2.2 Chemical composition of some non-metallic inclusions [17]

Type of weld	Constituent elements	Reported phases
C-Mn steel	Si, Mn, O, S (traces of Al, Ti, and Cu)	SiO_2, $MnOSiO_2$, MnS, (Cu_xS)
Low-alloy steel	Al, Ti, Si, Mn, O, S, N (Cu)	$MnOAl_2O_3$, γ-Al_2O_3, TiN, SiO_2, $MnOSiO_2$, α- and β-MnS, (Cu_xS)

The reactant concentration in the weld is affected by the solidification process. During the weld metal solidification solute elements segregate to the liquid at the solid/liquid interface, and the liquid concentration can reach high levels in the interdendritic spaces. The nonequilibrium lever rule or Scheil equation could be used to take into account this segregation, if the solid diffusion is neglected:

$$C_L = C_0 f_L^{\kappa_0 - 1} = C_0 (1 - f_S)^{\kappa_0 - 1} \qquad (2.1)$$

where C_0 is the bulk concentration in the weld pool, C_L is the concentration in the liquid at the interface, f_L and f_S are the liquid fraction and the solid fraction, respectively; and κ_0 is the equilibrium partition ratio [18-20]. Table A.1 in the annexes shows values for κ_0 for different solute that could be found in HSLA steel welds.

The concentration of different alloying solutes and the interaction between them are the factors affecting the formation of the simple or complex non-metallic inclusion during the welding process. The concentration of the different solute could be estimated using equation 2.1 and the interaction between them could be taken in account using the interaction coefficients

used in steelmaking processes [21, 22]. Several attempts have been made for the prediction of the inclusion formation in steel welds. Kluken and Grong[23] developed a theoretical model for inclusion formation in submerged arc (SA), gas metal arc (GMA), and flux cored arc (FCA) steel weld metals, where the homogeneous nucleation of oxide inclusions occurs as a consequence of the supersaturation in the weld pool during cooling. The reactions of deoxidation will be almost completed when the liquid metal reach a constant level of about 1550 °C. The growth of the particles may occur under this approximately isothermal condition until the temperature reaches the melting point of the steel. Figure 2.4 shows the sequence of events during the inclusion formation in the weld metal. In a later work, van der Eijk and Grong[24], working on Ti and Al-Ca deoxidised steels, proposed the mechanism for the formation of single phase and complex multiphase oxysulphides, based on experimental and thermodynamical analysis. They concluded that Ti-rich inclusions forms as a result of a series of reactions occurring in the liquid metal, during solidification and in the solid state, identifying the solid state products as MnS, TiN, and $MnOTiO_2$. In contrast the inclusions in the Al-Ca deoxidised steel were complex oxysulphides, where the thermodynamically more stable phase can be formed in the liquid metal. Figure 2.5 shows schematically the formation of those complex inclusions. These types of complex inclusions have been found in welds [14, 17, 23, 25-27].

The utilisation of computational thermodynamics[28] has permitted the prediction of the formation and competition between different non metallic inclusions and the construction of deoxidation diagrams similar to those presented in the figure 2.6, from the investigation of Babu and David [14, 26-27]. These diagrams predicted satisfactorily the formation of AlN and the inhibition of the Al_2O_3 and Ti(CN) reactions for the alloy (a) (figure 2.6 (a)) and the contrary situation for the alloy (b) (figure 2.6 (b)).

The construction of these diagrams shows the possibility to describe inclusion formation in a wide range of welding processes and compositions by employing equilibrium thermodynamic calculations that consider multicomponent interactions in liquid steels. However, this analysis is not complete without the modelling of the kinetics of formation and growth of inclusions. This kinetic approach could permit the estimation of the size, size distribution and density of non-metallic inclusions, characteristics that influence strongly the weld metal transformation and the final mechanical properties of the weldment.

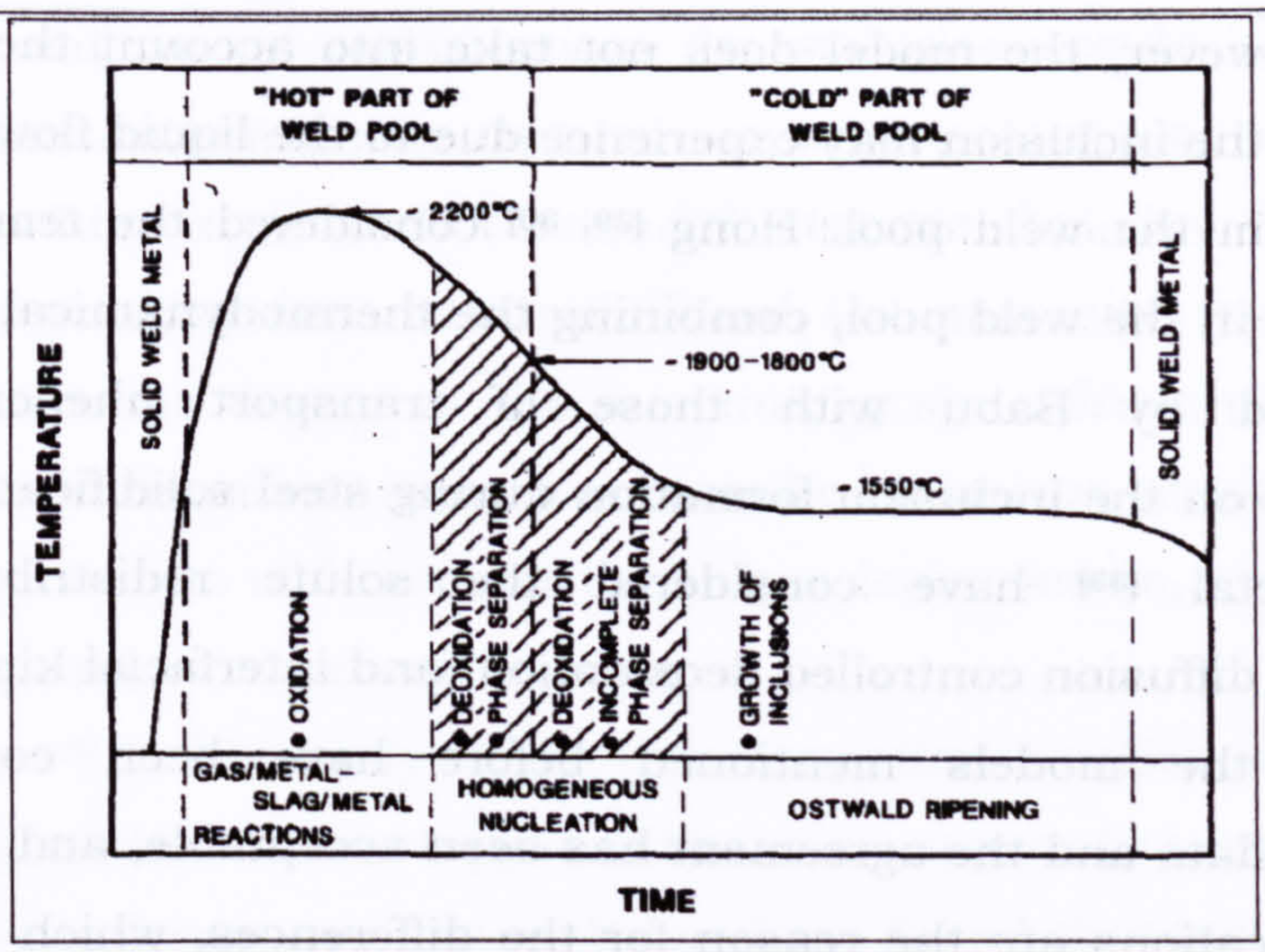

Figure 2.4 Schematic representation of the inclusion formation model proposed by Kluken and Grong [17, 23]

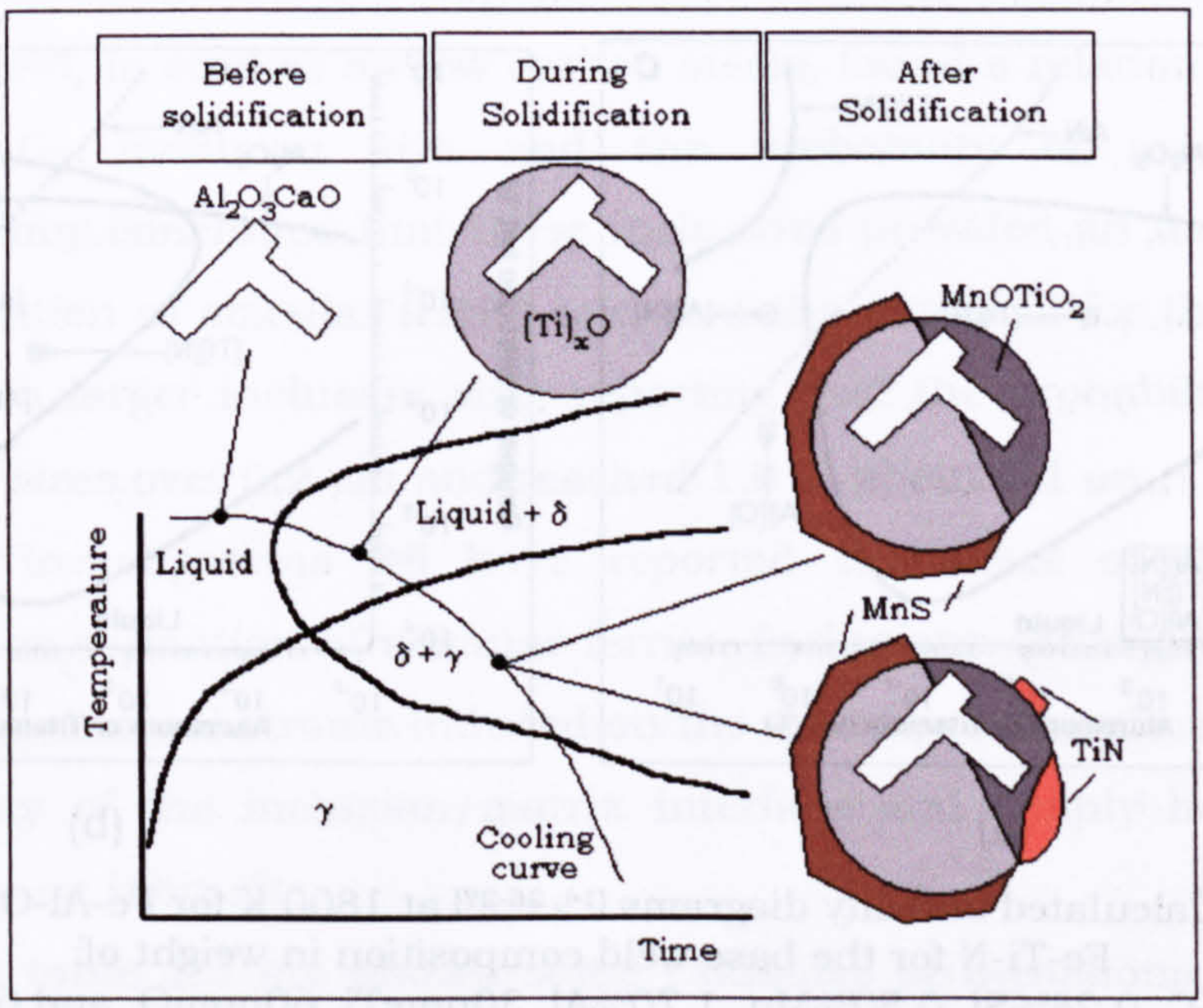

Figure 2.5 Schematic representation of sequence of inclusion formation in Ti deoxidised steels, superposed on a TTT diagram for the weld transformation. Modified from Grong [24]

Various investigations have been concerned with kinetic models for the precipitation of non-metallic inclusion during the steel solidification. Babu [26], Hong [29,30] and collaborators have developed a model for inclusion formation in liquid weld metal based on an overall kinetics approach using nucleation and growth rate expressions. In the model of Babu [26], the homogeneous nucleation rate was used to estimate the number of inclusions as a function of time and the inclusion growth was simulated taking in account the diffusion rates of the elements to the reaction interface. This model permits prediction of the deoxidation sequence in the liquid weld metal from calculated TTT

diagrams. However, the model does not take into account the temperature gradient that the inclusion may experience due to the liquid flow and the heat extraction from the weld pool. Hong [29, 30] considered the temperature and velocity fields in the weld pool, combining the thermodynamical and kinetical theories used by Babu with those of transport phenomena. Other investigations on the inclusion formation during steel solidification [31, 32] and on weld metal [33] have considered the solute redistribution during solidification, diffusion controlled deoxidation, and interfacial kinetics, in their models. All the models mentioned before have been compared with experimental data and the agreement has been acceptable, and indicates that some simplifications are the reason for the differences, which suggests that more has to be investigated in this area, particularly in the case of weld metals.

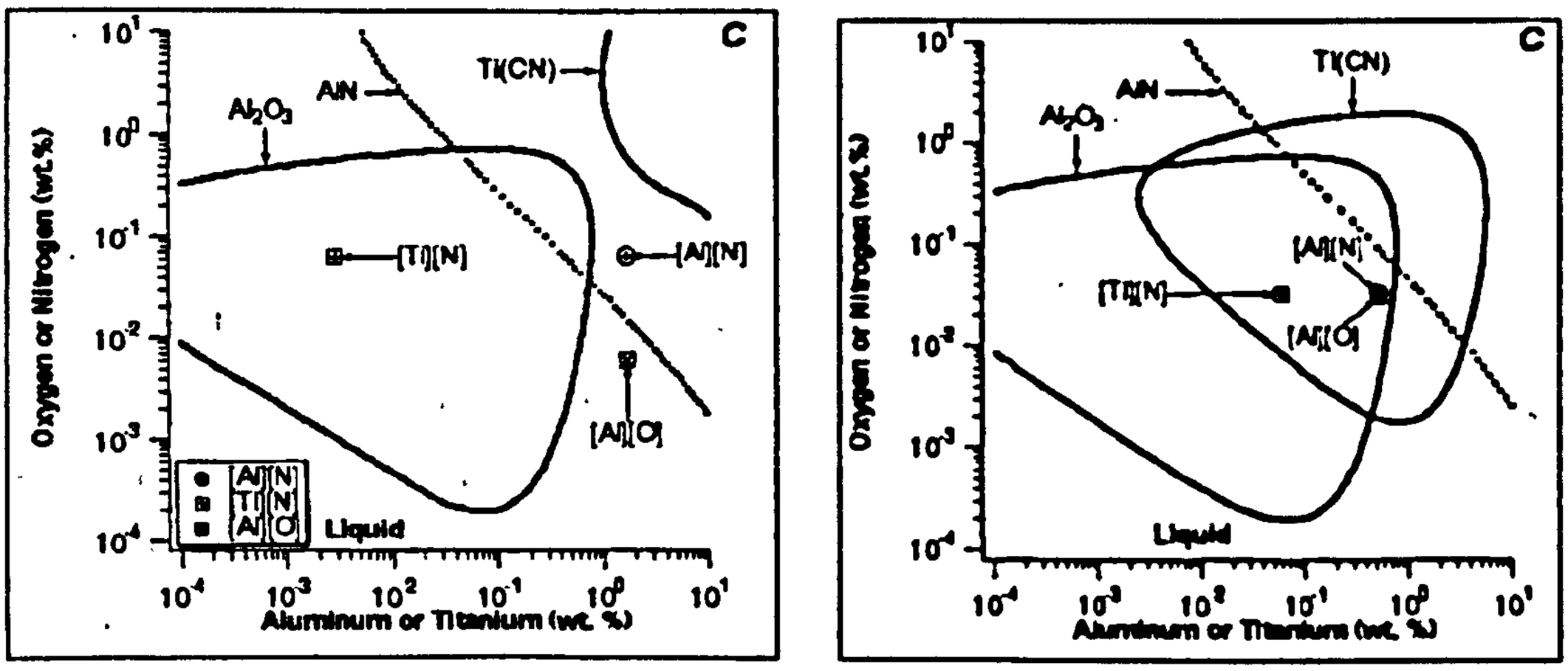

Figure 2.6 Calculated stability diagrams [14, 26-27] at 1800 K for Fe-Al-O, Fe-Al-N and Fe-Ti-N for the base weld composition in weight of:
(a) 0.23%C, 0.28%Si, 0.50%Mn, 1.70%Al, 30ppmTi, 60ppmO, and 640ppm N;
(b) 0.15%C, 0.30%Si, 0.64%Mn, 0.53%Al, 580ppmTi, 300ppmO, and 330ppm N

2.2.2 Non-metallic inclusions effect on the microstructure and mechanical properties HSLA steel weld metals

The composition, number density, size and spatial distribution of non-metallic inclusions in weld metals are critical factors in determining weldment microstructural development and, as a consequence, the properties. In general, the mechanical properties are affected negatively by the presence of non-metallic inclusions. However, under certain conditions, in low alloy steel welds, the existence of some kind of inclusions promote the formation of acicular ferrite, with which an improvement in toughness is produced [29].

During weld metal solidification, the inclusions could be formed and trapped in the interdendritic spaces as a consequence of the solute segregation in those regions. Cochrane [34] suggests that this distribution of the inclusions could reduce the mobility of the austenite grain boundary, contributing in some degree to the austenite grain refinement. During the austenite to ferrite transformation, non-metallic inclusions provide preferential sites for the nucleation of ferrite, particularly acicular ferrite, when the proper inclusion composition is present.

Thewlis [35] in his study of the transformation kinetics of ferrous weld metals concluded that different types of inclusion appear to have different free energy barriers to ferrite nucleation. It has been found that inclusions rich in titanium are most effective in acicular ferrite production, but specific compounds have not been identified. Many results suggest that inhomogeneous inclusions are responsible for the nucleation of acicular ferrite [36]. Lee et al. [37], in studies on low carbon steels, found a relation between the SiO_2-MnO-Al_2O_3 inclusion size and the probability of acicular ferrite nucleation. They concluded that these inclusions provided an inert substrate for the nucleation of acicular ferrite and that the potential for the nucleation increased with larger inclusion size, reporting that the probability enhanced markedly for sizes over 0.2 μm and reached 1.0 at about 1.1 μm.

Many investigations [36] have reported the effect of the inclusion composition on formation of acicular ferrite. Inclusions could promote ferrite nucleation by: thermal strains induced on the matrix, chemical heterogeneities in the vicinity of the inclusion/matrix interface and simply heterogeneous nucleation on an inert site.

In the table 2.3 are shown some examples of inclusions, which have been identified as effective or ineffective in the nucleation of acicular ferrite. The inclusions, as mentioned before, could act as inert sites for nucleation or on the contrary, they could react chemically: decarburizing the steel close to the NMI/matrix interface or consuming other alloying elements which are austenite stabilizers. As a consequence, ferrite nucleation is promoted. Inclusions acting as oxygen source have the ability to tolerate oxygen vacancies in their structures or to thermally decompose. Ti_2O_3 can dramatically reduce the Mn concentration of the adjacent steel, element that is considered an austenite stabilizer.

Other mechanisms are not yet clear. For example, TiO is effective as a ferrite nucleant and a good lattice match with ferrite may be the reason, but so does TiN, which is not effective in ferrite nucleation [36].

Table 2.3 List of ceramic oxides that have been tested for their potency in stimulating the nucleation of ferrite plates [36]

Effective: oxygen source	Effective: other mechanism	Ineffective
TiO_2, SnO_2, MnO_2, PbO_2, KNO_3	Ti_2O_3, TiO	TiN, $CaTiO_3$, $SrTiO_3$, NbC, α-Al_2O_3

2.2.3 Weld metal solidification

Solidification behaviour controls the size and shape of grains, the microstructure, the extent of segregation, the distribution of inclusions, the extent of defects such as porosity and hot cracks, and ultimately the properties of weld metal [38]. The weld solidification process has the following characteristics [39]:

(a) No nucleation event is necessary to initiate weld solidification. The molten weld pool wets partially melted grains in the base material, which has similar composition. These offer the solidification interface and when the weld pool is cooled the growth takes place with a minimum of supercooling.
(b) Macroscopic solidification rates in weldments are very rapid, being determined by the speed of welding, thermal gradient, etc
(c) Macroscopic shape of the solid/liquid interface remains constant over the major portion of the weld length.
(d) The motion of the molten metal within a weld pool during arc welding creates conditions of considerably turbulence due to the electromagnetic stirring. For this reason, there is good mixing of the molten weld pool.

In welds, the initial solidification takes place epitaxially, where the partially melted base metal grains at the fusion boundary act as nuclei for the columnar grains. The width of the columnar grain depends on the HAZ grain morphology, which subsequently will affect the weld austenite grain size. Most microalloyed steel welds solidify as delta ferrite, which later decomposes to austenite. Figure 2.7 shows schematically, the solidification structure of a weld metal that solidified as delta ferrite. The austenite grains will cross the

primary delta ferrite grain boundaries, thereby removing all traces of the prior structure. However, the mode of solidification depends on the weld metal chemical composition, and in some cases the delta ferrite can be completely suppressed [1].

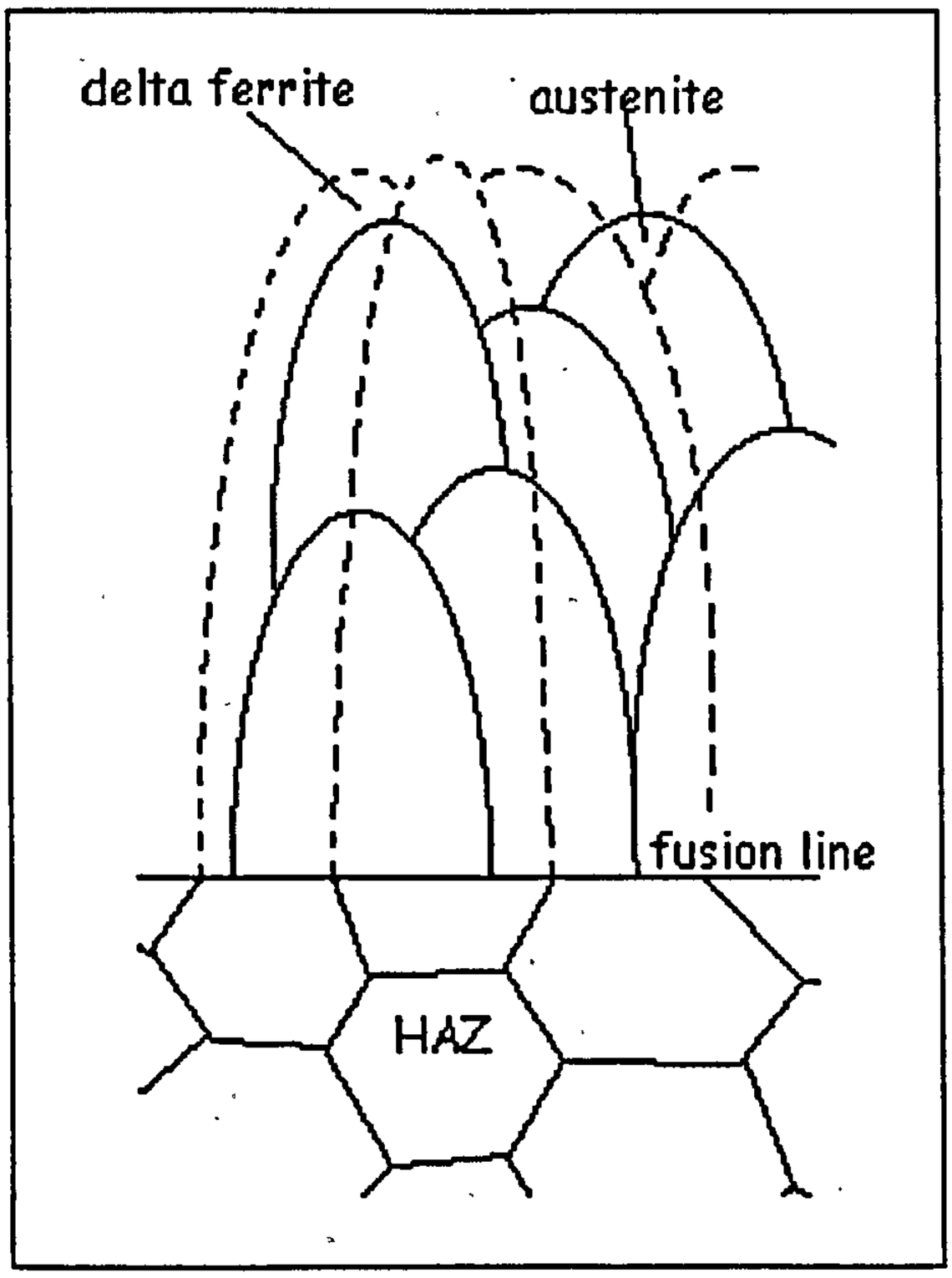

Figure 2.7 Schematic illustration of the solidification of delta ferrite columnar grains and the subsequent formation of austenite grains.

The columnar grain exhibits a substructure that depends on the stability of the solidification front, which is controlled by the extent of constitutional supercooling ahead of the advancing interface, and is therefore influenced by composition, the growth rate R and the thermal gradient G in the weld pool. The figure A.1, in annexes, presents the solidification modes depending of the temperature gradients and the constitutional supercooling. It can be seen that the higher the thermal gradient the lower the constitutional supercooling.

The reduction of the thermal gradient change the growth mode in the following order: planar, cellular, cellular dendritic, columnar dendritic, and equiaxed dendritic [1, 13, 17, 38, 40]. The various growth modes that may develop during normal solidification of fusion welds are shown schematically in figure 2.8 (a). Figure 2.8 (b), which is based on experimental observations, relates the gradient G, solidification rate R, and composition to the type of structure

developed. For a given alloy system; it has been found that the greater the C_o, the greater the tendency for constitutional supercooling and non-planar solidification [40].

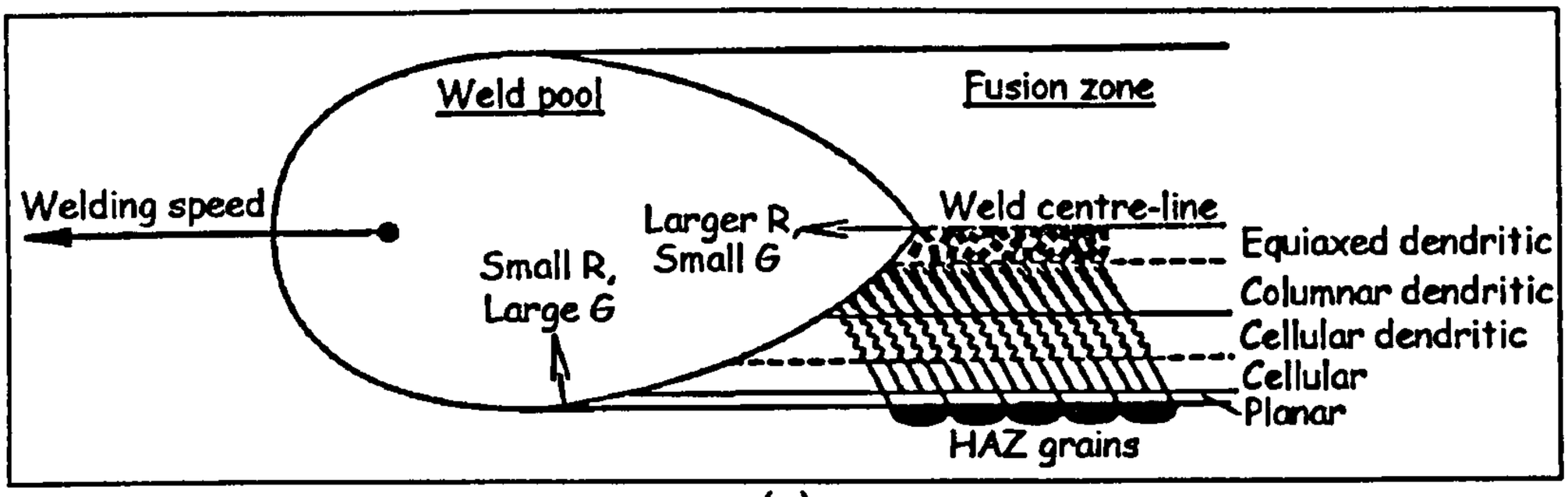

(a)

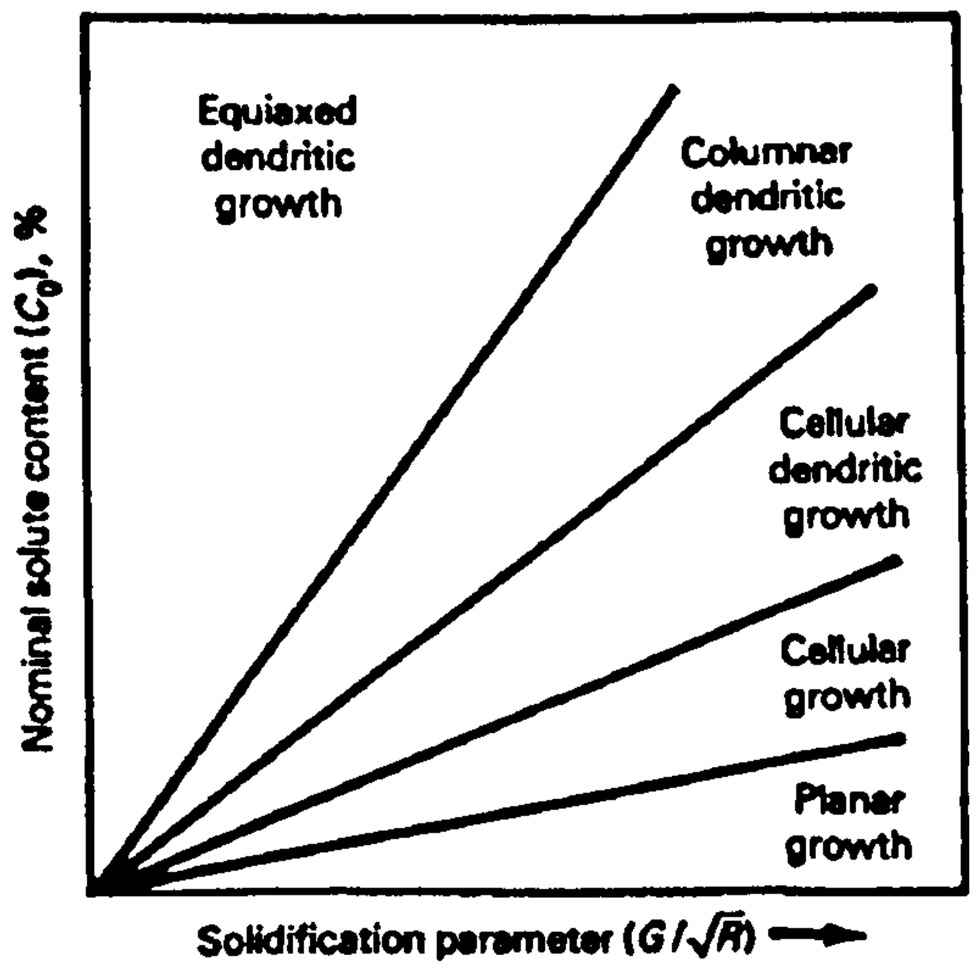

(b)

Figure 2.8 Schematic diagrams illustrating (a) structural variations in the weld metal solidification microstructure across the fusion zone, and (b) the effect of crystal growth rate R and the melt thermal gradient G [17, 38, 40].

The characteristic growth pattern of cellular and dendritic solidification in combination with the rapid cooling rates, presented in welding processes, produce extensive segregation of alloying and impurity elements (particularly carbon, oxygen, manganese, sulphur, and phosphorus) to the intercellular or interdendritic spaces. After the austenite/ferrite transformation, the segregation can lead to formation of coarse blocky laths of martensite and bainite along the solidification or the transformation sub-boundaries [1]. The segregation in the interdendritic regions is higher than that in the intercellular regions, as is shown in figure 2.9.

The segregation to these inter-columnar regions in weld metals could cause intergranular embrittlement. It has been demonstrated that the local tensile stress required for intergranular separation decreases monotonically as

the intergranular concentration of a particular solute increase. When hydrogen and intergranular impurities are present, the result is intergranular brittle fracture at lower stresses [41].

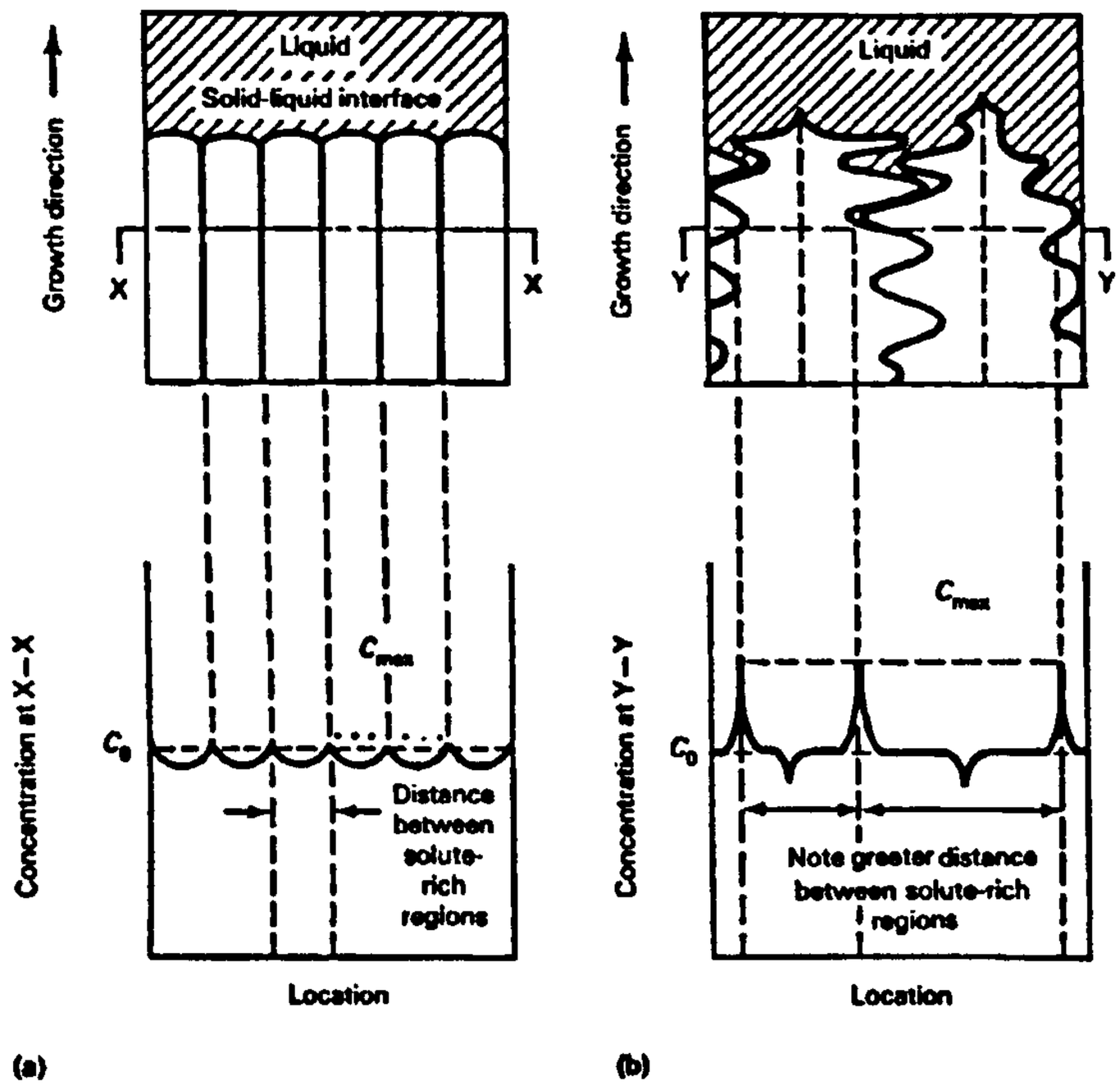

Figure 2.9 Solute distribution at the dendrite or cell core and the intercellular or interdendritic regions. (a) Cellular growth. (b) Dendritic growth [40].

2.2.4 Solid-state transformation and the microstructure of HSLA steel weld metals.

The properties of the weld metal are governed by the microstructure. For this reason, the various phases and micro-constituents must be identified using a system of nomenclature that is both widely accepted and well understood. In wrought steels, this need has been satisfied to a large degree by Dubé scheme for classifying the different morphologies of ferrite, as shown in figure A.2 in annexes. Similarly, the microstructures in ferritic steel weld metals have been largely resolved by the IIW classification scheme shown in figure A.3 in annexes [42]. Table 2.4 shows these categories and the abbreviations. Figure 2.10 presents a typical microstructure of HSLA steel weld metal using optical and electronic microscopy (SEM).

Cochrane [43] reviewed the transformation microstructure in an as deposited weld and presented continuous cooling transformation (CCT) diagrams for weld metals. The minor constituents (the 'microphases'), generally in quantities lower than 10%, are: retained austenite and/or martensite, martensite austenite carbides aggregates (MAC) or cementite.

These minor constituents are formed in the last region to transform and, while their distribution is influenced predominantly by the form adopted by the ferrite, certain other factors, including the addition of Nb and Mo, can influence their character [15].

Table 2.4 International Institute of Welding classification of microstructural constituents in ferritic steel weld metals [42].

Category	Abbreviation
Primary ferrite	PF
Grain boundary ferrite	PF(G)
Intragranular polygonal ferrite	PF(I)
Ferrite with second phase	FS
Ferrite with non aligned second phase	FS(NA)
Ferrite with aligned second phase	FS(A)
Ferrite side plates	FS(SP)
Bainite	FS(B)
Upper bainite	FS(UB)
Lower bainite	FS(LB)
Acicular ferrite	AF
Ferrite-carbide aggregate	FC
Pearlite	FC(P)
Martensite	M
Lath martensite	M(L)
Twin martensite	M(T)

Choi and Hill [44] give the transformation temperature ranges for the major constituents, which showed some dependence on composition. In table 2.5 are shown these temperature ranges and the product identified.

Table 2.5 Transformation temperature range in a steel weld metal [39]

T range [°C]	Microstructure associated	Nucleation site
1000-650	Grain boundary ferrite	Prior austenite grain boundary
750-650	Ferrite side plates	Prior austenite grain boundary
Below 650	Acicular ferrite	Within austenite grains
Below 500	Bainite	Linked with high dislocation density

It has been suggested (for submerged arc welds) that three broadly different types of microstructure may be linked to three regimes of weld metal oxygen content. Several factors influence the oxygen levels at which microstructural changes occur. In table 2.6, the effect of oxygen content on the microstructure of a steel weld metal is presented. A sufficiently high

volume fraction of inclusions can restrict austenite grain size in the weld metal, favouring the formation of ferrite side-plates. A reduction in the quantity, and possibly the size of the inclusions, added to an adequate composition of the weld and an appropriate cooling rate, provide the conditions for the formation of acicular ferrite. Finally, a sufficient reduction in oxygen content or increase in alloy content will inhibit the formation of acicular ferrite, permitting the formation of bainite [39]. Ito and collaborators [45] demonstrated that the increment of the oxygen content in the weld metal augment the number of inclusions in the microstructure and shift the transformations curves to short times, resulting in a detrimental effect on hardenability.

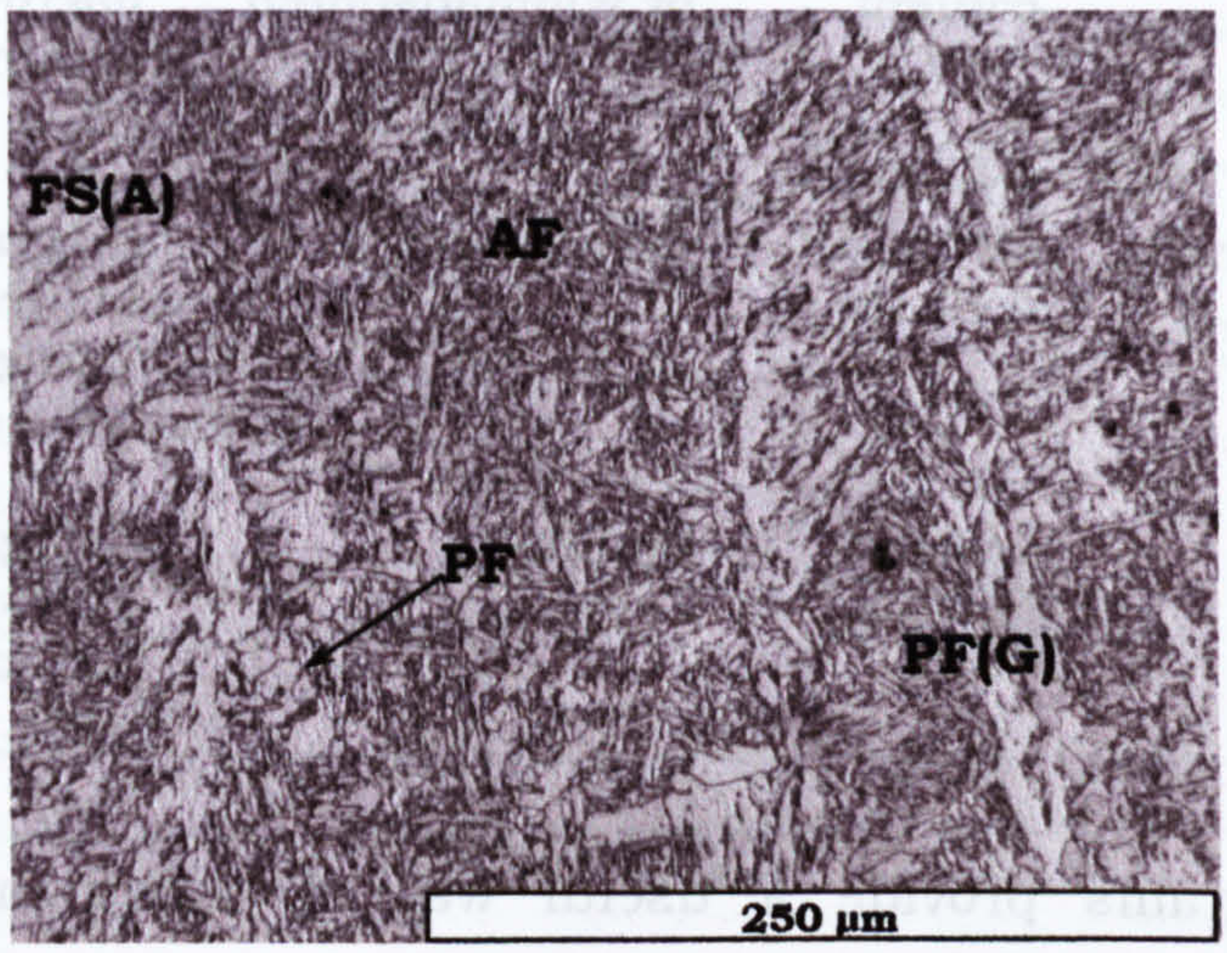

(a)

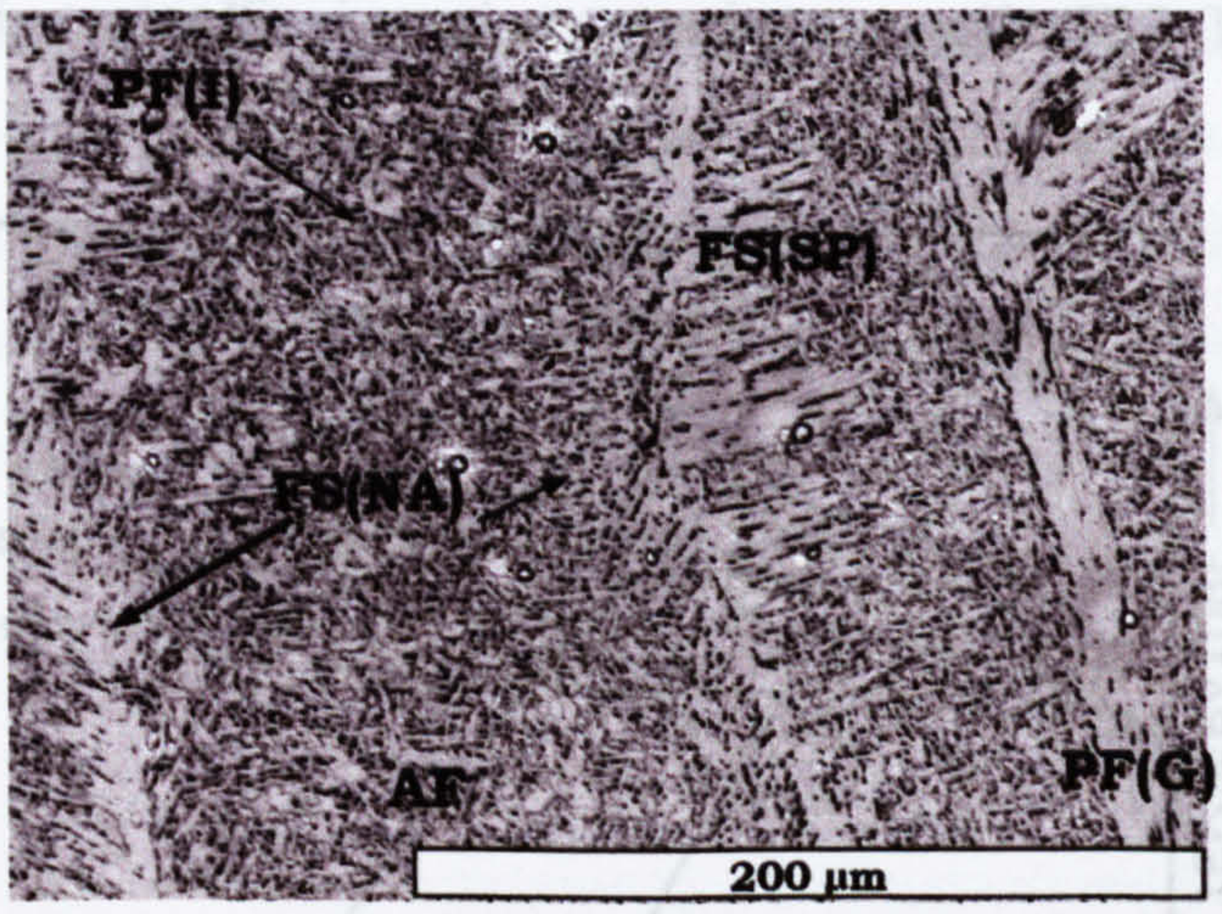

(b)

Figure 2.10 HSLA steel weld metal microstructures showing various microstructural constituents. Table 2.5 presents classification nomenclature. (a) Optical microscopy, and (b) SEM microscopy.

CCT diagrams provide a convenient way of describing microstructural development under non-equilibrium conditions, such as those encountered during welding. Weld metal CCT diagrams, and schematic weld metal CCT diagrams have played an important role in improving the metallurgical understanding of weld metal microstructural development [46]. Figure 2.11, a conventional CCT diagram applicable to weld metals, shows the effect on microstructural developments of alloying elements, oxygen content, and heat input.

Table 2.6 Types of microstructure linked to three regimes of oxygen contents [39].

Oxygen content	Inclusions	Mayor constituent	Microphases
≥ 0.06 weight %	High content	Ferrite side-plates or Widmanstätten	Elongated microphases within the ferrite laths.
~0.03-0.06 weight %	Medium content	Acicular ferrite	Irregular space between the intragranular laths of ferrite.
~0.01 weight %	Lower content	Bainite	Elongated microphases within the ferrite laths.

CCT diagrams provide a useful way of examining the effects of composition on the austenite/ferrite transformation behaviour during welding. The influence of different alloying elements and the prior austenite grain size on movement of CCT diagram phase regions is illustrated schematically in figure 2.12.

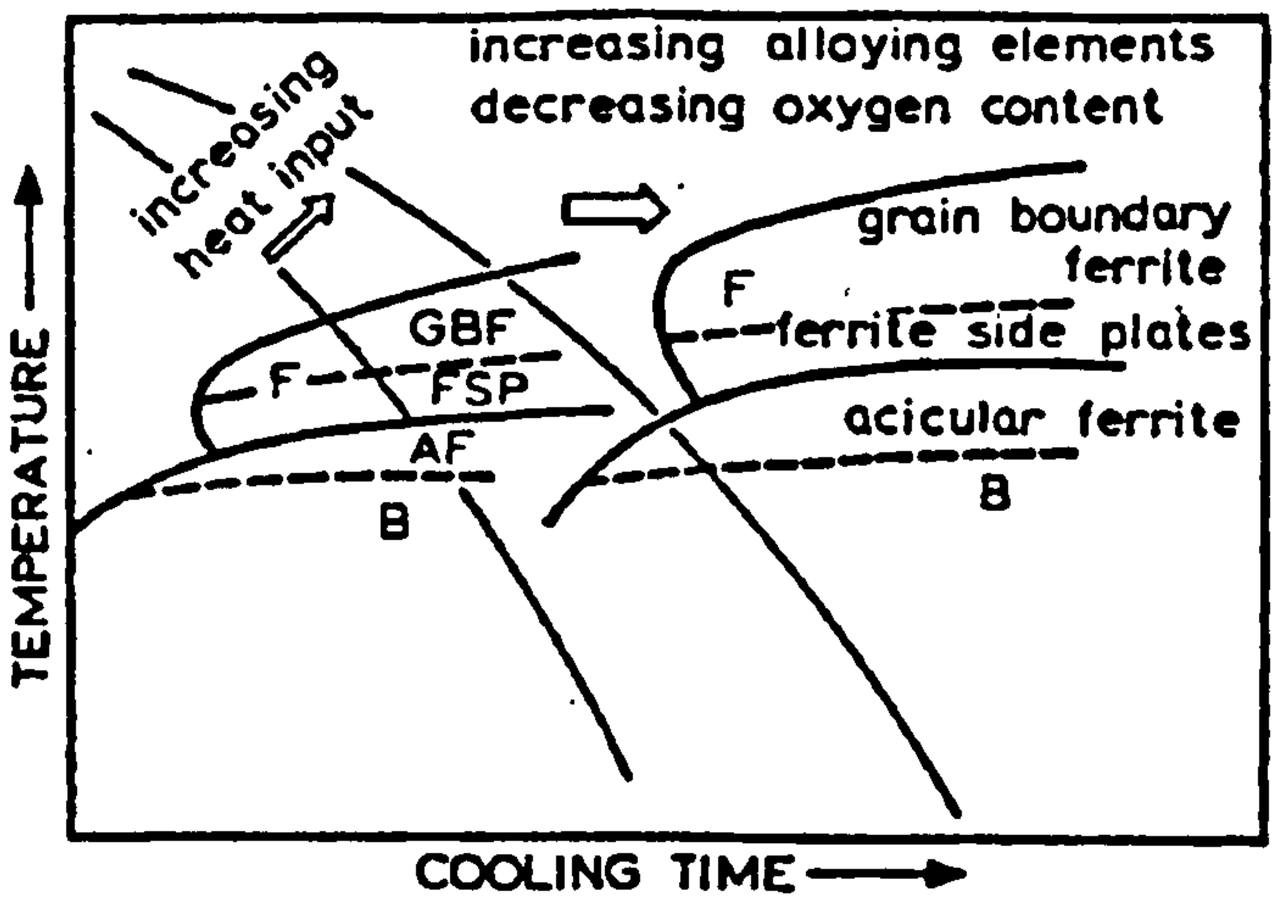

Figure 2.11 Schematic presentation of effect on the weld metal microstructures of the alloying elements and the heat input [46]

Carbon, Mn, Ni, Cr, Mo, and increased grain size all displaced the bainite and ferrite regions of the CCT diagram to longer times. Manganese and Ni displace all transformation temperatures to lower values and generally increase hardness. Molybdenum and Cr extend the bainite field. Niobium suppresses grain boundary pro-eutectoide ferrite and blocky pearlite. In weld metals with high oxygen levels and/or low hardenability, Nb promotes ferrite sideplates and upper bainite structures. On the other hand, Nb promotes acicular ferrite in the low oxygen and/or high hardenability type weld metals [46].

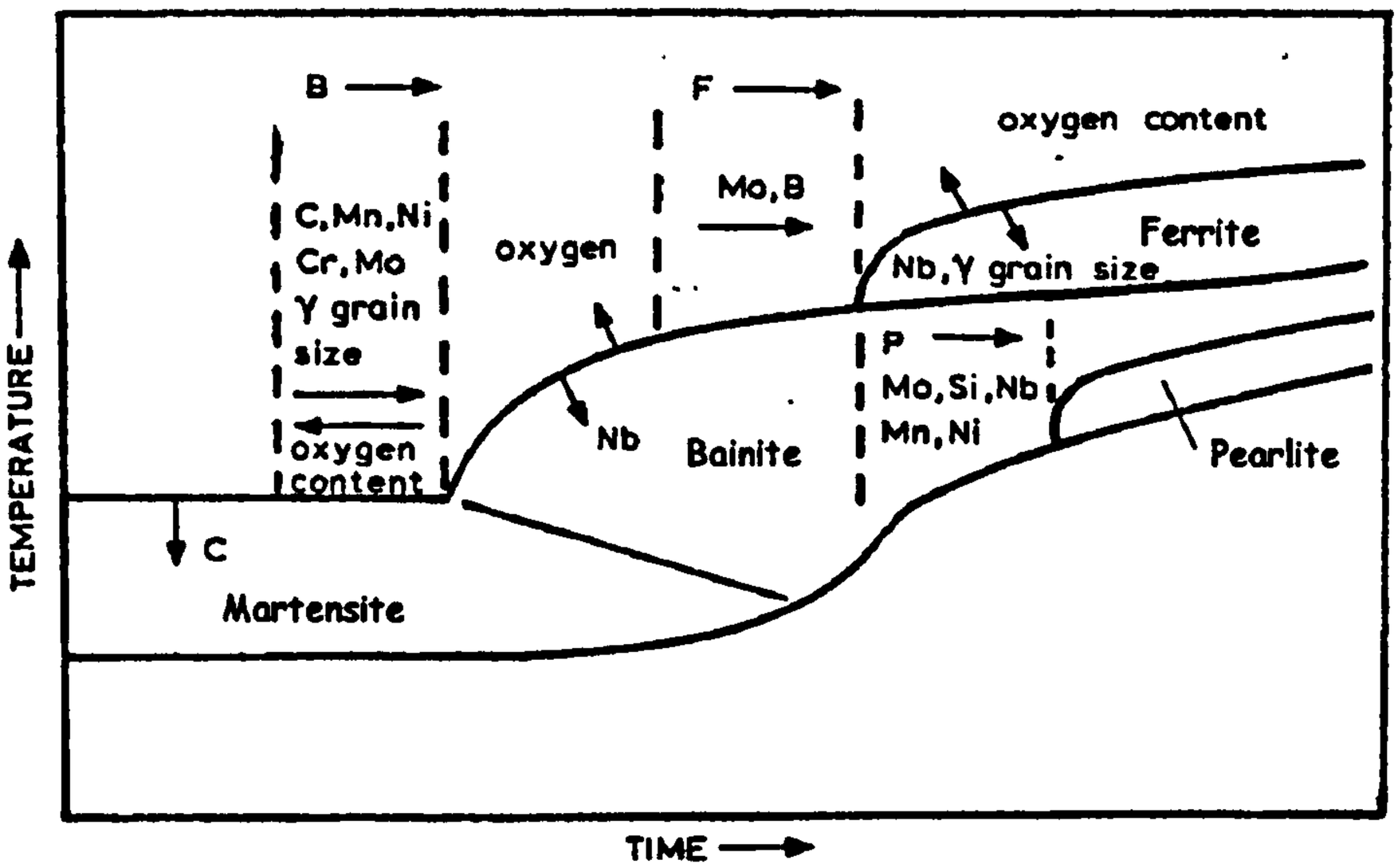

Figure 2.12 Schematic representation of the effect of alloying elements and the austenite grain size on CCT diagrams [46]

The understanding of the factors that influence the final microstructure of the steel weld metals will permit to determine the optimal composition and characteristics of consumables. These have to produce weld metal with an optimum combination of mechanical properties and resistance to hydrogen induced cracking.

CHAPTER THREE

HIGH STRENGTH LOW ALLOY WELD MICROSTRUCTURE AND MECHANICAL PROPERTIES

In the previous chapter, brief descriptions of the phase transformations that occur during welding were presented. It was shown that several factors influence the final microstructural development and hence the mechanical properties. From the chemical reactions in the liquid steel (inclusion formation) to the solid state transformation, passing throughout the solidification process, the welding parameters and the steel composition affect strongly the final properties of the weldment.

In the present chapter, attention is concentrated on the effect of alloying elements on the microstructure and mechanical properties of high strength low alloy steels.

3.1 Microstructure and Mechanical Properties

In low alloy steel weld metals there are several strengthening mechanisms that could contribute to the final strength of the weldment. These mechanisms are [12, 17]: grain refinement strengthening, solid solution strengthening, precipitation (or dispersion) strengthening and dislocation strengthening (or work hardening)

The influence of each mechanism on the final strength depends on the chemical composition and the weld thermal history, which is affected by the welding parameters. The number of variables involved in the welding process (heat input, multi-run welding, preheating temperature, post welding treatment, consumable type, position of welding, geometry of joint, etc.) and the effect of metallurgical variables (composition of parent plate, composition of filler metal, thermodynamic and kinetic of phase transformation, etc.) on the final microstructure and hence the mechanical properties, makes the modelling and prediction of weld metal properties a very challenging task.

Several models presented by Lalam [47] involve mechanical properties prediction by empirical approximation and by physical approximation. The first group use empirical equations [48], use linear regression analysis which take into account chemical composition, whilst maintaining the welding variables constants. The second group, by Bhadeshia and collaborators [49-51], attempt the mechanical properties prediction using physical variables such as: solid solution strengthening, grain size, phase proportions, dislocation density,

bainite and martensite lath width, etc.). The aim of these models is to design weld metals theoretically reducing the time consuming and costly mechanical tests and microscopy, at the same time of gaining knowledge on the behaviour of materials. In the following paragraph some models are briefly discussed.

3.1.1. The effect of the strengthening mechanisms.

Figure 3.1 shows a variation of the treatment for bainitic steels originally developed by Gladman and Pickering, reported by Grong [17] where the individual strengthening contributions in low carbon bainite weld metal, which includes both upper and lower bainite and acicular ferrite, are shown.

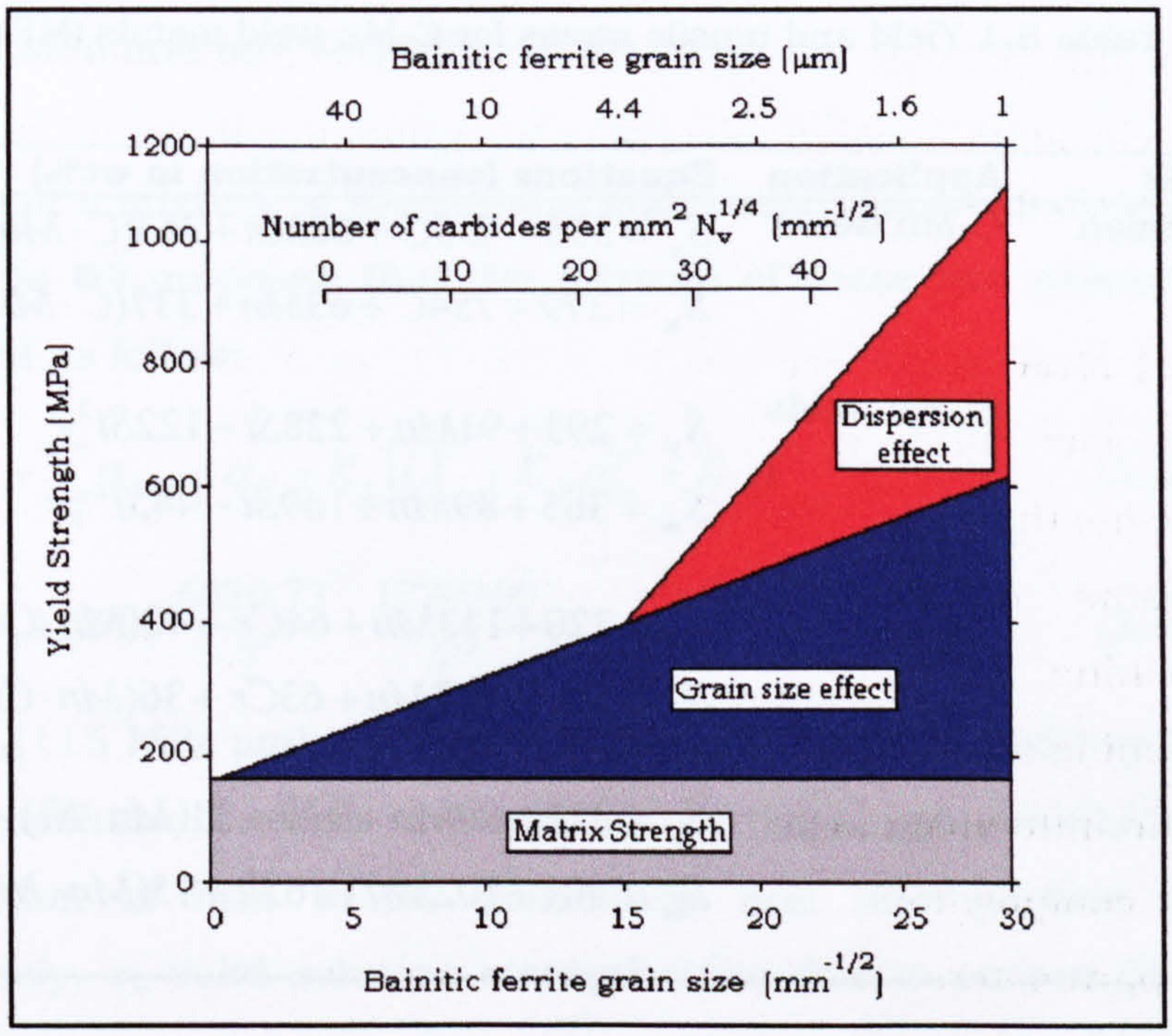

Figure 3.1 Influence of the different strengthening mechanisms on the yield strength in low-carbon bainite. Adapted from Grong [15]

The matrix strength is the result of the solid solution strengthening produced by alloying and impurity elements such as manganese, phosphorus, silicon and uncombined nitrogen. The matrix strength is increased by grain refinement, which in this case is determined by the reduction in the bainite lath size. However, the effect of the precipitates (dispersion strengthening) is only significant for small grain sizes and this is of great importance at the moment of the selection of the adequate microstructure to produce a good combination of toughness and strength, as the obtained by the introduction of acicular ferrite. Figure 3.1 implied that if higher strength levels than those produced by acicular ferrite (with a lath size of about 2 μm could produce a maximum yield strength of 650 MPa) are required it is necessary to decrease

the grain (lath) size through a refinement of the microstructure, which means that the acicular ferrite must be replaced by bainite or martensite. Following this idea, a new generation of high strength steel weld metals have been developed in the range from 650 to 900 MPa [17].

3.1.2 Empirical models for mechanical properties prediction

Empirical expressions are obtained under experimental condition applied to the studied weldments and for this reason they may be only applicable to those conditions. Some coefficients can be difficult to explain physically. In table 3.1 some equations are presented [47, 48].

Table 3.1 Yield and tensile stress for C-Mn weld metals (MPa) [47, 48].

Models	Application	Equations (concentration in wt%)
Regression	C-Mn welds	$S_y = 335 + 439C + 60Mn + 361(C \cdot Mn)$
		$S_m = 379 + 754C + 63Mn + 337(C \cdot Mn)$
	Si-Mn welds	$S_y = 293 + 91Mn + 228Si - 122Si^2$
		$S_m = 365 + 89Mn + 169Si - 44Si^2$
	Cr-Mn welds	$S_y = 320 + 113Mn + 64Cr + 42(Mn \cdot Cr)$
		$S_m = 395 + 107Mn + 63Cr + 36(Mn \cdot Cr)$
	Ni-Mn welds	$S_y = 332 + 99Mn + 9Ni + 21(Mn \cdot Ni)$
		$S_m = 401 + 102Mn + 16Ni + 15(Mn \cdot Ni)$

3.1.3 Models using physical metallurgy principles

The yield strength has been estimated throughout the application of physical metallurgy principles. The method assumes that the yield strength (σ_y) of steel microstructures can be factorised into a number of intrinsic components [49-53]: the strength of the pure annealed iron (σ_{Fe}), the solid solution strengthening effect of substitutional alloying elements ($\sum_i x_i \sigma_{SS_i}$), the carbon solid solution strengthening (σ_C), the grain size strengthening effect (Hall-Petch equation, $k_y\, d^{-1/2}$), the effect of dislocation density ($K_D\, \rho_D^{1/2}$), effect of lath size or width (martensite and bainite, $K_L\, (\bar{L})^{-1}$), the effect of dispersion strengthening ($K_p\, \Delta^{-1}$), effect of phase proportions (mixture law) and others. Some examples are listed in regard of the applicability of the equation:

1- Strength of as-welded weld metals containing grain boundary, acicular and Widmanstätten ferrite phases: This model by Sugden and Badeshia [49] is represented by the following equation:

$$\sigma_y = \sigma_{Fe} + \sum_i^n \sigma_{SSi} + \sigma_{Micro} \quad (3.1)$$

$$\sigma_{Micro} = \sum_1^n \sigma_i v_i = \sigma_{gb} v_{gb} + \sigma_{AF} v_{AF} + \sigma_W v_W \quad (3.2)$$

where σ_{Micro} is the mixture law, σ_{gb}, σ_{AF} and σ_W are the microstructural strength contributions and v_{gb}, v_{AF} and v_W are the volume fractions of the grain boundary, acicular and Widmanstätten ferrite phases, respectively. The values of the strength contribution are: σ_{gb}= 27 MPa, σ_{AF}= 402 MPa and σ_W= 486 MPa

2- Strength of a mixture of bainite and martensite (not welded): Young and Bhadeshia [50] proposed that the mixture of these two phases can be factorised as follow:

$$\sigma_y = \sigma_{Fe} + \sum_{i=1}^n \sigma_{SS,i} + \sigma_C + K_L\left(\bar{L}\right)^{-1} + K_D \rho_D^{0.5} + K_p \Delta^{-1} \quad (3.3)$$

$$\log\{\rho_D\} = 9.284 + \frac{6880.73}{T} - \frac{1780360}{T^2} \quad (3.4)$$

where K_L(115 MPa·μm), K_D(7.34 10^{-6} MPa·m^{-1}) and K_p (0.52·vp MPa·μm, v_p is the volume fraction of cementite particles) are constants for the contribution of lath width, dislocation and inter-particle distance, respectively, σ_C solid solution strengthening due to carbon (for bainite σ_C= 1722.5 $X_C^{1/2}$ and for martensite σ_C= 1171.3 $X_C^{1/3}$, X_C in weight%), $\bar{L}$ (μm) is the bainitic or martensitic ferrite plate width, ρ_D [m^{-2}] is the dislocation density (estimated by equation (3.4) where T is the transformation temperature in Kelvin) and Δ is the distance between any carbide particles. The strength of pure annealed iron, σ_{Fe} is around 219 MPa at 300 K.

3- The strength of ferritic microalloyed steels: this takes into account grain size and precipitation strengthening[12]:

$$\sigma_y = \sigma_i + \sum_{i=1}^n \sigma_{SS,i} + K_y d^{-1/2} + \Delta\sigma_y \quad (3.5)$$

$$\Delta\sigma_y = \left(10.8 f^{1/2}\right)\left(\ln\left(\frac{X}{6.125 \cdot 10^{-4}}\right)\right) \quad (3.6)$$

where σ_i is the friction stress for iron, K_y is the strengthening coefficient for grain size and d is the grain diameter. $\Delta\sigma_y$ is the dispersion strengthening (Ashby-Orowan relationship), where X is the particle diameter (μm) and f is the volume fraction of particles.

Neural network analysis, a more general form of regression, has been used to estimate the yield and tensile strength of ferritic weld metals and to provide an indication of the likely values for elongation and Charpy toughness, which are much more difficult to predict [52, 53].

3.2 Effect of the alloying elements in the weld metal microstructure and properties.

An incredible amount of research has been dedicated to the study of the different alloying elements on the microstructure and mechanical properties of steel weld metals and heat affected zones. The excellent work by Evans and Bailey [48] covering some 20 years of research illustrates the complexity of the influence of alloying elements on the mechanical properties of C-Mn weld metals and the role of microalloying . Earlier review by Abson and Pargeter [15] presents great quantity of data related with this subject. Both groups have shown clearly the importance in the design of the consumables with the optimum chemical composition to produce the desired mechanical properties of the weldment.

In this section, the effect of the different alloying elements on the modification of the microstructure and the mechanical properties will be explained briefly.

3.2.1 Effect of Carbon.

The carbon content influences the strength and toughness of the weld metal. The solid solution hardening effect of carbon is very high, but this is the little importance in most welds as the solubility of carbon in ferrite is about 0.01 wt% [15]. The main effect of C is to alter the microstructure [48]. Some effects of an increase in C are [15, 48, 54, 55]:

(a) Decrease the width of the columnar grains or reduces the austenite grain size, which seemingly promotes intergranular transformation
(b) Give thinner ferrite veins at prior austenite grain boundaries
(c) Increase the amount of secondary phases, such as martensite-austenite constituent (MA) or austenite-martensite-carbide (MAC).

Increase the proportion of retained austenite between the laths of acicular ferrite.

(d) Increase the aspect ratio of the ferrite lath, giving the classical Widmanstätten structure at high carbon levels.

The role of carbon, in defining the amount and distribution of the so-called 'microphases', is also important. The presence of retained phases (retained austenite) may be harmful for toughness if this is transformed to carbides or/and martensite.

3.2.2 Effect of Manganese

Manganese is used, in general, as a deoxidant and to control strength and toughness. The utilisation of Mn is a practical way of controlling mechanical properties without the necessity of more expensive alloying elements [48]. It has a moderate solid solution strengthening effect. Moreover, Mn has a great effect on the acicular ferrite formation. The effect of manganese can be summarised as follow:

(a) Promote acicular ferrite (AF). AF formation hardly occurs with manganese content less than 1.0wt%. At 1.4-1.8wt%Mn, the microstructure mainly consists of AF, giving the highest toughness. When this range is exceeded, upper bainite is expected to form and toughness decreases [56]

(b) Acicular ferrite is refined by an increase in Mn content [56]

(c) An increase in Mn content reduces the grain boundary ferrite and the ferrite with second phase

(d) Mn content seems not to affect the quantity of retained austenite in the weld metal

(e) Strength properties increase linearly with manganese content

(f) In terms of Charpy transition temperatures an optimum level is reached with 1.4wt%Mn

3.2.3 Effect of Silicon

Silicon and Mn are used as deoxidants. Si is used in quantities lesser than 0.5wt%, because it produces undesirable effects on the properties of the weld metal, such as the reduction in ductility. The influence of Si on the microstructure depends on the Mn levels of the weld [48, 54]:

(a) At high Mn: no significant changes are produced. However, an increase in the Si content increases the aspect ratio of the acicular ferrite.

(b) At low Mn: Si increases irregularly the proportion of acicular ferrite at the expense of other constituents.

(c) Si has been reported to increase the amount of retained austenite or the M/A constituent largely through its role in delaying cementite formation.

In regard to the Si effect on strength, an increase in the Si content produces an increase in the yield strength, but this effect is reduced when more Si is added [48]. The operating strengthening mechanisms is due to the solid solution of Si [15].

3.2.4 Effect of Nickel

Nickel is a much less potent strengthener of weld metals than manganese, chromium or molybdenum [48]. However, an increase in Ni improves considerably the toughness regardless of the change in microstructure. The effect of Ni can be summarised as follow:

(a) It could increase the proportion of acicular ferrite at the expense of both grain boundary ferrite and ferrite with second phase[48]

(b) At high Mn level and with a content more than 2.2wt%Ni, martensite is produced and the proportion of ferrite with second phase is increased

(c) Increases the aspect ratio of acicular ferrite

(d) Permit the retention of M/A constituent

Kang and collaborators [57] studied the effect of Ni and Mn in low-carbon steel weld metals and found that the hardness increased linearly with Mn and Ni, due mainly to solid solution strengthening and partially to the formation of hard phases. The effect of Ni on toughness depended on the quantity of Mn, improving this at low Mn content and deteriorating this property at high Mn levels, causing intergranular fracture.

3.2.5 Effect of Chromium

Together with nickel and molybdenum, chromium forms part of the major alloying elements added to steel weld metals. Chromium increases hardenability in a similar manner as Mn [48]. This is a strengthening element

that promotes the formation of acicular ferrite and as a consequence could improve toughness. The effects are:

(a) Reduces and could eliminate the amount of grain boundary ferrite veins.

(b) Cr increases the proportion of acicular ferrite and the optimum content to produce a maximum of this phase depends on the Mn content: for example, at 1wt%Mn the optimum Cr content is 1% and less than this value at higher Mn content (1.8wt%Mn)[48]. Further increase in Cr reduces AF and promotes the formation of ferrite with aligned second phase (bainite).

(c) Promote the formation of irregular and dispersed M/A constituent

(d) Both yield and tensile strengths increase linearly with Cr

3.2.6 Effect of Molybdenum

Molybdenum has an important strengthening effect. This effect is greater than that produced by Mn. However, Mo can cause detrimental effects on toughness. In general its effects on microstructure are [48, 54]:

(a) The addition between 0.2 and 0.3wt% of Mo suppresses grain boundary ferrite and promote the formation of acicular ferrite. However, subsequent additions could increase ferrite with aligned second phase, reducing the proportion of acicular ferrite.

(b) An increase of Mo up to 0.5wt% refines considerably the AF.

(c) Mo in combination with titanium could further facilitate the formation of acicular ferrite.

3.2.7 Effect of Titanium

It has been recognised that small titanium additions to C-Mn weld metal promotes considerably the formation of acicular ferrite. Evans and Bailey[48] reported that using 1wt% of rutile(TiO_2) in the consumable, which gives 15 ppm of Ti in the weld metal, produce a microstructure formed predominantly by acicular ferrite. The maximum content of acicular ferrite was found between 25 and 40 ppm of Ti. Ventrella et al.[58] in studies on the effect of boron and titanium on ferritic weld metals reported that 30 ppm of Ti produced a large volume fraction of acicular ferrite in B-free weld metals. The addition of 40 ppm of B and 400 ppm of Ti promoted the formation of the maximum proportion of acicular ferrite. This effect is due to the effect of B in

reducing the grain boundary ferrite formation and the effect of Ti on the formation of AF.

The influence of Ti on the AF formation is believed to be the result of the formation of Ti compounds (Ti-oxides) on the surface of the non-metallic inclusions, where the acicular ferrite nucleates [54]. In the table 2.2, chapter 2, the effectiveness of different Ti oxides can be compared.

Other effects of Ti on the microstructure and properties of steel weld metals are [48]:

(a) An increase in Ti content could increase the acicular ferrite aspect ratio
(b) The strength of the weld metal increases with the Ti content and the ductility is reduced slightly.
(c) Ti is effective to the formation of acicular ferrite in combination with sufficient Mn content; for weld with 1.4-1.8wt%Mn only 30 ppm Ti are required.

3.2.8 Effect of Boron

Boron increases the hardenability of engineering steels. Devletian and Heinel[59], in studies on carbon steel welds, found that the hardenability effect of B in weld metals was as potent as it was in wrought steels of the same composition. In low alloy steel weld metals, the segregation to grain boundaries inhibits the formation of grain boundary ferrite, due to the formation of boron nitride (BN) [54].

Boron is used in combination with titanium to promote the nucleation of ferrite intragranularly, due to the GBF suppression. However, in weld metal with Ti, an increase in the B content above 50ppm could increase the proportion of ferrite with second phase, reducing both grain boundary ferrite and acicular ferrite [48].

3.2.9 Effect of Aluminium

Aluminium is used as a deoxidant, having a stronger affinity to oxygen than Ti and Mn, and in some cases could be utilised to fix nitrogen, reducing the risk for strain-ageing embrittlement [48]. There is an optimum aluminium content for the formation of acicular ferrite. At low Al content, the microstructure consists of grain boundary ferrite and acicular ferrite, but if this is added in excess the microstructures becomes upper bainite, which affect the toughness [54]. The formation of upper bainite is the result of the

increase in Ti and B soluble in the weld metal, which produce an increase in the hardenability and reduce the formation of Ti oxide, affecting the formation of AF.

The effect of aluminium depends strongly on the oxygen potential in the weld metal. At high oxygen content, Al effect is insignificant. At low oxygen levels, the presence of Al do not permit the formation of Ti oxides and the soluble Ti and B increases, changing the microstructure, as described before.

3.2.10 Effect of Oxygen

The microstructure of the weld metal is affected by the oxygen content. Table 2.5 (Chapter 2) shows that varying the level of oxygen in the weld metal produces the variation of the microstructural constituent from bainite, at low oxygen content, to ferrite side plates (Widmanstätten ferrite) at high levels. Optimum oxygen contents between 0.03 and 0.06wt%O, are necessary for the formation of acicular ferrite [39]. A narrower range (0.02-0.035wt%O) has been reported by Potapov[60] for low alloy steel weld metals, based on the optimum mechanical properties, which must be related with the formation of acicular ferrite and the quantity of non-metallic inclusions. This critical oxygen content to form AF is affected by welding method, cooling rate, and alloying elements, and has been reported to be wide for these reasons (from 150 to 450ppm)[54].

A decrease in oxygen content lowers the start temperature for transformation and delays the transformation time as shown in figure 2.10 in chapter 2. These could be the result of the role of inclusion as a nucleation site and as austenite grain refiners [54]. The reduction in oxygen decreases the number of inclusions (rather than their size) [48].

To control the O levels in the weld metal, the quantity of deoxidants, such as Mn, Si, Ti, and Al, must be carefully balanced to permit the positive effect that these elements and the other alloying elements produce on the microstructural transformation and the mechanical properties of weld metals.

3.2.11 Effect of Nitrogen

Nitrogen is a strengthening element that has little effect on the macrostructure of C-Mn steel weld metals [48]. N in solid solution has a similar strengthening effect to that of carbon. The major problem regarding nitrogen is its role in promoting strain ageing embrittlement. Strain ageing is an interaction between free nitrogen (and free carbon) atoms in steels and

dislocations in the matrix. It can occur at room temperature and above. Strain ageing increases strength and reduces ductility and toughness [48].

The nitrogen content has to be maintained at levels lower than 200 ppm, because at higher values it could contribute to the formation of porosities. For optimum impact toughness N contents should be maintained lower that ~0.007wt% depending on the levels of Al and Ti present. Account has to be taken of the observation that the lower the N contents the lower the risk for strain ageing embrittlement.

3.2.12 Effect of Niobium and Vanadium

Niobium and vanadium are known to give toughness problems. Small amounts of these elements could enter the weld metal, either diluted from the parent steel, from impurities in rutile or other coating materials or from the core wire [48]. Dolby [61], in a review of the effects of these two elements on weld metal properties, concluded that low levels of Nb (<0.02wt%) and V (<0.05wt%) were not detrimental to Charpy toughness, behaviour that depended on the cooling rate and the Mn content of the weld metal. In the presence of high levels of V and Nb, the best weld metal toughness was found in microstructures consisting in acicular ferrite. The general effects of V and Nb on weld microstructure are summarised in table 3.2.

He and Edmonds [62], in studies on C-Mn steels, concluded that the acicular ferrite appeared to develop principally as a result of vanadium alloying between 0.2 and 0.5wt% V, without detrimental effects on toughness. They suggested that the formation of V-rich regions may facilitate the nucleation of acicular ferrite in these steels.

Table 3.2 V and Nb effects on the microstructure of steel weld metals [61]

Microstructural constituent	V effect on proportion of the constituent	Nb effect on proportion of the constituent
Grain boundary ferrite	Little change but may be increased	Reduced
Lamellar (sideplates) ferrite	Reduced, except in presence of Nb	May be increased depending on plate and welding consumables used
Acicular ferrite	Often increased, especially when lamellar ferrite is reduced. However, V alone cannot increase AF beyond 80%	Depends on consumables used. Generally decreased in lean deposit at slow cooling rates. It could be increased when using basic, alumina-basic and low silica, calcium silicate fluxes
Martensitic microphases	Increased	Increased

3.2.13 Effect of impurities: phosphorus and sulphur

Sulphur and phosphorus are generally recognized to be detrimental to toughness. Oxygen and sulphur are responsible for the formation of non-metallic inclusions, and for this if they are restricted the upper shelf Charpy toughness will improve [15].

Increasing the sulphur content decreased the proportion of acicular ferrite, which is replaced by ferrite with aligned second phase and as a consequence the toughness is deteriorated. Another effect of sulphur is to deteriorate the strength and reduction of area (ductility) of the steel. Moreover, as S is augmented the ductile-fragile transition temperature is increased [48].

On the other hand, phosphorus does not produce significant changes in microstructure of the weld metal and Evans [48] have reported that this element did not appear to change the tensile strength, yield strength and ductility values in the as-welded condition of the studied C-Mn weld metals.

The effect of the alloying elements mentioned before are complex when a combination of them is present in the weld metal. However, for the selection of the optimum combination of alloying elements it is important to take in account their individual behaviour and their interdependence. This has made the modelling of the welding metallurgy one of the more difficult subjects to develop because of the huge number of involved variables.

CHAPTER FOUR

HYDROGEN EMBRITTLEMENT AND HICC IN WELDS

The previous three chapters have been concerned with the welding of HSLA steels, their microstructure and properties relationships. The present chapter is dedicated to the literature review on one of the most frequent problems found in the welding of HSLA steels: the Hydrogen Induced Cold Cracking (HICC). Firstly, a general description of HICC problem in welding and some of the parameters, which affect its occurrence, are described. Consecutively, the theories about the general phenomena of hydrogen embrittlement are treated with some detail. It is worthy to emphasise at this point that the HICC is not more than a manifestation of the effect of hydrogen on the mechanical properties of metals, which in the case of steel weldments is the result of the introduction of hydrogen in the weld from different sources during the welding process. In other hydrogen embrittlement phenomena, the hydrogen could be introduced during electrolytic processes, such as electroplating, and/or during the structure service time, due to corrosion or cathodic protection.

A further section is devoted to the treatment of the trapping theories. The influence of the hydrogen trapping effect on the hydrogen transport, distribution and concentration in different regions of the microstructure is related with the susceptibility to HICC of the microstructure. Finally, the last section deals with the appearance of hydrogen embrittlement on the fracture surface. This last section elucidates the relationship between hydrogen content and distribution, the microstructure and the fracture mechanism. A special treatment is made to the micromechanism suggested for the effect of the hydrogen on the crack formation and propagation.

4.1 Hydrogen Induced Cold Cracking (HICC).

One of the most common causes of failure in welded structures, during and after the welding process, is hydrogen induced cold cracking (HICC). This is caused by the presence of hydrogen in the bulk of the steel, which originates from dissociation of hydrogen from various types of hydrogen containing compounds.

In this section the origins of the hydrogen which cause the damage are discussed, together with a description of the factors which influence the occurrence of hydrogen induced cold cracking.

4.1.1 Hydrogen sources and its diffusion into a metal

Hydrogen is dissolved in a weld metal during the welding process and the amount is proportional to the square root of the partial pressure of the hydrogen gas in the shielding gas [7]. Several sources can be identified. The following sources of weld metal hydrogen are considered in shielding metal arc welding [7, 16, 63]: hydrogen in core wire steel; organic substance, hydroxyl and water of mineral crystallisation in covering flux; moisture in binder for covering and extraneous hydrogenous material, e.g. moisture, grease, organic compounds, and paint.

The weld metal hydrogen content may vary strongly from one welding process to another. The lowest hydrogen levels are usually obtained with the use of low moisture basic electrodes or gas metal arc welding (GMAW) with solid wires. Submerged arc welding and flux cored arc welding, on the other hand, may give high or low concentration of hydrogen in the weld metal, depending on the flux quality and the operational conditions applied. The highest hydrogen levels are associated with cellulosic, acid, and rutile type electrodes [16]. In figure 4.1, a comparison of different welding processes, in terms of the hydrogen levels, could be observed.

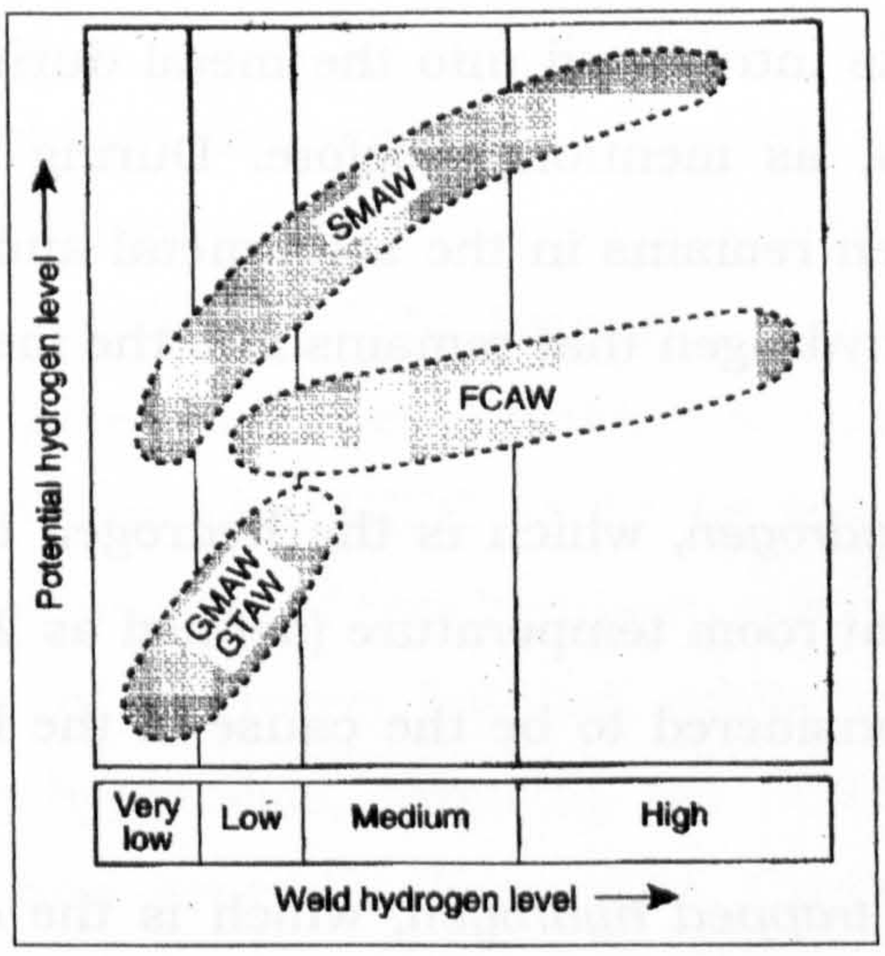

Figure 4.1 Schematic ranking of different welding process in terms of hydrogen level: shielded metal arc (SMA), flux-cored arc (FCA), gas metal arc (GMA) and gas tungsten arc (GTA) welding [16].

4.1.2 Conditions for hydrogen induced cold cracking (HICC)

As was mentioned in the introductory chapter, for the occurrence of HICC in the weld metal or in the HAZ of the weldment or both, four conditions have to be present simultaneously, as schematised in figure 4.2. These conditions are [6, 7, 49]:

1. Hydrogen at sufficient concentration
2. Sufficient stress for the crack initiation and propagation
3. Microstructure susceptible to hydrogen embrittlement
4. The temperature must be within a critical range

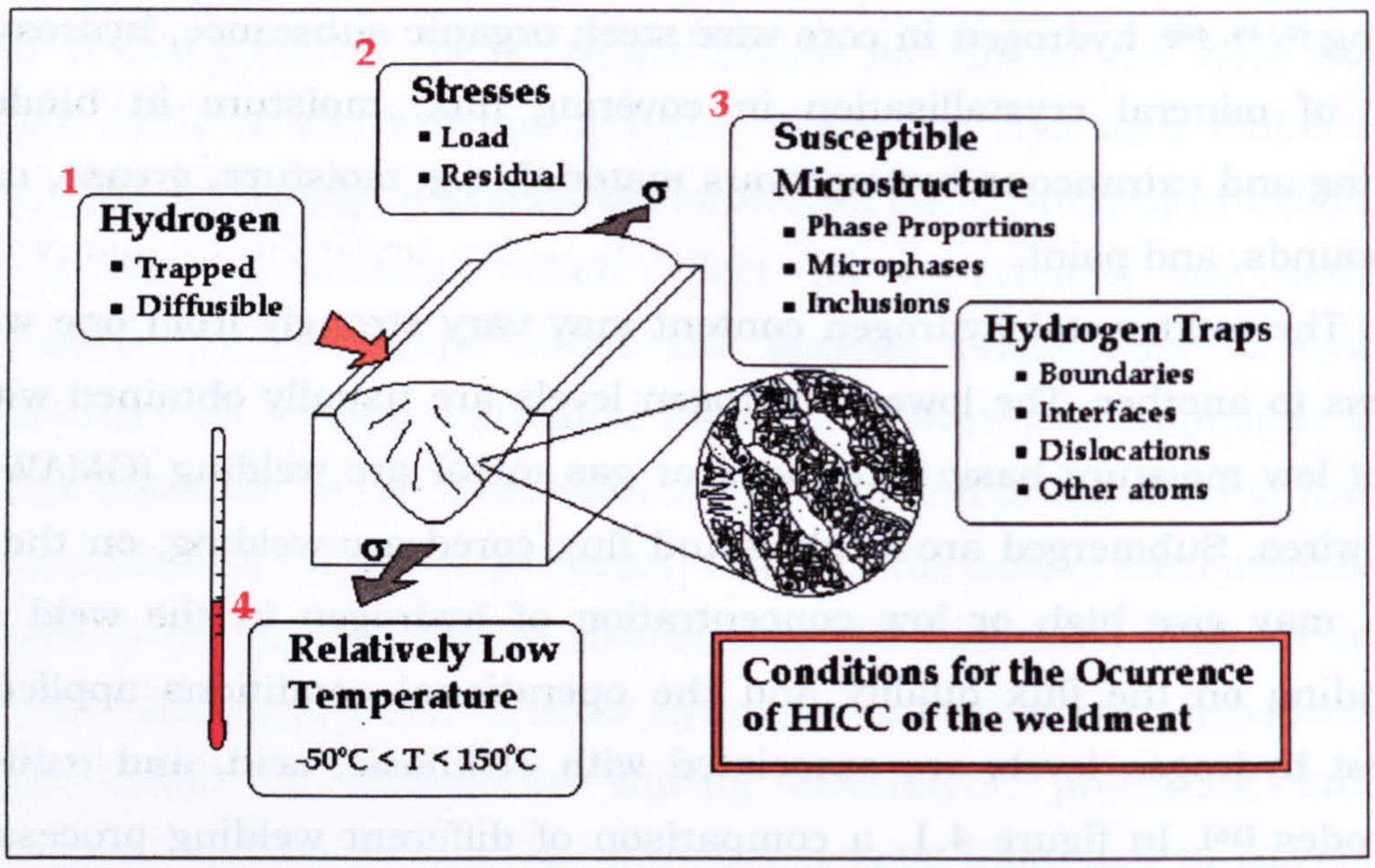

Figure 4.2 Necessary conditions for the occurrence of hydrogen-induced cold cracking of the weldment

The hydrogen is introduced into the metal during the welding process from various sources, as mentioned before. During and after the welding process some hydrogen remains in the solid metal and some could escape to the atmosphere. The hydrogen that remains into the metal could be present in two forms:

(a) *Diffusible hydrogen*, which is the hydrogen that can diffuse out of the sample at room temperature (defined as 25 ± 5°C)[64]. This is the hydrogen considered to be the cause of the hydrogen induced cold cracking.

(b) *Residual or trapped hydrogen*, which is the difference between the total amount of hydrogen in the metal and the diffusible hydrogen. This is the hydrogen trapped in different locations in the microstructure. It is relatively immobile and it is believed not to be harmful, although in some cases could transform to diffusible hydrogen.

The stresses, which are necessary for the formation and propagation of cracks, could be of two kinds: residual and/or the loads supported in service by the structure. The first kind could be introduced during the welding

process due to the occurrence of different phase transformations and the constraints imposed on the structure. The other stresses are those for which the structure was designed. Local stresses or local strains produce non-uniform distribution of hydrogen that could assist the formation and propagation of cracks.

If the hydrogen content is sufficient and the localised stresses occur near microstructural features susceptible to the formation of cracks, the micro-cracks are going to form. These cracks could grow until the failure of the structure is produced or could be arrested and remain in the material as a potential flaw, which could continue to propagate in the presence of sufficient stress. The temperature at which this process occurs is very important. As shown in figure 4.2, the temperature interval where the HICC is produced could be as low as -50°C and as high as 150°C. In this temperature interval the hydrogen diffusion may have the right value to affect the deformation and crack propagation processes in a delayed manner. If one of the four factors listed above is absent the hydrogen induced cold cracking would not occur.

4.2 Mechanisms of hydrogen embrittlement.

Several reviews have been written in relation with the phenomena of hydrogen embrittlement of steels. A survey of this subject is not complete without making reference to the works of Oriani [65] and Hirth [66]. In these reviews there is an excellent presentation of the fundamental basis for the understanding of the complexity of the hydrogen embrittlement phenomena. Yurioka and Suzuki [7] gave another excellent review in regard to the hydrogen assisted cracking in weldments. HICC could be termed a special case of hydrogen embrittlement because of how hydrogen is introduced in the metal.

The mechanism of hydrogen induced crack formation is still being investigated. An early hypothesis, involving the build up of hydrogen gas pressure in voids, is now generally discredited. Currently, the most widely accepted model involves the presence of pre-existing defect sites in the material: small cracks or discontinuities caused by minor phase particles or inclusions. In the presence of existing stress, these sites may develop high local areas of biaxial or triaxial tensile stress. Hydrogen diffuses preferentially to these dilated lattice sites of the microstructure. As the local hydrogen concentration increases, the cohesive energy and the critical stress to break the cohesion of the lattice decrease. When this critical stress falls below the local intensified stress level, fracture occurs spontaneously. Hydrogen then

evolves in the crack volume, and the process is repeated. This model is consistent with the relatively slow and discontinuous nature of the crack propagation found in the hydrogen induced cracking process [5].

The mechanisms of hydrogen induced cracking could be divided into two important groups: classic and modern mechanisms. The first group includes the earlier attempts to explain the phenomenon and the last one contains the modern theories in the field.

4.2.1 Classic Mechanisms

Hirth [66] summarised the following five major mechanisms proposed to explain hydrogen embrittlement of steels:

a. Internal pressure theory

b. Slip softening model

c. Surface energy model

d. Hydride formation model

e. Decohesion theory

These models are discussed briefly in the following paragraphs.

a. Internal Pressure Theory

In the internal pressure mechanism, proposed by Zapfee and Sims [67], the hydrogen reaches high internal pressures in voids and microcracks and as a result assists the formation and growth of the crack. The idea is that very large hydrogen gas pressures generated in internal microcracks and voids force their expansion either by plastic deformation or cleavage, leading to the coalescence of microcracks or microvoids [65]. A small external stress helps the spreading of the crack because the external stress and the internal pressure of H_2 are additive [68]. High-fugacity hydrogen environments are necessary for the occurrence of the pressure enhanced void growth, as demonstrated by blister formation in the absence of external stress. However, several authors have shown that crack propagation in dry hydrogen at sub-atmospheric pressures can occur and for this reason, this model can not be general [66].

The theoretical model for crack propagation in the pressure theory is based on Griffith's theory of brittle fracture. This theory is based in a thermodynamic treatment of the crack propagation, i.e., based on an energy balance concept. If a solid body under the action of external stresses can reduce its potential energy by forming cracks, then the equilibrium state of the body is reached when the fracture of the solid has occurred [69]. The critical

stress, σ_{cr} for spreading an elliptical crack of length 2c under plane strain state (thick plate) is:

$$\sigma_{cr} = \left[\frac{2 \cdot E \cdot \gamma}{\pi \cdot c \cdot (1-\nu^2)}\right]^{1/2} \quad (4.1)$$

where γ is the surface energy of the metal, ν the Poisson's ratio and E the Young's modulus. Then the condition for crack spreading in presence of a H_2 pressure (P_{H2}) inside the crack is modified as:

$$P_{H_2} + \sigma > \sigma_{cr} \quad (4.2)$$

where σ is the applied stress which is assumed to act normal to the plane of the crack [68]. The simple relation 4.2 shows that the stress to produce the fracture or the propagation of the crack in the solid with hydrogen is lesser than that without the presence of hydrogen.

The presence of microcracks and voids, where the hydrogen pressure can reach critical values, are necessary for the operation of this mechanism. However, many authors [70, 71] have shown that microcracks or cavities need not to be present to initiate embrittlement process. Microcracks could nucleate from dislocation pileups under the influence of an external stress.

b. Slip Softening models

In studies of hydrogen assisted cracking of steels, Beachem [72] proposed that hydrogen augments the dislocation motion. Hydrogen effect on dislocation motion is demonstrated by the softening behaviour due to the enhanced screw dislocation mobility, enhanced dislocation formation at surfaces, and the promotion of shear instabilities [66]. This increase in the dislocation mobility produces a softening effect. However, hardening effect could also be observed, and for this reason, the softening theory may not be a general one.

Linch [73] has noted the analogy between the liquid metal embrittlement and the intergranular crack propagation in high strength steels charged with or in the presence of hydrogen. As in the case of liquid metal embrittlement, the hydrogen effect is due to the adsorption of it and its major contribution is to promote the formation of dislocations at the crack tip, causing crack propagation by an alternate sliding off of the crack tip in a model similar to that suggested for fatigue crack growth [66].

c. Surface Energy Model.

Similar to the Griffith's crack model for brittle fracture, Petch and Stables [74] suggested that the adsorption of hydrogen decreases the surface energy at the surfaces created in crack propagation, reduces the needed work to produce fracture, and as a consequence promotes cracking. For a crack formed from a pileup of dislocations (Stroh crack) the well-known Petch equation for fracture stress is:

$$\sigma_f = \sigma_0 + 4 \cdot \left[\frac{3 \cdot G \cdot \gamma}{\pi \cdot (1-\nu) \cdot L} \right]^{1/2} \qquad (4.3)$$

where σ_f is the fracture stress, σ_0 is a constant, γ is the surface energy, 2L is the grain diameter, ν is the Poisson's ratio (0.30) and G the rigidity modulus (≈79GPa). In presence of H, the value of the surface energy is reduced to γ_H, as given by the following equation:

$$\gamma_H = \gamma - 2 \cdot N_s \cdot k \cdot T \cdot \ln\left[1 + (A \cdot P)^{1/2}\right] \qquad (4.4)$$

where N_s is twice the number of H atoms adsorbed per unit area of surface at saturation (Ns= 6.106 10^{10} m^{-2} for the (100) planes of α-Fe), k is the Boltzmann's constant, T is the absolute temperature, A is constant (≈$5 \cdot 10^7 m^{-1}$) originated from Langmuir isotherm and P the pressure of H_2. Substituting equation 4.4 into 4.3 and simplifying the expression to the Hall –Petch's popular form:

$$\sigma_f = \sigma_0 + K \cdot L^{-1/2} \qquad (4.5)$$

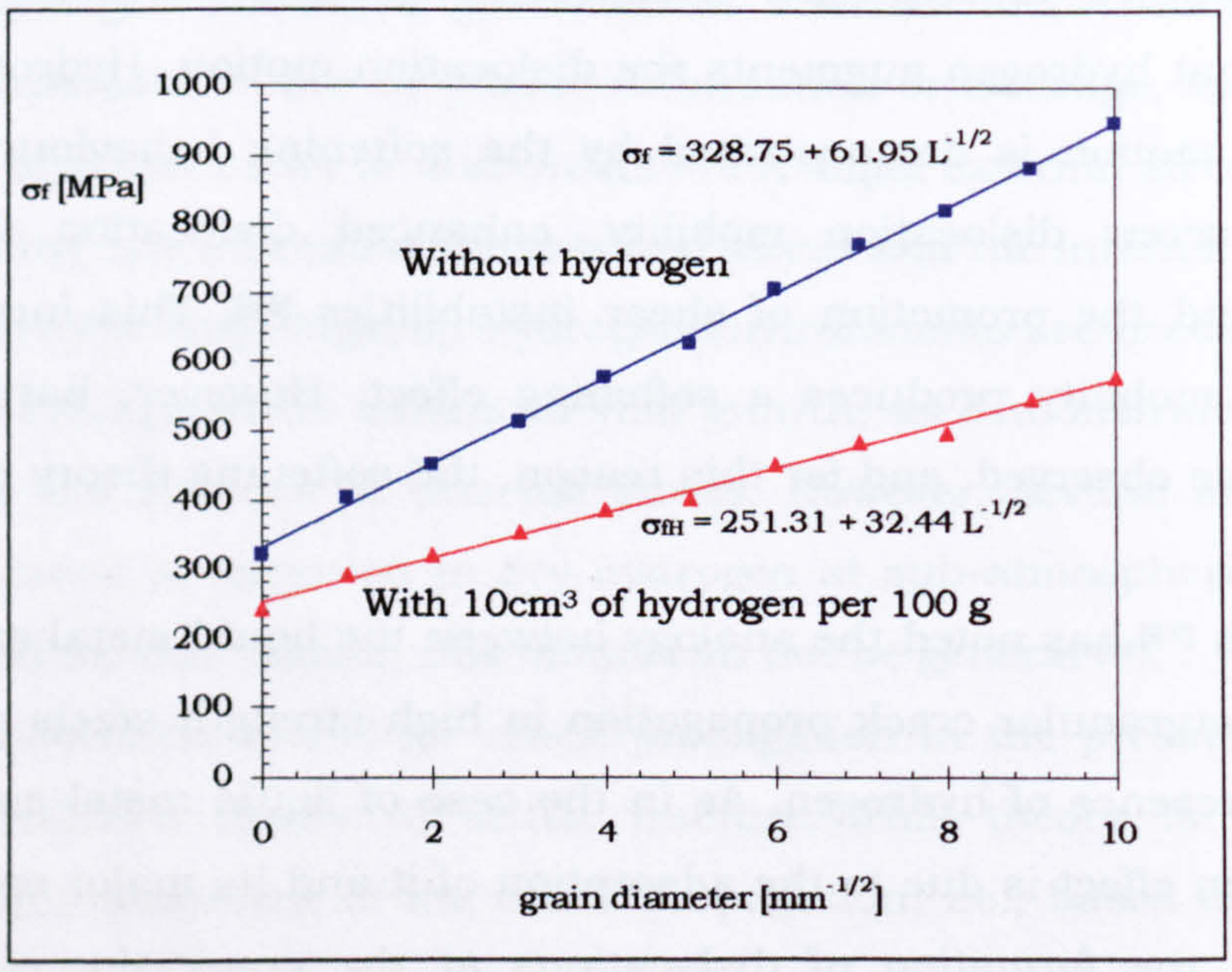

Figure 4.3 Hydrogen effect on the fracture stress of a mild steel at 291 K without and with $10cm^3$ of hydrogen per 100g of steel and different grain size. The reduction of σ_0 and K can be observed when hydrogen is introduced to the steel. Adapted from [75]

Petch found that the values of σ_0 and K, which are proportional to γ or γ_H, decrease as a consequence of the presence of H [68], as shown in figure 4.3. It can be observed that both σ_0 and K are reduced from 328.75MPa and 61.95 MPa·mm$^{1/2}$ to 251.31MPa and 32.44MPa·mm$^{1/2}$, respectively. Using equation 4.3 the ratio γ_H/γ could be estimated as 0.274, value that shows clearly the reduction in the surface energy due to the hydrogen absorption. Assuming γ to be around 1.2J/m^2, Petch's theoretically predicted value of σ_f-σ_0 = 147.1 MPa for $(2L)^{-1/2}$ = 5mm$^{-1/2}$ was in close agreement with the observed values of 169.7MPa [75].

Although the experimental evidence that support this theory exists, there are some arguments against this theory:

a) It greatly underestimates the needed work for fracture
b) It cannot account for the discontinuous cracking propagation mode characteristic of the hydrogen assisted cracking
c) It cannot explain why the tendency for delayed failure can be reversed on stress removal. This reversibility is likely connected with crack nucleation which can involve not only surface energy reduction by hydrogen but also local stresses associated with dislocation pileups and elastic incompatibility stresses (which can influence the local hydrogen concentration), all of which can be relaxed or recovered on removal of external stresses [66].
d) It cannot explain why oxygen, which has a greater heat of adsorption, not only fails to promote cracking but stops the hydrogen effect. One possibility for the role of oxygen is that it adsorbs at the crack tip and blocks hydrogen while also being in an atomic position unfavourable for crack propagation, where it could locally make bond breaking more difficult [66].

d. Hydride formation model

This model was proposed by Westlake[76] and the idea is that cracking occurs by the formation and cracking of metallic hydrides near the crack tip. The hydrostatic stress field at a stressed crack tip could stabilise hydride, as was demonstrated for embrittlement in niobium by Gahr et al [77]. Other metals and alloys, for example, Ti, Zr, V, U, Ta, $LaNi_5$, Fe-Ti, etc., form hydrides as well [68]. The modulus of elasticity and the molar volume of these hydrides are lower and larger than that of the metallic matrix, respectively. Even without the application of external stresses, the materials will fracture.

This model had not been considered in the case of iron and steels because iron hydride is stable at very high hydrogen pressures, which could be as high as 2 GPa. Nevertheless, calculations of the Fermi Dirac atmosphere of hydrogen at a stressed crack tip shows that saturation occurs at room temperature permitting the hydride formation. This suggests that the hydride formation model could be applied on an atomic scale [66].

e. Decohesion Theory

This is the most accepted qualitative model and proposes that hydrogen reduces cohesion of the second phase particles when pre-charged into steels. It was firstly proposed by Troiano [78] in his study of low strength steels. This model is in agreement with the general idea of decohesion as in the ductile fracture models, and as modelled for metalloid effects on the mode of fracture of several alloys [66]. It supposes that dissolved hydrogen at high concentrations lowers the maximum cohesive force between the atoms of the alloy in the iron alloy lattice, at grain boundaries and at interfaces.

On application of an external stress, H is supposed to diffuse preferentially into regions of triaxial stresses, where solubility is higher than other regions. Hydrogen accumulates at these regions and produces the weakening of the metal-metal bond. The fracture results when the local stress at the crack tip equals the fracture strength reduced by hydrogen [65, 68]. Plasticity at the crack tip such as dislocation pileups, intersection of slip bands, and regions of plastic incompatibility due to inhomogeneous plastic deformation provide the necessary conditions for hydrogen accumulation and its embrittlement effect [65]. In the next section these mechanisms are linked with theoretical calculations of the electronic density: the molecular approach to fracture.

4.2.2 Modern Mechanisms for hydrogen embrittlement

Many investigators have attempted to provide an explanation for the hydrogen embrittlement phenomenon for more than 130 years. The vast available literature shows that the search for a theory, capable of explaining H embrittlement for all metals and alloys, remains obscure. The modern mechanisms rely on the phenomenological treatments given previously for H embrittlement but attempt a quantum mechanical approach to hydrogen solubility and decohesion at interfaces. In the following paragraphs two of the

most interesting models are described. These theories are related to the decohesion theory described before.

a- The electronic density of states N(E) approach

This theory was proposed by Lee [79] and is based on the concept that hydrogen embrittlement could be related to the electron density of states $N(E_f)$ at the Fermi energy level. This relationship is characterised by a unique electrons per atom number (Zi), that must be determined both from its position in the periodic table and from the net charge transfer of electrons (ΔZ) which takes place upon alloying. In other words, hydrogen embrittlement is related to its effect on the electronic structure of metals and alloys. The general effect of the hydrogen on a particular alloy was described by the decohesion model that was proposed firstly by Troiano [78].

Lee [79] suggest a "universal" hydrogen embrittlement index (HEI) which is empirically derived to show a direct correlation with the electronic specific heat coefficient (γ) at high temperature. When plotting $N(E_f)$ or γ and HEI obtained experimentally using the change in area reduction after charging with hydrogen, a linear relationship can be noted, as in figure 4.4 for pure metals.

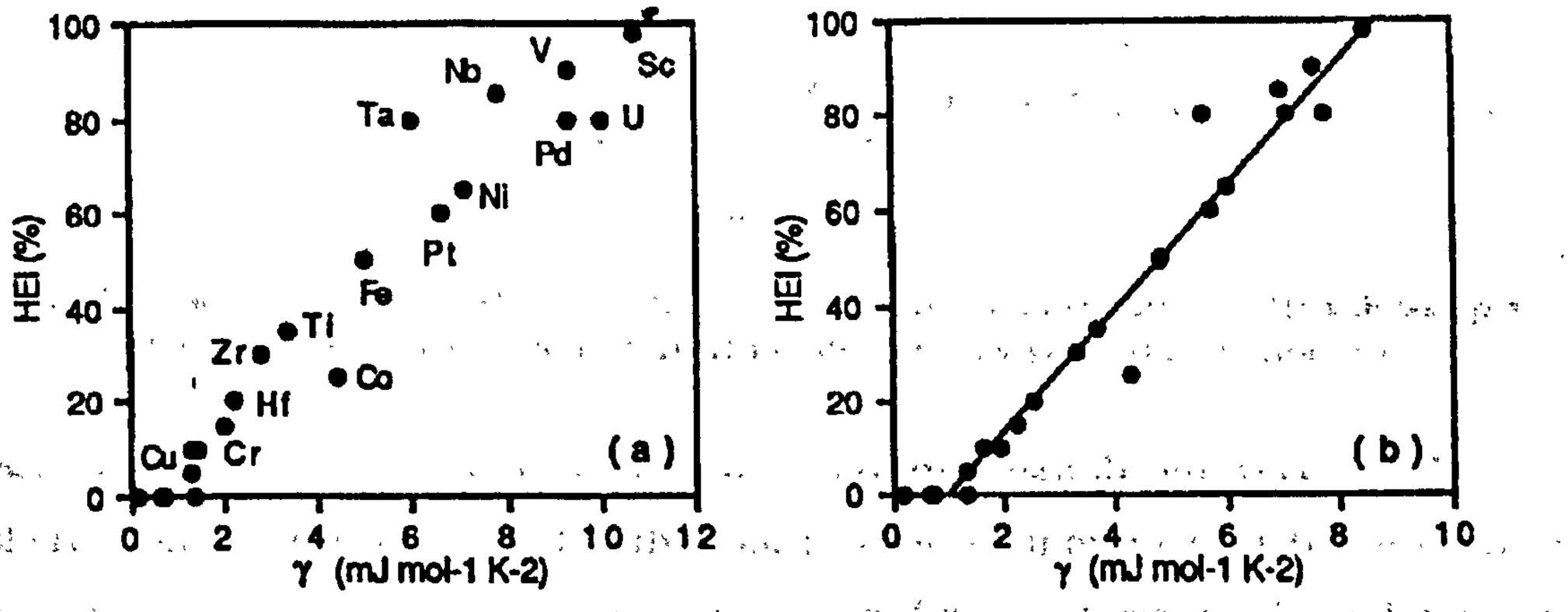

Figure 4.4 The electronic density of states approach of hydrogen embrittlement: (a) plot of γ versus HEI for 22 pure metals at low temperature and (b) at room temperature [79].

The figure 4.4(a) shows a linear relationship between the HEI and γ at low temperatures. This relation must be corrected to room temperature where the embrittlement effect is observed. In the figure 4.4(b) such correction is plotted and from this the following equation is obtained:

$$HEI = \alpha(\gamma) - b \approx 13\%(\gamma) - 13\% \qquad (4.6)$$

From this kind of approach and similar to the periodic law, it could be suggested that hydrogen embrittlement may vary systematically in going from one element to the next as arranged in the periodic table. Moreover, for any transition element the hydrogen embrittlement effect could be related with a particular electron per atom number (Z_i). Lee [79] showed that HEI could be predicted for a large quantity of binary alloys and more complex alloys following the same concept. The general form of the equation 4.6 is still applicable, but the γ_{alloy} must be estimated. Every element can contribute individually to the total HEI of an alloy. Zi for the alloy is not an average value but it will depend on the alloy concentration and the sign will depend on the ability for an element to lose or gain an electron when alloying [79]. The prediction for many austenitic stainless steels and nickel alloys is shown in the figure 4.5.

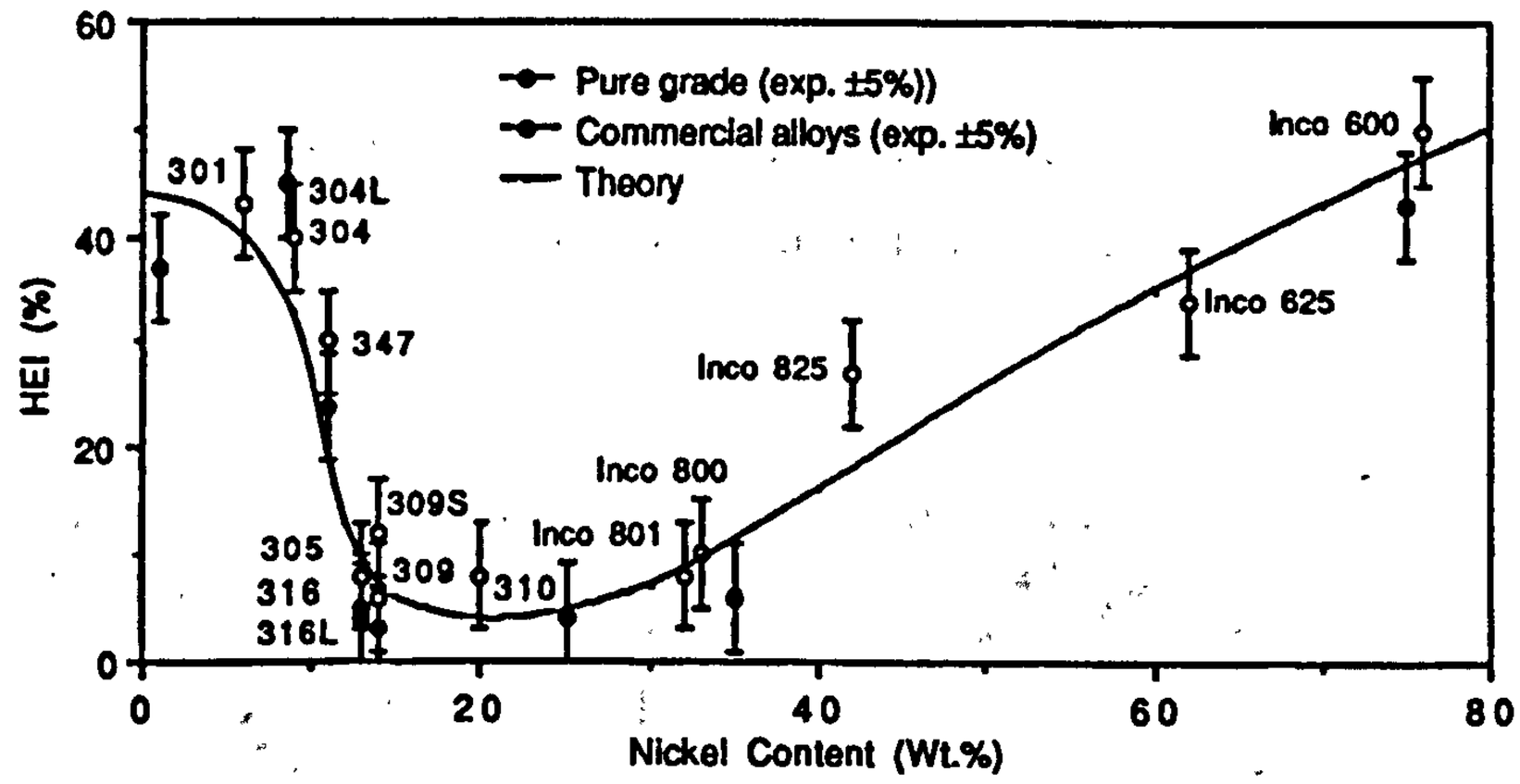

Figure 4.5 HEI predictions for austenitic stainless steels and Fe-Ni-Cr alloys as a function of Ni (wt. %) with Cr concentration mostly 16 to 20 wt. % [79].

The electronic density approach has some limitations when localised events related to a premature loss of local ductility at the tip of microcracks that lead to the formation and propagation of rapid cracks are taken into account. In this respect, the electronic density theory suggests that H embrittlement must begin at a particular site where the local $N(E_f)$ value is relatively high. However, the predictions of the HEI from the $N(E_f)$ of the bulk metal seem to indicate that the variations of the electronic density in this localised sites must be small and this suggests that a localised event is not of vital importance to the embrittlement effect. In addition to this, it is not clear yet how internal strains, dislocations, interfaces and other microstructural defects affect the average N(E) [79].

b.- The molecular orbital approach to fracture

The basic idea to model the embrittlement effect of a determined solute in a matrix is to use a cluster of atoms to represent the environment, in this case the grain boundary or an interface. Then the solute is located in a particular place and the molecular orbital theory (MO) is used to solve for the electronic structure of the cluster [80]. In this manner different solutes are studied and their effect on the cohesion of the matrix.

Messmer and Briant [81] used this approach to show the effect of S, P, C, and B as impurities on the intergranular embrittlement. They assume a tetrahedron as the structure of the clusters. Some of their results are shown in figure 4.6

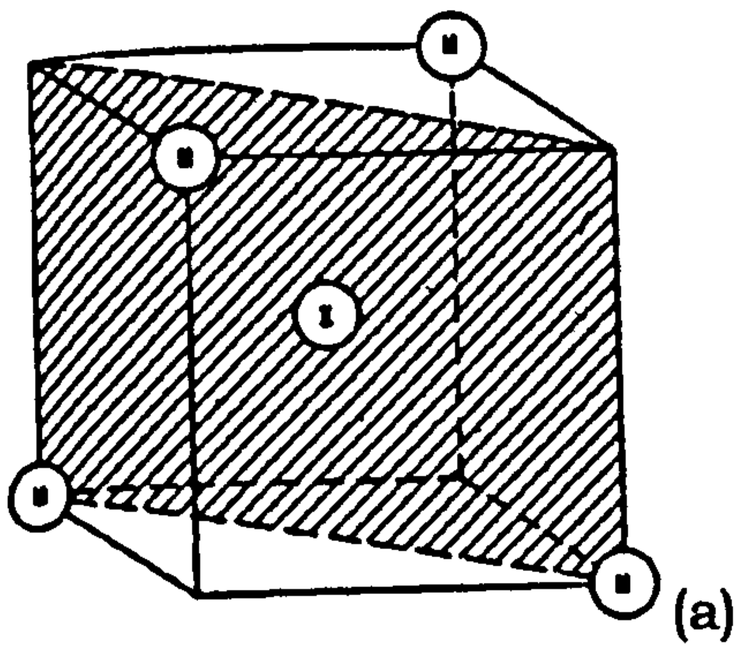

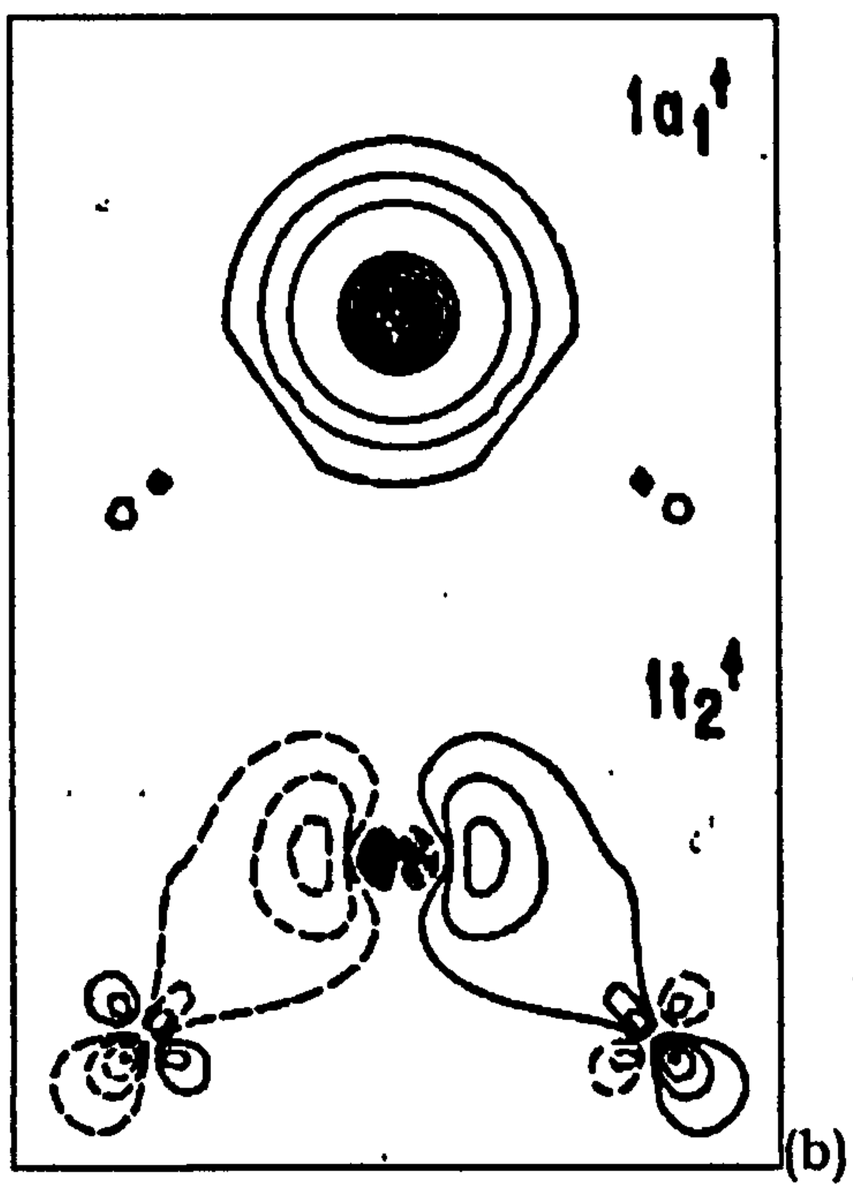

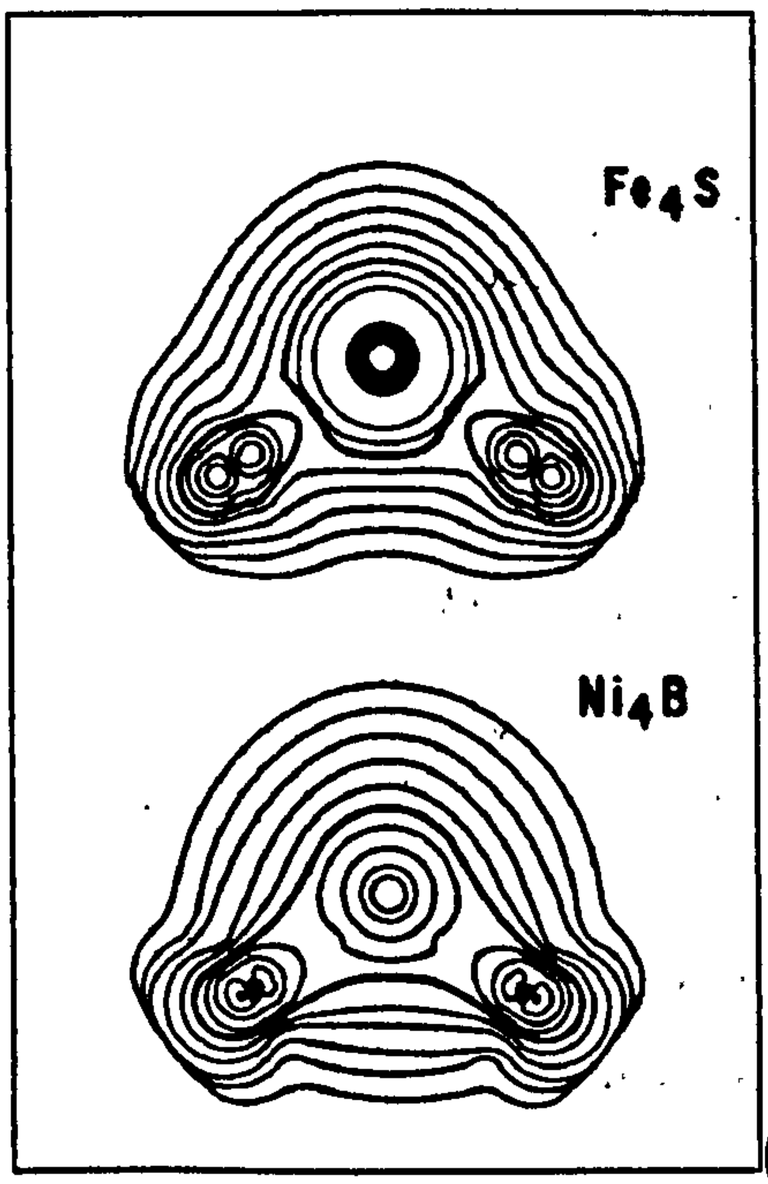

Figure 4.6 The MO theory applied to the grain boundary embrittlement. (a) Tetrahedron used as cluster of atoms M (Fe, Ni) and the impurity (S, B). (b) The orbital contour plots of the $1a_1$ and $1t_2$ orbitals in Fe_4S (crosshatched plane in (a)), and (c) The charge density for the tetrahedral cluster for Fe_4S and Ni_4B [81].

Figure 4.6(a) presents the tetrahedral cluster, where "M" represents the metallic atoms and "I" the impurity in the centre of the cube, used in the calculation of the orbital contour (4.6(b)) and the charge density distribution (4.6(c)). The energy level diagram for this system is showed in annex figure A.4. In these diagrams, the $1a_1$ and $1t_2$ levels are very important, because these two levels correspond to the wave functions that describe the metal-impurity interaction. The rest of the energy levels correspond to wave functions that are located either completely or almost completely on the metal atoms. For this reason, the orbital contour plots for the $1a_1$ and $1t_2$ levels are shown in figure 4.6(b). As can be observed in this figure for Fe_4S, the $1a_1$ orbital has practically no metal contribution and the $1t_2$ orbital also has little content on the metal atoms and are more concentrated on the impurity. Consequently, the bond has a hetero-polar character [81].

The special charge density plots are shown in figure 4.6 (c) for Fe_4S and Ni_4B to compare the effect of an embrittler element (S) and a cohesive enhancer (B). As is observed, the charge density is much greater on the S atom in the case Fe_4S than on the B atom in the case Ni_4B. For example, examining the sixth contour (from the most external contour) it can be observed to be broken in the case of Fe_4S but not in the case of Ni_4S. This suggests that the metal-metal bond has been weakened by the presence of the impurity, in the case of S in Fe, but it has been reinforced in the case of B in Ni. S is an embrittler and B not [81]. If an embrittler impurity is located in the grain boundary or other interface, the metal-metal bonds which hold these together will be weakened and the embrittlement will occur.

In a MO treatment of the embrittlement of Fe by hydrogen, the MO energy levels for a cluster of Fe atoms in the presence of hydrogen have showed results similar to the case of S in Fe or Ni. The basic idea is a chemical combination of H with Fe that could weak the Fe-Fe bonds [80]. This is not different to the phenomenological ideas about hydrogen embrittlement developed by Troiano [78]. Eberhart et al. [82] indicated that hydrogen which forms three centre bonds with the segregate could enhance the effect of the impurities in the grain boundary, and produce embrittlement at much lower concentration of impurities.

4.3 Hydrogen Trapping Theory

There is evidence that certain and localised sites in the material serve as hydrogen sinks. The hydrogen becomes trapped in these places where it

could remain or be liberated to diffuse, depending on condition such as temperature and the binding energy of the traps.

Evidence for hydrogen trapping in certain localised regions of the matrix is provided by the decrease in the diffusion coefficient of hydrogen in ferritic steels at temperatures below 200°C. This effect is shown in figure 4.7. The apparent diffusion rate of hydrogen in ferritic steels is slower than that for the diffusion in the lattice at temperatures below 200°C. Oriani[83], based on a hydrogen trapping theory, proposed the following equation for the apparent diffusion coefficient:

$$D_{app} = \frac{D_L}{1 + K \cdot \exp\left(\frac{E_b}{RT}\right)} \qquad (4.7)$$

Where

D_{app} apparent diffusion coefficient

D_L lattice diffusion coefficient

E_b binding energy between hydrogen and trap site

K density of trapping sites

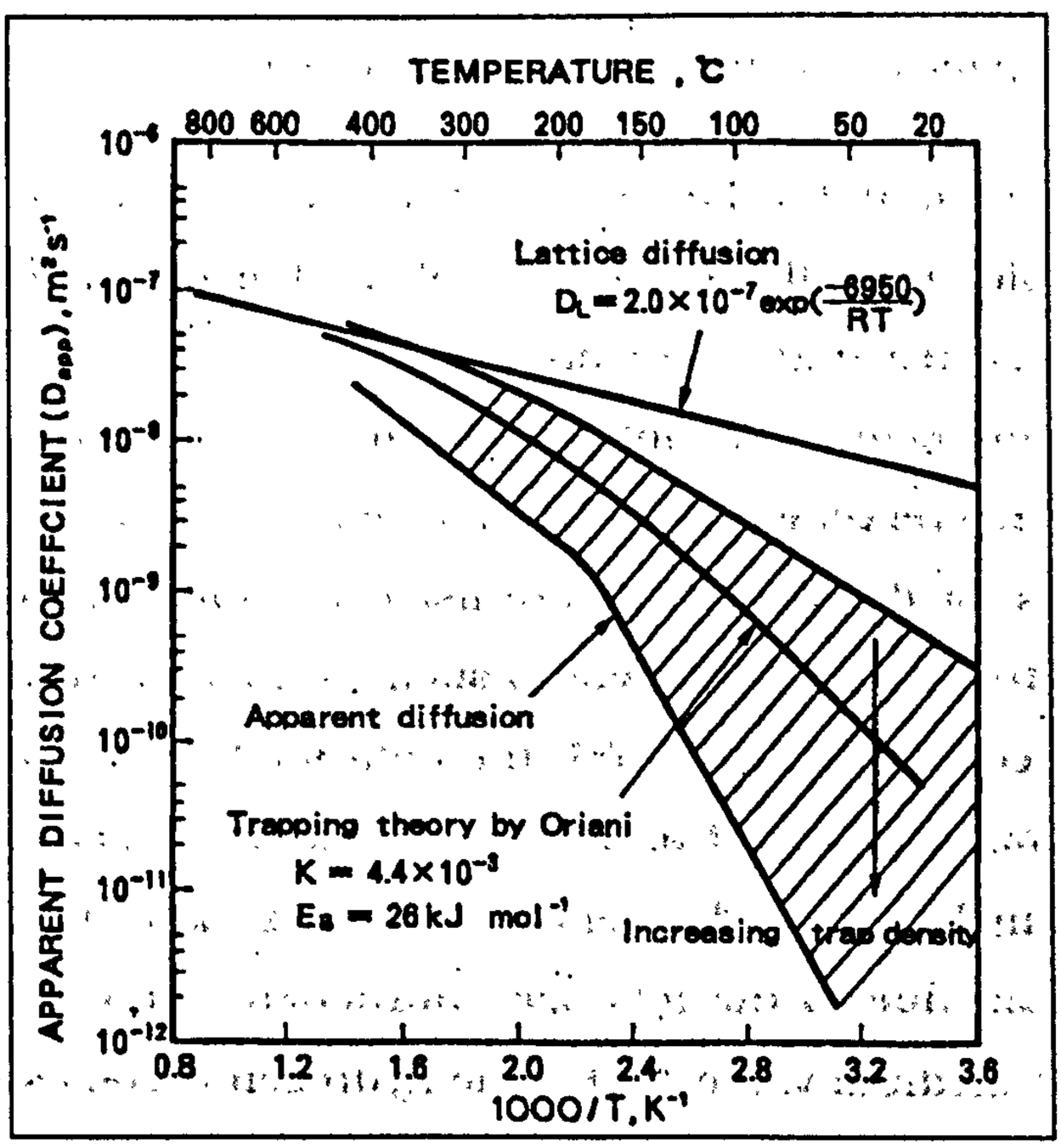

Figure 4.7 Hydrogen diffusivity coefficients for lattice diffusion (D_L) and for the experimentally (shaded region) and theoretically determined diffusivity in the presence of traps, apparent diffusion (D_{app}) [7].

The D_{app} predicted from equation 4.7 is plotted in figure 4.7 (for values of K = 4.4 10^{-3} and a E_b = 26 kJ/mol). The figure shows that D_{app} decreases if

an increase in trap density K occurs [7]. Moreover, an increase in the binding energy (E_b) between hydrogen and the trap site, which represents the intensity of hydrogen trapping or the quality of the trap, must decrease D_{app} as well. This is shown in figure 4.8.

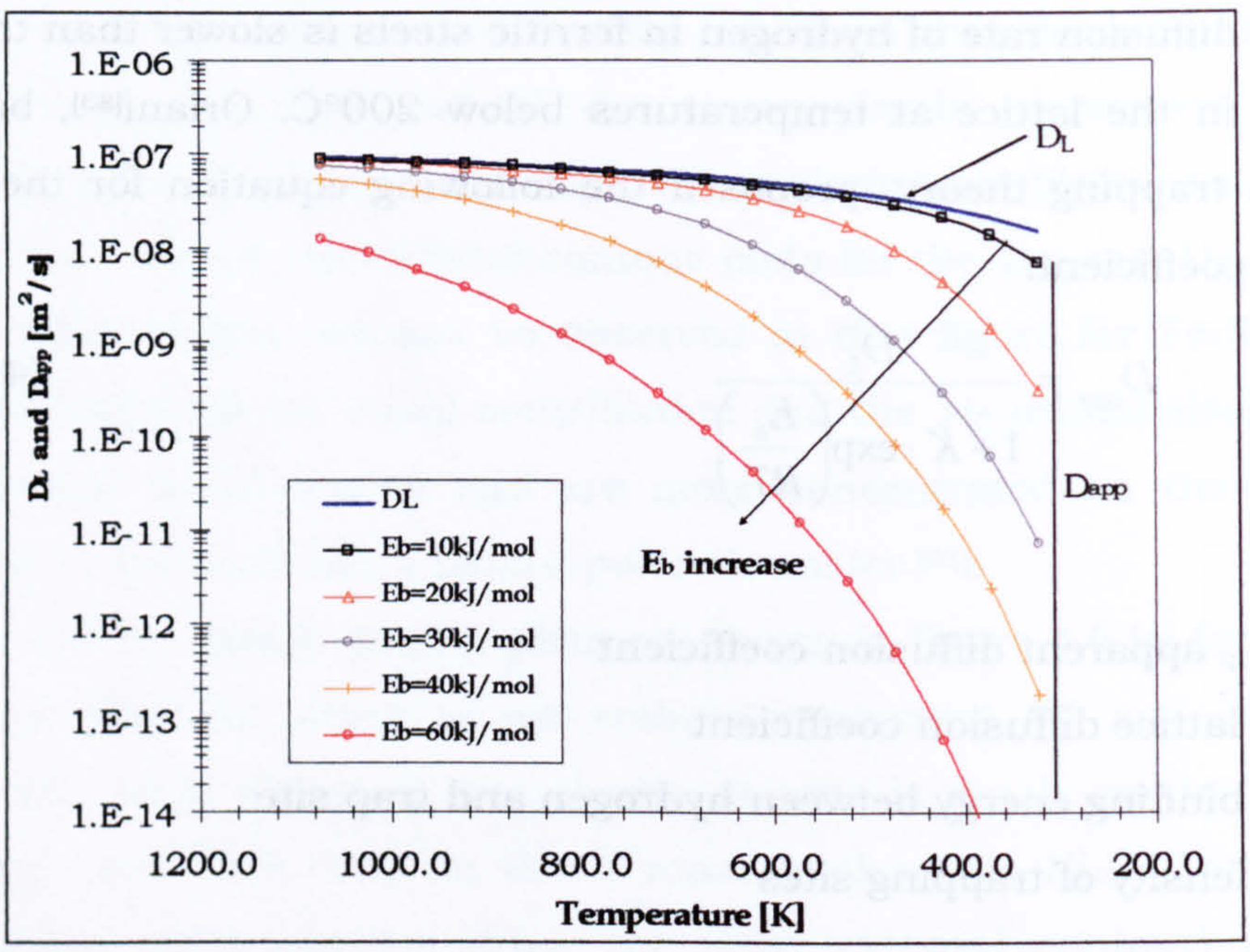

Figure 4.8 Variation of D_{app} with the increase of the binding energy of the hydrogen trap using equation 4.7. A K value of 4.4 10^{-3} was used.

Depending on the value of E_b, traps have been classified into two groups: reversible traps (E_b < 60 kJ/mol) and irreversible traps (E_b > 60 kJ/mol). It is reported that E_b for dislocations and hydrogen ranges between 20 and 60 kJ/mol, being reversible traps. On the other hand, TiC particles in a Ti-C steel are irreversible traps (strong traps) and their E_b is 96 kJ/mol [7]. Binding energies for different traps are listed in table 4.1 extracted from the review by Hirth [66] and other references such as the data related with retained austenite reported by Park et al. [84], the data for VC by Asahi et al. [85] and that for TiC reported by Lee et al. [86]. The traps are presented in the order of increasing trap-hydrogen binding energies. Reversible traps could complicate hydrogen diffusion due to the hydrogen attraction to the trap if the binding energy is low. At medium values of E_b, the hydrogen becomes strongly trapped but this could be released in the event of deformation when a dislocation passes near the reversible trap transporting this hydrogen to other sites. In contrast, the irreversible traps, as a consequence of their high binding energy, only capture hydrogen until saturation and its later release is very difficult [87]. The only means of releasing hydrogen from a irreversible trap is at elevated

temperatures, a characteristic that is used in the hydrogen thermal desorption (HDT) analysis for the study of trap binding energies.

As mentioned before, reversible traps can behave in two ways: they can act as simple sinks, where hydrogen accumulates and remains during the test; or they can exchange hydrogen with stronger traps, acting as hydrogen source as for example with dislocations. On the contrary, irreversible traps would be strong enough that they do not release hydrogen in the conditions imposed by the test [88].

Table 4.1 Hydrogen binding energies with different traps [66, 84-87]

Trap site	E_b [kJ/mol]
H-perfect lattice	0 (reference)
H-C	3.3
H-H	4.2
H-N	≥ 12.5
H-grain boundary	17.2 to 59
H-Ti	26.1
H-H_2 in void	28.6
H-dislocation core (screw)	20 to 30
H-VC interface	33 to 34
H-Austenite bulk trap	55
H-dislocation core (mixed)	58.6
H-AlN interface	65
H-free surface	70.7-95
H-MnS interface	72
H-Al_2O_3 interface	79
H-Fe_3C interface	84
H-TiC interface	86.9 to 94.6

4.3.1 Traps and hydrogen embrittlement

Traps definitively affect the susceptibility to hydrogen embrittlement of a metal or alloy as indicated by the general idea that some critical concentration of hydrogen (C_K) must be reached at potential crack sites for the initiation of cracks. As is shown in figure 4.9, a crack is initiated on a certain defect if the quantity of trapped hydrogen (C_H (t)) goes over C_K. Both C_K and C_H(t) are dependent on various parameters, but C_K depend specifically on the defect considered and its characteristics [88]:

(a) The shape of the defect: for example, an elongated MnS is more susceptible to initiate a crack than a spherical one. This means that for an elongated inclusion the value of C_K is lower than that for a spherical inclusion.

(b) The neighbouring structure of the defect: for example, C_K for an elongated MnS in martensite is lower than in ferrite.

(c) The defect coherency: for example, very incoherent grain boundaries are more susceptible to initiate a crack than more coherent ones.

(d) The defect orientation with respect to the applied stress: for example, a tensile stress perpendicular to the main axis of an elongated MnS lowers C_K.

(e) Other factors are the adsorbed impurities at the interface defect-matrix, the microstructure, the temperature, etc.

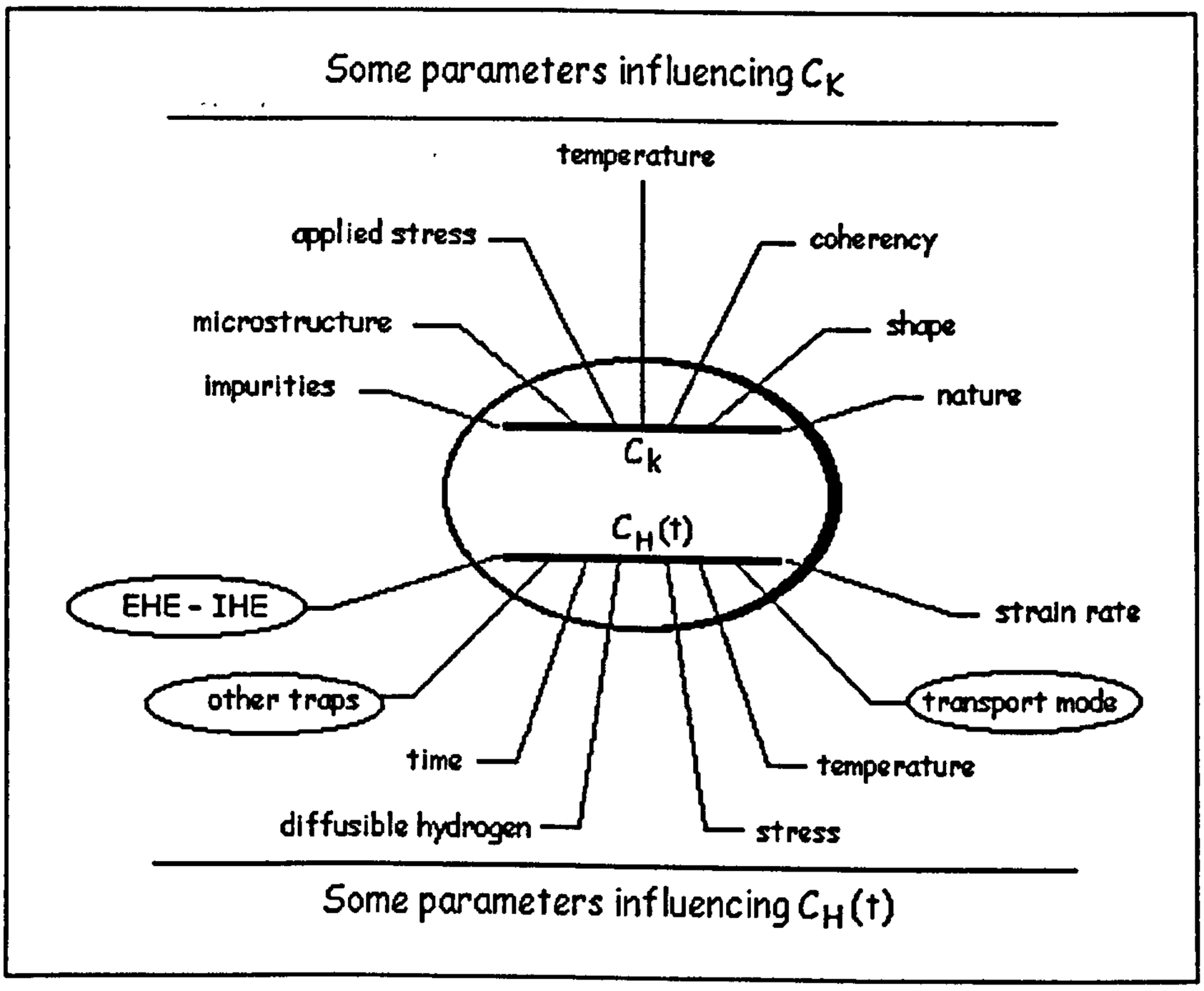

Figure 4.9 Critical concentration concept and related parameters. C_K is the critical concentration and C_H the hydrogen concentration trapped on the defect considered. EHE: external hydrogen embrittlement and IHE: internal hydrogen embrittlement [88].

In the same way, C_H (t) is influenced by numerous parameters, such as time, stress, temperature, amount of available hydrogen (diffusible hydrogen), other traps, transport mode, etc [88, 89].

The type of traps could be classified depending on the crack initiation sites and the propagation path. Following this idea, Gibala and DeMiglio [90] suggested that the crack path in hydrogen embrittlement could depend on the presence of strong traps that in adequate numbers can collect hydrogen from external sources or reversible traps and produce the cracks. Table 4.2 presents this statement in a general manner. However, this view has changed with time and research and as discussed below the presence of a homogeneous distribution of irreversible traps could reduce the risk of

hydrogen induced cracking due to the redistribution of hydrogen in local low concentration that are not enough to crack initiation and propagation.

Table 4.2 Crack classification for hydrogen assisted cracking (HAC) [90]

Microstructural trap	Nature of trap	HAC susceptibility
Solute atoms Microvoids Low angle boundaries Dislocations Coherent precipitates	Weak/ moderate Reversible $E_b \leq 60$ kJ/mol	Cracking along well-defined interfaces is not favoured
Pre-existing microcracks Propagating microcracks High angle boundaries Incoherent precipitates Incoherent interfaces	Strong Irreversible $E_b \geq 60$ kJ/mol	Cracking along interfaces that are irreversible traps is favoured.

Pressouyre [88, 89] has proposed two ways to explain the incidence of traps on the susceptibility to hydrogen embrittlement:

a- Some of these traps will be potential flaws for the crack nucleation. The formation of the crack depends on the trapping, on its critical concentration value, and on the quantity of hydrogen which will reach the trap site during the test. If the hydrogen concentration goes over the critical concentration, a crack will be nucleated.

b- Many traps will not nucleate cracks, but they will either prevent hydrogen from reaching potential flaws in sufficient quantities, acting as innocuous sinks, or they will assist potential traps to gain large amounts of hydrogen, playing the role of sources.

Two main factors influence the behaviour of the traps in the metal during a test to study the hydrogen embrittlement. Firstly, the initial state of the material prior to testing, for example, whether the material has been pre-charged or not. Secondly, the process by which hydrogen moves in the material. Hydrogen may diffuse throughout the lattice by interstitial jumps, as dislocation atmospheres, or along short circuits paths such as grain boundaries and interfaces [88, 89].

The trap theory of H embrittlement proposed by Pressouyre [88, 89] quantitatively describes the role of these three groups on the factors that affect $C_H(t)$, those are shown in figure 4.9: trap characteristics (reversible or irreversible), hydrogen transport mode (lattice, dislocation or fast path) and location of hydrogen during test (external or internal). Figure 4.10 represents schematically two cases where hydrogen is transported by dislocation

atmospheres: one with the hydrogen source external to the material during mechanical testing and the other where the material has been precharged with hydrogen before testing. The response of the material will be different in each case.

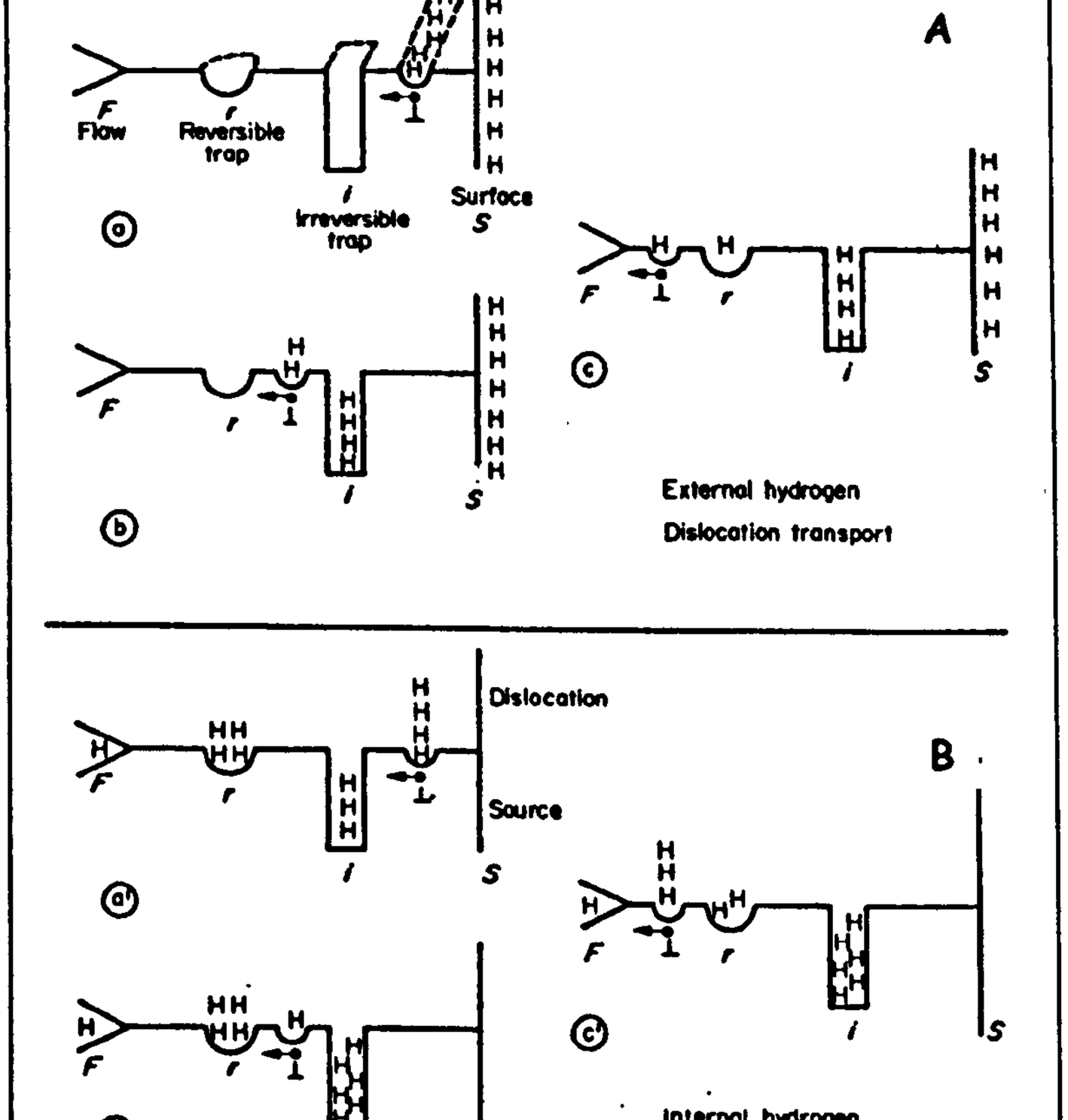

Figure 4.10 *(A)*. External hydrogen atmosphere and transport by dislocations. (a) The dislocation just nucleated at the surface has pick-up hydrogen and moves toward the flaw. (b) On passing over an irreversible trap, i, some hydrogen is lost by the dislocation. (c) Some more hydrogen is lost on the reversible trap, r. The flaws receive little quantity of H. *(B)*. Material precharged and transport by dislocations. (a') Hydrogen is distributed on all traps when the dislocation begins to move. (b') Some hydrogen is lost on the i traps. (c') Because the preceding loss, the dislocation recharges itself on the r trap. The flaw will receive more hydrogen than without the existence of r trap [89].

In the external hydrogen situation, the material is tested mechanically in an atmosphere with hydrogen or other hydrogen source such as corrosion reactions. The dislocations of interest are those nucleated at the surface where they can collect hydrogen. This hydrogen is transported in their atmospheres to the hydrogen free material and has to reach potential flaws for the formation of cracks. Transport by dislocations will provide hydrogen both to irreversible traps (i), and to reversible traps (r) which are initially without hydrogen. Consequently, the dislocations reach the flaw with much less

hydrogen than it collected at the surface. Under this circumstance, it will be more difficult to reach the critical hydrogen concentration (C_K) on the flaw to produce the crack initiation and the material seems to have low susceptibility to hydrogen induced cracking.

In the internal hydrogen situation, the material is precharged with hydrogen before the testing. In this situation, reversible traps (r) and irreversible traps (i) contain hydrogen before the test. The dislocations source may be located anywhere in the lattice or at the material surface. When dislocations are created, they collect hydrogen from the surrounding material. Dislocations move with their hydrogen atmospheres and would introduce more hydrogen to i traps. However, the situation with the r traps could be different. Dislocations that have lost hydrogen on i traps could replenish it when they meet the r traps. Therefore, the replenished dislocation will reach the flaw with more hydrogen than if there had not been r traps. This will result in an increasing chance of nucleating a crack, because is easier to exceed C_K [88, 89].

Application of this theory could explain the different response of a metal to different experimental conditions to study its susceptibility to hydrogen embrittlement. The dual role of the reversible traps could be one interpretation. On the contrary, a fine and homogeneous distribution of irreversible traps would be a method of improving the resistance to hydrogen embrittlement [89].

4.4 Fracture Modes, microstructure and Hydrogen embrittlement

Microscopic observation of fracture surfaces produced by hydrogen induced cracking is an important step in understanding the hydrogen embrittlement mechanisms and to elucidate the role of the microstructure on the promotion and control of the process of hydrogen assisted fracture [5].

The fracture modes found in hydrogen assisted cracking processes include different types: microvoids coalescence (MVC), quasicleavage fracture (QC), and intergranular fracture (IG). For this reason, it is necessary to understand these mechanisms of fracture and identify the relationship between, hydrogen content and microstructure so that the micromechanisms of fracture can be determined. In general, such processes can be divided into nucleation and propagation stages of the fracture event [91]. For example, in the case of MVC the micromechanism is the nucleation, growth and coalescence of microvoids [91, 92]. For the other fracture modes, however, the micromechanism is not clearly defined. Several models have been proposed.

The cleavage fracture of steels containing discrete carbides particles is nucleated by microcracks formed in the carbide particles, but the micromechanism is not established in the case of steels that do not contain brittle second phase particles [93]. Echeverría and Rodriguez-Ibabe [94] studied the brittle fracture of C-Mn-B steel conditioned for both bainitic and martensitic microstructure. They found that the rupture of coarse TiN particles of similar size triggers the brittle fracture. Lambert *et al.* [95] in studies on brittle fracture of a HSLA steel found that martensite/austenite constituents acts as initiators of arrested cleavage cracks. Several investigations have demonstrated that the fracture toughness of low alloy steels is influenced by the called metallurgical factors as prior austenite grain size, bainite packet size, martensite/austenite constituents and carbides [95]. In general, the larger the grain and the bainite packet size the lower the toughness. In the case of the MAC and the carbides, the higher the volume fractions of them could reduce the toughness of the steel.

The intergranular mode of fracture occurs when the grain boundaries are embrittled by the presence of precipitates, impurity phases or impurity elements. The fracture is produced after a minimal mechanical loading [96], which is lower than the required to produce cleavage or MVC. McMahon [97] suggested that the combined effects of hydrogen and segregated embrittling elements at grain boundaries, such as Mn, Si, P and S in commercial steels, cause the phenomenon of hydrogen-induced intergranular brittle fracture of steels. The presence of impurities at the grain boundaries reduces the cohesive strength of the steel and the mobile hydrogen increases this effect. The result is decohesion of the grains at very low stress intensities.

Although a great deal of effort has been made to explain how hydrogen alters or assists the various micromechanisms of fracture there are only qualitative descriptions of these processes. One of them was suggested by Beachem [72]. The author suggested a diagram based on qualitative observation (figure 4.11), where are shown the three factors known to affect the crack growth mode during stress corrosion cracking (SCC) and hydrogen assisted cracking (HAC) of quenched and tempered steels:

(a) The stress intensity factor (K), that depends on the applied stress and the crack geometry

(b) The dissolved hydrogen content (H) in the crack tip

(c) The microstructure

Basically, the model suggests that the presence of enough hydrogen dissolved in the lattice ahead of the crack tip contributes with the deformation and crack propagation processes. These processes depend on the stress intensity (K) and the microstructure. In the figure, the K values and hydrogen concentrations are the ordinate and abscissa, respectively, and the lines represent critical combination of K and hydrogen concentration to produce crack growth by the three fracture modes as determined by the microstructure: IG, QC, and MVC. Cracks would not be expected in the region labelled "NO HAC". The lines that divide the regions of fracture modes depend on the microstructure, but the order of the regions is fixed. These converge at the K_C value, which is the critical fracture stress factor (Kc). H_{IG}, H_{QC}, and H_{MVC} represent the critical hydrogen concentration to allow crack nucleation at the edges of sub-microscopic interfaces (sub-microscopic cracks, interfaces or other defect) by whichever mode. The increase in hydrogen content, in the case of no applied stress, is sufficient to cause cracking. In the case of test specimens or components in service, the applied loads increase the K factor and reduce the amount of hydrogen to produce the crack. During the process the stress intensity factor augments from zero or its initial value to K_C. When K_C is reached, the failure occurs [72].

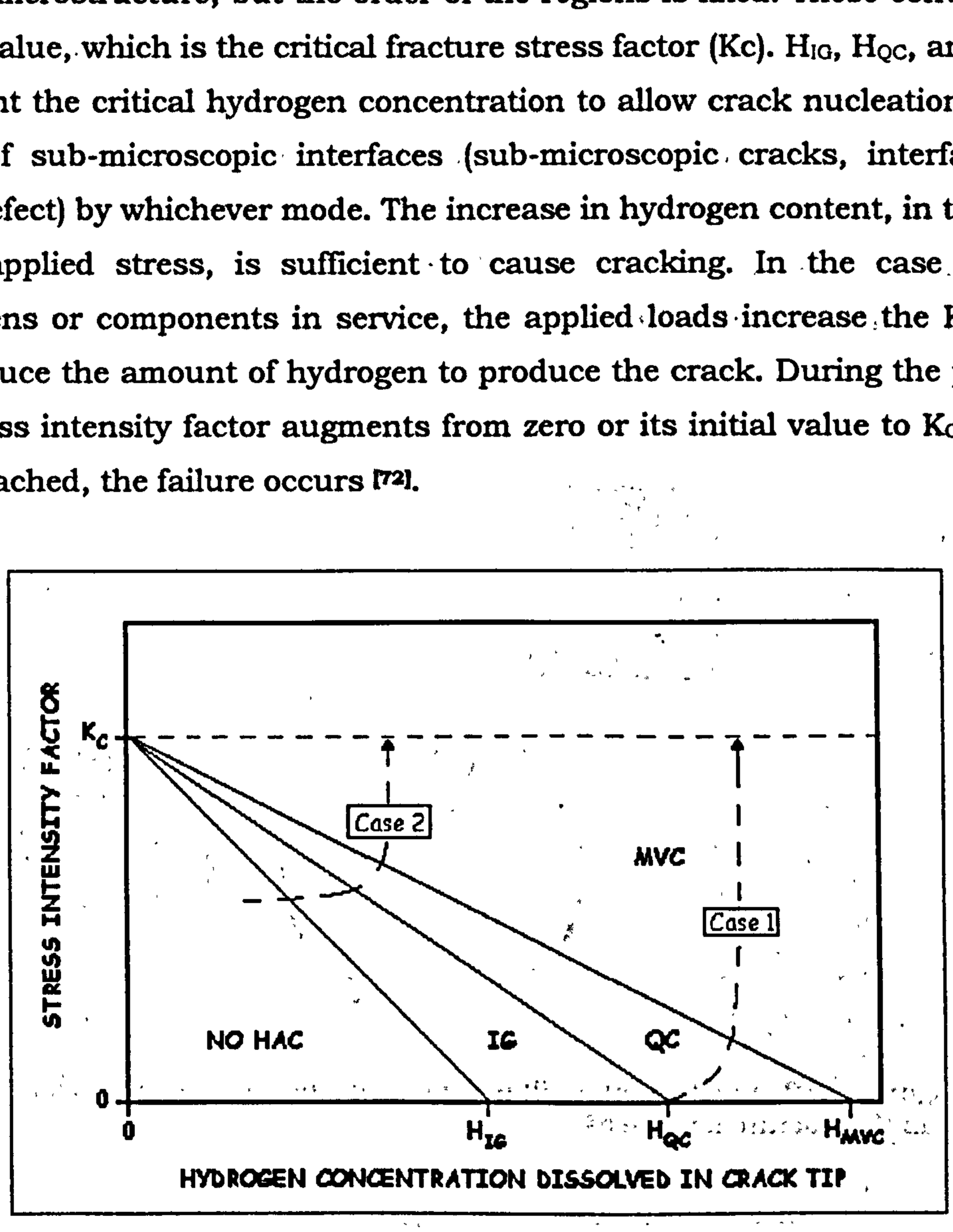

Figure 4.11 Suggested interrelationships between stress intensity factor, dissolved hydrogen content, and HAC mode in microscopically small volumes of crack tip, adapted from Beachem [72].

As examples, two cases are shown in the figure 4.11. The case 1 may explain the changes in the fracture mode with crack growth from the initial QC to final fracture by MVC in low alloy steels, when external stress is not

applied[72]. In this case, the crack growth may be assisted by residual stresses and/or hydrogen pressure. When the conditions reached K_C the failure occurs. Case 2 represents conditions where a pre-cracked or components cracked in service are under stress producing initially a finite value of K. At the beginning, the crack or microcrack has a sub-critical size, is held under constant load and growth does not occur. Then, hydrogen diffuses to the crack tip and consequently the critical condition for IG is reached. HAC initiates and the conditions change continuously through the other modes (QC and MVC) until K_C is reached [72]. Finally, the failure occurs.

The fracture modes observed by Beachem[72] have been observed by other authors, although some differences can be apparent. Ishikawa et al. [98] suggested that a possible mechanism of hydrogen assisted fracture is that cracking starts at the subsurface non-metallic inclusion resulting in a QC facet, followed by an IG facet and MVC region. This is shown in figure 4.12. In this case an inversion of position between the QC and IG regions seems to occur in figure 4.11. However, this behaviour could be explained as follow:

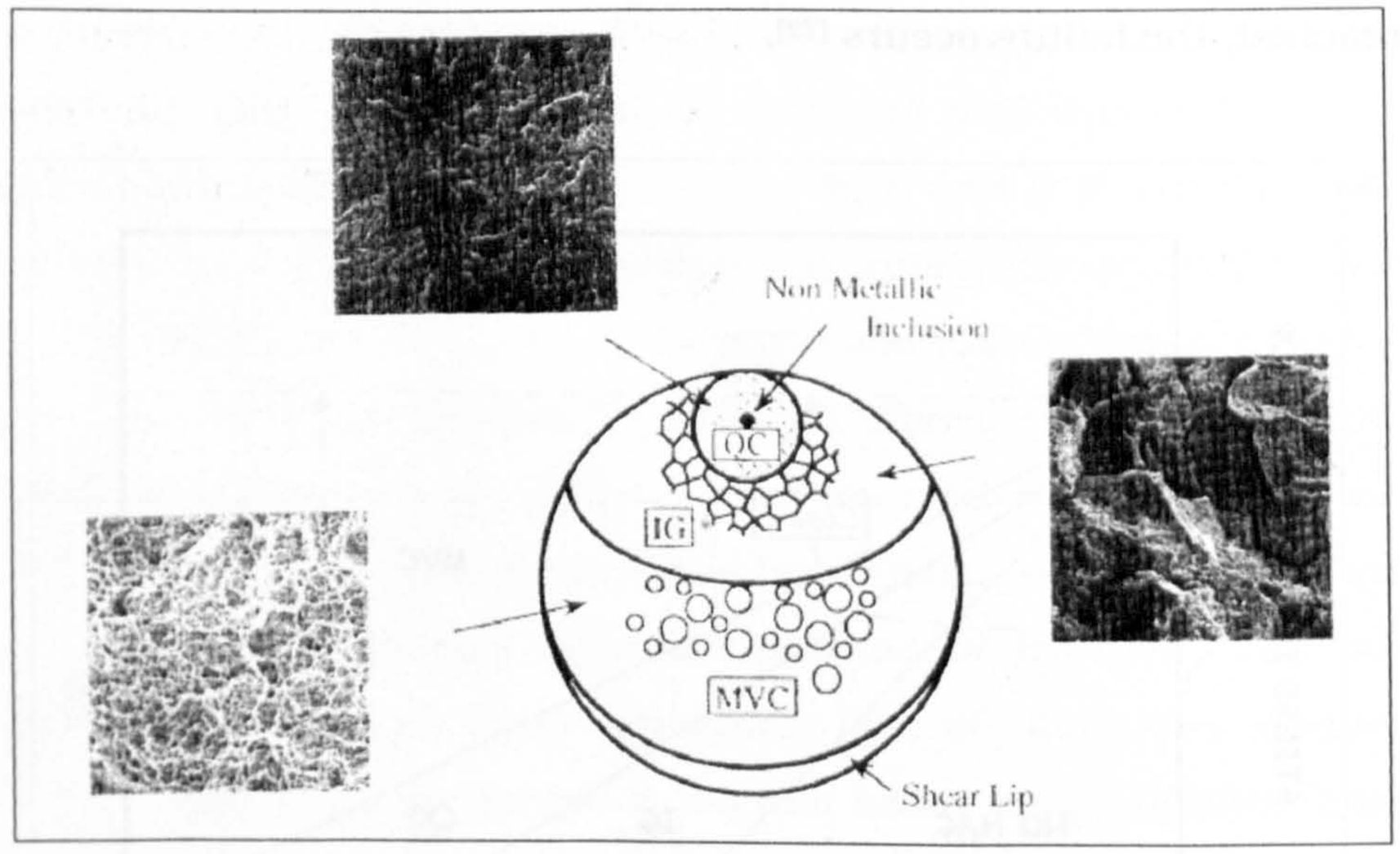

Figure 4.12 Fractographic illustration of the hydrogen cracking process appeared in the fracture surface [98]

a- An accumulation of hydrogen occurs around the inclusion. In this way, the concentration of hydrogen is locally raised and at a certain stress level the crack propagates in a QC mode.

b- Due to the formation of a QC fracture around the NMI, where there was a high hydrogen content, the region ahead of the crack could find lower hydrogen levels and as a consequence

the fracture changes from QC mode to IG mode. The crack grows in an IG form producing an increment of K.

c- The crack continues growing, increasing the stress intensity factor K. This change in K value could occur sharply and as a result the fracture process could proceed under the MVC mode. However, the transition from the IG mode to the MVC should pass through the QC region, but this transition region could be small because the increase in K is large and the conditions for MVC mode of fracture are favoured.

As has been noted, the Beachem's approach, which is qualitative, described the effect of hydrogen content and the stress intensity factor (or the effect of the mechanical loads) on the fracture modes found in HAC processes. However, the model does not take in account the effect of the heterogeneous distribution of hydrogen due to the effect of the microstructure or trapping. The example described above could be one way of taking into account the local accumulation of hydrogen in certain regions of the material, in this case the NMI. Other considerations that are not clearly explained include the effect of different microstructural features, such as grain boundary ferrite, acicular ferrite, bainite, retained austenite, MAC islands and other phases on the fracture mode in the presence of hydrogen. In this investigation an attempt is made to correlate these factors.

Chapter Five

Techniques Used in Hydrogen Measurement, Transport and Trapping Studies

In this chapter, the different techniques used in the measurement of the hydrogen content, transport and trapping are described. The first section treats briefly the classical techniques related with the measurement of the potential hydrogen levels (those in consumables, fluxes and shielding gases) and the hydrogen content in welds (after the welding process). These techniques have been used to classify the welding methods and the consumables on the basis of the different risks of producing hydrogen induced cold cracking or HICC.

Later sections deal with the experimental techniques to determine hydrogen transport and trapping, which are of great importance in understanding the process of hydrogen diffusion and distribution in the material and its effect on the mechanism of failure and assistance to crack growth. It is generally accepted that diffusible hydrogen is responsible for the reduction in ductility and toughness. On the contrary, the trapped hydrogen could have different effects:

1- The trapping of hydrogen could reduce the risk for embrittlement due to the reduction in diffusible hydrogen.
2- The trapped hydrogen could be transformed to diffusible hydrogen. In this case the traps act as a source of hydrogen and this may increase the risk for embrittlement
3- The trapped hydrogen could exceed a critical concentration for the microstructure and as a consequence of the local stresses cracks are initiated in this site, crack growth is then assisted by diffusible hydrogen liberated from the trap.

A knowledge of the critical hydrogen content to produce embrittlement, its diffusion paths and trapping sites for different weldment microstructure could elucidate ways of improving the resistance to hydrogen induced cold cracking of a welded alloy.

5.1 Classic techniques to measure hydrogen content.

There are several techniques in this field but they can be classified into two groups: those that measure the potential level of hydrogen that could be found in the weld and those that produce information about the levels of hydrogen after welding.

5.1.1 Measurement of potential hydrogen levels

These techniques include those that measure the moisture in the electrode coatings, welding fluxes and shielding gases. These moisture levels are related with the amount of hydrogen that is potentially available for absorption in the weld pool during the welding process. For this reason, these procedures allow a classification of the consumables and welding processes with respect to the potential risk of introducing certain quantities of hydrogen in the weldment. Depending on the susceptibility of the steel to HICC, the methods are selected to reduce the risk for cold cracking. In table 5.1 several consumables and fluxes are compared with respect to the potential hydrogen levels that can be produced.

Table 5.1 Typical potential hydrogen levels produced for different consumables and fluxes. Adapted from Bailey [6]

Electrodes or Fluxes	Moisture Content (% by weight)
Consumables	
Cellulosic type	10.0
Rutile type	3.50
Basic type (re-baked)	0.075
Fluxes	
Agglomerated submerged-arc	0.050
Fused submerged-arc	0.035

In the selection of a method for welding not only has the data from table 5.1 to be taken in account but also the atmospheric humidity where the welding process is being applied. The principles used for the measurement of potential hydrogen are shown in table 5.2. For more detailed description the reference of Bailey et.al.[6] is recommended.

Table 5.2 Techniques used for the measurement of potential hydrogen produced by consumables and fluxes. Adapted from Bailey [6].

Measurement	Principle
Moisture in electrode coatings and fluxes	The sample is ignited in the presence of pure dry oxygen and the water produced in the process is absorbed and weighed.
Moisture in shielding gases	An electrolytic hygrometer is used
Hydrogen potential of welding consumables by encapsulation	The consumable is encapsulated in a mild steel container that allows fast hydrogen effusion at high temperatures. The hydrogen that evolved from the capsule is measured.

5.1.2 Measurement of weld metal hydrogen levels

This type of measurement is used to determine the quantity of hydrogen that is absorbed during the welding process. They are generally used to characterise the welding consumable, under standard conditions, based on the hydrogen levels in the weldment. Using these methods the diffusible, the residual (trapped) and the total hydrogen content could be measured. A knowledge of these factors is of vital importance in revealing the susceptibility of the weldment to hydrogen cracking and the risk of the process in producing this failure.

Table 5.3 Typical weld hydrogen levels for different consumables and welding processes. Adapted from Bailey [6]

Welding process or consumable	**Hydrogen amount (mL/100g of metal)**
Covered electrode, rutile coating	20.0-30.0
Cored wires	2.50-12.5
Submerged arc	2.50-12.5
Covered electrodes, basic coating	2.50-10.0
Gas shielded metal arc, Ar & CO_2	1.0-5.0

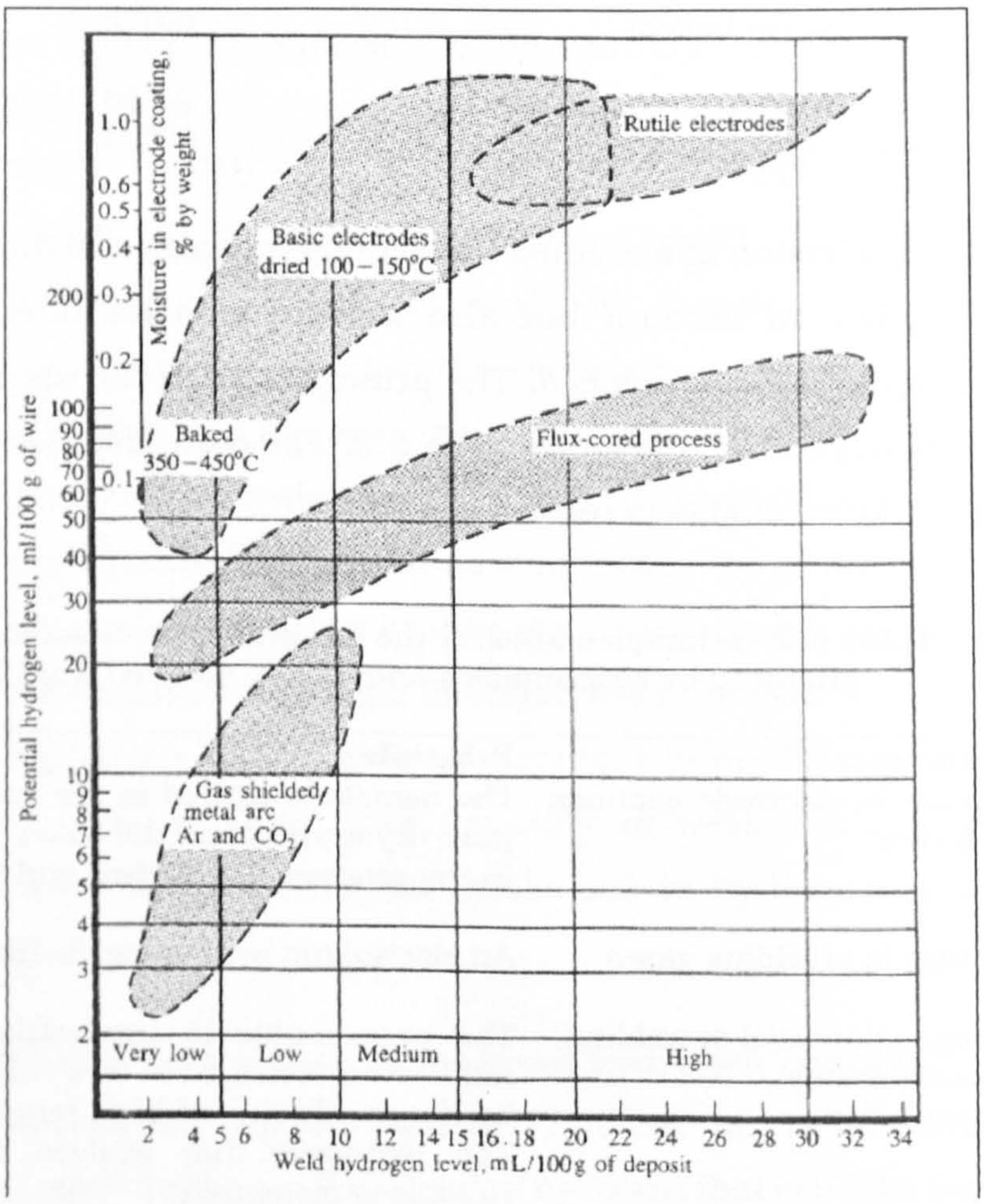

Figure 5.1 Relationship between potential hydrogen levels and weld hydrogen content for different consumables and welding processes [6]

In table 5.3, the typical hydrogen levels obtained for different consumables and welding processes are shown. The highest values of hydrogen are the result of the use of rutile coatings in covered electrodes. The lowest hydrogen levels are reached using gas shielded metal arc (Ar and CO_2). Figure 5.1 summarises the hydrogen levels in weldment obtainable with different consumables and welding processes. This classification can be used as a guide for the selection of the process. At the bottom of this figure the levels of hydrogen are classified as very low, low, medium and high. This does not mean that the risk to HICC corresponds to this hydrogen levels, the risk also depends on the microstructure of a specific alloy. The graph only gives some indication of the quality of the consumable or the welding process necessary to achieve the shown hydrogen level.

Table 5.4 summarises the two most common methods of measuring diffusible, residual and total hydrogen content in weld beads after the welding process has been applied. Other techniques based on the same principles have been used to measure the hydrogen content in a weld [7]:

a- The glycerine replacement method, which immerses the weld sample in glycerine bath at 45°C for 48 h

b- The silicone oil replacement method, which uses this liquid as an immersion media at 100°C for 90 min.

c- The gas chromatography method, which involves placing a sample in a chamber at 150°C, filled with argon as a gas carrier. The hydrogen is transported to a chromatograph, where is analysed.

Table 5.4 Techniques used for the measurement of diffusible hydrogen produced in welds. Adapted from Bailey [6]

Measurement	Principle
Determination of diffusible hydrogen in ferritic steels BS 639 Parts 1-5	A single weld bead is deposited under carefully controlled conditions and then quenched. The weld is immersed in mercury at room temperature and its diffusible hydrogen content is measured by volumetric methods and reported as hydrogen volume per mass of either deposited or fused metal.
Determination of diffusible, residual or total hydrogen in ferritic steel weld metals	A single weld bead is deposited under carefully controlled conditions and then quenched. To measure the diffusible hydrogen the sample is analysed at room temperature. To measure the residual hydrogen the samples are heated to 650°C to extract the hydrogen. In both cases the hydrogen content is determined volumetrically using vacuum apparatus or an inert carrier gas technique.

5.2 The determination of hydrogen distribution in welds

During the welding process, hydrogen is introduced in the weld pool from the consumable, the atmosphere or impurities on the surface of the parent plate. During cooling this hydrogen diffuses through the microstructure in the weld metal and the HAZ of the weldment. Depending on the different microstructures and the stresses in these regions the hydrogen could be heterogeneously distributed, due to differences in the diffusion coefficient and solubility. Moreover, the existence of voids, inclusions and microphases, such as retained austenite and MAC islands, could contribute to the non-uniform distribution of the hydrogen in the weld. As a consequence the hydrogen becomes trapped and distributed in specific regions of the weldment. For example, the hydrogen content in the HAZ could reach higher levels in comparison with the weld metal. The opposite could well occur. For these reasons, methods of determining the hydrogen distribution have been designed.

The determination of the local accumulation of hydrogen in steel welds has been experimented by several methods [7]:

a- Microsectioning of different weld zones at low temperature followed by hydrogen extraction.

b- Bubble counting on the polished cross-section of a weld covered by a thin film of glycerine

c- Microprinting of a polished cross-section utilising a neodymium film or an emulsion silver bromide, normally used in conjunction with the radioactive isotope, tritium, of hydrogen.

d- Spot fusion of a weld cross-section by laser beam followed by mass spectrometric analysis of evaporated hydrogen.

These methods must be capable of measure the hydrogen content in small and localised regions of the weldment and this objective is best reached producing the local evolution of hydrogen using a concentrated heating, for example, a laser beam. Between them are the following:

1- Laser Induced Breakdown Spectroscopy (LIBS)

2- Laser ablation/ Gas Chromatography (LA/GC)

3- Laser ablation/Mass Spectrometry (LA/MS)

These three techniques were evaluated by Smith et al.[99] and their results shows that the more suitable of the methods was LA/MS. This method can detect very low hydrogen concentration and it is capable of distinguishing between the isotopes from deuterium gas (D_2), which is used as a hydrogen

tracer, and those from other sources, such as contaminants on the weldment surface. Using this technique it is possible to obtain qualitative hydrogen profiles that are consistent with the theory of non-uniform hydrogen distribution in welded steel as a function of differences in microstructural transformation. Figure 5.2 shows schematically a result of the hydrogen distribution for a gas metal arc welded 100 HSLA steel using 0.5% D_2/Ar shielding gas, obtained by Smith and collaborators [99].

Smith et. al.[100] developed a hydrogen sensor that permits the detection of hydrogen in the actual welded structure and in short times (less than an hour). The sensor is based on the chemochromic reaction (colour change due to a chemical reaction) of certain transition metal oxides with hydrogen in air. The reaction is catalyzed by a thin film of Pd or Pt on the WO_3 oxide film, which is sensitive to hydrogen. Both films are deposited on a polymer optical fiber. The changes are detected visually or spectroscopically. The sensor promises to be an excellent device to detect hydrogen in welds and the distribution of it, provided an array of sensors is used. However, refinement of the design is needed to improve the performance of the detector in the field.

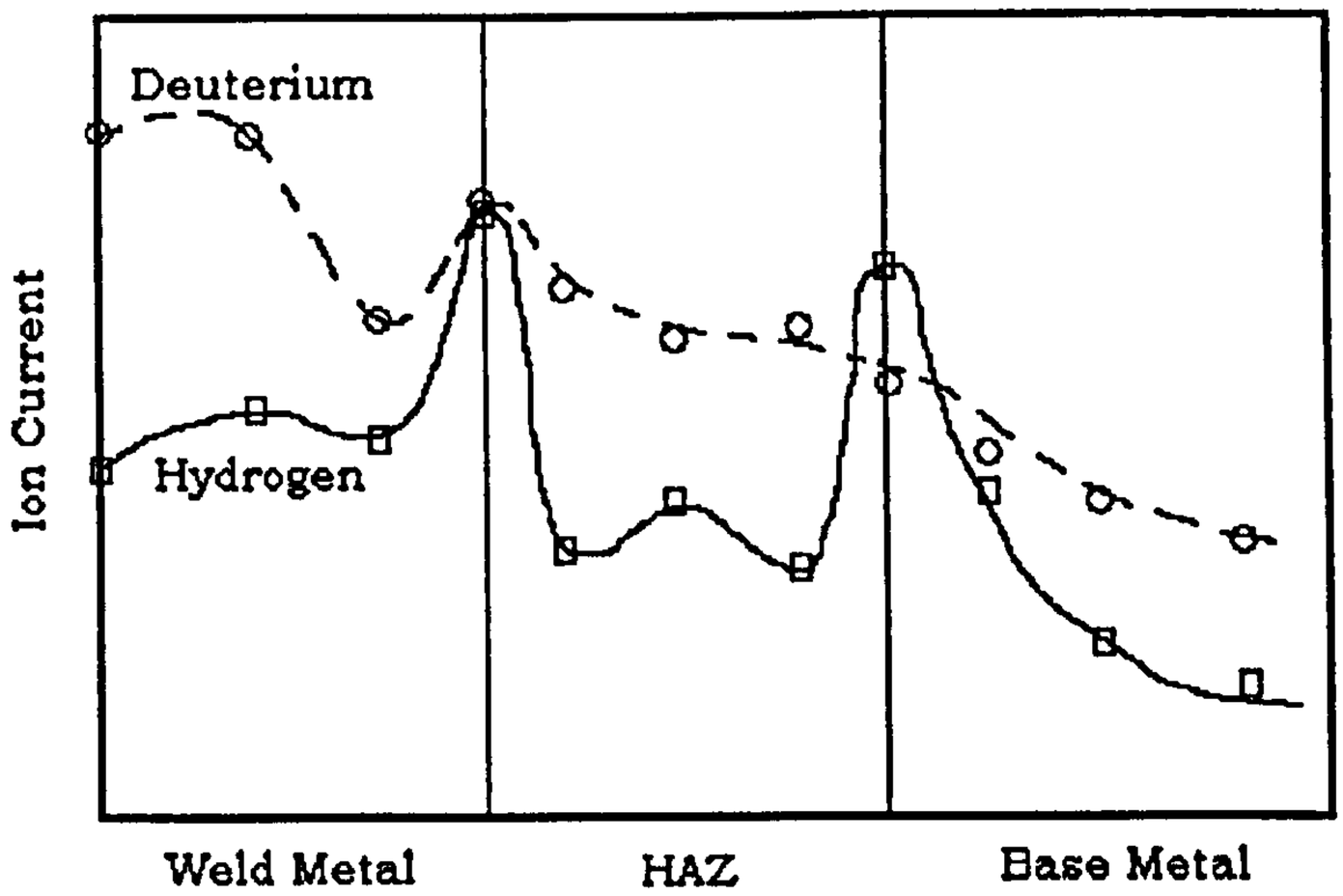

Figure 5.2 Schematic representation of a LA/MS hydrogen/deuterium distribution profiles for gas metal arc weld. Adapted from Smith[98]

5.3 Electrochemical techniques to study H diffusion and trapping

In this section, some electrochemical techniques to study the hydrogen diffusion process and hydrogen trapping in metals and alloys are briefly described. Attention is concentrated in a complete description of the technique and analysis of data proposed by Pound and collaborators [101-105] because this technique is used in the present investigation to qualitatively characterise the trapping behaviour of the different weld metals used in this research.

Measurements of hydrogen "on" and hydrogen "in" metals has been the subject of several investigations. The metal surface could be corroding or dissolving anodically while H from the surface is studied. The fundamentals of some of these techniques are described briefly as follow:

(a) *The Fourier Transform Infrared Spectroscopy (FTIR) approach to surface hydrogen.* It was found by Bockris et al. [80] for H on Fe that FTIR determinations could distinguish two peaks which corresponded to those expected for vibrations of H chemically bonded to Fe. This technique is used to determine the surface coverage of adsorbed hydrogen atoms per unit area (θ_H). Low and accurate numerical values of θ_H could be obtained, but the method gives $\partial \ln \theta_H / \partial V$, which is an indicator of the mechanism of adsorption [80].

(b) *Devanathan-Stachurski (D-S) Permeation Method for Internal Hydrogen.* This method gives the diffusivity of H (D_H) in the metal and the concentration of H just below the surface of the Fe ($C_{O,H}$) which are useful in the study of the diffusion and trapping of H in the metal. A thin Pd membrane is used to protect the anodic side of the Fe. The method allows the determination of $C_{O,H}$ and the partial molar volume of hydrogen in metal ($\overline{V}_H$) as a function of potential, surface occupation by inhibitors, etc. The permeation-time (P_H-t) data indicates the potential region in which the metal breaks down due to the onset of internal cracking: before that potential, it is reversible, but afterwards the P_H-t relations cannot be repeated [80].

(c) *Determination of internal H by means of Laser-Pulse evaporation.* A laser is used to evaporate holes of about 20 μm diameter. The H_2 released is registered on a mass spectrometer. The Fe and steel specimens are precharged with H at various fugacities. This method gives the concentration of H in the metal at a controlled spot and at a controlled depth. It is helpful in finding the distribution of H, for example, near points of stress [80]. This technique was described above, in the section 5.2.

(d) *Double pulse approach.* H_2 is evolved on the metal at a chosen over-potential (η), and two constant-current potential-time measurements are then recorded. In the first, the potential from which the anodic sweep starts is produced when the over-potential (η) is eliminated. The anodic current during this pulse involves that from the dissolution and re-oxidation of H and that from the dissolution of Fe. A second pulse is then made which starts from an anodic region and therefore involves only dissolution of Fe. Both signals are subtracted and the signal corresponding to the re-oxidation of hydrogen is obtained. Electrochemical kinetic equations allow a basic coulometric value of θ_H (the hydrogen coverage) to be derived, but the determination involves an iterative procedure [80].

5.4 A Potentiostatic double-step method for measuring hydrogen atom diffusion and trapping in metals.

Pound *et al.* [101-105] proposed a general model to study experimentally and mathematically the effect of trapping on the diffusion of hydrogen by modifying Fick's second law of diffusion. The modification takes in account the effect of hydrogen trapping. Experimentally, the metal electrode is polarised as shown in figure 5.3 which shows the potential step programme and the resulting current transient. E_A is slightly below the corrosion potential (E_{corr}) to minimise the effect of corrosion of the metallic electrode. The experiment commences by stepping the cathodic potential to E_c for a period t_c, the charging time, during which the steady cathodic current, i_c, will flow and the electrode becomes charged with H atoms. Then the electrode potential is stepped in the positive direction back to E_A, and the anodic current transient is recorded during a period of time, t' [101].

Mathematically, the modification of Fick's law is made to include a trapping term, k·c, in which the rate of trapping is assumed to be proportional to the concentration c(x,t) of diffusing hydrogen.

$$\frac{\partial c}{\partial t} = D\frac{\partial^2 c}{\partial x^2} - k \cdot c \qquad (5.1)$$

The density of traps and the probability of capture of hydrogen by a trap determine the magnitude of the trapping rate constant (k). Several assumptions and boundary conditions are necessary in this model because the short time used in the experiments:

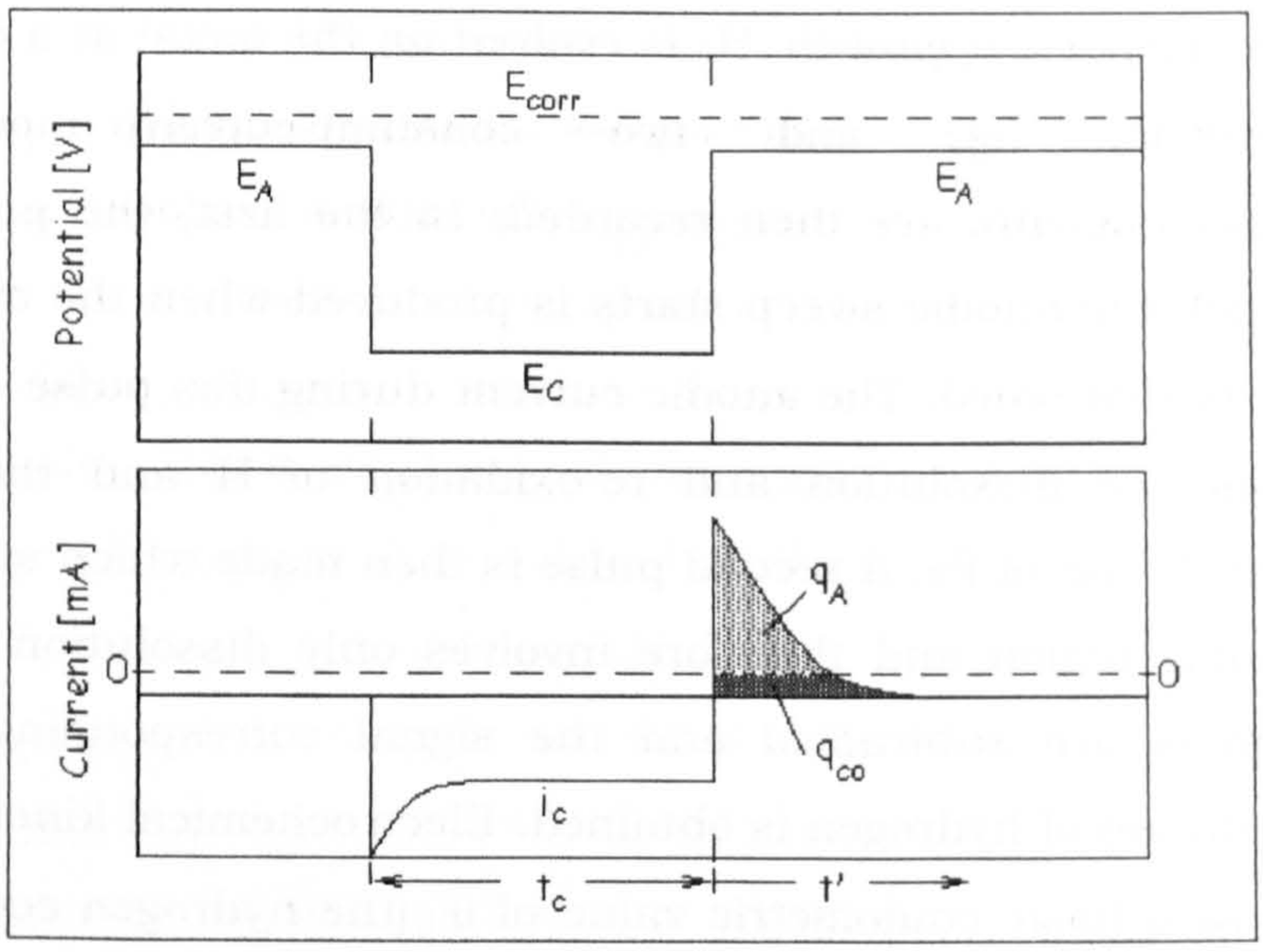

Figure 5.3 Schematic potential programme and expected current response during the double potentiostatic pulse experiment. q_A is the anodic charge value read from the digital coulometer, and q_{co} is the charge correction arising from the small cathodic current. Modified from Pound [101]

(a) The trapping is irreversible and for this reason, there is no significant release of H atoms from the traps.

(b) The traps are not considered to become saturated. This implies that k must be a constant.

(c) Mass balance at the interface requires that the difference between the H flux into and out of the metal is balanced by the diffusion flux carrying hydrogen into the bulk metal, i.e.

$$k_{in}\theta = k_{ex}c(0,t) - D\left(\frac{\partial c}{\partial x}\right)_{x=0} \qquad (5.2)$$

where the term $k_{in}\theta$ is the flux into the metal, $k_{ex}c(0, t)$ is the flux out of the metal, and θ is the surface coverage of adsorbed hydrogen atoms per unit area.

(d) The ingress flux $k_{in}\theta$ is considered constant at a given charging potential E_c.

The diffusion equation 5.1 is solved analytically for two cases that are characterised by the rate-determining step for the transfer of adsorbed hydrogen into the metal during the cathodic reduction. These cases are: diffusion control and transfer control. In this investigation, it is assumed that the diffusion control operates in the cases that were studied. Further justification is made in following chapters.

I.- Diffusion control case

In this case, H atom transfer across the iron/electrolyte interface is very rapid. The H concentration just below the metal surface is assumed in equilibrium with the adsorbed H layer, and reaches the C_S value almost instantly after the polarisation at E_c. This is due to the small value of the second right hand side term in equation 5.2, which gives the relation:

$$k_{in}\theta = k_{ex}c(0,t) = k_{ex}C_S \tag{5.3}$$

The rate of hydrogen ingress is then controlled by the diffusivity of H in the metal. The non-dimensional anodic current I', and charge Q', as a function of time after stepping back to E_A have been calculated:

$$I'(T') = \frac{e^{-R\cdot T'}}{\sqrt{\pi\cdot T'}} - \frac{e^{-R\cdot(1+T')}}{\sqrt{\pi\cdot(1+T')}} - \sqrt{R}\cdot\left(erf\sqrt{R\cdot(1+T')} - erf\left(\sqrt{R\cdot T'}\right)\right) \tag{5.4}$$

$$Q(T') = \left[\frac{1}{2\sqrt{R}} + \sqrt{R}\cdot T'\right]\cdot erf\sqrt{RT'} + \sqrt{\frac{T'}{\pi}}\cdot e^{-RT'} - \left[\frac{1}{2\sqrt{R}} + \sqrt{R}\cdot(1+T')\right]\cdot erf\sqrt{R\cdot(1+T')} - \sqrt{\frac{1+T'}{\pi}}\cdot e^{-R(1+T')} + \left[\frac{1}{2\sqrt{R}} + \sqrt{R}\right]\cdot erf\sqrt{R} + \frac{1}{\sqrt{\pi}}e^{-R} \tag{5.5}$$

In these equations I', Q', T' and R are non-dimensional terms of current, charge, time and trapping rate constant respectively, defined as follows:

$$I' = \frac{i'}{F\cdot c_s\sqrt{\frac{D}{t_c}}} \tag{5.6}$$

$$Q' = \frac{q'}{F\cdot c_s\sqrt{D\cdot t_c}} \tag{5.7}$$

$$T' = \frac{t'}{t_c} \tag{5.8}$$

$$R = k\cdot t_c \tag{5.9}$$

where i' is the current density at the surface of the metal at time t' after the anodic step from E_C to E_A. q' is the charge consumed in oxidising the diffusional hydrogen [101].

II.- Interface control

If the rate of transfer of hydrogen atoms across the interface is very slow, then this process controls the velocity of hydrogen ingress. Under these conditions of interface control, the second term on the right hand side of equation (5.2) is dominant. Then the following relation is obtained:

$$k_{in}\theta = -D\left(\frac{\partial c}{\partial x}\right)_{x=0} = J \qquad (5.10)$$

where J is the hydrogen ingress flux which is constant for a given value of E_C. At sufficiently long times, the assumption of a constant concentration gradient at the surface may not be valid. On the contrary, the concentration immediately below the surface, c(0,t), could approach the equilibrium value (C_S) and a transition to diffusion control could then occur.

5.5 Utilisation of the potentiostatic double-step method.

The double step method or the potentiostatic double pulse (PDP) technique has been used by Pound [102-105] in the study of different alloy systems:

a- High strength alloys: AISI 4340 steel, Monel K500 and MP35N
b- Work-hardened alloys: Inconel 625 and Hastelloy C-276.
c- Precipitation-hardened alloys: Inconel 718, Incoloy 925 and 18Ni maraging steel.
d- High strength steels: AISI 4340, AerMet 100 and H11.

In all these cases, Pound has tried to relate the value of the trapping rate constant (k) with the hydrogen embrittlement susceptibility and the trap population in the alloy. In the study for high strength alloys the author found a close relation between the MnS inclusion density and the density estimated from the value of k using the following equation:

$$k = \frac{4\pi d^2 N_T D_L}{a} \qquad (5.11)$$

These estimations were made under the assumption of spherical traps of radius d and a surface area $4\pi d^2$. N_T is the concentration of traps and "a" is the diameter of the metal atoms. If the value of the diffusivity constant in the lattice (D_L) is known the k value could be related to the N_T. In the case of the steel 4340, the MnS density, which are assumed to be the principal traps acting in the steel, was estimated around $2\ 10^8\ m^{-3}$ and the determined through metallographic characterization was $2\ 10^9\ m^{-3}$. However, for the case

of the Monel alloy K500 and the alloy MP35N this value was uncertain. For the last two alloys the traps were assumed to be sulphur and phosphorous clusters at grain boundaries [102]. Table 5.5 present a summary of the results reported by Pound [103-105] for the values of k for different alloy systems and the irreversible traps identified to be related to k.

Pound [101-105] associated the k value for the different alloy systems to the intrinsic susceptibility of the alloy to hydrogen embrittlement (HE). As a general rule, the higher the value of k the higher is the susceptibility to HE. Following this tendency it could be expected that the susceptibility to HE decrease from the steel 4340 to the annealed AerMet 100 alloy. In some cases, where the values of k show only a small difference, the tendency to embrittlement is similar for two alloy systems.

Table 5.5 Irreversible trapping constant for different alloy systems obtained by the PDP technique [103-105]

Alloy	k (s^{-1})	Irreversible Trap
4340 steel	4.0	MnS inclusions
H11 steel	3.5	MnS inclusions
18 Ni maraging steel	1.50	TiC/Ti(CN) particles***
AerMet 100 (482°C aged)	0.66	M_2C carbides (M=Cr, Mo)****
AerMet 100 (270°C aged)	0.44	Fe_3C rod-shaped carbides
Inconel 718	0.128	NbTi(CN) particles
Hastelloy C-276 (27% c. w.)	0.090	P at grain boundaries
Monel K500	0.040	S and P impurities*
Incoloy 925	0.034	TiC particles
MP35N	0.026	S and P impurities*
Hastelloy C-276 (27% c. w.)	0.019	Unidentified**
Inconel 625 (17% c.w.)	0.014	NbTi(C) particles
AerMet 100 (annealed)	0.000	No irreversible traps

* The inconsistency was attributed to segregation and clustering of S and P
** These are unidentified quasi-irreversible traps that saturates
***This alloy presented a quasi-irreversible traps with a higher k value (k=3)
****Very small Fe_3C rod-shaped carbides could be found

Another effect that is worthy of mention from table 5.5 is the effect of the aging temperature on the trapping constant for the AerMet 100 alloy. As can be seen the increase of the aging temperature from 270 to 482°C increase the k value [105]. This could be attributed to the precipitation of the M_2C type carbides which increases the population of irreversible traps. The annealed alloy presented a k value of virtually zero. Moreover, in the case of the 4340 steel with different heat treatment to obtain higher yield strengths, it was found that the k value increases with the increasing strength [105]. This is probably associated with some variation in the microstructure.

As can be observed, the determination of k could be used as an index of susceptibility to hydrogen induced cold cracking. However, the interpretation of results needs careful analysis for the following reasons:

a- The value of k is a trap constant that reflects the effect of irreversible and reversible traps. It is very difficult to separate the effect of both types of traps and within each type different trap quality and quantity could be present. For this reasons, to determine which group of hydrogen traps are producing a predominant role to produce the hydrogen embrittlement effect is not easily possible. Moreover, it is recognised that the diffusible hydrogen is responsible for the embrittlement effect and that the traps could be simple hydrogen sources or sinks, although they could be located in a susceptible microstructure to form cracks and in which case they may act as crack initiators.

b- The k value has been related to irreversible traps such as MnS in steels, some carbides and carbo-nitrides in steel and other alloys and in some Cu-Ni alloys with segregated S and P. Although these play an important role in the hydrogen assisted cracking process, they should not be taken as the only sites for crack initiation. The microstructure of the alloy has an important influence in the initiation and propagation of cracks: interfaces and inter-phases regions, retained phases, voids and micro-shrinkages, micro-cracks, dislocation arrangements, etc. This list could be expanded and taken into account to analyse the susceptibility of the alloy to HIC or HICC.

c- The suggestions made by Pound have certain degree of disagreement with the theory of hydrogen trapping mentioned in the previous chapter. It is accepted by that theory that the presence of irreversible traps homogeneously distributed in the material could be beneficial to the resistance to hydrogen embrittlement. This is due to the beneficial effect of the distribution of hydrogen in those traps reducing the diffusible hydrogen that is signalled to be the responsible of the reduction in ductility of the material, as was mentioned previously.

To overcome the effect of the reversible traps on the value of k, which is defined as the apparent irreversible constant, Pound[103-105] suggests a relation between k and k_i, the irreversible trap constant:

$$k_i = k\frac{D_a}{D_L} \tag{5.12}$$

where D_a is the apparent diffusivity constant for the alloy and D_L is the lattice diffusivity constant. The first has to be determined using permeation methods for the alloy in study and the second diffusivity constant has to be determined or estimated for the equivalent high purity alloy where some elements have been removed to eliminate their influence on the diffusion of hydrogen through faster paths such as grain boundaries, interfaces, etc.. In any case, to estimate the k_i value from the apparent irreversible trap constant, k, determined experimentally, specific diffusion data is required. In some cases this data may not be available and should be determined in the laboratory.

CHAPTER SIX

EXPERIMENTAL METHODOLOGY

6.1 The weld metal and welding process

The weld metals used in the present work were selected and designed by Wildash[8] in a previous work; two types of consumables were available: commercial and modified. These had produced different microstructures and this allowed study of their effect on the HICC resistance. A detailed description of the experimental methodology is described elsewhere [8-11]. Sections 6.1.1 to 6.1.4 summarises the procedures followed and are included in this text due to the importance of defining the microstructure, the mechanical properties and the resistance to HICC of the several weld metal studied in this investigation.

6.1.1 Welding Procedure

The welding process used to obtain the different weld metal utilising both commercial and modified consumables was Gas Metal Arc welding (GMAW). The general welding conditions applied are shown in the table 6.1. Other welding parameters are shown in the tables A.2 and A.3 in the annexes. The tensile samples were obtained from the final weld bead made over the groove machined into the cladding, as is shown in figure 6.1.

Table 6.1 Welding conditions applied to each weld bead of the cladding and each final weld bead, deposited in the machined groove, where a heat input of 1.0 kJ/mm was required. Data from Wildash [8]

Parameter	***Value***
Preheat (°C)	150
Heat Input (± 0.2 kJ/mm)	1.0
Polarity	DC + or -, Appendix A [6]
Shielding gas Composition	Argon 80% - CO_2 20%
Shielding gas flow (L/min)	21
Stand off (mm)	15
Arc Mode	Dip or spray transfer
Current (A)	188 ± 4
Potential (V)	27.0 ± 2.5

After application of the final weld bead, the weld metal was degassed for 20 h at 150 °C. Tensile samples were then obtained from the fusion zone of the final weld bead and charged with hydrogen as described later.

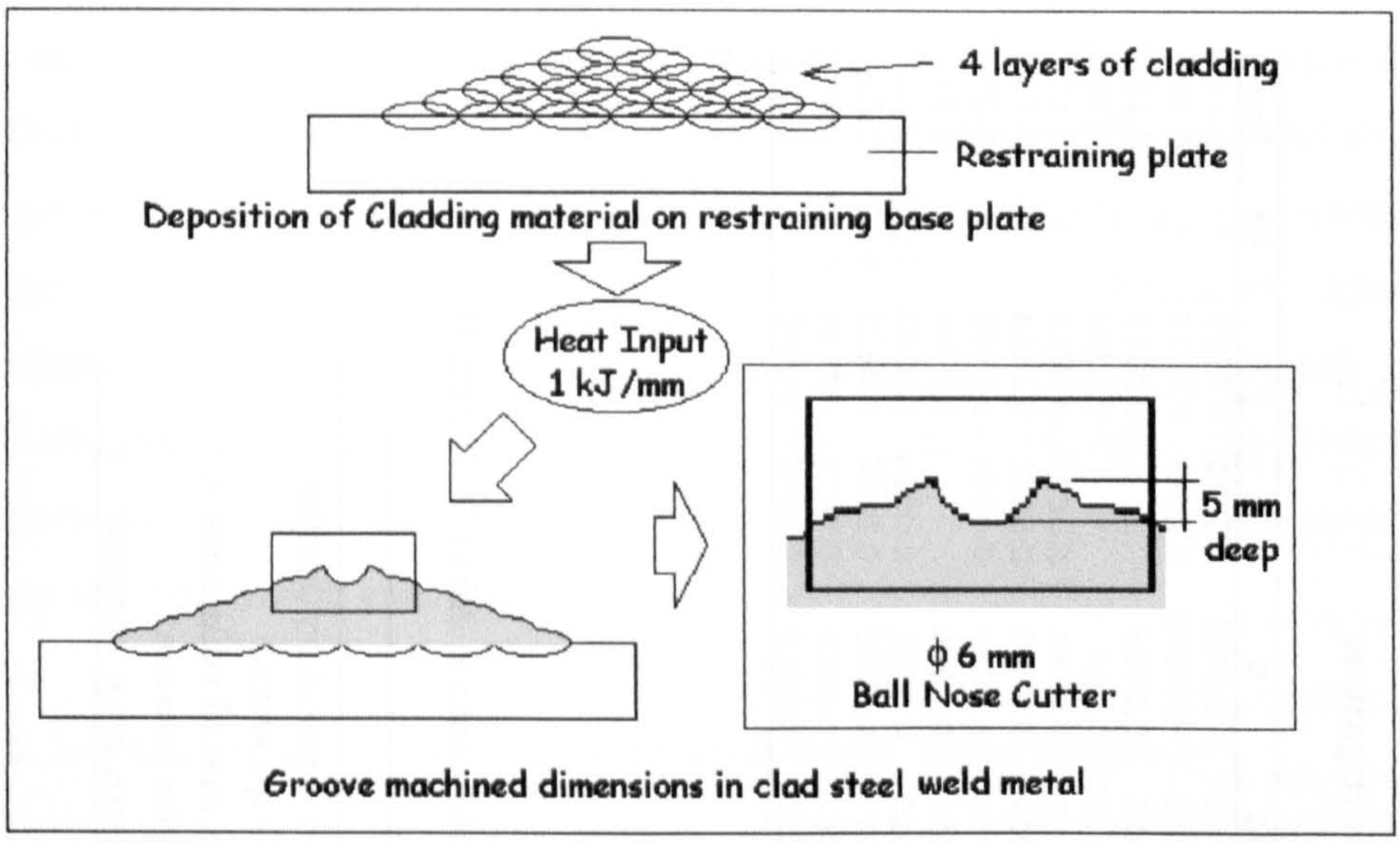

Figure 6.1 Procedure to obtain the tensile sample of every weldment. Adapted from Wildash [8].

6.1.2 Weld Metal Composition

The composition of the weld metals obtained using commercial and modified consumables are shown in table 6.2. The commercial consumables are those with the following identification: 15171, 14001, and 14031. The so-called modified consumables are those with the identification number preceded by CWX or VCX. In the table the P_{cm} value was calculated using the equation:

$$P_{cm} = \%C + \frac{\%Mn + \%Cr + \%Cu}{20} + \frac{\%Si}{30} + \frac{\%V}{10} + \frac{\%Mo}{15} + \frac{\%Ni}{60} + 5 \cdot \%B \qquad (6.1)$$

The weld metals were divided by Wildash [8] into 5 groups as is shown in the table 6.3, presented here as a reference. This table shows roughly the effect of consumable composition on the microstructure. This could be used as a guide and does not limit comparison between weld metals of different groups. In tables A.2 and A3 (annexes) the different weld metals are classified as basic, metal cored and rutile depending on the consumables types.

6.1.3 Hydrogen Charging

Hydrogen charging of the tensile test samples was carried out electrochemically by Wildash [8]. The detailed procedure is found in his work. The principal variables are presented here as a reference.

Table 6.2 Chemical composition for weld metal studied in this investigation.

Wid	C	Si	Mn	P	S	Mo	Cr	Ni	Cu	Nb	V	Ti	Al	B	N	O	Ce	Pcm
CWX181gb	0.037	0.31	0.93	0.008	0.009	0.006	0.02	0.87	0.015	0.011	0.020	0.03	<0.005	<0.0005	0.0080	0.0559	*	0.11
CWX351	0.083	0.56	0.25	0.010	0.009	0.005	0.02	0.04	0.02	<0.005	0.007	0.007	0.012	<0.0005	0.0049	0.0816	*	0.12
14001	0.046	0.67	1.25	0.013	0.009	<0.005	0.02	0.02	0.02	<0.005	0.009	0.007	0.013	0.0006		0.0818		0.13
15171	0.058	0.29	0.86	0.011	0.006	<0.005	0.02	0.94	0.01	0.012	0.020	0.020	<0.005	0.004		0.0536		0.15
VCX2561	0.059	0.28	0.99	0.011	0.009	0.009	0.04	1.02	0.010	0.012	0.020	0.02	<0.005	0.0060	0.0068	0.0511	*	0.17
CWX361	0.079	0.52	0.74	0.010	0.009	0.590	0.02	0.03	<0.01	<0.005	0.010	0.009	0.019	0.0005	0.0051	0.0681	*	0.18
CWX201	0.059	0.34	1.64	0.009	0.007	<0.005	0.02	1.02	<0.010	0.018	0.030	0.04	<0.005	0.0050	0.0044	0.0408	*	0.20
14031	0.037	0.47	1.59	0.008	0.009	0.54	0.02	1.75	<0.01	<0.005	0.009	0.007	0.013	0.0006		0.0744		0.20
CWX71	0.046	0.51	1.56	0.009	0.010	0.56	0.02	1.89	<0.010	<0.005	0.007	0.006	0.012	0.0006	0.0054	0.0845	0.002	0.21
CWX91	0.063	0.50	1.63	0.009	0.012	0.53	0.02	1.79	<0.010	0.006	0.010	0.008	0.015	0.0008	0.0058	0.0628	0.004	0.23
CWX81	0.067	0.50	1.65	0.009	0.013	0.53	0.02	1.76	<0.010	0.005	0.010	0.010	0.017	0.0009	0.0071	0.1338	0.004	0.24
CWX331	0.069	0.67	1.86	0.008	0.008	0.64	0.02	2.32	<0.010	0.005	0.012	0.064	0.020	0.0009	0.0085	0.0692	*	0.27

Table 6.3 Grouping of the different weld metals based on the microstructural modification. After Wildash [81].

Group	Weld metal identification	Purpose
1	15171, CWX181gb, CWX201, VCX2561	To vary grain boundary ferrite
2	14001, 14031, CWX351, CWX361	To vary MAC quantity
3	CWX71, CWX331	To vary weld metal refinement
4	CWX71, CWX181o	To vary oxygen content
5	CWX71, CWX81, CWX91	To vary Cerium trap content

The solution utilised was 0.1 N H_2SO_4 with different quantities of sodium arsenite as inhibitor of corrosion and promoter of H entrance into the metal. Different inhibitor concentrations (inhibitor strength) were employed to introduce a certain quantity of hydrogen into the steel. Hydrogen contents in the range from 0.2 to 15 ml/ 100 g of weld steel were obtained. Specimens were cathodically precharged using a current density of approximately 6 A/m^2 during 48h employing a platinum counter electrode [9, 11]. After the precharging and before the tensile test, the specimens were stored in liquid nitrogen to minimise the hydrogen evolution.

6.1.4 Mechanical Testing and hydrogen measurement

Tensile tests of the weld metals without and with different hydrogen content were carried out by Wildash[8]. A schematic representation of the tensile sample is given in the figure 6.2. These samples were obtained from the final weld bead. After precharging and before the tensile test, the stub was cut to measure the diffusible hydrogen (HD) in the sample using a gas chromatographic analyser. The strain rate used in all the tensile tests was 0.5 mm/min.

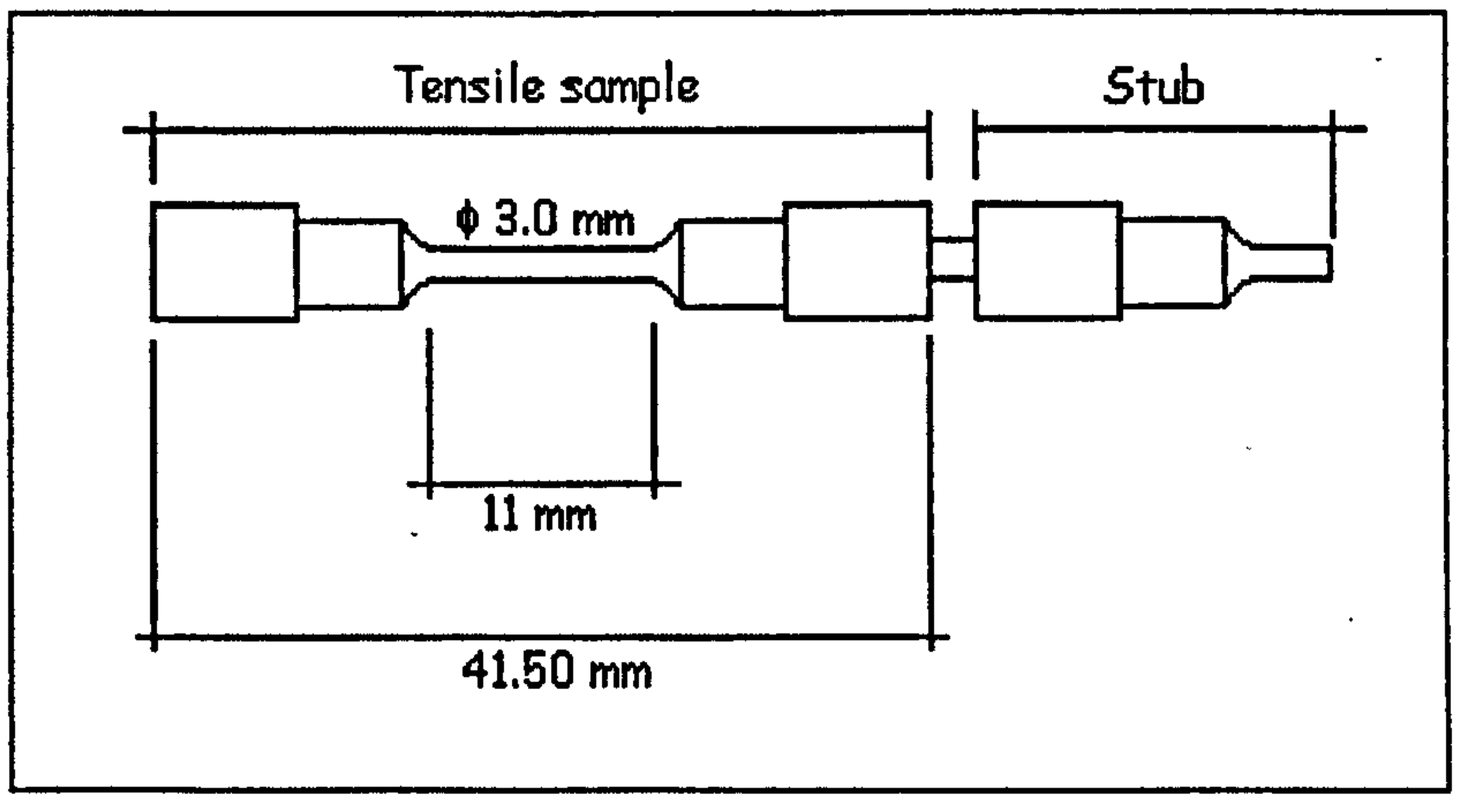

Figure 6.2 Tensile sample and stub made of weld metal.

6.2 Weld Metal Characterisation

In the understanding of the mechanical properties and resistance to hydrogen induced cold cracking, the microstructure must be completely characterised. This characterisation took account of:

(a) Microstructure present in every weld metal. This includes major and micro phases present

(b) Volume fraction of phases present in the microstructure

(c) Non-metallic inclusion volume fraction, size distribution and spatial distribution

(d) Size and distributions of micro-phases

For the microstructural characterisation optical and electron microscopy will be used. SEM and TEM will be utilised as principal tools of microphase's observation.

6.2.1 Optical Microscopy

The optical microscopy is useful in studying the general microstructure of the different weld metal. Weld metal microstructures are examined using standard specimen removal and preparation techniques. Microstructural characterisation of welds has the purpose of relating the microstructure present to mechanical properties and resistance to hydrogen induced cracking. Phase proportion and distribution have to be taken in account. The presence of microphases, such as retained austenite, austenite/martensite islands, and carbides, must be carefully studied because their effect on the material properties. In general, the effects of a process and parameters on microstructure are due to the compositional and thermal effects. The compositional effects are principally limited to the fusion zone and the thermal cycles affect both the fusion zone and HAZ [106].

The optical microscopy techniques include:

- Standard metallographic procedure
- Light and deep etching
- Non-metallic inclusion assessment (size and spatial distribution)

6.2.1.1 Standard Metallographic Procedure

A transverse section was studied, which is most often used to observe and document welded joint macrostructure and microstructure.

The metallographic procedure was the standard. An optically flat surface of the material was obtained using a low-speed cutter with a diamond-impregnated wheel, in order to avoid mechanical damage or overheating the sample. Because the small size of the sample, this had to be mounted using polymer resin or Bakelite. Once the sample is mounted, the sample surface must be ground flat and polished. Grinding was made using silicon carbide paper of 240, 320, 400, 600 and 1000grit. After this, the sample surface has to be mechanically polished using cloth polishing wheels impregnated with

diamond paste of grit from 6, 3, 1 and 0.25 μm. Finally, the surface was chemically etched. The chemical etching was 2.5% Nital for the entire weld metals. The etchant composition and the microstructure that is revealed are listed in the table 6.4, selected from the standard ASTM E 340-95.

Table 6.4 Etchant for microscopic examination of the weld metals [107]

Etchant	Composition	Purpose or characteristic revealed
Nital	2.5 ml HNO_3 in 100 ml ethanol (95%) or methanol (95%)	Develops ferrite grain boundaries in low carbon steels; produces maximum contrast between pearlite and cementite or ferrite network; develops ferrite boundaries in structures consisting of martensite and ferrite

6.2.1.2 Light and deep etching

For the study of the microstructure on the optical microscope at low magnifications (50X, 100X, 200X and 400X) short etching times were used. The time of etching was slightly different for each weldment, depending on the chemical composition. The times varied between 10s and 20s. The sample surface, maintained upward, was covered by the etchant and the progress of the etching was observed constantly during the procedure to avoid over etching.

In the case of OM studies at higher magnification (1000X) and for electron microscopy examinations a more deep etching was used. The time for etching was between 30 and 100s and the sample surface was covered with Nital and observed as described before. However, the solution was renewed several times during the etching procedure to permit fresh etchant in contact with the sample.

6.2.1.3 Non-metallic inclusion assessment (density, size and spatial distribution)

The inclusions were studied on a transverse section of the weld metal which was prepared metallographically as described before, but taken special care in the final step of polishing with 0.25 μm diamond paste, to avoid or minimise the scratches that could introduce difficulties in the automatic counting and measuring process. Optical microscopy was used to obtain at least 12 photographs of the weld metal at 1000X. Care was taken to avoid repetition of the photographed inclusions and to take representative regions of the weld metal surface. Not less than 1500 inclusions were counted. The range

of inclusions counted was between 1500 and 3500. The minimum inclusion size measured was around 0.2 μm. The total of inclusions per surface area was counted. The number of inclusions per unit area with size less than 1 μm in diameter and greater than 1μm are reported as well. For counting and diameter measuring of the inclusions, KS400 (version 4.0) software was used. For the automatic counting and sizing the MACRO 1 was implemented. The instructions utilised is shown in the annexed section A.7.

The average diameter measured on the surface will be called the arithmetic mean two dimensional particle diameter, $\bar{d}_a$, as named by Kunklen and collaborators [108]. This 2-D diameter is related with the arithmetic three dimensional particle diameter, $\bar{d}_v$, by the theory of polydispersed system of spheres, developed by Fullman and reported in the work of Kunklen and Grong [108], and presented in the simple equation:

$$\frac{\bar{d}_v}{\bar{d}_a} = \frac{\pi}{2} \tag{6.2}$$

Equation (6.2) was used to calculate the 3-D diameter of the inclusions. Other important inclusion characteristics and the way of calculating them from the measurement on the sample surface (2-D) are shown in the following group of stereometric relationships [108]:

$$N_v = \frac{6V_v}{\pi(\bar{d}_v)^3} \tag{6.3}$$

$$N_a = N_v \bar{d}_v \tag{6.4}$$

$$S_v = \pi N_v (\bar{d}_v)^2 \tag{6.5}$$

$$\lambda_v = 0.554\left(\frac{1}{N_v}\right)^{\frac{1}{3}} \tag{6.6}$$

where N_a is the number of particles per unit area, N_v is the number of particles per unit volume, V_v is the inclusion volume fraction, S_v is the total particle surface area, and λ_v is the mean particle centre to centre volume spacing.

The inclusion spatial distribution was measured indirectly using a procedure designed to take in account the area around the inclusion (on the surface of the metallographic sample), instead of using the distance between the nearest neighbour, the second nearest, and the successive nearest neighbour, which can make the automatic calculation difficult from the mathematical and programming point of view. The following procedure was considered simpler for programming and analysis:

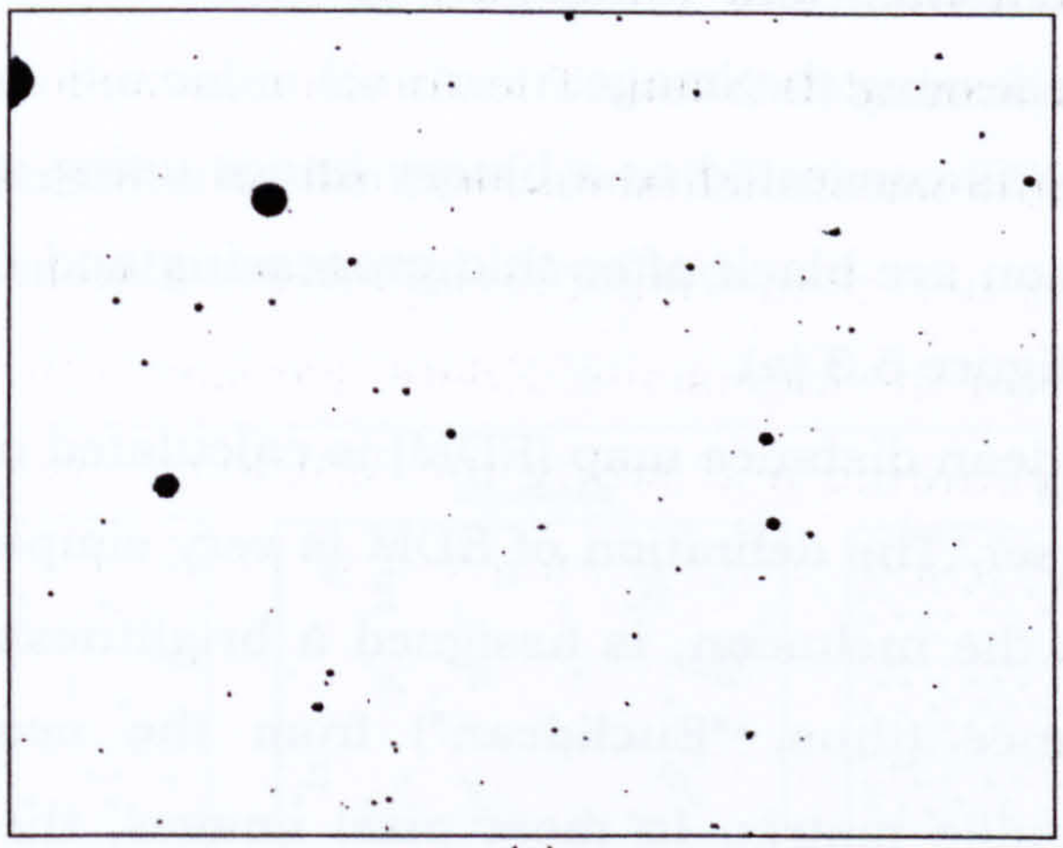

(a)

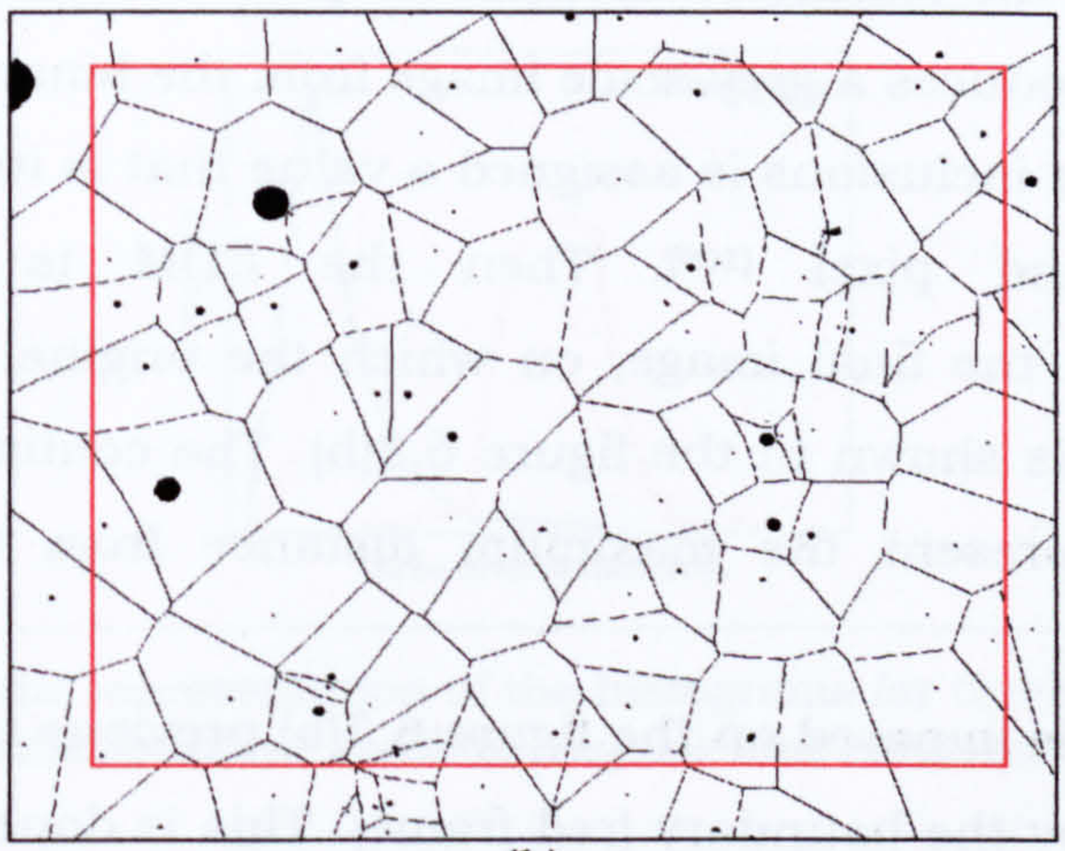

(b)

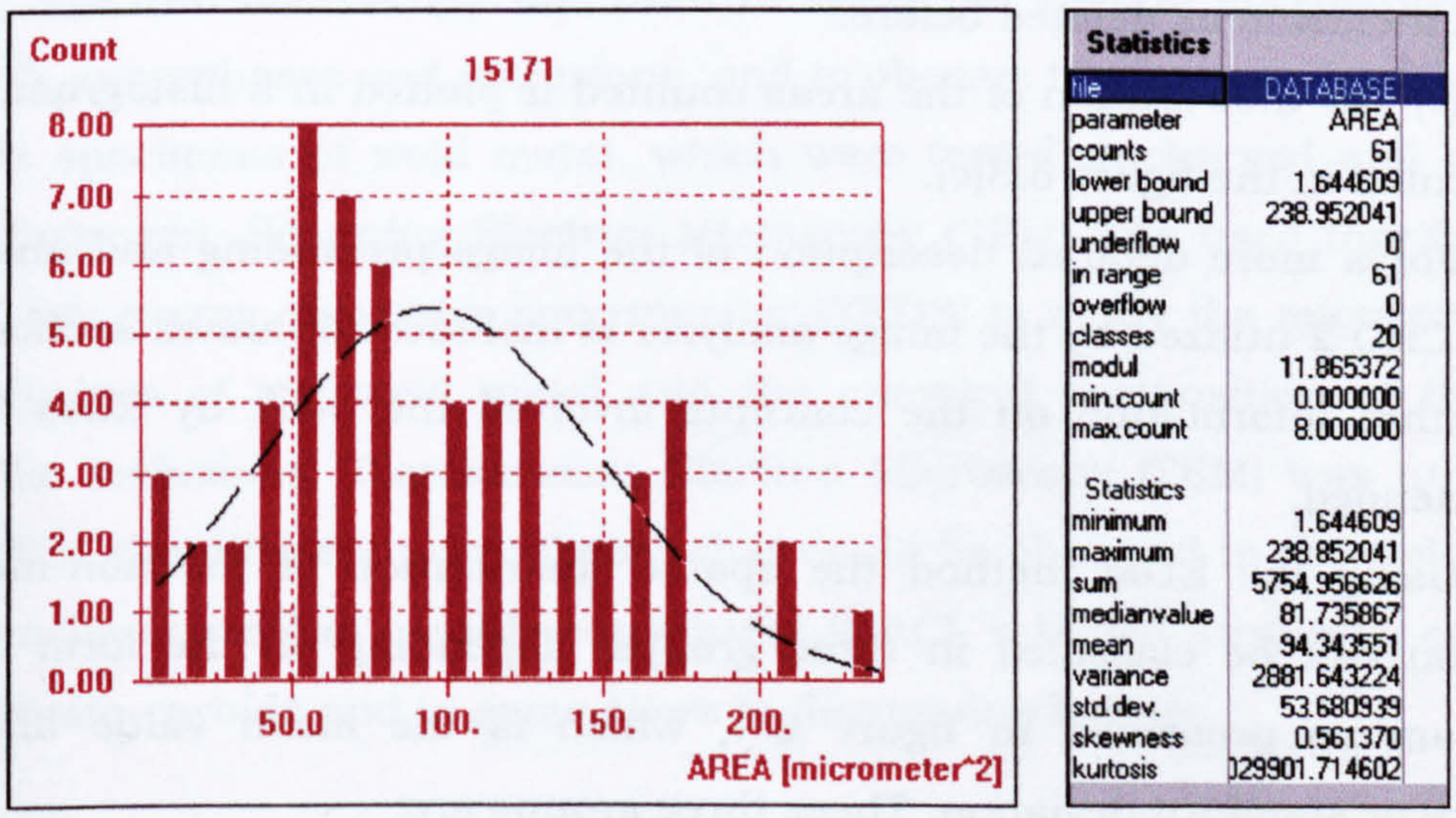

Statistics	
file	DATABASE
parameter	AREA
counts	61
lower bound	1.644609
upper bound	238.952041
underflow	0
in range	61
overflow	0
classes	20
modul	11.865372
min.count	0.000000
max.count	8.000000
Statistics	
minimum	1.644609
maximum	238.852041
sum	5754.956626
medianvalue	81.735867
mean	94.343551
variance	2881.643224
std.dev.	53.680939
skewness	0.561370
kurtosis	029901.714602

(c)

Figure 6.3 Non-metallic inclusion distribution, (a) Binary image of the inclusions in the steel obtained by OM at 1000X, (b) The Euclidean distance map (EDM) after "skeletonisation" and the measuring frame (in red) superposed on the image (a), and (c) area distribution of the regions only inside the frame.

(a) The image is enhanced using any graphic software available, changing the brightness and contrast to make the inclusion to appear clear on

the picture. Any scratches and luminosity gradient on the image has to be corrected before processing the image.

(b) The image is converted to a binary image using specialized software for this. The inclusion are black after this processing and the matrix is white, as is shown in the figure 6.3 (a).

(c) The Euclidean distance map (EDM) is calculated on the binary image by the image analyser. The definition of EDM is very simple: each pixel in the foreground, that is the inclusion, is assigned a brightness value equal to its straight line distance (thus, "Euclidean") from the nearest point in the background or metallic matrix. In most pixel images, the distance is taken from each pixel in the feature to the nearest pixel in this is the background. This calculation produces a grey-scale image from the binary picture, in which every pixel between inclusions is assigned a value that is its distance from the nearest background pixel [109]. Then the EDM is thresholded and "skeletonised" and the final image, on which the original binary image has been superposed, is shown in the figure 6.3(b). The continuous lines around the inclusions represent the maximum distance from the matrix to the inclusions.

(d) A frame is imposed on the figure 6.3(b) previous to the calculation of the areas limited by the boundary (red frame). This is done to avoid the areas formed with the edges of the photograph, which does not represent the area around inclusion as defined before.

(e) The distribution of the areas counted is plotted in a histogram, as is represented in the figure 6.3(c).

For a more detailed description of the image processing and analysis, the MACRO 2 utilized by the image analyzer is included in annex section A.7. For further information on the concepts involved the book by Russ [109] is recommended.

Using the EDM method the spatial distribution of the non-metallic inclusion can be classified in three groups, depending on the form of the histogram as presented in figure 6.4, which is the mean value and the variance or standard deviation. These three groups are:

a- Random distribution: it is characterised by higher variance and standard deviation values than the corresponding values for clustered and regular distributions.

b- Clustered distribution: the median value and the variance may be lower than the corresponding values for random distribution.

c- Regular distribution: in this case, the standard deviation may be lower than the value for clustered and random distributions.

Following this criteria, the spatial distribution of the inclusions in the different steel weld metals could be determined.

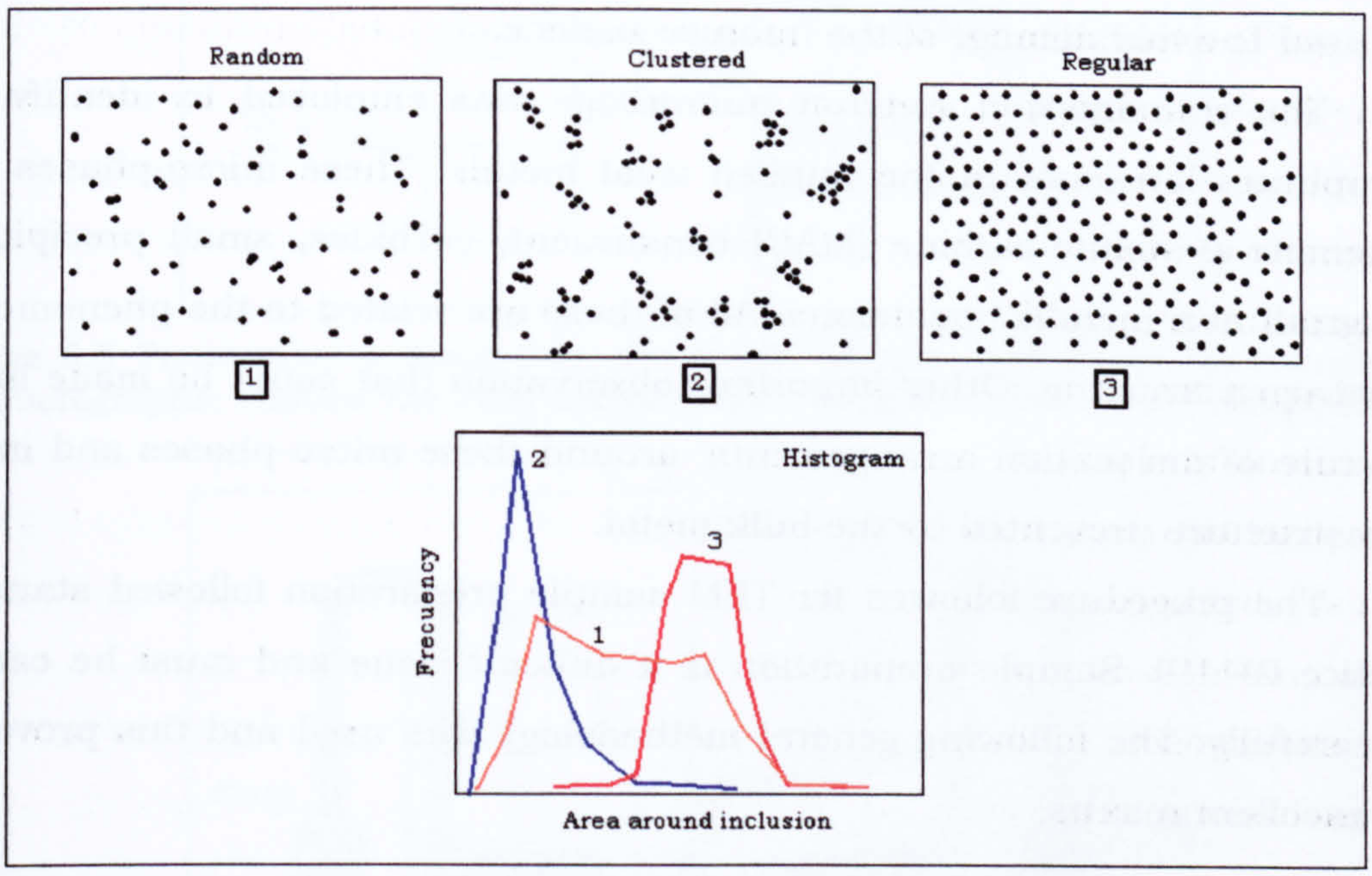

Figure 6.4 Schematic representation of the histograms for three different inclusion distributions: random, regular and clustered.

6.2.2 Electron Microscopy, general methodology.

Electron microscopy was used to study the general microstructure, to identify microphases and inclusions, and to observe the fracture surface of the tensile specimens of weld metal, which were tested uncharged and charged with hydrogen. Scanning Electron Microscopy (SEM) was used together with the X-ray energy dispersive spectrometer (XEDS) to study the microstructural constituents of the weld metal and the chemical composition of the non-metallic inclusions. Transmission Electron Microscopy (TEM) was utilised to identified the different microphases that could be observed in the weld metal: martensite-austenite- carbide constituent (MAC), retained austenite, carbides, martensite-carbide and in some cases to distinguish bainite.

6.2.2.1 Sample preparation for Electron microscopy.

No special preparation is required for the observation of the microstructure and the fracture surface using SEM.

For the observation of the microstructure the same procedure for grinding and polishing was used (see section 6.2.1.1). Long etching times are necessary to reveal the different micro-constituents. The reagent used was the

same as the utilised in optical microscopy: 2.5% Nital. Times from 30 to 100 seconds were employed. After etching the sample was immersed in acetone and cleaned using an ultrasonic bath.

In the fractographic studies the fracture surface was observed after a cleaning process in an ultrasonic bath using acetone. No chemical cleaning was used to avoid damage of the fracture surface.

The transmission electron microscope was employed to identify the microphases presents in the studied weld metals. These micro-phases are: martensite-austenite-carbide (MAC) constituent, carbides, small precipitates and small non-metallic inclusions. All of these are related to the phenomenon of hydrogen trapping. Other important observation that could be made is the structure of dislocation arrangements, around these micro-phases and in the microstructure presented by the bulk metal.

The procedure followed for TEM sample preparation followed standard practice [110-111]. Sample preparation is a difficult issue and must be carried out carefully. The following general methodology was used and this proved to give excellent results.

A- Pre-treatment of the specimen.

Samples for TEM were taken from the base of the tensile samples showed in the figure 6.5. Disc of 250 μm thick and approximately 5 mm in diameter were cut using a low speed diamond saw to minimise mechanical damage. Planar grinding with a 1000 grit SiC-paper was utilised to reduce the thickness of the disc between 150 and 200 μm. After that 3 mm discs were punched out and then were ground further, using a holder where the sample can be introduced and the thickness controlled rotating a screw on the opposite end of the holder. The final thickness of the 3 mm discs were between 80 and 100 μm.

B- Final thinning of the discs

The final thinning was carried out utilising a Struers TenuPol-5 twin jet polisher. The schematic representation of the process is shown in figure 6.6. This normally consists in polishing the 3 mm disc specimens with the 1 mm jets. The polishing is carried on until a small hole appears, when the process is stopped automatically using a light stop value, selected previous to the thinning process, reacting as soon as a hole is established [112-113].

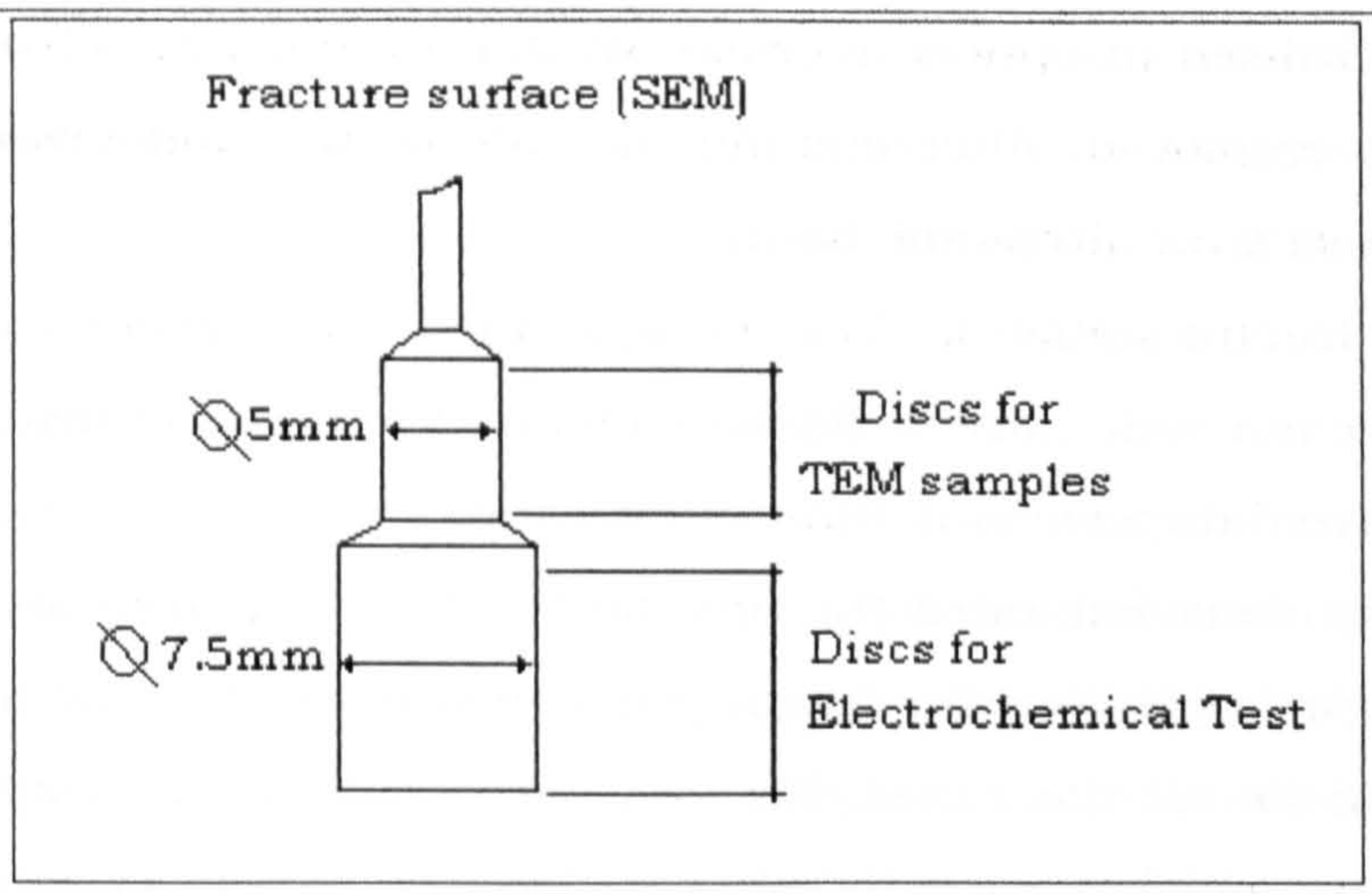

Figure 6.5 Transversal sections from the tensile sample used to extract samples for the fractographic studies, the TEM samples and the electrochemical test samples.

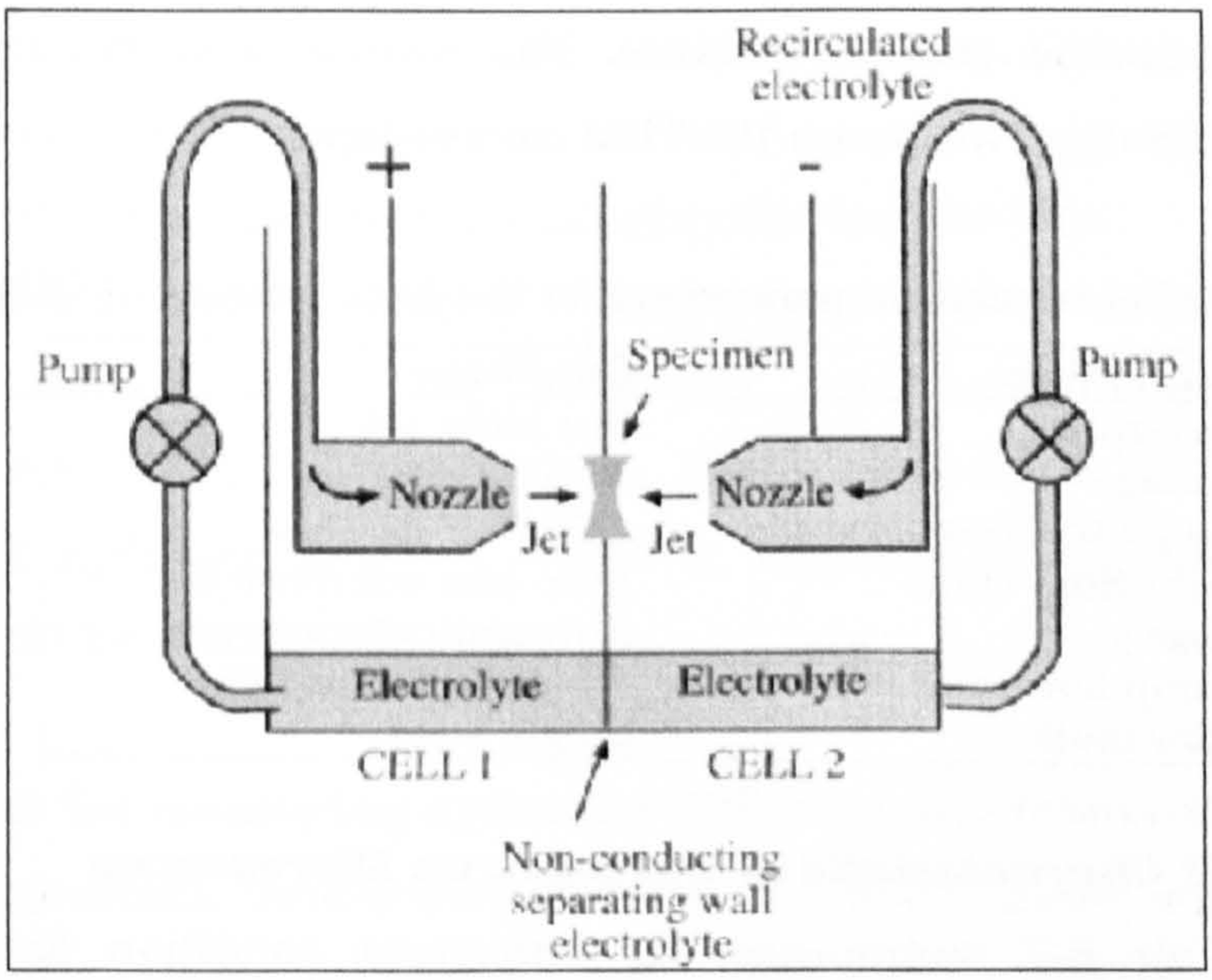

Figure 6.6 Schematic of a twin jet electro-polishing equipment. The positively charged specimen is held in a Teflon holder between the jets. A light pipe (not show) detects perforation and terminates the polishing [112].

The electrolytic solution used for the electro polishing has the composition presented in the table 6.5. The chemicals have to be mixed in the order showed in the table and this operation must be carried out very carefully and following the correct safety procedures. Whilst mixing, the solution has to be constantly stirred.

Table 6.5 Chemical composition for the electro-polishing solution

Substance	Concentration (% volume)	Volume (mL)
Ethanol + 4.8% Methanol	60	900
2-Butoxyethanol (99%)	30	450
Perchloric Acid (60%)	10	150

The polishing condition, such as voltage, temperature, flow mode and rate were established after some trials. The polishing voltage was determined for every sample to be prepared, obtaining the current-voltage curve under the condition for electro-polishing. The voltages used were between 22 and 30 V, depending on the weld metal. Some recommended conditions are listed in table 6.6. Lower temperatures than the maximum recommended in the table were used and these extended the time for the thinning process, but improve considerably the conditions for a thin polished sample. A single moderate flow rate was used for all the cases. The time of polishing was controlled by an infrared sensor, which constantly measure light emitted from an infrared light source placed on the opposite side of the sample.

After the electro-polishing process was finished, the sample was cleaned up in methanol and then in ethanol. The sample was stored immersed in ethanol until its observation on the TEM microscope.

Table 6.6 Recommended parameters for the final thinning of TEM samples

Parameters	Condition
Electrolyte	See table 3.4
Voltage	22 – 30 V
Maximum Temperature	-15° C
Light Stop value	Auto (see reference 66)
Time	Automatically stopped
Pump flow rate	35 (see reference 66)
Flow mode	Single flow

6.2.2.2 Characteristic of the Electron Microscopes

The table 6.7 summarise the important condition for the different microscopes used in this investigation. Important parameters for the microscopes are: type of filament, accelerating voltage (E), working distances (WD), electron detectors type (EDT) and spot size (SS).

Table 6.7 Important parameters for the different microscopes used

Equipment	Filament type	E (kV)	WD (mm)	SS	EDT
CamScan4	Thermoionic emission (W)	20	18-22	1-5	SE BE
FEG-SEM	Field emission	5-10	5-12	30 μm*	SE SE-in-lens
CM-20 TEM	Thermoionic emission (LaB_6)	200	λL=1 m**	2	Screen Film

* The size of the spot is controlled by different apertures (standard 30 μm)
**This is the camera length used for electron diffraction analysis

The CamScan4-SEM was used for general observation of the microstructure, chemical analysis of NMI and general fractography. The FEG-

SEM permitted the observation of the microstructure and the fracture surface at very high resolution. The CM20-TEM was utilised for the identification of the microphases using electron diffraction techniques.

6.3 Scanning Electron Fractography

To study the fracture mechanism and its relation with the microstructural components of the weld metal and the hydrogen content, scanning electron microscopy (SEM) was used. Special attention was made to both the morphology of the fracture surfaces and the microstructure possibly related with the fracture surface characteristic.

A special methodology is not necessary in the SEM observation of the fracture surface of the tensile samples. If dust or corrosion products are present, some cleaning procedures should be necessary. Care has to be taken in the selection of the procedure to be used because it could result in the dissolution of the fracture surface, changing the morphology.

In the fracture morphology of hydrogen assisted cracking, quasicleavage (QC), intergranular (IG), and microvoid coalescence (MVC) fracture mechanisms are observed. Using SEM, the relationships between fracture morphology of hydrogen assisted cracking, microstructure, and mechanical properties could be elucidated.

6.4 Test for measuring hydrogen diffusion and trapping

A potentiostatic double-step method or double pulse technique (PDP) was used to study hydrogen ingress and egress for the different weld metals. The technique consists of generating hydrogen atoms at a constant cathodic potential on the metallic surface and in the presence of a hydrogen entry promoter (for example As^{+3}, S^{-2}, etc.), and then step the potential to a more positive value below the corrosion potential. During this step, the anodic current and the charge associated with the re-oxidation of H from the electrode are recorded. This technique was proposed by Pound and collaborators [101-105, 114]. They showed that a mathematical model for the diffusion and trapping of hydrogen (chapter 5, sections 5.4 and 5.5) under the condition imposed by this technique could quantitatively account for the experimental results obtained. Using this technique, the trapping characteristic of the weld metal could be obtained, through the determination of the k, the trapping rate constant.

6.4.1 Weld metal electrode preparation

Discs of weld metal about 0.5 cm^2 and 1-1.5 mm thick were taken from the base of the tensile samples (see figure 6.5) using a slow cutting machine with a diamond disc. After the cutting, both faces of the discs were ground with 1000 grit SiC-paper and then cleaned with acetone. A copper wire was soldered to the discs, obtaining the electrical contact necessary. This wire was passed through an L-bent glass tube previously to the soldering on the sample surface. Soldering was made using 60Sn-40Pb wire. The sample of weld metal was located as near as possible of the L- shaped extreme of the tube and then, using a digital voltmeter, the electrical conductivity was checked.

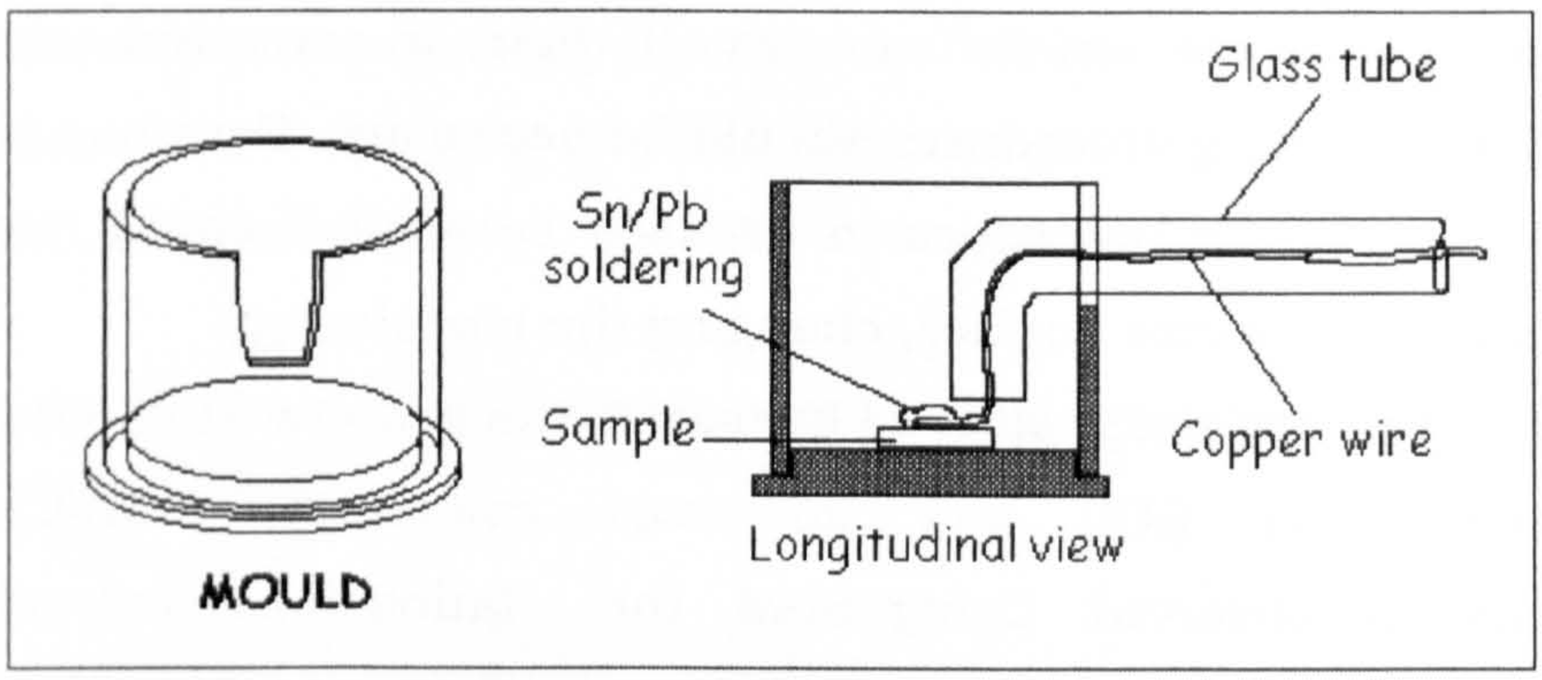

Figure 6.7 Especial mould used to mounting the electrode.

After that, a mounting with epoxy resin utilising a special mould (figure 6.7) was made to permit contact only between one of the surfaces of the sample and the electrolyte. A schematic representation of the electrode is given in the figure 6.8. This type of electrode has the advantage of easier handling at the time of grinding, polishing and degreasing of the metal surface.

6.4.2 Surface preparation of the electrode.

After the resin has cured, the electrode surface was ground with SiC paper of 1000 grit to obtain a flat surface. Then the surface was polished using a diamond abrasive compound from 6 to 1 μm of particle size. Finally, the surface was cleaned and degreased in an ultrasonic bath with ethanol during 5 minutes then dried in the air and immediately immersed in the electrolyte. It is very important to prepare the sample just before the PDP test to avoid the formation of corrosion products on the surface that could affect its electrochemical condition.

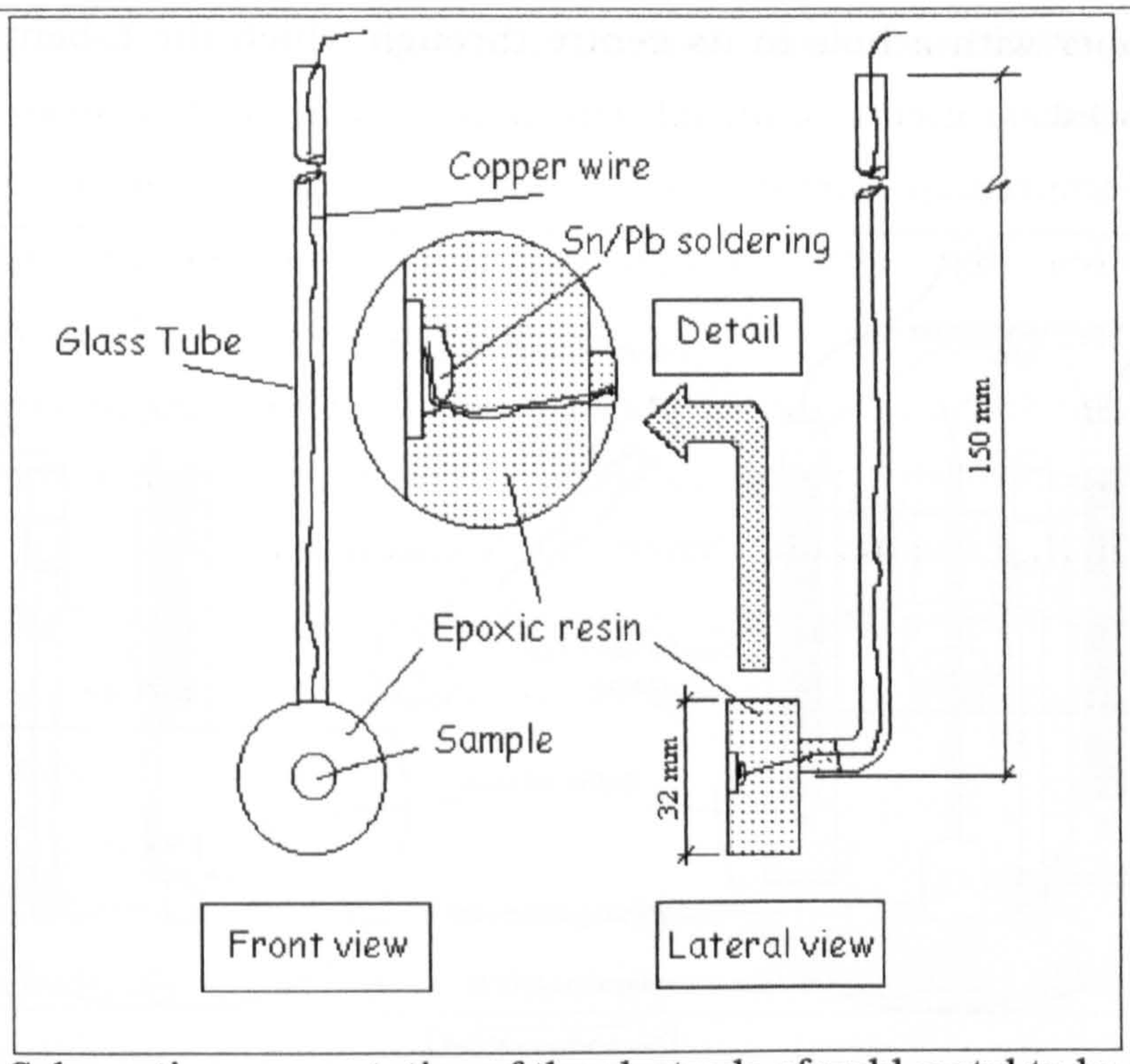

Figure 6.8 Schematic representation of the electrode of weld metal to be used in the electrochemical test.

6.4.3 Preparation of electrolytic solutions

The electrolyte was a sodium acetate buffer of composition: 0.87 mol/L acetic acid ($C_2H_4O_2$) and 0.5 mol/L sodium acetate ($C_2H_3NaO_2$) containing 15 ppm sodium meta-arsenite ($AsNaO_2$) as a hydrogen entry promoter. It was prepared mixing 51.3 ml of acetic acid 96%, 42 g of sodium acetate, 1 mL of a 15.6 g/L aqueous solution of sodium meta-arsenite and distilled water to complete 1 litre of solution. The calculated pH for this buffer electrolyte was 4.52. This solution was de-aerated continuously with nitrogen 1 hour before the sample immersion and throughout the measurements.

6.4.4 Description of the electrochemical cell and equipment.

The electrochemical cell that was used for the hydrogen ingress/egress experiments is shown in the figure 6.9. This consists of a six-necked flask, a Lugging capillary, a saturated Calomel electrode (SCE) as a reference electrode (RE), two glass cylinders with a porous base to introduce the two platinum counter electrodes (AE), and the nitrogen inlet. The counter or auxiliary electrodes were introduced into the cylindrical container to avoid the dissolution of oxygen in the electrolyte, which is formed on their surface during polarization. The Lugging capillary was filled with the same buffer solution used for experiments. The working electrode (WE) was held by a

rubber stopper with a hole in its centre through which the L-bent glass tube was introduced.

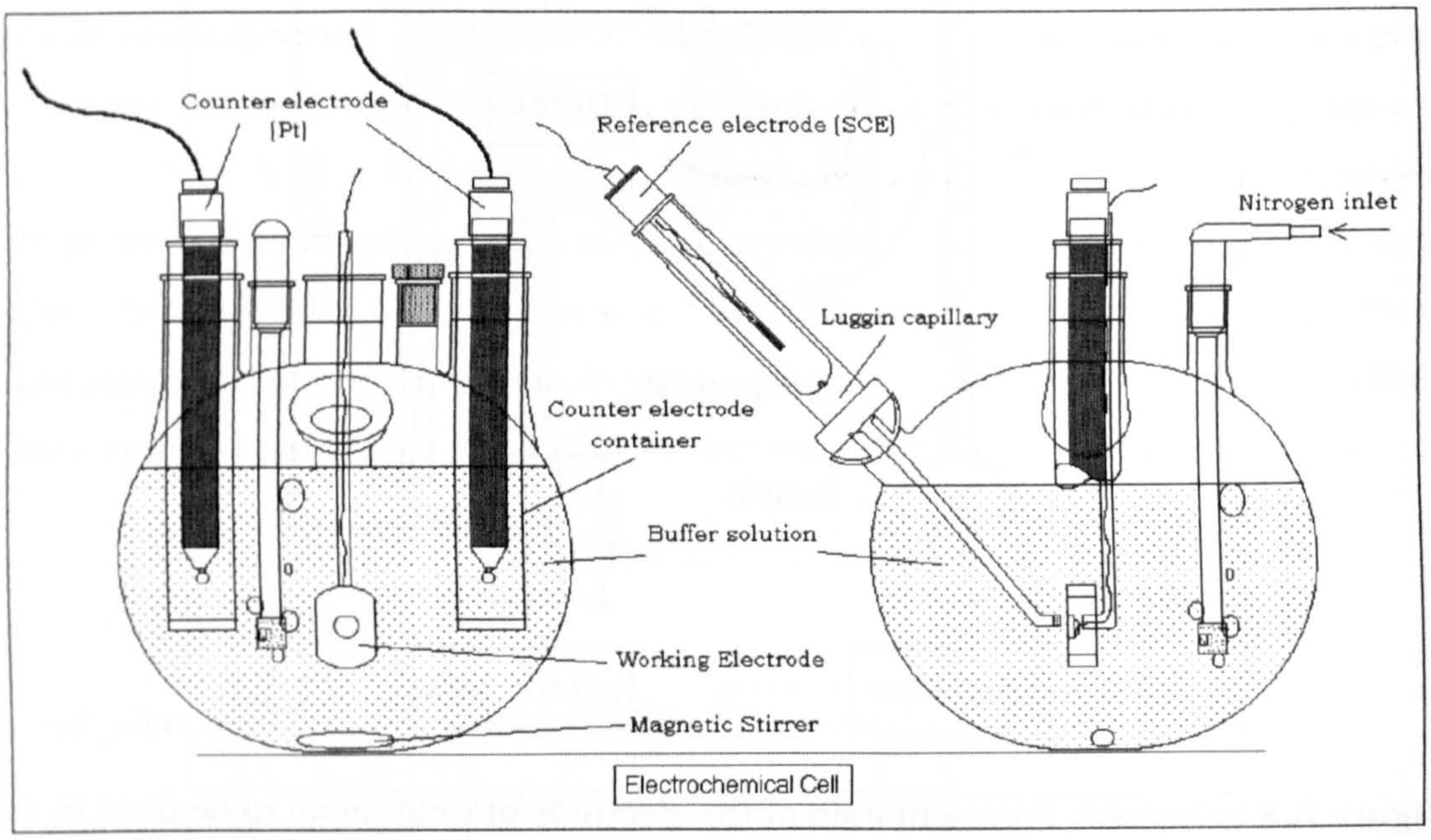

Figure 6.9 Schematic of the electrochemical cell.

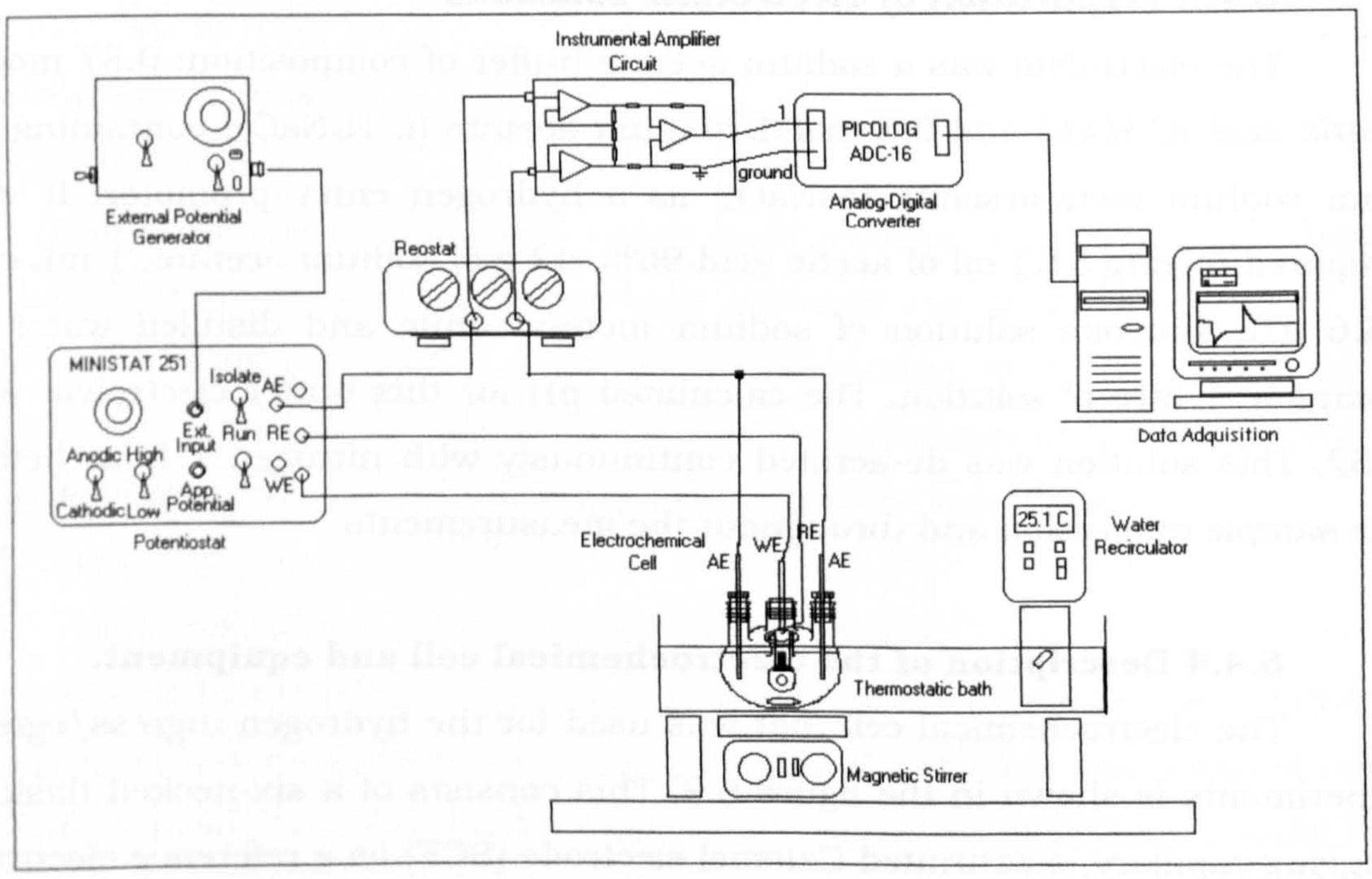

Figure 6.10 Schematic illustration of the instrumentation for the electrochemical test.

The potentiostatic double pulse experiment of the weld metal electrode was carried out with a Ministat-251 potentiostat. The figure 6.10 shows schematically the instrumentation. It was necessary to design and build an instrumental amplifier to permit the measurement of the current transient during the test. Detailed description of the differential amplifier circuit is

shown in figure A.5 in annexes. This amplifier was connected to a rheostat which was connected in series with the line of the counter electrodes (AE). For the potential pulse generation, a stable potential source was built and was operated manually. Details of its circuit are presented in figure A.6 in annexes. An analogue to digital converted (Picolog ADC-16) was utilised to record the current transients in a personal computer.

The electrochemical cell was immersed into a thermostatic bath with water and the temperature was controlled by a water recirculator at approximately 25.0 ± 0.1 °C. For the continuous stirring of the solution inside the cell, a magnetic stirrer was used in combination to a stirring plate placed outside the bath (see figure 6.10).

6.4.5 Electrochemical test procedure

The electrochemical test was carried out with standard electrode-kinetic instrumentation described previously in this chapter.

Firstly, the buffer solution was de-aerated continuously with pure N_2 at least 1 h before the immersion of the sample and throughout the realisation of the experiment. It was stirred continuously. The temperature of the solution was maintained at 25.0 ± 0.1°C during the whole process using a thermostatic bath described before. The preparation of the sample surface was started just 30min before its immersion in the solution, so the sample was introduced into the solution just after the 1h de-aeration process was completed and just after the preparation of its surface. This procedure permits the minimisation of the corrosion of the sample surface in the air.

Once the sample is in the electrolytic solution, its corrosion potential (E_{corr}) is measured with respect to the SCE, during 30 min every 5 min. This allows the starting point for the realisation of the polarisation. Before the culmination of the 30 min period, the potentiostat is set up to the value of E_{corr}-10 mV. This is the E_A potential. At this stage, the cell must be properly connected to the potentiostat but the cell must be isolated. The potentiostat has a switch to permit this state. At the same time, the external potential source is set up to the overpotential (η_C) needed to reach the E_C potential value, which is

$$E_C = E_A + \eta_C \qquad (6.7)$$

E_C was selected to permit the reduction of hydrogen on the weld metal surface without the formation of H_2 bubbles in excess that could interfere with the H covering of the electrode surface, which at the same time could decrease

the ingress of H atoms into the weld metal. For the weld metals studied the value of η_C was selected at -150 mV, which is expected to be located inside the Taffel region of the polarisation curve. Visual observation of the electrode surface during polarisation permitted corroboration that the formation of excessive H_2 bubbles was avoided, i.e. no bubbles were observed.

After the measurement of E_{corr} the sample was polarised at E_A during exactly 1 min, time considered to be sufficient for the stabilisation of the polarised electrode surface. During this time the cathodic current was followed. At E_A the cathodic current will be called I_A for future explanations.

The recording of the current with respect the time using the analogue to digital converter (Instrumentation amplifier + Picolog DC-16) was started 10s before the culmination of the period of 1min. The table 6.8 shows the settings for the data acquisition using the Picolog software. One of the most important parameters is the sampling interval, which will permit the recording of the current transients. These transients are expected to occur very fast.

Table 6.8 Important parameters for the data acquisition using Picolog ADC-16

Parameter	Value or Condition
Recording type	Real time continuous
Sampling interval	100ms
Reading per sample	Single
Resolution	13bits
Conversion time	78ms

After 1 min at E_A, the potential was stepped to the E_C value, in the cathodic direction. At this moment, the process of hydrogen charging begins, that is the ingress of hydrogen into the weld metal electrode. The charging process at E_C is maintained constant during a determined period of time and the charging current (I_c) is recorded. Three charging times (t_c) were used: 10, 20 and 30 s. This selection, as will be explained below, permits the study of the hydrogen egress process taken in account the two possible cases that could be controlling the behaviour of the evolution of H: diffusion control in the weld metal and interface control. This was explained in chapter 2. Moreover, by using different times it may be possible to study the saturation of the traps in the weld metal, by following the changes in the trapping constant k.

At the end of the charging period, the potential is returned to the E_A value. An anodic current transient is registered after this step. This anodic

current is produced by the re-oxidation of the H that is diffusing out of the electrode, the diffusible hydrogen (H_D). This current transient is the most important part of the whole experiment. This permits the characterisation of the trapping rate constant (k) for the different weld metals. The method for this determination is explained in the next section.

The current recording process is stopped when the current is stabilised approximately to the original I_A, the cathodic current measured before the E_C step. The time passed between the appearing of the anodic current transient and the end of the recording was called t'. The figure 6.11 shows schematically the potential program and a possible current response.

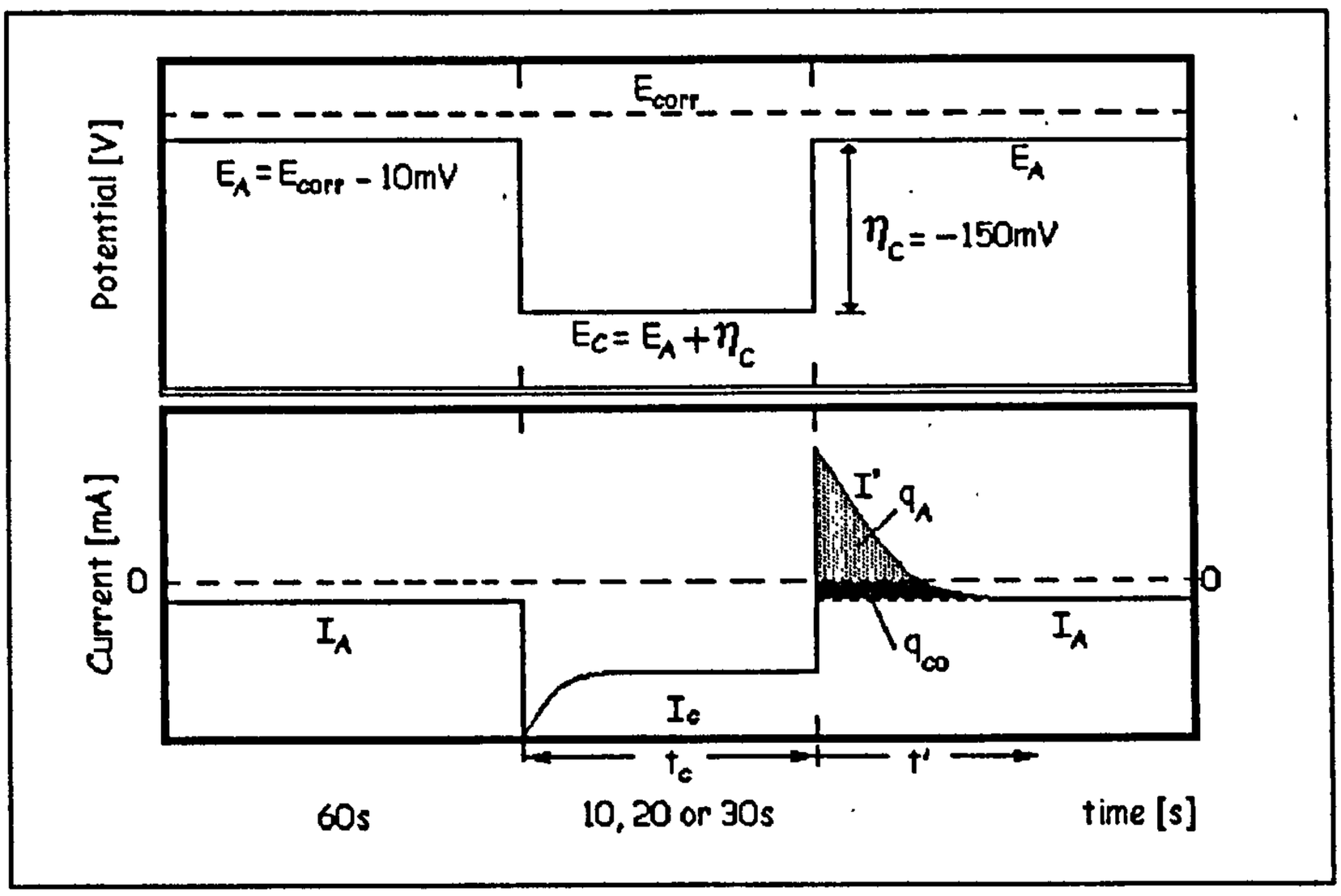

Figure 6.11 Schematic potential programme and expected current response during the potentiostatic pulse experiment. Modified from Pound [101, 114]

In figure 6.11, the area below the anodic transient has been shaded. Two regions are shown: the upper region where the current is positive (q_A) and the lower one where the current is negative (q_c). The addition of these two charges is equivalent to the total hydrogen that evolves from the interior of the weld metal electrode. For this reason, if the total amount of hydrogen that egresses from the sample is required, the shaded area has to be calculated. Mathematically this could be done easier if the current curve is shifted to more positive values until I_A becomes nil. This is equivalent to adding the absolute value of I_A ($|I_A|$) to the anodic current transient (I'). This will be explained in the next section.

6.4.6 Methods for the analysis of the hydrogen egress

The analysis of the experimental data can be examined in terms of the diffusion control presented in the section 5.4 in chapter 5. From the application of this, parameters such as the rate constant for trapping (k) were evaluated for the different weld metals.

The method for the determination of the trapping constant k consists in the matching of the equation for I'(T') (equation 5.4 in chapter 5) with the experimental data obtained for the anodic current density transient. The equation 5.4 is the solution of the modified equation for second Fick's law of diffusion that takes in account the trapping of hydrogen. This solution was obtained by Pound and collaborators [101]. In the equation I', T' and R are non-dimensional terms of current, time and trapping rate constant, respectively, defined in the expressions from 5.6 to 5.9 [101, 114] (see chapter 5, section 5.4).

Before the utilisation of the analytical equation to match the experimental data, the latter has to be modified to take in account the small cathodic current (I_A) imposed by the potential E_A, which is slightly below the corrosion potential, E_{corr}, of the weld metal. Figure 6.12 shows the concept that is needed to explain the modification of the anodic curve. The left hand side picture shows the theoretical electrochemical behaviour of the metal M, that is the independent curve for the anodic reaction and the corresponding cathodic reaction. On the right hand of the figure, the potentiostat response to the polarisation process is represented, this shows basically the difference between the anodic and the cathodic currents. For example, at E_{corr} the anodic current density (oxidation of the metal) equals the cathodic current density (reduction of hydrogen), and the potentiostat response is zero current because the different between these is nil. However, at E_A the anodic current density (i_{A1}) is much less than the cathodic current density (i_{A2}) (logarithmic scale) and as a consequence the potentiostat reports a total cathodic current almost equal to the value of i_{A2}, that is $i_A \approx i_{A2}$. This implies that during the hydrogen egress, the anodic transient, so determined, is in reality the difference between the anodic transient and the cathodic current at E_A. This suggests that the anodic current due to the re-oxidation of hydrogen is equal to the anodic current reported by the potentiostat plus the absolute value of the cathodic current at E_A. Such a modification facilitates the comparison between the responses for different weld metals and simplifies the mathematical processing.

An iterative process was involved for the determination of the C_s and k values, the surface concentration of hydrogen and the trapping constant, respectively. A simple method was used for the iteration: firstly, a spreadsheet was created to plot the equation 5.4, where the input data was C_s, t_c, k, t', the hydrogen diffusivity (D) and the Faraday's constant (F); then this theoretical curve was superimposed on the experimental curve and finally, the values of C_s and k were changed until the theoretical curve matches the experimental one. Following this procedure the trapping rate constant k was obtained.

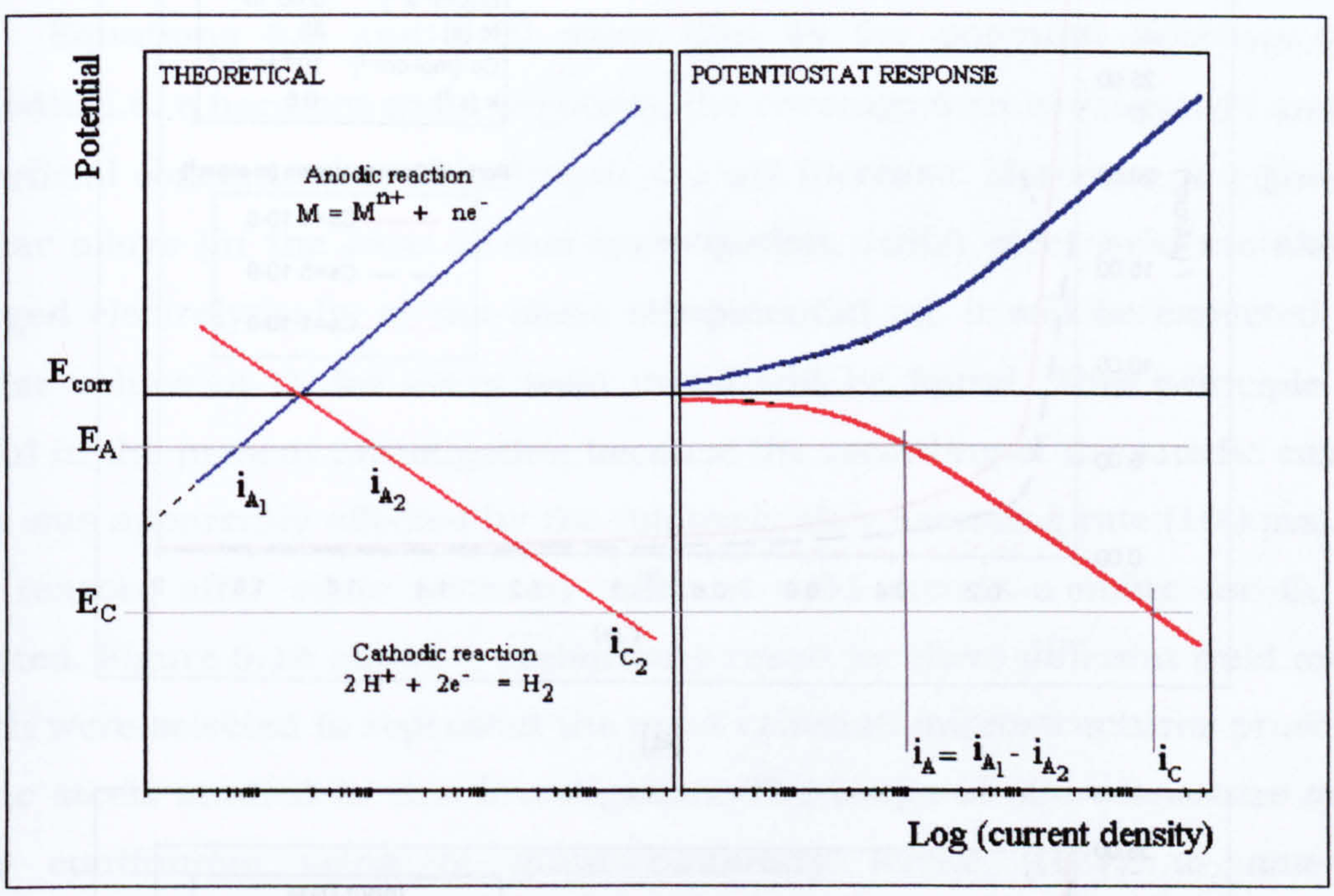

Figure 6.12 Schematic representation of the theoretical and potentiostatic response during polarisation of a metal in an acid aqueous solution. i_A is the cathodic current density at E_A and i_C is the cathodic current density at the charging potential .E_C.

It is very important to know how to interpret these results, and the effects of C_s and k on the anodic current density transient. Figure 6.13 presents the effect of these two parameters on the anodic current theoretically calculated. Figure 6.13(a) shows that the changes in the concentration of hydrogen on the surface of the electrode, from $1 \cdot 10^{-9}$ to $1 \cdot 10^{-8}$ mol/cm^3, causes an important decrease of the anodic current density peak at t'=0. It has been demonstrated that the value of C_s depends on the cathodic charging potential or overpotential (η). McBreen and Genshaw [115], presented an electrochemical analysis of the hydrogen evolution kinetics, mechanisms and adsorption on metals and concluded that one of the most important parameters in the entry of hydrogen into metals is the coverage of absorbed H on the metal surface, θ, which for low coverage gives the Langmuir expression:

$$\theta = \theta_0 \exp\left(-\frac{\eta \cdot F}{R \cdot T}\right) \tag{6.8}$$

where θ_0 is the value of θ at zero overpotential and F, R and T are the Faraday's constant, the Universal Gas constant and the temperature, respectively.

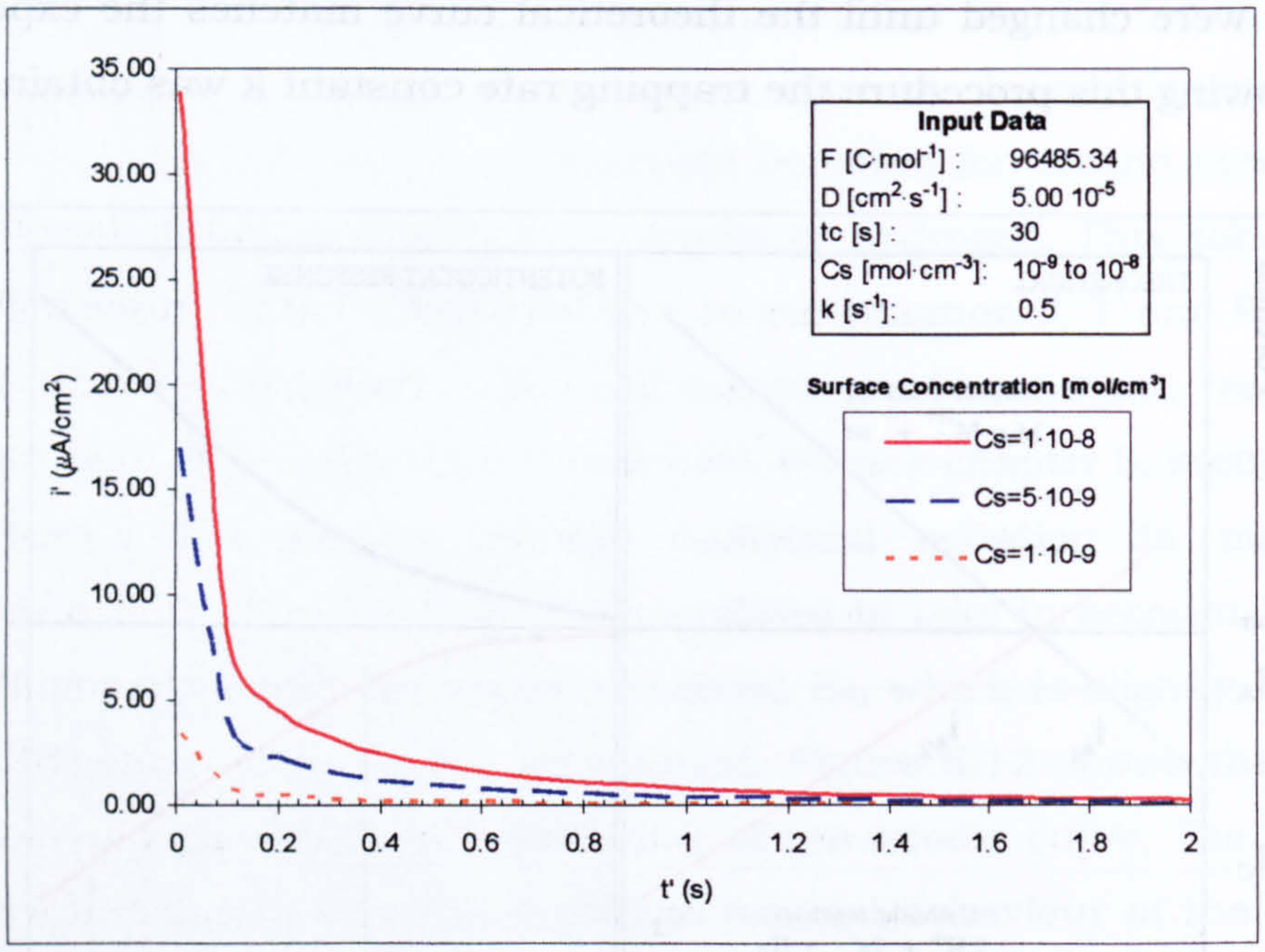

(a)

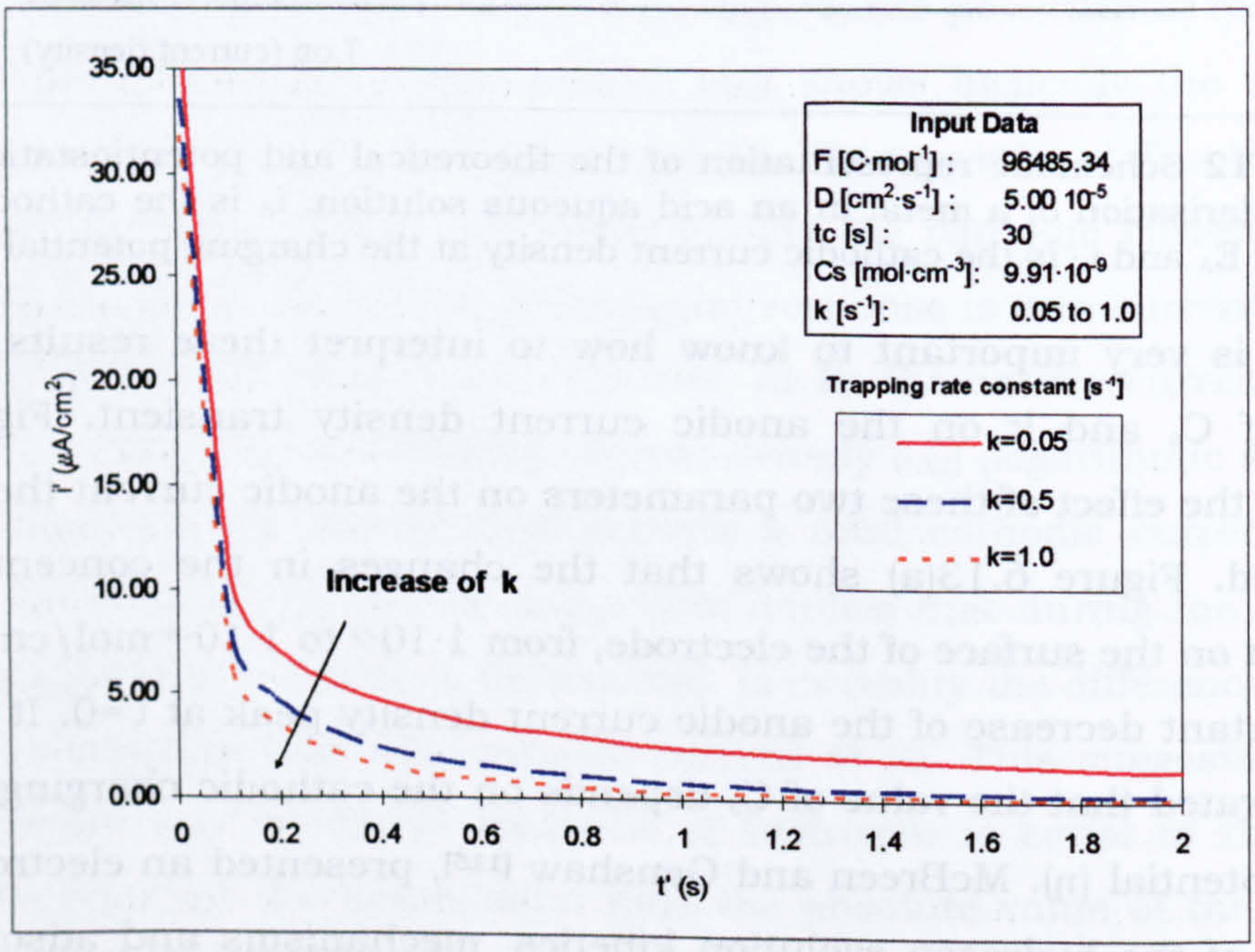

(b)

Figure 6.13 Schematic representation of the anodic current density due to the re-oxidation of hydrogen. (a) Effect of the superficial hydrogen concentration (Cs) and (b) effect of the trapping rate constant (k), on the current density response

The hydrogen coverage can be related with C_s using the equilibrium constant K_{abs}, representing the equilibrium across the interface between the absorbed and dissolved hydrogen:

$$K_{abs} = \frac{C_S}{\theta} \qquad [6.9]$$

By substituting equation 6.8 into 6.9 and modifying the latter, it is possible to obtain a relationship between C_s and η:

$$\ln C_s = \ln(\theta_0 \cdot K_{abs}) - \frac{\eta \cdot F}{RT} \qquad (6.10]$$

Equations 6.8 and 6.10 show that as the potential becomes more cathodic (i.e. η becomes more negative), the coverage with hydrogen (θ) and the superficial concentration of hydrogen (C_s) will increase. Moreover, if a group of similar alloys (in the case of this investigation, HSLA steel weld metals) are charged electrolytically at the same overpotential (η), it will be expected that similar values of C_s for every weld metal will be found. This principle was useful in the present investigation because the recording of the anodic current peak was apparently affected by the relatively slow sampling rate (100 ms). For this reason, after some tests on different weld metals a value for C_s was selected. Figure 6.14 shows a preliminary result for three different weld metals which were selected to represent the most common microstructures presented in the steels studied in this investigation. The range of microstructure varies from continuous veins of grain boundary ferrite (GBF) to non-GBF morphologies. As can be seen in the graph, the peak of the anodic current density appears to be between 30 and 35 $\mu A/cm^2$, which using the procedure for the determination of C_s and k described before and schematised in figure 6.13, the values for the three weld metals in figure 6.14 were: $8.70 \cdot 10^{-9}$, $9.60 \cdot 10^{-9}$, and $9.95 \cdot 10^{-9}$ mol/cm^3, for the weld metals 15171, 14031 and VCX2561, respectively. With these values as a guide, all the anodic current density results for the egress of hydrogen were studied to determine k. After the processing of all the curves, it was apparent that the value for C_s, suitable to compare the totality of the weld metal samples was $9.91 \cdot 10^{-9} mol/cm^3$. This C_s value was selected to permit comparison of the k values for the weld metals studied. This value may or may not represent the true value for Cs for all the weld metals; however it permitted at least a qualitative comparison between them, from the trapping point of view.

For the presentation of the results of the egress of hydrogen, the peak related with the value of Cs was omitted and the maximum scale used in the

graph was 5 μA/cm² which did permit the comparison of the experimental data obtained for the different samples that were studied.

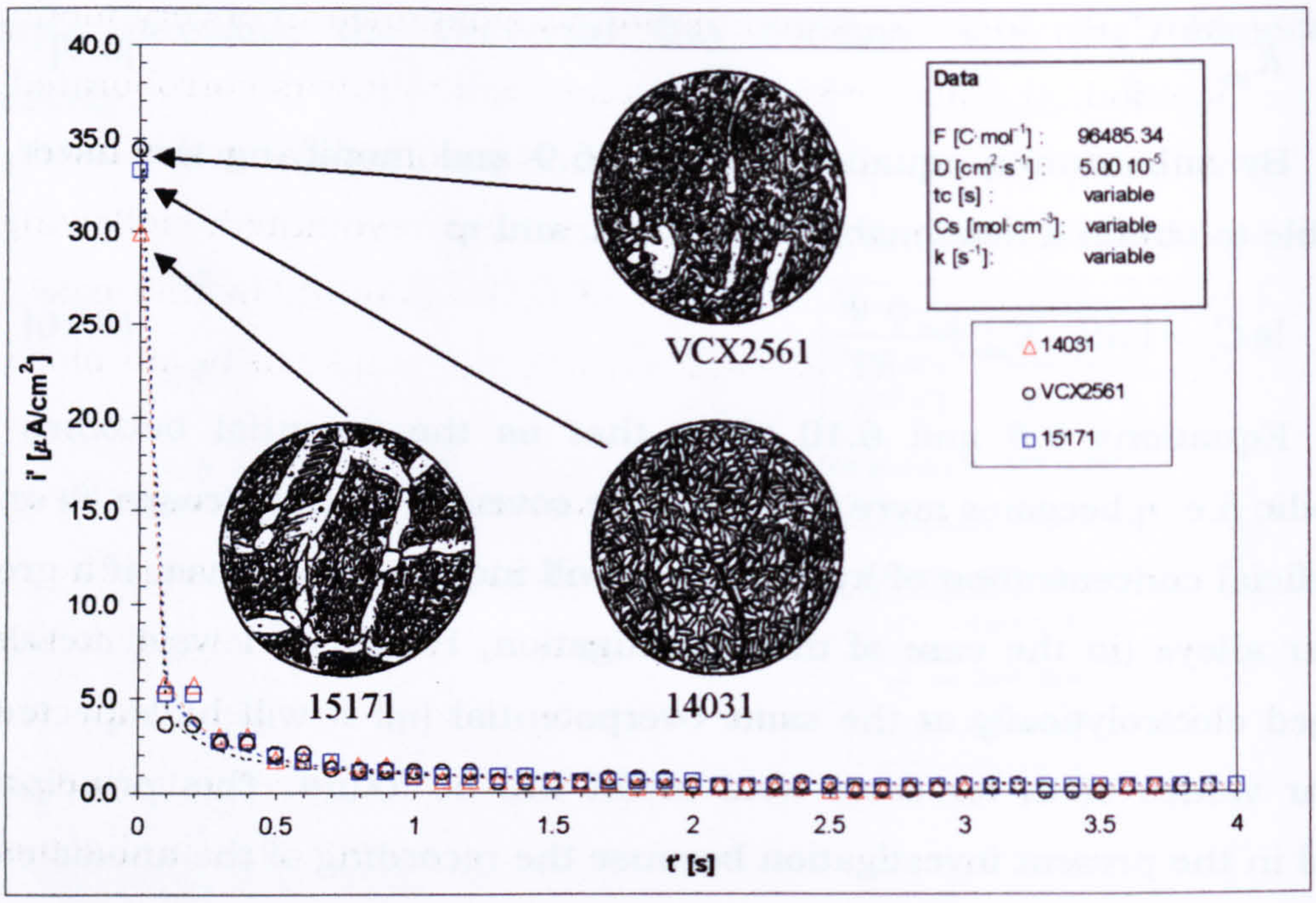

Figure 6.14 Anodic current densities for three different weld metal microstructures. The microstructures are: continuous grain boundary ferrite veins (15171), discontinuous grain boundary ferrite (VCX2561) and no grain boundary ferrite (14031). The rest of the microstructure is acicular ferrite, and variable contents of bainite and microphases. The microstructure for each weld metal is represented schematically in the figure based on real results.

6.4.7 Determination of the trapping rate constant (k)

Once the value of C_s was selected as described before, the determination k is done through iteration until the theoretical curve of anodic current density matches the experimental data. The criteria to compare the trapping rate constant for the different weld metals is schematised in the figure 6.13(b) where the effect of the value of k is shown. As can be observed in the figure, an increment of the k value produces the reduction of the anodic current density. For this reason, the variation of the k value is associated with the increase of the trap density in the weld or the variable quality of traps that could be found. The quality of the traps is the capacity of the trap to attract and immobilise the hydrogen in the material.

Other applications of the study of the k value at different charging times could be the saturation of the traps. If the sample is charged at consecutively increased times, a reduction of the k value could be related to the saturation of the traps. This criterion was employed to compare the k values and in the same weld the effect of the time of charging.

6.5 Experimental data and analysis.

In this investigation, as mentioned before, original data was taken from a previous work by Wildash[8]. This data includes:

1- *MAC proportion.* This information was obtained by a very meticulous method, and after revision of some results it was corroborated their validity. For this reason this set of data was used. The corresponding scatter of results was estimated, following the recommendations of the appropriated standard. In this case, as is discussed later the potential error is estimated to be no more than 5%.

2- *Mechanical properties.* All the results from the tensile test were employed. This data was manipulated to clearly present the results without oversimplifying. This original data was analysed following a different approach to elucidate the weld metal behaviour and the effect of hydrogen. Due to the lack in statistical information, the potential scatter of the results was estimated. This is discussed in detail later.

3- *Diffusible hydrogen measurement.* This measurement was made using gas chromatography and was utilized as was reported originally. No further manipulation was done.

As is described in this chapter, the work that was carried out during this investigation involves:

1- *Detailed metallographic analysis.* Weld metal samples were prepared in different manners to study: microstructure of the weld metals (OM, SEM and TEM), NMI characterisation (some compositional analysis, size and spatial distributions, morphology, number density, etc.), MAC identification and characterisation (location, morphology, size, etc.). The finality of this analysis is to clarify the relationship between composition, microstructure, mechanical properties and hydrogen induced cold cracking resistance.

2- *Fractographic analysis.* The fractured tensile samples were studied in some detail throughout SEM. Basically, the study was concentrated in identify the relation between microstructural features and the behaviour of the hydrogen charged samples. Especial attention was taken to the effect of hydrogen on the

fracture micromechanisms, the crack initiation and the associated microstructure or microconstituent.

3- *Thermodynamics and other theoretical calculations.* Some effort was made to apply current models to the analysis of the weld metals samples. TTT and CCT diagrams were calculated to support the effect of composition on microstructure of weld metals. Estimation of transformations temperatures (B_s, B_f, M_s and M_f) taking into account composition and size effect, in the case of the estimation of the probability in the retention of austenite in the MAC constituent. NMI stability diagrams were obtained for each weld metal with the intention of associate composition with type of expected inclusions. Other calculation involving NMI, was the effect of solidification of the weld metal on the formation of the different inclusions. Other minor mechanical estimations were employed to support the analysis of results.

4- *Trapping capacity of the weld metals.* The pulse technique described in this chapter was applied to the weld metal samples to estimate their hydrogen trapping capacity. This technique had not been employed before on weld metals. For the application of this technique some electronic circuitry was fabricated by the author to be adapted at the facilities of the laboratory. Detail of this electronic circuits are described in this volume.

5- *Statistical analysis.* When appropriate a t-student analysis was carried out to establish the significance of the results. In the case of the electrochemical test to estimate the trapping constant, due to limitation in the volume of sample each test was made maximum three times. This small size sample requires an especial statistical treatment. Confidence intervals were estimated when needed.

CHAPTER SEVEN

RESULTS AND DISCUSSIONS

PART I

THE MICROSTRUCTURE OF THE HSLA STEEL WELD METALS

In the present chapter the results of metallographic studies carried out during this investigation are presented. They were obtained using optical and high resolution-electron microscopy (FEG-SEM). Twelve weld metal samples were selected from a group of 40 compositions obtained by Wildash and collaborators [8-11], which were made with two heat inputs: 1 and 3 kJ/mm. For convenience, the weld metals produced with a heat input of 1 kJ/mm were selected, as the effect of heat input on microstructure and properties is well understood. These weld metals were utilised to cover a wide range of compositions, microstructures and strengths. Some efforts are made to classify the different weld metal microstructures. Proportion variations of grain boundary ferrite (PF(G)), acicular ferrite (AF), ferrite sideplates (FS(SP)), bainite (FS(B)), and martensite (M), were related to composition. The effect of composition on microstructure is interpreted using theoretically calculated TTT and CCT diagrams and other models for the calculation of the proportion of phases.

Attention was concentrated on identification of phases and microphases in the weld metal, as well as their volume fraction and spatial distribution. The microconstituents of the weld metal such as retained austenite, martensite-austenite-carbide islands (MAC), and non-metallic inclusions (NMI), are studied with some detail because their hydrogen trapping capacity. Effort at the identification of MAC and retained austenite was made. Theoretical calculations to try to predict the presence of retained austenite in the MAC constituent are presented. In the case of the NMI, their size and spatial distribution were assessed, and some chemical analysis was used to identify the principal types and compositions of inclusions. Some thermodynamical calculations were carried out as an attempt to predict the types of inclusions that could form from a determined weld metal composition. The purpose of these assessments is to characterise as complete as possible the microstructural features that could influence: the mechanical properties of the weld metals; the transport, distribution and trapping of hydrogen in the weld; and their resistance to hydrogen induced cracking or HICC.

7.1 General microstructure of the weld metals.

Figure 7.1 shows a general view of the weld metal CWX351. In this photomicrography, two regions in the microstructure of the weldment can be clearly differentiated:

a) The fusion region or weld metal region. This is formed mainly by columnar grains decorated by grain boundary ferrite surrounding a darker region of a fine constituent, which could be a mixture of acicular ferrite and other microconstituents such as bainite, martensite, carbides, retained austenite and MAC islands. In some welds, due to variations in composition, the presence of grain boundary ferrite is inhibited.

b) The heat affected zone (HAZ) or reheated regions in a multi-pass welding. These regions content fine ferrite grains and some darker regions, which could be MAC constituents.

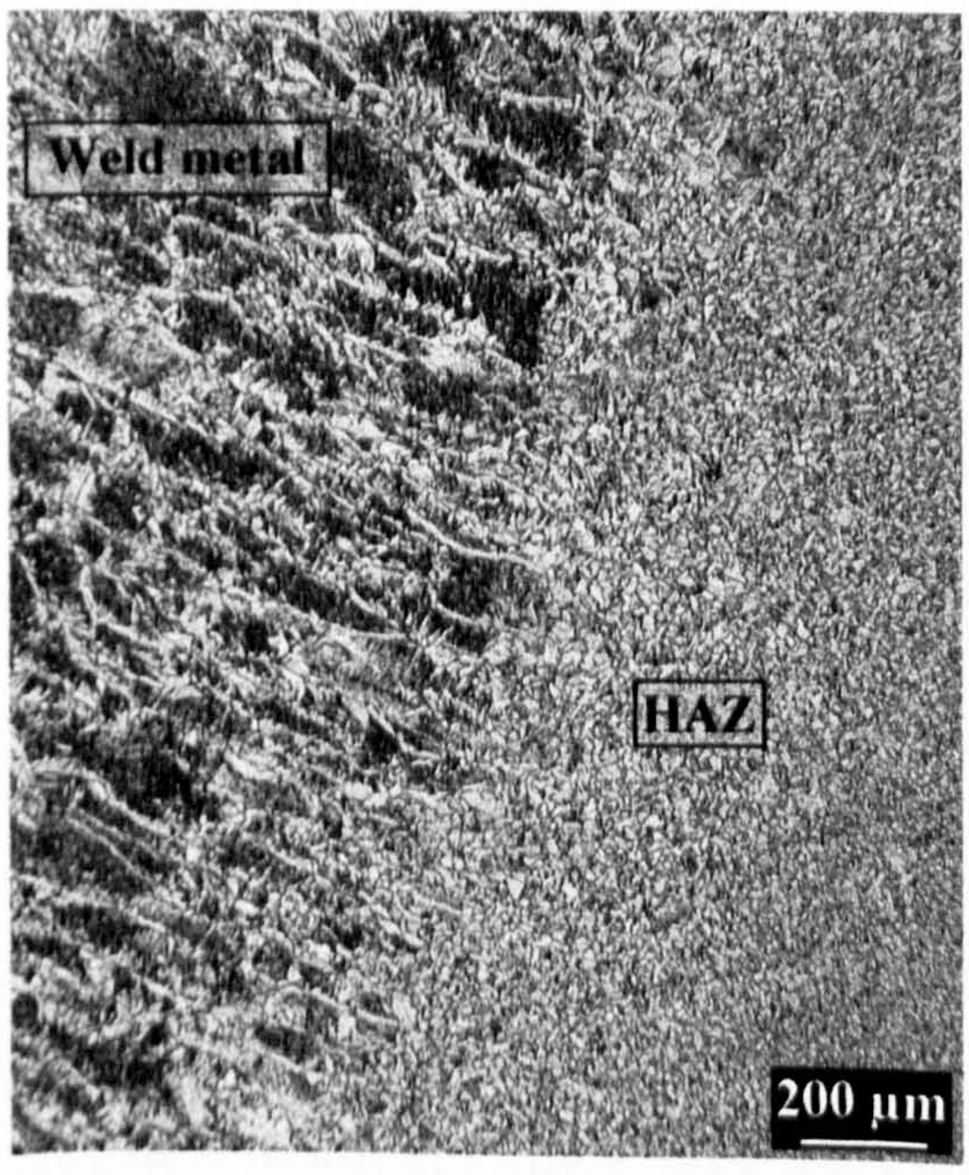

Figure 7.1 Weld metal and reheated zone of the weldment obtained with the consumable CWX351 using a heat input of 1 kJ/mm

The microstructural study in this investigation is concentrated in the weld metal region, where HICC is expected to occur in HSLA steels welds.

In the arc welding process, the weld metal composition, microstructure and mechanical properties such as strength and toughness are mainly determined by the following factors:

a- the composition of the consumables;

b- the composition of the parent metal;

c- the heat input and the thermal history of the weldment, which depends on the geometry of the workpiece.

The composition and microstructure of the weld metal were varied by Wildash[8-11] through the utilisation of different types of consumables and maintaining the other parameters similar, using 1 kJ/mm and a multi-pass bed to avoid dilution of the weld metal due to the effect of the parent plate. The composition of the consumables affects microstructure through all stages of the transformation of the weld: from the formation of inclusions in the weld pool to the solid state transformation of the weld metal, passing throughout the solidification process.

7.2 Effect of weld metal P_{cm} value on general microstructure.

Figures 7.2 and 7.3 present the general microstructure of the weld metals which were studied in this investigation. Table 6.2 in chapter 6, shows the composition of these weld metals. It can be noted in this table that the analysis was complex and no attempts were made to identify clearly the influence of compositional variables on microstructure. This complication is increased by the difficulty of recognising or differentiating the various microstructural constituents. To overcome this problem the P_{cm} value, equation 7.1 which is a measure of composition, was used as a reference to compare the different weld metals:

$$P_{cm} = \%C + \frac{\%Mn + \%Cr + \%Cu}{20} + \frac{\%Si}{30} + \frac{\%V}{10} + \frac{\%Mo}{15} + \frac{\%Ni}{60} + 5 \cdot \%B \qquad (7.1)$$

In figures 7.2 and 7.3, the different constituents of the HSLA steel weld metals: grain boundary ferrite (PF(G)), Widmanstätten ferrite (FS(SP)), acicular ferrite (AF), bainite (FS(B)) and martensite (M), can be identified. From these figures the following observations could be extracted:

1- An increase of the P_{cm} value produces the reduction in grain boundary ferrite proportion, the refinement of the microstructure and the formation of low temperature transformation products: bainite and martensite. This basically is due to the increase in hardenability of the weld metal, that is, the displacement of the TTT or CCT curve to longer times and lower temperatures.

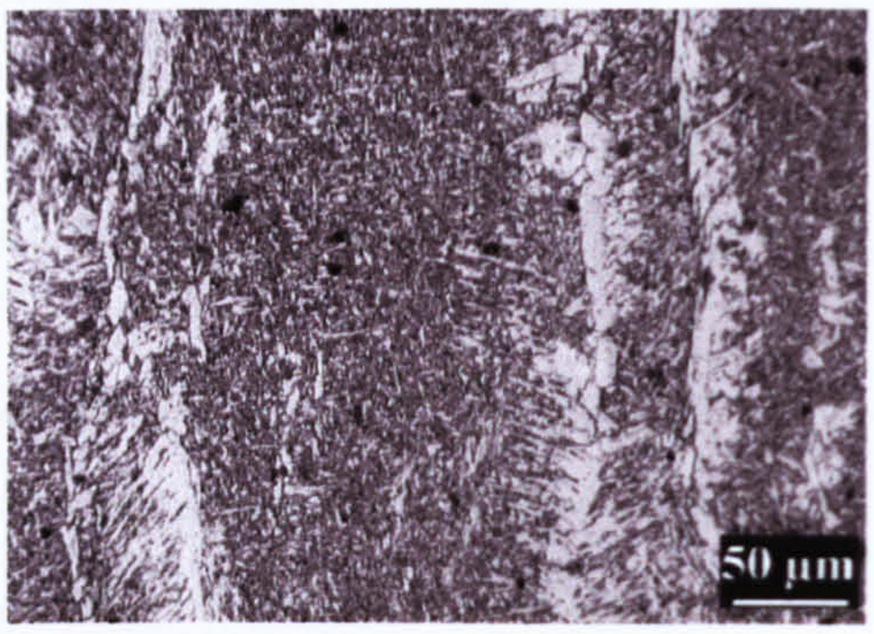

(a) P_{cm}=0.11

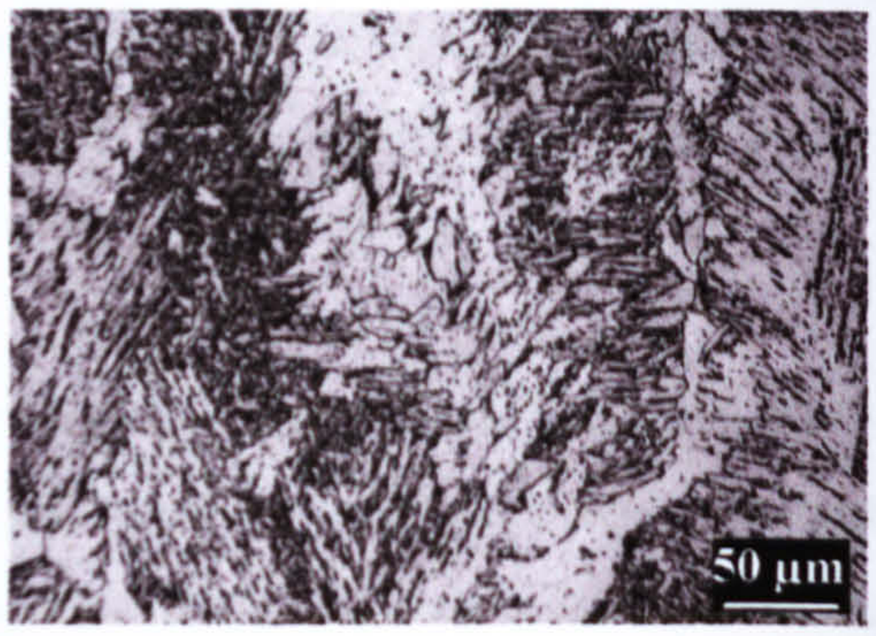

(b) P_{cm}=0.12

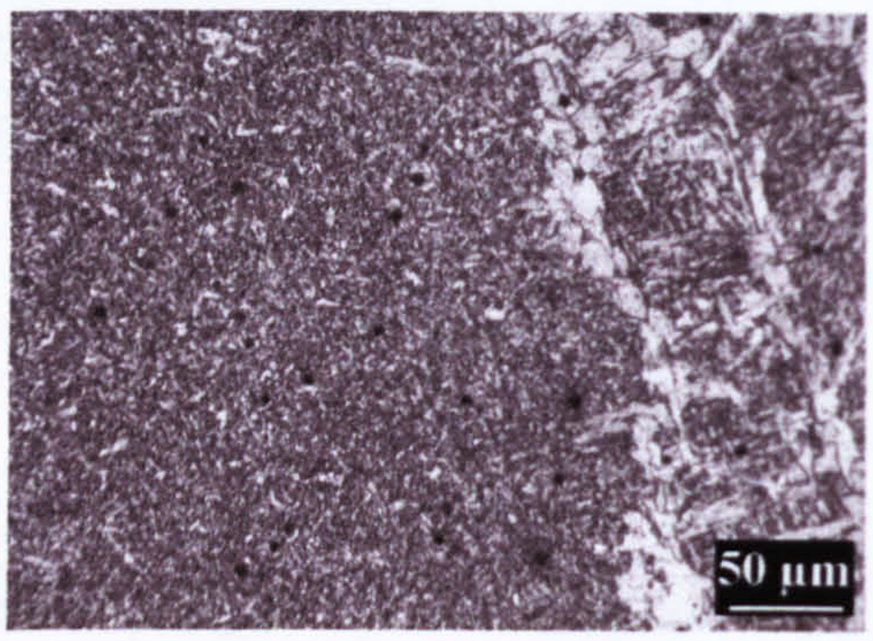

(c) P_{cm}=0.13

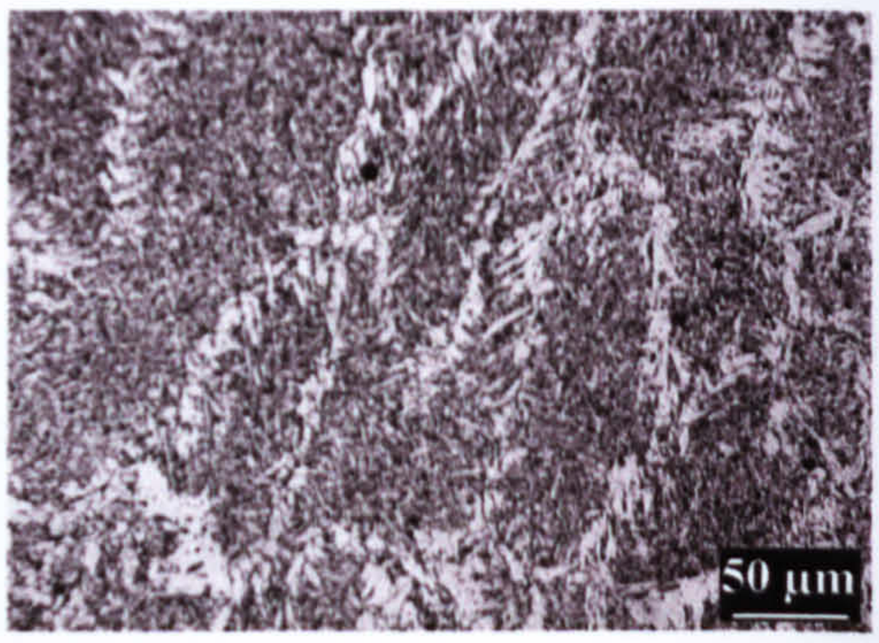

(d) P_{cm}=0.15

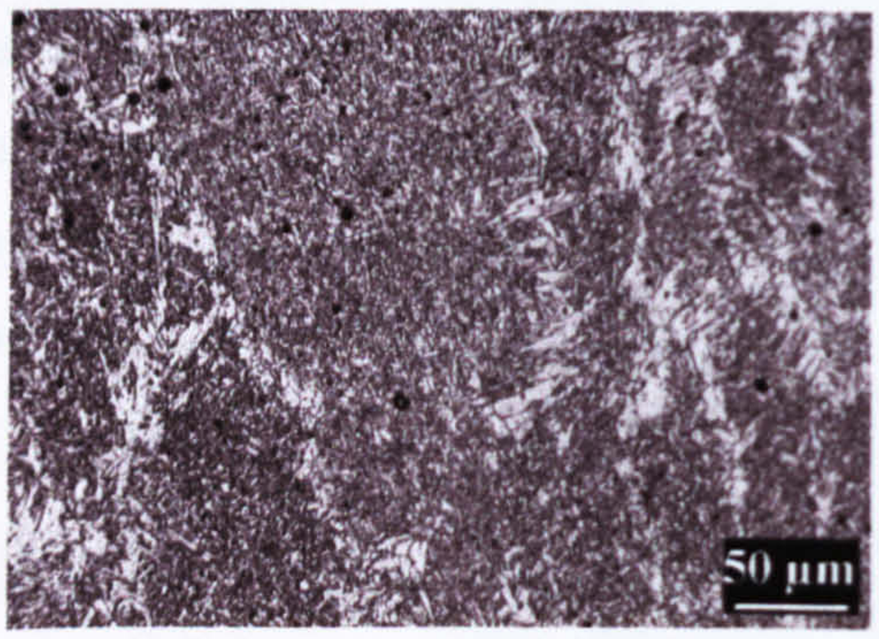

(e) P_{cm}=0.17

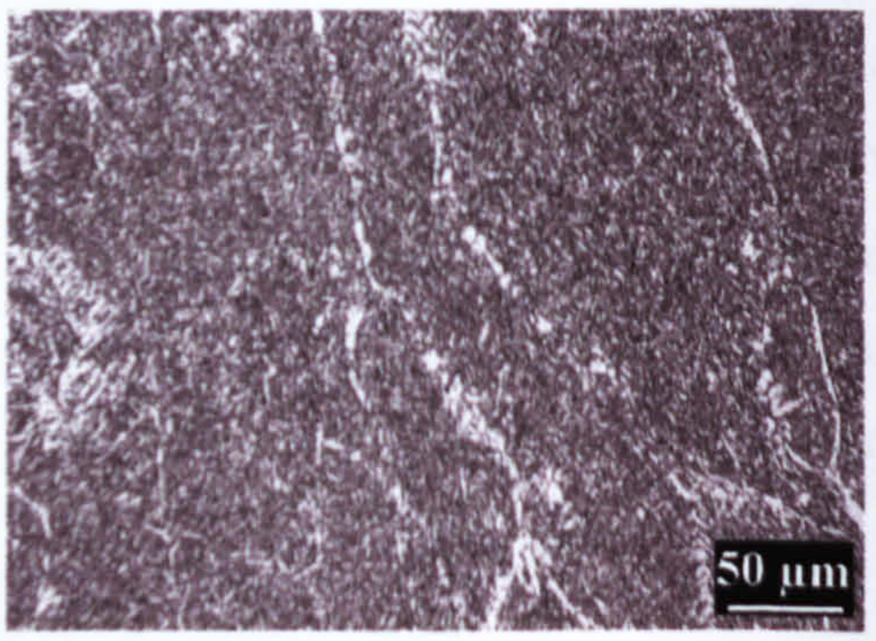

(f) P_{cm}=0.18

Figure 7.2 Effect of composition (P_{cm}) on the microstructure of six different weld metals obtained with a heat input of 1 kJ/mm: (a) CWX181, (b) CWX351, (c) 14001, (d) 15171, (e) VCX2561 and (f) CWX361.

2- In the group of weld metals that contain grain boundary ferrite, two sub-groups could be delineated: those containing a continuous network of grain boundary ferrite and those accommodating a discontinuous network. This feature has been previously shown by Wildash[8] to have a significant effect on the HICC behaviour of the weld metals.

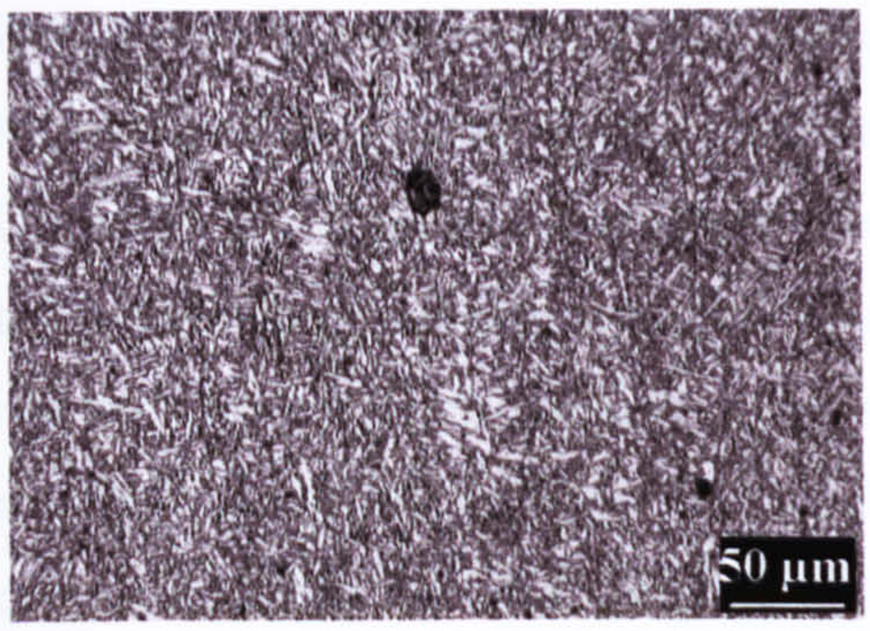

(a) P_{cm}=0.20

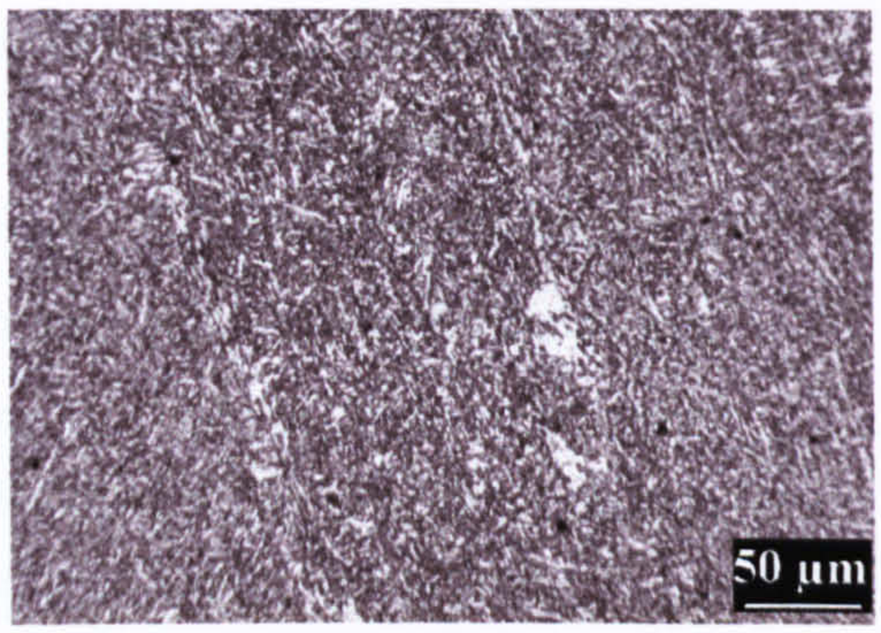

(b) P_{cm}=0.20

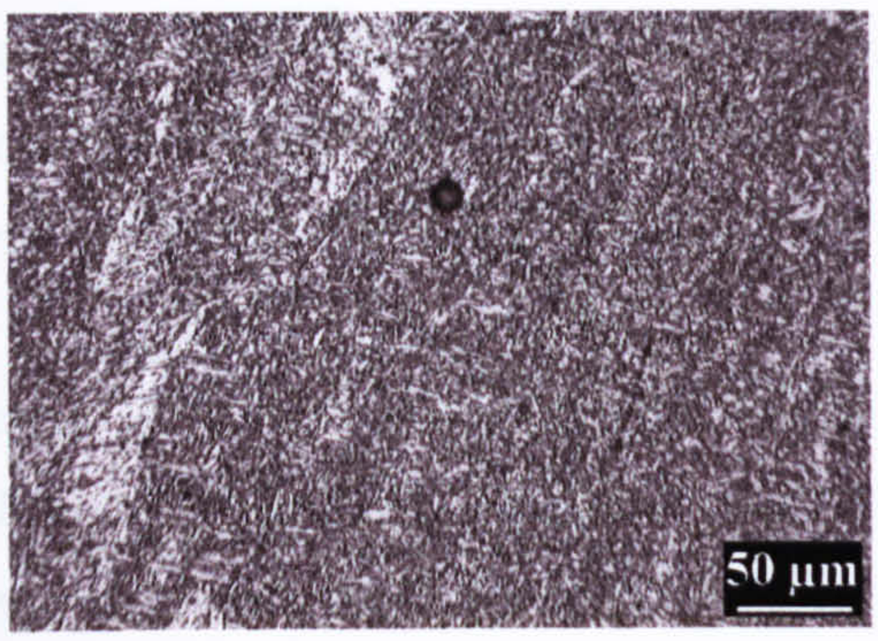

(c) P_{cm}=0.21

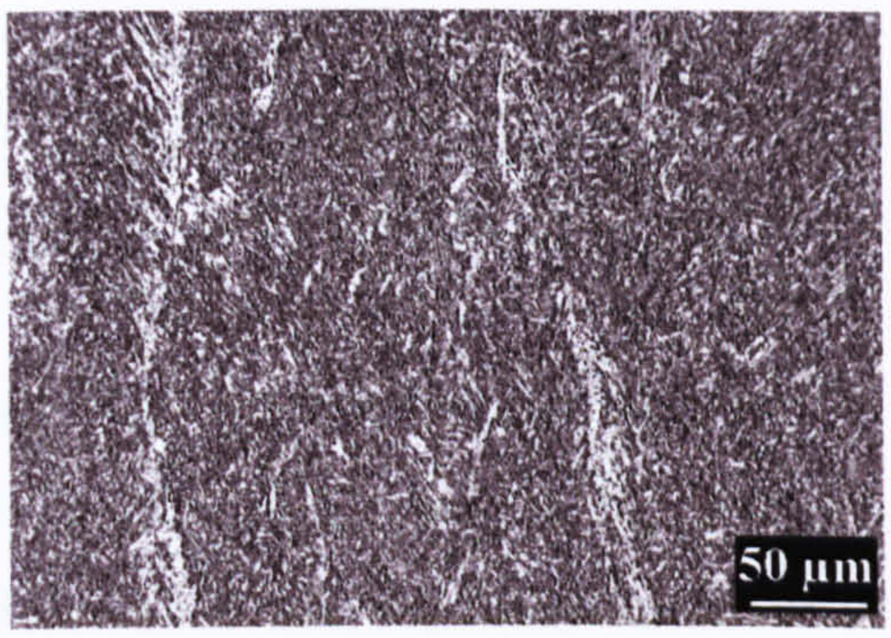

(d) P_{cm}=0.23

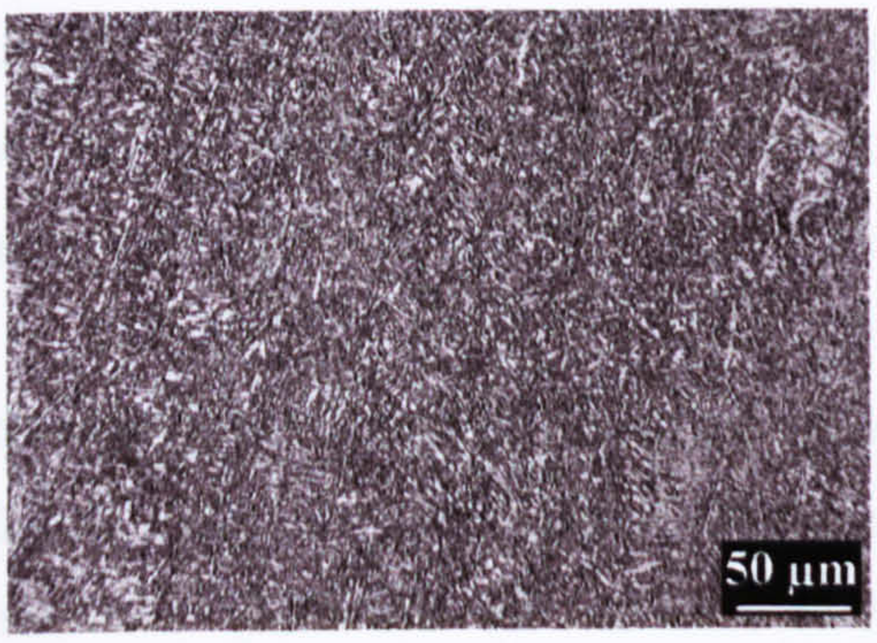

(e) P_{cm}=0.24

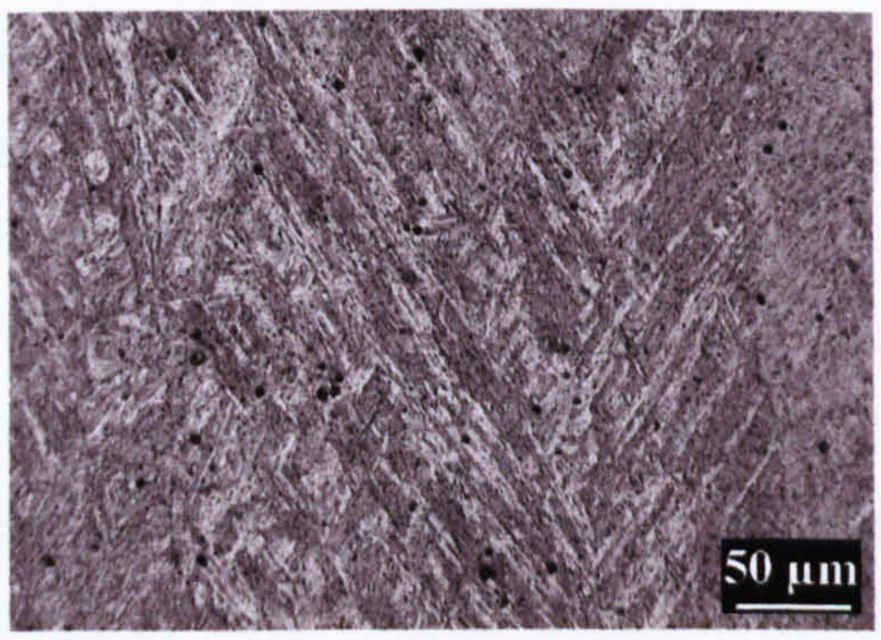

(f) P_{cm}=0.27

Figure 7.3 Effect of composition on the microstructure of six different weld metals obtained with a heat input of 1kJ/mm: (a) CWX201, (b) 14031, (c) CWX71, (d) CWX91, (e) CWX81 and (f) CWX331.

3- The size (width and length of columnar grains) vary slightly between weld metals with no particular relation with the increase P_{cm} value. Cooling rate and heat input are important to control the size of these columnar grains. The prior austenitic columnar grain is observed clearly in the weld metal with PF(G) and hardly in those without this constituent decorating the grain boundary. The austenite grains are

formed during the solidification process and/or the transformation of δ-ferrite to austenite and are affected by: the grain size of the parent steel (in this case previous weld pass), the non-metallic inclusions density, size and distribution, and the alloy content. The reduction in grain size could be the consequence of: the variations in C content and/or the non-metallic inclusion density. An augment in C has been reported [14, 48, 55-56] to reduce the columnar grain width and size, which could be due to the formation of carbides that could control the austenite grain growth. Moreover, a high non-metallic inclusion density could affect the nucleation and growth of the new grains. This change in grain size influences the solid-state transformation due to the increase of places for the nucleation of grain boundary ferrite, bainite or another transformation product.

The weld metal microstructure in the lower P_{cm} range (<0.20), changes from a mixture of grain boundary ferrite (PF(G)), Widmanstätten ferrite (FS(SP)) and acicular ferrite (AF) to almost 100% acicular ferrite (AF), as observed in figure 7.2 and 7.3(a). However, at higher P_{cm} values (>0.20) the appearance of bainite could be observed, constituent which appear to compete with the formation of acicular ferrite, as shown in figures from 7.3(a) to 7.3(e). At the highest P_{cm} value of 0.27, a martensitic microstructure can be found, which also contains an amount of bainite which is difficult to distinguish using the optical microscope.

Micro-constituents such as retained austenite and martensite-austenite-carbides islands (MAC) are present in small proportions in all the welds mentioned above. This proportion is affected by the alloy content and cooling rates, as is discussed in the next section.

7.3. Details of weld metals microstructure and composition effect.

Figures 7.4 to 7.6 present in more detail representative microstructure of weld metals. The proportions of each phase are shown, in figures, adjacent to the microstructures. In some cases, the phases can be clearly identified as grain boundary ferrite (PF(G)), acicular ferrite (AF) and ferrite with aligned second phases (FS(A)), in which is included Widmanstätten ferrite or ferrite side plates (FS(SP)) and bainite (FS(B)). When no alignment between second phase and ferrite is found, the phase is identified as FS(NA). However, in other welds the distinction between the different features was very difficult. In these

cases a mixture of microstructural features are reported, such as: AF+FS(NA) and FS(A)+M, as in figures 7.4(c) and 7.5. Evolution of the microstructure with P_{cm} value is shown in table 7.1. In annexe A.10 the phase proportion of all the weld metals is presented. Figures from 7.4 to 7.6 are representative of them. The following observations are worthy of comment:

1- The microstructure of the studied weld metals is a mixture of various features. At low P_{cm} values grain boundary, Widmanstätten and acicular ferrite forms predominates. At higher P_{cm} values bainite apparently compete with the formation of acicular ferrite and it is possible to produce martensite.
2- Microphases are found in all the weld metals. As is discussed in next section, the proportion of microphases such as retained austenite, MAC islands and carbide depends on the amount of particular alloying elements. The austenite transformation to acicular ferrite tends to leave a significant amount of untransformed austenite between the intersecting ferrite laths as a consequence of its chaotic interlocking nature. These regions later transform to either ferrite-carbide aggregates, martensite or remains as retained austenite, depending on cooling rate and composition. In next section, an attempt to predict the retention of austenite is made.
3- At high P_{cm} values and due to the variation of some alloying elements such as Mn, Cr, Ni and Mo, it is promoted the formation of bainite, which is found as isolated islands as shown in figure 7.6 for several welds. Manganese, chromium and nickel are typically used to produce low carbon bainite steels [115]. Probably, a fully bainitic weld metal is not obtained due to the large size of the prior austenite grain. The sulphur content as been reported to promote the nucleation of bainite at the grain boundary, where this impurity segregates [116].

Table 7.1 Evolution of the weld metal microstructure with composition. The weld metal is a representative example of that microstructure

P_{cm} value	Microstructure*	Weld metal
$P_{cm}<0.17$	PF(G) [continuous] + AF + FS(A) + microphases	CWX181
$0.17<P_{cm}<0.20$	PF(G) [discontinuous] + AF + microphases	CWX361
$P_{cm}\geq0.20$	AF + FS(B) + FS(NA) + microphases	CWX201
$P_{cm}=0.27$	M + FS(B) + microphases	CWX331

*PF(G): grain boundary ferrite, AF: acicular ferrite, FS(A): Widmanstätten ferrite, FS(B): bainite, FS(NA): ferrite with non aligned second phase or degraded ferrite with MAC constituents and M: martensite.

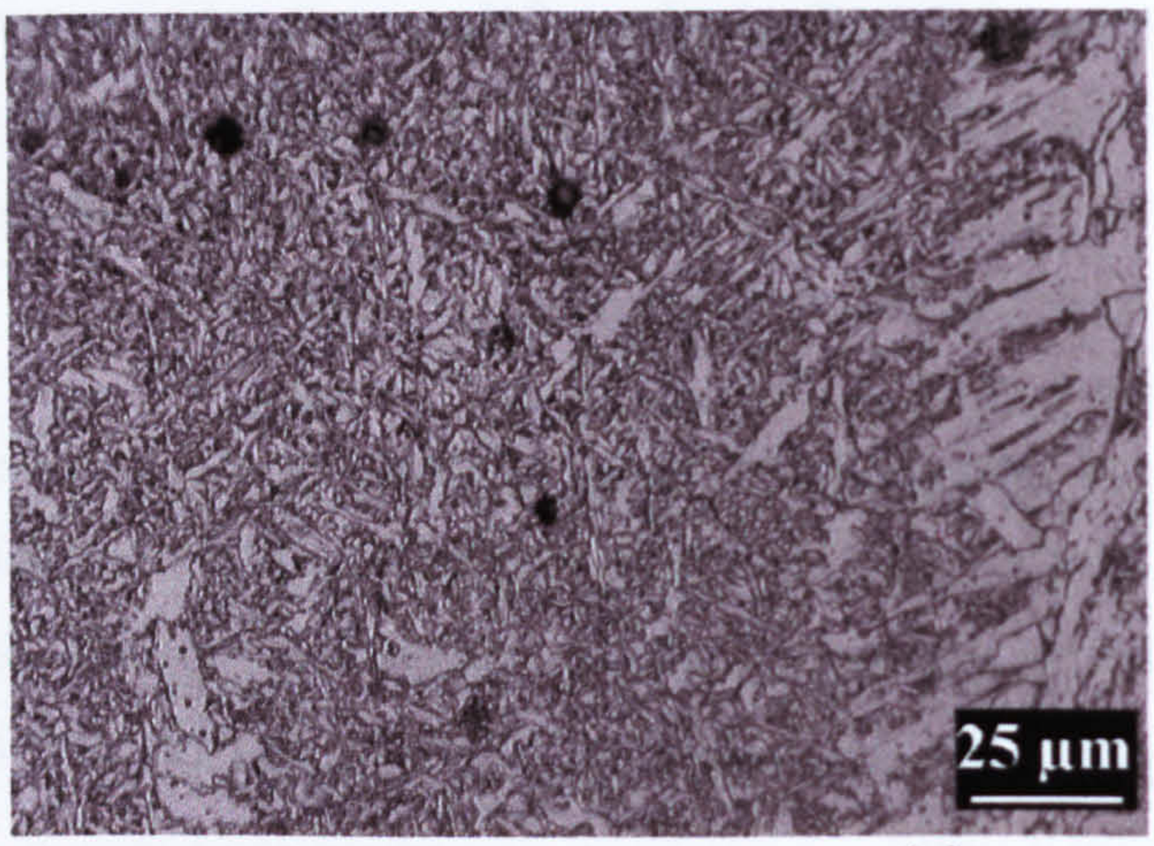

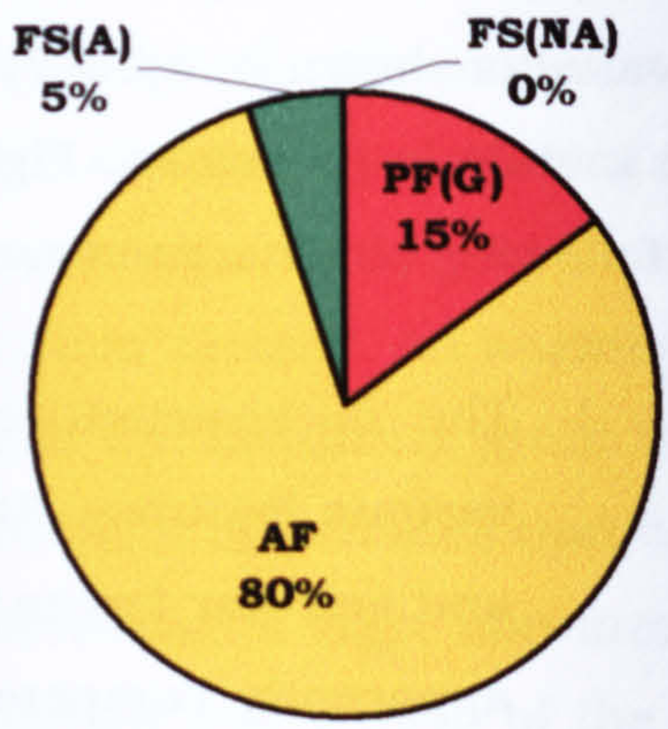

(a)

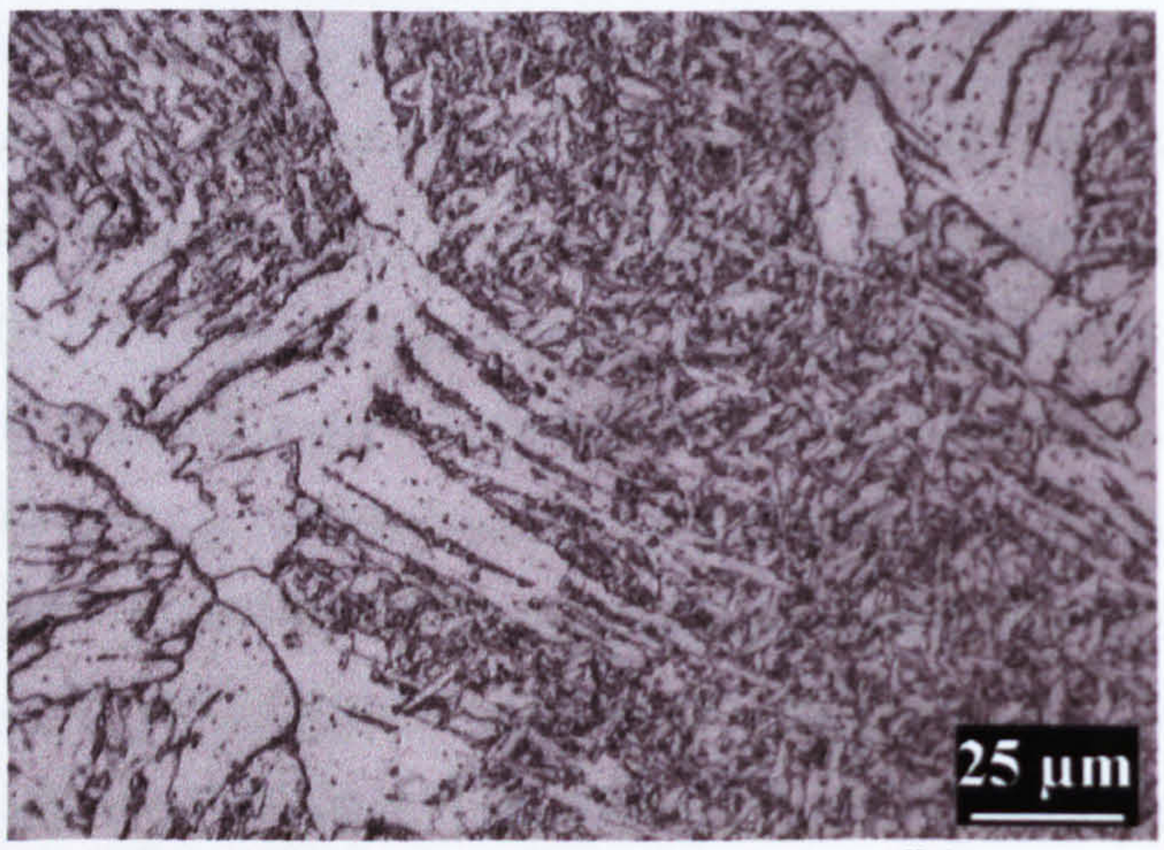

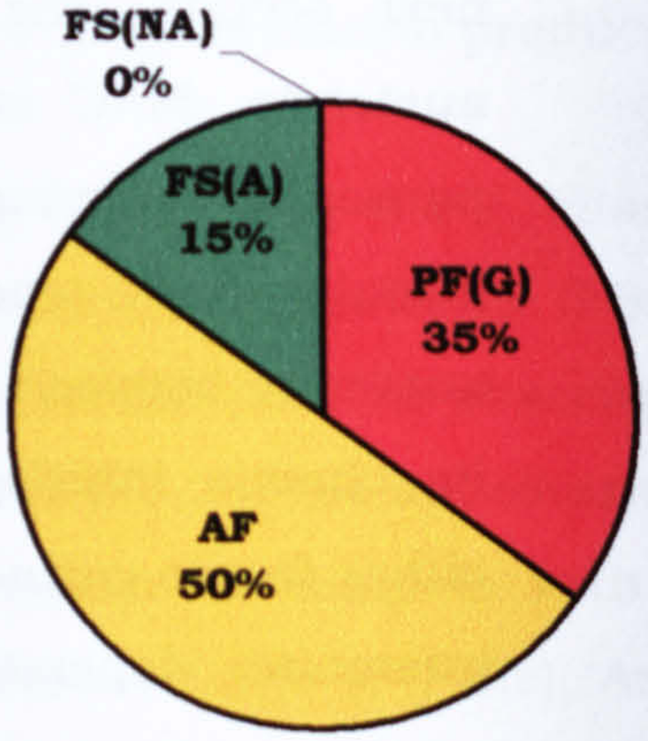

(b)

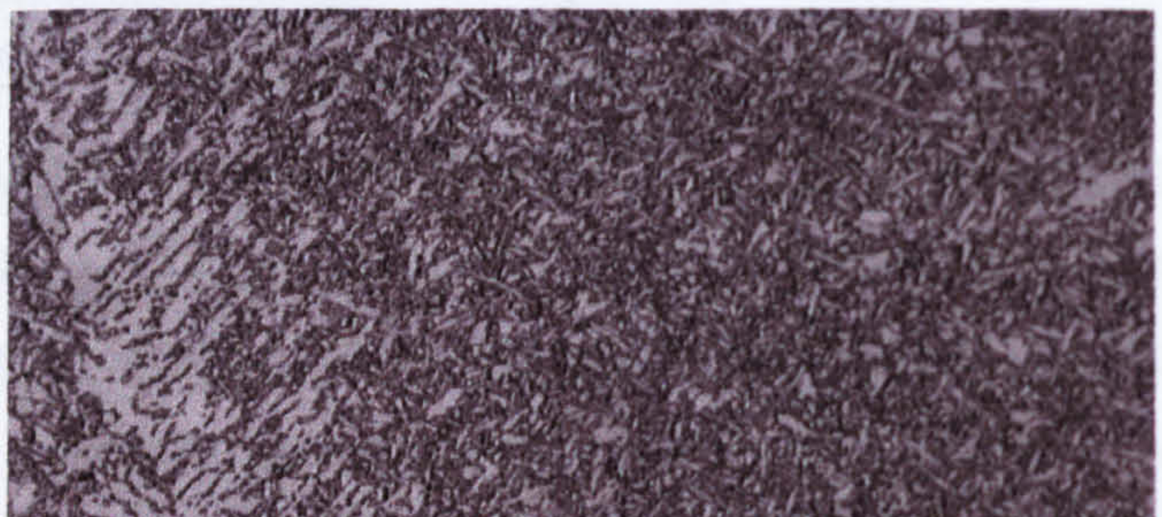

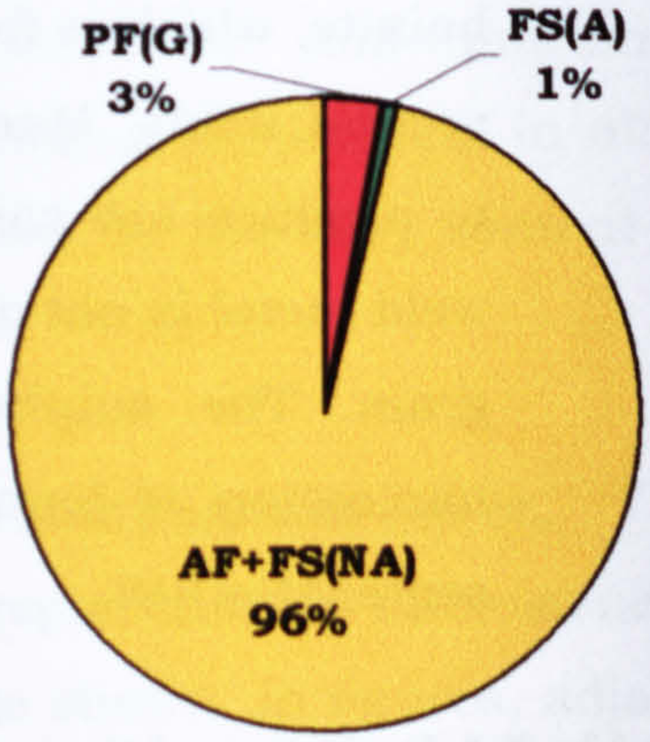

(c)

Figure 7.4 Microstructural changes due to the composition of different weld metals: (a) CWX181gb, (b) CWX351 and (c) CWX361. The P_{cm} values are 0.11, 0.12 and 0.18, respectively, as seen in table 7.1.

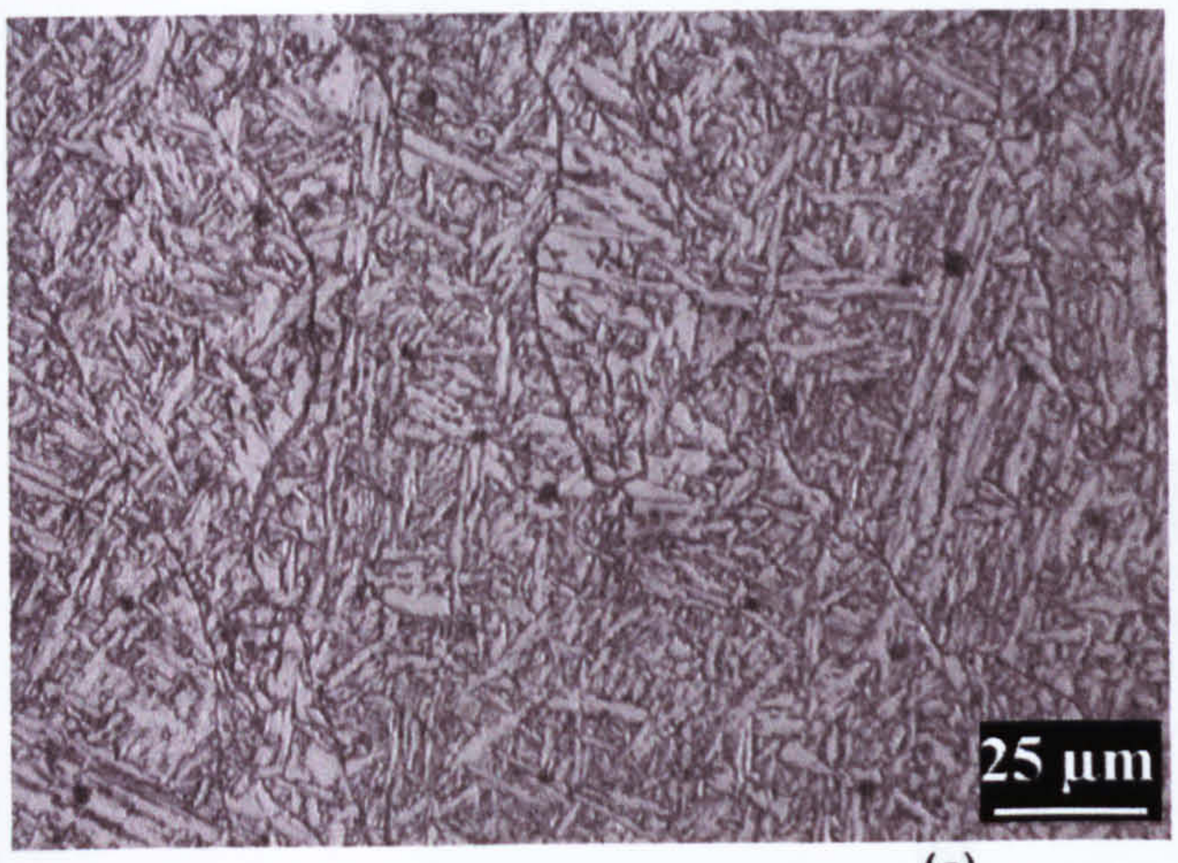

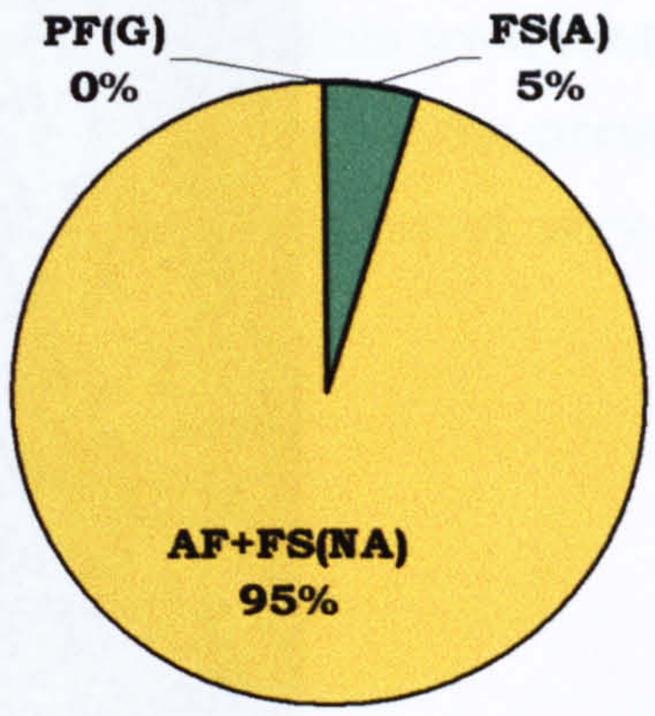

(a)

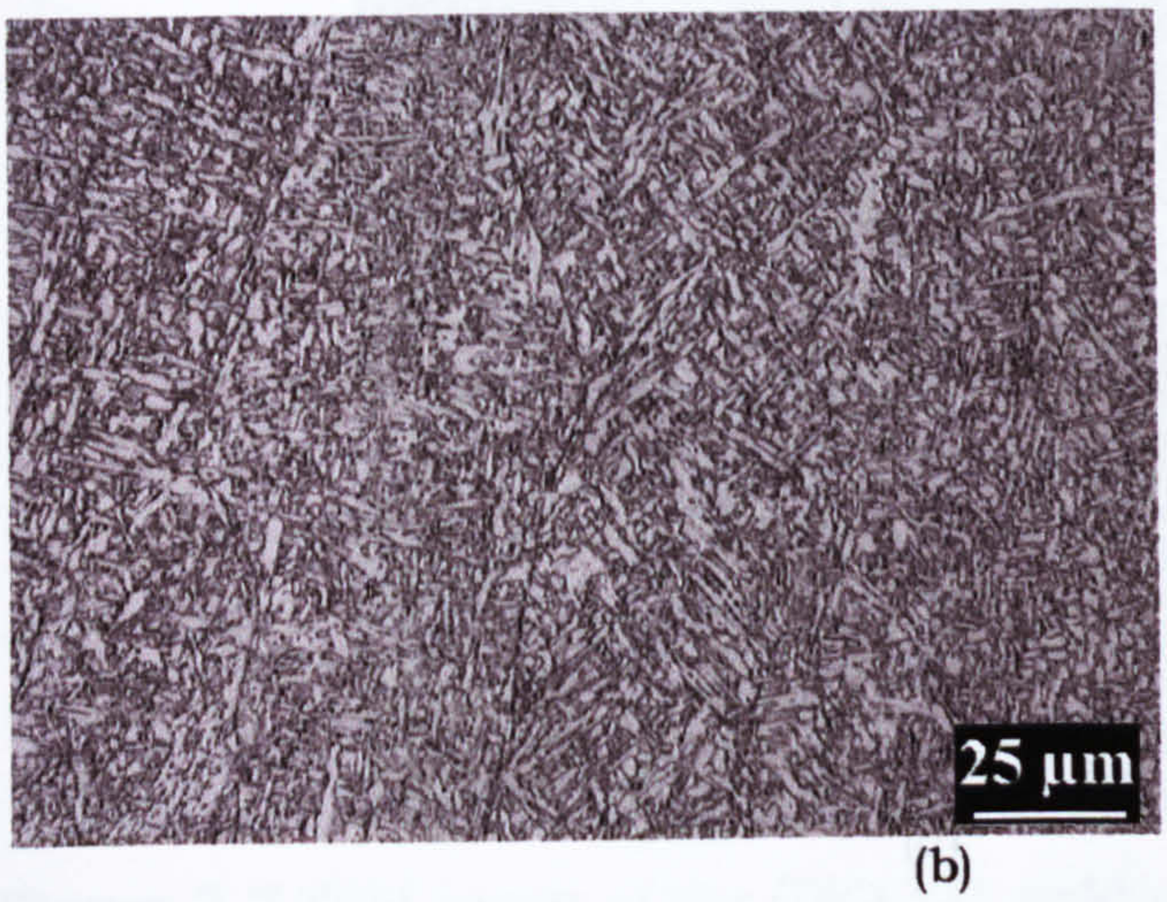

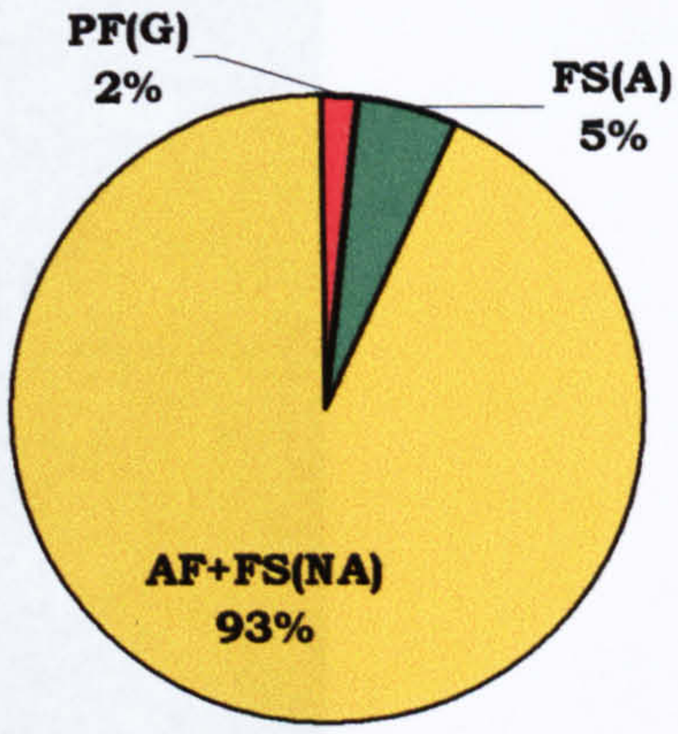

(b)

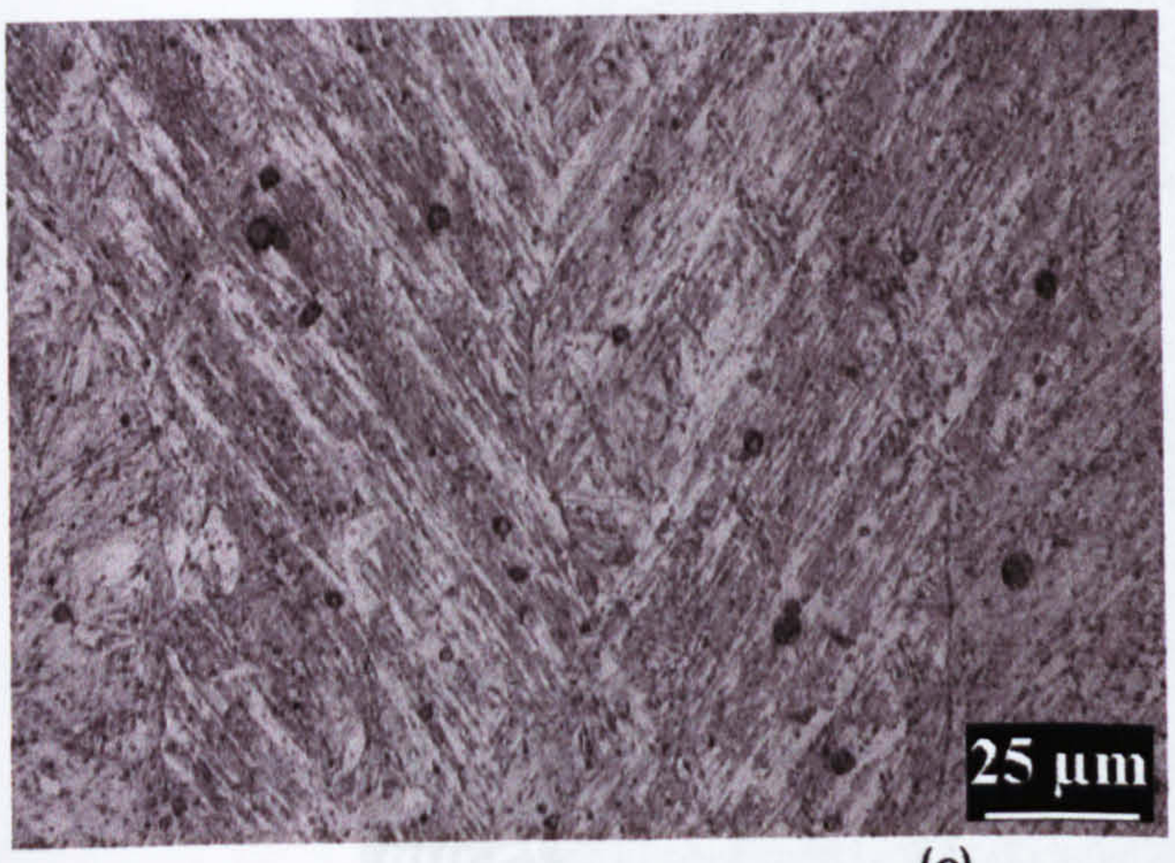

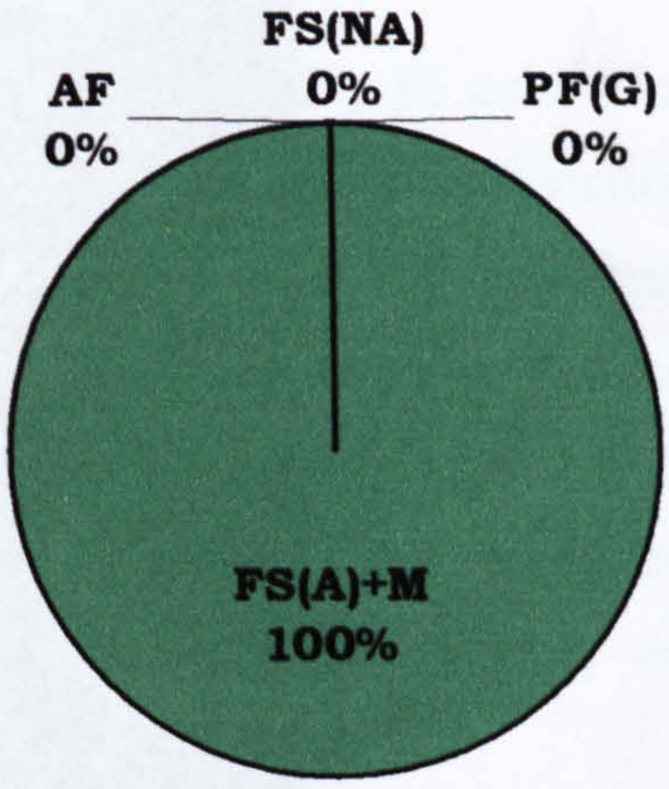

(c)

Figure 7.5 Microstructural changes due to the composition of different weld metals: (a) CWX201, (b) CWX81 and (c) CWX331. The P_{cm} values are 0.20, 0.24 and 0.27, respectively, as seen in table 7.1.

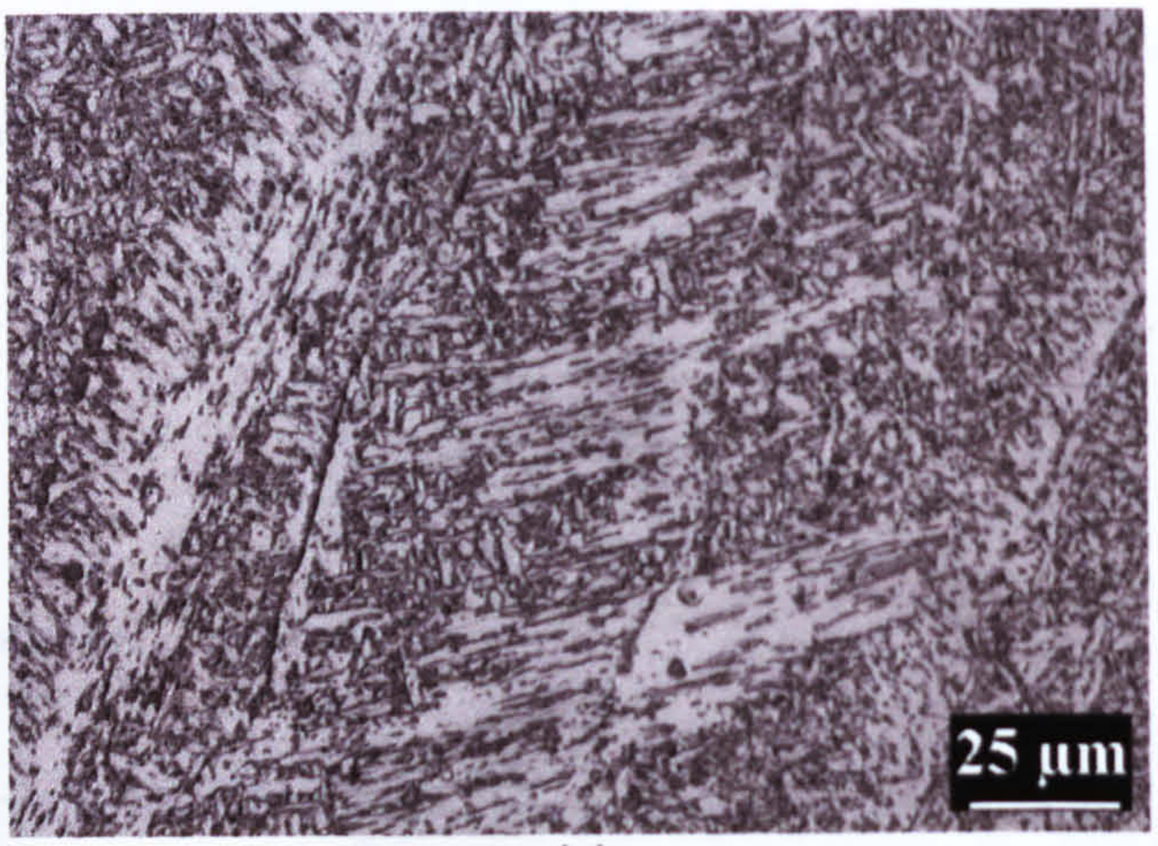

(a)

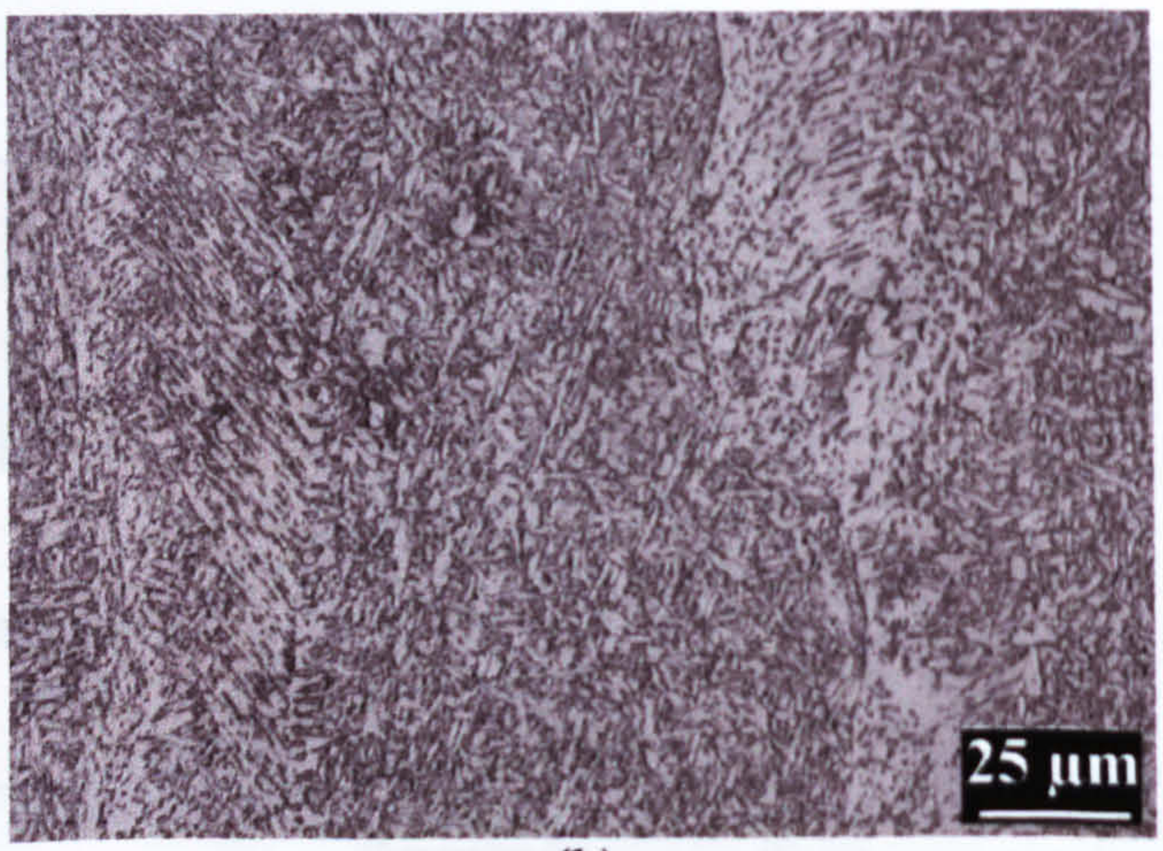

(b)

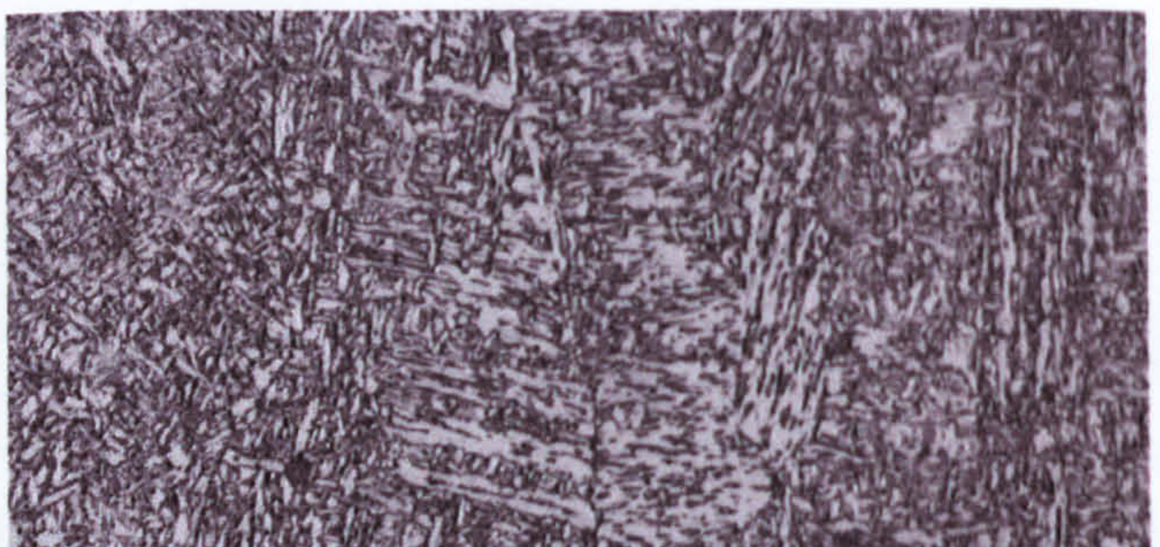

(c)

Figure 7.6 Isolated islands of FS(A) or bainite in three weld metals: (a) CWX71, (b) CWX81 and (c) CWX91.

4- High content of Ni and Mo promotes the formation of martensite as is the case of the CWX331 weld metal, which seems to be a mixture of lower bainite and martensite. The TEM image of this weld metal is presented in figure 7.7. It can be observed in this figure the presence of bainitic ferrite laths and the high dislocated region of very fine martensite laths.

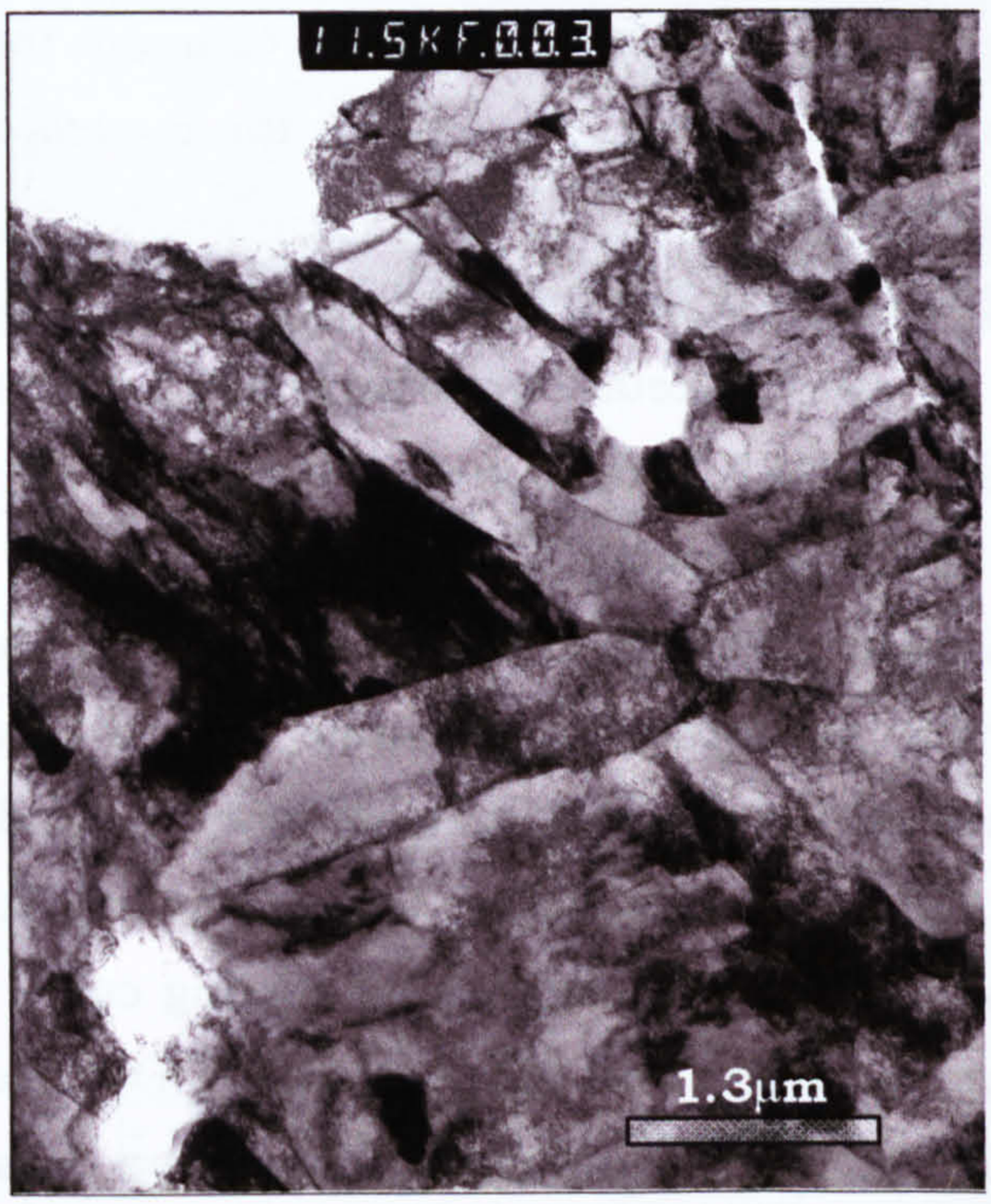

Figure 7.7 TEM image of the CWX331 weld metal containing bainite and martensite (dark region on centre left of picture).

5- The increase in some alloying elements such as Cr, Ni and Mo, as expected, produces the refinement of the weld metal microstructure as can be observed comparing CWX201 with CWX71 in figures 7.5 (a) and (b), respectively. This could be the result of the retardation of the austenite transformation, which reaches lower temperatures to convert to ferrite, thus refining the microstructure. The formation of precipitates from the microalloying additions (Nb, V, Ti) could contribute to this effect.

This general description of the variation of the weld metal microstructure, as discussed previously, permits to provide a basis for understanding the wide spectrum of weld metal strength (from 400 MPa to 1000 MPa) in the as-welded condition.

7.4 Calculated TTT and CCT diagrams for the HSLA steel welds

In the last section the effect of the composition on the microstructure of the weld metal was briefly elucidated. In this section, the effect of the composition on the weld metal hardenability and phase proportion is treated using two computer programs based on simple thermodynamic and kinetic models. For calculation of the TTT and CCT diagrams the models first presented by Bhadeshial[118] were used by Babu et.al.[119] to produce a suitable software. The other program that was used to estimate the phase proportion was made by Babu et. al.[120] and implements the models reported by Ashby, Easterling and Ion[121-122].

TTT and CCT diagrams are a convenient way of presenting the effect of the composition on weld metal transformation. Figure 7.8 shows the calculations for the CWX181 weld metal. Figure 7.8(a) shows the actual microstructure of the weld metal, figure 7.8(b) presents the TTT and CCT diagrams for this weld metal and figure 7.8(c) plots the variation of the proportions of ferrite, martensite and bainite with the cooling rate. Figure 7.8(a) shows a microstructure consisting of grain boundary ferrite (PF(G)), ferrite sideplates (FS(A)) and acicular ferrite. Figure 7.8(b), showing the transformation diagrams and the calculated cooling curve for the weld metal near the centre line, indicates that this general form of microstructure is well predicted. The calculation of the cooling rate curve, based on Rosenthal's equations, is explained in annex A.9. Using this cooling curve, it should be noted that the formation of PF(G) is expected in agreement with the actual microstructure. However, the diagram fails to show clearly the range of transformation for ferrite sideplates and acicular ferrite, regions that must appear between the PF(G) initiation curve and the bainite start line. These transformation boundaries can be only obtained experimentally. Harrison and Farrar [123-124] present more complete CCT diagrams and phase proportion for C-Mn weld metals. Figure 7.8(c), where the variation of the phase proportion with the cooling rate is shown, could supplement diagram 7.8(b). This figure presents the proportion of ferrite, bainite and martensite after the solid state transformation, information that is not contained in the previous diagram. In this case, it is predicted the formation of 80% ferrite and 20% bainite, but no distinction is made about grain boundary, acicular ferrite or ferrite side plates. Similar diagrams to figure 7.8(c) were calculated for the rest of weld metals but the phase proportion predictions not were satisfactory for weld metals with P_{cm} values above 0.20.

(a)

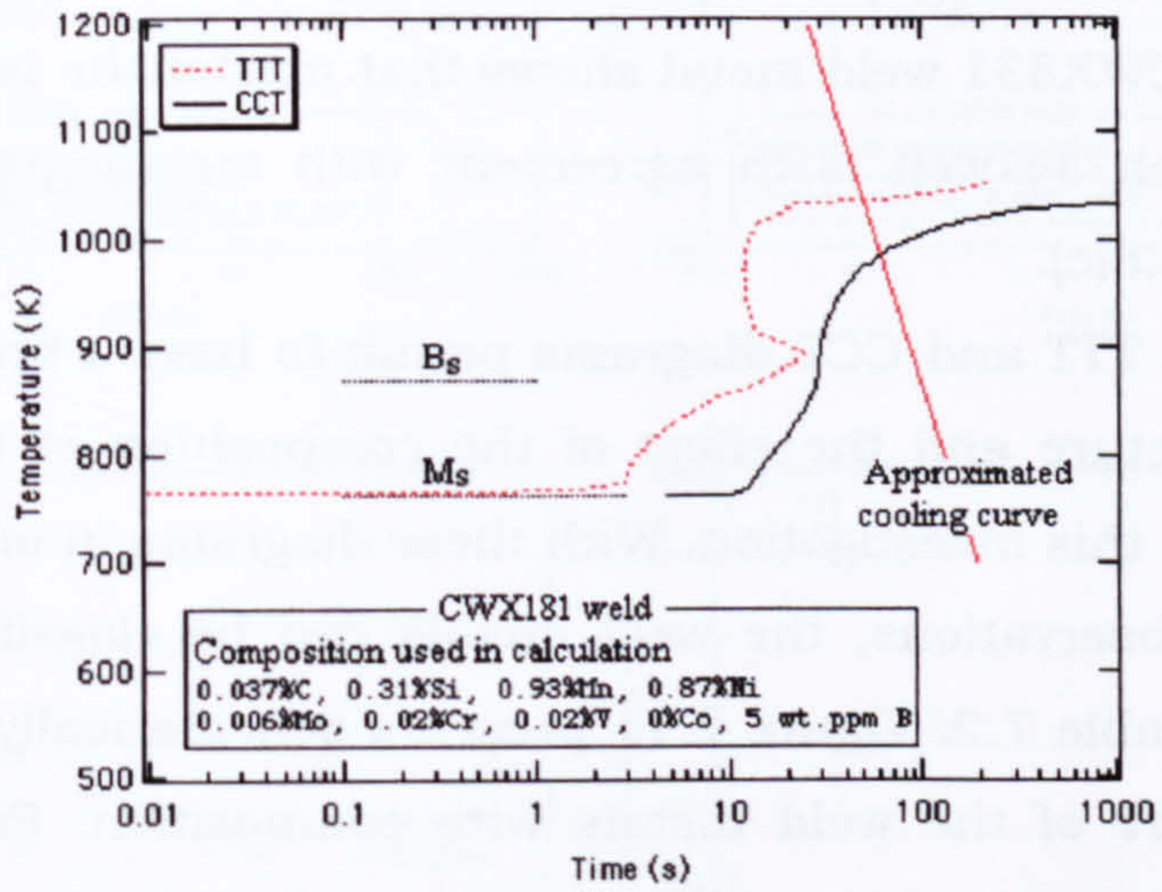

(b)

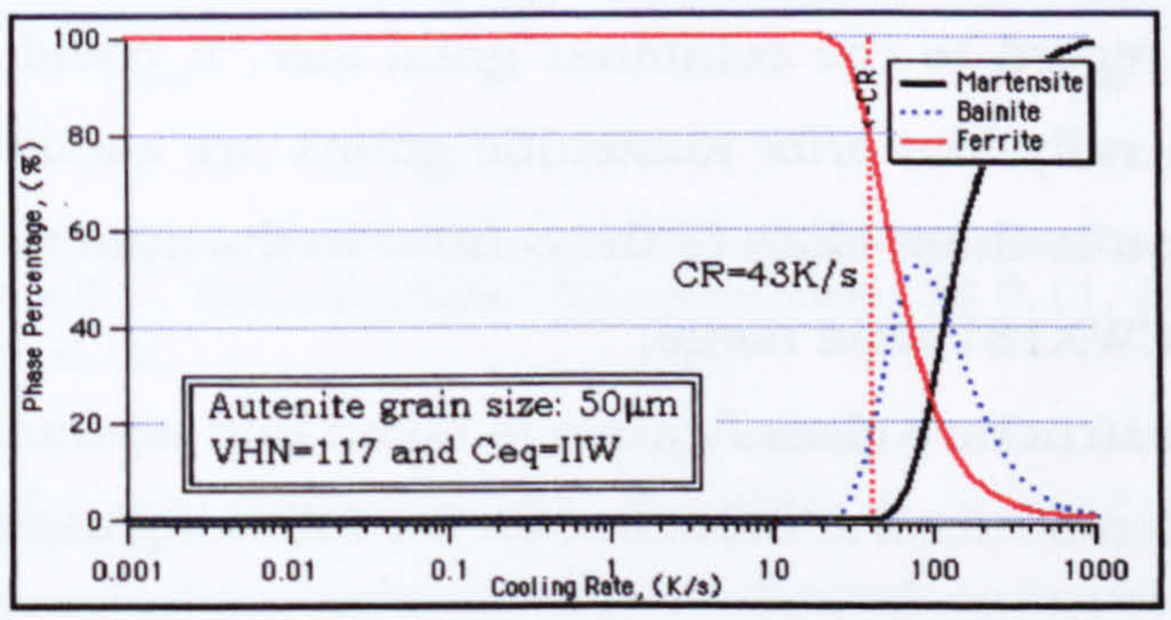

(c)

Figure 7.8 Microstructure of the weld metal CWX181gb (a) Actual microstructure showing PF(G), FS(A), AF and microphases, (b) TTT and CCT diagram with the cooling curve superposed and (c) Calculated phase proportion of the weld metal at CR=43 K/s. Bs and Ms are the start transformation temperature for bainite and martensite, respectively.

In figures 7.9 and 7.10, calculated TTT (red dotted line) and CCT (continuous black line) for all studied weld metals are presented. On each diagram the estimated cooling curve is superimposed. Figure 7.9, it can be noted that the formation of grain boundary ferrite is expected for this group of weld metals, results that are in agreement with experimental observations. In contrast, figure 7.10 do not predict the formation of grain boundary ferrite but bainite. It can be observed that for the case of CWX201 weld metal (figure 7.10(a)) the cooling curve intercepts the CCT diagram in a region between polygonal ferrite and bainite, slightly above B_s temperature, the initiation temperature of bainite. In this region it is expected to occur the formation of acicular and/or bainite. Experimental observations confirm this microstructure (see figure 7.5(a)). Weld metals represented in figures 7.10(b) to (f) indicate that bainite is expected, as shown experimentally in figure 7.3. The diagram for the CWX331 weld metal shows that martensite is expected in this weld metal, which as well is in agreement with metallographic results, as shown in figure 7.5(c).

Calculated TTT and CCT diagrams permit to have a broad visualisation of the microstructure and the effect of the composition of the various weld metals studied in this investigation. With these diagrams in mind and from the metallographic observations, the weld metals can be classified as shown in figure 7.11 and table 7.2. Figure 7.11 presents schematically the evolution of the microstructure of the weld metals with composition. Five types can be observed and table 7.2 indicates which weld metals pertain to each type. Weld metals in the same group have different proportions of the phases and/or composition. In regard to the columnar grain size, it could vary in the same weld metal. Generally, the prior austenitic grains are smaller near the fusion line in comparison to those close to the centre. In the annexe A.11 is shown an example for the CWX181 weld metal.

This microstructure classification is taken into account in next chapters to explain the microstructural influence on the following aspects:

1- The changes in fracture micromechanisms of the weld metal with and without hydrogen. The presence of microstructural features that could initiate cleavage cracks could be: grain boundary ferrite, bainite, martensite, etc.

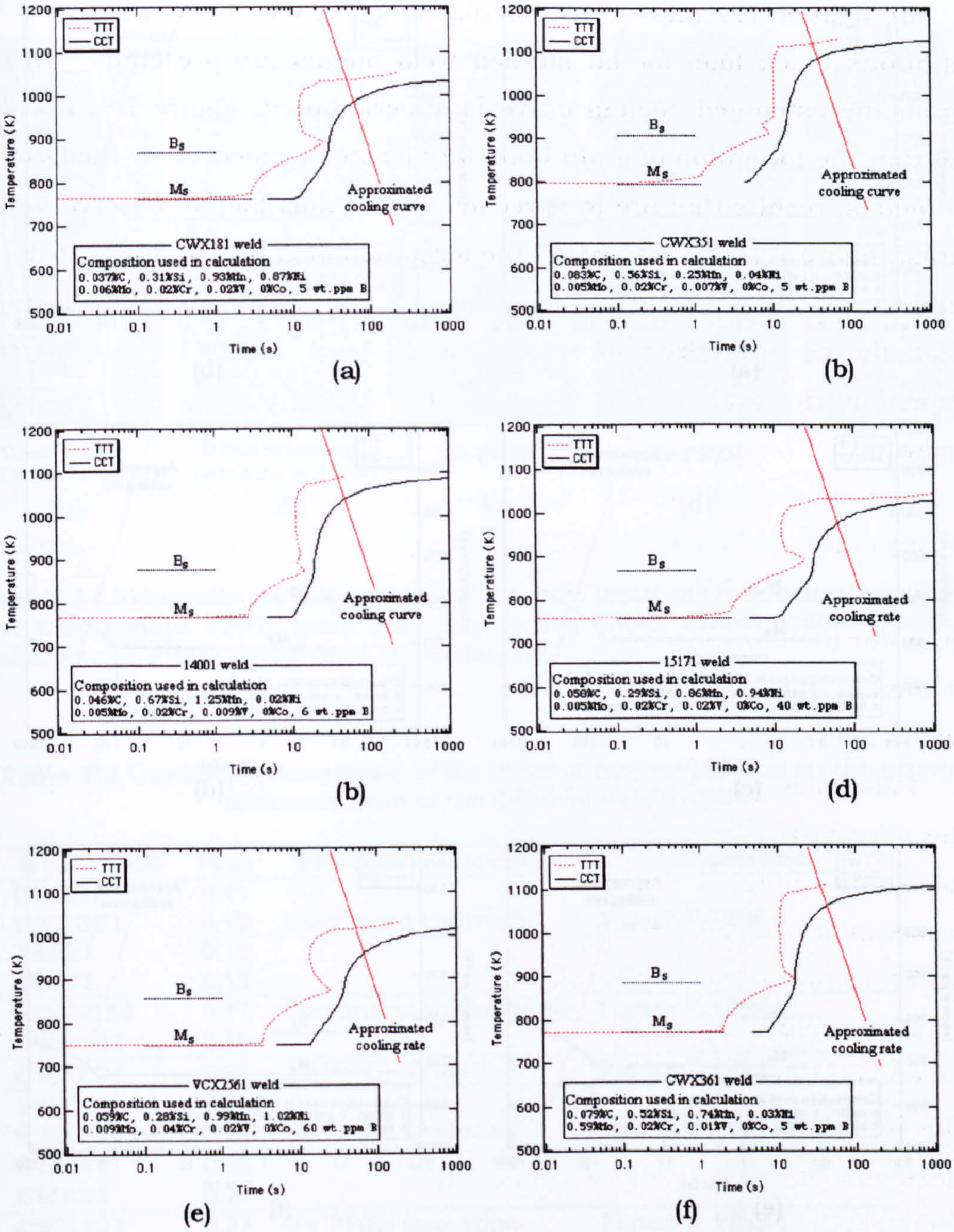

Figure 7.9 Theoretically calculated TTT and CCT diagrams for the different steel weld metals listed in table 7.1. The calculated P_{cm} values are: (a) 0.11, (b) 0.12, (c) 0.13, (d) 0.15, (e) 0.17 and (f) 0.18.

2- The hydrogen diffusion and trapping. It is expected, for example, that a continuous network of grain boundary ferrite could contribute to the transport of hydrogen into the weld and outside to the atmosphere. The diffusion throughout the microstructure could be difficult due to heterogeneous features. Moreover, high proportion of MAC constituent, which could be located between ferrite side plates and acicular ferrite laths, could increase the hydrogen trapping of the weld metal.

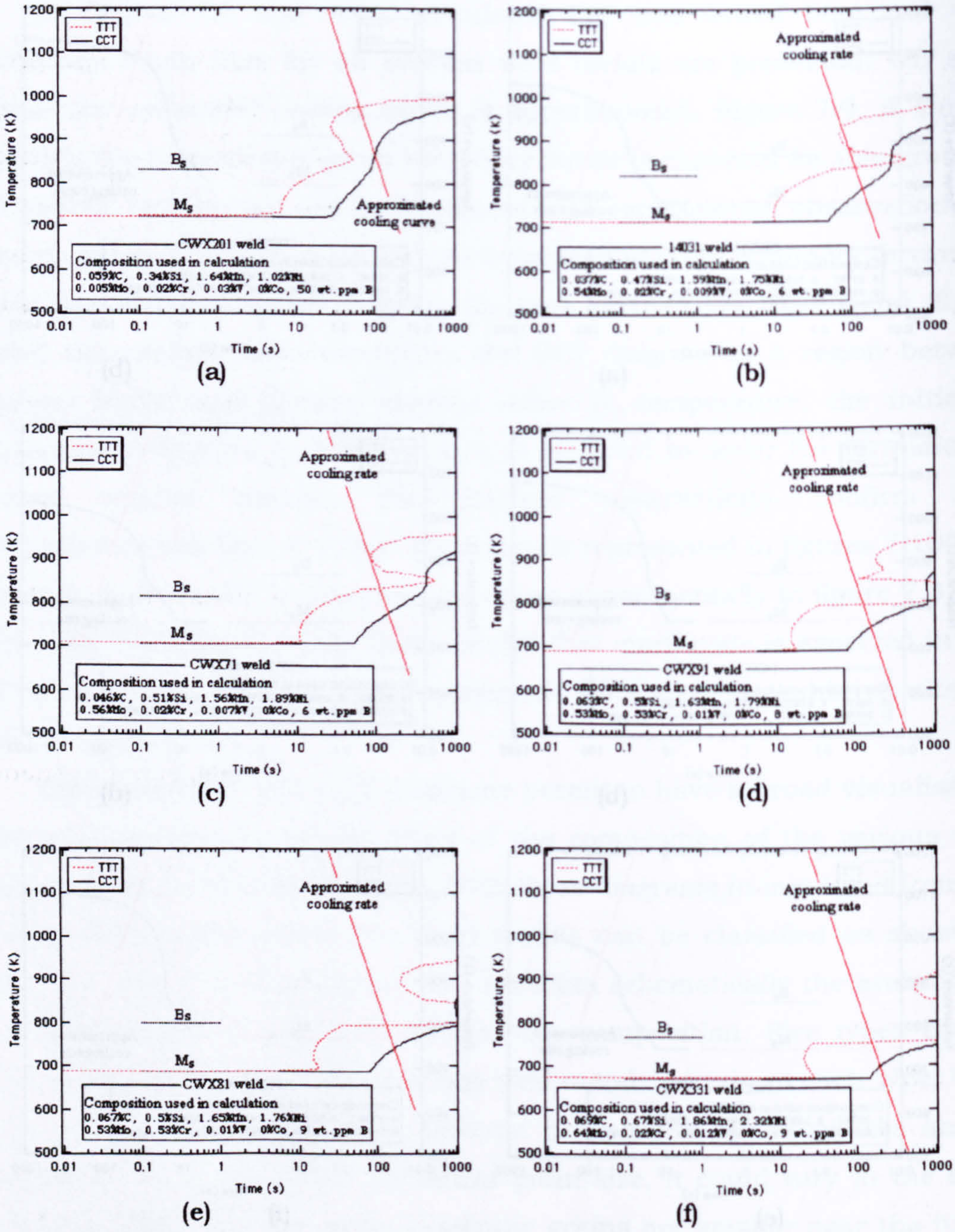

Figure 7.10 Theoretically calculated TTT and CCT diagrams for the different steel weld metals listed in table 7.1. The calculated P_{cm} values are: (a) 0.20, (b) 0.20, (c) 0.21, (d) 0.23, (e) 0.24 and (f) 0.27.

The general classification presented in figure 7.11 and table 7.2 summarises the range of microstructure of the weld metals which were analysed in this research. This was one of the reasons for the selection of these 12 compositions. These figures simplify the microstructural support that is needed in the next discussion chapters, when dealing with relationships between the microstructure, the mechanical properties and the resistance to HICC of the weld metals, making the discussion more comprehensive and effortless.

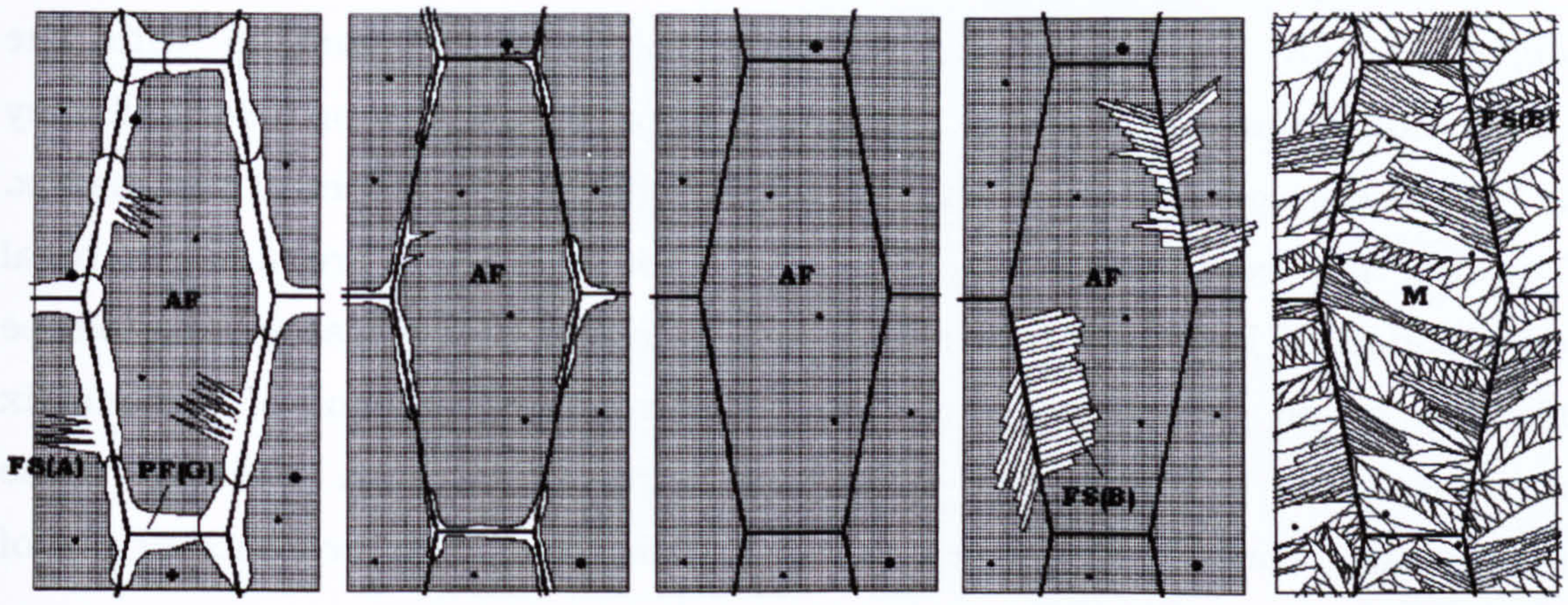

Figure 7.11 Schematic representations of the weld metal microstructures in different HSLA weld metals. PF(G): grain boundary ferrite, FS(A): Widmanstätten ferrite, AF: acicular ferrite, FS(B): bainite and M: martensite.

Table 7.2 Qualitative description of the effect of the composition on the general microstructure of the different weld metals

Weld metal	Pcm	PF(G) characteristic	Schematic
CWX181gb	0.11		
CWX351	0.12	Continuous network	Figure 7.12(a)
14001	0.13		
15171	0.15		
VCX2561	0.17	Discontinuous network	Figure 7.12(b)
CWX361	0.18		
CWX201	0.20	No PF(G) formation	Figure 7.12(c)
14031	0.20		
CWX71	0.21	No PF(G) formation	Figure 7.12(d)
CWX91	0.23		
CWX81	0.24		
CWX331	0.27	No PF(G) formation	Figure 7.12(e)

7.5 Microstructure and micro-constituents of the weld metals

There is considerable evidence from other studies about the effect of micro-constituents (retained austenite, martensite/austenite islands and martensite/austenite/carbide particles (MAC) on: the effect of retained austenite (γ_R) on the properties of TRIP steels [125-127], the mechanical properties of weld metals [16, 128-129] and hydrogen trapping by retained austenite or MAC [87]. Wildash [8] identified MAC constituents as one of the factors that influence the HICC resistance of HSLA steel weld metals. The presence of microphases affects in different ways the properties of the weld

metal. Firstly, these micro-constituents could reinforce or weaken the matrix depending on their individual strength and their relationship with the surrounding phases. Secondly, when the metal is stressed or deformed they act as stress concentrators which could facilitate the fracture of the matrix. Thirdly, they could be strong traps sites for hydrogen, producing a local distribution of hydrogen that may reach a critical concentration to produce fracture or on the contrary, reducing the hydrogen content of the matrix increasing its resistance to hydrogen induced fracture. Finally, these microphases could itself be the crack initiation sites in the presence or not of hydrogen.

In this section, the microstructure of the HSLA steel weld metals is studied in some detail using FEG-SEM and TEM observations. The objective of this section is to make a more detailed assessment of the weld metal microstructure than is possible by optical microscopy. In addition to this, it is intended to identify and locate the different types of micro-phases that could be found in these welds.

Figure 7.12 presents a picture of a weld metal microstructure, where can be observed polygonal or grain boundary ferrite and acicular ferrite. This high resolution photomicrograph permits to appreciate the continuous character of the polygonal ferrite (PF) and chaotic nature of the acicular ferrite (AF). For this reason, for example, polygonal ferrite is an easy path for crack propagation and acicular ferrite is an intricate path for the growth of the crack. From the point of view of the hydrogen diffusion, the acicular ferrite offers more resistance to hydrogen transport and the contrary occurs for the grain boundary ferrite which could be a fast path for hydrogen to diffuse. This is discussed in detail in chapter 9.

Figure 7.12(b) shows a detailed image of the section marked on figure 7.12(a). In this figure can be appreciated the presence of what has been called micro-constituents or microphases: retained austenite, martensite-austenite-carbides islands (MAC), carbides and non-metallic inclusions (NMI). These micro-phases are located mainly in between the grains of acicular ferrite (black arrows) and at interfaces around grain boundary ferrite (red arrows). The number density and distribution of micro-constituents in the weld metal microstructure are affected by the composition and the thermal history of the weld.

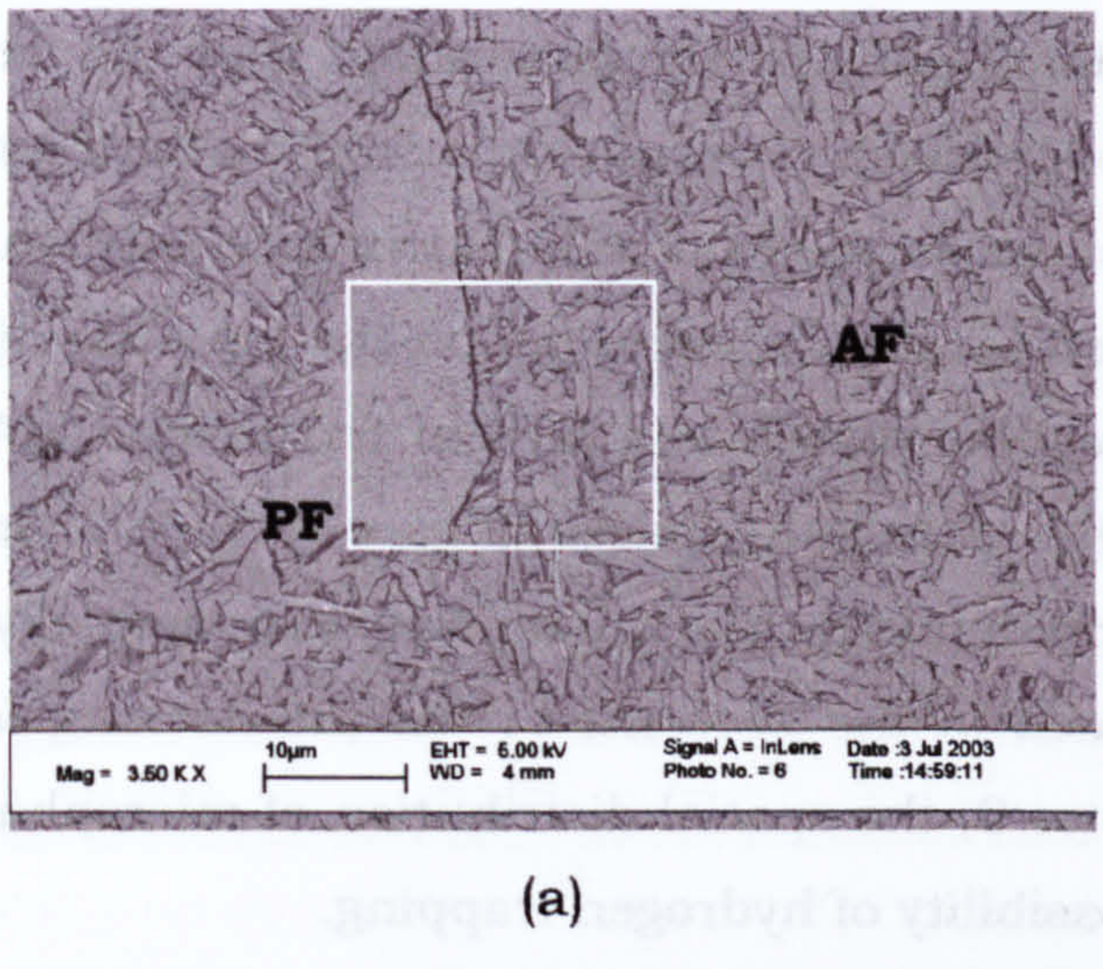

(a)

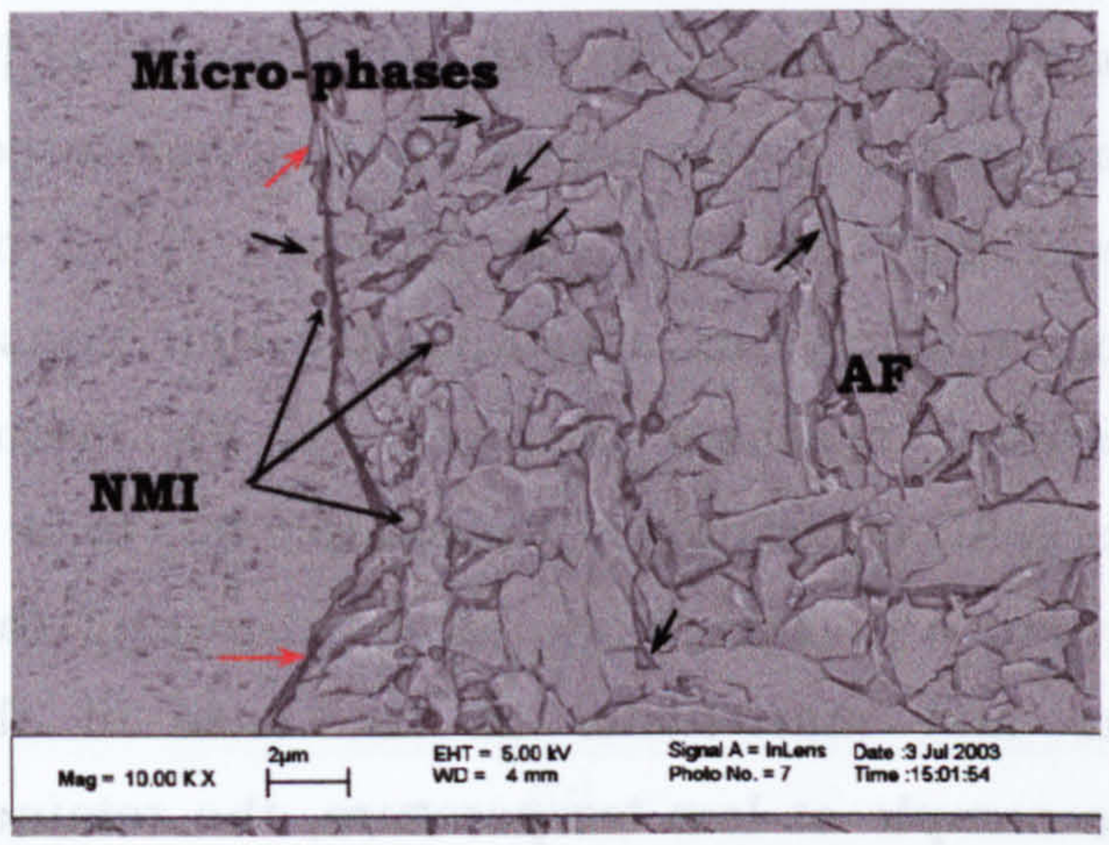

(b)

Figure 7.12 FEG-SEM image of microstructure presented in the CWX361 weld metal, (a) Polygonal ferrite(PF) and acicular ferrite(AF) and (b) Detail of the region in (a): micro-phases (short arrows) and NMI (long arrows)

The microphases are the last regions to form or transform in the weld metal and for this reason adopts the shape that is permitted by the morphology of the ferrite. When polygonal ferrite is present the microphases are trapped between ferrite grains or located along the polygonal ferrite/acicular ferrite interface often having an irregularly elongated shape (see figure 7.13). In the case of parallel laths of ferrite as in ferrite sideplates and bainite, the microphases are located at the inter-lath region and can have laminar or thin films shapes (see figure 7.14). In acicular ferrite these occupy the irregular spaces between the ferrite grains as shown in figure 7.15, and for that reason adopt a wedge shape.

In regard to the spatial distribution of the microphases, it is expected to be influenced predominantly by the form adopted by the ferrite at least in the case of the MAC constituents, because the NMI distribution is inherited from the solidification stage. In the case of a matrix with polygonal ferrite, the MAC could be distributed sparsely, depending on the grain size (figure 7.13). If the matrix contains regular distributed lath of ferrite, the MAC are distributed regularly along the inter-lath spaces (figure 7.14(a)). On the contrary, if acicular ferrite is predominant the microphases are spatially distributed closer to each other located in the sites left by the interlocking ferrite grains. As is discussed in chapter 9, the spatial distribution of microphases could increase or decrease the possibility of hydrogen trapping.

To clearly identify the different type of microphase is a very difficult task. It is necessary to make use of high resolution SEM (for example, FEG-SEM) and in many cases transmission electron microscopy (TEM) will be essential. Whichever the case, the identification could be affected by the sample preparation, making this assessment a time consuming experiment when analysing several weld metal compositions. For example, in the case of SEM observation of MAC constituents, the sample has to be etched carefully to reveal the substructure of the microphase permitting the identification of retained austenite and martensite. In the case of the TEM thinning preparation of the sample at low temperature, the retained austenite could transform to martensite.

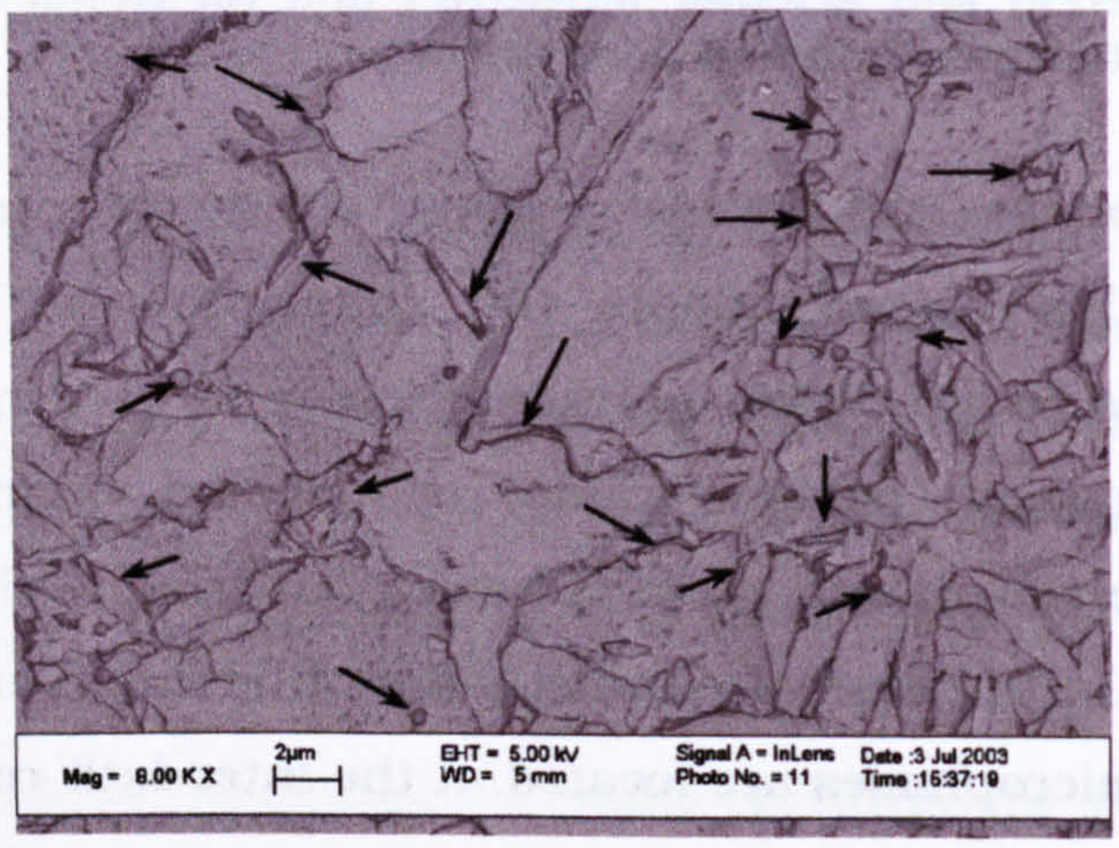

Figure 7.13 Weld metal microstructure formed by polygonal ferrite and acicular ferrite; the arrows indicate some of the micro-constituents: MAC islands, retained austenite and NMI

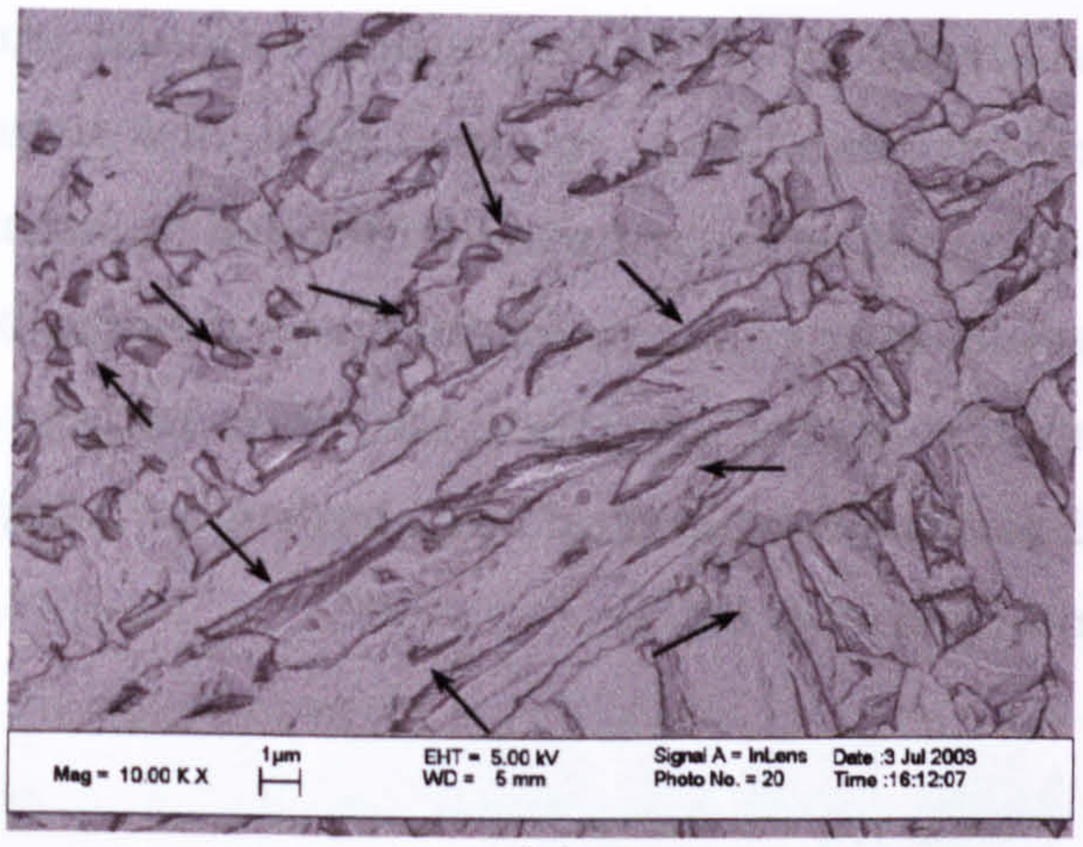

(a)

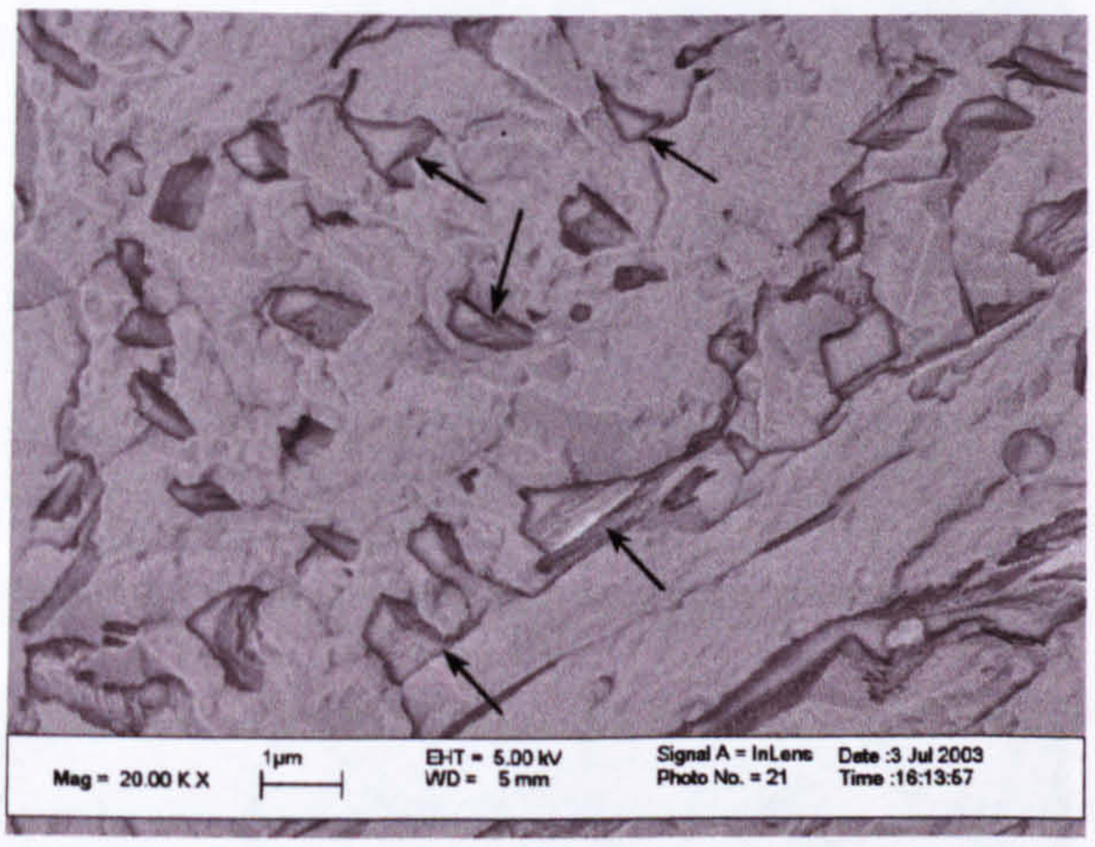

(b)

Figure 7.14 Weld metal microstructure presenting the morphology and distribution of microphases. (a) Elongated and irregular microphases and (b) detail of the figure (a).

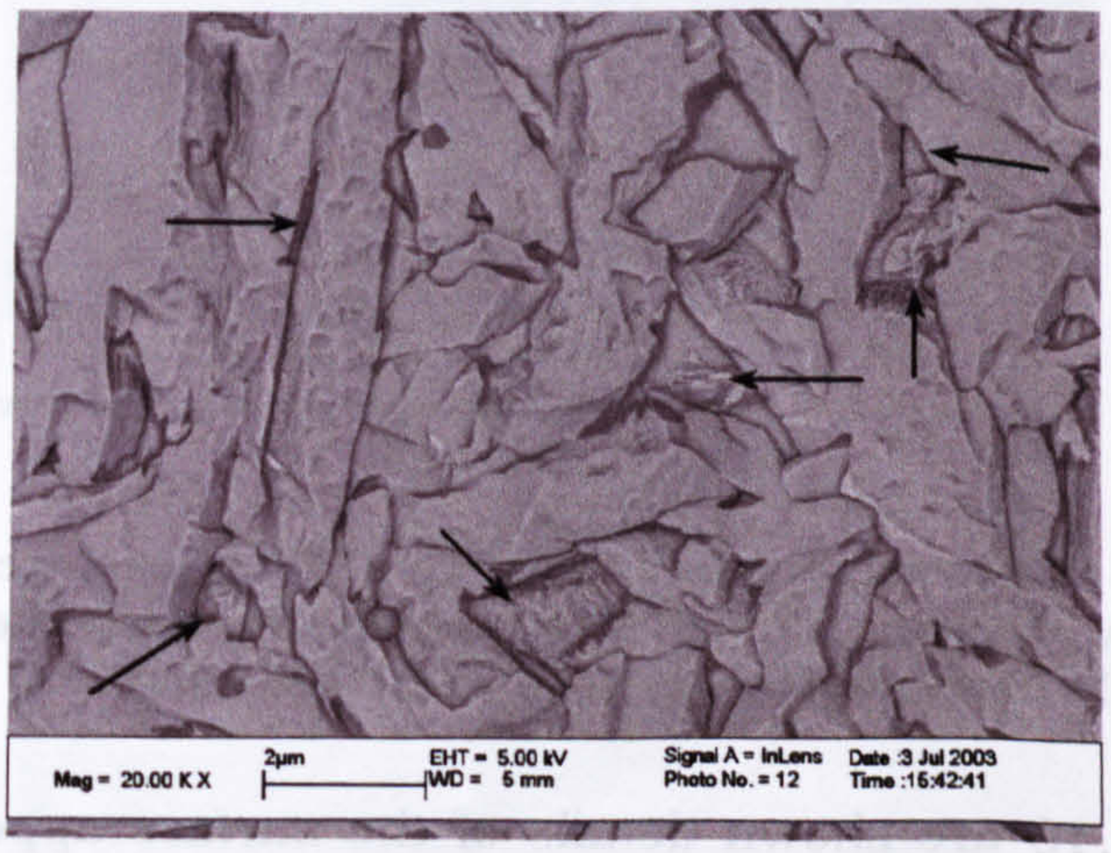

Figure 7.15 Detail of an acicular ferrite microstructure showing the wedge-shaped micro-constituents. Arrows indicate the microphases.

It is important to identify whether the MAC islands are formed by retained austenite, martensite or a mixture of them and carbides. The hydrogen solubility in austenite is higher than in ferrite, whilst the diffusivity

is lower in austenite than in ferrite [16, 130] and probably in martensite. For this reason, retained austenite or MAC containing retained austenite are better traps for hydrogen. The stability of retained austenite have to be taken into account, because if a hydrogen saturated retained austenite transforms for whichever the reason to martensite or ferrite and carbides the hydrogen will be liberated to the matrix increasing the risk of cracking. On the contrary, stabilised retained austenite will retain its hydrogen trapped during service due to the high binding energy [87].

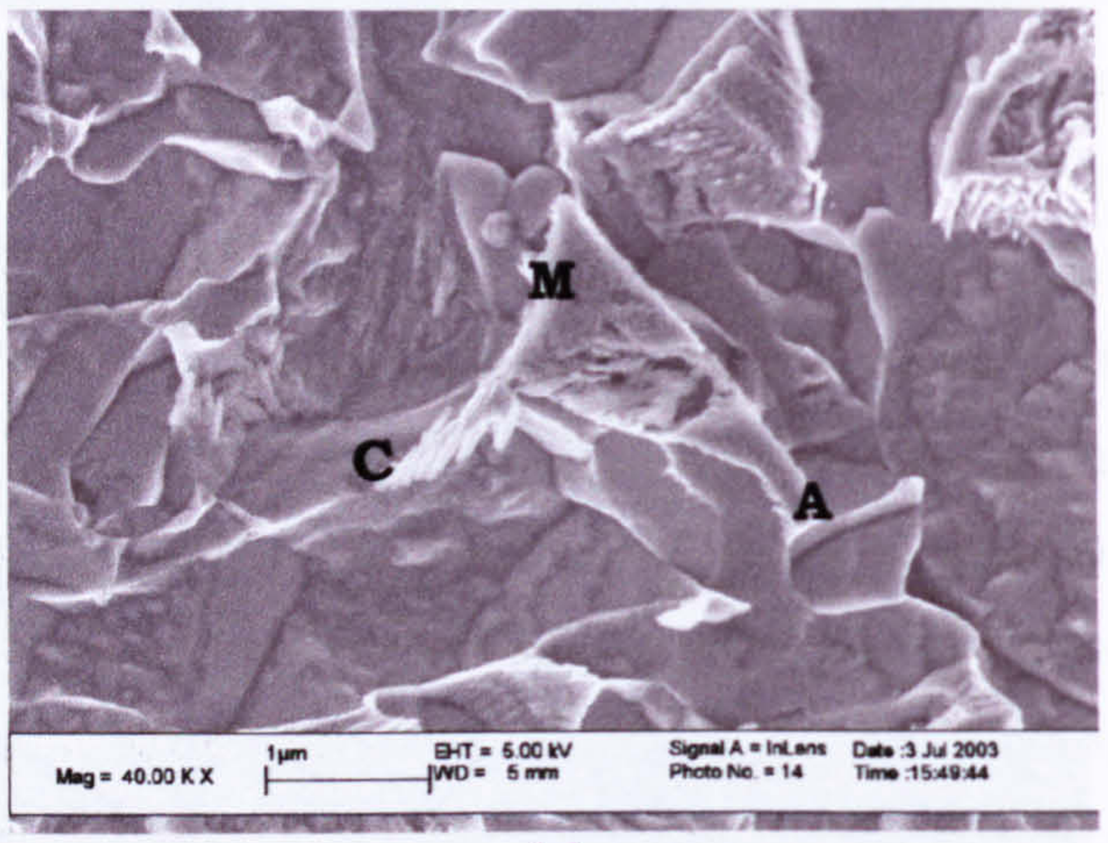

Figure 7.16 Detail of the microphases found in a HSLA steel weld metal, the central feature could be a MAC island, formed by martensite(M), austenite(A) and carbides (C); (a) positive FEG-SEM image and (b) negative FEG-SEM image.

In figure 7.16 are shown details of the surface appearance of some of the microphases presented in figure 7.15. These high resolution FEG-SEM images allow identification of martensite, retained austenite and carbides. The martensite (M) is identified by the observation of substructures on the surface. Carbides (C) can be seen as elongated precipitates. The smaller and blocky regions seem to be retained austenite, because generally they do not show

substructure on their etched surface. Using transmission electron microscopy this substructures and the configuration of similar microphases could be observed in more detail.

Figure 7.17, shows a TEM image of a MAC constituent in the weld metal CWX201. It can be noted the wedge shape of the central region of martensite, which fills the space between the acicular ferrite grains. The right hand corner of the wedge seems to be untransformed austenite, which has a lower dislocation density than the martensitic region. The high dislocation density of martensite and the high hydrogen solubility of austenite make them potential hydrogen traps, but crack initiators when a critical hydrogen level is reached.

Figures 7.18(a) and (b) show a more detailed SEM image of the substructure found in a martensite island in the CWX201 weld metal. The martensite island appears to be located in a region between the acicular ferrite (AF) and the ferrite sideplates (FS(A)). Moreover, it seems to be located between two ferrite laths that have grown from the upper right region in the figure to the centre. This region was enriched in C and other elements during transformation raising hardenability and as a consequence promoting the formation of martensite. An elongated region, marked in figure 7.18(b) by arrows, can be noted that has probably formed by martensite in the inter-lath region, the last region to transform.

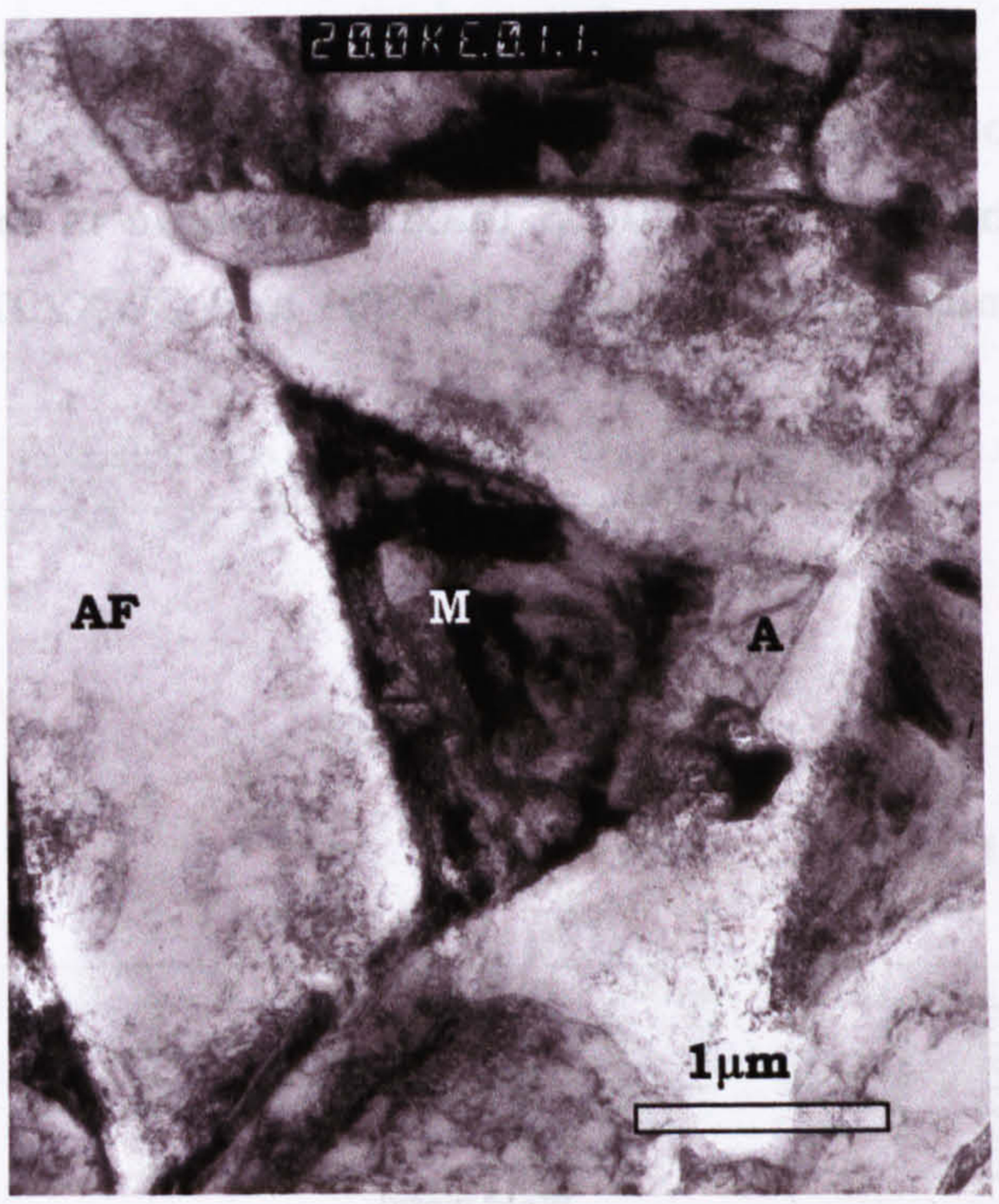

Figure 7.17 TEM image of a MAC island showing the substructures in the martensitic region. It can be observed the acicular ferrite grains (AF), martensite (M) and retained austenite (A).

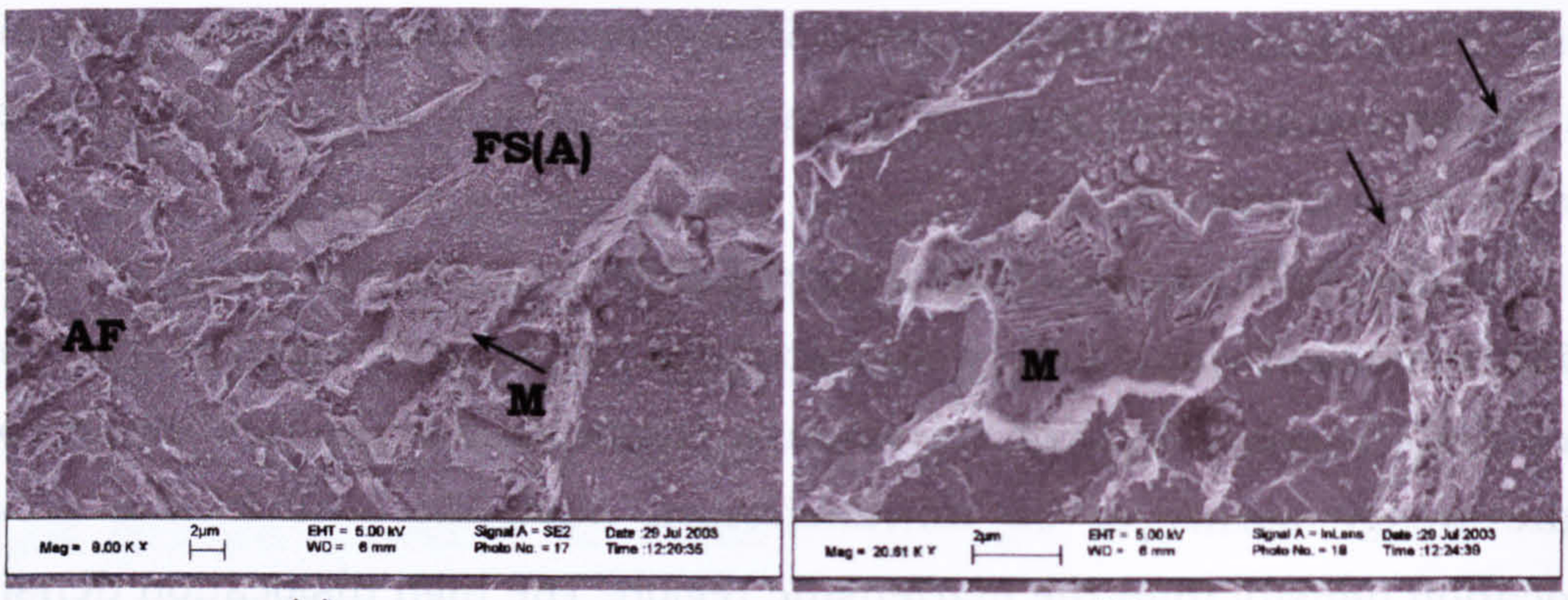

Figure 7.18 SEM image of a MAC island. Note the substructure in the martensite island and the martensitic elongated inter-lath region signalled by arrows, (a) low resolution image showing FS(A) and M; (b) detail of the figure (a). The micro-mark in the figure is 2 µm

7.6 The relation between composition and MAC proportion.

Microphases exert a significant influence on the properties of the weld metals. As a consequence, the determination of the volume fraction of MAC for each weld allows a correlation with mechanical properties and the resistance to hydrogen induced cold cracking. In figure 7.19, the variation of the proportion of MAC constituent with the composition of the weld metal can be observed as a function of the P_{cm} value. This figure was constructed using data from the work of Wildash[8]. It is anticipated a progressive increase in the MAC content with the increase in alloying elements due to the expected increase of the hardenability of the steel, permitting the formation of the microphases. However, as is noted, the MAC proportion does not show a uniform increase with respect to the P_{cm} value and a maximum value is found for two of the weld metals with medium P_{cm} values: CWX361 and CWX201.

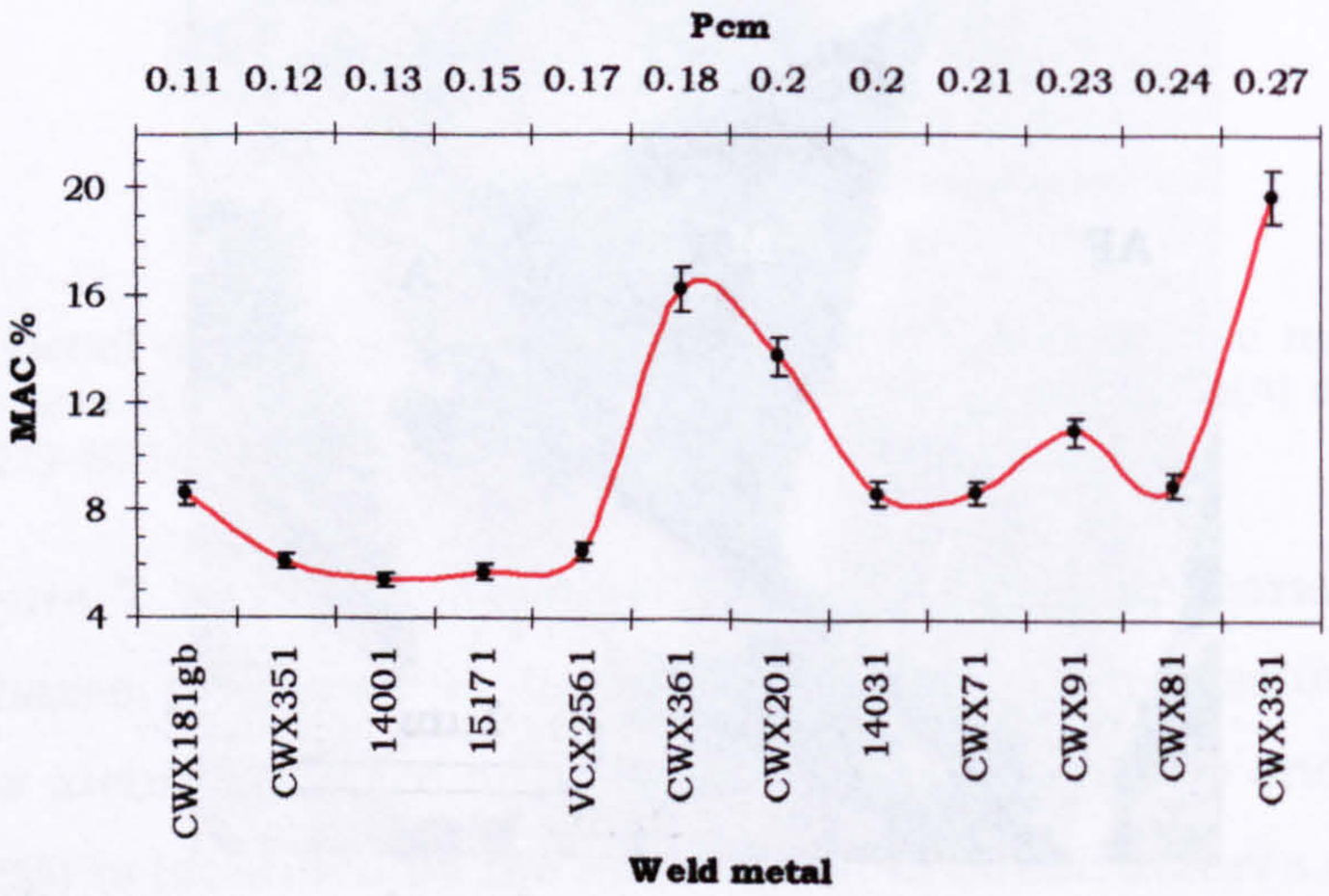

Figure 7.19 MAC proportion for different HSLA steel weld metals. The relative error, based on BS7590, was estimated to be ≤ 5 %. Data taken from Wildash [8]

Figure 7.20 presents the variation in the experimental and the predicted MAC content with the Pcm value for each of the studied weld metals. In addition, the proportions of C, Si, Mn, Mo, Cr and Ni are shown to try to find whether the changes in MAC content correspond to variation in one or several alloying elements from this list. A multiple regression was used to obtain the empirical equation 7.2 which relates weld metal composition and MAC proportion. The equation is:

$$MAC(\%) = 155 \cdot C + 10 \cdot Mo + 6.6 \cdot Mn - 11 \cdot Cr - 7 \cdot Si - Ni - 4 \qquad (7.2)$$

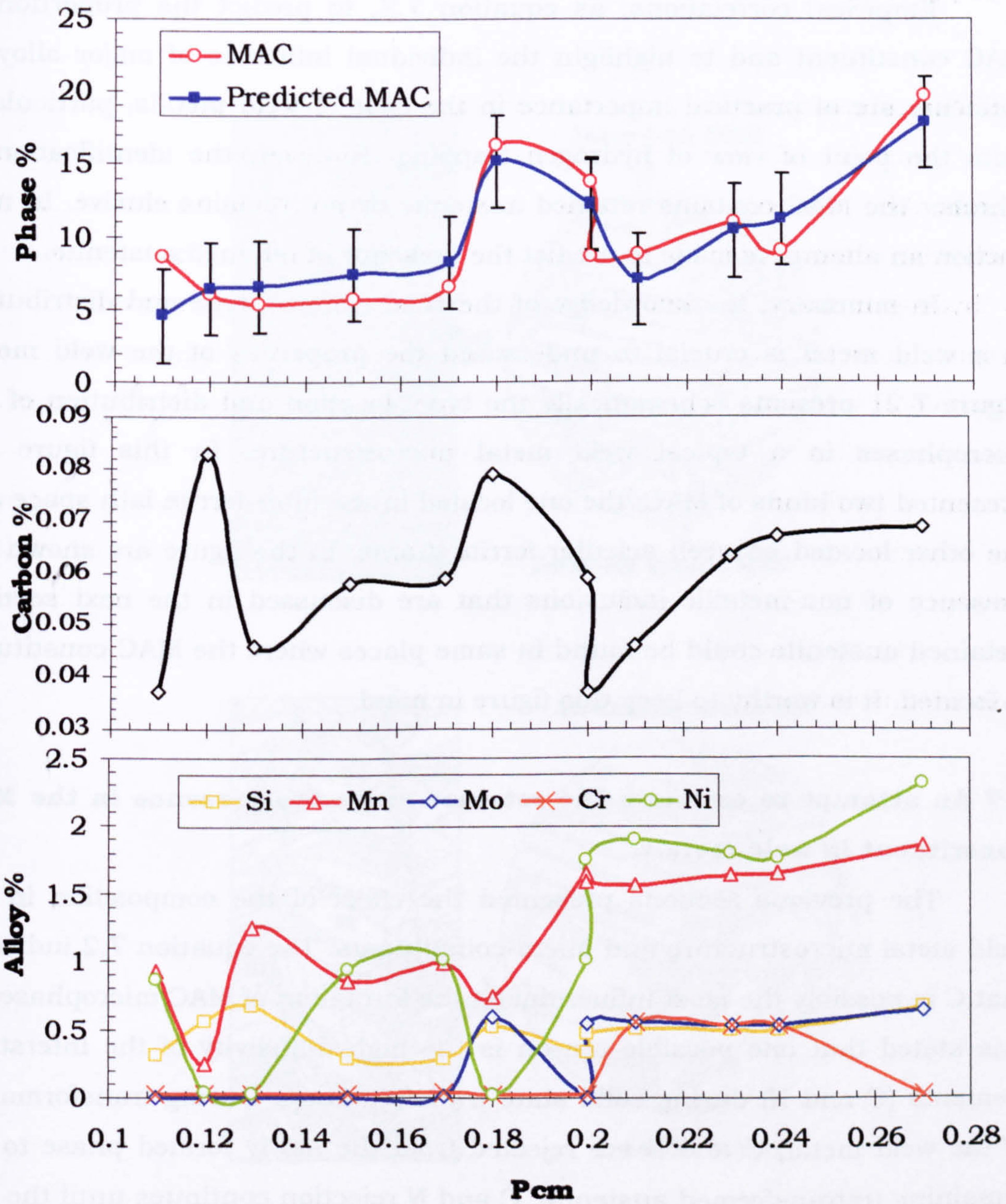

Figure 7.20 Variation in MAC and C, Si, Mn, Mo, Cr and Ni content with P_{cm} value as identifier of the weld metal.

Equation 7.2 correlates well with the experimental results as can be observed in figure 7.20. This equation shows that C is the alloy element that affects markedly the MAC content the most, other elements such as Mo and Mn are less effectives. Carbon influence on the formation of MAC constituent could be due to its high diffusivity in the weld metal and readily segregation during the transformation of the weld metal to the remaining untransformed austenite. However, whilst in general the variation in MAC is explained by variation in C content, the high C content of weld metal CWX351 do not produce a MAC proportion similar to those found in CWX361 and 14031. This is the result of the lower Mn and Mo content, which counteract the effect of C.

Empirical correlations, as equation 7.2, to predict the proportion of MAC constituent and to highlight the individual influence of major alloying elements are of practical importance in the case of weld metals, particularly from the point of view of hydrogen trapping. However, the identification of whether the MAC contains retained austenite or not remains elusive. In next section an attempt is made to predict the presence of retained austenite.

In summary, the knowledge of the MAC content, type and distribution in a weld metal is crucial to understand the properties of the weld metal. Figure 7.21 presents schematically the type, location and distribution of the microphases in a typical weld metal microstructure. In this figure are presented two kinds of MAC: the one located in the inter-ferrite lath space and the other located between acicular ferrite grains. In the figure are shown the presence of non-metallic inclusions that are discussed in the next section. Retained austenite could be found in same places where the MAC constituent is located. It is worthy to keep this figure in mind.

7.7 An attempt to estimate the retained austenite presence in the MAC constituent in weld metals.

The previous sections presented the effect of the composition in the weld metal microstructure and micro-constituents. The equation 7.2 indicates that C is possibly the most influential on the formation of MAC microphases. It was stated that one possible reason is the high diffusivity of the interstitial elements (C and N) during solid state transformation. During transformation of the weld metal, C and N are rejected from the newly formed phase to the remaining untransformed austenite. C and N rejection continues until the last portion of austenite is saturated with these elements. Substitutional elements are not expected to be partitioned significantly due to their lower diffusivity.

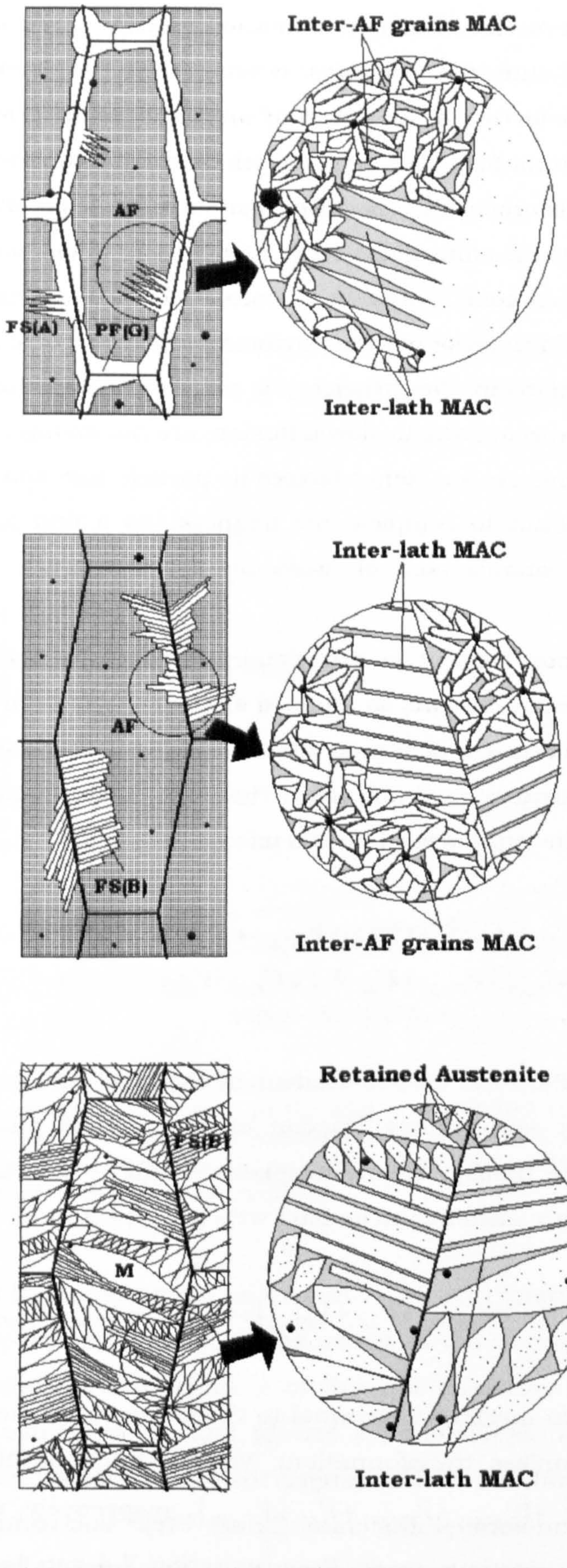

Figure 7.21 Schematic representation of the weld metal microstructure showing the type and location of MAC constituent and/or retained austenite.

C and N saturation and the presence of other alloying elements in austenite could have two effects: stabilise austenite at room temperature or permit the transform to martensite. However, only compositional factors are not responsible for the stabilization of austenite islands. Retained austenite stability is controlled by the C content, the size, distribution and morphology of the austenite particles, the microstructure that surround the retained austenite, the stress state and the strength of the retained austenite [131-138].

The carbon content and the presence of alloying elements such as Ni, Mn and N, could depress the martensite start temperature (Ms) and stabilise the austenite particle. Nevertheless, a complete partitioning of C and Mn (which is not expected due to slow diffusion) are not enough to shift this below 0 °C [136]. For this reason, other factors as particle size and shape have to be taken into account to complete the analysis. As a first approximation, the compositional stabilisation of austenite is discussed in the following paragraphs.

The carbon content in the remaining austenite, which transforms to MAC constituent or remains as retained austenite, has been estimated using a mass balance equation of carbon which takes into account the experimental proportion of ferrite phases and MAC. The mass balance equation is in general as follows for the various weld metals microstructures:

$$C_{WM} = C_{PF(G)} \cdot V_{PF(G)} + C_{FS(SP)} \cdot V_{FS(SP)} + C_{AF} \cdot V_{AF} + \\ + C_{FS(B)} \cdot V_{FS(B)} + C_{M} \cdot V_{M} + C_{MAC} \cdot V_{MAC} \qquad (7.3)$$

where C_{WM} is the total carbon content of the weld metal, C_i and V_i are the carbon content and volume fraction of each ferrite phases. If carbon in polygonal ferrite (PF(G)), ferrite sideplates (FS(SP)), acicular ferrite (AF) and bainite (FS(B)) are assumed to be 0.02 wt% ($C_{ferrite}$) equation 7.3 becomes:

$$C_{WM} = C_{ferrite} \cdot \left(V_{PF(G)} + V_{FS(SP)} + V_{AF} + V_{FS(B)}\right) + C_{M} \cdot V_{M} + C_{MAC} \cdot V_{MAC} \qquad (7.4)$$

Carbon in martensite is equal to the carbon in austenite from which is formed (diffusionless transformation). Volume fractions of MAC and ferrite, V_{MAC} and $V_{ferrite}$ $\left(V_{PF(G)} + V_{FS(SP)} + V_{AF} + V_{FS(B)}\right)$, respectively, were measured by Wildash [8] in a previous work. From equation 7.4 can be noted that the C content in remaining austenite depends on the total volume fraction of ferrite

phases. In figure 7.22 is plotted the C content in retained austenite versus the ferrite volume fraction, estimated throughout the mass balance of equation 7.4, which gives identical results as the equation proposed by Bhadeshia [139], and slightly higher by the analytical equation given in Wang [137]. Both results are shown for two weld metal C contents: 0.037 and 0.083 wt%. These correspond to the minimum and maximum carbon content found in the studied steel weld metals. As expected the carbon partitioning increase with the reduction in remaining austenite proportion depending on C content of the steel. For example, the carbon content in retained austenite (volume fraction 0.10) is around 0.2 and 0.7 C wt%, if the steel C level is 0.037 and 0.083 C wt%, respectively.

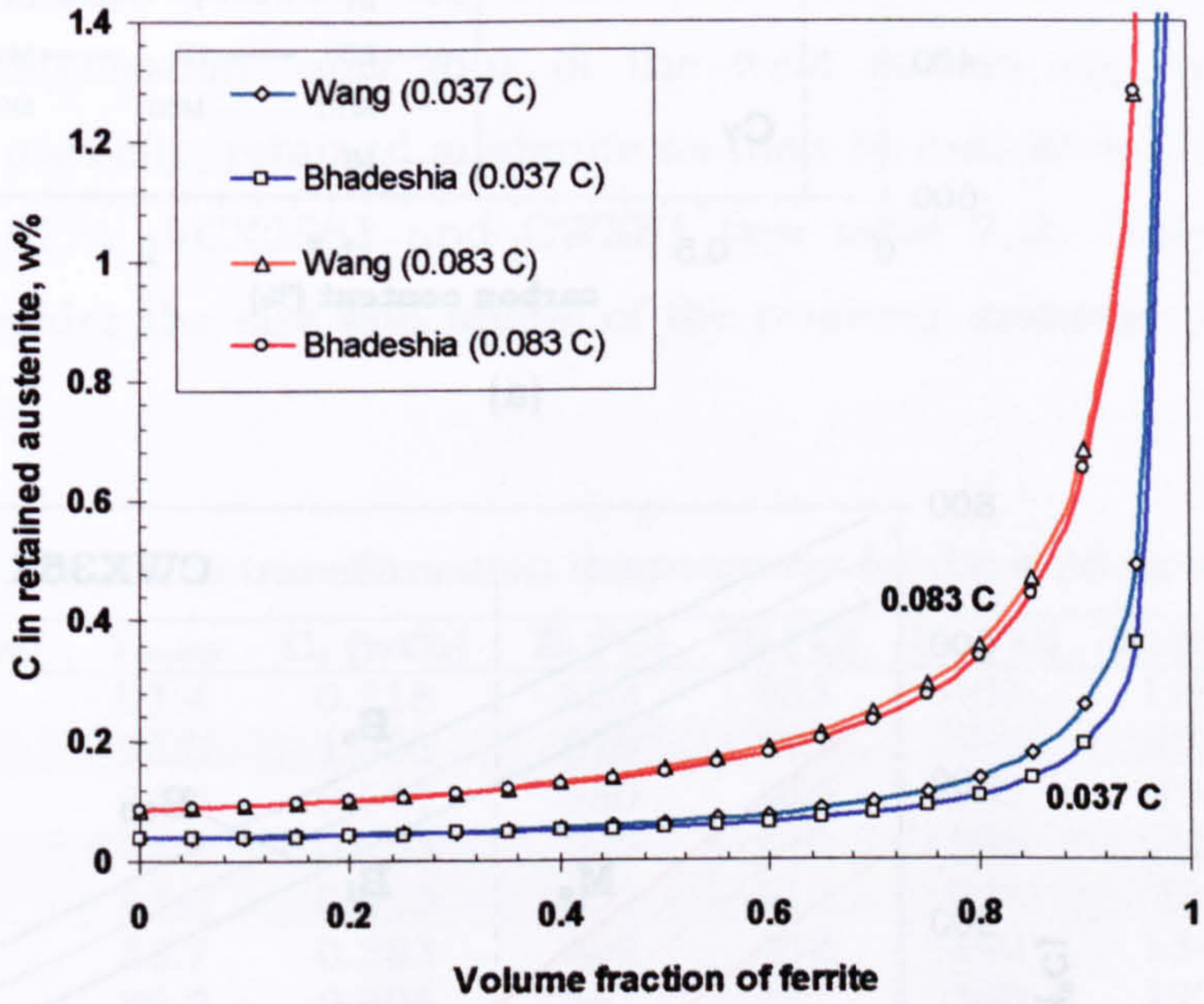

Figure 7.22. Estimated austenite carbon content with respect to ferrite volume fraction in steels. A minimum C content in the alloy was selected as 0.037 w% and a maximum of 0.083 w%, the interval of carbon content in the studied weld metals. Equations based on mass balance (Chang and Bhadeshia [139]) and analytical treatments (Wang et. al. [137]) were implemented.

The M_s and M_f temperatures, martensite start and finish transformation temperatures, respectively, determine the extent of the transformation of the remaining austenite. If the C content of the last austenite to transform is known, and the values of M_s and M_f are estimated from the weld metal composition, it is possible to estimate approximately the extent of austenite retention for a particular weld metal, just taking into account chemical composition considerations. For the calculation of the transformation

temperatures for bainite and martensite, equations reported in the literature [140-142] were used and are listed in annex A.12.

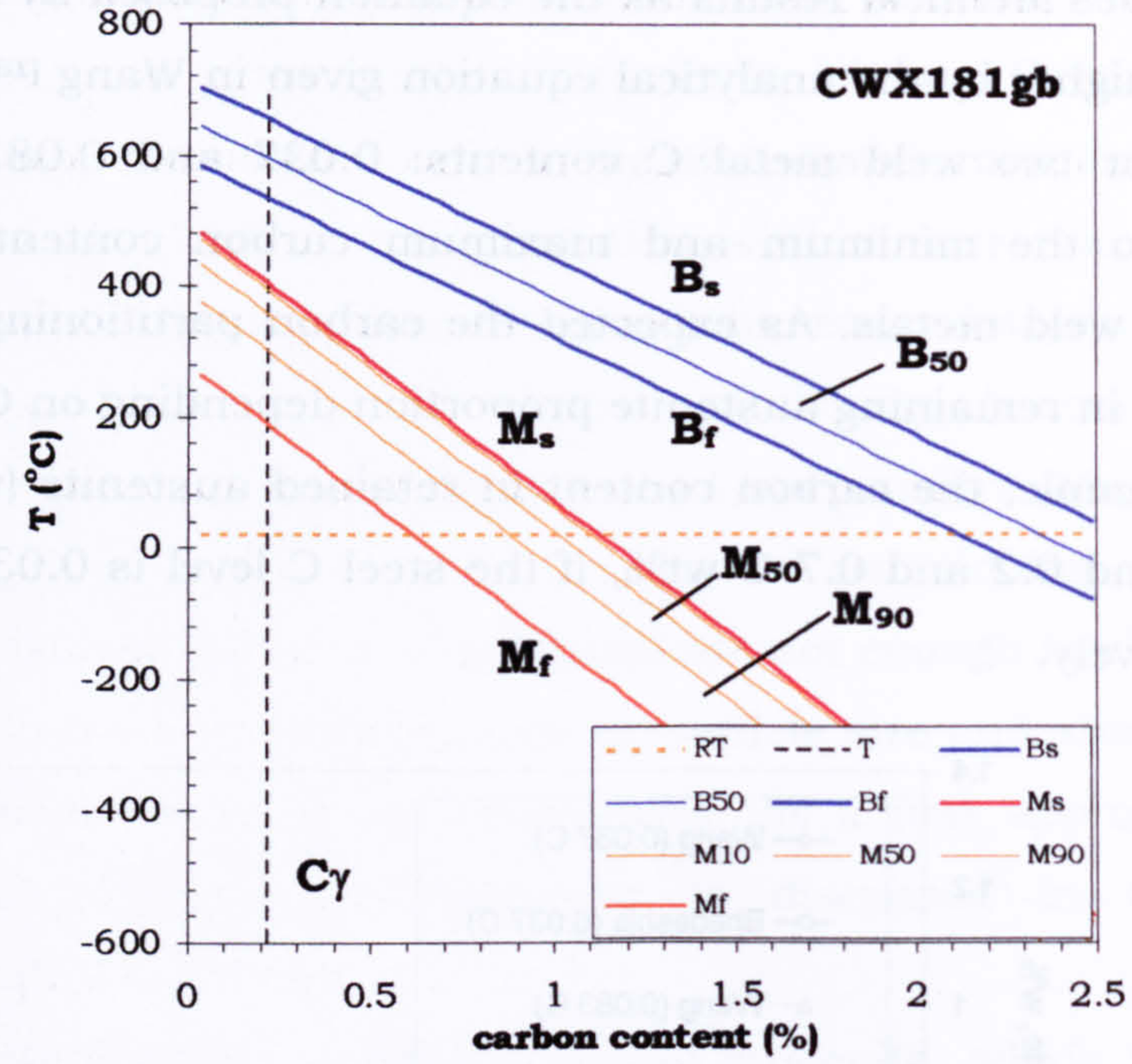

(a)

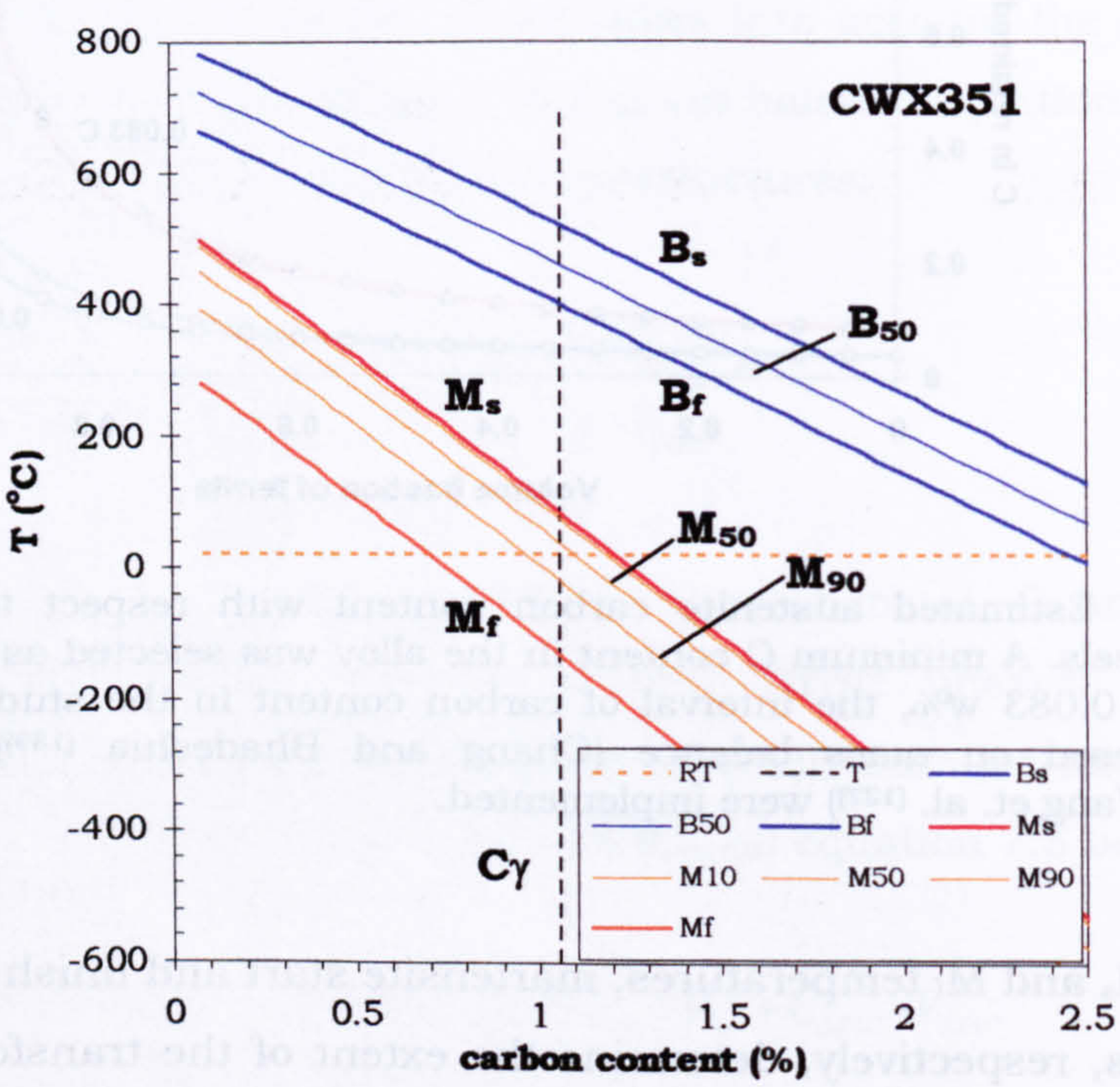

(b)

Figure 7.23 Calculated transformation temperatures for bainite (B_s, B_{50} and B_f) and martensite (M_s, M_{10}, M_{50}, M_{90} and M_f) versus carbon content in the last untransformed austenite (containing C_γ, vertical line). Room temperature is the horizontal line. (a) CWX181gb and b) CWX351. Note that in weld metal CWX351 M_f is below room temperature.

Two examples of the transformation temperature estimation are shown in figure 7.23 for weld metals CWX181gb and CWX351. The vertical line represents the carbon content present in the last untransformed austenite from where MAC constituent forms. The transformation temperatures are plotted against carbon content. Some retained austenite is expected when the M_s and M_f temperatures are below room temperature. In the examples shown in figure 7.23, retained austenite could be partially expected for the weld metal CWX351 (figure 7.23(b)).

Table 7.3 presents the calculated bainite and martensite transformation start and finish temperatures for all the studied weld metals and shows the volume fraction of ferrite ($V_{ferrite}$), the carbon content in the last untransformed austenite (C_γ), B_s, B_f, M_s and M_f. From point of view of the austenite compositional stabilisation, only four of the weld metals are expected to contain, at least partially, retained austenite as their M_f indicates. These welds are: CWX351, 15171, VCX2561 and CWX81 (see table 7.3). However, it is necessary to consider the size and shape of the retained austenite to make a complete analysis.

Table 7.3 Calculated transformation temperatures for the weld metals.

Weld metal	$V_{ferrite}$	C_γ (wt%)	B_s (°C)	B_f (°C)	M_s (°C)	M_f (°C)
CWX181	91.4	0.218	653	533	403	188
CWX351	93.9	1.056	519	399	84	-131
14001	94.6	0.501	580	460	288	73
15171	94.3	0.693	529	409	203	-12
VCX2561	93.5	0.620	532	412	228	13
CWX361	83.7	0.383	609	489	349	134
CWX201	86.2	0.304	561	441	342	127
14031	91.4	0.217	517	397	364	149
CWX71	91.3	0.319	486	366	319	104
CWX91	89.0	0.413	424	304	273	58
CWX81	91.0	0.545	388	268	217	2
CWX331	80.0	0.265	451	331	324	109

Several investigations on dual-phase steels have found an austenite size effect on the stability of austenite. Balliger and Gladman [133] have reported that austenite islands of less than about 1 μm in diameter were retained, slightly larger than 1 μm were partially transformed to martensite and in islands greater than about 10 μm, retained austenite was seldom found. In simulated heat affected zone of V treated HSLA steels, Chen et. al.[143] reported M-A constituents between 1 and 5 μm, approximately. No mention was made to distinguish whether the small blocky M-A constituent was retained austenite or a mixture of retained austenite and martensite. They associated

large M-A constituent to low toughness of the HAZ, probably due to the presence of martensite in the largest M-A particles. Jacques[144-146] has reported retained austenite with a very fine size of the order of 1 and 2 μm in TRIP steels. Rigsbee [136] reported that the particles of retained austenite are smaller than the martensite ones: 0.75 and 2.0 μm, respectively. In this investigation particles of retained austenite of sub-micron size have been found as was presented in figures form 7.12 to 7.18. Moreover, when larger than 1 μm particles were found, they were partially transformed to martensite (see figures 7.16, 7.17 and 7.18). All these examples demonstrate qualitatively that the smaller is the retained austenite particle the greater is its stability. This effect could be related to a decrease in M_s.

Wang and collaborators [137] have studied the stabilisation mechanisms of retained austenite: chemical and size stabilisation. They discussed that the reduction in the austenite particle size could be a consequence of: a decrease in the probability of finding heterogeneous nuclei inside the austenite island and a stabilisation effect due to an increase in interfacial energy. An increase in the interfacial energy is the result of the decrease in the austenite particle size. The effect of size reduction produces a shift of Ms to lower temperatures. In figures from 7.24 and 7.25 are shown several examples about the effect of the austenite particle size for the studied weld metals. These figures were obtained following the approach suggested by Wang et. al.[137] with few modifications. In annex A.13 is presented the procedure that was utilised in the present work.

In figures 7.24 and 7.25, it is observed that a reduction in the austenite particle size, as expected, decreases the M_s and M_f temperatures for the transformation of austenite to martensite for the weld metals. This effect is accentuated at particles sizes below 1 μm, approximately. Taking room temperature as a reference (segmented horizontal line), it can be noted that, depending on the steel composition, austenite particles below 0.1 μm should be retained, as in the case of all the weld metals except for CWX351. In the particular case of the CWX351 weld metal, an austenite particle with a diameter equal or less than 0.6 μm should be retained (see figure 7.24(b)). This behaviour as important implication with respect to the hydrogen trapping capacity of the weld metals as discussed later.

For weld metals where no retained austenite is expected, the effect of the particle size of the remaining austenite could stabilise it completely or partially. For example, the CWX91 weld metal which has a value of M_f around

58 °C (see figure 7.25(b) and table 7.3) could reduce this temperature below room temperature. As a consequence, in this weld metal small particles could be partially retained as austenite. The same occurs to the weld metal: 14001 in figure 7.25(a).

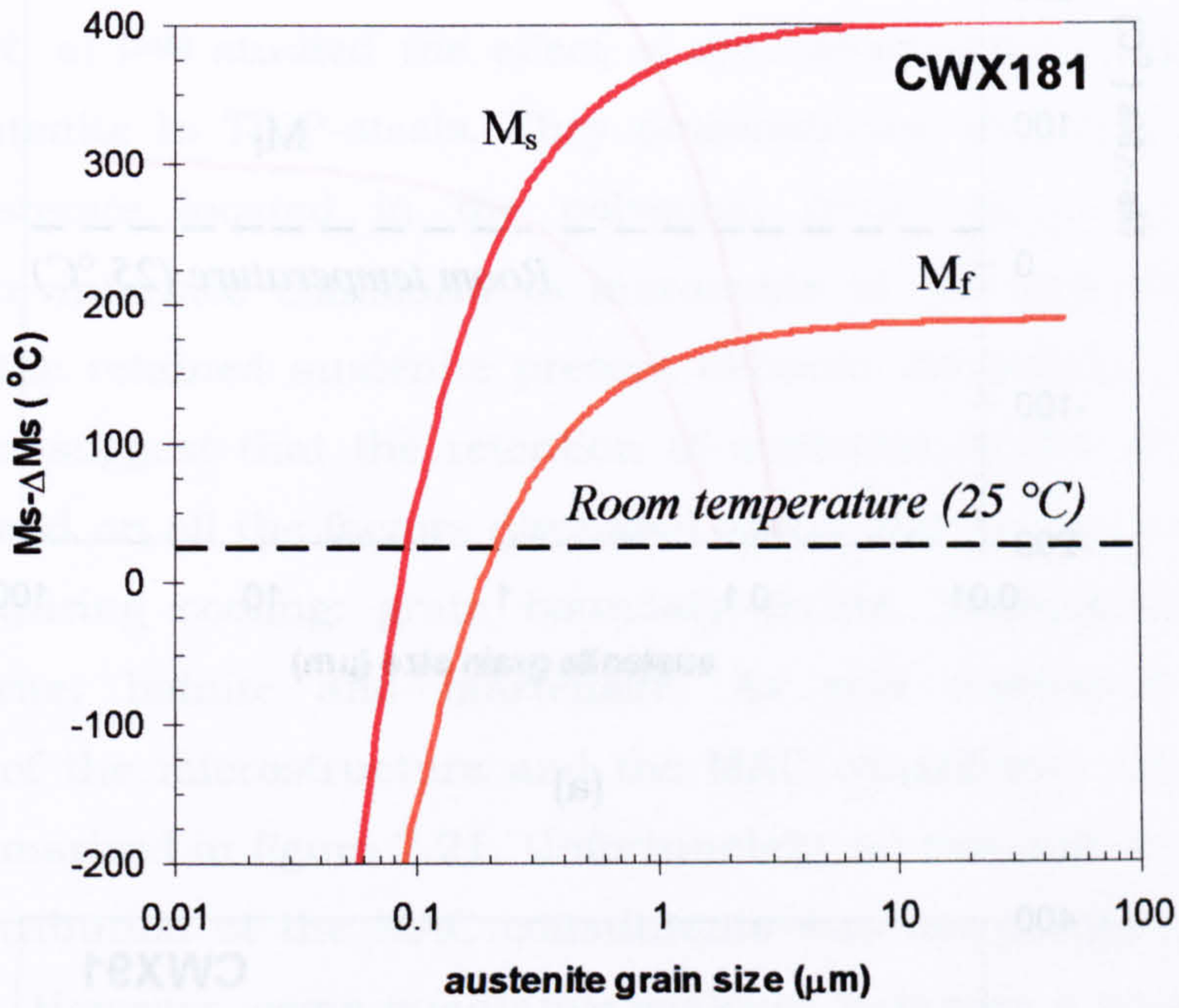

(a)

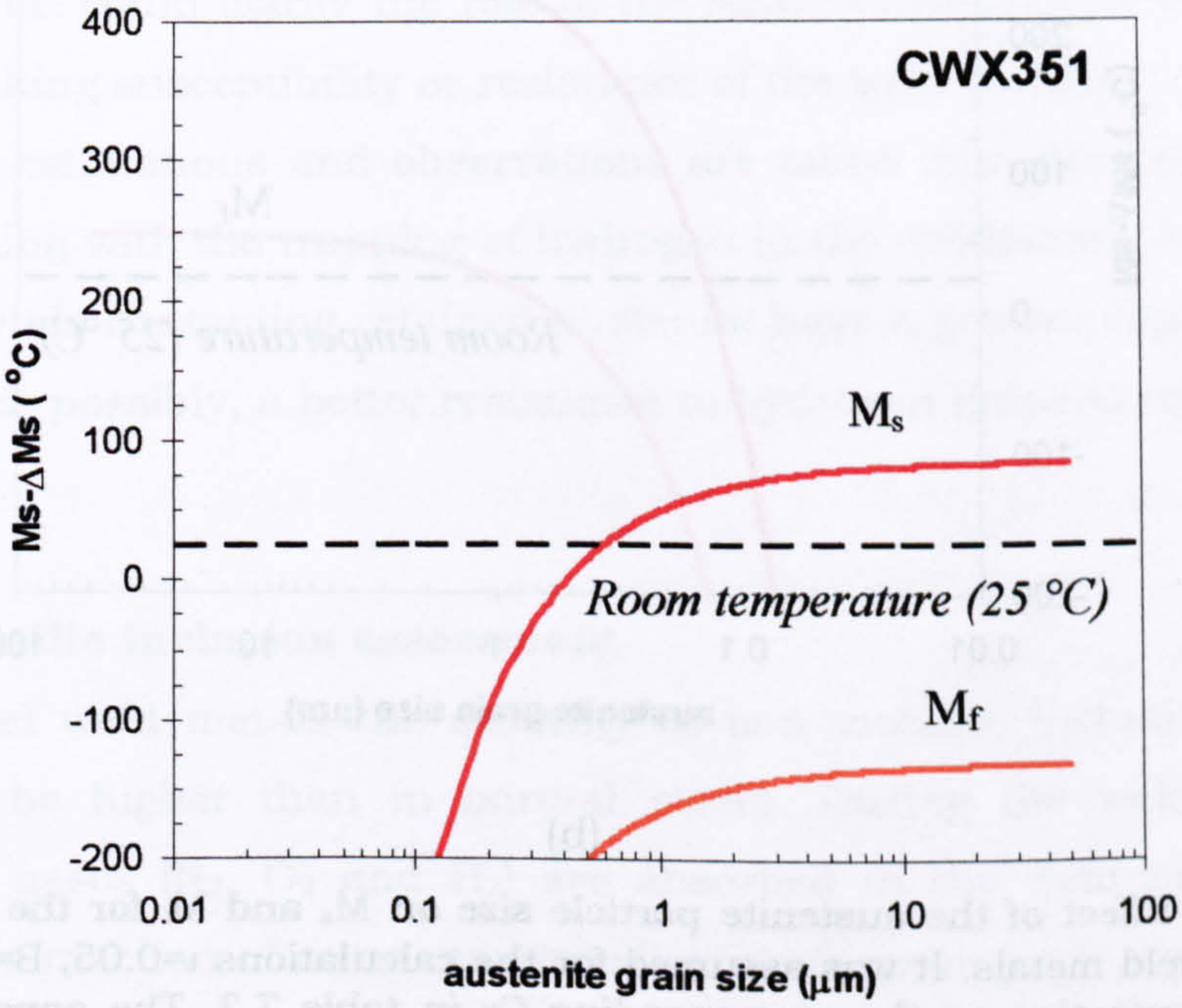

(b)

Figure 7.24 Qualitative estimation of the austenite particle size on Ms and Mf. It was assumed for the calculations ι=0.05, B=1.234 and the carbon concentration as the corresponding Cγ in table 7.3. The approach that was used is presented in annex A.13. Estimations for: (a) CWX181 and (b) CWX351

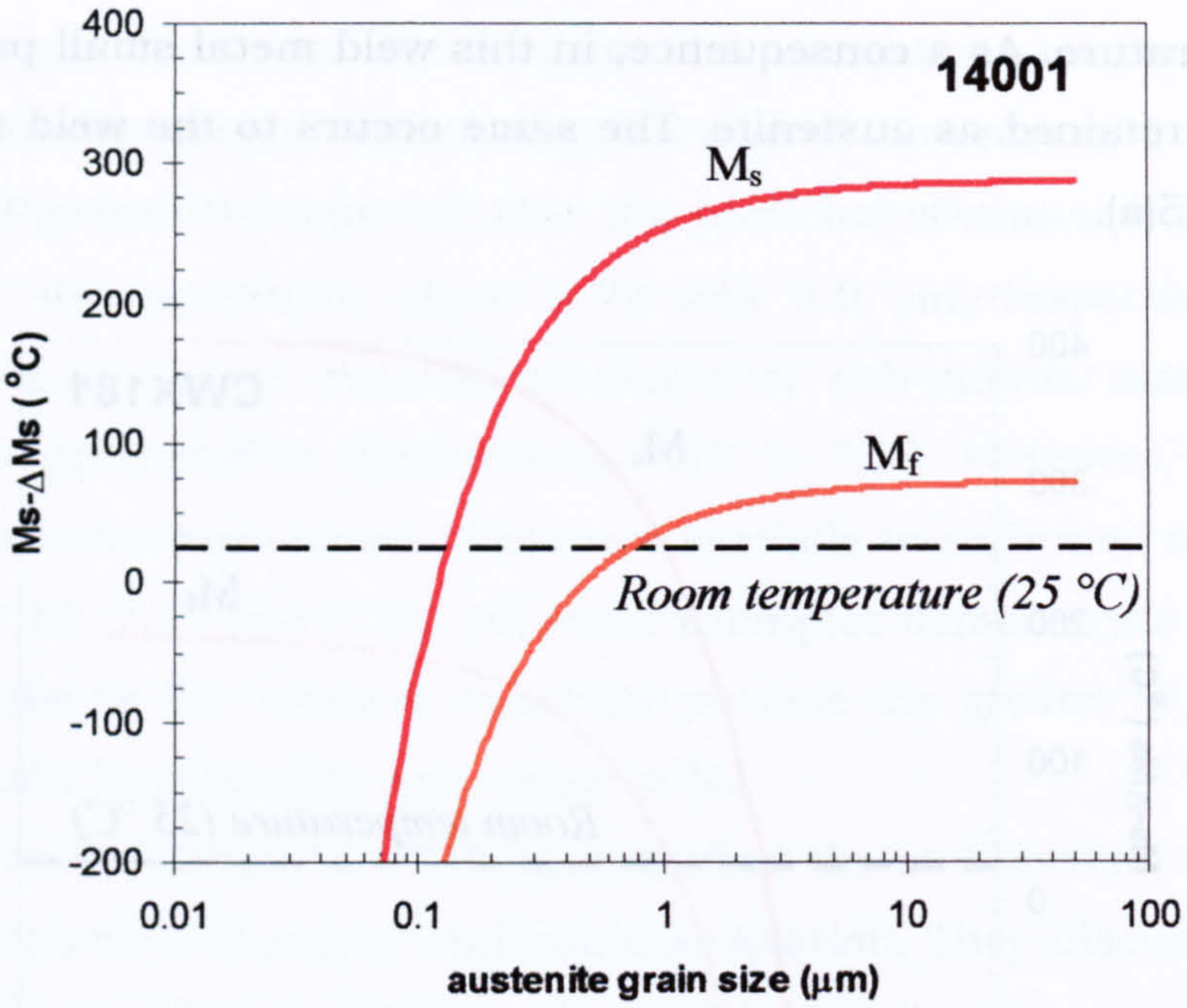

(a)

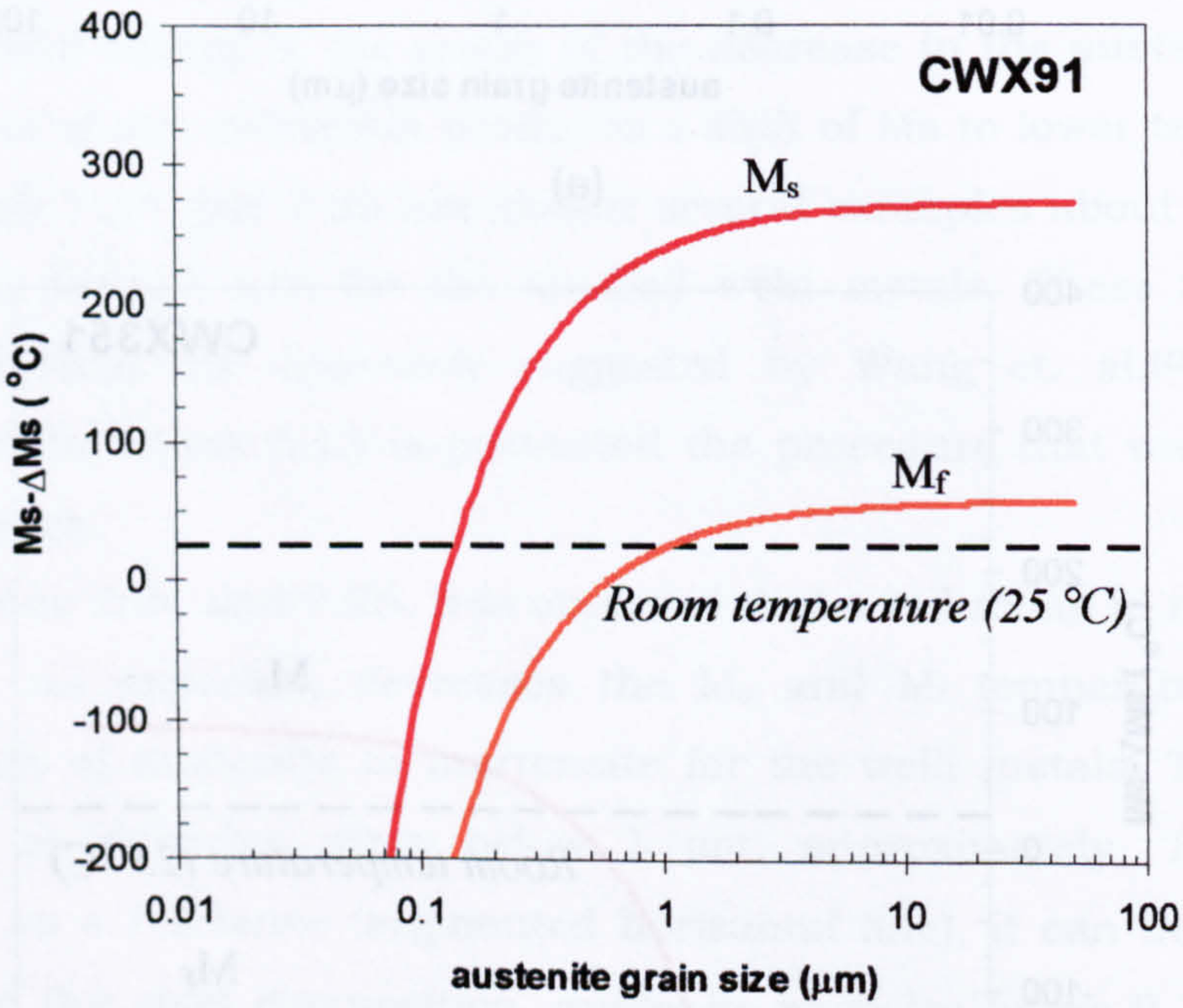

(b)

Figure 7.25 Effect of the austenite particle size on M_s and M_f for the 14001 (a) and CWX91 (b) weld metals. It was assumed for the calculations ι=0.05, B=1.234 and the carbon concentration as the corresponding $C\gamma$ in table 7.3. The approach that was used is presented in annex A.13.

In annex A.13 are presented the totality of the results of the estimations for the effect of particle size on the retention of austenite. It is worthy to mention that the steel composition seems to be the most important factor that

affects the stability of the retained austenite. The complexity of the prediction of the retention of austenite is due to the existence of factors that combined can control the stability of the retained austenite: carbon and alloy content, particle size, morphology and distribution within the microstructure. This subject continues to be an incentive for further investigations. Recently, Timokhina et. al [148] studied the effect of microstructure on the stability of retained austenite in TRIP-steels. They demonstrated that coarse blocks of retained austenite located in the polygonal ferrite or at the polygonal ferrite/bainite interface transform to martensite at low deformation levels, easier than the retained austenite present between the bainitic ferrite laths. These results suggest that the retention of austenite in the weld metals is going to depend on all the factors discussed above and on the microstructure that forms during cooling: grain boundary ferrite, Widmanstätten ferrite, acicular ferrite, bainite and martensite. As was discussed before the morphology of the microstructure and the MAC constituent are interrelated and are summarised in figure 7.21. Unfortunately, an exhaustive study on the size and distribution of the MAC constituents was not possible during this investigation. However, some qualitative evidence indicates a good correlation with the discussion above. A more detailed study is proposed for further work, a research that could clarify the role of the MAC constituent in the hydrogen induced cracking susceptibility or resistance of the weld metals.

These estimations and observations are taken into account in chapter 9, when dealing with the trapping of hydrogen in the weldments. It is expected that weld metals containing retained austenite have a greater capacity to trap hydrogen and, possibly, a better resistance to hydrogen induced cracking.

7.8 Non-metallic inclusion assessment

In steel weld metals the quantity of non metallic inclusions (NMI) is expected to be higher than in normal steels. During the welding process atmospheric gases (N_2, O_2 and H_2) are absorbed in the weld pool. NMI are formed by the reaction of some reactive alloying elements with oxygen such as Al, Ti, Mn and Si. They are complex compounds which can contain mixtures of oxides, sulphides and nitrides. Their effect on weld metals microstructure and properties include: a contribution as nucleation sites during transformation of the weld metal, participation in the formation of voids during deformation, distribution of hydrogen in the weld metal due to trapping capacity, initiation

of cracks, etc. For these reasons as complete as possible characterisation of the NMI in the weld metals is relevant to this investigation, particularly hydrogen trapping and distribution and initiation of cracks.

The assessment of the NMI characteristics is presented in this section. It was divided in experimental characterisation and thermodynamical calculation. The experimental assessment of the NMI was divided in two parts: the general NMI characteristics (shape, content, size and spatial distribution) and the NMI specific nature (chemical and morphological). Due to the impracticality of completely characterising the NMI types and composition, thermodynamic calculations were used. In this respect, stability diagrams were obtained to predict the composition and type of inclusions that could be formed during solidification.

7.8.1 NMI number density, size and spatial distribution.

Using the procedure described in the section 6.2.1.3 (chapter 6), the number of inclusions on a 2 dimensional (2D) transverse surface through each weld metal were determined. The apparent size and number on this plane were converted to true 3-dimensional (3D) using equations 6.2 to 6.6. Tables A.5 and A.6, in annex A.14, show these results. Table A.5 reports the cross-sectional superficial-density of the NMI (N_a) and the average two (apparent) and three-dimensional (true) diameters and their respective standard deviation. It could be noted that more than 90% of the total inclusion number has a true diameter less than 1.6 μm as a consequence of the rapid cooling rate experienced by the weld metal. The remaining inclusions are larger than 1.6 μm in diameter, as shown in table A.6. In general, the average inclusion true diameters are between 0.75 and 0.95 μm, as can be observed in table A.5. However, the dispersion of the true diameters, as determined by the standard deviation, varies in each weld metal.

Figure 7.26 shows the values of d_v, the true diameter, for the various low alloy steel weld metals. In general, the NMI average size is similar for all the weld metals that were evaluated. Moreover, it was observed that there was a wide dispersion of inclusion diameters and this was particularly wide for weld VCX2561. This range in inclusion diameters is related to the presence of particularly large inclusions, which can jeopardize the mechanical properties of the weld metal.

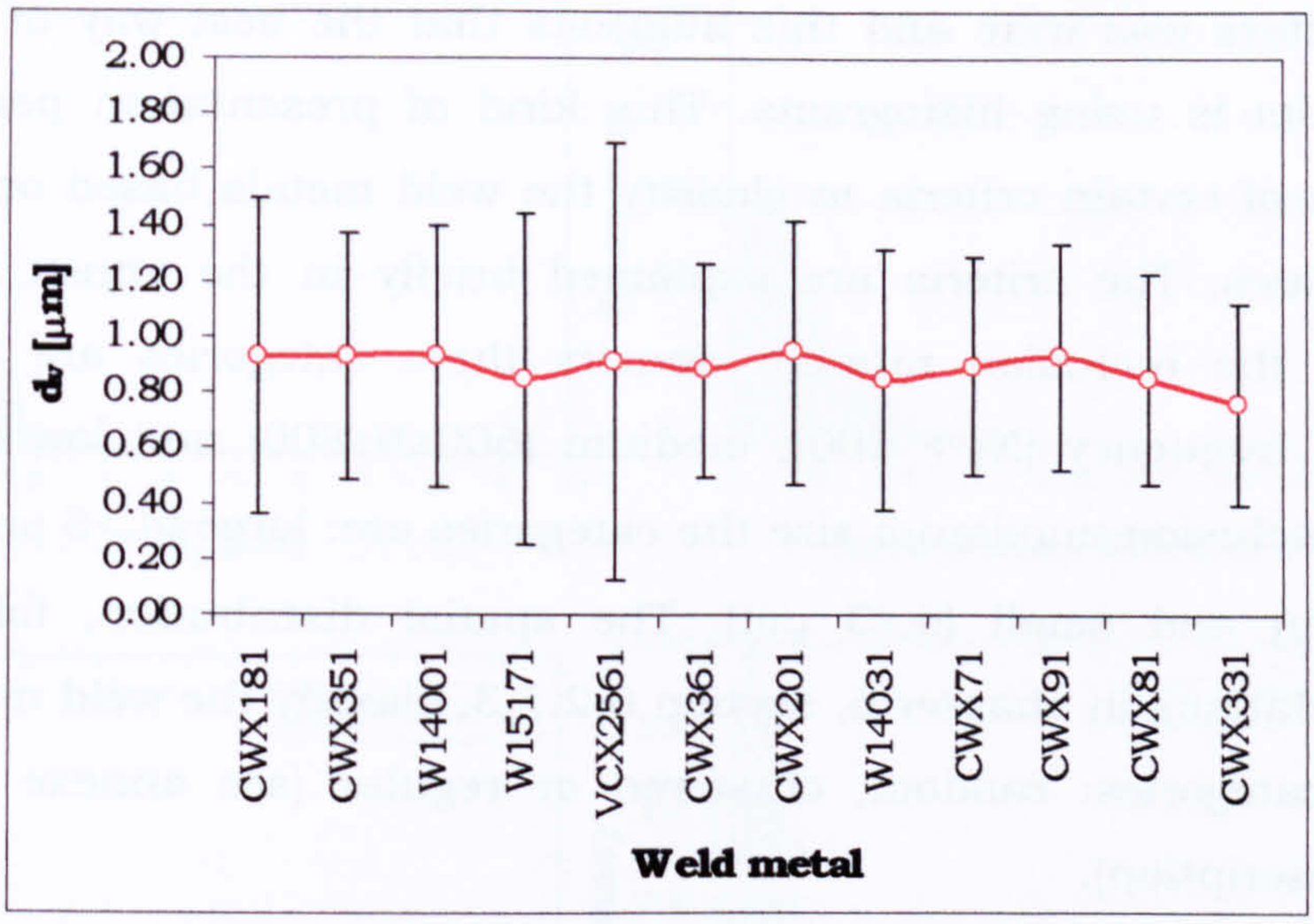

Figure 7.26 3D or true diameters (d_v) for the HSLA steel weld metals, which were studied in this investigation.

Figure 7.27 presents the 3D or true inclusion number for the steel weld metals. It can be noted that the number of inclusions vary considerably for each weld metal, showing a minimum value for CWX201 and the maximum for the CWX351 and CWX81 welds.

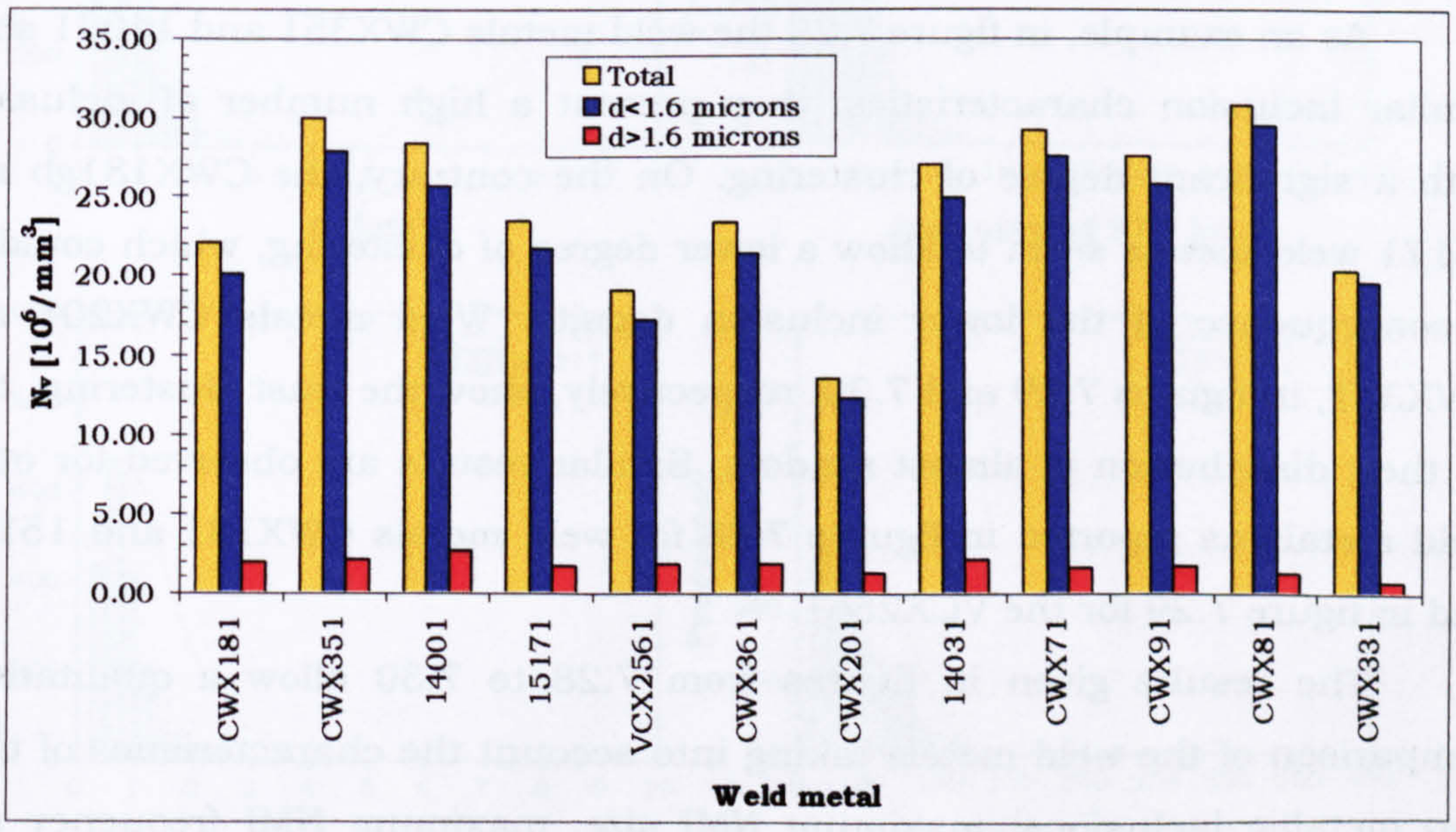

Figure 7.27 NMI numbers for the HSLA steel weld metals, which were studied in this investigation. The Pcm value for each weld metal increases from left to right.

It has already been mentioned that the dispersion of the values of the NMI diameters was wide and this suggests that the best way of presenting these results is using histograms. This kind of presentation permitted the application of certain criteria to classify the weld metals based on their NMI characteristics. The criteria are explained briefly in the annex A.15. With respect to the inclusion number density three categories are used: high (maximum frequency (N) > 800), medium (600≤N≤800) and low (N≤600). In regard to inclusion maximum size the categories are: large (d_v>5 μm), medium (3<d_v≤5 μm) and small (d_v≤3 μm). The spatial distribution, following the recommendations in chapter 6, section 6.2.1.3, classify the weld metals in the following categories: random, clustered or regular (see annexe A.15 for a detailed description).

Figures 7.28 to 7.30 expose the size and spatial distribution of the NMI in the different low alloy steel weld metals, which were analysed using the methods already described. In the figures, the histograms on the left-hand side are the results for 3D or true diameter (d_v) distribution of each weld. This distribution obeys a log-normal distribution.

Histograms on the right-hand side of the figures, show the spatial distribution which was indirectly estimated by the NMI-free area around each inclusion. The curves on these histograms correspond to a normal distribution and allow classification of the distribution in random, clustered or uniform, as was mentioned above and is proposed in chapter 6.

As an example, in figure 7.28 the weld metals CWX351 and 14001 show similar inclusion characteristics: they present a high number of inclusions with a significant degree of clustering. On the contrary, the CWX181gb and 15171 weld metals seem to show a lower degree of clustering, which could be a consequence of the lower inclusion density. Weld metals CWX201 and CWX331, in figures 7.29 and 7.30, respectively, show the least clustering, that is, their distribution is almost random. Similar results are observed for other weld metals as reported in figures 7.25 for weld metals CWX181 and 15171, and in figure 7.29 for the VCX2561.

The results given in figures from 7.28 to 7.30 allow a qualitatively comparison of the weld metals taking into account the characteristics of their non metallic inclusions: maximum NMI size, maximum NMI frequency and spatial distribution, as mentioned above. Table 7.4 shows this qualitative classification.

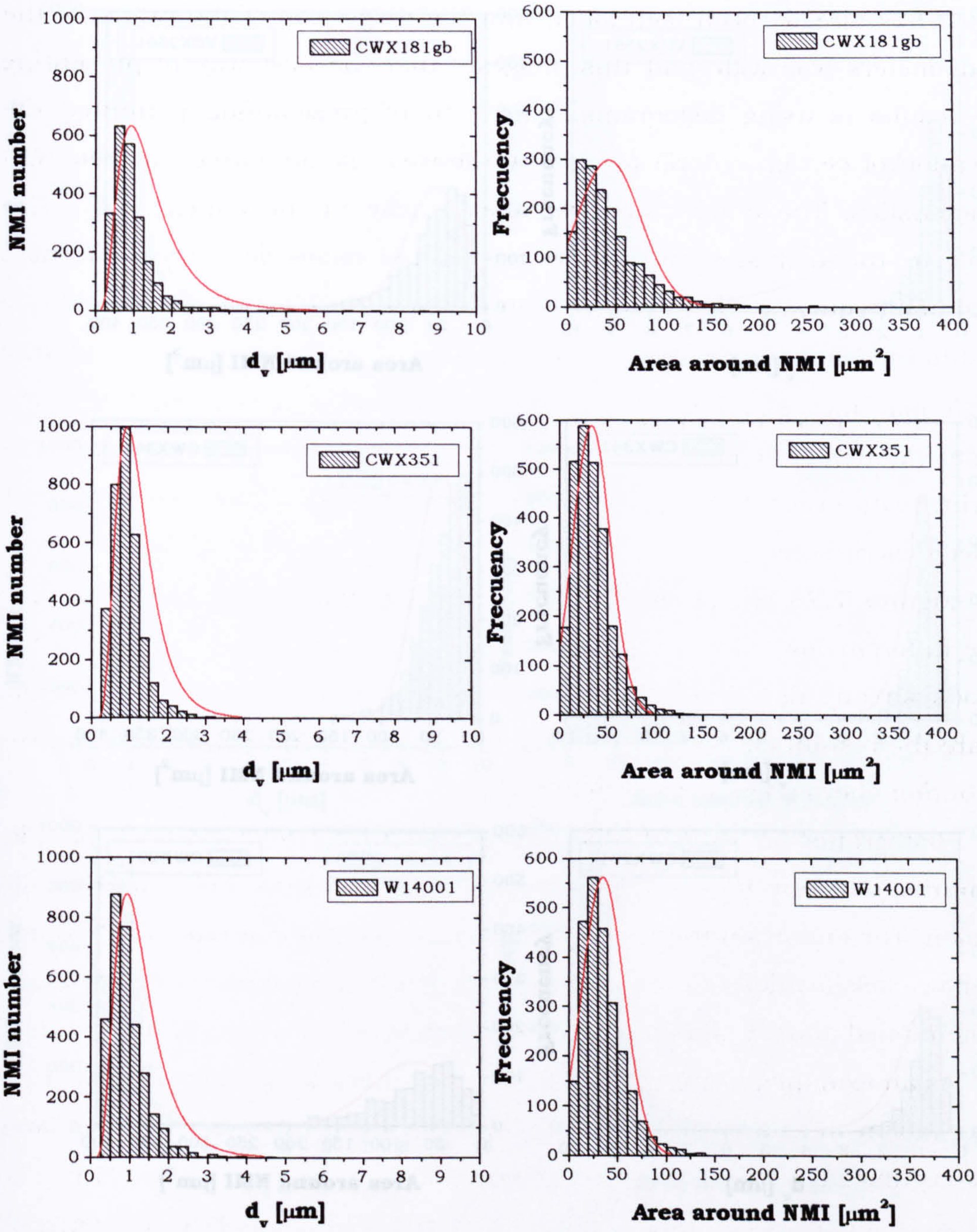

Figure 7.28 NMI size and spatial distribution for the analysed weld metals: CWX181, CWX351, 14001 and 15171. The method used for the estimation of the spatial distribution is presented in section 6.2.1.3 in chapter 6.

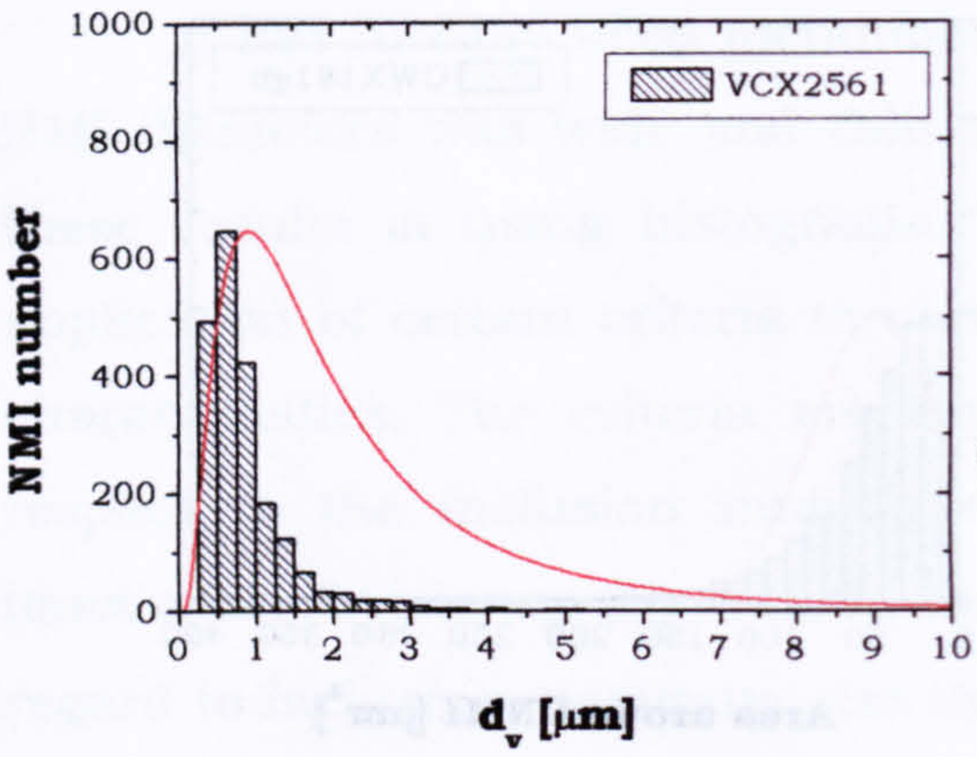

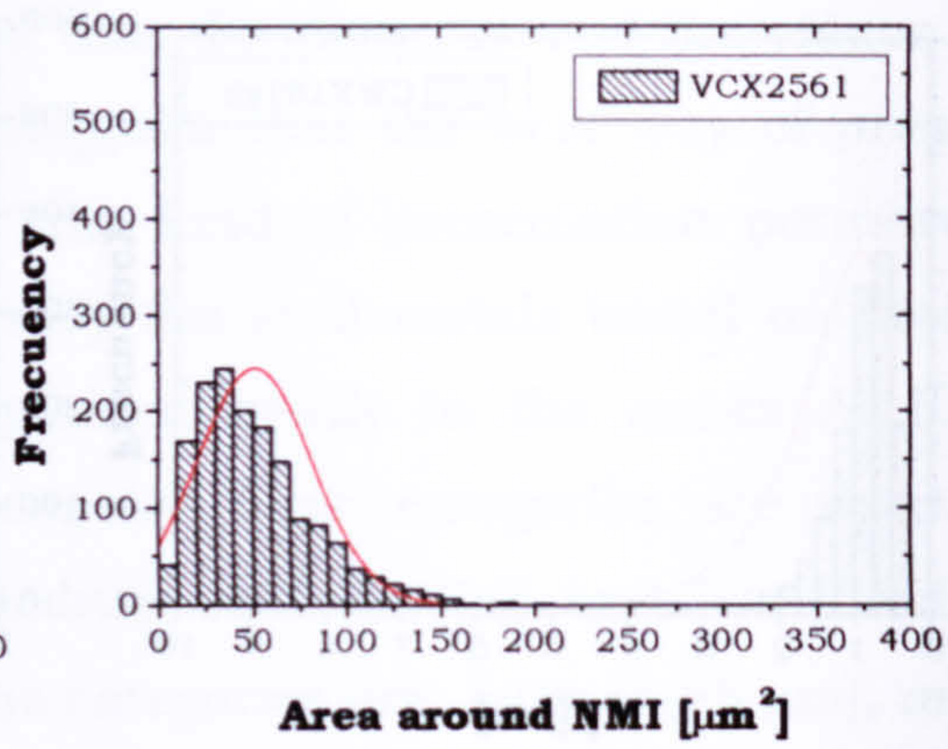

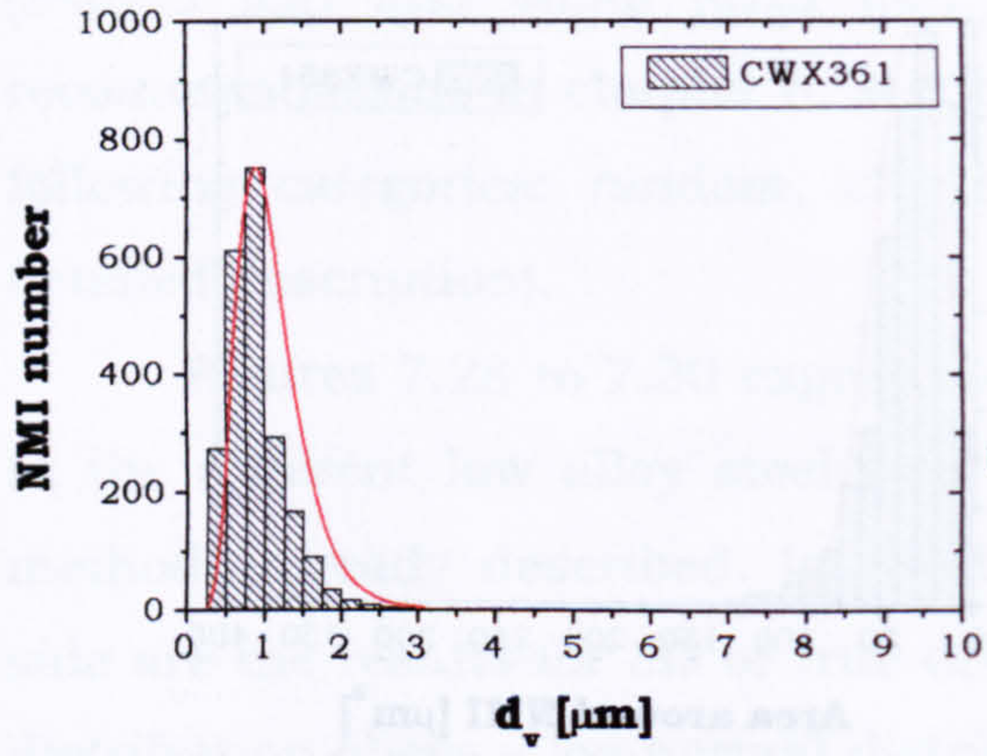

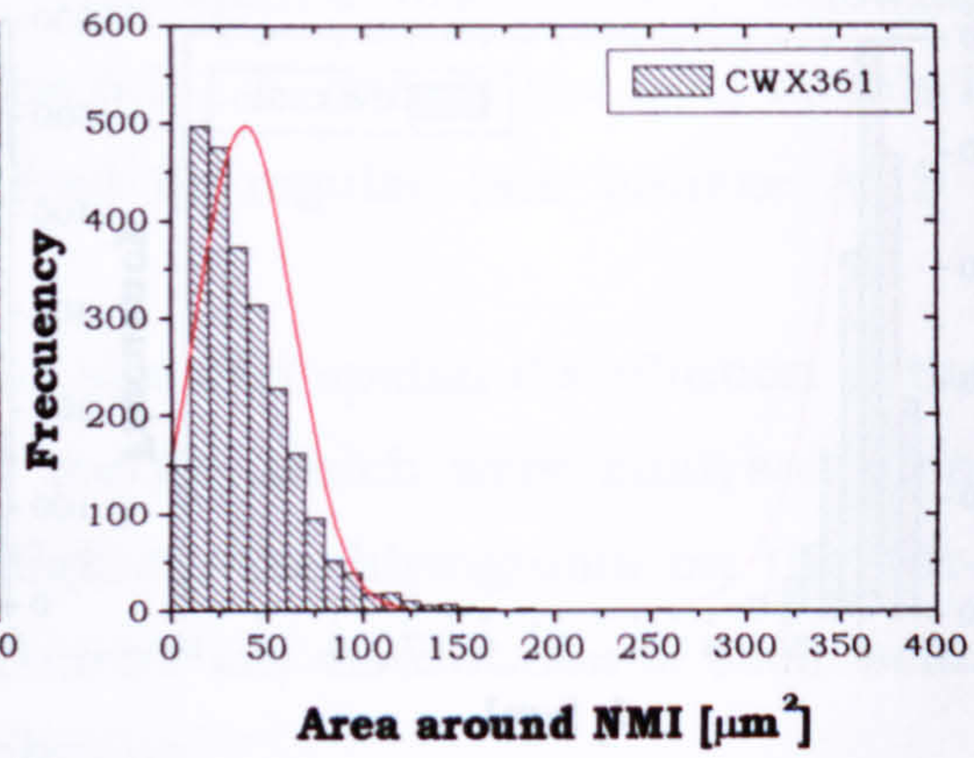

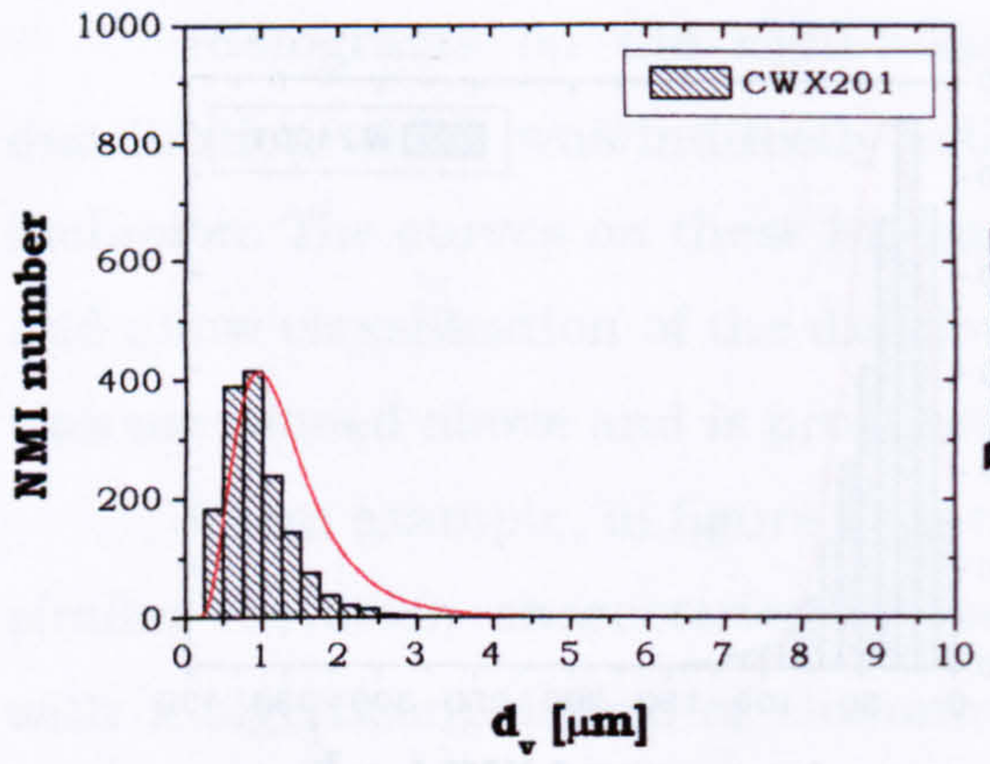

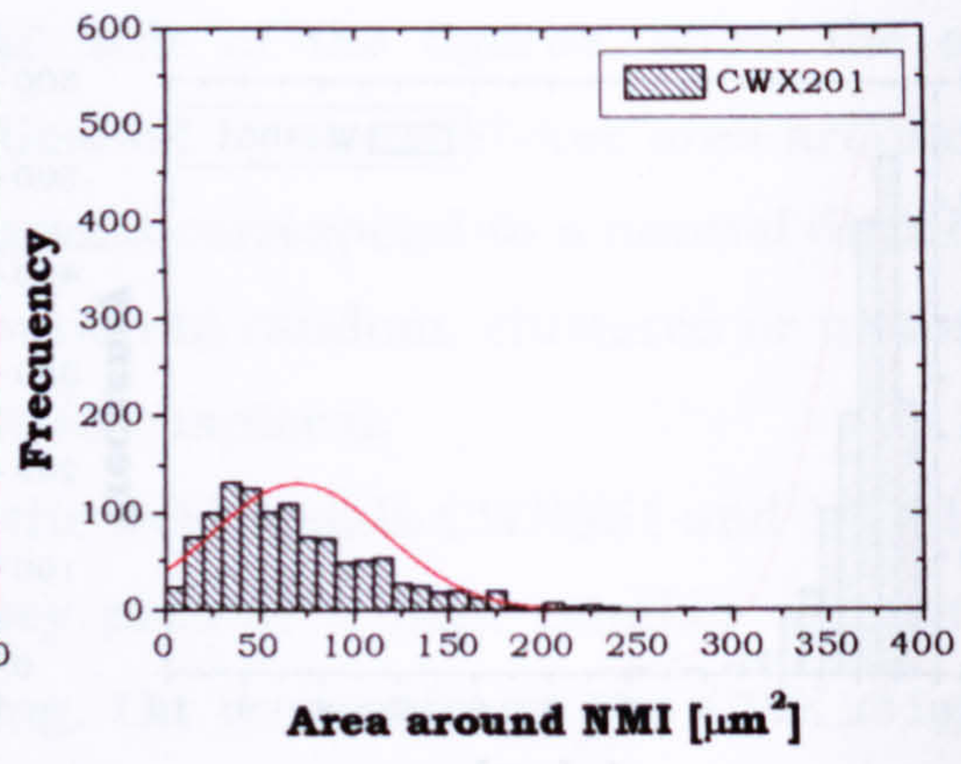

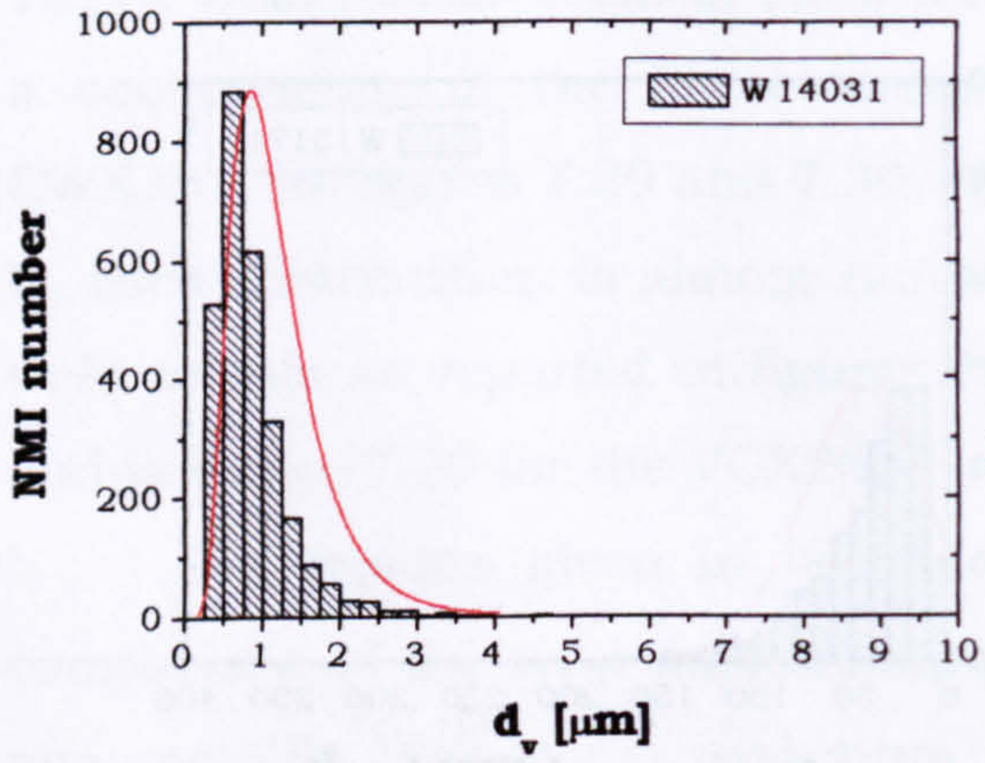

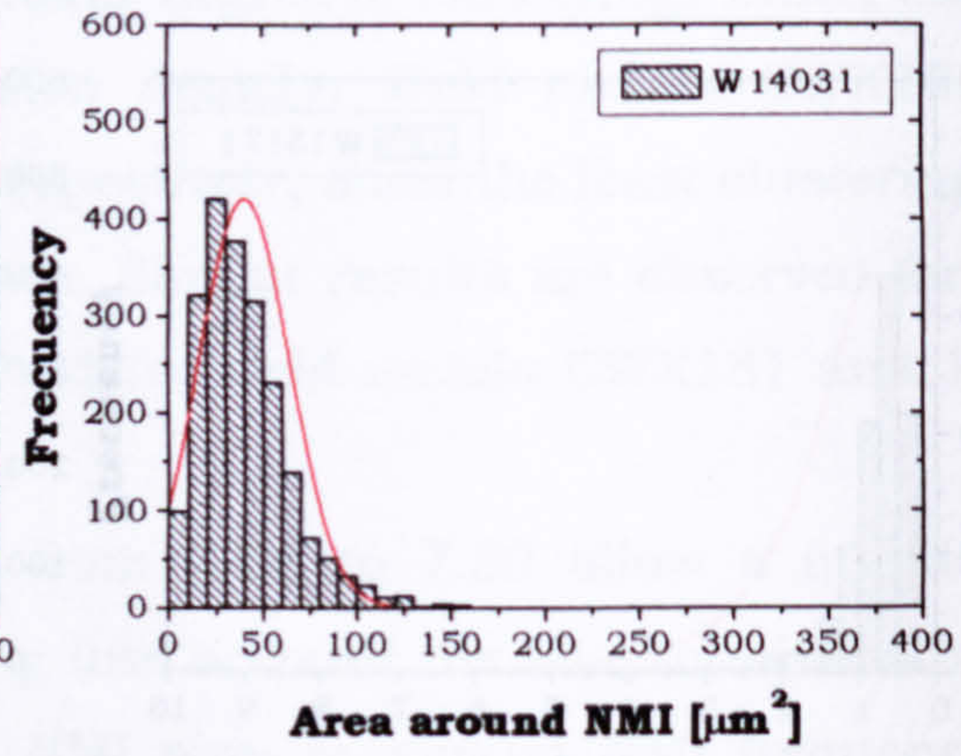

Figure 7.29 NMI size and spatial distribution for the analysed weld metals: VCX2561, CWX361, CWX201 and 14031. The method used for the estimation of the spatial distribution is presented in section 6.2.1.3 in chapter 6.

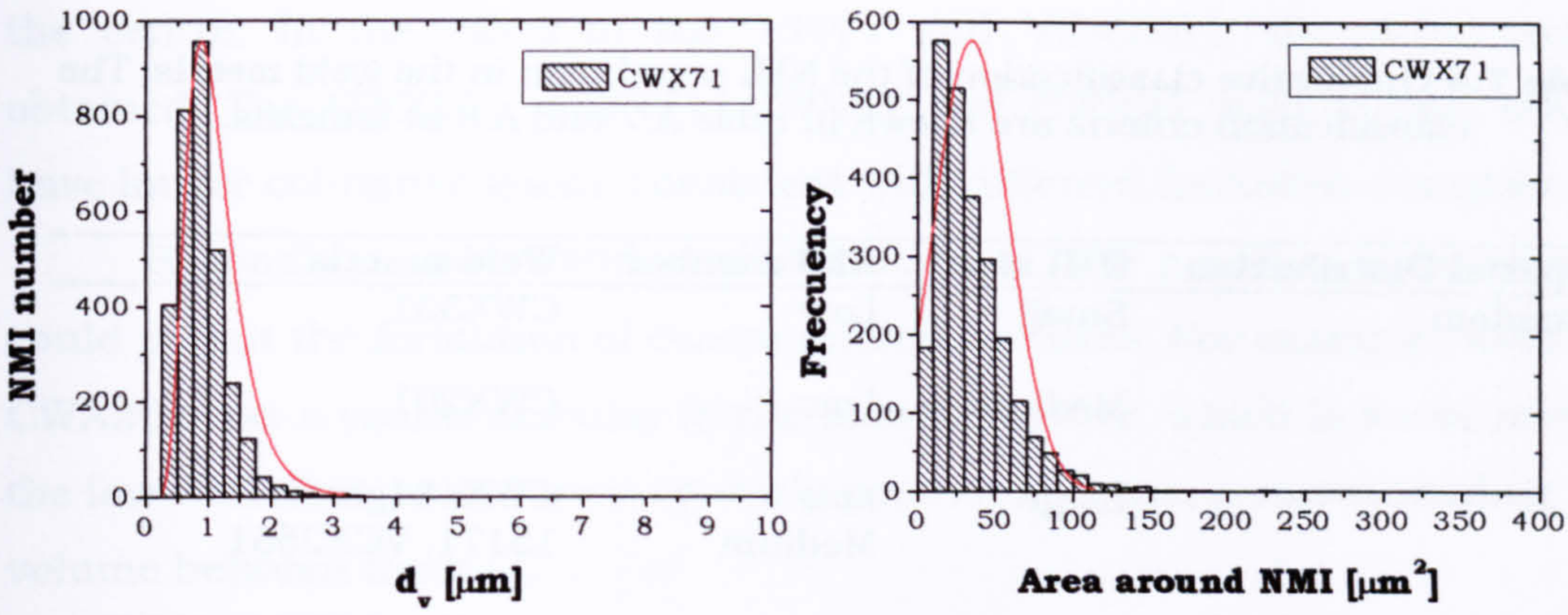

Figure 7.30 NMI size and spatial distribution for the analysed weld metals: CWX71, CWX91, CWX81 and CWX331. The method used for the estimation of the spatial distribution is presented in section 6.2.1.3 in chapter 6.

Table 7.4 Qualitative classification of the NMI population in the weld metals. The classification criteria are shown in table A.7 and A.8 in annexes.

Spatial Distribution	NMI size*	NMI number	Weld metals
Random	Small	Low	CWX331
	Medium	Low	CWX201
	Large	Low	CWX181gb
		Medium	15171, VCX2561
Clustered	Small	High	CWX71, CWX81, CWX91
		Medium	CWX361
	Medium	High	CWX351
		Medium	14031
	Large	High	14001

*maximum inclusion size observed in the original data and on the histogram

The weld metals were only grouped into two spatial distribution classes: random and clustered. Regular distributions were not found. Average volume around inclusion clusters in the random group is larger than that expected for inclusions showing clustered distribution. There are further sub-divisions in each group based on maximum NMI true size and NMI number. Each weld metal pertains to a determined group. For example, weld metal CWX201 has a unique combination of NMI inclusion characteristics: random distribution, medium NMI maximum true size and low NMI number. Weld metals CWX71, CWX81 and CWX91 are in the same group: clustered distribution, small NMI size and high number density of inclusions.

Such a qualitative classification of the weld metals based on their NMI characteristics can be used to compare the influence of inclusions on the mechanical properties and the hydrogen induced cold cracking. These aspects are discussed in greater length in chapter 8 and 9. However, with respect to the weld metal microstructure it is known that the size, type and distribution of NMI influence the solid state transformation in several different ways.

Firstly, the presence of NMI could affect the grain size. They could inhibit the grain growth during solidification and solid state transformation reducing the size of the prior columnar austenite. Depending on volume fraction, small NMI size could affect less than large. For example, weld metal CWX351, which has a high number of medium sized inclusions, had smaller columnar grains in the regions near fusion line and upto some distance from

the centre. In the cases of the 15171 and VCX2561, the same result is obtained. The CWX331, CWX71, CWX81 and CWX91 weld metals seems to have longer columnar grains consistent with different inclusion densities.

Secondly, a more random distribution of NMI possibly encourages and could permit the formation of coarse microstructures. For example, weld metal CWX201 has a coarse acicular ferrite microstructure, which is associated with the low NMI density and their sparsely populated areas, a corresponding larger volume between them.

Finally, highly clustered inclusions would mean that there are regions of the weld metal free of NMI, hence the formation of microstructures not requiring inclusions as a nucleant could occur. Examples of this are the isolated islands of bainite found in the weld metals 14031, CWX71, CWX81 and CWX91 or Widmanstätten ferrite in the CWX351.

7.8.2 NMI composition and morphology

Non-metallic inclusions have complex structures formed from various oxides, nitrides and sulphides. Some of the compounds that could be found in steel weld metals are: $MnOAl_2O_3$, γ-Al_2O_3, SiO_2, $MnOSiO_2$, TiN and MnS.

Figure 7.31 shows the composition of typical randomly selected NMI's found in CWX181gb. Figure 7.31(a) shows the backscattering electron image (BEI) where could be appreciated the size and location of some inclusions which have the typical NMI composition presented in the figures from 7.31(b) to (d). Generally, microanalysis of the inclusions in the studied weld metals revealed the presence of elements such as Mn, Si, Al, Ti, O, N and S.

Figure 7.32 shows other examples of NMI composition that were found in other HSLA steel weld, which were studied in this investigation. Figure 7.33 presents more evidence about the elemental distribution of Mn, Si, Ti and Al in a weld metal surface. This NMI composition results could imply the presence of compounds such as those mentioned above. There are concordances between the NMI composition results in this investigation and those reported by several authors [1, 16, 23-34, 149].

The complex composition of the non-metallic inclusions indicates that they are formed by several oxides, compound oxides, sulphides, carbides and nitrides, which implies that the NMI's can not be treated as monocrystalline and homogeneous particles. Moreover, many inclusions are amorphous materials. It has been reported that the amorphous inclusions represent the 50 to 60% of the inclusions that could be found in low alloy steel weld metals.

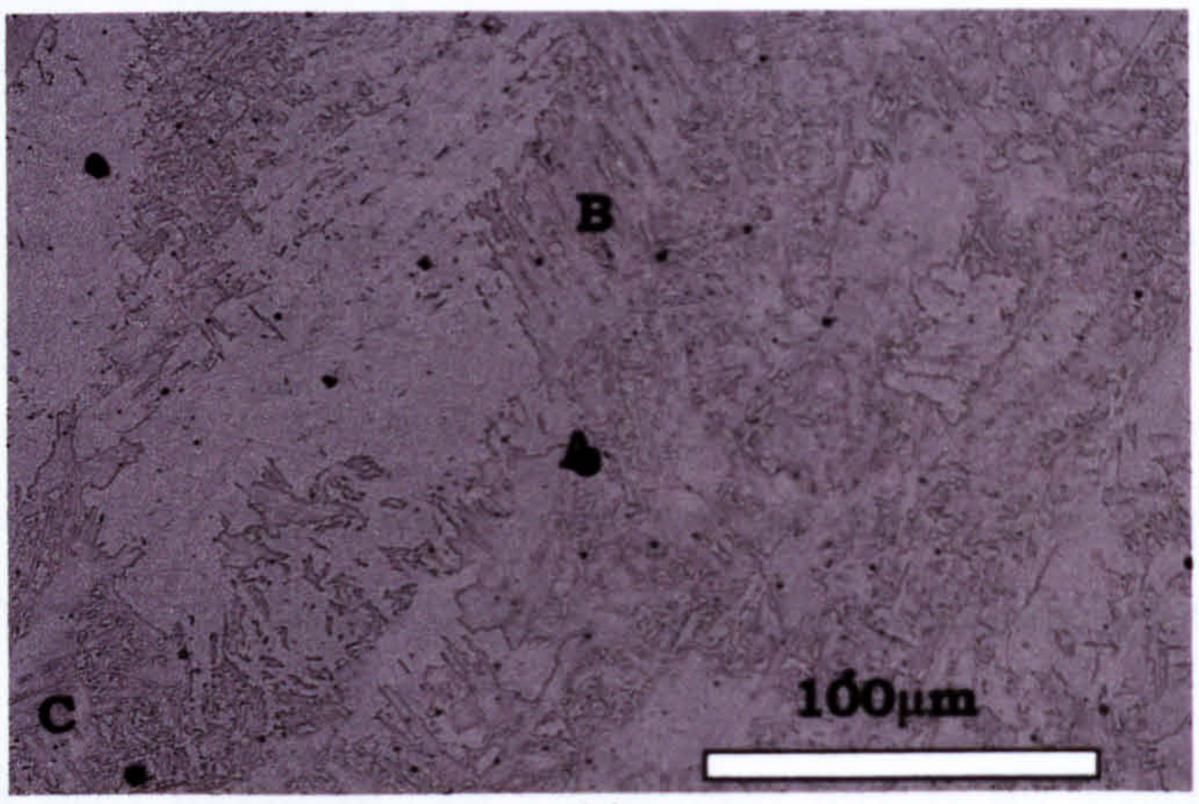

Figure 7.31 NMI composition in the CWX181gb weld metal, (a) BE image of the surface, (b), (c) and (d) are the composition of NMI A, B, and C, respectively.

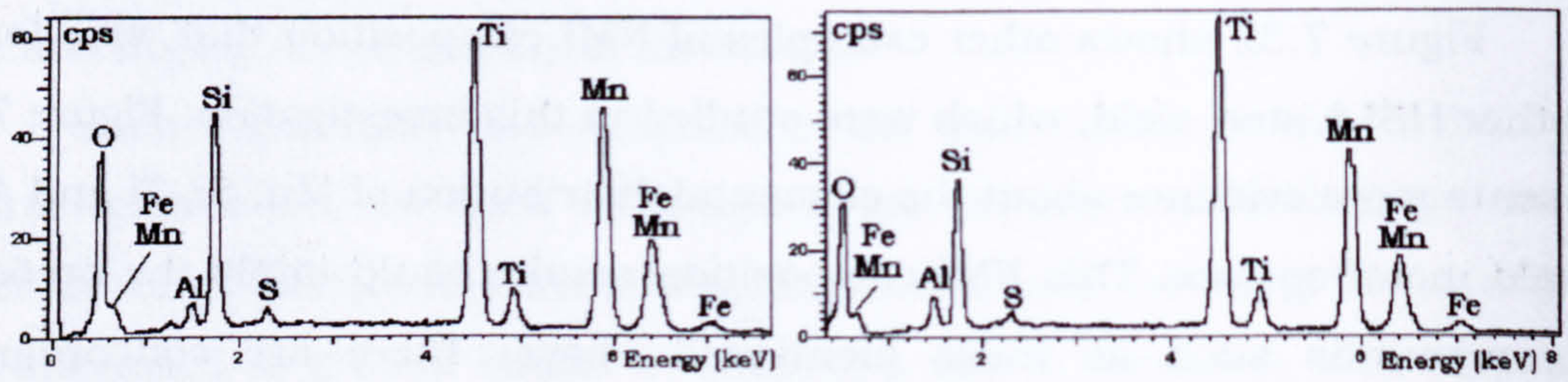

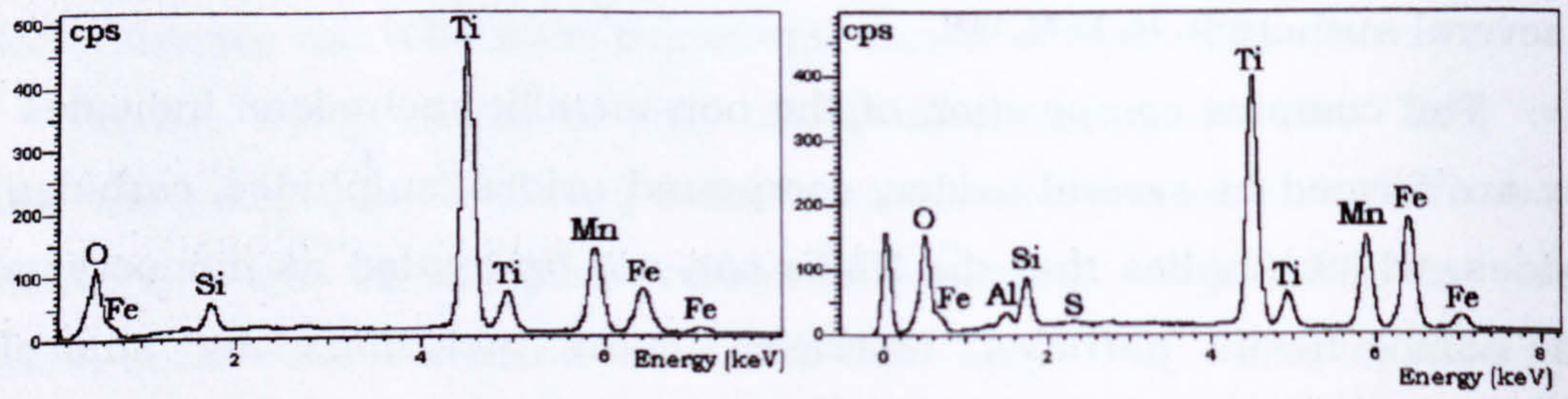

Figure 7.32 Typical chemical composition of the NMI for several HSLA steel weld metals which were studied in this research.

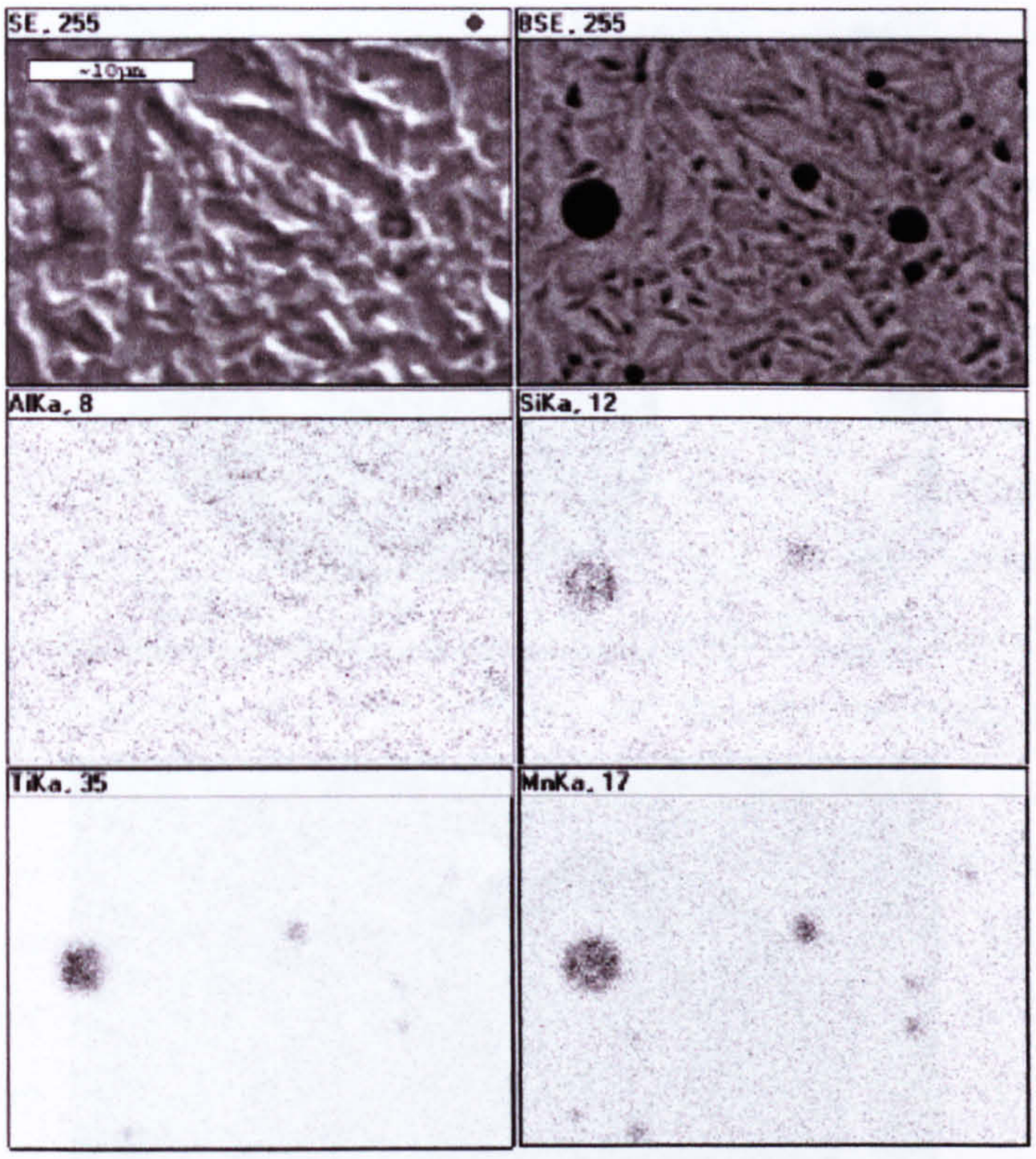

Figure 7.33 Elemental composition mapping presenting the distribution of Al, Si, Ti and Mn in the VCX2561 weld metal.

Between these inclusions, the majority are glassy silicates [149]. Figure 7.34 presents two examples of complex non-metallic inclusions, which were found in two different weld metals in this work. These NMI were found on the fracture surface of the tensile sample. It can be noted the composite nature of them and the complex structure that could be formed.

The determination of the NMI composition and morphology may permit the identification of those kinds of inclusions, which produce beneficial or detrimental effects on the phase transformation processes, the mechanical properties and the hydrogen distribution in the weld metals. Study of the nature of inclusions, chemically and morphologically, is a very complex task and the detailed study may not lead to any precise result. For example, in the case of studies related to the effect of NMI on the formation of acicular ferrite in weld metals, there have not been unambiguously demonstrated, what chemical composition of inclusions or orientation relationship promotes the preferential formation of acicular ferrite [149].

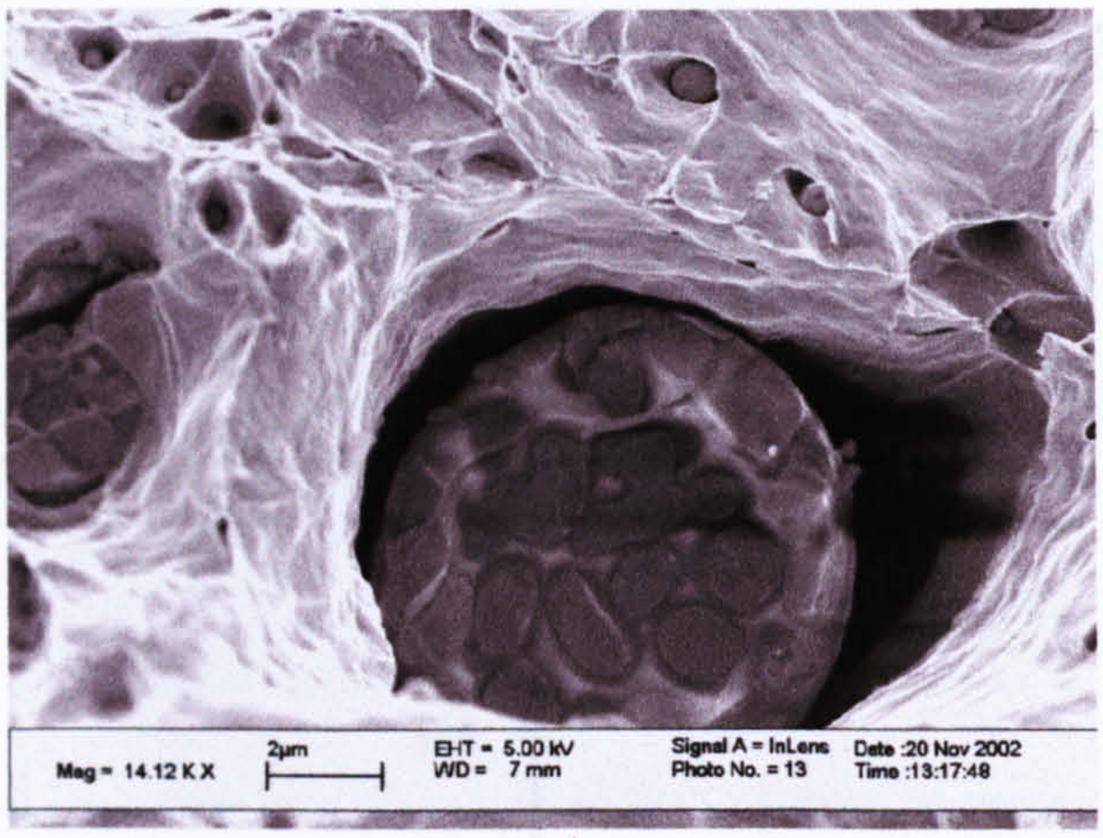

(a)

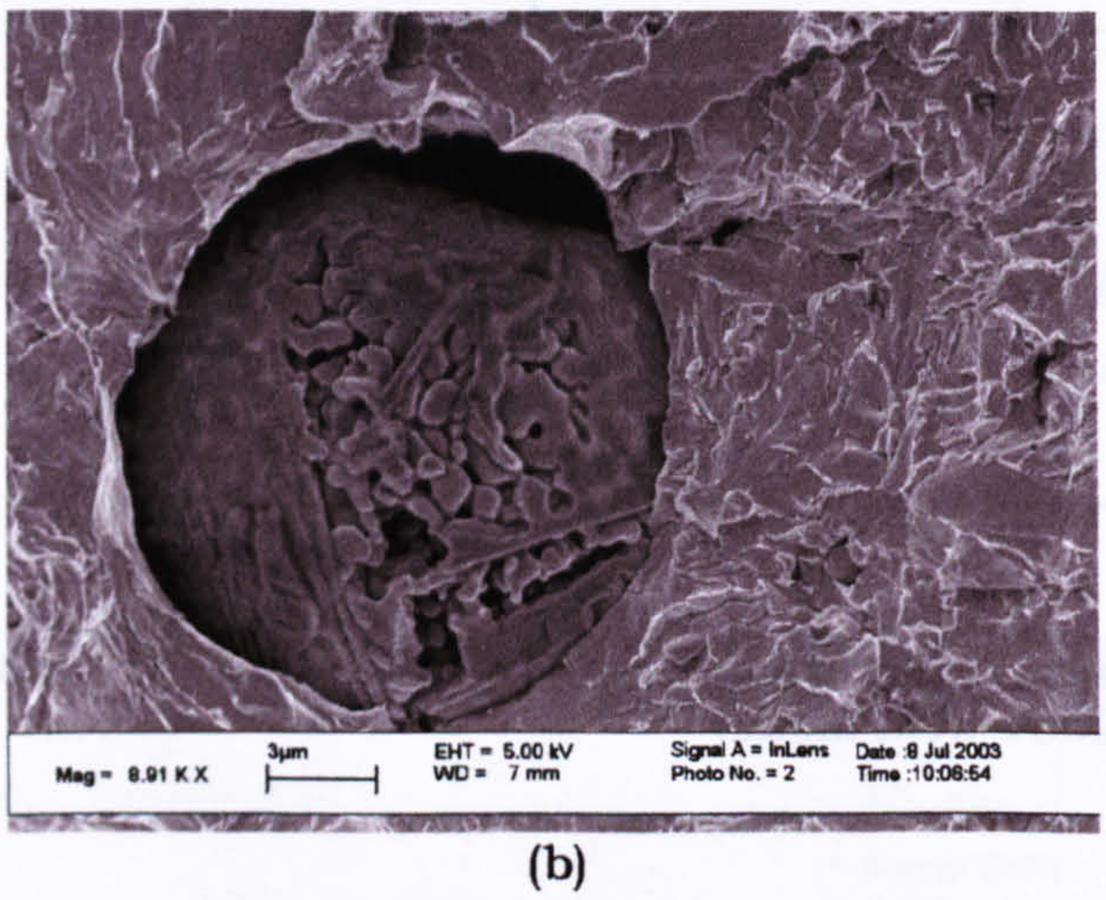

(b)

Figure 7.34 Complex morphology of some inclusions in low alloy steel weld metals, (a) 15171 and (b) CWX181gb weld metals.

7.8.3 Thermodynamic calculations

The effort required for quantitative analysis of the inclusions in all of the welds was considered impractical and, although useful, would have been impossible in the timescale. One way of overcoming the complexity of the inclusion is through thermodynamical calculations. Such calculations are capable of predicting the types of non-metallic inclusions that would be expected based on the chemical composition of the weld metal or the consumables and the shielding gases. Moreover, segregation during the solidification process, which produces changes of alloying elements as the fraction of liquid decreases, can be accounted in the prediction. Segregation could promote or inhibit the formation of certain inclusions or precipitates, but models based on the Scheil approach can, in principle, indicate the sequence of inclusion formation.

7.8.3.1 NMI stability diagrams

It is possible, using thermodynamic data on dilute iron alloys, to construct non-metallic inclusion stability diagrams. These diagrams describe the inclusion formation employing equilibrium thermodynamic calculations by considering multicomponent interactions in liquid steel. The equations and the thermodynamical data utilised for the calculation of the diagrams are given in the annex A.16.

Figure 7.35 presents two stability diagrams for the major non-metallic inclusions: Al_2O_3, SiO_2, MnO and $MnOSiO_2$. These are isothermal diagrams in this case the temperature selected was 1873 K, where the liquid iron is stable. The axes of the diagram are the activity or weight percent of the involved metallic elements (M = Al, Mn and Si, for example) and the oxygen dissolved (O) in the liquid metal. The continuous lines represent the equilibrium activities for M and O for the formation of a particular oxide. If the activities of M and O are located above this line, the respective oxide is formed. On the other hand, the ovoidal regions of stability for determined compound are obtained when interaction coefficients between alloying elements are taken into account (see appendix A.16. If the weight percent of M and O are located inside the ovoidal regions of a particular compound, this is formed. On the contrary, if the M and O activities is below the equilibrium line or their weight percent is outside the stability regions, the compound is not formed. In this way it is possible to predict the potential oxides or other compounds such as nitrides and sulphides that could be formed in the weld metal during welding or during solidification if the appropriated isothermal diagram is obtained.

In figure 7.35, weld metals are grouped into two classes: those with comparatively contracted regions for SiO_2 and $MnOSiO_2$ and those with an expanded region for the same compounds. The stability regions for Al_2O_3 and MnO are similar for all the studied weld metals. The nominal contents of Si, Mn, Al and O for each weld metal are plotted on the figures and, as can be observed, they are located in certain regions. This indicates similarities between NMI in the weld metals studied.

In the case of Al_2O_3, SiO_2 and $MnOSiO_2$, the diagrams confirm their formation in all the welds. However, in the case of the weld metals CWX361, 14031, CWX71, CWX91, CWX81 and CWX331, it could be expected a major thermodynamical tendency, due to the expanded fields for SiO_2 and $MnOSiO_2$ (figure 7.35(b)), and the location of the corresponding composition inside the stability regions. In regard to the formation of MnO, it is noted that it is

possible for all the weld metals except for the CWX351, which has the lowest Mn content, about 0.25 wt%. This weld, observed in figure 7.35(a) on the left in the oval corresponding to Mn and O combination, has a composition that falls outside the stability region of MnO oxide.

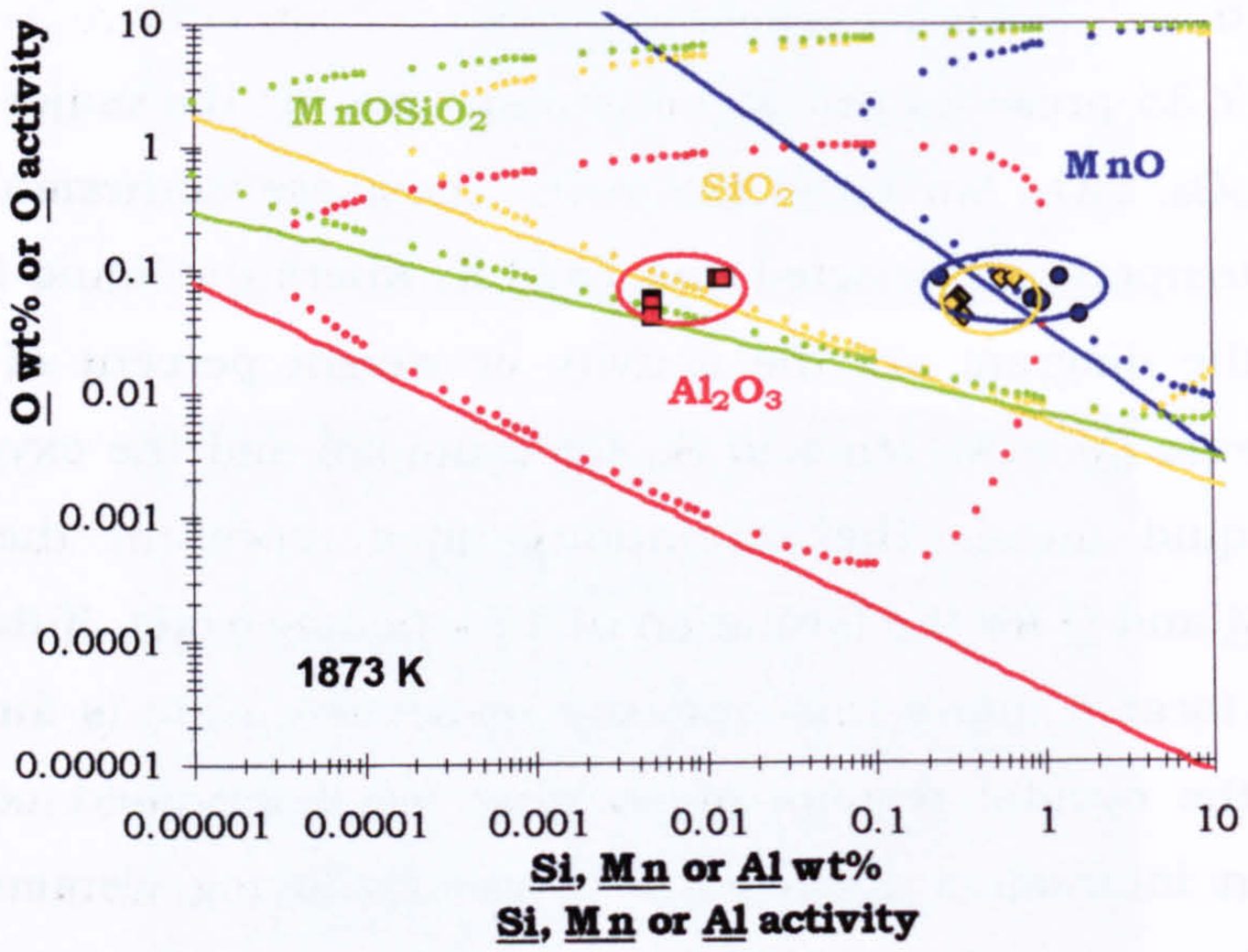

(a)

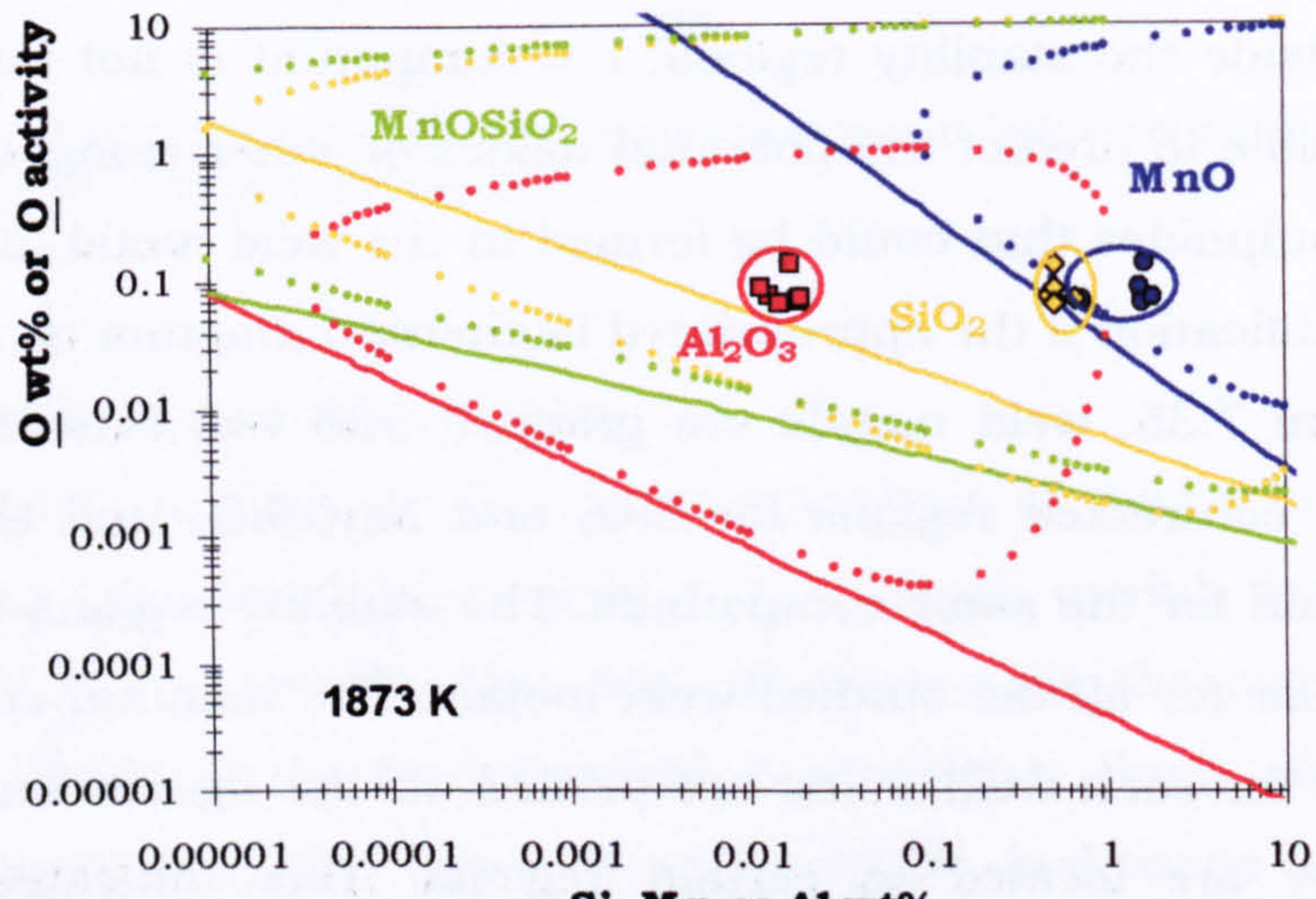

(b)

Figure 7.35 NMI stability diagrams for the oxides Al_2O_3, SiO_2, MnO and the complex oxide $MnOSiO_2$ calculated for the weld metals studied in this investigation: (a) Contracted $MnOSiO_2$ field: CWX181gb, CWX351, 14001, 15171, VCX2561 and CWX201; (b) Expanded $MnOSiO_2$ field: CWX361, 14031, CWX71, CWX91, CWX81 and CWX331

Figure 7.36 presents the diagrams for the formation of titanium oxides: TiO, Ti_2O_3, Ti_3O_5 and TiO_2. Similarly, the weld metals were grouped in three classes: expanded, intermediate and contracted oxide fields. In the first two groups the formation of all the Ti-oxides is possible. In the expanded group (figure 7.36(a)) the thermodynamical tendency for the formation of Ti-rich oxides is larger than for the rest, possible similar to the case of Al_2O_3, SiO_2 and $MnOSiO_2$ formation. In figure 7.36(c), the Ti and O content are located so close to the stability boundary that a decrease in oxygen due to the formation of other more stable oxides, could inhibit the formation of Ti-oxides.

The figure 7.37 shows the stability diagrams for MnS, TiN and AlN in the studied weld metals. As for the case of Ti-oxides, the weld metals have been classified in three groups depending on the size of their TiN field because MnS and AlN fields do not present appreciable changes. It can be noted that for the first group (figure 7.37(a)), it could be expected the formation of TiN in the liquid steel. For the welds in the intermediate group (figure 7.37(b)), the TiN precipitation could occur during solidification. However, the formation of Ti-oxides could reduce this possibility due to the consumption of Ti, which could maintain the Ti-N composition outside the stability region. For the case of the weld metals in the contracted group (figure 7.37(c)), due to the reduction in the stability region of the TiN, it is not expected to form this nitride.

The thermodynamical calculations for the formation of NMI in weld metals, presented in form of stability diagrams in figures 7.35 to 7.37, can be useful to predict the type of inclusion that could form depending on composition. However, in the present investigation the difference in weld metal composition does not seem produce significant changes in the NMI types. In the next section a Scheil approach is used to study theoretically the effect of solidification on the formation of different NMI.

7.8.3.2 Effect of solidification on the formation of NMI's

The formation of inclusions in the weld metal is affected by the simultaneous formation of other inclusion and by the segregation of alloying elements due to the solidification process of the weld metal. Other factors that could influence the formation of inclusions are: the magnetic and thermal stirring of the weld pool, the composition of the protecting gases, the cooling rate, the heat input and other external factors [1, 23-34].

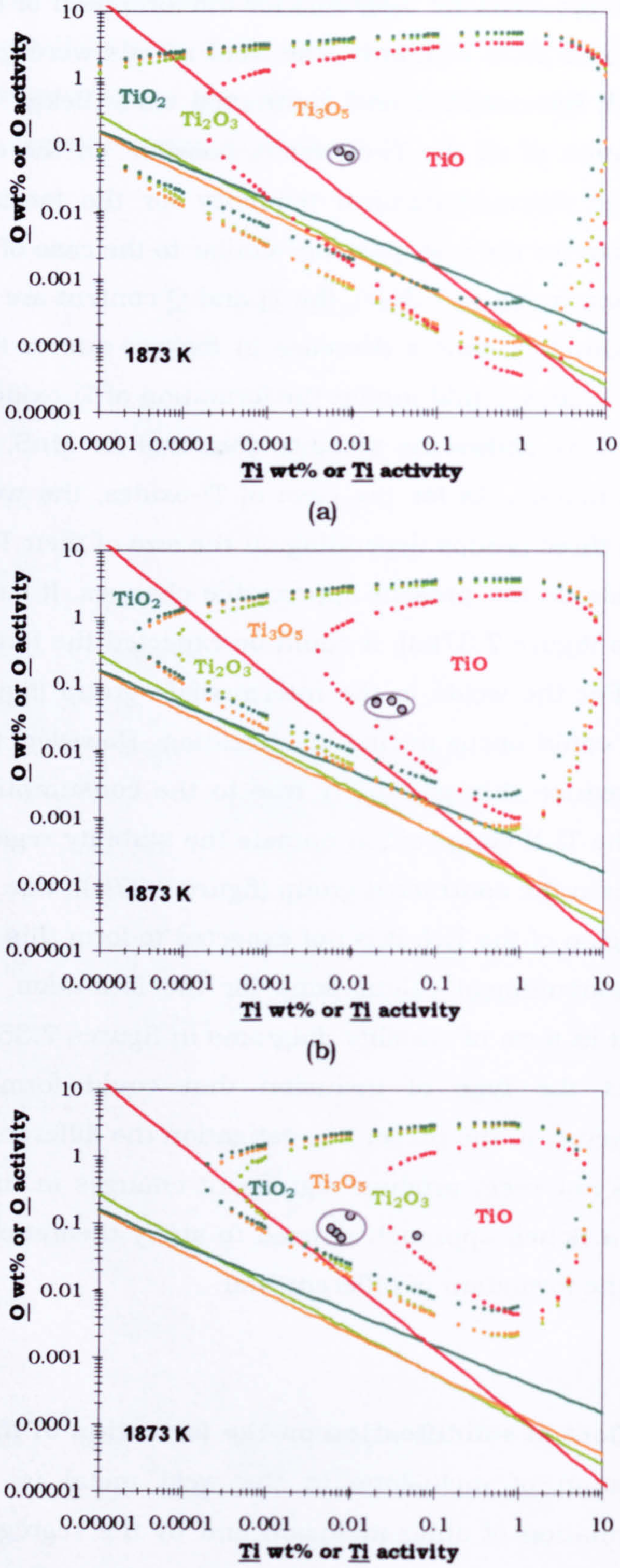

Figure 7.36 NMI stability diagrams for the Ti oxides in the weld metals studied in this investigation: (a) Expanded fields: CWX351, 14001 and CWX361; (b) Intermediate fields: CWX181gb, 15171, VCX2561 and CWX201; (c) Contracted fields: 14031, CWX71, CWX91, CWX81 and CWX331

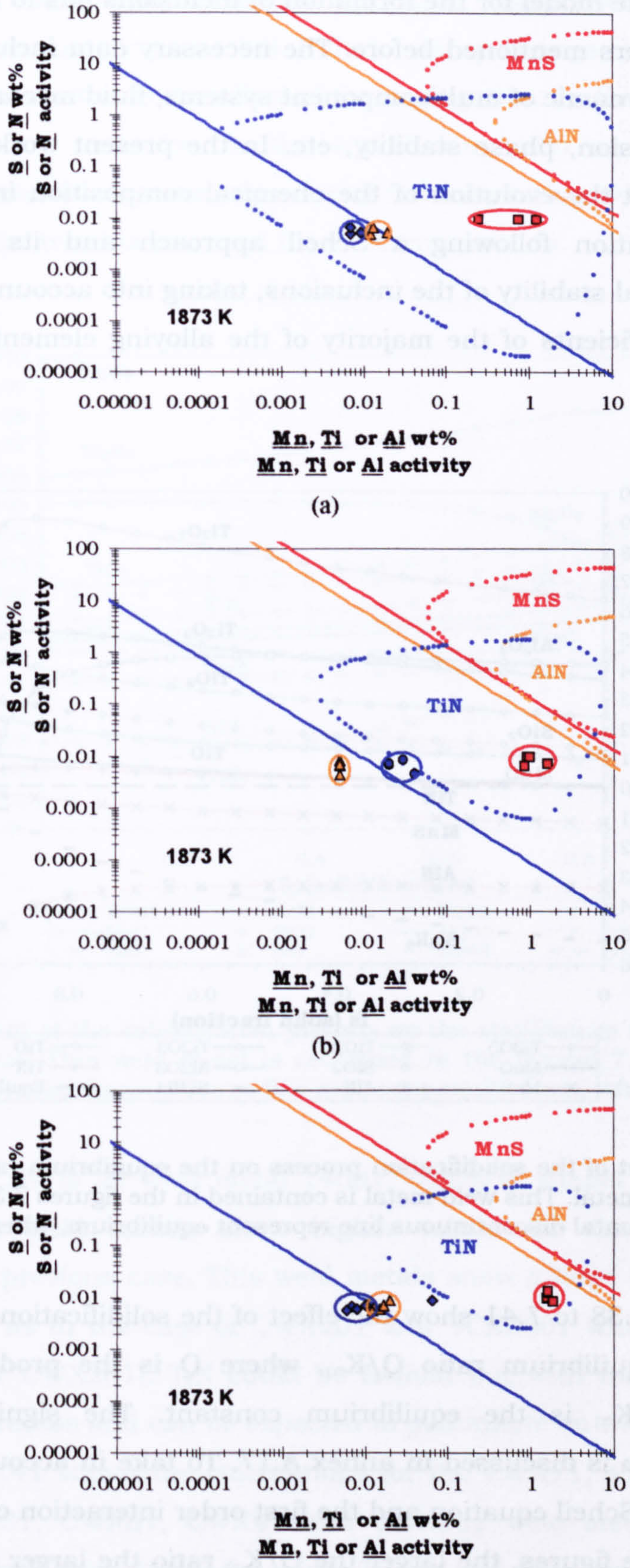

Figure 7.37 NMI stability diagrams for MnS, TiN and AlN in the weld metals studied in this investigation: (a) Expanded fields: CWX351, 14001 and cwx361; (b) Intermediate fields: CWX181gb, 15171, VCX2561 and CWX201; (c) Contracted fields: 14031, CWX71, CWX91, CWX81 and CWX331

A complete model for the formation of inclusions has to take in account all the parameters mentioned before. The necessary data include information about: thermodynamic of multicomponent systems, fluid mechanics, inorganic chemistry, diffusion, phase stability, etc. In the present work an attempt is made to present the evolution of the chemical composition in the weld pool due to segregation following a Scheil approach and its effect on the thermodynamical stability of the inclusions, taking into account the first order interaction coefficients of the majority of the alloying elements in the liquid steel weld pool.

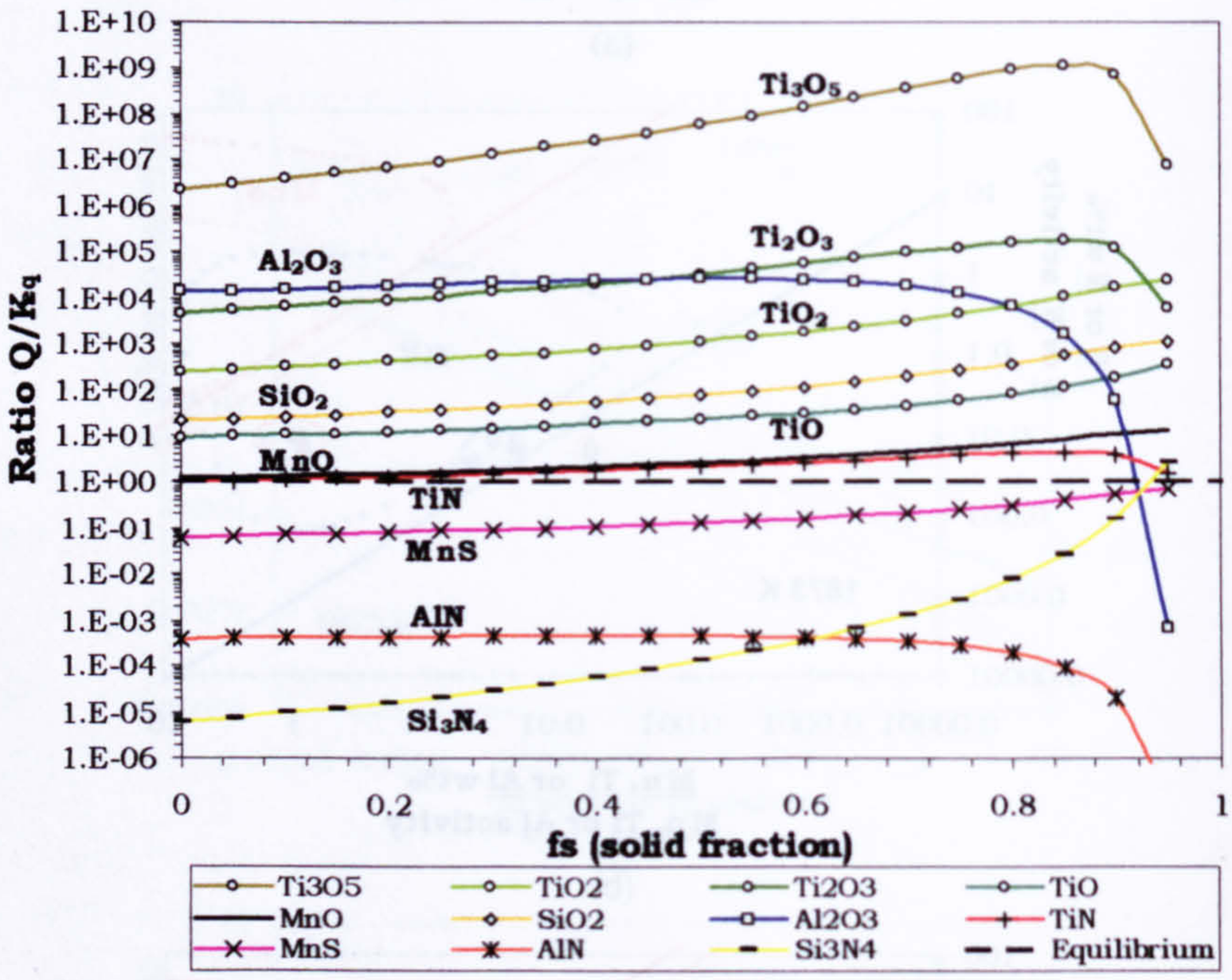

Figure 7.38 Effect of the solidification process on the equilibrium ratio Q/K_{eq} for the CWX181gb weld metal. This weld metal is contained in the figures 7.32(a), 7.33(b) and 7.34(b). The horizontal discontinuous line represent equilibrium, where $Q/K_{eq}=1$.

Figures 7.38 to 7.41 show the effect of the solidification process on the value of the equilibrium ratio Q/K_{eq}, where Q is the product of element activities and K_{eq} is the equilibrium constant. The significance of the equilibrium ratio is discussed in annex A.17. To take in account the effect of segregation the Scheil equation and the first order interaction coefficients were employed. In the figures, the larger the Q/K_{eq} ratio the larger is the tendency to the formation of the specific inclusion. The inclusion is not formed when the equilibrium ratio is less than 1.

Figure 7.38 presents the variation of Q/K_{eq} ratio for the CWX181gb weld metal. The 15171 weld metal present similar behaviour. In both cases, the

inclusions with major tendency to form are: Ti_3O_5, Al_2O_3, Ti_2O_3, TiO_2, SiO_2, TiO and in less extension MnO and TiN. This tendency changes with the increase of the solid fraction due to the effect of the segregation. In the case of Al_2O_3, it could be noted a reduction in the equilibrium ratio at the end of the solidification process as a consequence of the interaction with other alloying elements. Similar trend is observed for other compounds.

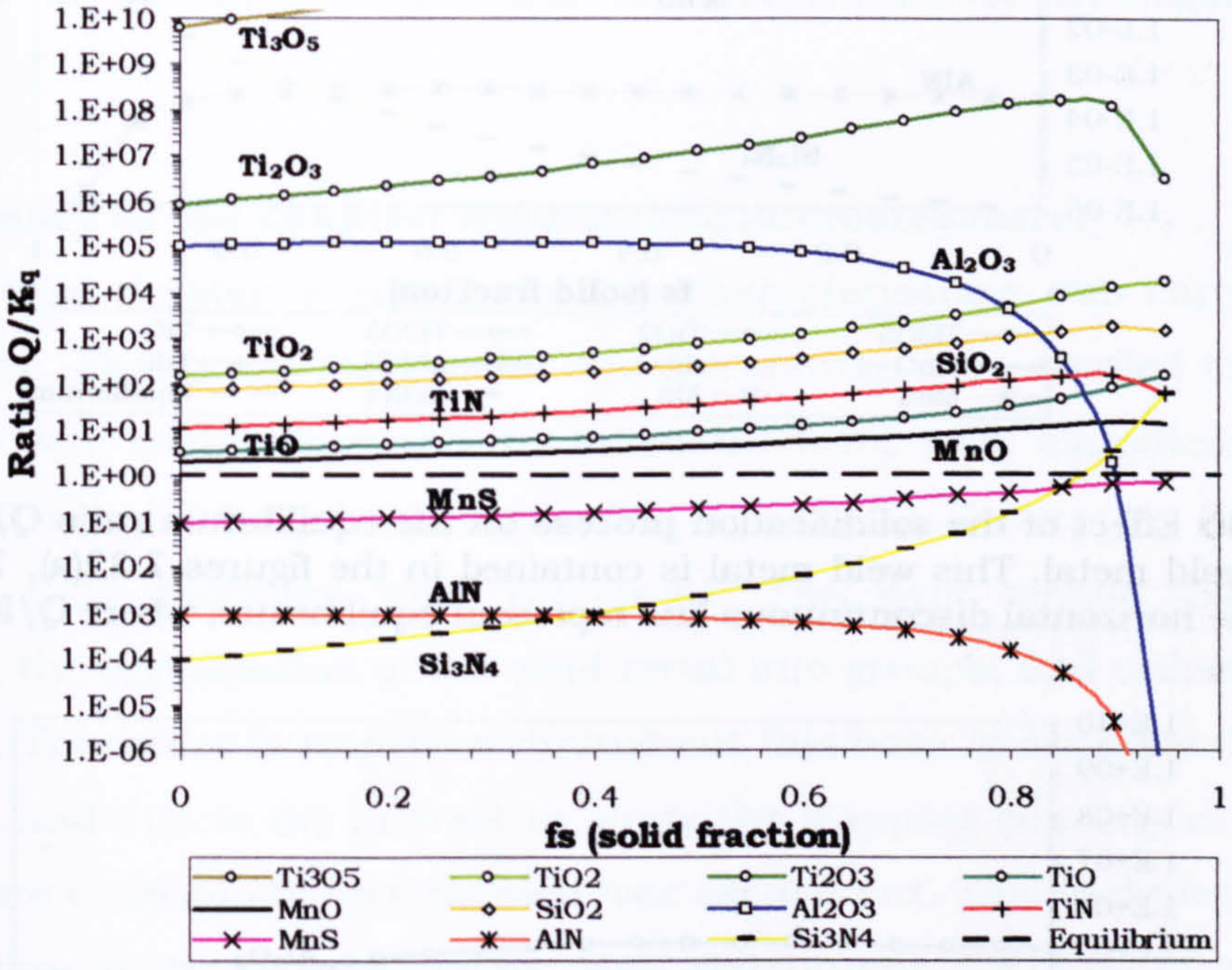

Figure 7.39 Effect of the solidification process on the equilibrium ratio Q/K_{eq} for the 14001 weld metal. This weld metal is contained in the figures 7.32(a), 7.33(a) and 7.34(a). The horizontal discontinuous line represent equilibrium, where $Q/K_{eq}=1$.

Figure 7.39 is for weld metal 14001, which is similar to CWX351 and CWX361. This weld metals show higher values for the ratio Q/K_{eq} in comparison to previous case. This weld metals show a large tendency to form Ti-rich oxides, as in the case of CWX201 and VCX2561 which are shown in figure 7.40 (for CWX201). TiN could be formed but with the advance of the solidification process and can be expected to precipitate on the NMI particles.

Figure 7.41 shows the calculations for the CWX71, which is similar to those for: 14031, CWX81, CWX91 and CWX331 weld metals. The highest tendency to form is for the Al_2O_3 oxide. Ti, Si, and Mn oxides could form as well but the driving force is lesser than for the rest of the weld metals. The TiN is not predicted to form. As a consequence, in this group of welds Al-rich NMI are expected.

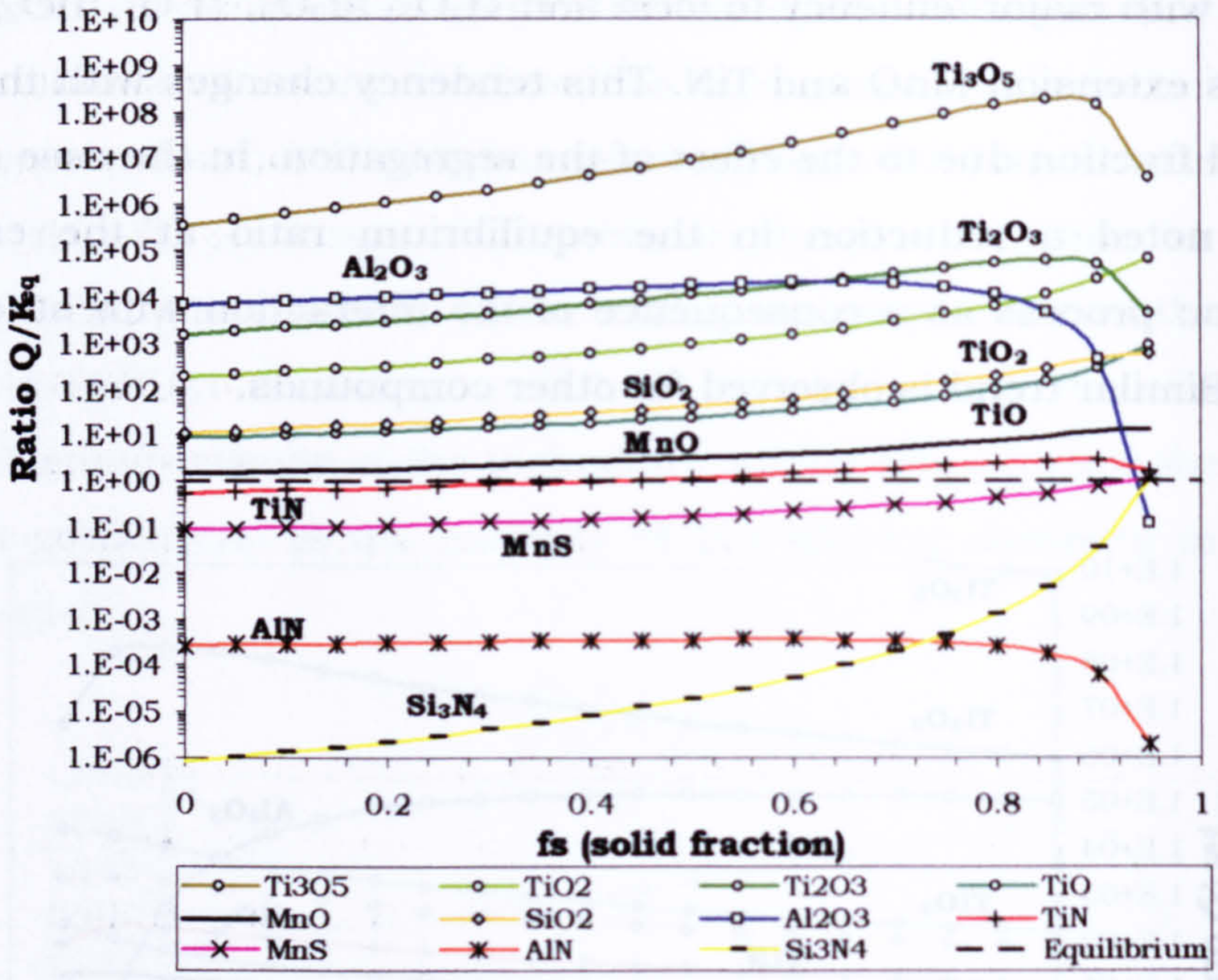

Figure 7.40 Effect of the solidification process on the equilibrium ratio Q/K_{eq} for the CWX201 weld metal. This weld metal is contained in the figures 7.32(a), 7.33(b) and 7.34(b). The horizontal discontinuous line represent equilibrium, where $Q/K_{eq}=1$.

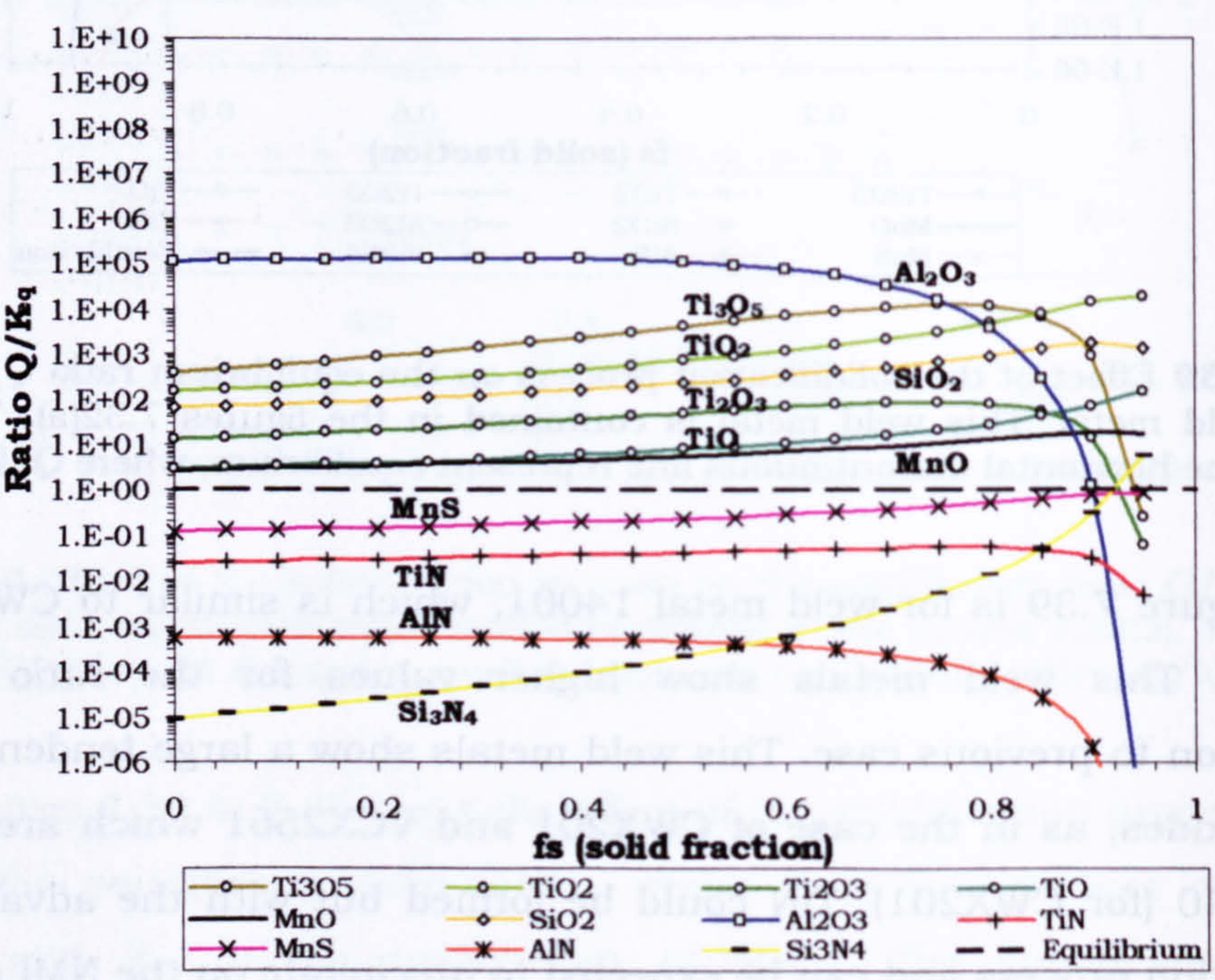

Figure 7.41 Effect of the solidification process on the equilibrium ratio Q/K_{eq} for the CWX71 weld metal. This weld metal is contained in the figures 7.32(b), 7.33(c) and 7.34(c). The horizontal discontinuous line represent equilibrium, where $Q/K_{eq}=1$.

As a summary, the thermodynamical calculation for the formation of NMI can predict the type of inclusion that can be formed in the weld metal. However, due to the similarities in composition between the studied weld

metals no significant differences were found. Refinement of the calculation taken into account the decrease in composition caused by simultaneous NMI formation can be useful as the determination of the formation sequence. The weld metals can be broadly classified as containing Ti-rich inclusions (CWX181, CWX351, 14001, 15171, VCX2561, CWX361 and CWX201) and Al-rich inclusions (140131, CWX71, CWX91, CWX81 and CWX331). Further work is necessary identify the types of inclusions and to clarify their role in the properties of the weld metals and their resistance to hydrogen induced cracking.

7.9 Summary of the chapter: Weld metals microstructure.

In this chapter, a metallographic characterisation was carried out in some detail. Firstly, the weld metal microstructures were studied to establish a relation with composition. All the microstructures were classified as shown in tables 7.1 and 7.2, and schematised in figure 7.11. To support the analysis TTT and CCT diagrams were calculated. The weld metals classification permitted the organisation of the weld metal into groups, and ordered by their P_{cm} value. This order is respected throughout this book to facilitate discussion. Secondly, and due to the interest in study the trapping capacity of each weld metal, more detailed characterisation was carried out. This includes the study of the micro-phases in weld metals: MAC constituent, NMI and other features that could act as hydrogen sinks. The presence of retained austenite is particularly important due to its high hydrogen solubility and binding energy. Due to difficulties encounter to identify retained austenite in thin foils using TEM, a theoretical approach was used to estimate the probable retention of this constituent in the MAC particles. Throughout empirical and thermodynamical calculation, considering chemical (carbon and alloy content) and size stabilisation, was possible to identify the weld metal samples with chance to retain austenite partially or totally. They are the following well metals: CWX351, 15171, VCX2561, CWX91 (if size effect is considered) and CWX81. Depending on the weld metal composition and MAC proportion, the austenite particle size that reduces Ms below room temperature is in the submicrons range (particles smaller than 0.1 μm in diameter can be retained). Using high resolution SEM the MAC constituent was characterised in a general way: their morphology and location in the microstructure was elucidated as schematised in figure 7.21.

Thirdly, a detailed characterisation of NMI number density, size and spatial distribution was carried out. However, it was not possible to fully characterise the inclusion composition and type and some thermodynamical calculations were used to overcome this limitation. With respect to the NMI density, size and distribution some differences were established between weld metals. This permitted the classification of the weld metals following the criteria presented in table 7.4: random and clustered distribution; large, medium and small maximum sizes; and high, medium and low NMI number (defined in annexe A.15). This characterisation is taken in consideration in the chapter 9, where the trapping capacity of the weld metals is studied. The NMI stability diagrams permitted a general differentiation of the weld metals depending of the extension of the stability of determined NMI types: aluminium oxide, titanium oxides, silicon oxide, manganese oxide and sulphide and, finally, some nitrides. These calculations are complemented with some estimation following Scheil approach.

Finally, in this chapter are established some important microstructural issues that can contribute to understand the behaviour of the weld metal when affected by hydrogen charging, in an attempt to find relationships between microstructure and resistance to hydrogen induced cold cracking of the different weld metals.

CHAPTER EIGHT

RESULTS AND DISCUSSIONS
PART II

THE EFFECT OF HYDROGEN ON THE MECHANICAL PROPERTIES AND FRACTURE BEHAVIOUR OF HSLA STEEL WELD METALS

In chapter seven the relations between weld metal composition and microstructure were described for various selected HSLA steel weld metals studied in this investigation. This chapter deals with the effect of hydrogen content on the mechanical properties and the fracture behaviour of these weld metals.

The effect of hydrogen content on the fracture micromechanisms of the weld metals and the possible role of the different phases and micro constituents were investigated. Special attention was dedicated to the factors that contribute to:

1- Crack initiation (on non metallic inclusions, cavities, voids, MAC constituents, precipitates, interfaces, etc.)
2- The changes in micromechanisms of fracture due to stress intensity factor and/or hydrogen content and weld metal strength
3- The changes in the propagation of cracks (hydrogen level, different phases, grain boundaries, NMI and different precipitates).

The results on the effect of hydrogen on mechanical properties were obtained by Wildash [8-11] in a previous thesis and are revised and analysed to be fully understood: firstly, the intrinsic mechanical properties of the weld metals; and secondly, the effect of the hydrogen content on the strength and ductility. A brief summary is given in the next section of this chapter on the mechanical properties, more detailed information could be found elsewhere [8]. With respect to the effect of hydrogen on the weld metal properties, some results are shown here in a clearer manner, avoiding the oversimplification found in Wildash [8]. The intention of this analysis is to correlate microstructure, properties and hydrogen induced cold cracking of the different weld metals.

Based on fractographic analyses a phenomenological model is proposed which describe and relate the occurrence of different micromechanisms of fracture with microstructure, mechanical properties and hydrogen heterogeneous distribution in the weld metal.

8.1 The as-welded tensile properties of the HSLA steel weld metals

The diversity of microstructures and the variation of particular alloying elements in the studied weld metals have produced a wide range of mechanical properties: yield strengths (S_y) between 400 and 900 MPa, tensile strengths (S_m) between 600 and 1100 MPa and fracture stresses between 900 and 1500 MPa, in the as-welded condition. These levels of strength are commonly reached in structural steels throughout quenching and tempering or other heat treatment such as ageing.

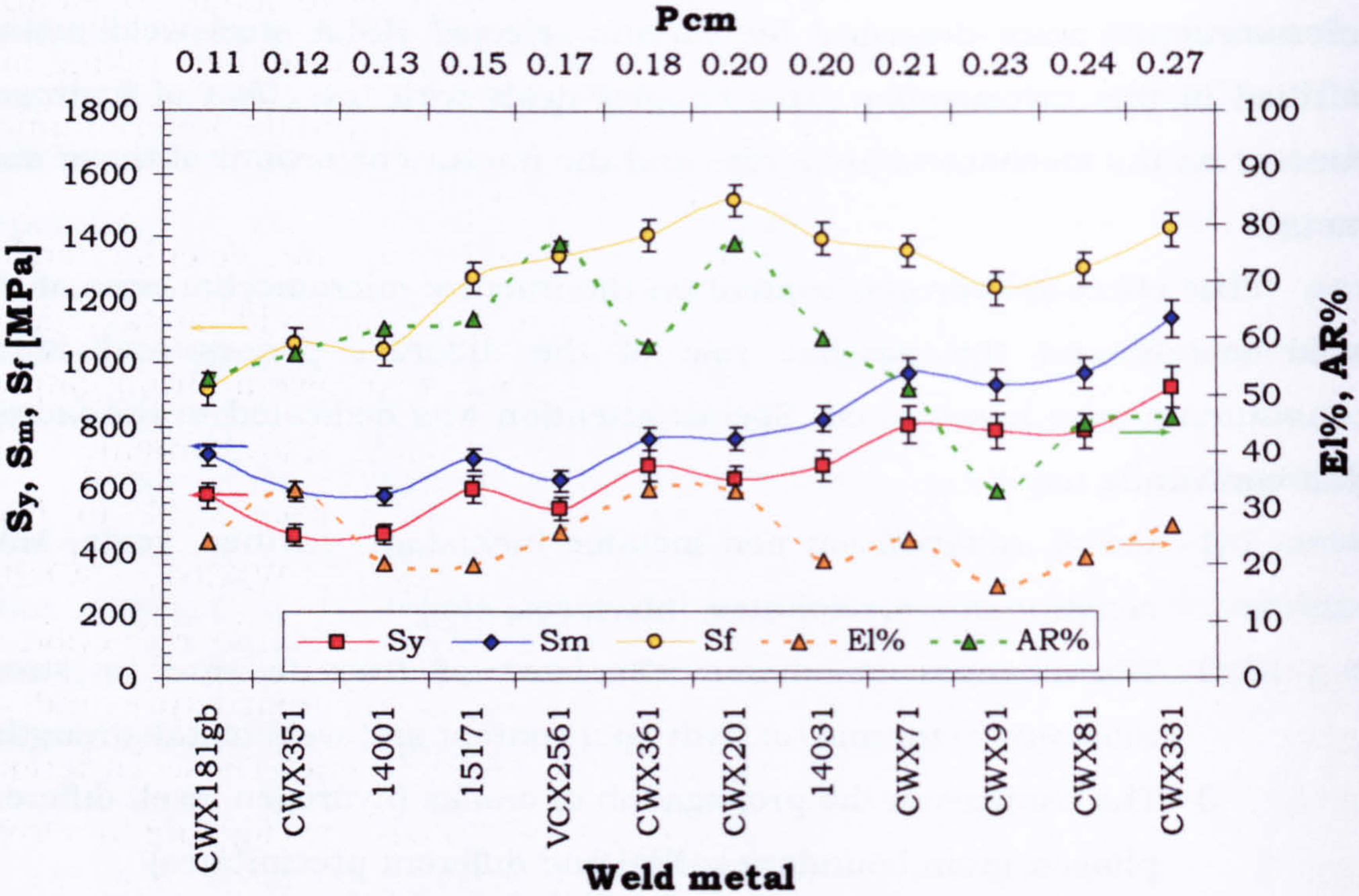

Figure 8.1 Tensile mechanical properties of the HSLA steel weld metals, which were studied in this investigation. The strength and ductility of the weld metals are presented as a function of the P_{cm} value. Based on data obtained by Wildash[8-11]

Figure 8.1 presents the tensile properties of the selected weld metals, as a function of their P_{cm} value. The values of S_y, S_m, and S_f are shown together with the values of ductility, which were determined by the elongation (El%) and the area reduction (AR%). Although, the original information utilised to construct this figure does not include scatter of values, it is possible to estimate the potential variability of them. It is known that for materials property data, such as yield strength, hardness, and fracture toughness, coefficients of variation ($\delta_x = S_x / \bar{x}$, where S_x and $\bar{x}$ are the standard deviation and sample mean, respectively) are generally in the range 0.05 to 0.20, that is, 5% to 20% [150]. Typical values of δ_x for S_y and S_m of metals are 7 and 5%, respectively. In the case of the tensile strength of welds δ_x= 10%, and for this

reason δ_x for S_f should be around 10-15%. These coefficients of variation are included in figure 8.1 to give an idea of the potential variation around the measured value. These Y-error bars have to be taken as illustrative of the potential variation of the weld metal property due to unknown scatter in the original data.

Figure 8.1 shows that S_y, S_m and S_f values increases with P_{cm} value, but this increase shows some irregularities. These irregularities could be associated with the variations of different alloying elements in each weld metal. As mentioned in chapter seven, no attempts were made to identify clearly the influence of compositional variables on microstructure, taking one element at a time. As a consequence, complexity is added to the determination of the relationship between composition and properties.

Changes in the proportion of grain boundary ferrite, acicular ferrite, bainite, martensite and the micro-constituents of the weld metals (MAC islands, retained austenite, NMI and other precipitates) have a strong impact on the mechanical properties, which in turn depend on its alloy content:

1- For weld metals in the range of P_{cm} values from 0.11 to 0.20 (CWX181gb, CWX351, 14001, 15171, VCX2561, CWX361, CWX201 and 14031), the mayor microstructural variation is the reduction in grain boundary ferrite, the refinement of the microstructure and an increase in the proportion of the MAC constituent. These variations could increase strength, but compositional differences impede this to be monotonically.

2- For weld metals with P_{cm} values in the range 0.20-0.24, such as CWX71, CWX81 and CWX91, the yield and maximum strengths are maintained similar. As presented in figure 7.6 there are no significant differences in the microstructures, all of which are characterised by a very fine ferritic constituent (degenerated acicular ferrite or ferrite with non aligned second phase) and some isolated bainite islands. However, in table 6.2 can be observed slightly differences in C, Mn, Mo, Ni, V, Ti and N, which could explain discrepancies.

3- Weld metal CWX331 (P_{cm} equal to 0.27) gave the highest yield and maximum stress values. The microstructure of this weld metal is a mixture of martensite and bainite, as can be observed in figures 7.5 and 7.7, producing a high strength. This type of microstructure is some times avoided in the welding of high strength low alloy steels because their brittle behaviour in the presence of hydrogen. However,

martensite presence is needed to produce high strength welds when C is low.

8.2 The effect of hydrogen content on the strength and ductility of the weld metals and the critical hydrogen content for embrittlement

Figures 8.2 and 8.3 present the fracture surface for three different weld metals: CWX181gb, CWX201 and CWX331 in the as welded and degassed condition. The fracture of these welds occurs by the coalescence of microvoids: the MVC mechanism. This kind of ductile fracture is present in all the weld metals prior to hydrogen charging, even though differences in microstructure and strength between the weld metals exist.

An association between the microvoids and the NMI can be observed. The number, shape and size of the dimples depend on [151]: the number, size and spatial distribution of the NMI and other precipitates which contribute to the formation of cavities and the ductility of the material. As can be observed on the fracture surfaces of the three weld metals, each dimple could be associated with particles and NMI of different nature.

Figure 8.4 shows, as an example, the relation between true fracture stress (S_f) and the NMI number density (N_v). As can be noted, the maximum fracture stress is presented by the CWX201 weld metal which contains coarse acicular ferrite and the lowest NMI density. This and other examples indicate that the strength and ductility of weld metals strongly depend on their NMI characteristics and this is important to keep in mind through the discussion in this chapter.

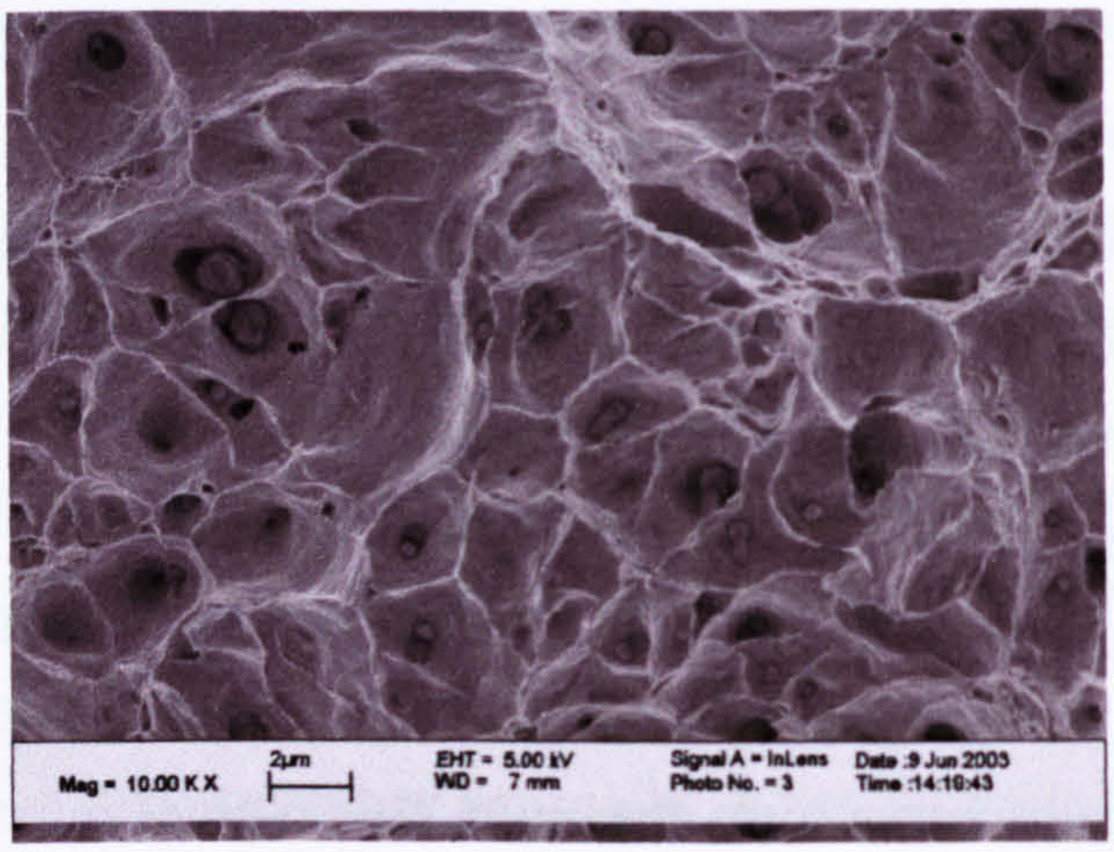

Figure 8.2 Fracture surface of CWX181gb weld metal presenting MVC fracture. The presence of grain boundary ferrite could be the reason of the appearance of the smooth flat regions on the surface.

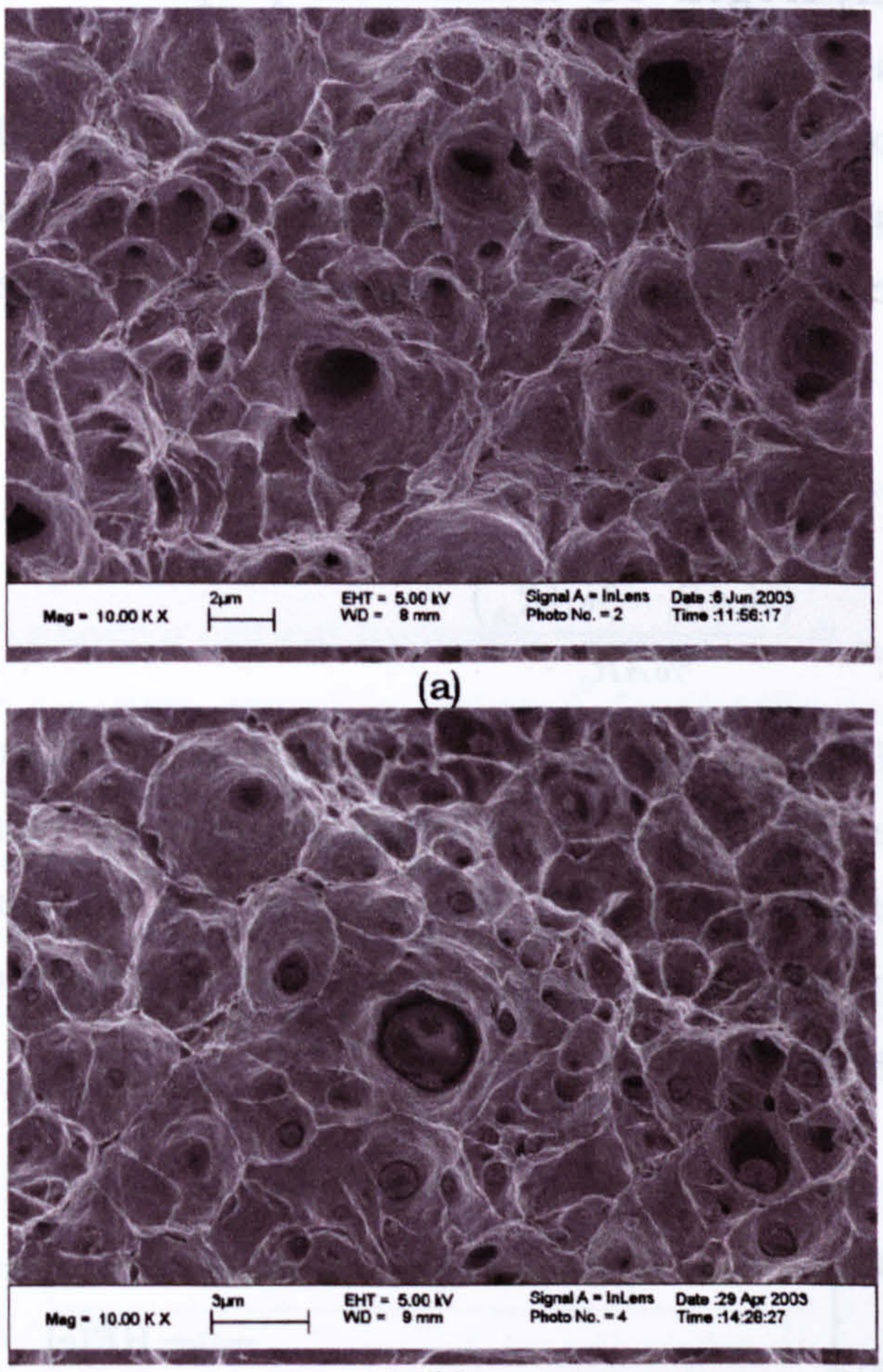

Figure 8.3 Fracture surfaces of two weld metals presenting MVC fracture: (a) CWX201 and (b) CWX331. These weld metals do not present PF(G), and the smooth flat regions are absent (compare with 8.2).

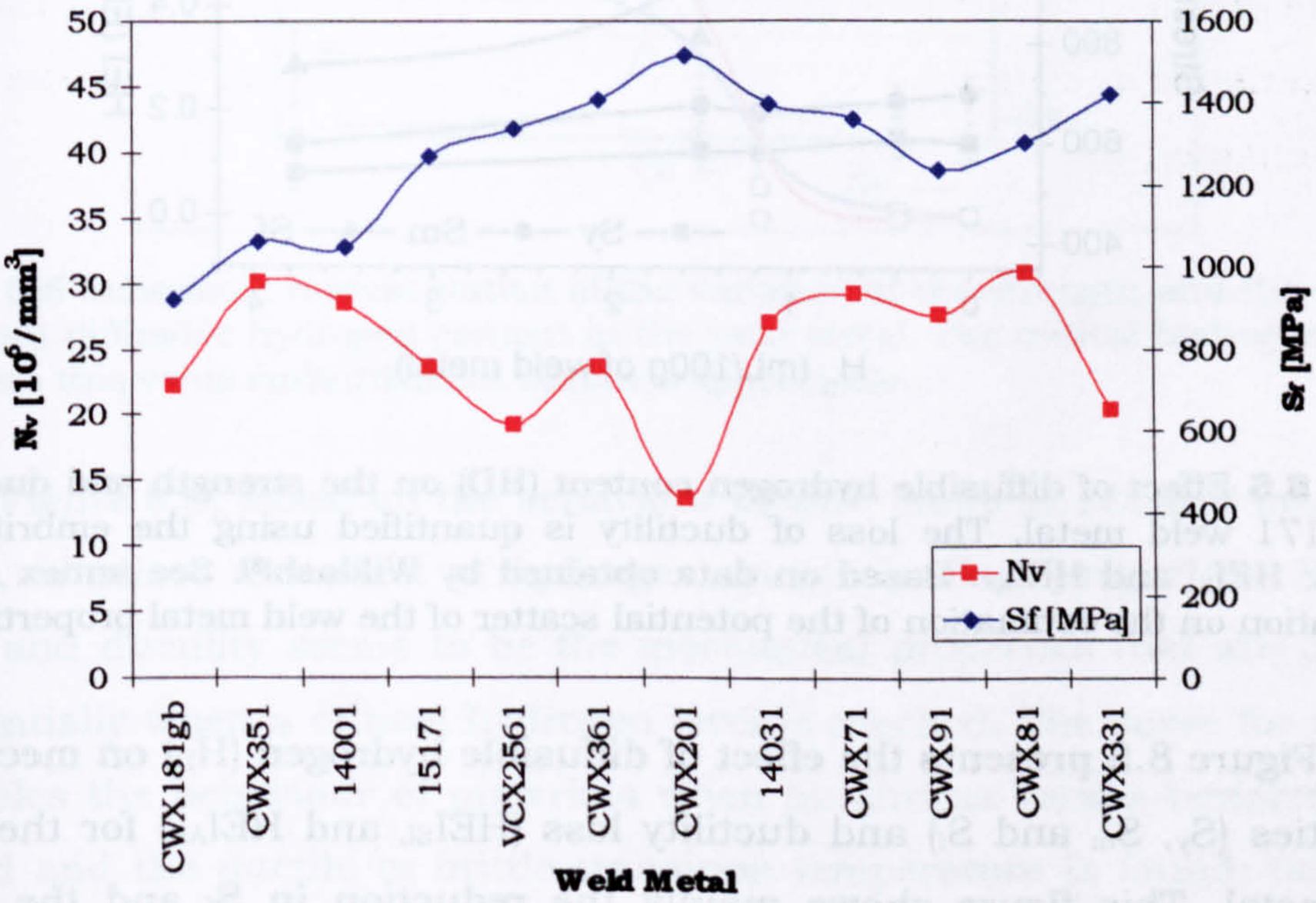

Figure 8.4 Variation of the fracture stress and the three-dimensional density (Nv) of NMI for the studied weld metals. Based on data obtained by Wildash[8] and the NMI characterisation in this investigation.

8.2.1 Effect of hydrogen on mechanical properties and the hydrogen embrittlement indexes (HEI).

The effect of hydrogen on weld metals is to reduce ductility and assist cracking. The magnitude of hydrogen embrittlement is characterised through the utilisation of certain indexes. Equations 8.1 and 8.2 are examples of such equations:

$$HEI_{EL} = \frac{(\%El_0 - \%El_{ch})}{\%El_0} \qquad (8.1)$$

$$HEI_{AR} = \frac{(\%AR_0 - \%AR_{ch})}{\%AR_0} \qquad (8.2)$$

where HEI_{el} and HEI_{AR} are the hydrogen embrittlement indexes obtained by the calculation of the changes with hydrogen content of: elongation (%El) and transversal area reduction (%AR) percentages. The subscripts "0" and "ch" indicate that the property was measure without hydrogen charging and after hydrogen charging, respectively.

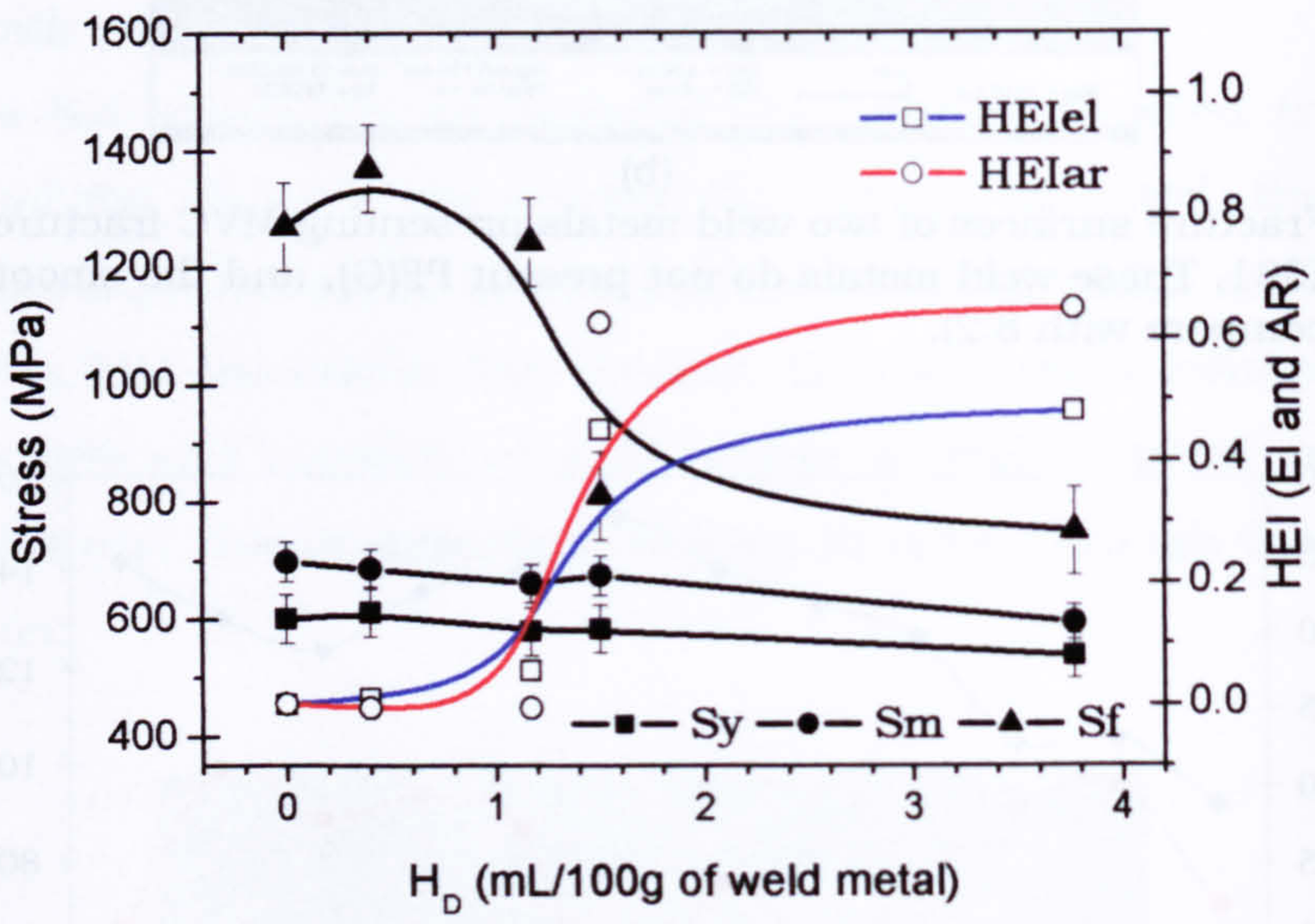

Figure 8.5 Effect of diffusible hydrogen content (HD) on the strength and ductility of the 15171 weld metal. The loss of ductility is quantified using the embrittlement indexes: HEI_{El} and HEI_{AR}. Based on data obtained by Wildash[8]. See annex A.18 for information on the estimation of the potential scatter of the weld metal properties.

Figure 8.5 presents the effect of diffusible hydrogen (H_D) on mechanical properties (S_y, S_m and S_f) and ductility loss (HEI_{EL} and HEI_{AR}) for the 15171 weld metal. This figure shows mainly the reduction in S_f and the loss of ductility with the increase in H_D. This example illustrates the concept of the critical hydrogen content for embrittlement, C_k. As discussed in chapter 4, this

critical concentration depends on: microstructure, applied stress, temperature and the hydrogen distribution due to trapping. For the weld metal 15171 this critical hydrogen content seems to be around 1.2 ml/100 g. Below this value the weld metal does not present a reduction in ductility or the true fracture stress, S_f. Above this critical hydrogen level the ductility is reduced almost 60%.

From figure 8.5 three observations must be highlighted:

1- The loss of ductility (as measured by equations 8.1 and 8.2) is observed above a critical hydrogen value, C_K.

2- The true fracture stress is reduced drastically to levels close to S_y and S_m or lower (in other cases discussed later), when the hydrogen content exceeds the C_K value.

3- An increase in the H_D content does not seem to affect drastically the yield and maximum stress of the weld metal 15711, even at high hydrogen levels.

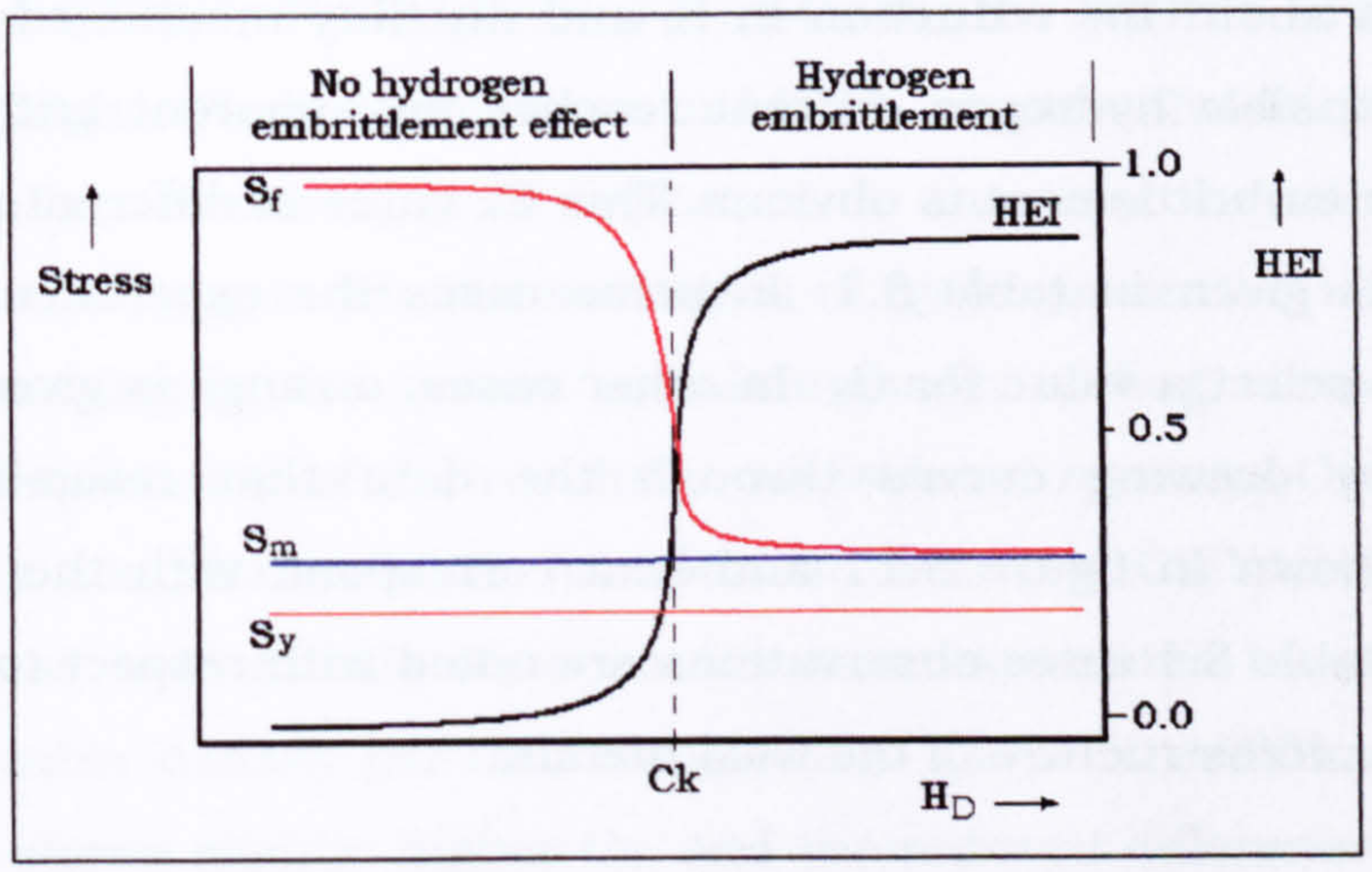

Figure 8.6 Schematic representation of the variation of the strength and the ductility (HEI) with diffusible hydrogen content in the weld metal. The critical hydrogen level is C_K. Above this value embrittlement becomes appreciable.

Figure 8.6, based on the behaviour of weld metal 15171 and other weld metals, idealises the effect of hydrogen on mechanical properties. Fracture stress and ductility seems to be the mechanical properties that are changed substantially when a critical hydrogen level is reached. The curve for the HEI resembles the behaviour of materials when toughness versus temperature is studied and the ductile to brittle transition temperature is found: below the ductile to brittle transition temperature the steel is brittle and above C_K the material becomes brittle. Unfortunately, the idealised behaviour was only observed clearly in the case of the 15171-weld metal and in some degree in

cases such as CWX351, 14001, CWX201, 14031 and CWX81. The rest of the weld metals presented the general response to hydrogen content without following the behaviour shown in figure 8.5: reduction in S_f and ductility with hydrogen content. However, it could be extracted from the different curves that there exists a critical hydrogen level over which embrittlement is appreciated clearly. Figures from A.15 to A.18, in annexe A.19, show details of the effect of diffusible hydrogen on the strength and ductility of all the weld metals studied in this investigation. From these figures, as discussed below, the C_k is estimated as the diffusible hydrogen content that produces a HEI_{AR} of 0.5, i. e., a 50% of loss in ductility. Due to the absence of statistical information in the original data [8], the potential scatter in the measured properties of the weld metals was estimated following the suggestions in annex A.18. These estimations are considered in the discussion that follows.

8.2.2 The hydrogen critical level for embrittlement (C_K)

Figures in annex A.19, apart from being consistent with general observations about the reduction in S_f and ductility mentioned before, show that the diffusible hydrogen content reaches an apparent critical level (C_K) above which embrittlement is obvious. This C_K value is different for each weld metal and is given in table 8.1. In some cases the experimental data was sufficient to select a value for C_K. In other cases, a range is given, which was estimated by drawing curves through the data that resemble the ideal behaviour shown in figure 8.11 and best correspond with the experimental data. From table 8.1 three observations are noted with respect to the possible effect of the microstructure of the weld metals:

Table 8.1 Apparent critical hydrogen content for different weld metals, which produces 50% of ductility loss

Weld metal	C_K [mL/100g]	C_K interval [mL/100g]
CWX181gb	2.6	*
CWX351	5.4	*
14001	3.2	2.6-3.6
15171	1.5	*
VCX2561	1.6	*
CWX361	4.0	3.6-5.0
CWX201	2.0	*
14031	1.0	0.7-1.2
CWX71	1.8	1.6-2.4
CWX91	1.0	0.6-1.2
CWX81	3.0	2.6-3.4
CWX331	1.2	0.8-2.0

1- The C_K values for the weld metals with grain boundary ferrite are apparently higher than the values for the weld metals without this constituent. Weld metal CWX351, which contains grain boundary ferrite and Widmanstätten ferrite, exhibits the highest C_K level. Weld metals with less or without grain boundary ferrite show lower C_K levels.

2- In combination with the microstructure characteristic, the presence of NMI seems to favour the hydrogen tolerance of the weld metal, i.e., increase the C_K level. This can be illustrated using two comparisons. The first example is presented by the pair 14001 and 15171. Both weld metals have similar microstructure (see table 7.2) and similar MAC content (see figure 7.19). It can be observed from figure 7.27 and table 7.4 that the main difference between weld metals is their NMI characteristics: 14001 has higher Nv (number density of NMI) than 15171. This could be the reason for the higher C_K level for 14001. The other example involves weld metals: 14031 and CWX71. The higher value of C_K for the CWX71 could be due to its higher Nv in comparison to 14031, because the microstructure is similar. However, it is important to mention that several factors contributing to the redistribution of hydrogen in the weld metal are operating in the system simultaneously, adding complexity to the interpretation of the results in an isolated manner. One example of this complexity is the comparison between CWX181 and 14001. These weld metals show similar microstructures but different NMI number density per unit volume (N_v). The weld 14001 with a higher N_v shows slightly higher C_K, and the reduced difference in C_k values could be due to differences in the proportion of MAC (higher proportion in CWX181), as discussed below. This suggests that there exists a combination of factors that contribute simultaneously to the susceptibility to hydrogen cracking, as represented by C_K. Other examples are discussed in chapter 9.

3- The high proportion of MAC in the CWX361 seems to be responsible for the elevated C_K value if compared with the VCX2561, which has a similar microstructure, only slightly higher N_v and lower MAC content. This is probably indicative of the beneficial effect of MAC presence in the microstructure. The case for the CWX201 seems to corroborate this behaviour. This weld metal content coarse acicular

ferrite, the lowest NMI density and approximately 13.75 % of MAC (lower than CWX361). The value of C_K for the CWX201 is half the value of the critical hydrogen content for the CWX361. However, as explained before several other factors influence the value of C_K. In chapter 9 this is discussed in detail.

These observations apparently indicate that the tolerance of the weld metal to hydrogen is influenced by: the grain boundary ferrite content, the MAC proportion and the NMI density. However, there is no general rule for the variation of C_K for different welds. It is clear that a combination of several factors interacting simultaneously provide the resistance to hydrogen embrittlement. These factors could be:

a- The microstructure constitution (phase proportion and distribution of PF(G), AF, FS(B), FS(A), FS(NA), etc.)

b- The microphases content and distribution (MAC, retained austenite, carbides)

c- The NMI density, size and spatial distribution.

The influence of these factors on the weld metal resistance to hydrogen induced cold cracking is discussed in the next chapter in more detail and from the point of view of the hydrogen trapping behaviour.

It is important to stress that the values determined for C_K have to be reached with caution as they represent the total hydrogen content measured in the weld metal. They do not take in account the heterogeneous distribution of hydrogen in the weld due to different features: voids, cavities, residual stresses, traps of different capacities (different binding energies and size), microcracks, non metallic inclusions and retained phases (retained austenite, MAC, etc.). All these microstructural features could induce local accumulations of hydrogen and the impairment of the weld metal mechanical behaviour in those regions.

8.2.3 The effect of H_D on S_y and S_m of the weld metals.

Diffusible hydrogen content affects the values of S_y and S_m. This effect depends on the microstructure and strength of the weld metals. In annex A.19 are shown the results for each selected weld metal. As can be observed, for weld metals below S_y values of 650 MPa, such as CWX181, CWX351, 15171, VCX2561, CWX361, CWX201 and 14031, the changes in S_y and S_m due to the

increase in H_D content are not dramatic at low and medium hydrogen levels. The exception was weld metal 14001 which shows changes in these stresses. However, at high hydrogen levels weld metals CWX181; CWX201 and 14031 show marked variations. On the other hand, weld metals with S_y values above 650 MPa suffered considerable variations of these two stresses (CWX71, CWX81, CWX91 and CWX331) in the range of hydrogen levels which were produced by electrolytic charging.

Various investigators [61, 152-154] have shown that the effect of hydrogen on yield stress (S_y) is not unambiguous. It has been found a softening and a hardening effect. A reduction in S_y due to an increase in hydrogen content could mean that hydrogen promotes or assists the movement of dislocations. If the contrary occurs, hydrogen reduces the movement of dislocation and a strengthening effect could be observed. On the other hand, reports on the effect of hydrogen on the maximum tensile stress (S_m) seem to be scarce.

S_m is the stress at which the material suffers a localized and intense deformation in its weakest region. This results in the formation of the neck in a sample during a tensile test. Plastic deformation occurs before the S_m stress is reached and the material experiences strain hardening. A simple way to quantify the strain hardening capacity is throughout the S_y/S_m ratio [117]. Hydrogen affects this ratio. Figures 8.7 and 8.8 present the variation of the S_y/S_m ratio with the increase of diffusible hydrogen content. To interpret this result, the following approach is used: weld metals with low S_y/S_m ratio have a large capacity to strain harden before fracture and the contrary is true to weld metals with high S_y/S_m ratio. If for a determined weld metal this ratio increases with the hydrogen content, its strain hardening capacity is reduced, which means that deformation before fracture is decreased. This reduction could be the consequence of the following effects:

1- Hydrogen increases dislocation mobility and the weld metal does not strain harden considerably and S_y and S_m become closer in value. The increase in dislocation mobility must produce a reduction in strength or softening of the steel. In reviews by Hirth [66, 152] is reported that in pure iron the role of hydrogen is to increase the mobility of screw dislocations by the promotion of the formation of double kink nucleation and slip planarity.

2- Hydrogen interacts with dislocations and impedes their movement. Due to this impediment the weld metals do not deform easily and

fracture is promoted. This must result in an increase in yield stress or hardening. Hirth [66] suggest that when deformation occurs by cross slip, hydrogen charging could make difficult the deformation process due to the preferential softening of {110} slip planes, the increase in dislocation density and the changes in their arrangements. Hydrogen in dislocation cores could make dislocation intersection more difficult as well.

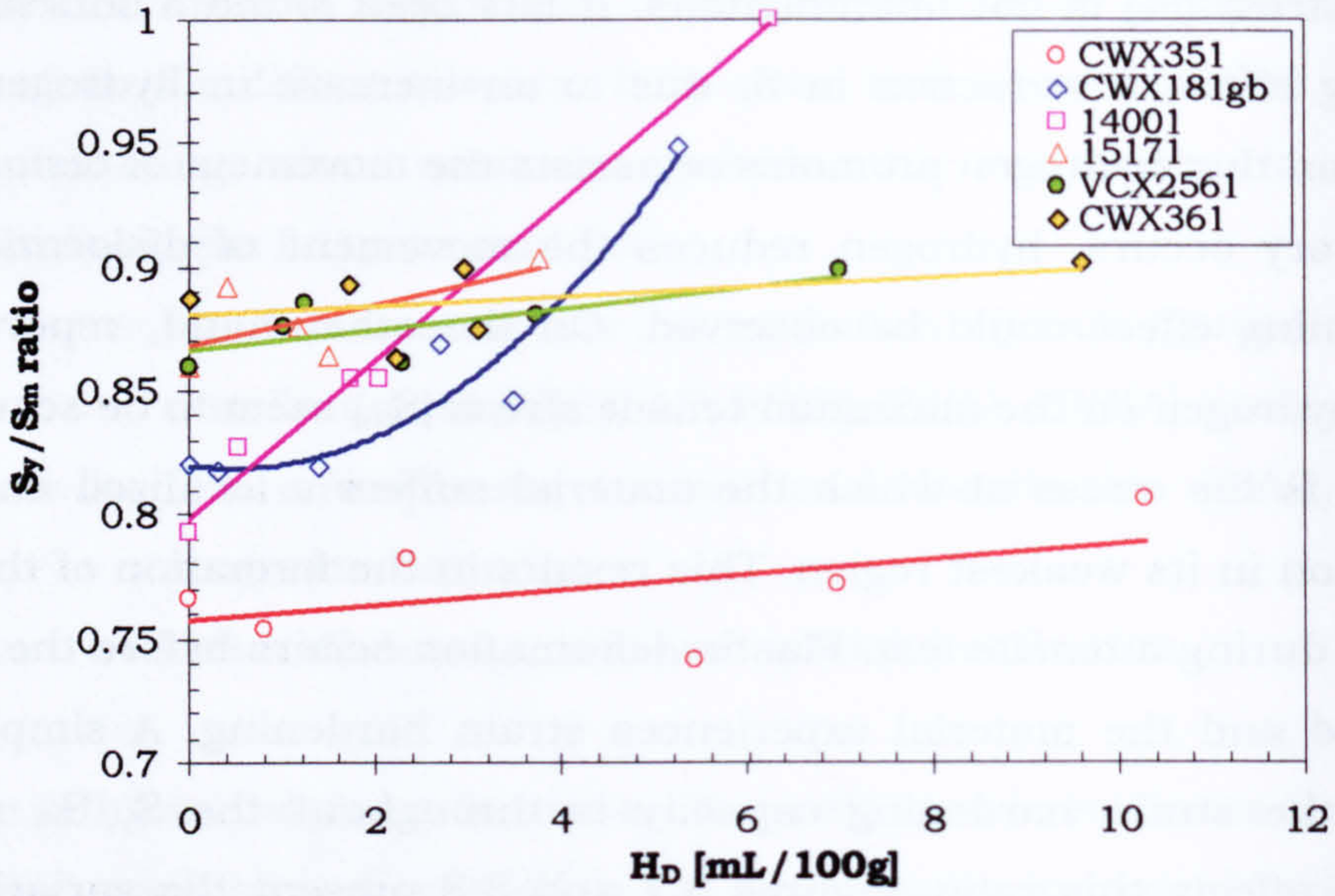

Figure 8.7 Effect of diffusible hydrogen (H_D) on the S_y/S_m ratio for weld metals with Pcm values below 0.20: CWX181, CWX351, 14001, 15171, VCX2561 and CWX361. Based on data obtained by Wildash[8]

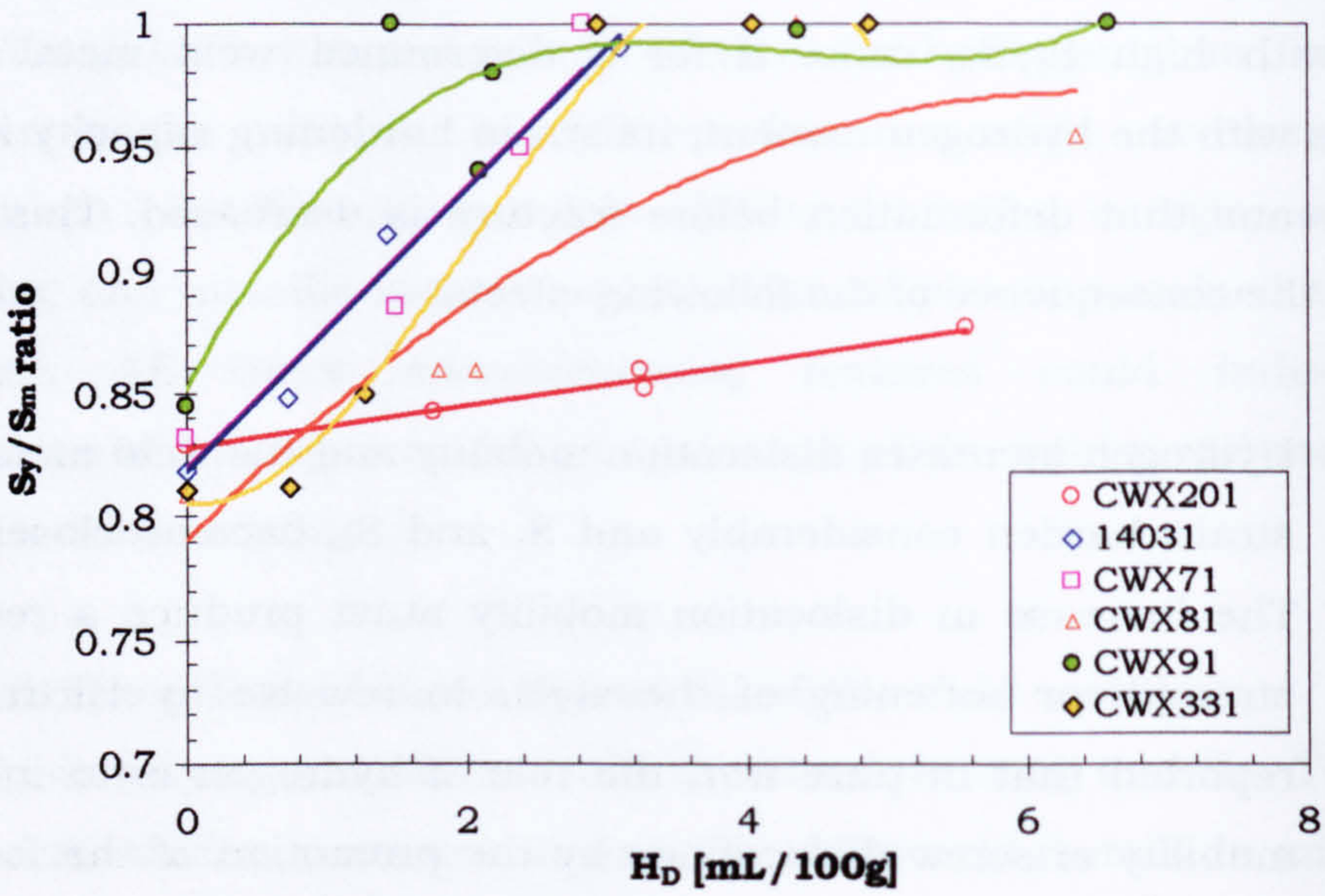

Figure 8.8 Effect of diffusible hydrogen (H_D) on the S_y/S_m ratio for weld metals with Pcm values above 0.20: CWX201, 14031, CWX71, CWX91, CWX81 and CWX331. Based on data obtained by Wildash[8]

3- Hydrogen contributes to the multiplication of dislocations and as a result the material strain hardens quickly. Consequently, the movement of dislocation is made difficult rapidly, the weld metals lose their capacity to deform and fracture occurs easily at lower stresses. S_y/S_m ratio is increased. The formation of microcracks, which act as stress risers, could increase locally the dislocation density and the multiplication occurs at lower global stresses.

The behaviour described above is affected by the microstructure of the weld metal and the dislocation density associated with the various ferrite phases that can form during solid state transformation. At high temperatures, products such as grain boundary ferrite and ferrite side plates are expected to have low dislocation density. As the transformation temperature is decreased, the dislocation density is increased. Martensite, which forms at much lower temperatures than the other ferrite phases, has the highest dislocation density of all. The dislocation density of these phases and their interaction with hydrogen causes the impairment of the mechanical properties and induces fracture.

In figures 8.6 and 8.7, it can be observed that the H_D content generally increases the S_y/S_m ratio. The variation is pronounced for some of the weld metal, whilst for others the ratio is only slightly augmented and could be related to the strength level and/or the microstructure of the different weld metals:

1- *Weld metal whose S_y/S_m ratios are affected markedly by hydrogen content.* These weld metals are 14001 and CWX181 given in figure 8.7; 14031, CWX71, CWX81, CWX91 and CWX331 in figure 8.8. The first two weld metals contains around 15% of PF(G), around 80% of AF and between 2 to 3% of FS(A). The rest of the weld contain fine AF, FS(B) and M, CWX331 containing a mixture of FS(B) and M. High dislocation density is expected for the last group of weld metals and it may explain the lower capacity to deform due to the interaction of dislocations and hydrogen. On contrast, weld metals 14001 and CWX181, which contain high transformation temperature products, should tolerate more deformation or strain hardening due to their expected lower dislocation density. No clear

explanation has been found for this behaviour but it could be related somehow to the coarseness of the microstructure.

2- *Weld metals whose S_y/S_m ratios are affected slightly by hydrogen content.* These weld metals are: CWX351, 15171, VCX2561 and CWX361, given in figure 8.7 and CWX201, in figure 8.8. These weld metals do not lose their strain hardening capacity as the previous group with the increase in hydrogen content. Excepting CWX351, these weld metals contain low proportions of grain boundary ferrite (PF(G)) and the rest of the microstructure is acicular ferrite (AF). Their S_y/S_m value without charging is between 0.83 and 0.89 and as is noted this values do not change markedly with hydrogen. Such increase could be related to the hydrogen interaction with the expected medium dislocation density. However, CWX351 weld metal, which contents the highest proportion of grain boundary ferrite (35%) and possesses the lowest S_y/S_m ratio without charging (about 0.76), seems to withstand the hydrogen effect due to the expected lower dislocation density at grain boundary ferrite.

From the results presented, it can be suggested that there exists a competition between hydrogen softening and hardening effect. For example, it is observed clearly that, S_y and S_m for the case of the 14001 weld which is presented in figure A.14 (c), increase slightly at low hydrogen levels and then decrease for higher H_D contents, illustrating the occurrence of hardening and softening effect of hydrogen. This effect is observed to a lesser degree in other welds. This behaviour could indicate that depending on microstructure and strength level, certain critical hydrogen contents are needed to produce hardening or softening to the weld metals, as summarised:

1- At low hydrogen levels a softening effect could be observed in microstructures with expected low dislocation densities due to the increase in dislocation mobility and multiplication.

2- At low hydrogen levels a hardening effect could be observed in microstructures with expected high dislocation levels and high number of precipitates, which could promote multiple or cross slip motion of dislocations.

3- At high hydrogen levels, quantity that depends on microstructure, the "softening" effect could be associated with damage of the material. This damage involves the formation of microcracks and voids in those susceptible regions where a high hydrogen content and stress are combined to initiate fracture or voids. The internal stress concentration at the microcracks and voids enhances local plastic flow, which could produce global deformation at lower stresses implying reduction in S_y.

8.2.4 Variation of S_f with diffusible hydrogen content.

As has been mentioned before, the increase of H_D content mainly reduces the true fracture stress of the weld metals. A marked effect of hydrogen on S_f is observed in comparison to its influence on S_y and S_m. Three different types of behaviour can be distinguished in figures from A.15 to A.18 in annexe A.19.

Firstly, for the cases of weld metals with continuous network of grain boundary ferrite, such as CWX181, CWX351, 14001 and 15171, at low H_D levels S_f appears to increase slightly until a maximum is reached and then further reduction occurs gradually. The variation in transversal area reduction with H_D supports this trend: at low H_D the index HIEar (equation 8.2) becomes slightly negative and then positive when hydrogen increases. This behaviour is not noted for the rest of the weld metals. It has been reported [8] that the grain boundary ferrite is detrimental to low temperature toughness: it is a preferential and easy path for crack propagation. However, it seems to increase the C_K level for cracking, as was discussed above and additionally, to increase the hydrogen cracking resistance at low hydrogen levels in the weld metal. The role of grain boundary ferrite could be explained as follow:

a- The transformation of austenite to grain boundary ferrite occurs at high temperatures and for this reason it is expected that its dislocation density were lower than the other products which transform at lower temperatures. This makes PF(G) a softer microstructure and a relatively free path for hydrogen diffusion. The easy hydrogen diffusion throughout the continuous network of grain boundary ferrite could permit the redistribution of hydrogen in the weld metal and its escape to the atmosphere. This is discussed in the next chapter in more detail.

b- The PF(G) deforms before the rest of the microstructural constituents until work hardening permits transfer of strain to the remaining harder phases. At low hydrogen levels hydrogen may increase the dislocation mobility and inhibit work hardening increasing ductility.

c- It is possible to find NMI in the ferrite and a negligible quantity of other micro-constituents at which cracks could be initiated due to the effect of hydrogen accumulation. This should reduce the possibility of the crack initiation in PF(G). A more critical region is the interface between PF(G) and the rest of the interior of the columnar grain, where segregation is expected and acicular ferrite and MAC constituents can be found.

These observations suggest, firstly, that the presence of grain boundary ferrite could be beneficial at hydrogen levels below 2 ml/100 g of weld metal. Moreover, the slight reduction in PF(G) proportion, mostly as a result of a reduction of the width of the continuous network, could contribute to the reduction in the probability of initiating cleavage in this region of the weld metal maintaining toughness at acceptable levels in the presence of hydrogen and preserving the path for hydrogen to escape after welding.

Secondly, the effectiveness of grain boundary ferrite in maintaining toughness in the presence of hydrogen is reduced at high H_D levels and when the continuity of the PF(G) veins are lost in the weld metal microstructure. Examples are the weld metals VCX2561 and CWX361, whose behaviour is shown in figure A.16. Any discontinuity of the grain boundary ferrite network could reduce its capability to redistribute hydrogen. Moreover, the reduction in S_f begins at low H_D levels.

Finally, weld metals without grain boundary ferrite seem to tolerate less hydrogen content. S_f values for these weld metals decrease considerably at low hydrogen levels, as shown in figures from A.16(c) to and A.18 (annex A.19). This reduction in the true fracture stress of the weld metals could be associated to the formation of microcracks during charging or during the tensile test. The growth of microcracks is assisted by the stress concentration at crack tips and the hydrogen content. Cracks could form around inclusions, microvoids, MAC islands, carbides and other interfaces. In next section this is discussed in some detail.

8.3 Effect of hydrogen, microstructure and properties of weld metals on fracture micromechanism: MVC, QC and IG.

Hydrogen embrittlement of steels manifests itself in a variety of ways on the fracture surface, depending on the hydrogen content and the microstructure of the weld metal. The appearance of the fracture surface of hydrogen embrittled steels or weld metals could include the following micromechanisms, which were introduced in chapter 4:

1- Microvoids coalescence fracture features (MVC)
2- Quasicleavage fracture features (QC)
3- Intergranular fracture features (IG)

The occurrence of these fractographic characteristics could depend not only on the hydrogen content and microstructure but stress/strain levels. In the following sections this relationship is discussed. Firstly, crack initiation based on the fractographic analysis of the charged and tensile fractured weld metals is studied. Secondly, the changes on the fracture surface due to the increase in hydrogen content are analysed in some detail in an attempt to relate changes to microstructure of each weld metal type. A model that describes the relation between hydrogen content, stress concentration factor, microstructure and weld metal strength is proposed.

8.3.1 The initiation of the hydrogen induced cracks.

Numerous examples of brittle cracks initiation in steels can be found in the literature and both NMI and MAC islands appear to initiate them. These brittle cracks, and particularly quasicleavage (QC) fractures, have been associated with: NMI, microphases and hard coarse particles (carbides and nitrides). Echeverría and Rodriguez-Ibabe[94] reported that the fracture of coarse TiN particles were responsible for the cleavage initiation in a C-Mn-B steel with bainitic and martensitic microstructures. Lambert and collaborators [95] associated cleavage nucleation with cracked M-A islands. Several dislocation mechanisms have been proposed in the case of cleavage nucleation not associated to a brittle particle. In the case of C-Mn weld metals, Tweed and Knott[155] have reported non-metallic inclusions as cleavage crack initiators sites. The occurrence of these micromechanisms for cleavage fracture nucleation depends on the availability of the hard particles, their strength, their size and spatial distribution.

8.3.1.1 NMI as a quasicleavage initiator. Effect of size and spatial distribution on hydrogen trapping

Figure 8.9(a) shows a QC facet on the fracture surface of the CWX181 weld metal which was charged with 1.39 mL/100 g of hydrogen. In the centre of the QC facet is found a NMI of around 5 μm in diameter. The slip lines or striations that can be observed around the inclusion (figure 8.9(b)) suggest that the initiation of the crack is related to the inclusion and that the crack grew from the centre (NMI) to the surroundings. Moreover, the striations are evidence of the discontinuous growth of the crack assisted by hydrogen diffusion to the crack tip. Tong and Knott[156] have found such kind of evidence in low strength steel charged with hydrogen and tensile tested at different temperatures.

In general, the inclusions found in this investigation on the QC facets were of sizes above the average for each weld metal. The tessellated stresses, the microstructure and the accumulated hydrogen around the inclusion could be the factors that contribute to the crack initiation.

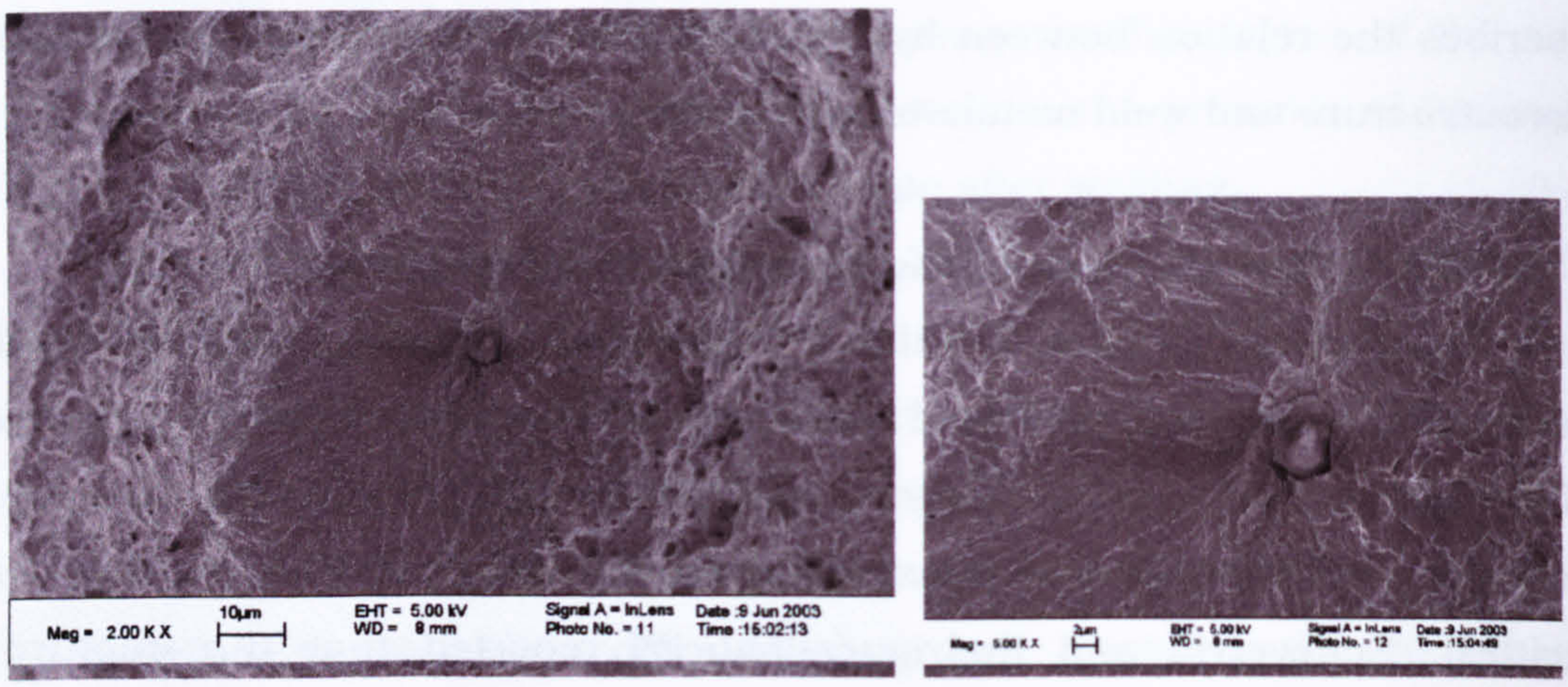

(a) (b)

Figure 8.9 Fish eye associated to a 5 μm inclusion in the CWX181 weld metal charged with 1.39 ml/100 g of hydrogen and fractured by tensile test. (a) NMI surrounded by QC fracture and (b) detail of the figure (a) where can be observed the slip lines on the QC surface. This slip lines or striations could be produced by the discontinuous growth of the crack.

Tessellated stresses around a NMI depend on the following factors: the inclusion shape, size and distribution, the nature of the inclusion (single, duplex or multiple compounds), the thermal expansion coefficients and elastic moduli of the inclusion and matrix [157-162]. The stresses around inclusions or precipitates arise as a consequence of the differential thermal contraction and are of the general form:

$$\sigma_{tessellated} = \pm\Phi[(\alpha_2 - \alpha_1)\Delta T] \quad (8.3)$$

where Φ is a function of the factors mentioned above, α_1 and α_2 are the coefficients of thermal expansion of the inclusion and matrix, respectively. ΔT is the change in temperature. Depending on the value of the term (α_2-α_1) the NMI inclusions are considered as: inclusions with stress raising or void forming potentials, see annexe A.20 for more detail. The nature and value of the tessellated stresses around NMI can be calculated using the expressions in annex A.21, for the case of an elastic-plastic deformation of the steel matrix.

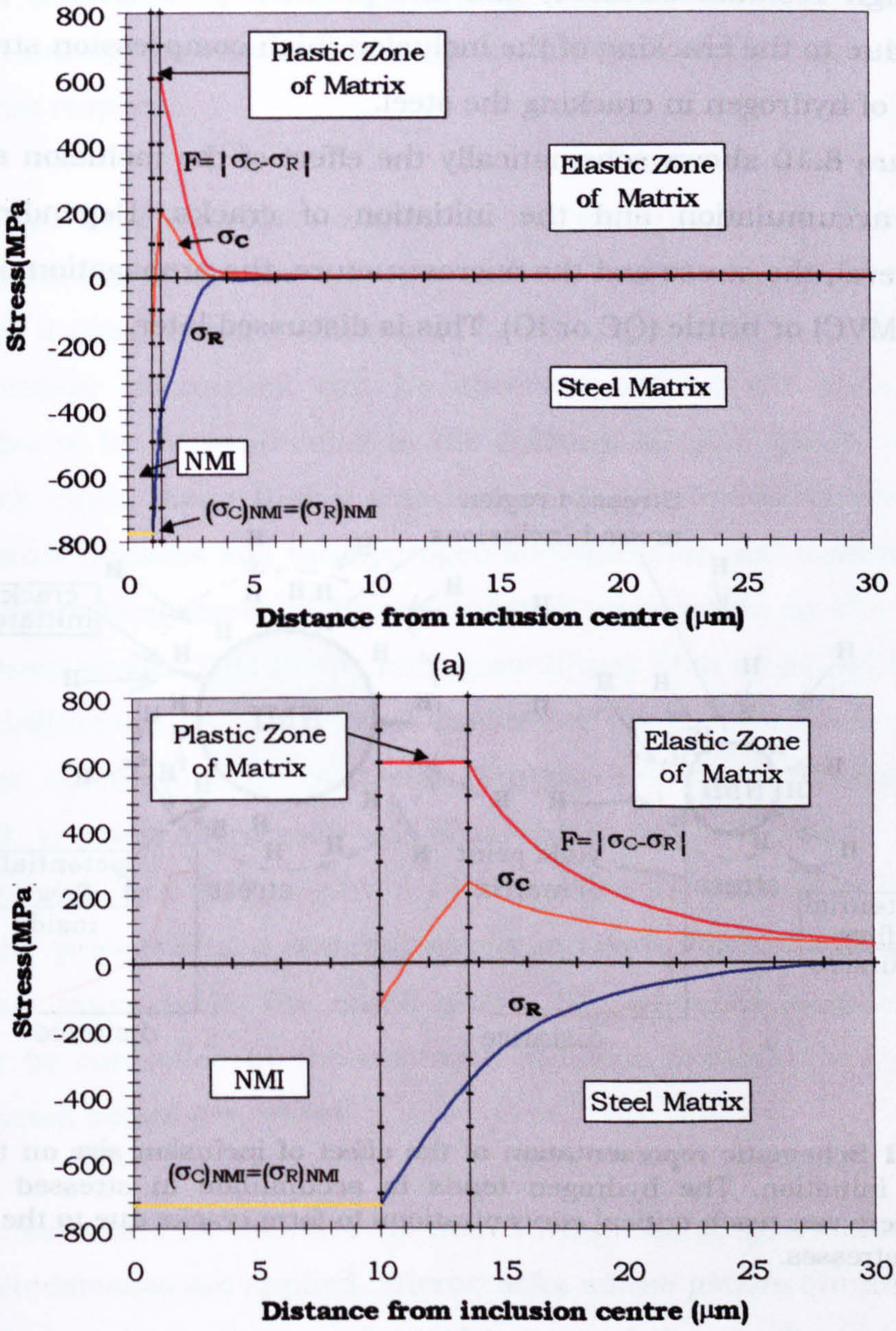

Figure 8.10 Calculation of the tessellated stress around the non-metallic inclusions of different size: (a) 2 μm and (b) 20 μm in diameter. It was supposed a single compound inclusion of Al_2O_3 (α_1=8 10^{-6} 1/°C, E_1=3.89 10^{11} Pa, ν_1=0.25) and steel (α_2=8 10^{-6} 1/°C, E_2=3.89 10^{11} Pa, ν_2=0.25) with 600 MPa of yield strength.

As an example, the regions of influence for two Al_2O_3 inclusions of different sizes has been calculated and presented in figure 8.10. The figure shows stress variation on the steel matrix versus the distance from the centre of the inclusion. From figure 8.10, it can be elucidated that the bigger the inclusion the larger the stressed/strained region. As a result of the expansion of the matrix more hydrogen could be accumulated around of large inclusions and more possibilities to initiate a crack exist if a potential flaw is reached by the stress field or the matrix cohesion strength is overwhelmed. The initiation of the crack depends on the microstructure surrounding the inclusion, its strength and the quantity of hydrogen. Inclusions in high strength steels could produce high residual stresses, and the probability to form a microcrack increases due to the cracking of the inclusion (high compression stress) or the assistance of hydrogen in cracking the steel.

Figure 8.10 shows schematically the effect of the inclusion size on the hydrogen accumulation and the initiation of cracks. Depending on the hydrogen level, the stress and the microstructure, the propagation of the crack is ductile (MVC) or brittle (QC or IG). This is discussed later.

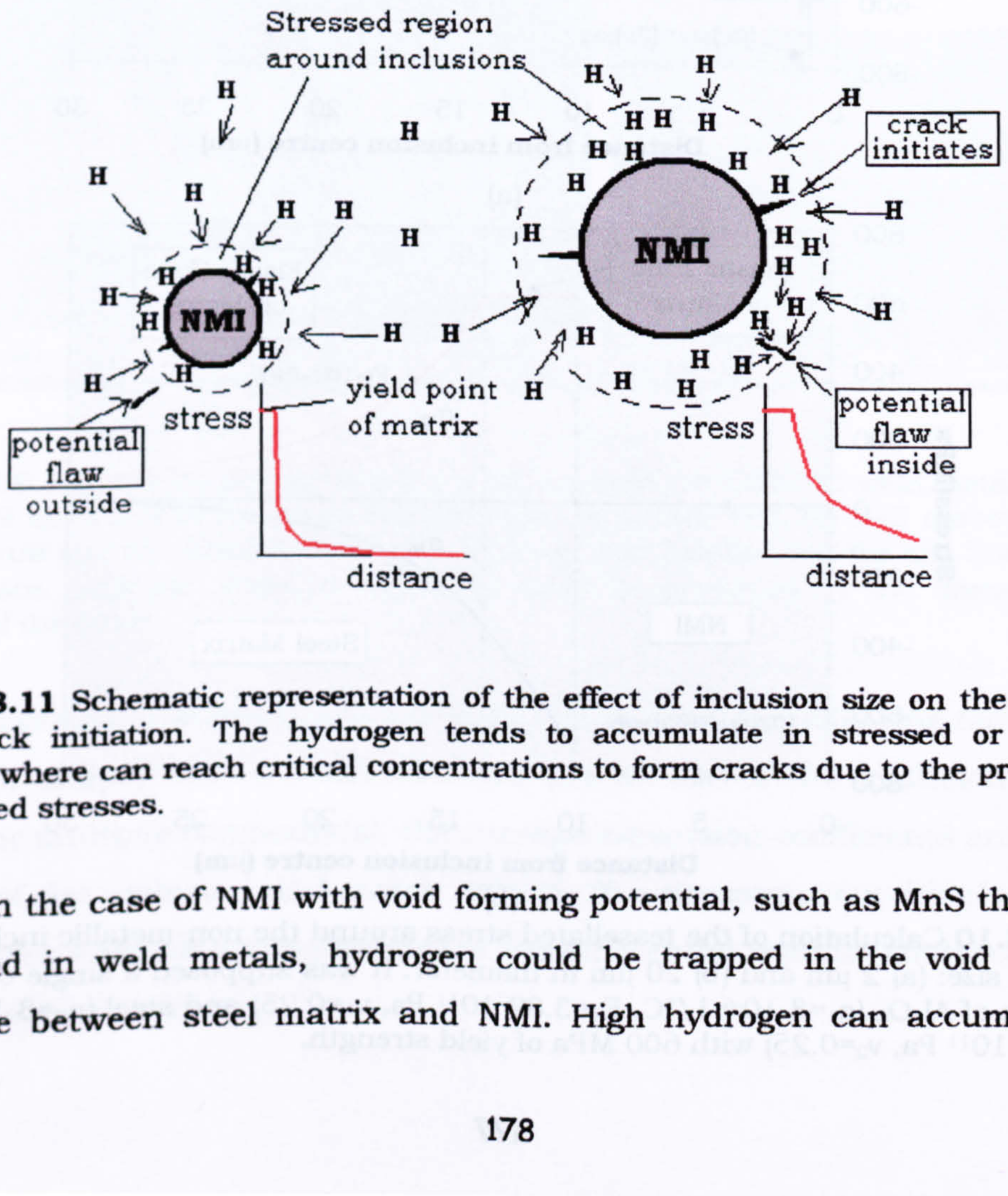

Figure 8.11 Schematic representation of the effect of inclusion size on the trapping and crack initiation. The hydrogen tends to accumulate in stressed or strained regions, where can reach critical concentrations to form cracks due to the presence of tessellated stresses.

In the case of NMI with void forming potential, such as MnS that could be found in weld metals, hydrogen could be trapped in the void and the interface between steel matrix and NMI. High hydrogen can accumulate in

voids and at high pressures the matrix could crack. This type of NMI can be beneficial to trap hydrogen that is introduced during welding.

Figure 8.12 illustrates the effect of the inclusion in the formation of quasicleavage facets at different hydrogen levels. Two general situations could be described based on the hydrogen level:

1- *At low total hydrogen content in the weld metal.* The steel around the inclusion could accumulate enough hydrogen that during tensile test the region could fracture in a QC mode instead of a MVC micromechanism. Not necessarily, the crack is formed during charging as a consequence of the low hydrogen level (see figure 8.12(a)). They form during the tensile test. Large inclusions could be more detrimental in this respect.

2- *At high total hydrogen content in the weld metal.* In this case, the residual stress and the hydrogen content could be sufficient to initiate a crack during charging. This could be evidenced in figure 8.12(b) where a secondary microcrack can be observed around the inclusion. This seems to be perpendicular to the fracture surface (main crack path), which could mean that it was formed during hydrogen charging. The residual stresses and the hydrogen accumulation and assistance would be the driving forces of the microcrack propagation in the absence of external stress. This microcrack growth may stop when the crack tip is not influenced by the residual stresses or the microcrack is arrested by other microstructural obstacles. Further evidence is shown in figure 8.13, where a microcrack was observed on the NMI/matrix interface of a hole left by a NMI. Figure 8.14 illustrates the assistance of hydrogen in the presence of a residual stress to the formation and growth of a brittle microcrack. The crack grows in a discontinuous manner and may be controlled by the hydrogen diffusion towards the crack tip, as reported before [156, 163-165].

The microcracks that are formed during charging are going to grow when tensile stresses are applied. Microcracks whose planes are normal to the tensile axis may begin to grow from the start of the tensile test, when the stress concentration around the crack is sufficient to propagate the crack in a particular manner (QC or MVC).

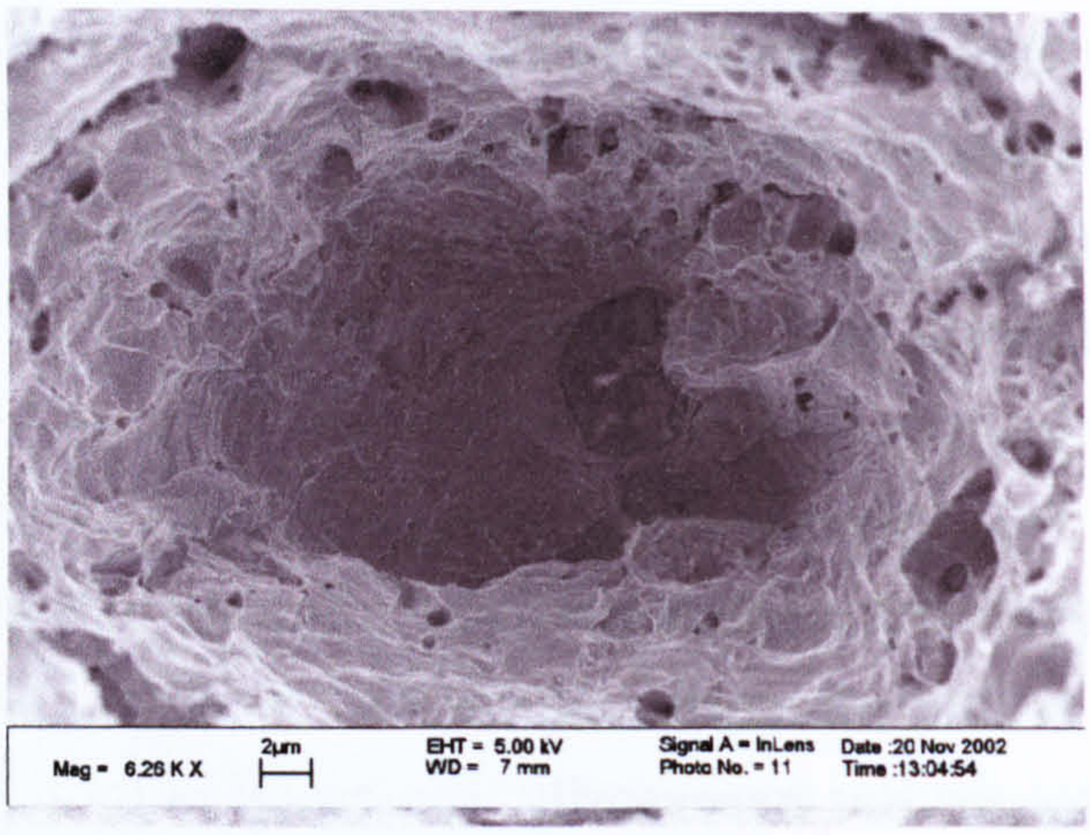

(a)

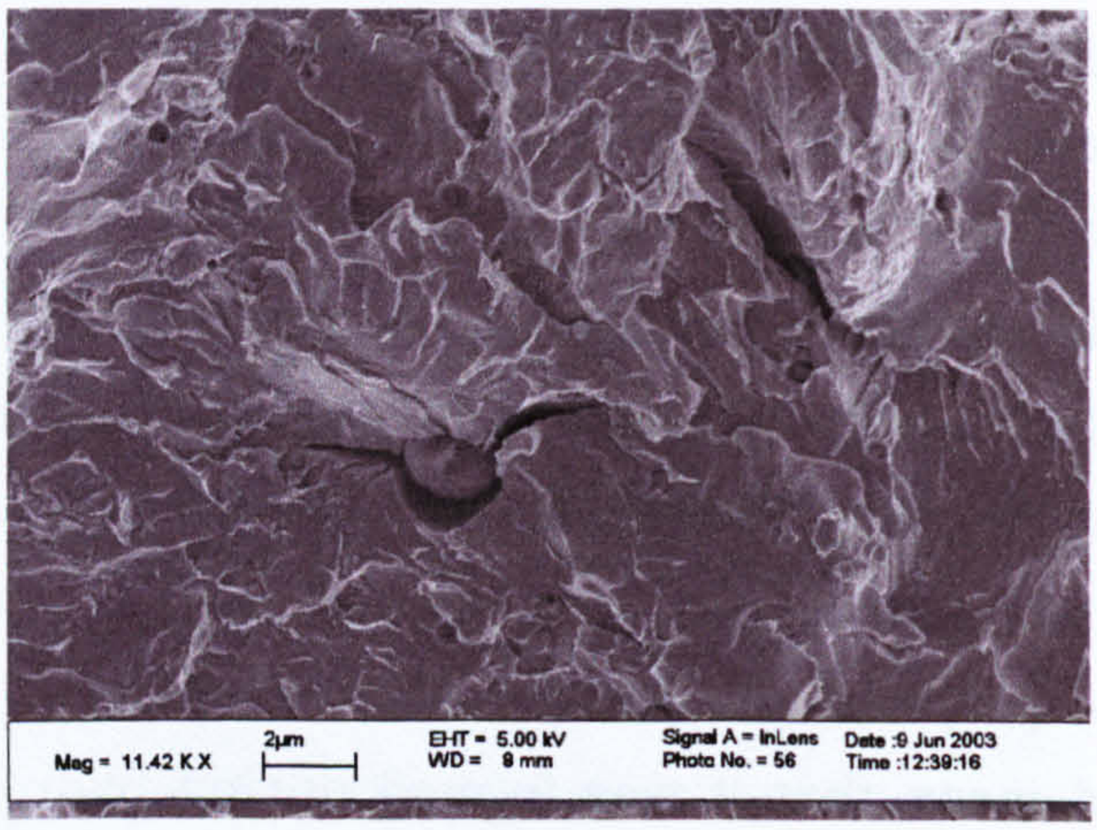

(b)

Figure 8.12 Relation between the inclusion, the brittle fracture of the matrix and the hydrogen content. (a) Inclusion of around 5 µm in diameter in the 15171 weld metal charged with only 0.4 mL/100 g of hydrogen. (b) Cracking of the matrix around the inclusion (2 µm in diameter) at high hydrogen levels in the CWX201 weld metal with 11.72 mL/100 g of hydrogen.

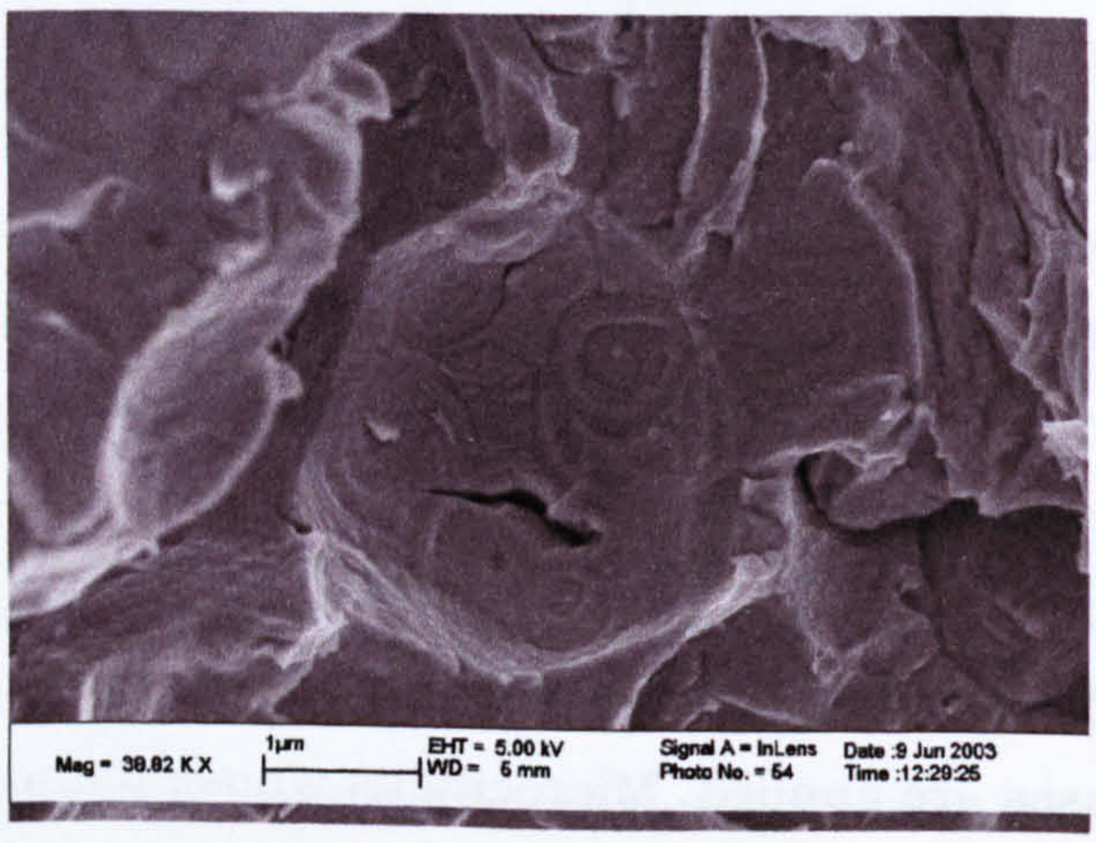

Figure 8.13 Microcrack formed around a NMI in CWX201 weld metal charged with 11.72 mL/100 g of hydrogen. The microcrack plane seems to be perpendicular to the interface surface

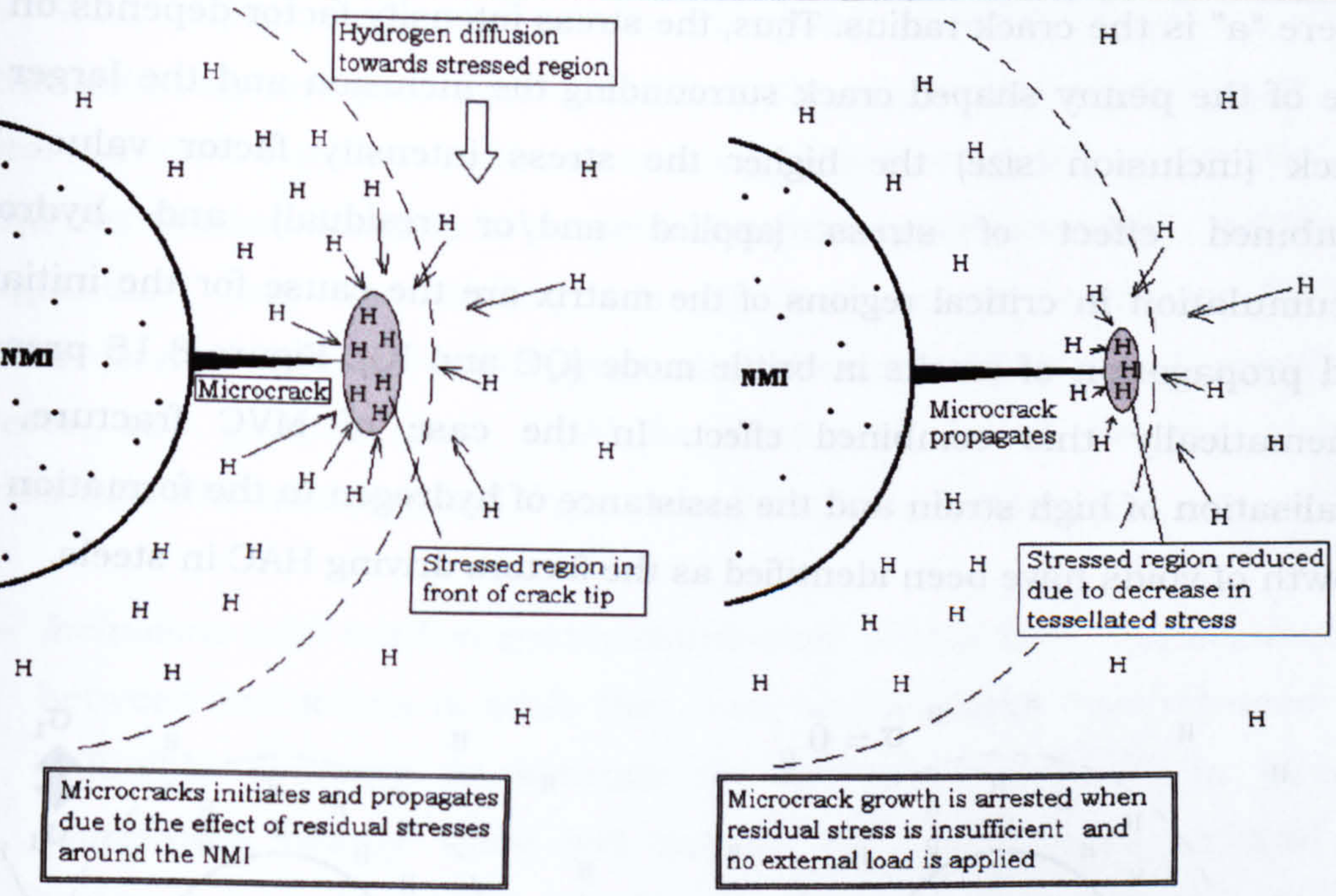

Figure 8.14 The initiation and propagation of a crack around an inclusion due to the effect of residual or tessellated stresses without the application of external loads. The growth of the crack stops when the residual stress is low and the assistance of hydrogen is not enough to propagate the crack.

A fracture mechanics approach [166-168] to stress concentration around an inclusion and inclusion + cracked matrix could give the order of magnitude indicator of the stresses that could be found in such regions. The stresses around a NMI could be approximated to the stresses around a spherical hole if it is supposed that no strong interaction exists between the inclusion and the matrix. Timoshenko and Goodier [169] have calculated for perfectly elastic materials, estimations for the case of steels which gives that the stress around the equatorial plane $(\sigma_{\theta\theta})$ can be twice the applied stress ($(\sigma_{\theta\theta})_{max} \approx 2\sigma$). This is the tensile stress that the matrix around the inclusion suffers during the tensile test, when there is not microcrack to intensify it significantly. This stress, or the associated strain, could produce enough hydrogen accumulation to promote the initiation and propagation of the cracks in a brittle manner.

In the case of a microcrack formed during charging, this could be taken as penny shaped cracks surrounding the inclusion. In this case no strong interaction between NMI/steel interfaces is supposed as before. The equation 8.4 allows an estimation of the stress intensity factor (K) for a circular embedded crack as follow [167]:

$$K = \frac{2}{\pi}\sigma\sqrt{\pi a} \qquad (8.4)$$

where "a" is the crack radius. Thus, the stress intensity factor depends on the size of the penny shaped crack surrounding the inclusion and the larger the crack (inclusion size) the higher the stress intensity factor value. The combined effect of stress (applied and/or residual) and hydrogen accumulation in critical regions of the matrix are the cause for the initiation and propagation of cracks in brittle mode (QC and IG). Figure 8.15 presents schematically this combined effect. In the case of MVC fracture, the localisation of high strain and the assistance of hydrogen to the formation and growth of voids have been identified as the factors driving HAC in steels.

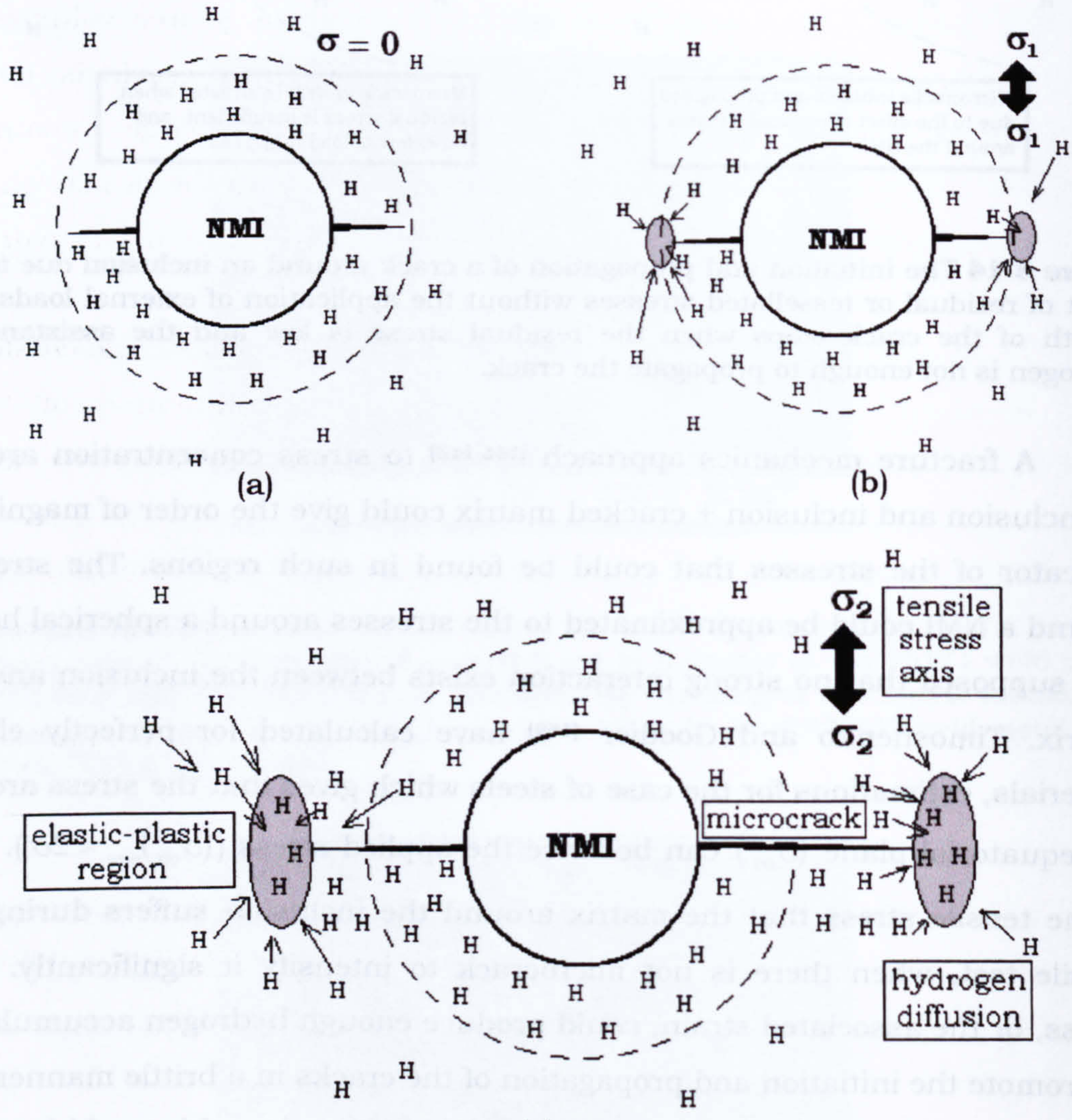

Figure 8.15 The propagation of a microcrack during the tensile test in a quasicleavage mode. (a) The microcrack is formed around the inclusion and its growth is stopped due to reduction in stress. (b) Applying load during test, stress concentration due to microcrack produces the growth of the crack assisted by hydrogen diffusion towards crack tip. (c) The cracks continue to propagate due to increase of stress in a QC mode. When stress intensity reaches a critical value the crack continues to growth but in a MVC fashion.

With respect to the NMI density and spatial distribution and its effect on the initiation and propagation of QC cracks, a precise correlation of the several variables such as: inclusion size, shape and composition, population, spatial distribution, location in the microstructure (grain boundary, interface, intragranular) and surrounding microstructure (grain boundary ferrite, acicular ferrite, bainite, martensite, micro constituents, etc.) is complex. However, two general cases could be mentioned, based on the spatial distribution, NMI numbers and the accumulation of hydrogen:

1- *Inclusions with random spatial distribution:* In this case, the separation between inclusions is such that there are no large free volumes for diffusible hydrogen to saturate the matrix. If a crack is formed somewhere nearby there will not be sufficiently large amount of hydrogen to assists its growth. As a consequence the crack may change from brittle to ductile due to the low concentration of hydrogen assisting cracking.
2- *Inclusions with clustered spatial distribution:* In this case, the clustering of inclusion could have two effects: the accumulation of larger quantities of hydrogen at the cluster sites and the existence in the matrix of large volumes of material where diffusible hydrogen can stay and saturate the matrix. The consequences are clear: the initiation of cracks is more likely to occur at clusters and there will be enough diffusible hydrogen to assist their growth which could be the hydrogen liberated by the cluster and/or the hydrogen saturating the matrix from those free volumes of steel.

The effect of the NMI size and spatial distribution on the HAC of the weld metals is discussed in more detail from the point of view of hydrogen diffusion, distribution and trapping in chapter 9.

8.3.1.2 Cavities or micro-shrinkages as quasicleavage initiators.

In some of the weld metals studied enormous QC facets were associated with cavities or micro-shrinkages. Figures from 8.16 to 8.19 show examples of these crack initiators. The size of the QC facet is around 300 μm in diameter (figure 8.16(a)) and the origin of the crack is a complicated network of cavities that must have been formed during the solidification of the weld metal (figures

8.16(b) and (c)). The effect of these cavities is to collect large quantities of hydrogen. The hydrogen could recombine as hydrogen gas in the cavity thereby pressurising it. If sufficient pressure is accumulated the cavity would induce the cracking of the matrix which is saturated by atomic hydrogen.

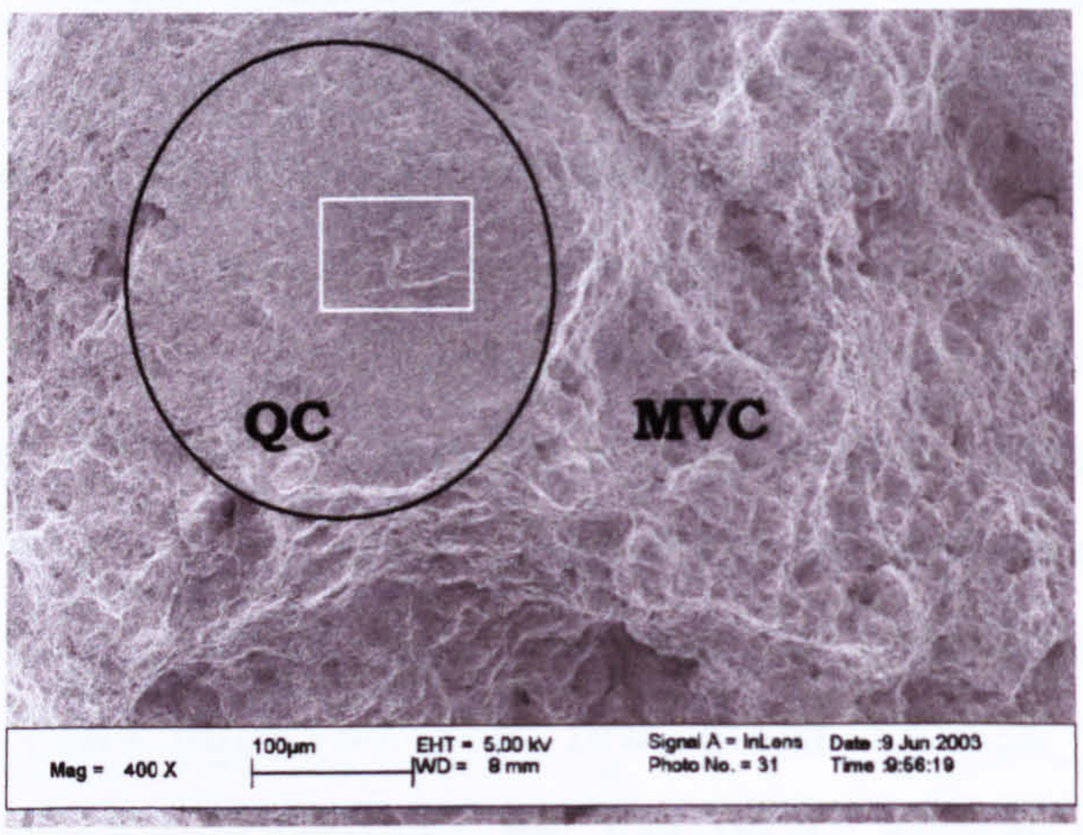

(a)

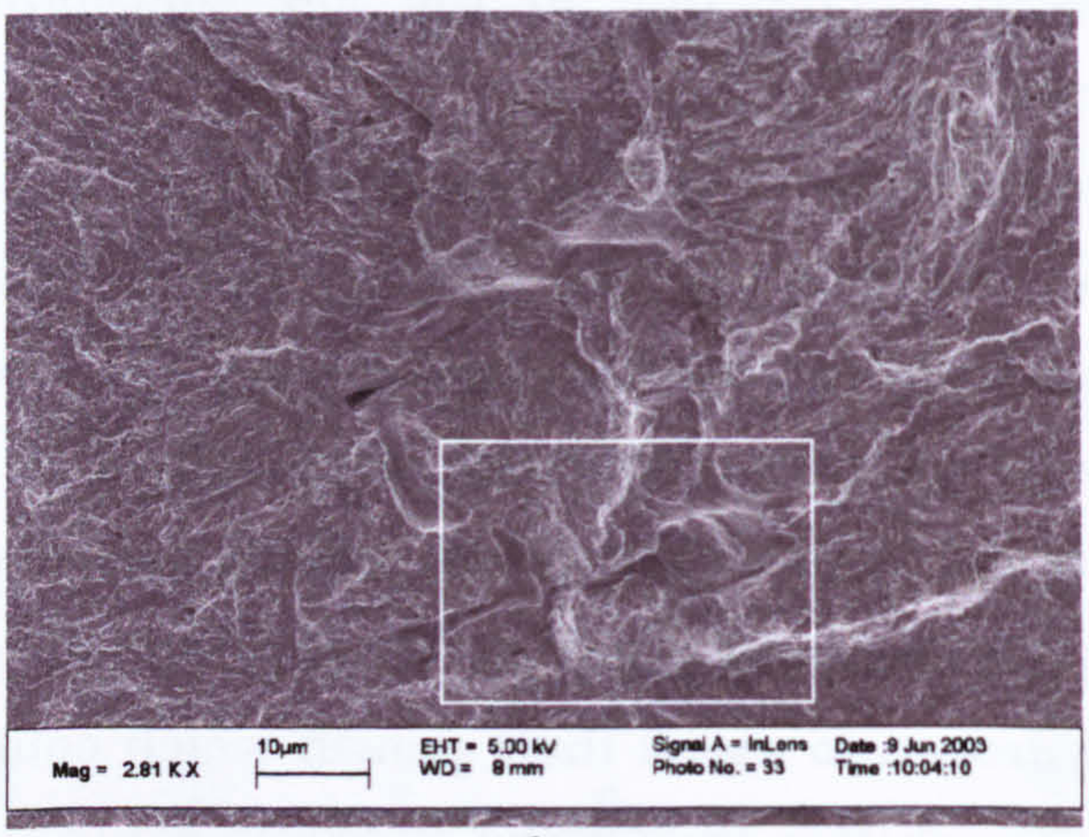

(b)

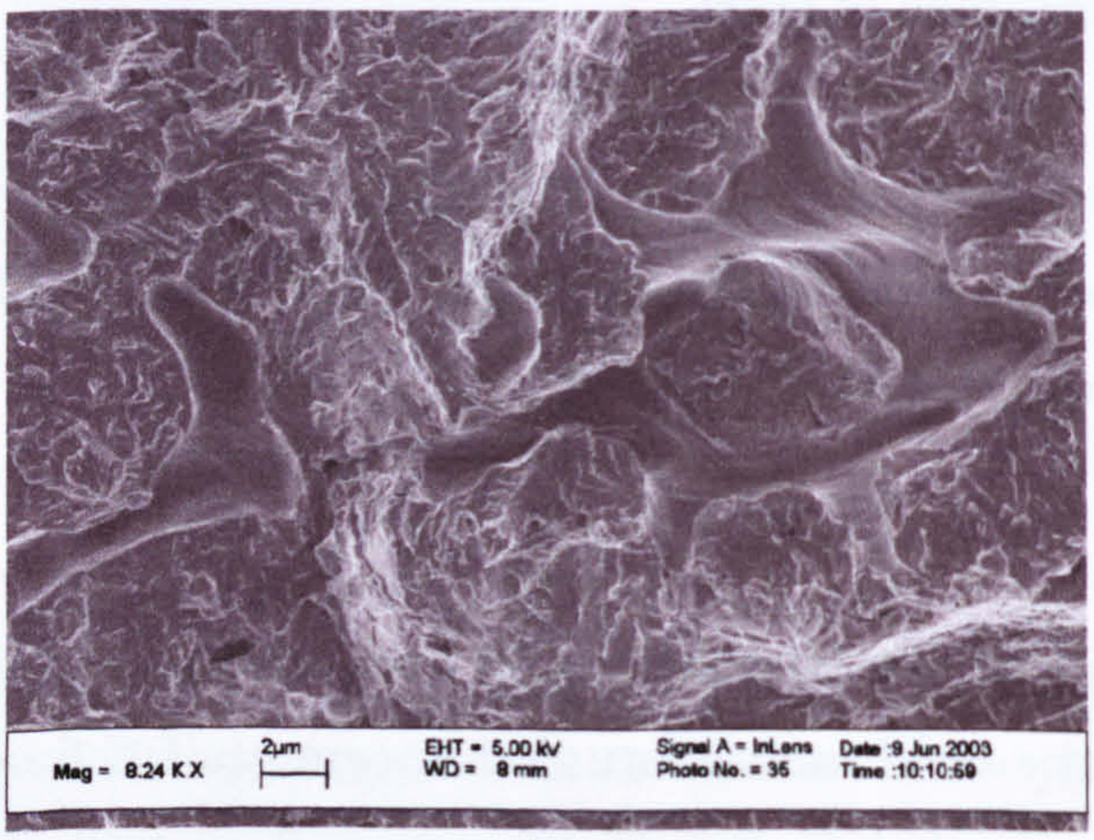

(c)

Figure 8.16 Cavities and micro-shrinkages as initiators of cracks in CWX201 weld metal with 3.24 mL/100 g of hydrogen after tensile test. (a) QC facet of 300 µm in diameter surrounded by a ductile fracture (MVC), (b) and (c) details of the origin of the brittle fracture.

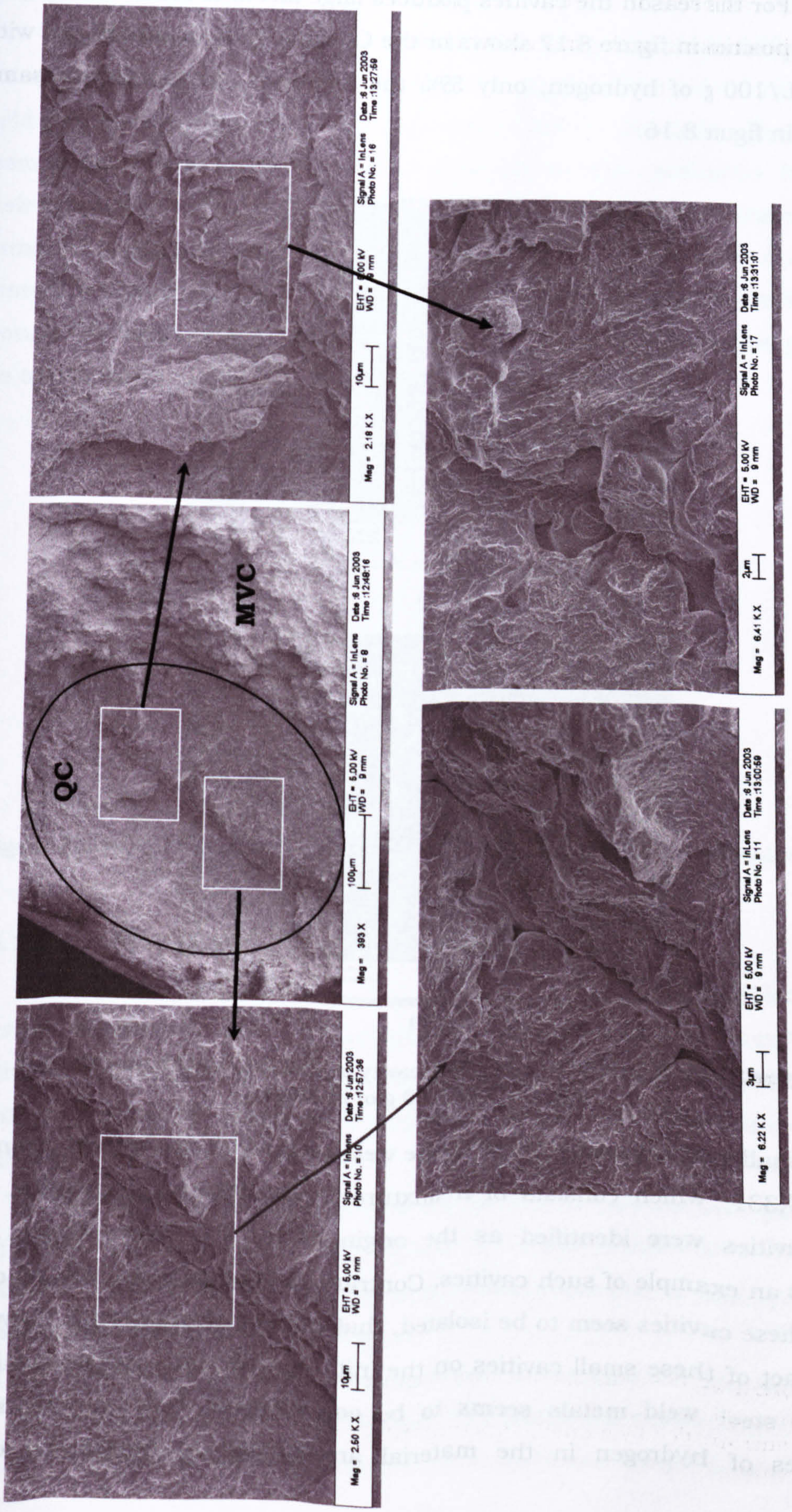

Figure 8.17 Large QC facets found after tensile test in CWX201 weld metal charged with 1.77mL of hydrogen. The composition illustrates the impact of the presence of this kind of complex network of cavities (micro shrinkages) on the hydrogen assisted cracking process.

Cracks would then form around the defect and their propagation assisted by the large amount of hydrogen inside cavities and the diffusible hydrogen in the matrix. For this reason the cavities produces large facets of brittle fracture, as the composition in figure 8.17 shows for the CWX201 weld metal charged with 1.77 mL/100 g of hydrogen, only 55% the hydrogen content for the same sample in figure 8.16.

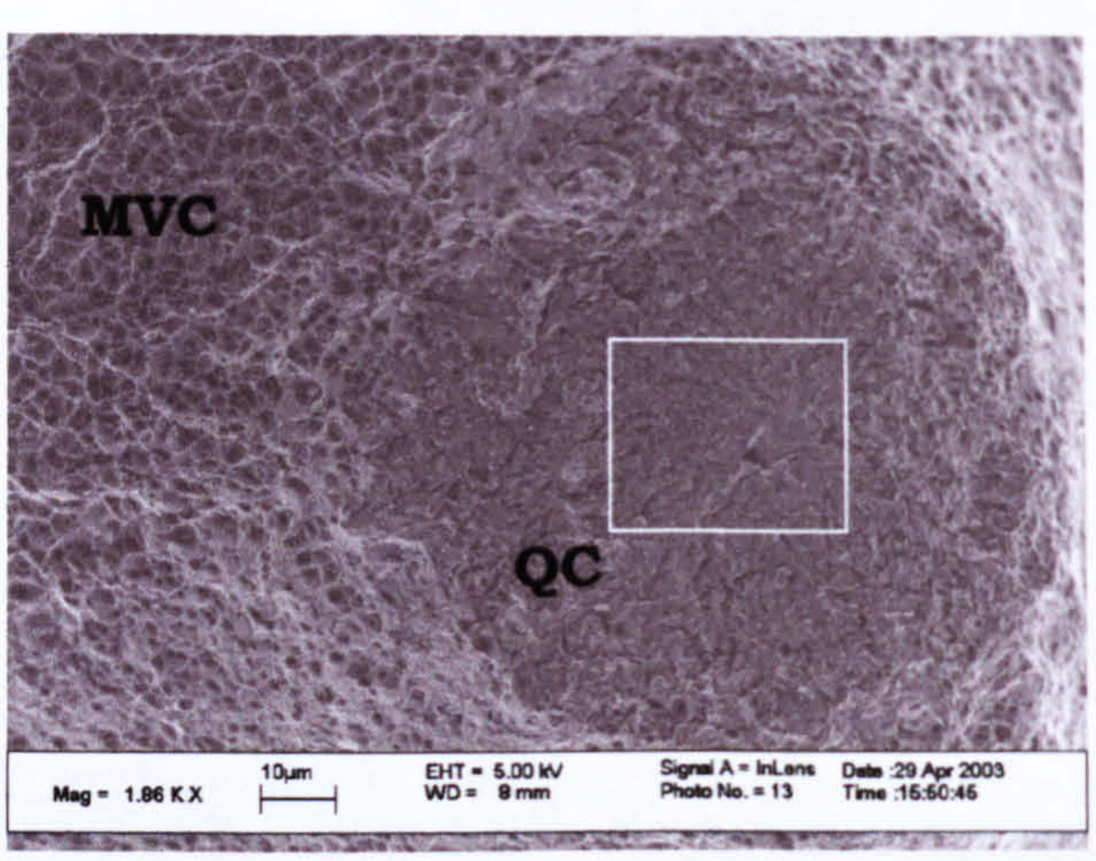

(a)

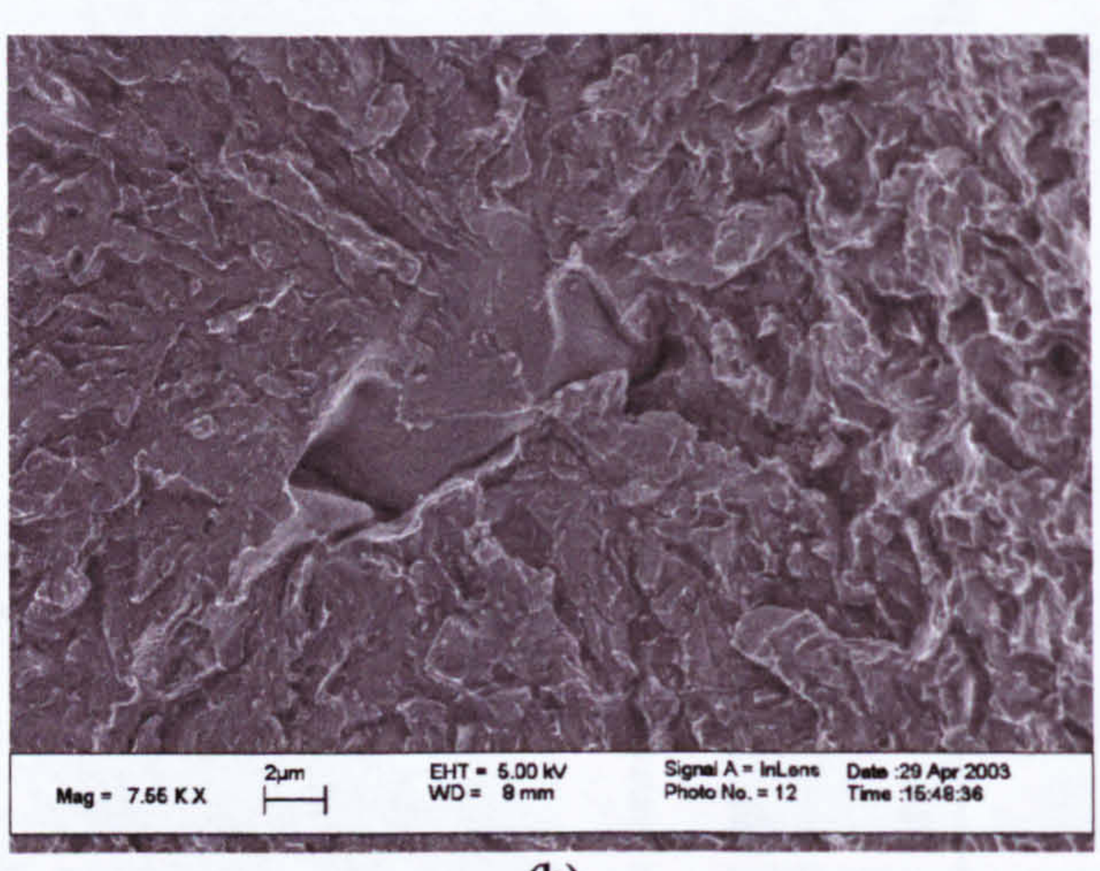

(b)

Figure 8.18 QC facet originated by a cavity in CWX331 weld metal charged with 1.27 mL/100 g of hydrogen.

Smaller cavities were found in the weld metal with the highest strength: the CWX331, which consists of a mixture of bainite and martensite. The micro-cavities were identified as the origin of the QC facet. Figure 8.18 presents an example of such cavities. Contrary to the cavity network reported above, these cavities seem to be isolated, that is not interconnected. However, the impact of these small cavities on the initiation of brittle cracks in higher strength steel weld metals seems to be considerable, because only small quantities of hydrogen in the material are needed to trigger the crack

formation. In the case of the CWX331 weld metal, the hydrogen level was as low as 0.73 mL/100 g and was sufficient to produce a QC facet associated with a small cavity, as shown in figure 8.19.

The presence of cavity networks or micro-shrinkages, like those presented above, was not found in the fractographic study of the rest of the weld metals. However, their existence should not be discarded. The cavities seem to be at least as detrimental as large non-metallic inclusions. However, their capacity to trap hydrogen is expected to be greater as is illustrated by the formation of blisters in steels exposed to corrosive environments. Such high quantities of hydrogen should be liberated to the matrix when fracture occurs around the cavity. As a consequence, cavities or micro-shrinkages probably are traps and/or sources of hydrogen during HICC.

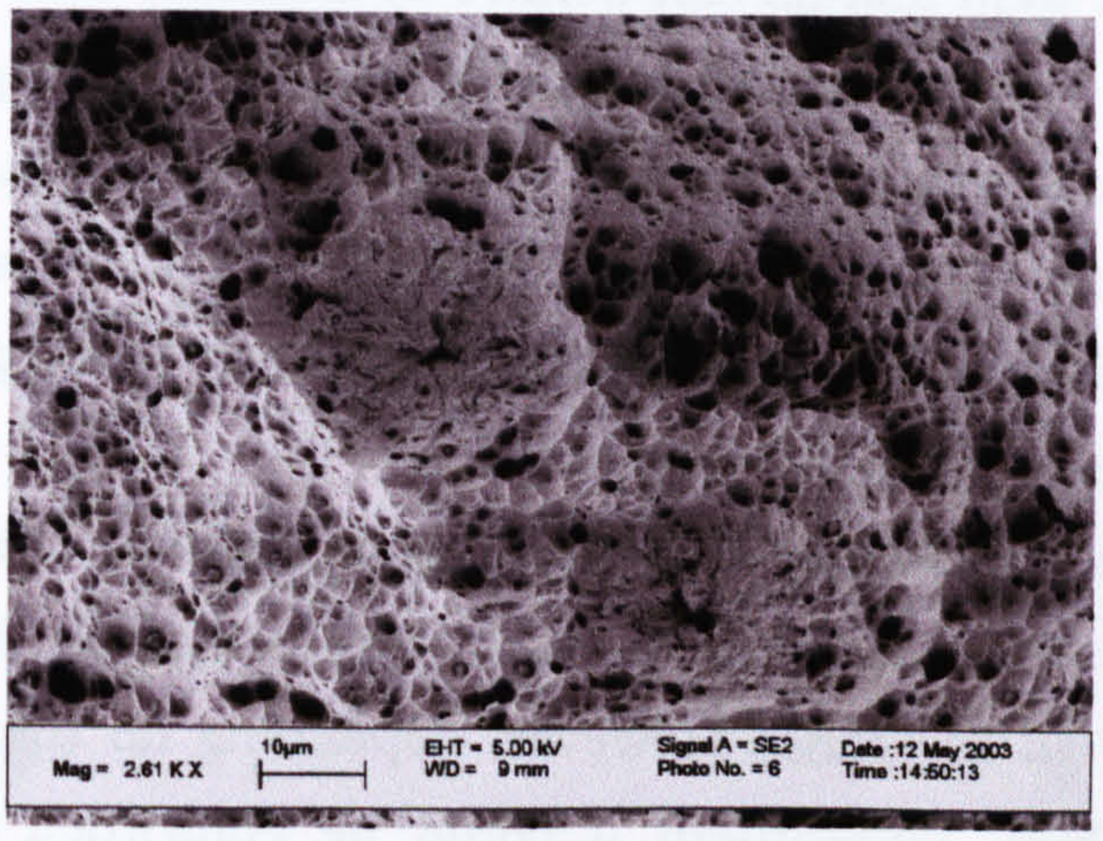

Figure 8.19 QC facet of around 30 µm in diameter associated with a small cavity in the CWX331 weld metal at 0.73 mL/100 g of hydrogen

8.3.1.3 The MAC as a nucleation site for quasicleavage.

In this investigation the MAC constituent was not identified on the fracture surface of the fractographically analysed tensile samples after hydrogen charging. Nevertheless, some QC facets were found with no clear identification of the micro-constituent responsible for their appearance or initiation.

The effect of MAC particles on mechanical properties and particularly toughness of steels have been subjects of several studies [133, 170-172]. The findings of these studies are useful to understand the role of MAC particles in low alloy steel weld metals. These are:

1- Martensite islands have been found to contribute to the formation of voids, most of them by the interfacial decohesion of the ferrite martensite interface [170, 171]. Wildash [8] has found similar evidence

in regions close to the fracture surface of HSLA weld metal tensile samples.

2- Brittle cracks propagate primarily in the ferrite matrix rather than into or throughout the martensite [171].

3- During tensile deformation the martensite islands do not deform until high strains are attained, which are above the maximum uniform strain [133].

4- The M-A volume fraction, spatial distribution and size strongly influence the strength and work hardening of the dual-phase steels, both increase with the augment of the volume fraction. The work hardening rate retards void growth during deformation and as consequence the total strain at fracture is expected to increase.

The MAC in weld metals can behave in a similar manner. In the case of hydrogen charged samples, MAC might be expected to trap hydrogen at the interface or inside when retained austenite, which has high hydrogen solubility, is present. Considering the observations above and supposing the MAC constituent as a solid particle which could trap hydrogen in the charged weld metals, during tensile test they could:

a- Support the deformation of the matrix without cracking itself at low and medium strains. Without fracturing the hydrogen remains trapped in the MAC. However, depending on the hydrogen content of the MAC constituent it could be embrittled and fracture may occur at low and medium strains. Then, cracks could propagate in a brittle manner if the matrix hydrogen level and stress concentration factor are sufficient. Hydrogen might be liberated to the steel matrix where it can continue to assist crack propagation.

b- Contribute to the formation of voids when the hydrogen content in the matrix is low and at high strain levels. If the hydrogen content in the MAC and the matrix is high, both could fracture in a brittle manner. Hydrogen contained in the MAC and the matrix will assist the propagation of the crack in conjunction with the stress concentration factor produced by tensile stress.

This simple observation about MAC, based on considering it as a hydrogen trapping hard-particle, is complicated by the constitution of the MAC. If the MAC is mostly formed by retained austenite, the solubility of hydrogen is high, which make it an excellent hydrogen container. However, austenite may be softer than ferrite, depending on C content, and can deform

during the tensile test. Deformation could transform the retained austenite to martensite and the trapped hydrogen is liberated saturating the steel matrix around, increasing the possibilities of embrittlement. The presence of carbides and ferrite, bainite or pearlite adds further complications to the behaviour of the MAC particle from the point of view of mechanical properties and hydrogen trapping.

The MAC constituent has been identified as detrimental to toughness in the heat affected zone (HAZ) of high strength low alloy steels, as has been reported by several authors [173-176]. All reports identify the martensite island as the initiators of cracks (ductile or brittle) depending on the morphology of the MAC islands and the temperature of the impact test. A summary of their observations is in annexe A.22. Figure 8.20 summarises these mechanisms of fracture involving MAC particles.

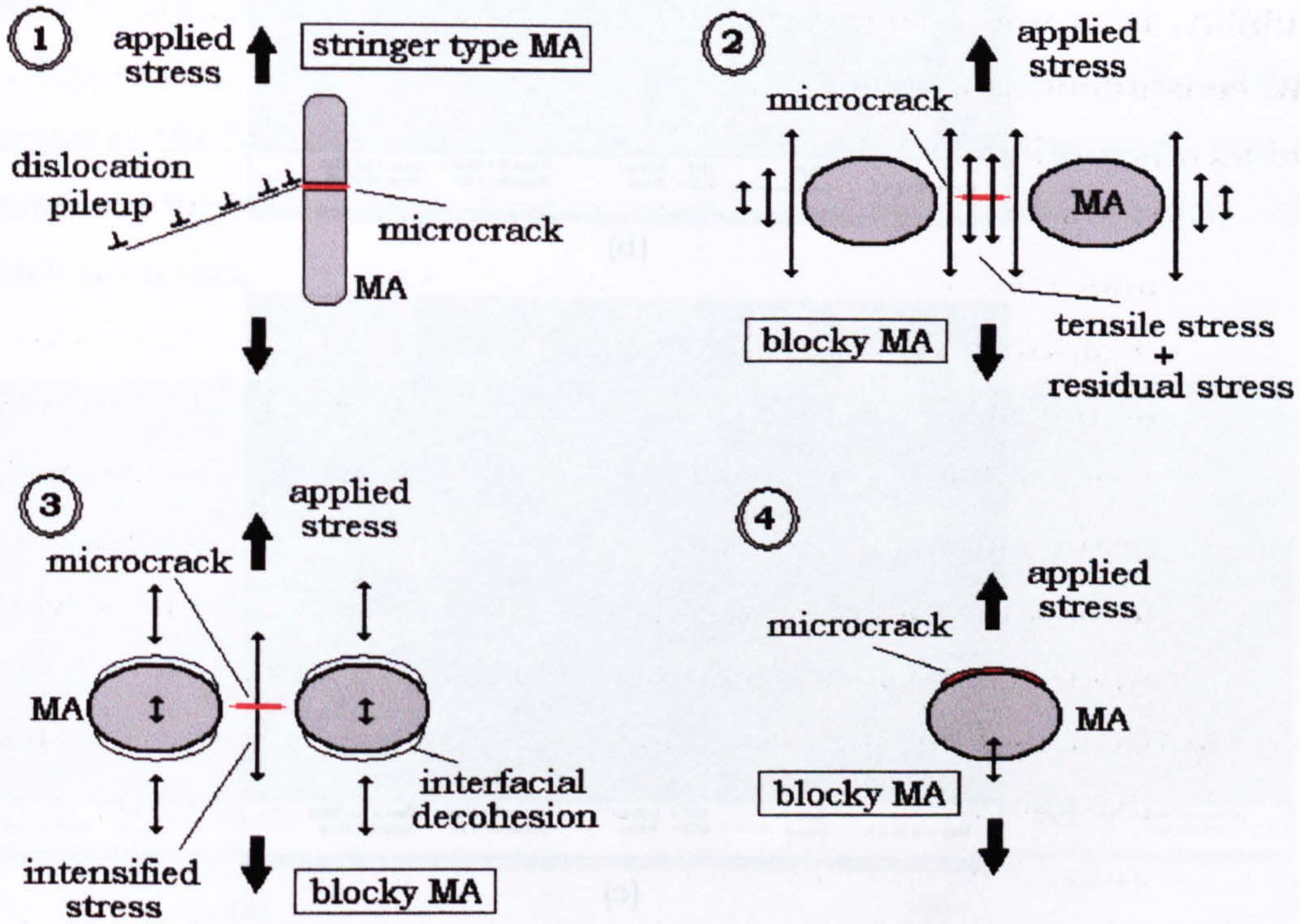

Figure 8.20 Schematics of the mechanisms proposed for the initiation of cleavage in the intercritical zone in weldments of high strength low alloy steels. 1- The elongated-type MA constituent cracks readily, initiating cleavage in the ferrite matrix. 2- Overlapping of transformation-induced residual stresses between blocky MA and applied tensile stress assists the cleavage of the ferrite matrix. 3- Strength mismatch leads to interfacial decohesion increasing stress in the matrix between particles. 4- Brittle debonding resulting in a microcrack at the MA/matrix interface could then propagate in a cleavage manner. Based on figure 18, Davis and King [174].

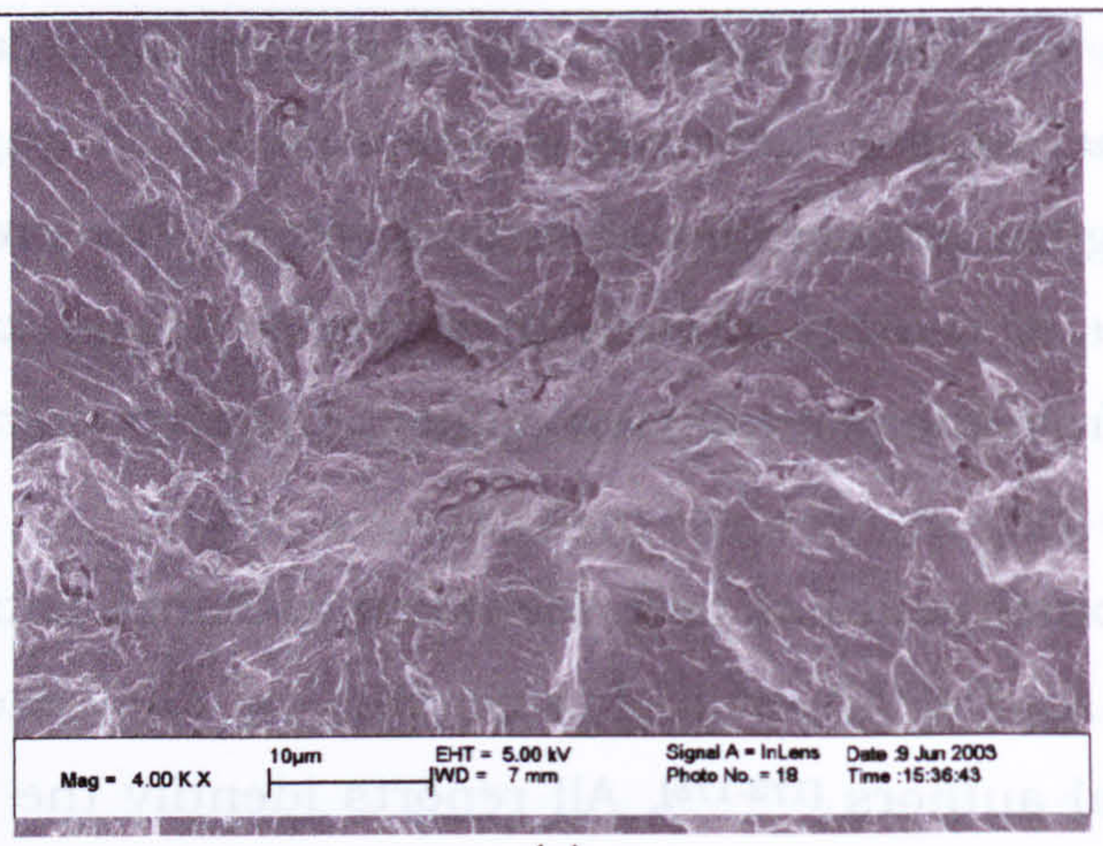

(a)

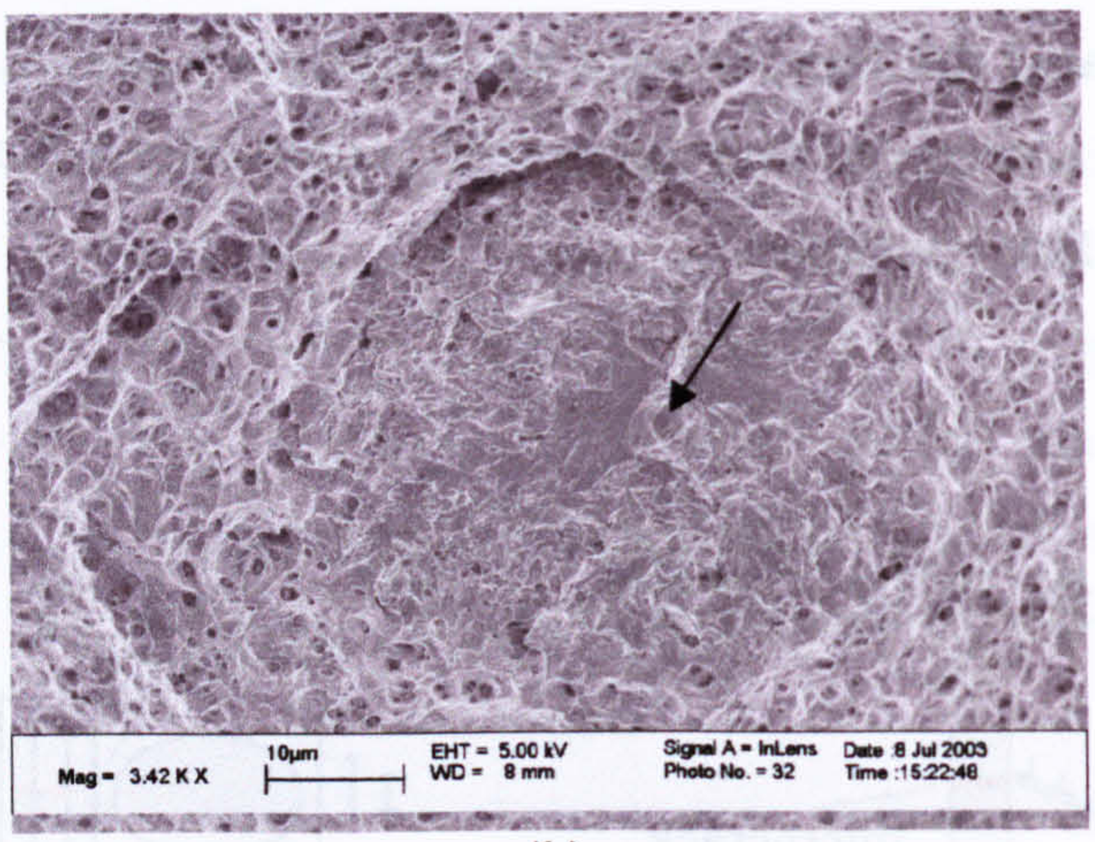

(b)

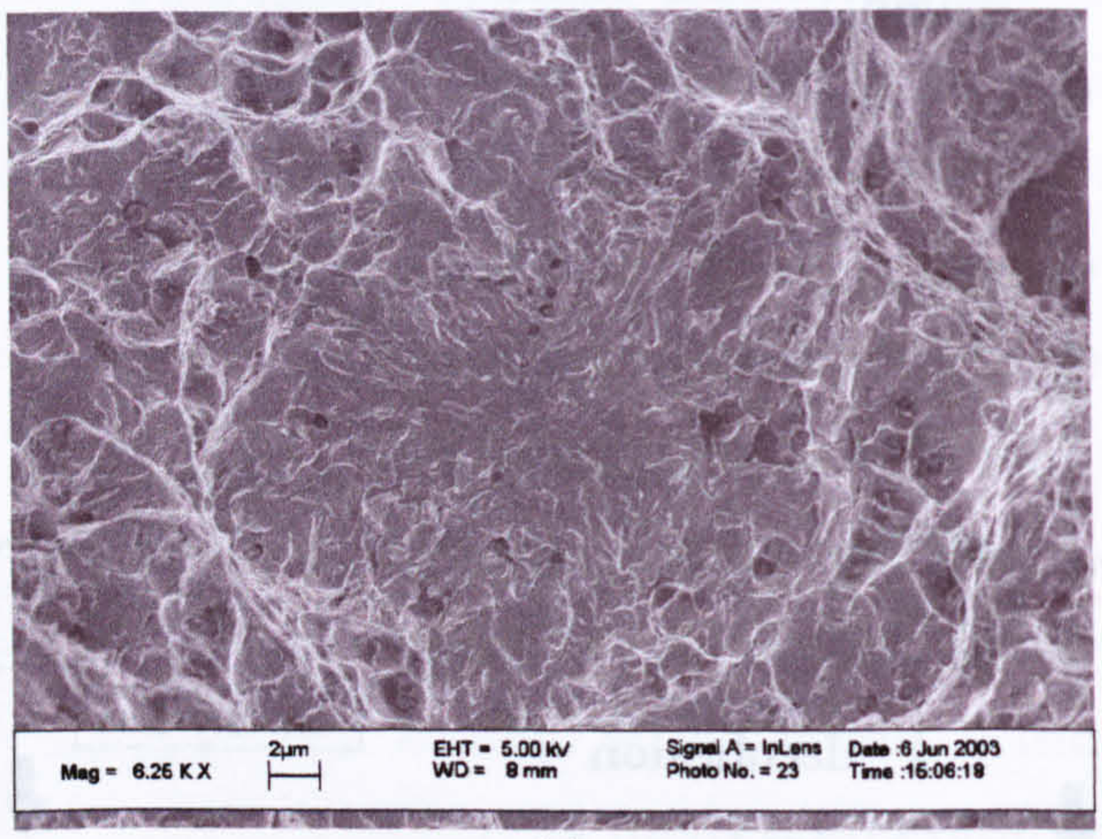

(c)

Figure 8.21 Examples of unidentified QC origins for three weld metals with different hydrogen content (mL/100 g): (a) CWX181 (2.70), CWX361 (2.95) and CWX 201 (5.58).

Figure 8.21 shows some examples of QC facets not associated with NMI, as a crack initiator as discussed before. Although the micro-feature which initiated the QC was not clearly identified, it is probable that one of the mechanisms summarised in figure 8.20 is operating. For example, if mechanisms 1 or 4 in figure 8.20 are initiating the crack, in the first case, the MAC could be recognised after etching (see arrow on figure 8.21(b)) and in the

second case, the MAC particle could be underneath the fracture surface (see figure 8.21(c)). Mechanisms 2 and 3 in figure might be easily recognised because the crack initiates between two MAC particles. No evidence was found in this study. Other mechanisms not involving MAC can not be discharged. For example, the weld metal CWX181 (figure 8.21(a)), which contains grain boundary ferrite (15%), could have initiated the QC crack in those regions due to the presence of a stress concentrator. Voids beneath the fracture surface could be other type of crack initiators. No clear evidence was found in this investigation.

If the MAC islands were the crack initiation sites, they should have been observed in those weld metals with high MAC proportion. CWX361 weld metal has one of the highest proportion of MAC constituent (16.3%) followed by CWX201 weld metal with 13.8%, both fracture surfaces in figures 8.21 (b) and (c), respectively. However, features like these were seldom found in these samples or in other samples. The majority of the QC facets were related to the presence of NMI, at least at low hydrogen levels.

Figure 8.22 shows QC facets which were found in weld metal CWX331. The origin of the facets seems to be the hole left by a particle of small size, the size expected for MAC islands. Further work is needed to clarify the MAC effect on crack initiation.

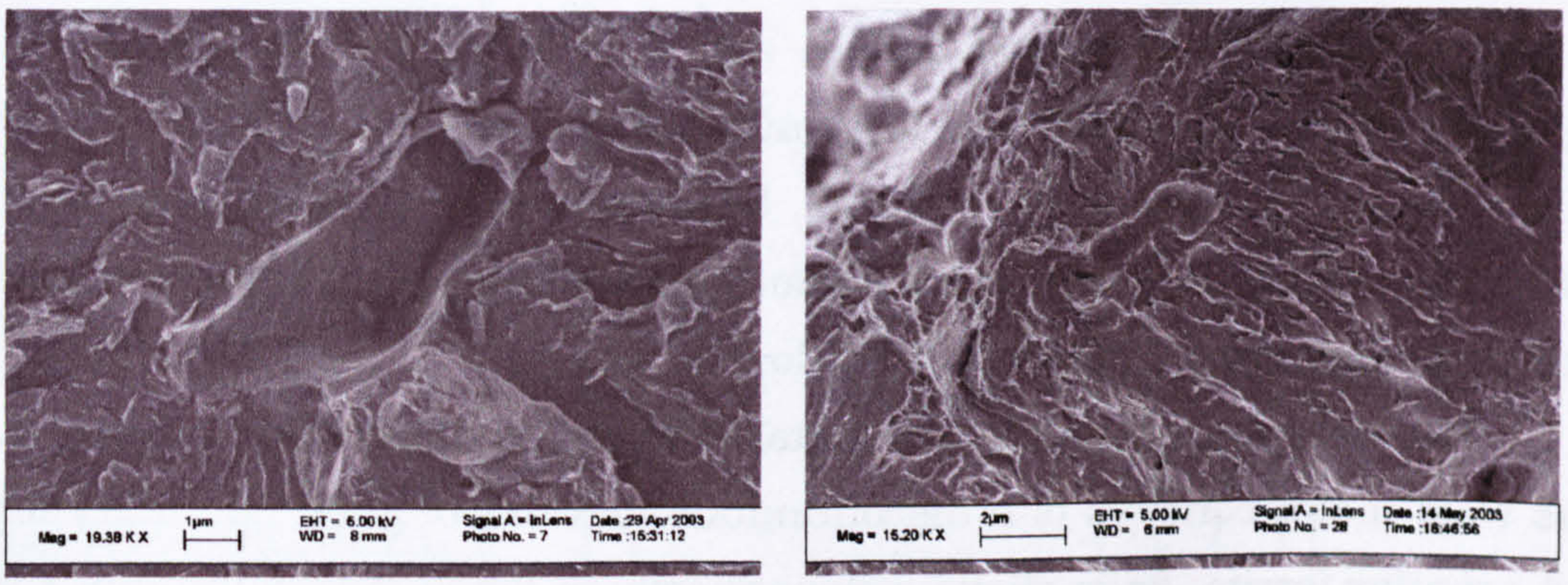

(a) (b)

Figure 8.22 Possible MAC particle decohesion initiating the QC facet in CWX331 weld metal with hydrogen content of: (a) 1.27 mL/100 g and (b) 4.88 mL/100 g.

8.3.2 Evidence for modification of fracture micromechanism by hydrogen content in the weld metals

Given the observations presented earlier in this chapter, it appears likely that the details of the fracture micromechanisms will depend on details of the microstructure and hydrogen content. The following sections deal with the the evidence that is going to support the proposed model that describes the

relation between microstructure, stress, mechanical properties and the hydrogen content of weld metals.

Figures 8.23 and 8.24 show the results for weld metals CWX181 and 15171, respectively. These welds are characterised by a continuous network of grain boundary ferrite and acicular ferrite in different proportions. As can be observed, at low hydrogen level (approximately 0.2-0.3 mL/100 g of weld metal) the fracture occurred by the MVC mechanism (figures 8.23(a) and 8.24(a)). At somewhat higher hydrogen contents, transgranular quasicleavage is observed, generally associated with the larger NMIs as observed in figures 8.23(b) and 8.24(b). Regions with dimples, indicating a mixed fracture micromechanism, surround these quasicleavage features or "fish eyes", as these are more commonly known. At this hydrogen level (1-1.4 mL/100 g), no significant reduction in S_f is observed despite the presence of a few QC facets with diameters below 100 μm. It seems to indicate that these weld metals with hydrogen levels around 1 mL/100 g, could withstand few penny shaped cracks of this size without severely affect the S_f value. However, further increase in H_D, between 1.2 and 4 mL/100 g, produces an appreciable decrease in S_f, which is related to the increase of QC on the fracture plane including facets with diameters between 100 and 300 μm and smaller ones. At even higher hydrogen contents (above approximately 4 mL/100 g), a larger number of QC features link up together to produce large quasicleavage areas, as those observed in figures 8.23(d) and 8.24(d). In addition to these QC regions, long cracks, which in a large number of cases appear to be coincident with regions of grain boundary ferrite, begin to appear. It could represent the initiation of the IG fracture mechanism. This evolution of the fracture surface with H_D is discussed in more detail below.

The behaviour for the weld metal CWX361 is illustrated in figure 8.25. This weld metal consists of a discontinuous network of grain boundary ferrite and acicular ferrite, as is shown schematically in figure 7.11 and table 7.2. In addition, CWX361 possess one of the highest MAC proportion of all the weld metals studied (16.3%). Similar to the previous welds, the influence of hydrogen on the fracture characteristics is demonstrated by changes in fracture micromechanisms from pure MVC in the weld without hydrogen (and probably very low H_D content) to the presence of QC facets together with evidence of MVC at high H_D. Even at the highest H_D content, the MVC fracture micromechanism is still observed (result not shown due to poor image quality).

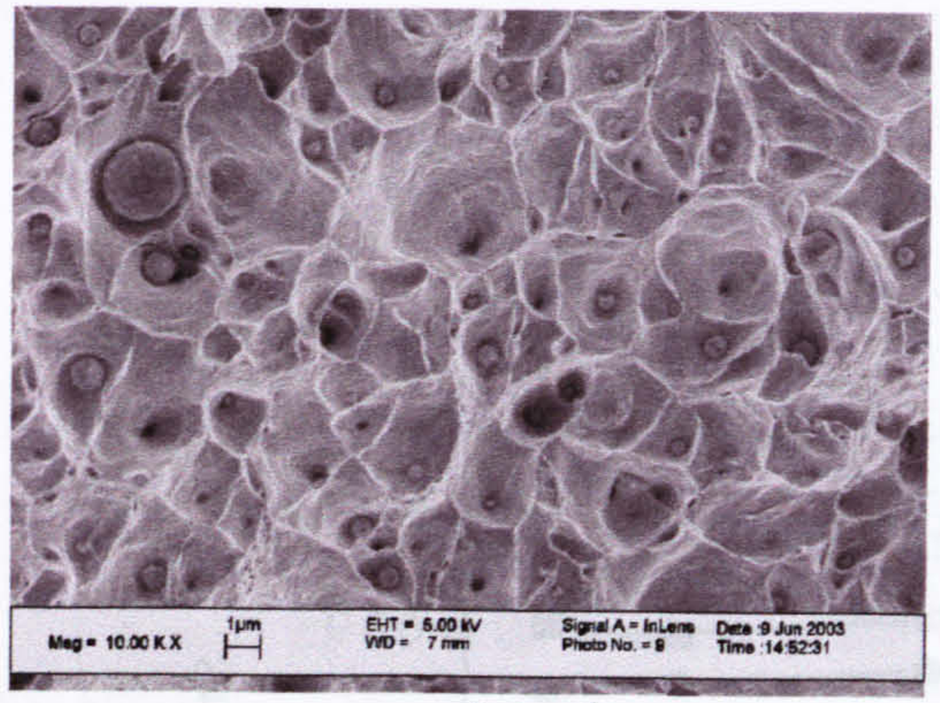

(a)

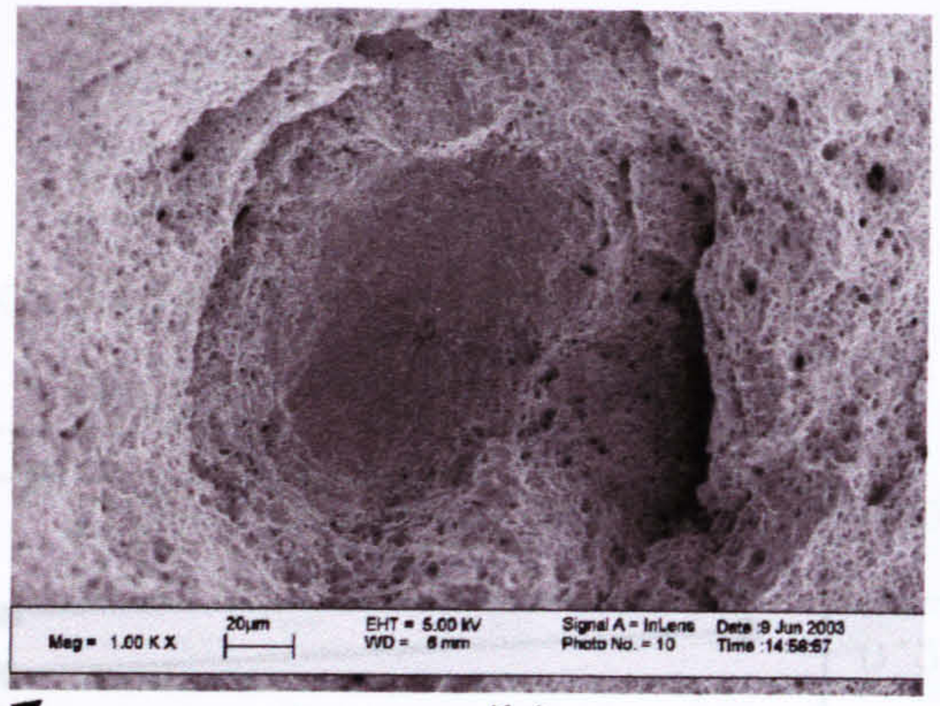

(b)

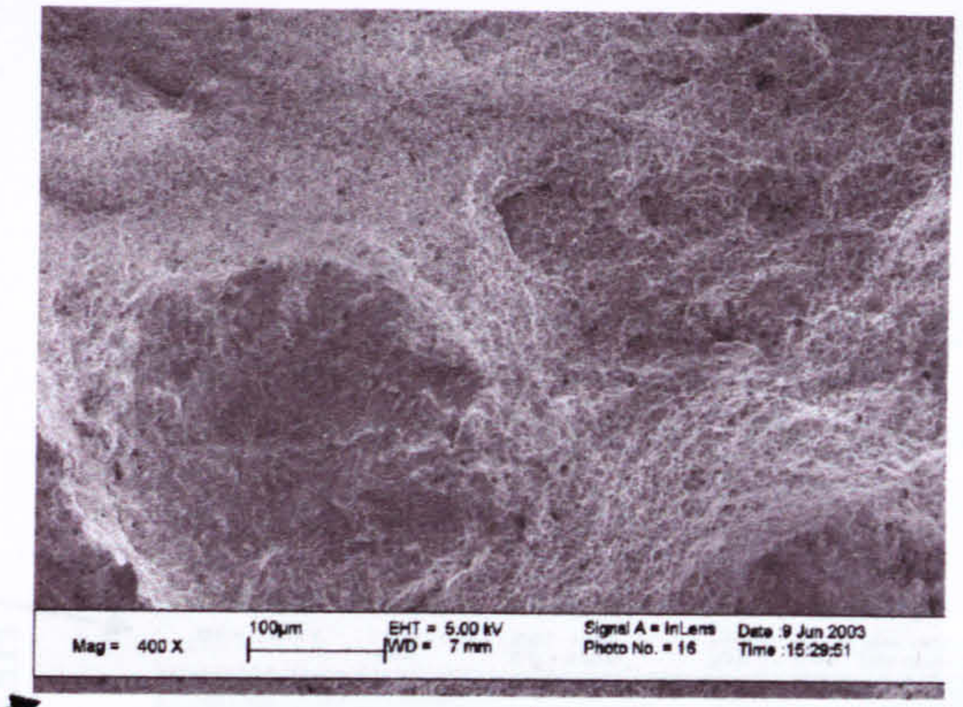

(c)

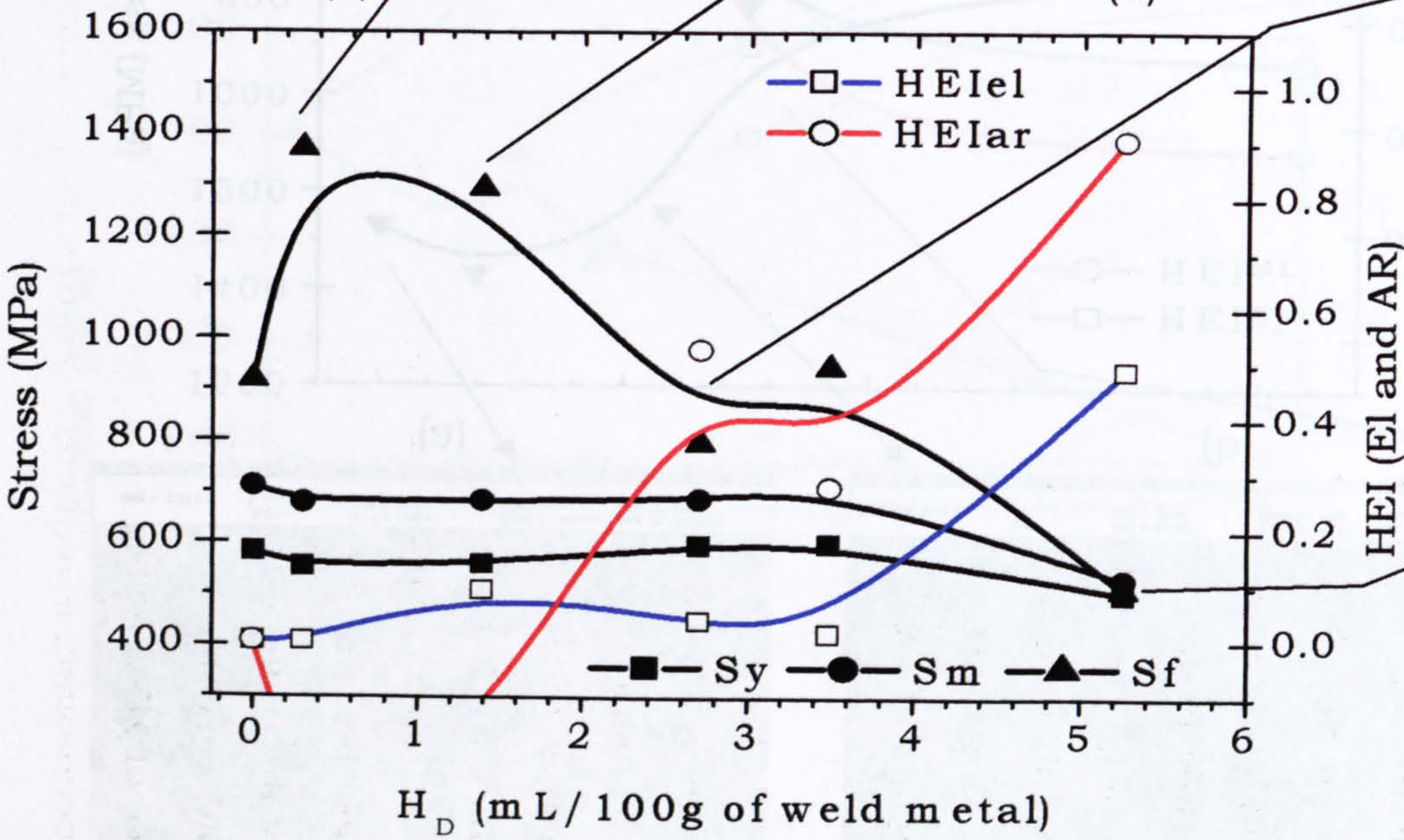

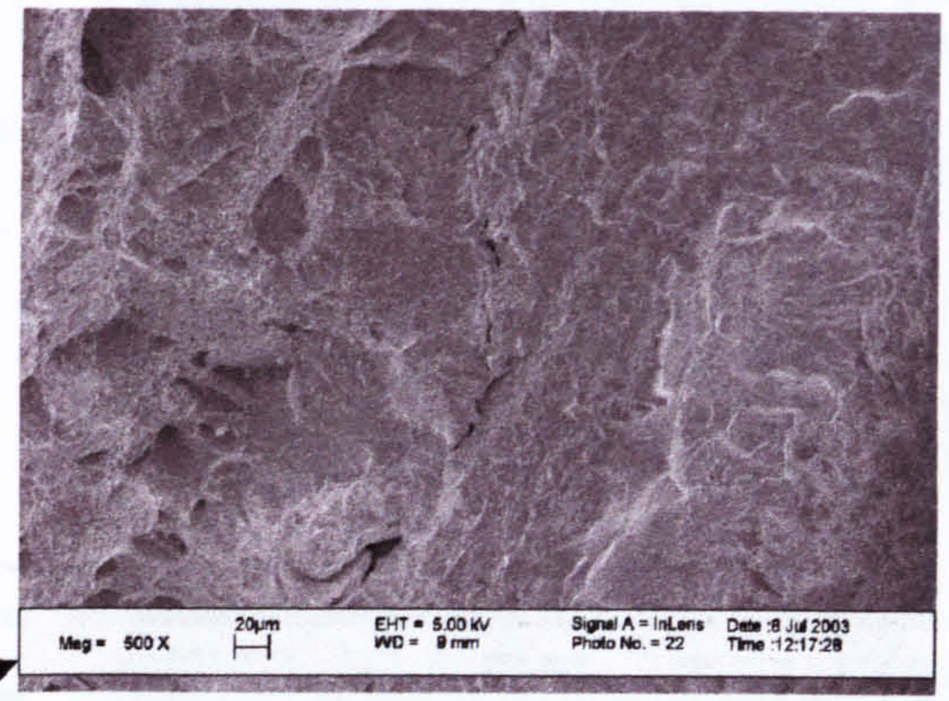

(d)

Figure 8.23 Effect of the diffusible hydrogen content on strength and the fracture surface of the CWX181gb weld metal.

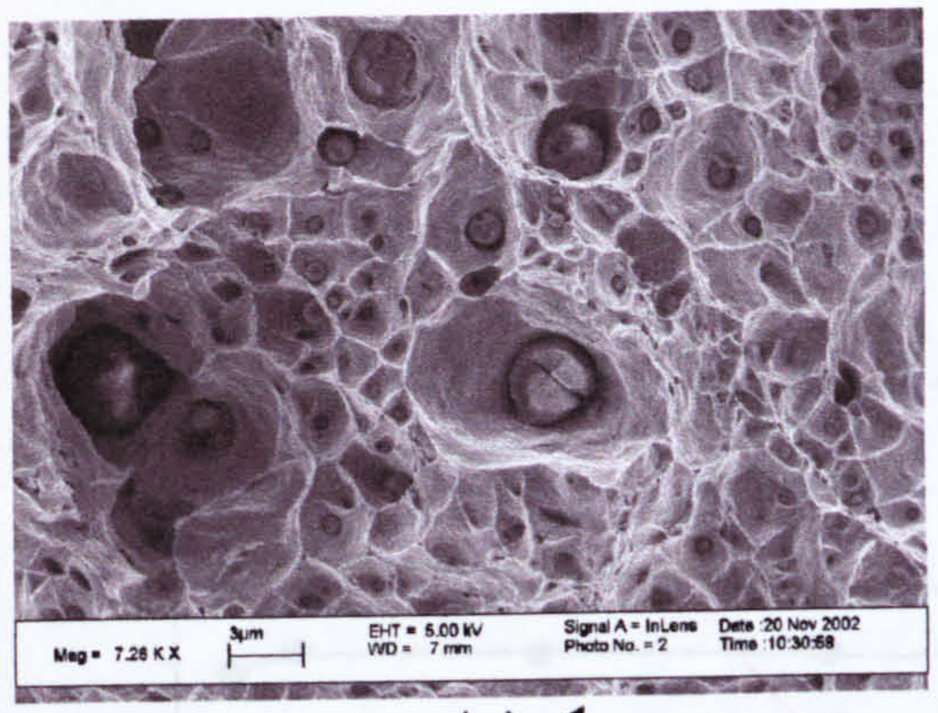

(a)

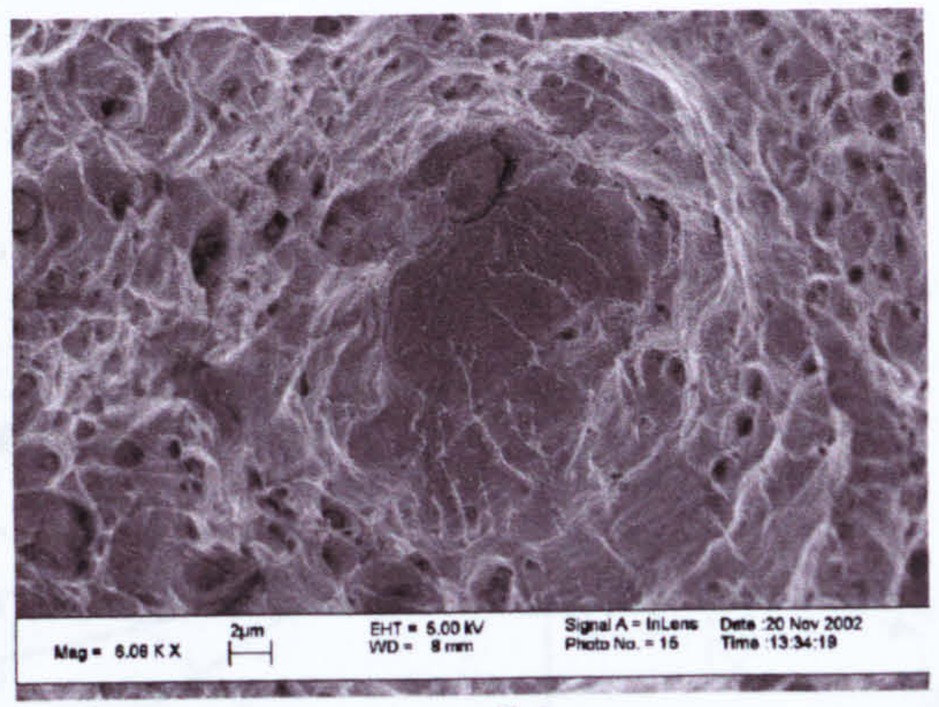

(b)

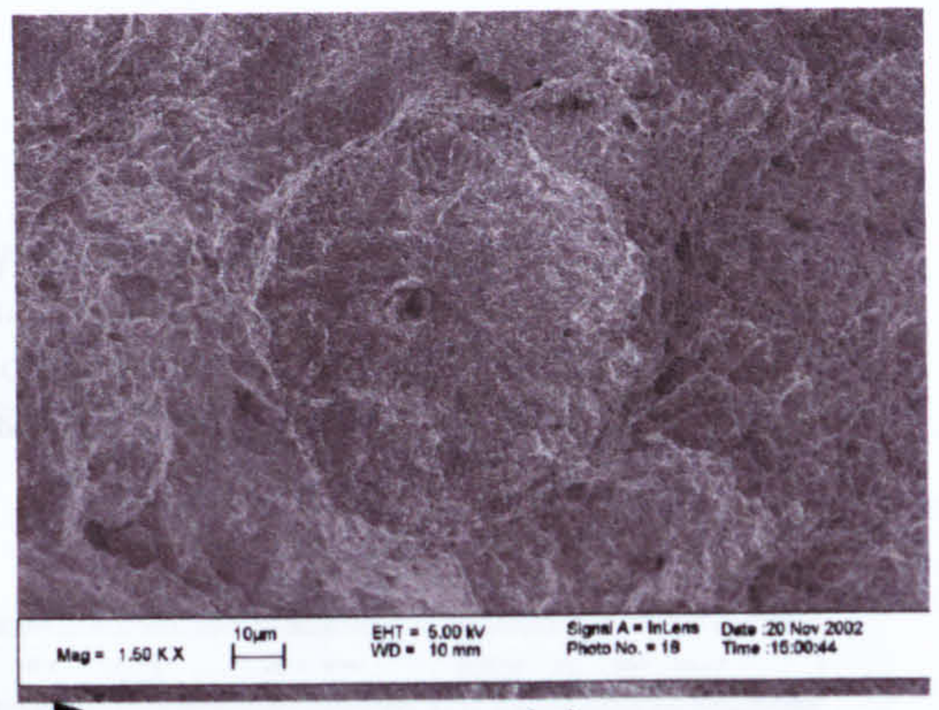

(c)

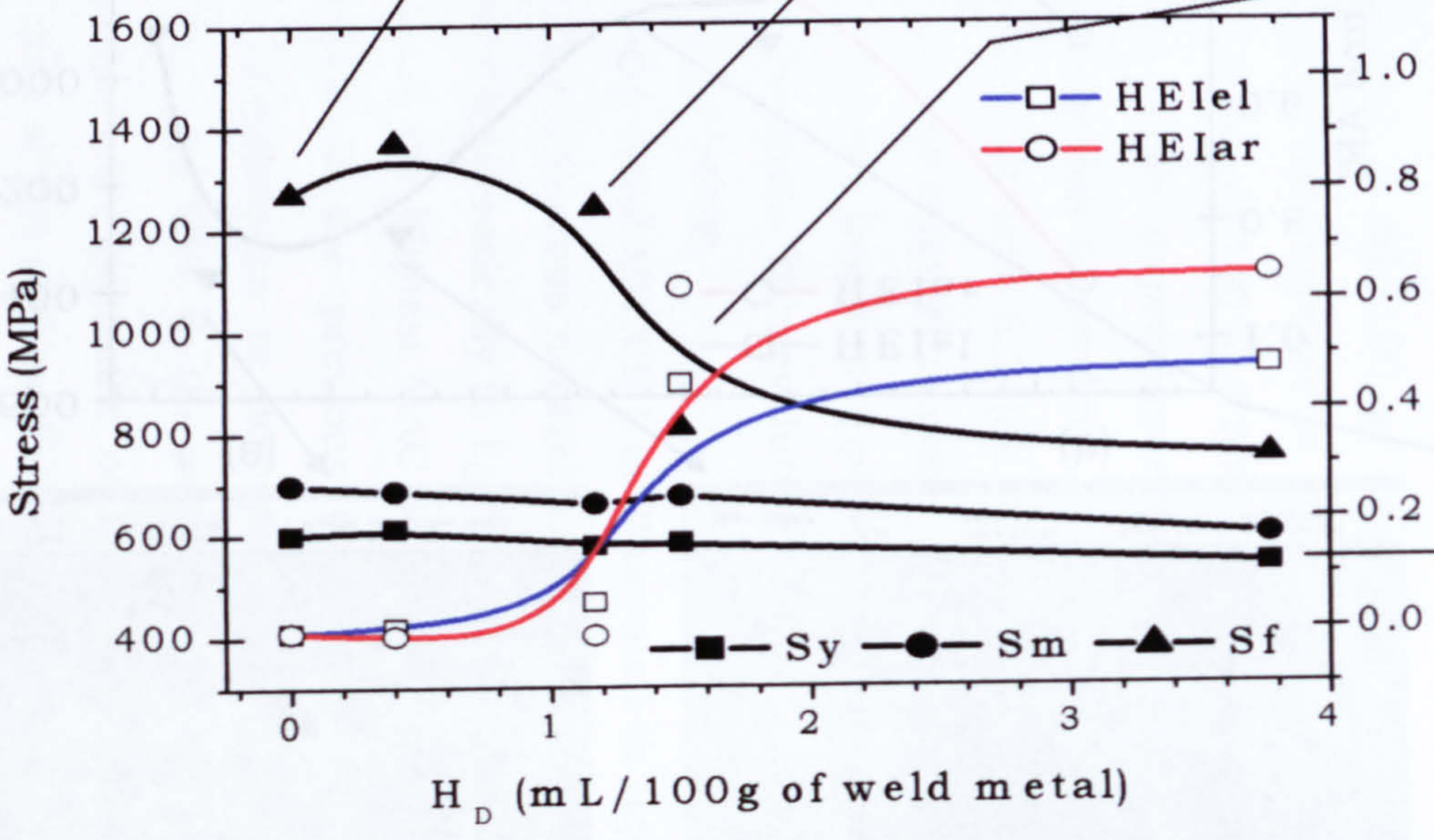

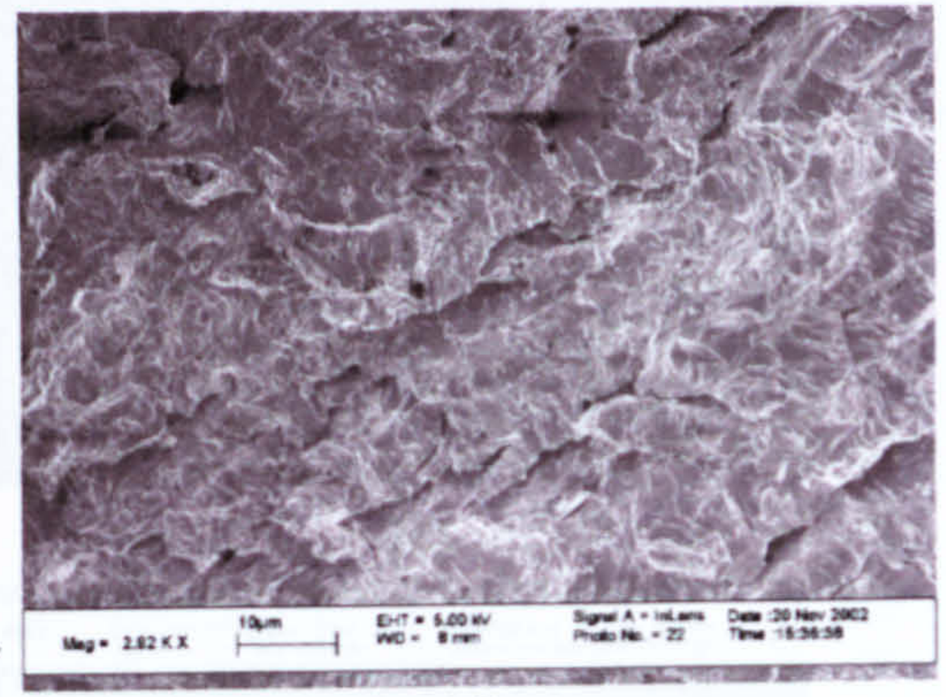

(d)

Figure 8.24 Effect of the diffusible hydrogen content on strength and the fracture surface of the 15171 weld metal.

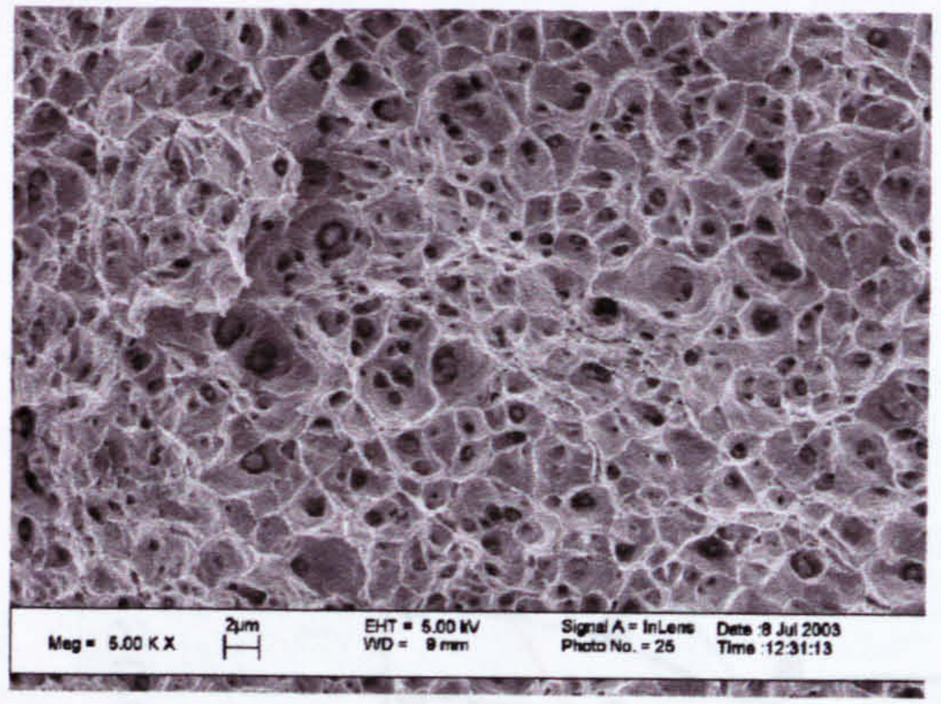

(a)

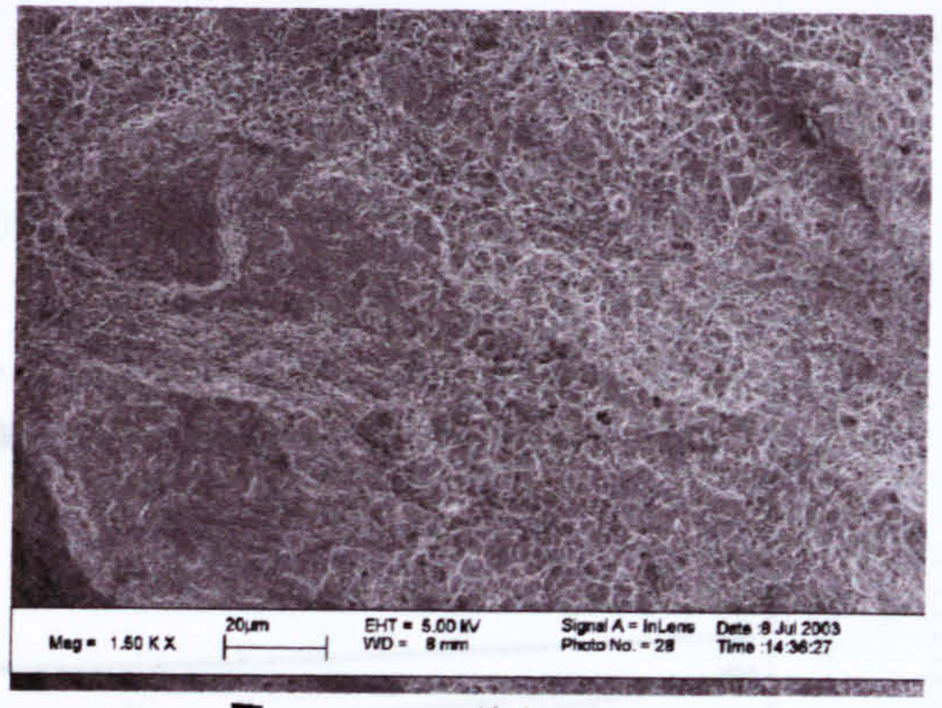

(b)

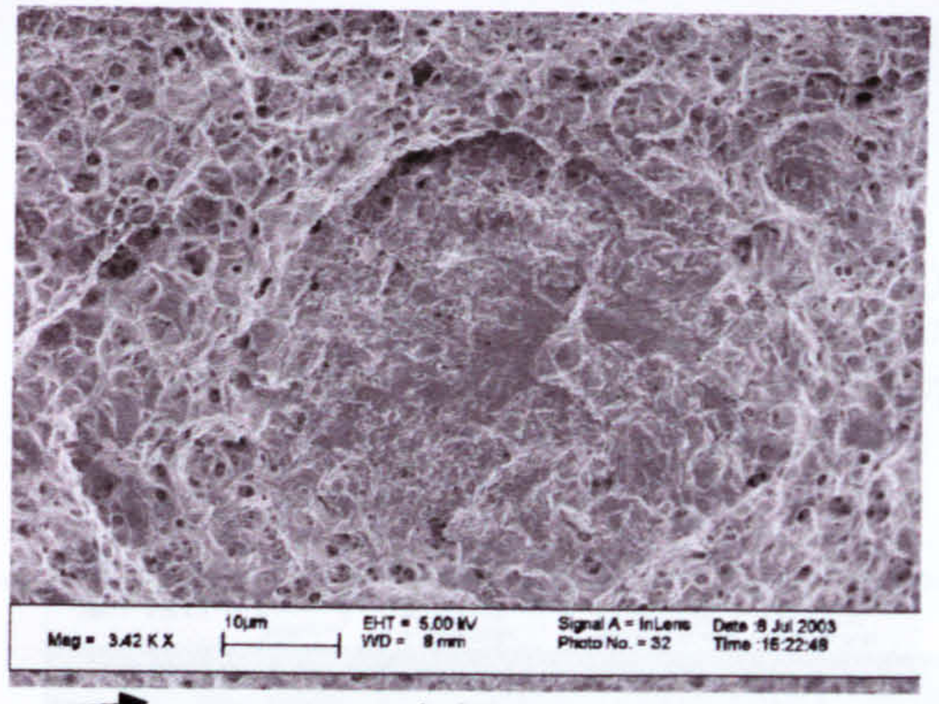

(c)

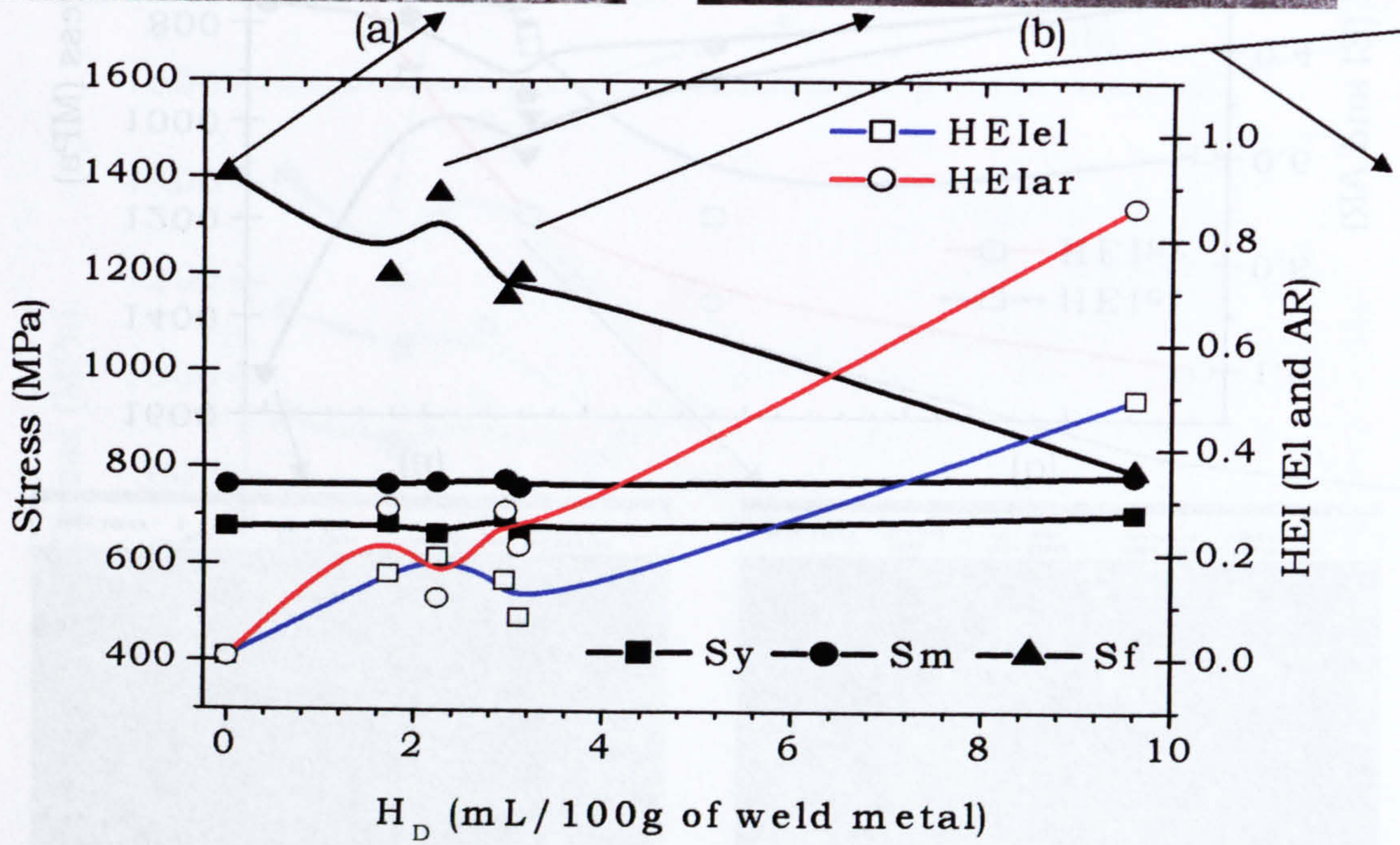

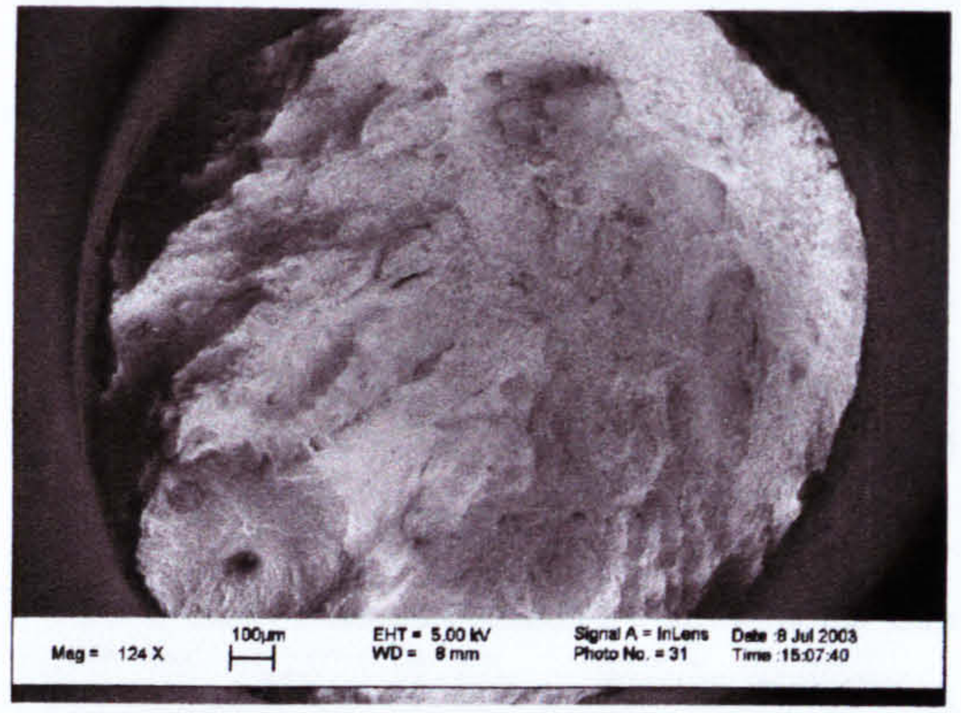

(d)General view

Figure 8.25 Effect of the diffusible hydrogen content on strength and the fracture surface of the CWX361 weld metal.

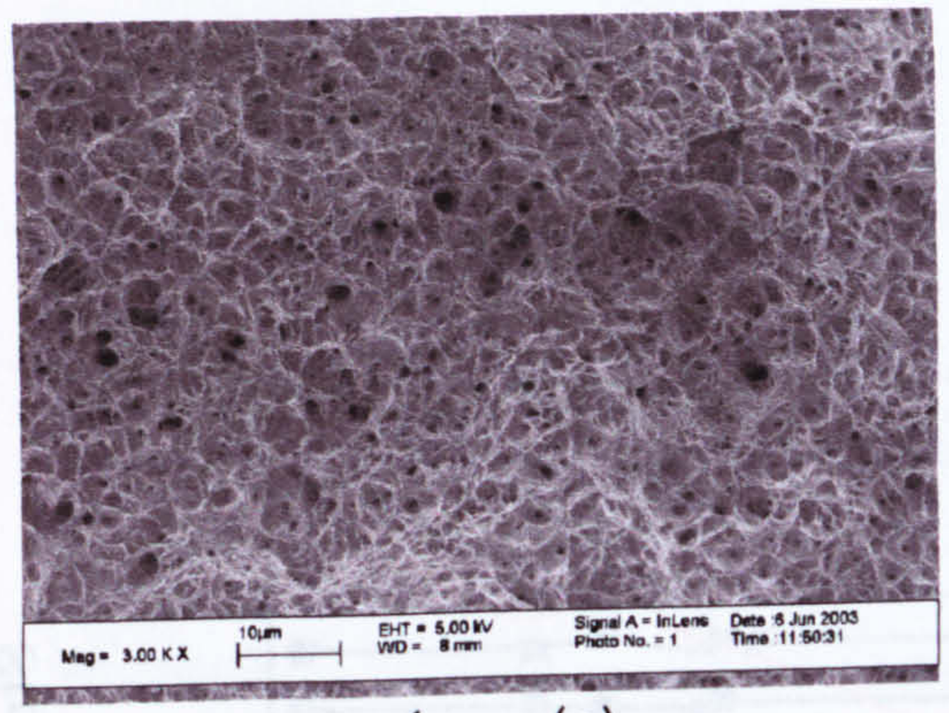

(a)

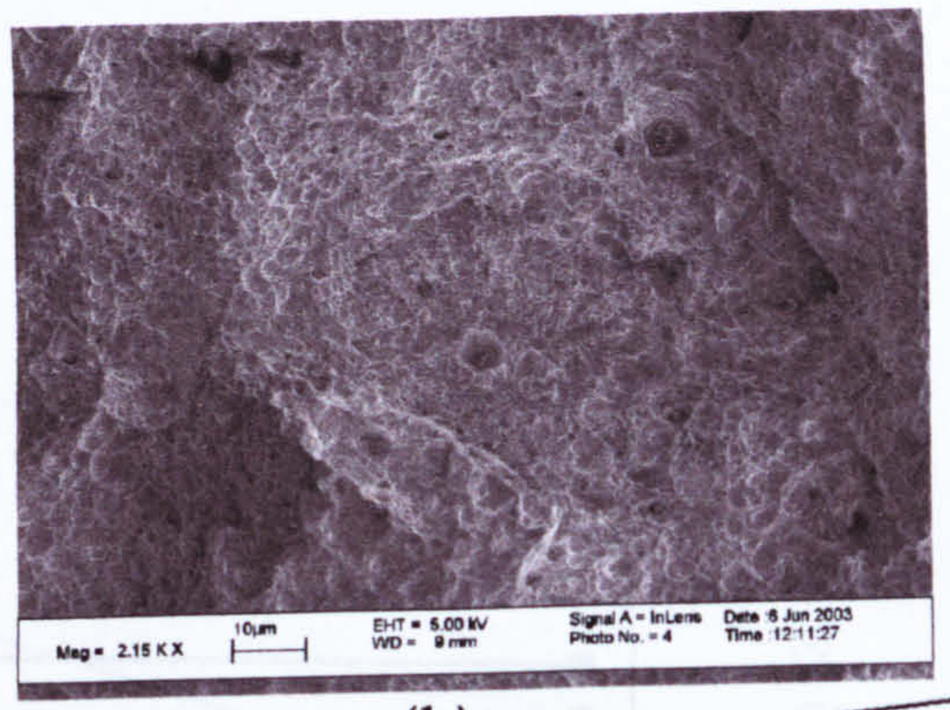

(b)

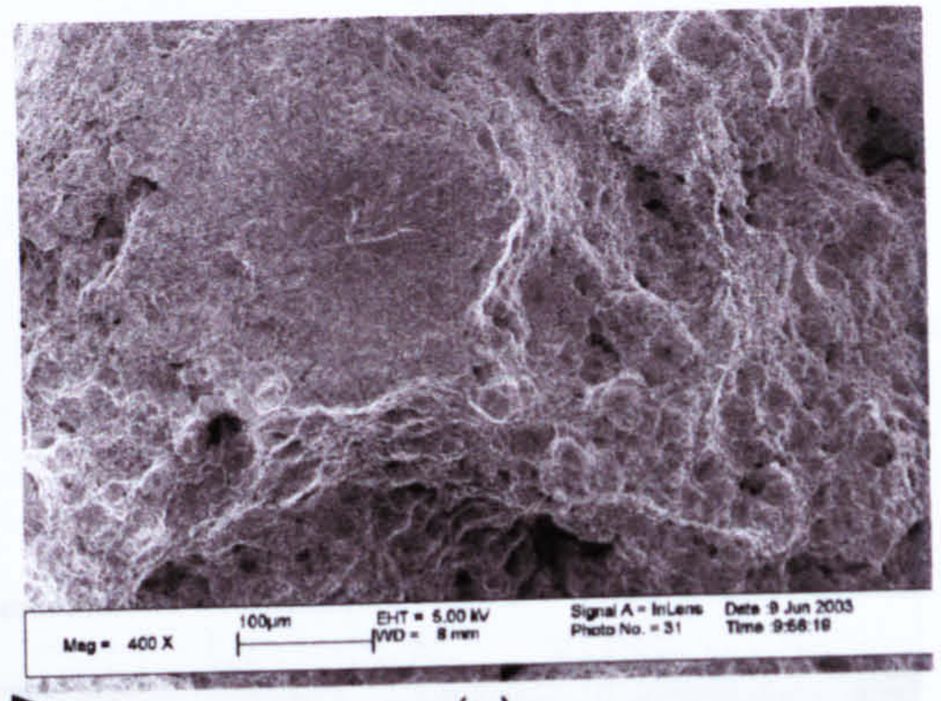

(c)

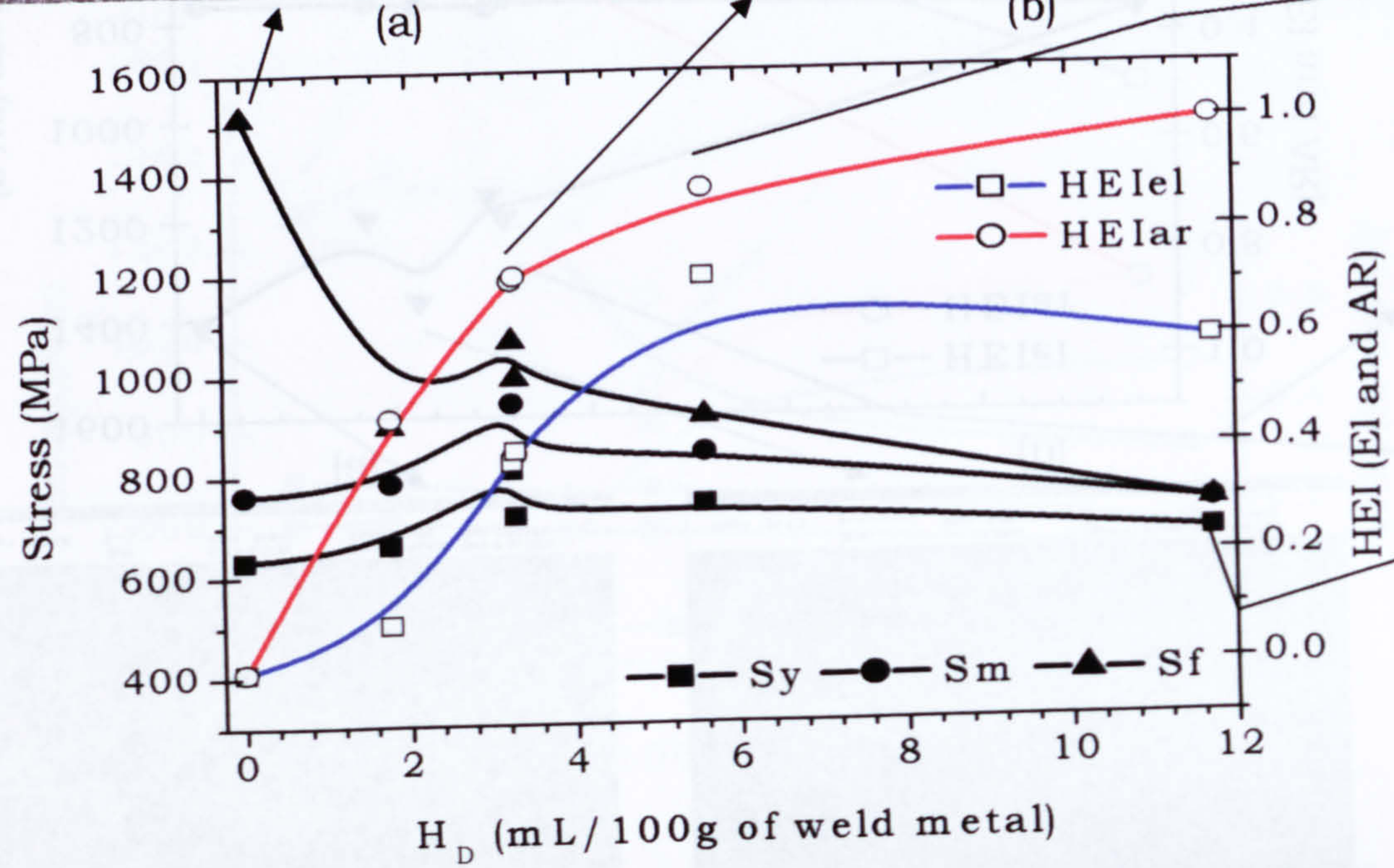

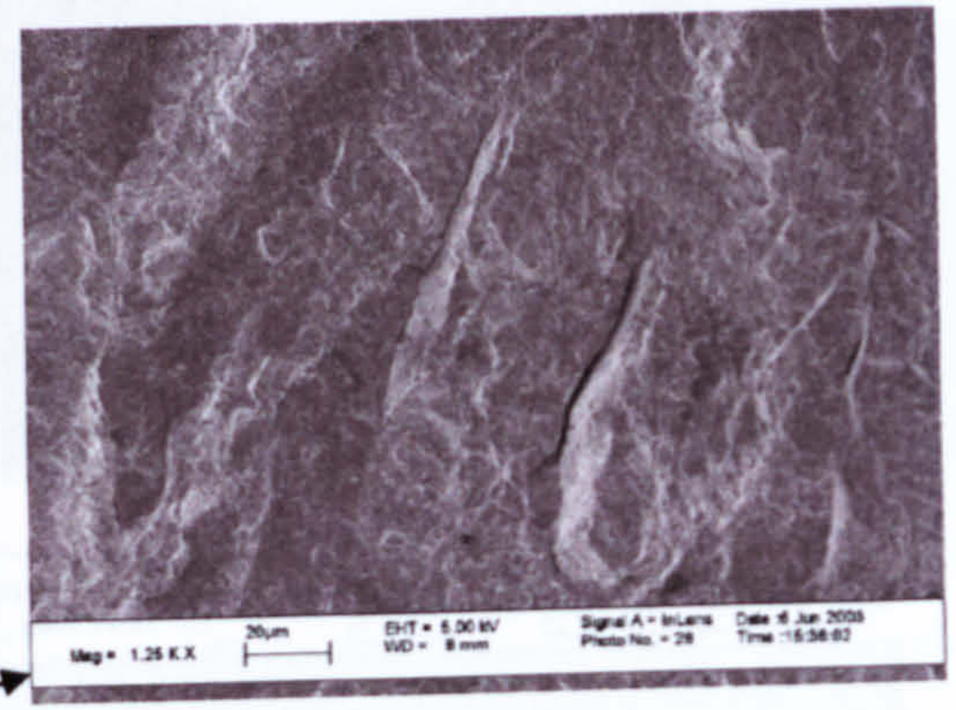

(d)

Figure 8.26 Effect of the difusible hydrogen content on strength and the fracture surface of the CWX201 weld metal.

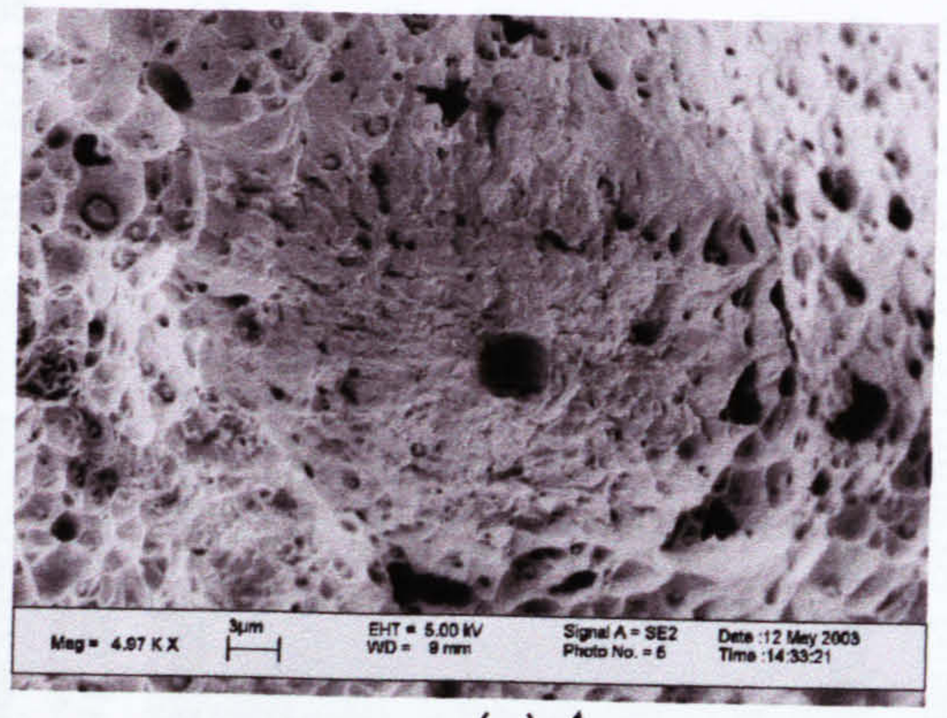

(a)

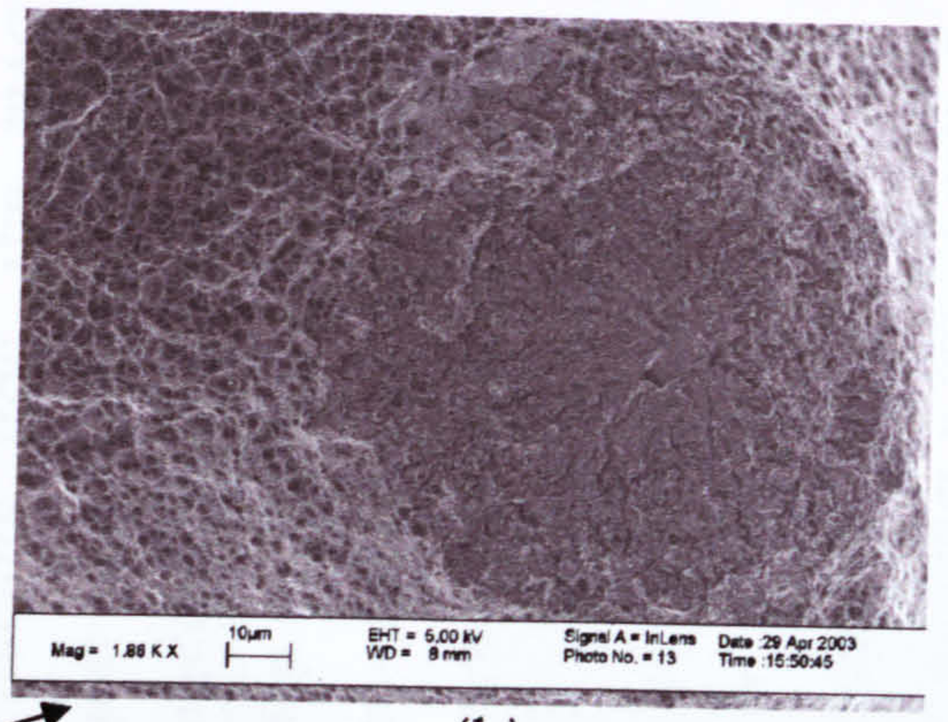

(b)

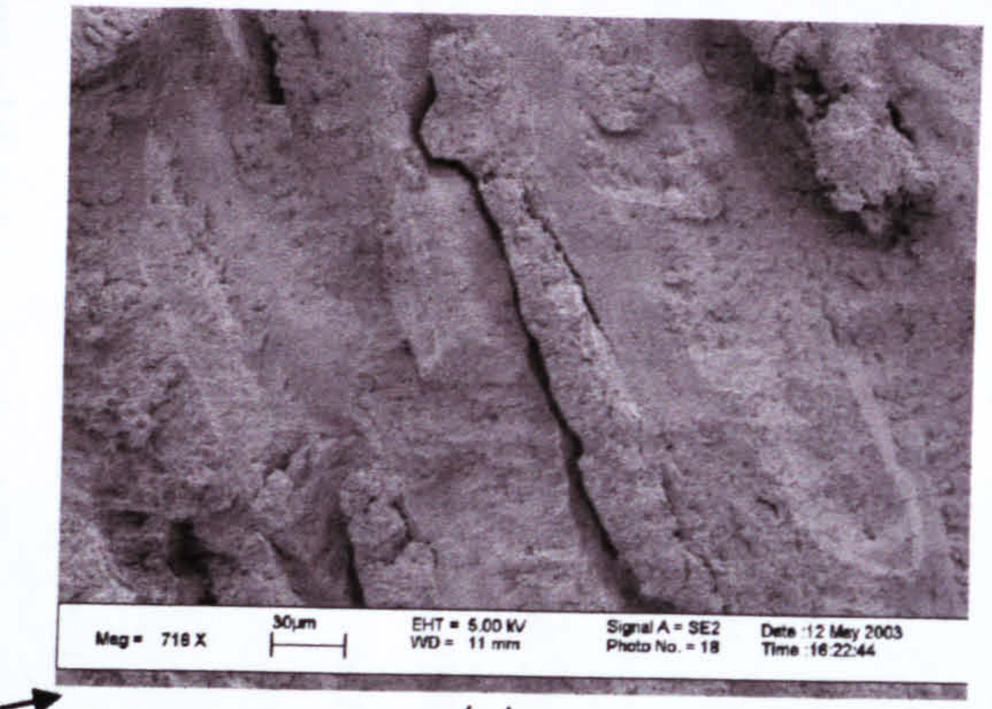

(c)

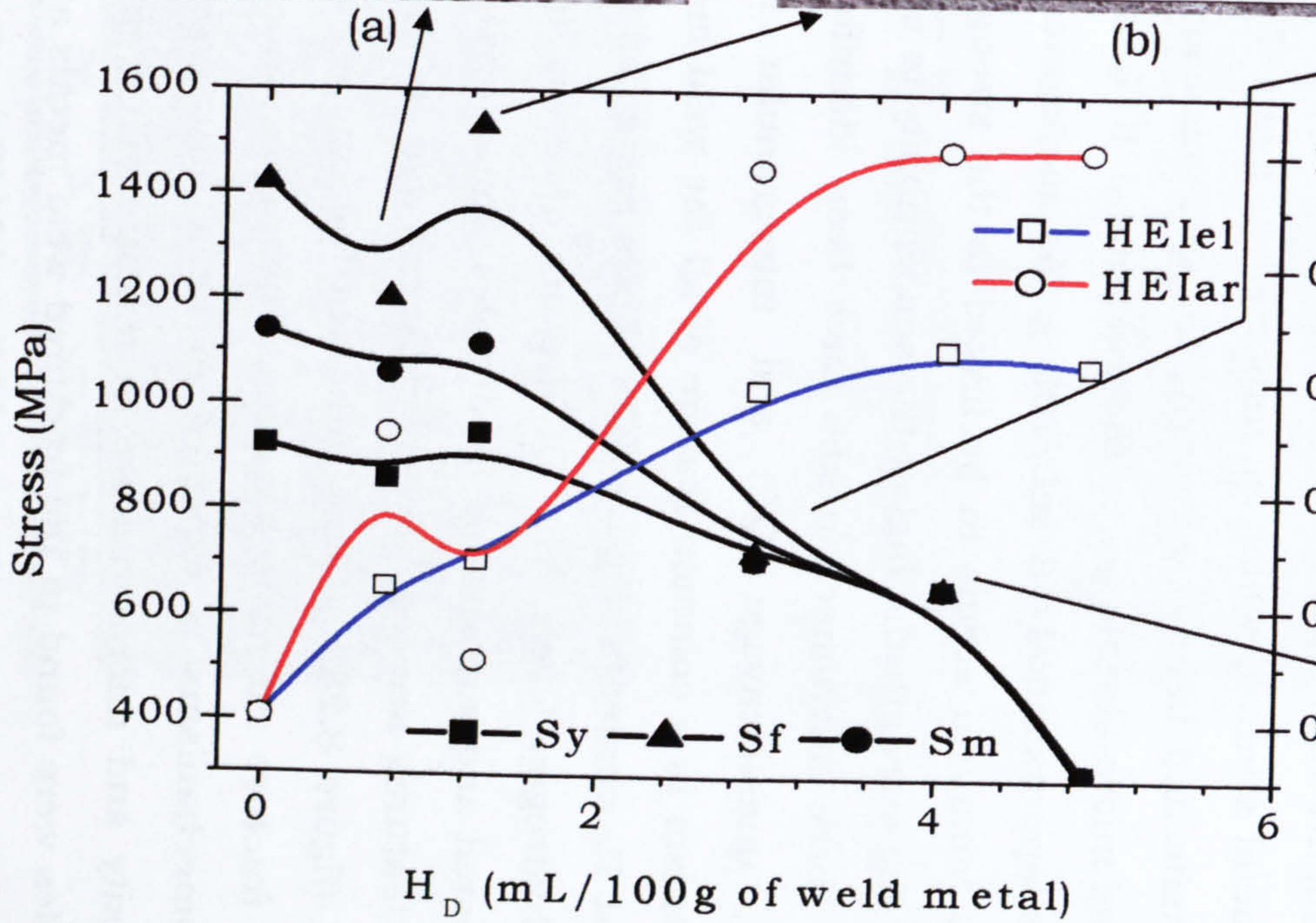

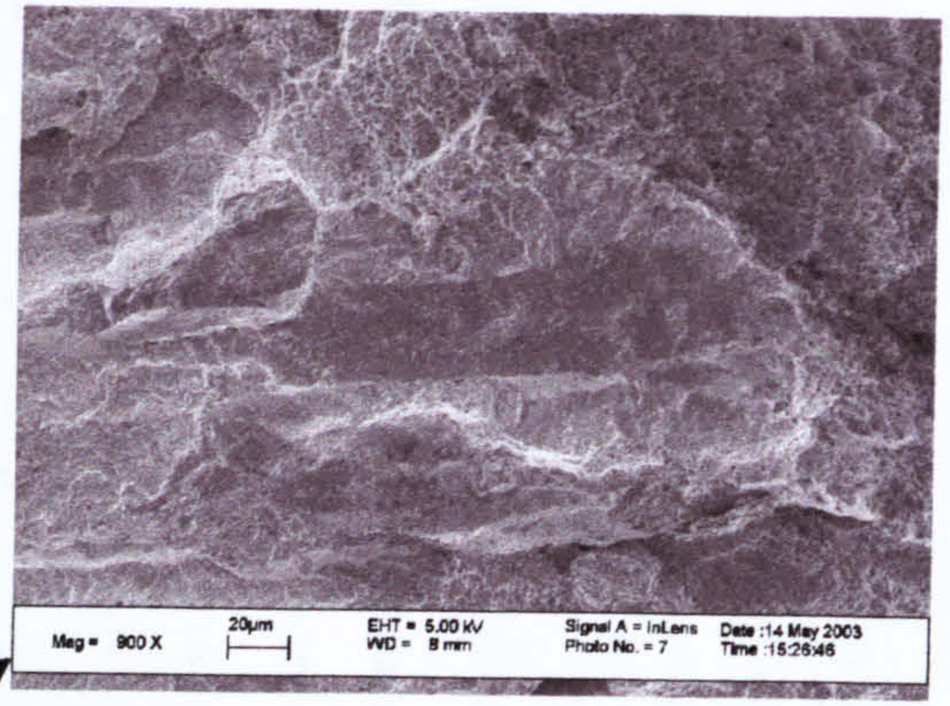

(d)

Figure 8.27 Effect of the difusible hydrogen content on strength and the fracture surface of the CWX331 weld metal.

Figure 8.26 shows the variation of the fracture surface appearance with hydrogen content for the weld metal CWX201, predominantly consisting in coarse acicular ferrite (see figure 7.5(a) and 7.11). As can be noted, similar behaviour to CWX361 is found. The fracture surface changes gradually with H_D content, from being mainly dimpled fracture (MVC) to a mixture of QC and MVC features. The QC areas are associated with NMI as before. However, it is found that some of these brittle regions are linked with what seems to be micro-shrinkage cavities, which was discussed in previous section. Another difference on the fracture surface appearance of the weld metal CWX201, in contrast to previous welds, is that at high hydrogen levels (5.58-11.72 mL/ 100 g) there is evidence for intergranular fracture (figure 8.26(d)). These regions of IG fracture are not general on the surface, but remain localised. This may indicate that for previous cases (CWX181, 15171 and CWX361) the critical hydrogen content to induce IG fracture is higher than for this case. In other words, the increase in strength of the material can make it susceptible to the hydrogen induced IG fracture at lower hydrogen levels.

Figure 8.27 shows the behaviour of weld metal CWX331, the strongest weld metal studied, which as indicated in figure 7.11, contains a mixture of martensite and bainite. Similarly, the quasicleavage fracture is originated at NMI and micro-shrinkages in the weld metal. IG fracture occurs at H_D levels as low as approximately 3 mL/100 g. As mentioned before, the IG fracture micromechanism seems to be linked to the strength of the weld metal, the higher the strength the higher the susceptibility to intergranular fracture.

Three micromechanisms have been identified: microvoid coalescence (MVC), quasicleavage (QC) and intergranular fracture (IG). The MVC mechanism is a common feature of all the weld metal examined even at the highest H_D contents. Figure 8.28 shows examples for CWX181 and 15171 at high hydrogen levels. The QC feature observed in figure 8.28(a) has been delineated and surrounded by dimples characteristic of the MVC. In contrast, such features are less clearly differentiated in the case of the 15171 weld metal (figure 8.28(b)). This indicates the competition between both QC and MVC fracture micromechanisms. The appearance of one or both of these micromechanisms is expected to be a function of: hydrogen level, stress intensity and microstructure. A mixture of QC facets surrounded by MVC dimples were found in the fractured weld metals at different hydrogen levels. Figure 8.29 shows a mixture of QC and MVC fracture modes at 2.95 mL/100 g of diffusible hydrogen.

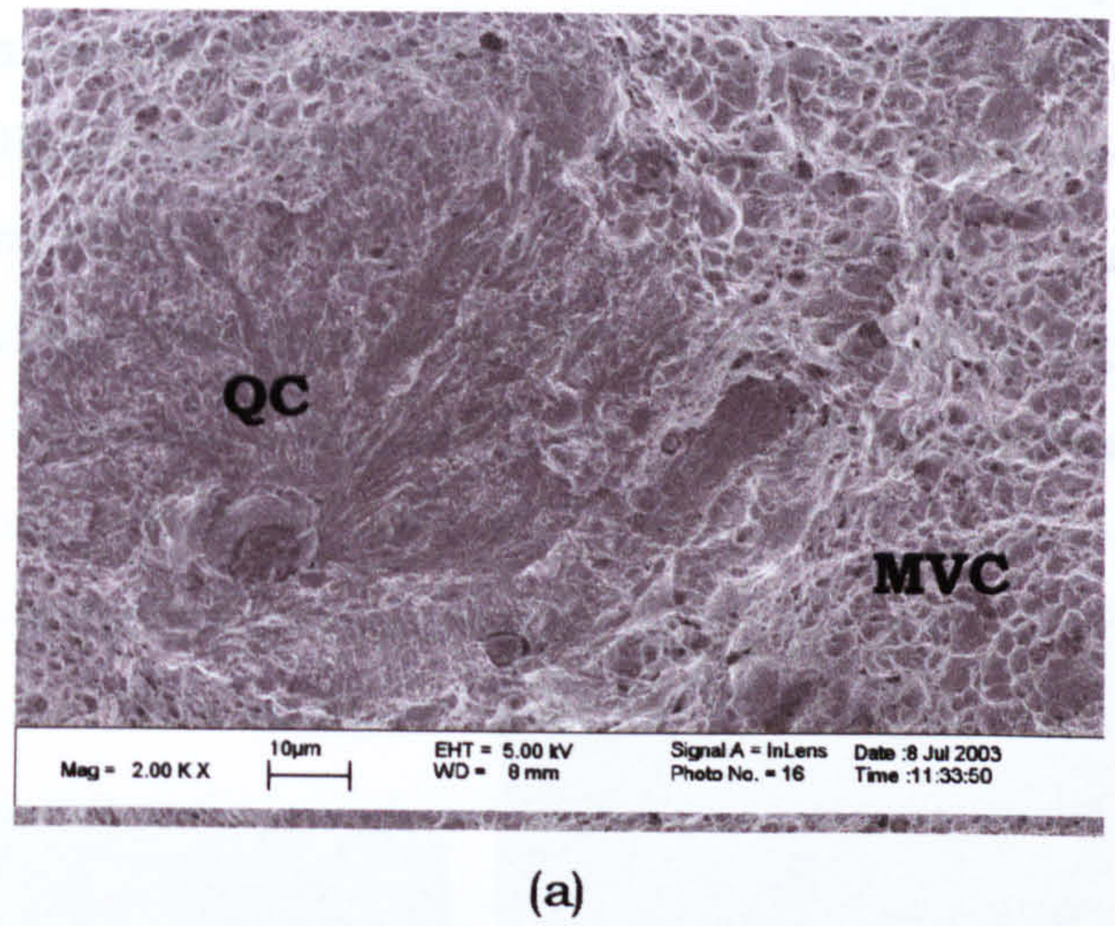

(a)

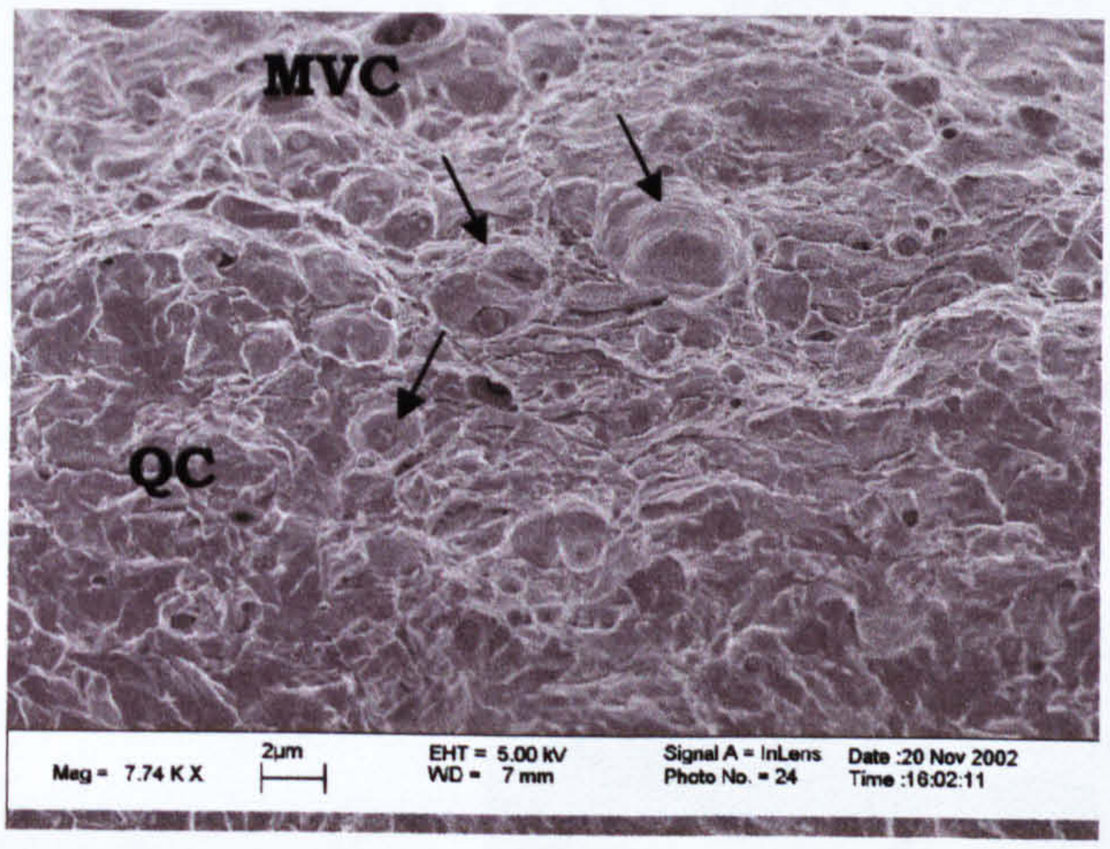

(b)

Figure 8.28 Fracture surface for the highest hydrogen content present in the weld metals where it is observed the mixture of QC and MVC micromechanisms: (a) CWX181 (5.26 mL/100 g) and (b) 15171 (3.77 mL/100 g). Arrows show isolated dimples.

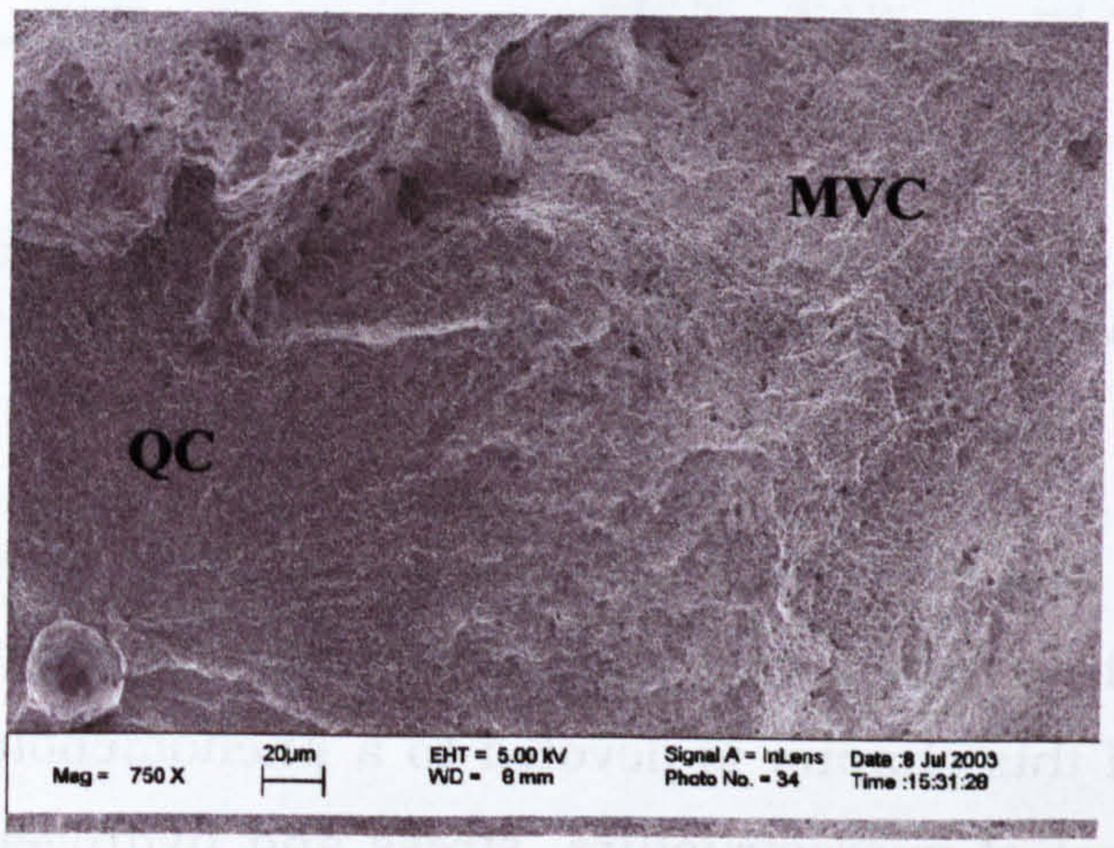

Figure 8.29 Fracture surface of the CWX361 weld metal with 2.95 mL/100 g of diffusible hydrogen, showing mixture of QC and MVC fracture micromechanism.

Figure 8.30 presents the IG fracture noted for weld metals CWX201 and CWX331. In both cases, the shape of the columnar grains present in the weld metal can be appreciated. In the case of the CWX201, the IG fracture is only noted between the columnar grains, but the QC fracture dominates the surface. On the other hand, in the case of the CWX331, the IG fracture extension covers several grains.

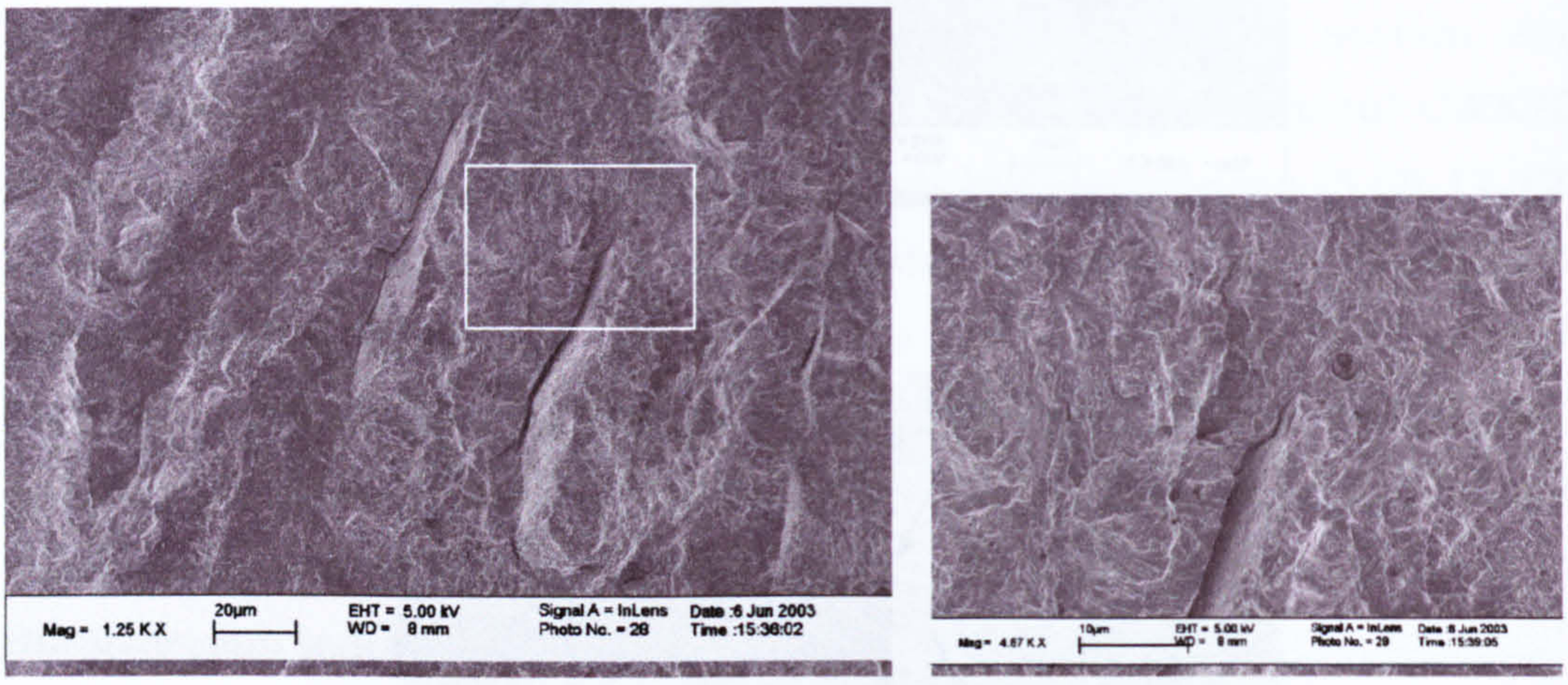

Figure 8.30 IG fracture found in two weld metals at high hydrogen content: (a) and (b) CWX201 (5.58 mL/100 g); (c) and (d) CWX331 (4.88 mL/100 g).

It is clear that there is a continuous spectrum of change in fracture appearance which is linked with microstructure and hydrogen content. The remaining part of this chapter is devoted to a phenomenological model which describes the effect of microstructure, stress and hydrogen content on these changes in fracture micromechanisms.

8.4 A phenomenological model describing the changes in micromechanism of fracture due to the combination of stress intensity factors and hydrogen content.

The first attempt to present a diagram which linked the stress intensity factor and the hydrogen content with fracture micromechanism (IG, QC and MVC) for steels under SCC or HAC conditions was proposed by Beachem [71]. Figure 4.11 in chapter 4 shows schematically this diagram and some examples were discussed there. One suggestion of the diagram is that the three fracture micromechanisms can occur at whichever hydrogen level and stress. Evidence in this investigation and others shows this is not totally true. Pyun and collaborators [177, 178] proposed a modification of the Beachem's diagram based on a theoretical model for the transition of fracture micromechanisms for hydrogen assisted intergranular cracking of high strength steels. The diagram is shown schematically in annexe A.23. The model predicts the occurrence of MVC at low hydrogen levels but QC fracture mode is not taken into account. Gerberich et.al. [163- 165] and other investigators [179-181], presented experimental evidence of the appearance of QC facets at certain hydrogen content or stress condition.

Based on the fractographic observations in this investigation, and the previous studies mentioned above a modified model for hydrogen assisted cracking is proposed. This model modifies the Beachem's diagram and completes, adding the QC curve to it, the Pyun's proposal. The reasons for the modification are detailed in the following paragraph:

1- Experimental fractographic evidence of hydrogen charged weld metals demonstrates that MVC mechanisms is predominant or only observed when the weld metal is not charged with hydrogen and at very low hydrogen content. Beachem's diagram predicts the formation of the three modes: MVC, QC and IG fractures even at low hydrogen levels. As a consequence, a threshold stress for the occurrence of ductile fracture (MVC) should appear at low hydrogen contents. This region was suggested by Pyun et. al. [177-178].

2- At low hydrogen content, IG fracture evidence is not observed. Beachem's diagram predicts the appearance of this fracture mode. Pyun et. al. [177-178] suggests that at low hydrogen concentration the

threshold stress necessary to cause IG fracture is so high that it is difficult to occur.

3- Quasicleavage fracture is observed at low hydrogen content. In the case of the QC facets found in the weld metals charged at a low hydrogen level, these are generally associated with stress raisers such as NMI and/or coarse precipitates. As a consequence, a threshold stress intensity factor for QC fracture (K_{QC}) higher than that for MVC (K_{MVC}) is expected. It is proposed that this K_{QC} value for low hydrogen content could be between the threshold stress intensity for IG fracture (K_{IG}) and that for MVC, K_{MVC}.

4- The hydrogen content of the weld metals affects their K value. Several investigations [177-181] have reported experimental evidence for the reduction of the threshold stress intensity factor caused by hydrogen content. Beachem's diagram shows this effect for each fracture mode, but the author supposed that the failure of the steels occurs at a constant K_C, the critical stress intensity factor for fracture, which is not affected by hydrogen. In the modified diagram, failure is expected to occur at the highest K value depending on hydrogen content and microstructure. An exception could be found at very low hydrogen contents, where K_{IG} is very high and is not reached before fracture of the material by other fracture micromechanisms occurs.

Figure 8.31 presents the changes to Pyun[177-178] original diagrams. As in the original diagram the vertical axis gives the threshold stress intensity factor and the horizontal axis hydrogen content. The diagram now shows the variation of the threshold stress for each type of fracture micromechanism that could be found in hydrogen induced cracking of steels weld metals: microvoids coalescence (MVC), quasicleavage (QC) and intergranular (IG). Hydrogen content reduces the K values for each fracture type. The diagram allows an explanation for the changes in micromechanisms of fracture with hydrogen and stress intensity factor:

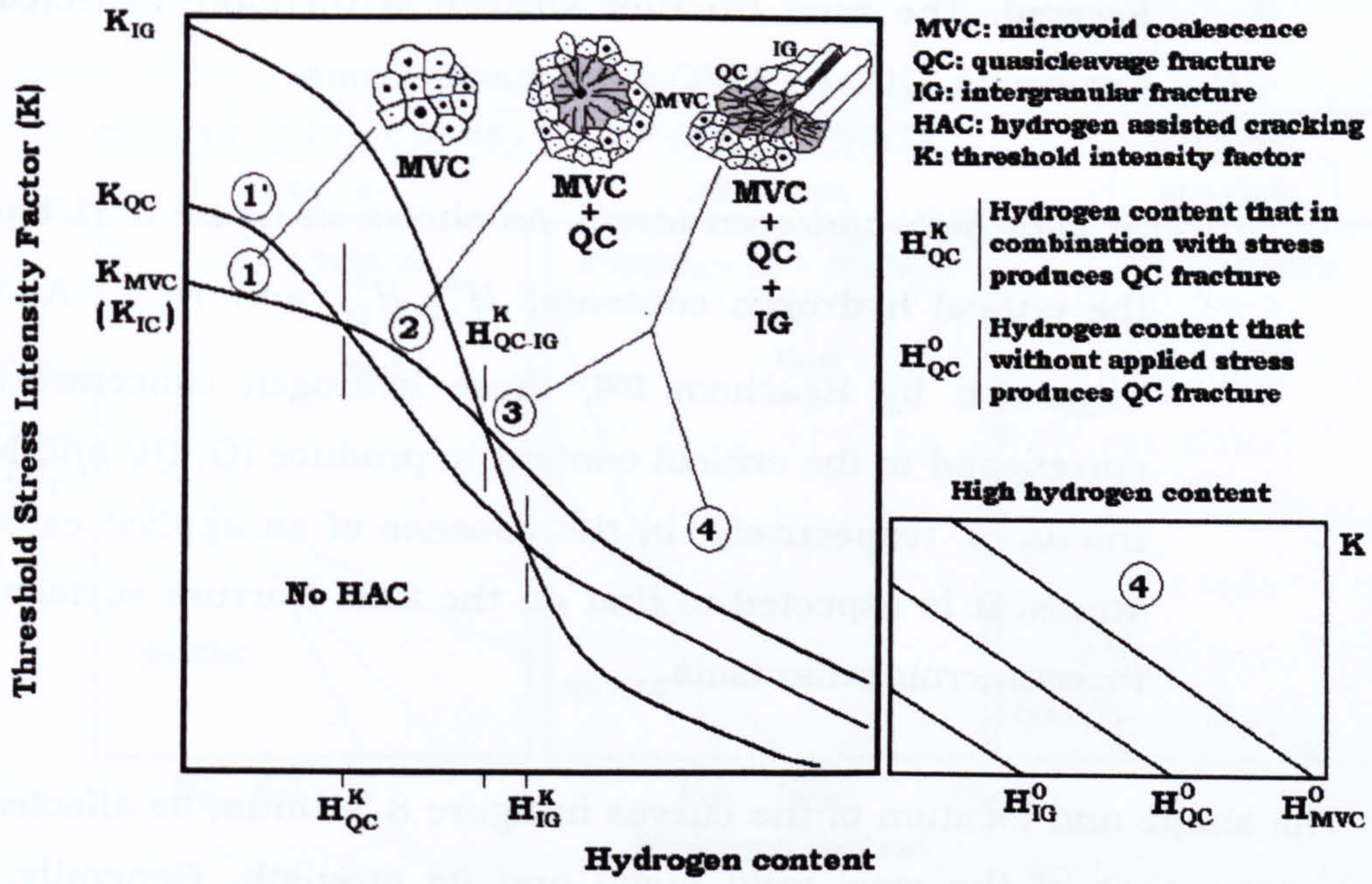

Figure 8.31 Schematic diagram that represent the effect of the threshold stress intensity factor (K) and the hydrogen content on the fracture micromechanisms. The Pyun's diagram [177-178] was completed by the addition of the curve for QC micromechanism, which is based on the fractographic evidence obtained in this investigation.

a- *At low hydrogen content region (H content < H^K_{QC}).* In samples without hydrogen or low hydrogen content the fracture micromechanism expected is MVC. In this region only high stress intensity factor could produce QC fracture. For example, in high strength steels with some microcracks or a fractured hard particle could reach locally the K level to triggers QC or cleavage fracture. In softer steels the microcracks are expected to blunt reducing the stress concentration at the tip, favouring the MVC mechanisms.

b- *At hydrogen levels between H^K_{QC} and H^K_{QC-IG}.* The K_{QC} is lower than the K_{MVC} and for this reason the quasicleavage micromechanism is promoted. The increase in K due to the growth of the brittle crack under load, favoured the formation and growth of dimples. QC facets surrounded by dimples could form the final fracture surface.

c- *At hydrogen levels above H^K_{QC-IG} and H^K_{IG}.* At these higher levels, the threshold stress intensity to produce IG fracture is

lowered. The final fracture surface is therefore expected to involve IG, QC and MVC micromechanisms.

d- *At very high hydrogen levels.* As shown in figure 8.31 shows the critical hydrogen contents: H^0_{IG}, H^0_{QC} and H^0_{MVC}. As was suggested by Beachem [72], these hydrogen concentrations correspond to the critical content to produce IG, QC and MVC fractures, respectively, in the absence of an applied external stress. It is expected to find on the final fracture surface the three micromechanisms.

The shape and location of the curves in figure 8.31 must be affected by the microstructure of the steel weld metal and its strength. Generally, the higher the strength of the weld metal the lower the threshold stress intensity factor for the occurrence of fracture. Figure 8.32 shows, schematically, this trend for the weld metals studied. These diagrams for each group of weld metals are based on the proposed model in figure 8.31 and takes into account experimental observations. For example, the IG fracture mechanism has been found to occur at 3 mL/100 g of hydrogen for the weld metal CWX331, the strongest of the weld metals. At same level of hydrogen, none of the weld metals shown in figures 8.23 to 8.26 (CWX181, 15711, CWX361 and CWX201, respectively) and other not shown (14001and VCX2561), suffer IG fracture. IG fracture was appreciably observed for weld metal CWX201 when its hydrogen content was around 5.58 mL/100 g. These observation suggest, as can be observed in figure 8.32, that for weld metals with low strength (S_y<450 MPa) the critical hydrogen/stress intensity factor for IG mode are expected to be higher than for stronger weld metals. For the case of weld metal CWX201 the critical hydrogen content for IG fracture might be around and 5.58 mL/100 g, where the initiation of IG fracture was observed. In contrast, for the CWX331, this critical hydrogen level is between 1.2 and 3 mL/100 g, considerably lesser than CWX201.

In regard to the hydrogen critical levels to induce QC fracture it was more difficult to estimate for the weld metals studied because the hydrogen content increments were, in some of the cases, sufficiently large to produce changes on the fracture surface but not conveniently fine to detect the initiation of changes. In addition to this, the QC initiation, as was discussed in previous section, is dependent upon the hydrogen accumulation. This means

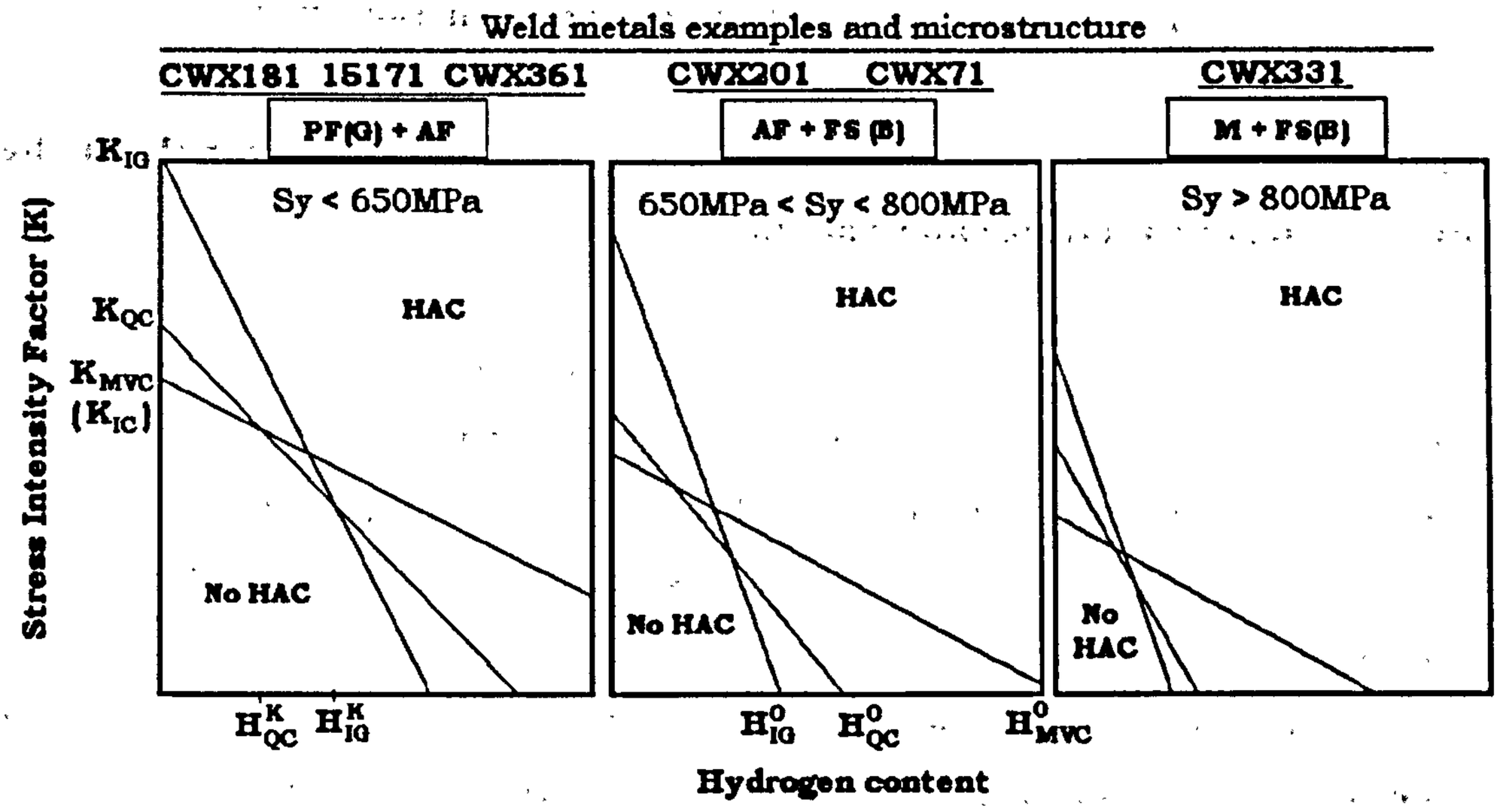

Figure 8.32. Schematic representation of the effect of microstructure, mechanical properties and hydrogen content on the hydrogen induced cracking (HAC) of the weld metals. On the top of each figure is shown the microstructural features and examples of the most representative weld metals. The strength, represented by S_y, the yield stress.

that the measured diffusible hydrogen does not reflect the hydrogen level which is locally accumulated. Small isolated and very few QC facets were observed on the fracture surface of weld metal 15171 at hydrogen levels between 0.4 and 1.17 mL/100 g, mostly associated with large inclusions. In weld metal CWX181 was not found evidence of QC at 0.3 mL/100 g. However, for the case of CWX331, several QC facets were observed on the surface at 0.73 mL/100 g of hydrogen, which were related to micro-cavities and NMI. Other experimental observations indicate that the QC facets became more appreciable, i. e., their numbers increase, at hydrogen levels that seem to be lower for weld metals with higher strength. For example, in the case of the weld metal CWX181, the QC facets are appreciable at around 2.7 mL/100 g, approximately 1.5 mL/100 g for 15171; around 1.0 mL/100 g for VCX2561, probably below 1.77 mL/100 g for CWX201 and 0.73 mL/100 g for CWX331. The order in which these weld metals are sorted correspond to an increase in strength (see figure 8.1).

The figure 8.32 summarises a possible effect of strength and microstructure on the hydrogen induced cracking. As expected and confirmed by the actual experimental observations, the figure indicates that the higher the strength the greater the susceptibility of the steel weld metals. Further work is needed to clarify the effect of these important factors over the shift of

the different curves representing the three kinds of fracture micromechanisms and to try to determine the critical levels of hydrogen for each mechanism.

8.5 Effect of hydrogen accumulation or trapping and crack growth on the changes in fracture micromechanisms.

The diagram in figure 8.31 could be used to follow the changes in fracture micromechanism that are found in the weld metals which were charged with different quantities of hydrogen. The hydrogen introduced into the weld metal is likely to be heterogeneously distributed between the various microstructural constituents.

Figure 8.33 presents schematically a transversal view of the fracture surface profile of a weld metal charged with different hydrogen levels. As the hydrogen content increases, the fracture surface shows evidence of changes in fracture micromechanism and this generally is evidenced by the observation of micromechanisms mixtures. As found in steels, it may be possible to find fracture surfaces 100% QC or 100% IG, however, these were not found in this investigation even at very high hydrogen contents (12 mL/100 g). Figure 8.33 shows schematically that brittle fracture is initiated at particular features of the microstructure: NMI (shown in figure for simplicity), cavities and possibly MAC islands depending on the applied stress.

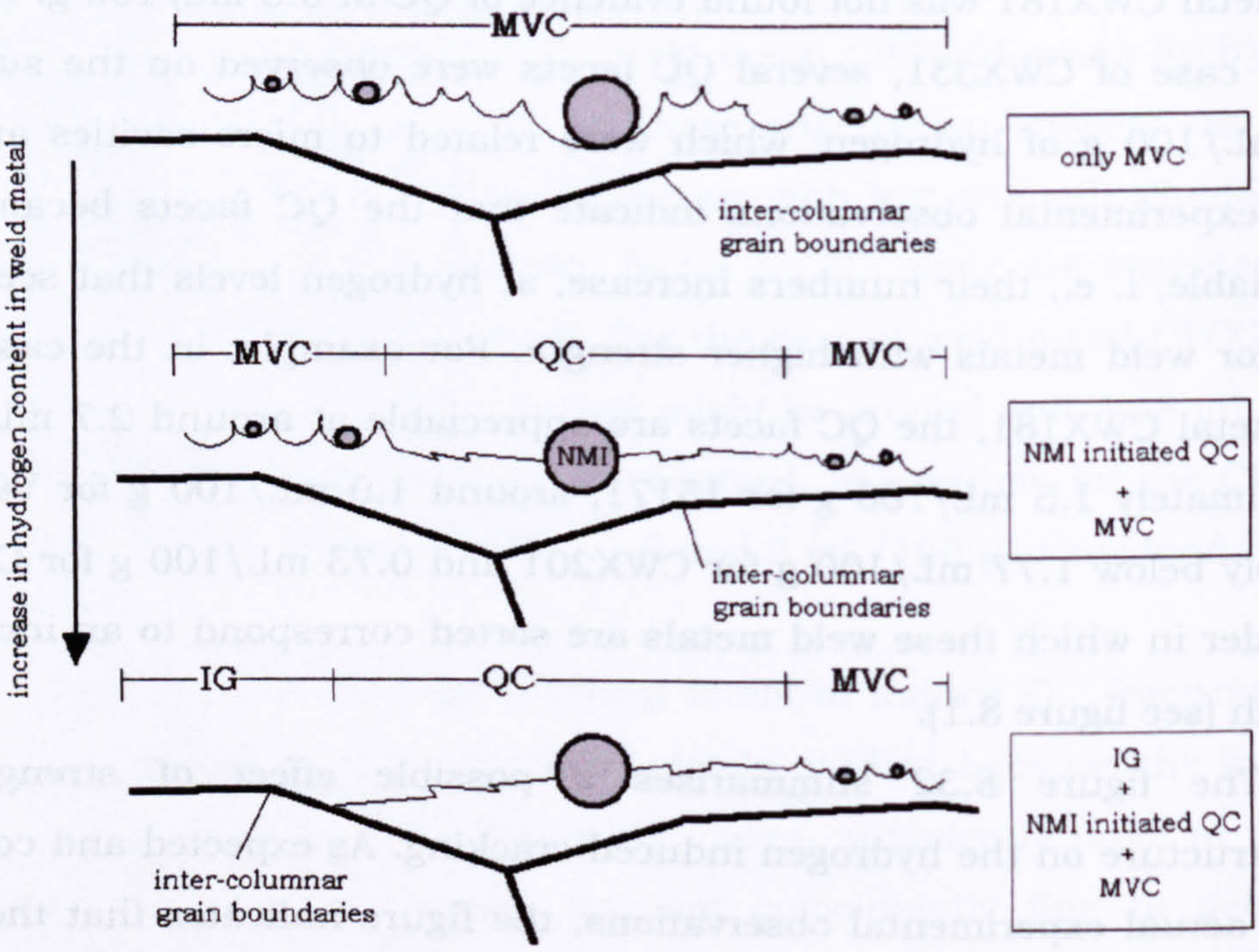

Figure 8.33 Schematic representation of the fracture surface profile and the effect of microstructural factors and hydrogen content.

It should be recognised that, although the measured H_D content represents an average value, there can be accumulation, or trapping, of hydrogen in specific regions of the microstructure such as around NMI, at dislocation sites in the AF, at particles interfaces, etc. Several authors [182-188] have estimated this hydrogen accumulation using various models and numerical methods taking into account stress. Essentially, the hydrogen accumulation in stressed regions has the form:

$$C_\sigma = C_0 \exp\left[\frac{V_H \cdot \sigma}{RT}\right] \tag{8.5}$$

where, C_σ is the stress modified hydrogen concentration, C_0 is the equilibrium concentration of hydrogen in the unstressed lattice, V_H is the partial molar volume of hydrogen (2 10^{-6} m^3 mol^{-1} in steels) and σ is the hydrostatic stress (=$1/3[\sigma_1 + \sigma_2 + \sigma_3]$, where σ_1, σ_2, and σ_3 are principal stresses). The expected increase in concentration estimated by equation 8.5 is presented in figure 8.34. The window shows the C_σ/C_0 ratio expected for the weld metals studied, taking their yield strength as the maximum stress field. It can be noted that C_σ/C_0 ratio factor between 1.4 and 2 could be found for stresses of the order of the yield stress. Equation 8.5 does not consider the effect of the hydrogen traps which could be found in the stressed regions. Gerberich [165] proposed that considering the trap binding energy (E_b) the equation 8.5 then changes to:

$$C_\sigma = C_0 \exp\left[\frac{E_b + V_H \cdot \sigma}{RT}\right] \tag{8.6}$$

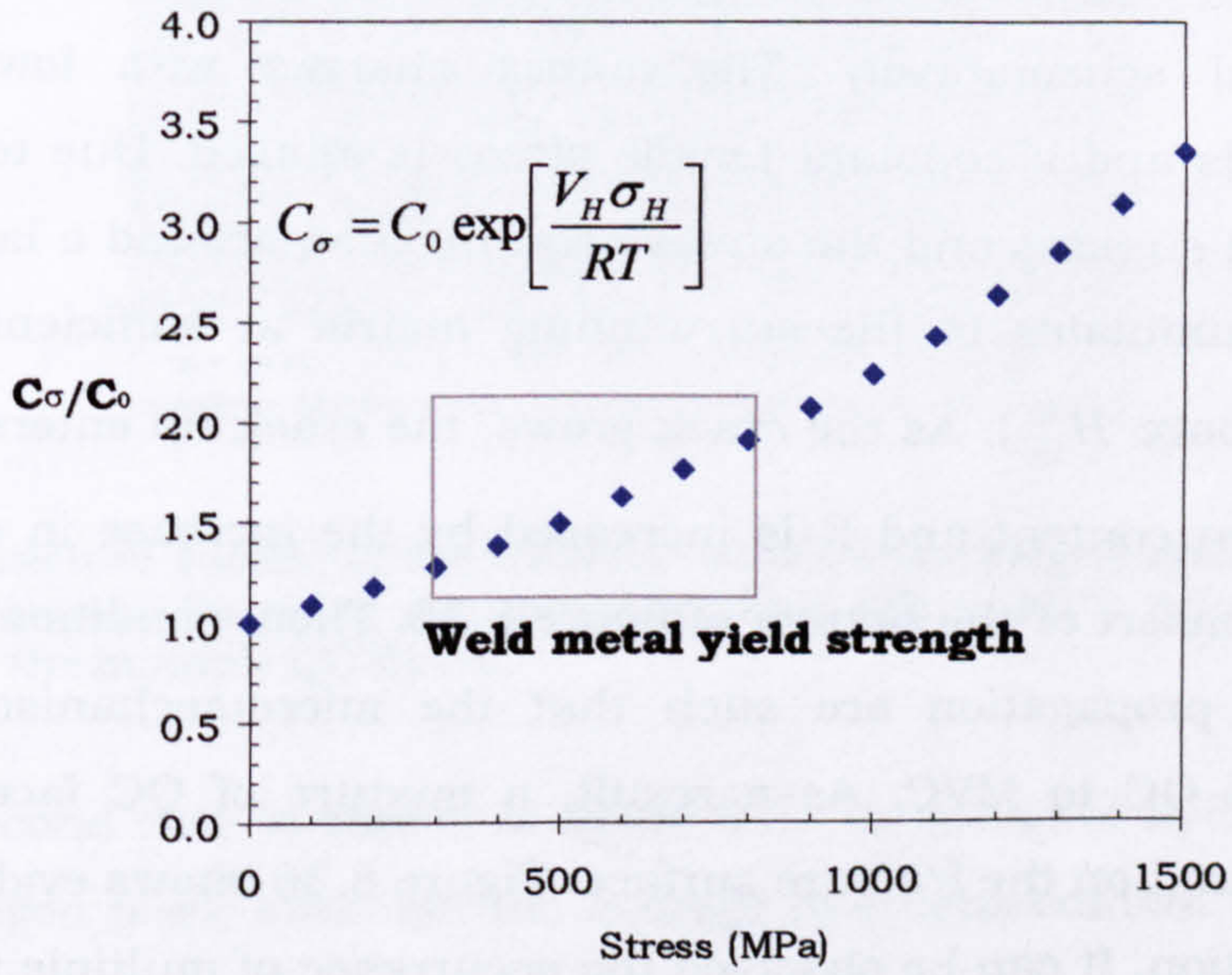

Figure 8.34 Estimation of the accumulation of hydrogendue to the effect of stress fields.

Table 4.1 shows binding energies (E_b) of different types of traps. Taking, for example, values of E_b around 20 kJ/mol, the value of the C_o/C_0 ratio could be of the order of 5 10^3, for stresses around 600 MPa, which is the value of the hypothetical steels used in calculations of stress around NMI in figure 8.10.

Although the average hydrogen level is below the critical value for the occurrence of QC (H^{κ}_{QC}) some regions of the weld metal could have hydrogen levels above this critical values (the large NMI in figure 8.33, for example). As a consequence, it is probable that the stress concentration factor and the hydrogen reach their critical value to produce the initiation and propagation of a crack in a QC mode. The growing of the crack increases the value of K and the crack penetrates regions with less hydrogen concentration. Both factors switch the mechanisms of fracture to the MVC mode. The growth of the crack (increase in K) affects the hydrogen accumulation as suggested by Yokobori et al [186, 188]. They proposed a physical model for hydrogen diffusion and accumulation around crack tip and carried out numerical analysis taking into account the effect of diffusivity constant, strength of the material and the stress concentration factor. The hydrogen accumulation is increased by the yield strength of the material and decreased by the value of the stress concentration factor, which correlates with the model proposed in this investigation (figure 8.31).Their more important findings are presented in annex A.24.

Following the considerations above, diagram from figure 8.31 could be used to interpret two cases where mixtures of fracture micromechanisms were found. The first case is shown in figure 8.35 where a mixture of QC and MVC is represented schematically. The matrix charged with low to medium hydrogen levels and a constant tensile stress is applied. Due to the effect of the tessellated stresses and the stress concentration around a large inclusion, hydrogen accumulates in the surrounding matrix at sufficient amounts to initiate QC (above H^{κ}_{QC}). As the crack grows, the crack tip enters regions with lower hydrogen content and K is increased by the increase in crack size, as shown in the insert at the bottom of figure 8.35. Then, conditions (H level and K) for crack propagation are such that the micromechanism of fracture changes from QC to MVC. As a result, a mixture of QC facets plus MVC surfaces is found on the fracture surface. Figure 8.36 shows evidence found in this investigation. It can be observed the occurrence of multiple QC facets due to the presence of inclusions. Each brittle facet is surrounded by dimples, evidencing the change in micromechanism due to the growth of the crack.

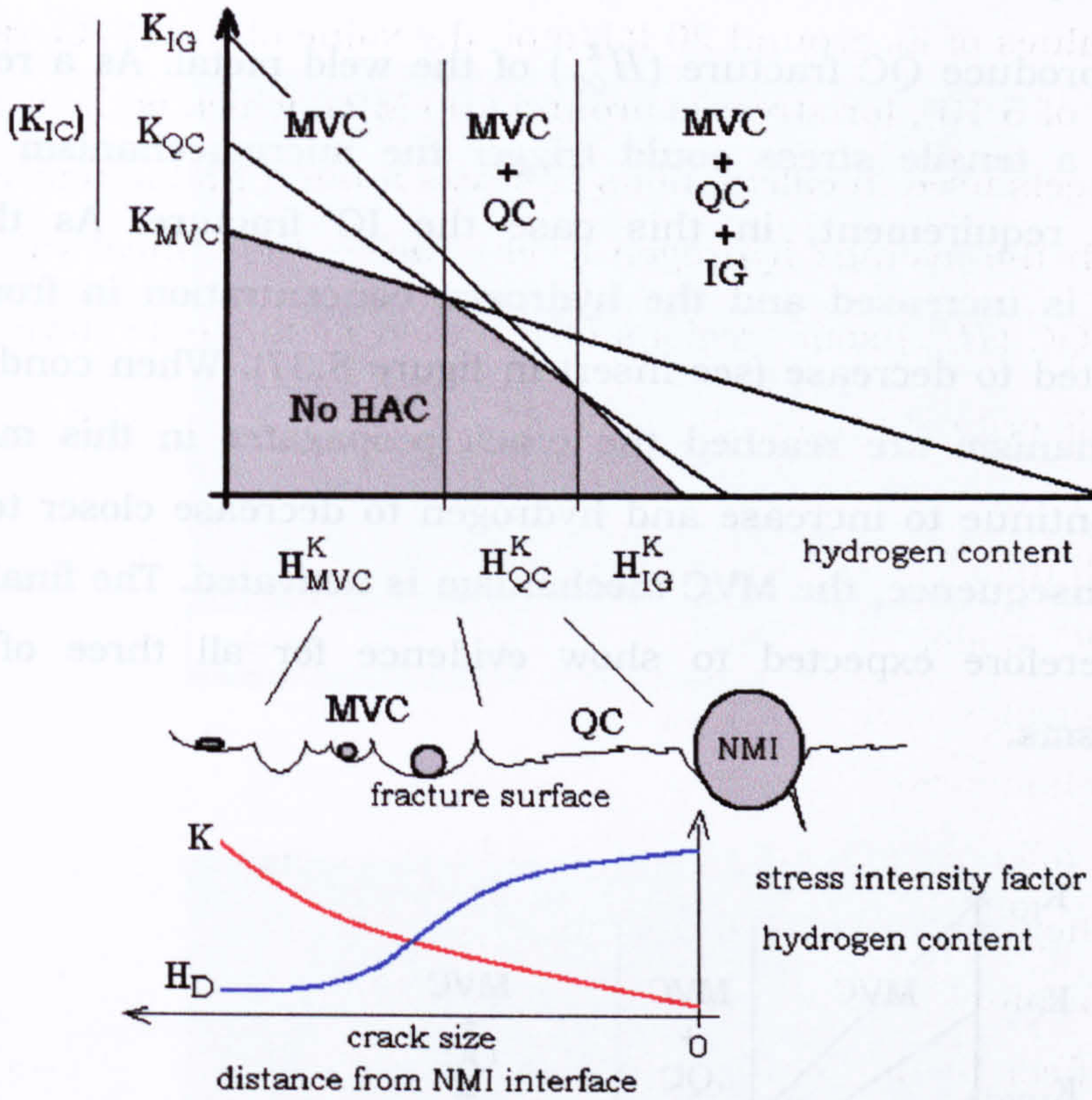

Figure 8.35 Effect of heterogeneous concentration of hydrogen and the stress concentration factor in the micromechanism of fracture for a steel that is charged with low to medium hydrogen content. The result is a mixture of QC facets surrounded by dimples from the MVC mechanism.

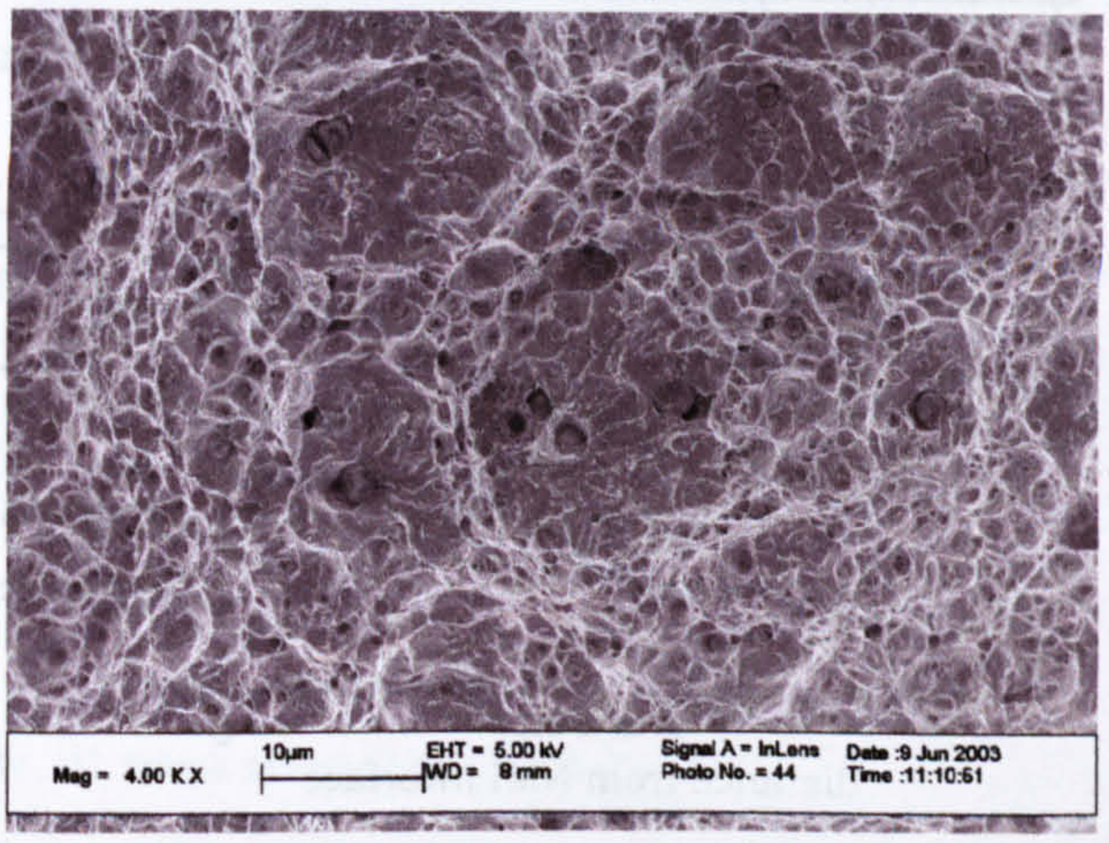

Figure 8.36 Fracture surface of the CWX201 weld metal charged with 3.24 mL/100 g of hydrogen. It could be noted the transition from QC to MVC micromechanism of failure around the multiple QC facets.

The second case is shown in figure 8.37 for a higher hydrogen content. At this hydrogen level, although the average hydrogen content could be close to the limit for the transition from MVC to QC (H^K_{QC}), the accumulation of hydrogen could be found in excess of the critical levels required at grain

boundaries to produce IG fracture (H^K_{IG}) or at cavities or non metallic inclusions to produce QC fracture (H^K_{QC}) of the weld metal. As a result, the application of a tensile stress could trigger the micromechanism with the lowest energy requirement, in this case the IG fracture. As the crack propagates, K is increased and the hydrogen concentration in front of the crack is expected to decrease (see insert in figure 8.37). When conditions for QC micromechanism are reached the crack propagates in this manner. K would then continue to increase and hydrogen to decrease closer to average value. As a consequence, the MVC mechanism is activated. The final fracture surface is therefore expected to show evidence for all three of fracture micromechanisms.

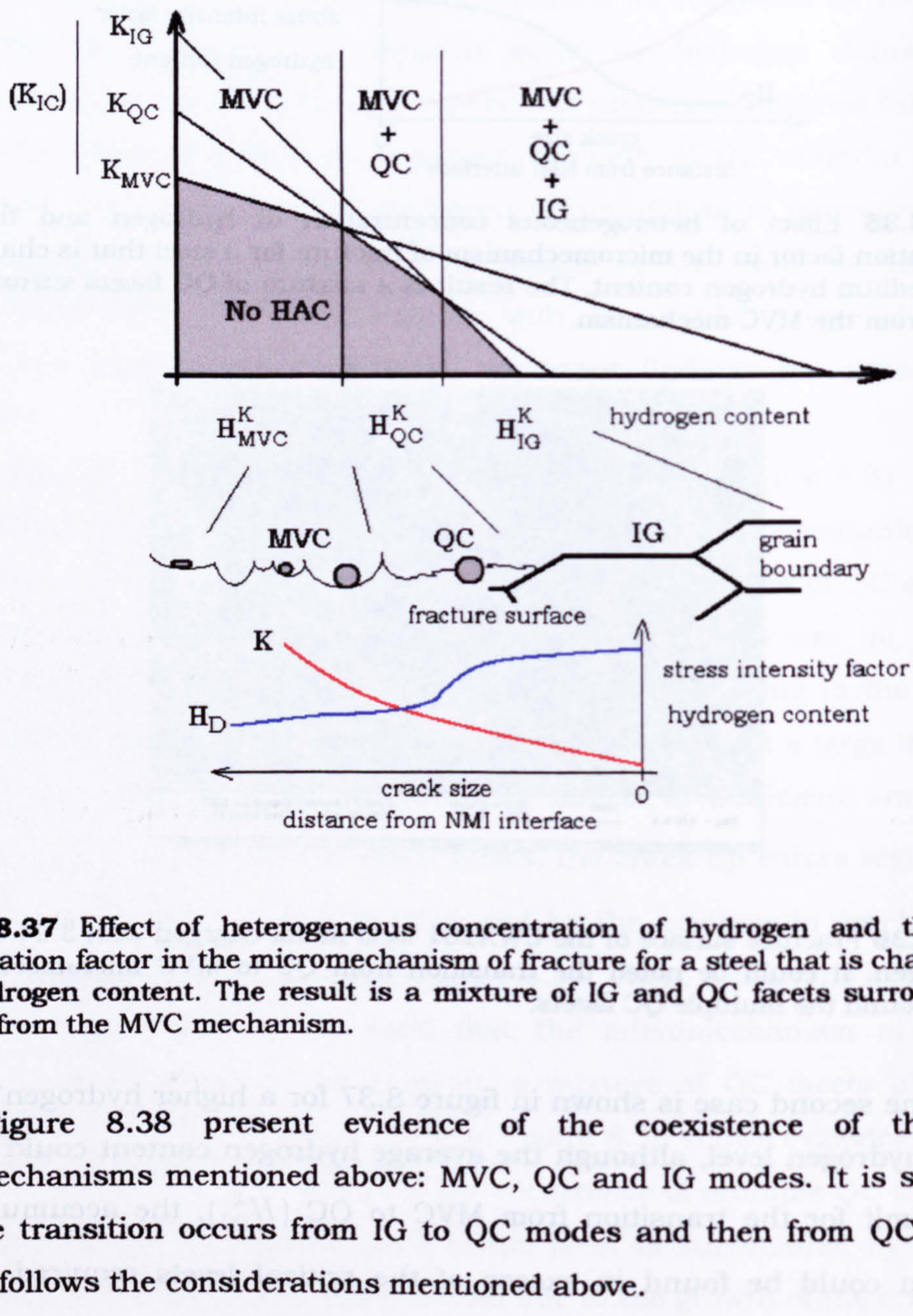

Figure 8.37 Effect of heterogeneous concentration of hydrogen and the stress concentration factor in the micromechanism of fracture for a steel that is charged with high hydrogen content. The result is a mixture of IG and QC facets surrounded by dimples from the MVC mechanism.

Figure 8.38 present evidence of the coexistence of the three micromechanisms mentioned above: MVC, QC and IG modes. It is suggested that the transition occurs from IG to QC modes and then from QC to MVC modes, follows the considerations mentioned above.

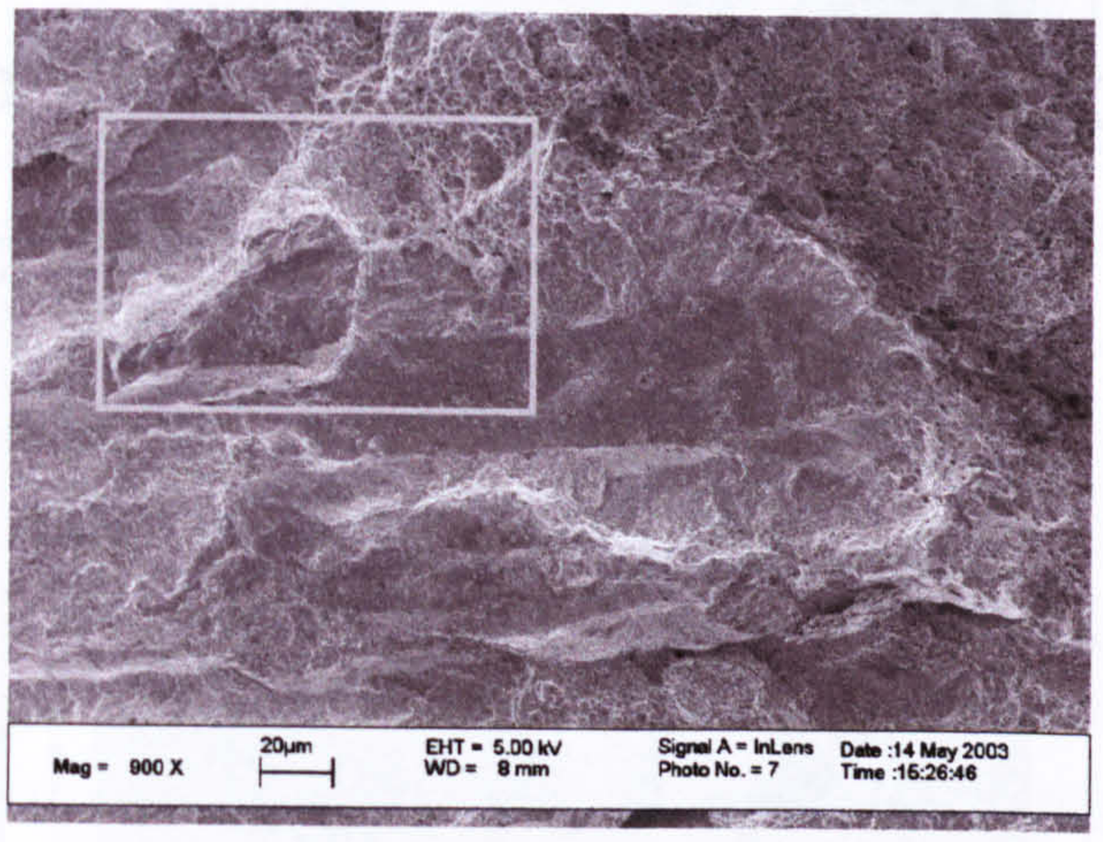

(a)

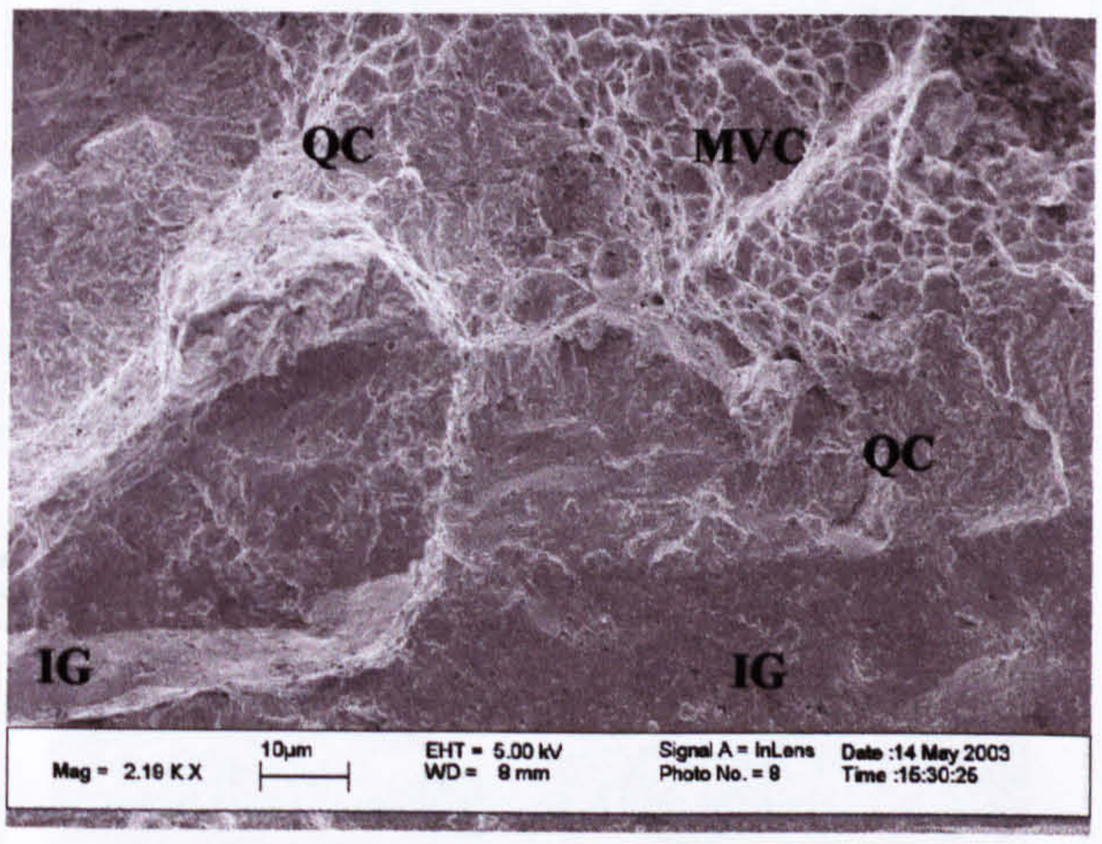

(b)

Figure 8.38 Fracture surface of CWX331 weld metal charged with 4.04 mL/100 g of hydrogen after tensile test. Note the existence of microvoids coalescence (MVC), quasi-cleavage (QC) and IG fracture micromechanisms in (a) and (b). (b) is a detail of (a).

Furthermore, it was mentioned before that theoretically it is possible to find fracture surfaces with 100% QC or 100%IG. The condition for that is that the hydrogen content and the stress concentration factor remains in their respective ranges suggested in figure 8.31. Figure 8.39 suggests that this could be possible at very high hydrogen contents. It is shown large areas of IG and QC fracture. At the top of the figure could be noted the transition IG→QC→MVC.

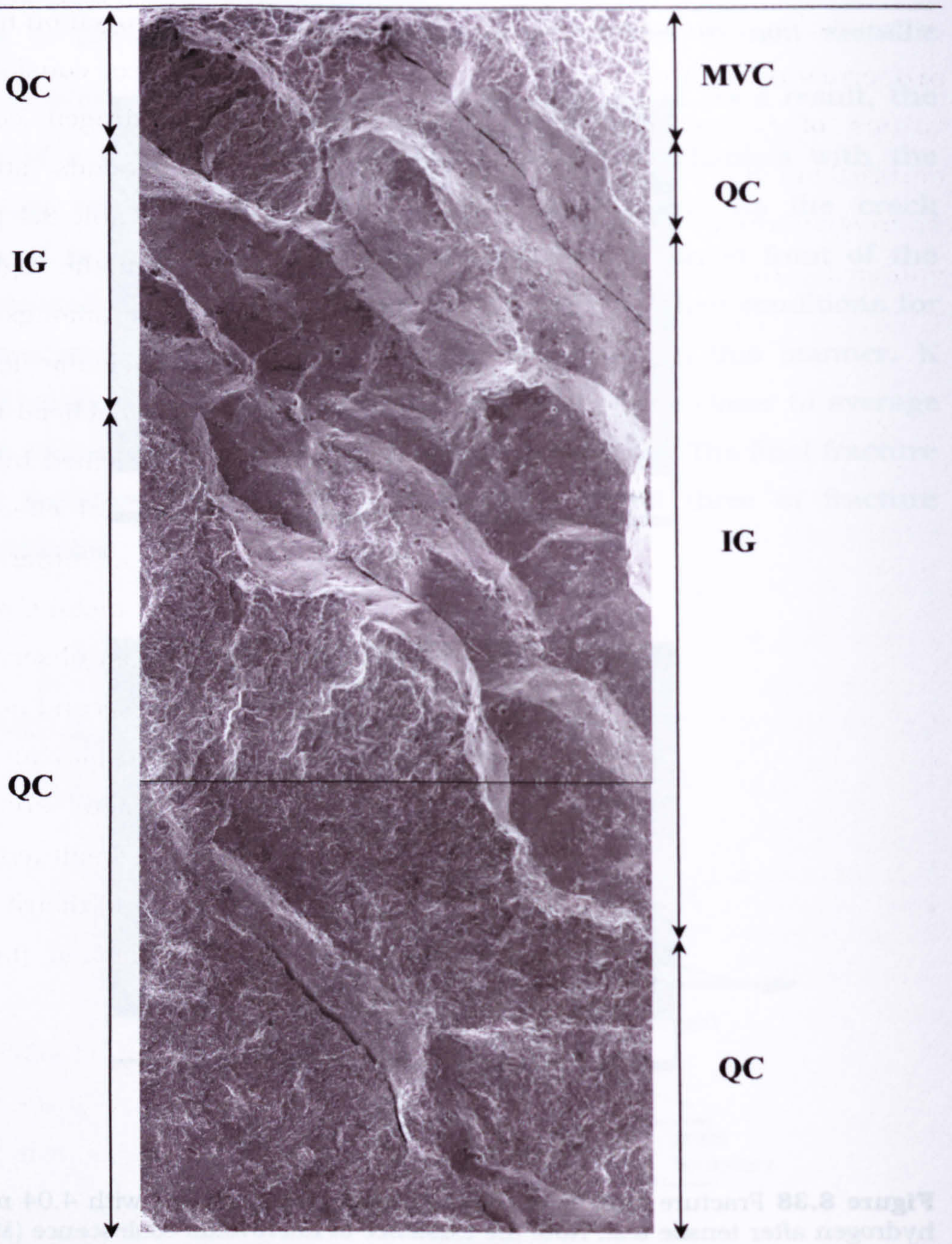

Figure 8.39 Fracture surface of CWX331 weld metal charged with 4.88 mL/100 g of hydrogen after tensile test. Figure shows large areas of IG and QC fracture.

8.6 Summary of chapter: Effect of microstructure, strength and hydrogen content on hydrogen induced cracking of weld metals

In this chapter, the influence of the hydrogen content on the mechanical properties and fracture of the weld metals is studied in some detail. The main tool used was the fractographic analysis using high resolution SEM.

Firstly, the effect of diffusible hydrogen content on S_y, S_m, S_f and ductility, originated from the work of Wildash[8], is presented and analysed carefully avoiding oversimplification. Figure 8.5 is an example of the new data

presentation. A conceptual idealisation of the effect of hydrogen on mechanical properties of the weld metal suggested that hydrogen affect considerably the values of S_f and ductility, indicating the critical hydrogen content for embrittlement, C_k. This critical hydrogen content depends strongly on microstructure and trapping capacity of the weld metals. Table 8.1 present C_k values for the different weld metals. The weld metal with the highest C_k is CWX351. Weld metals CWX181, CWX351 and 14001 are amongst the weld metals containing grain boundary ferrite (PF(G)) and acicular ferrite (AF), suggesting that a continuous network of PF(G) could be beneficial to improve the resistance to hydrogen cold cracking. However, as indicated by the lower C_k value for 15171 (weld metal with PF(G)), the beneficial effect of grain boundary ferrite depends on its proportion, continuity and other important factor like the MAC content and NMI characteristics. Weld metal CWX361 and CWX 81, with Ck of 4.0 and 3.0 mL /100 g confirm the last observation. The first weld contain a discontinuous film of PF(G), while the second is formed by fine AF and isolated bainite islands. The other factors that play an important role in increasing the hydrogen tolerance of the weld metal are: the MAC content and the presence of retained austenite in this constituent; and the NMI characteristics, like inclusion size, number density and distribution. The effect of these microstructural features on the Ck value and the trapping constant, k, is discussed in detail in the next chapter.

Secondly, throughout fractographic analysis with FEG-SEM (high resolution), it was studied the micromechanisms of fracture of the weld metal and how this behaviour can be affected by hydrogen charging. It is proposed a phenomenological model to correlate stress intensity factor and hydrogen content. There are three modes of fracture that where identified: coalescence of microvoids (MVC), quasicleavage (QC) and intergranular fracture (IG). The model intent to explain the effect of hydrogen, stress and crack like flaws on the fracture observed experimentally. Figure 8.31 presents a schematic representation of the model. The strength of weld metals was suggested to affect the critical combination of hydrogen content and stress intensity for changes in micromechanisms: H^K_{QC}, H^K_{IG}, H^0_{IG}, H^0_{QC} and H^0_{MVC}.

Finally, the role of NMI, MAC constituent and micro shrinkages is elucidated with respect to the initiation of cracks and as hydrogen accumulators. Large NMI and the microcavities were identified as very detrimental to the resistance to hydrogen assisted cracking. The evidence of the role of MAC particles was not explicit.

CHAPTER NINE

RESULTS AND DISCUSSION

PART III

HYDROGEN TRAPPING BEHAVIOR AND ITS RELATION WITH THE HYDROGEN INDUCED CRACKING (HIC)

In previous chapters, an attempt was made to relate the microstructure, the mechanical properties and the hydrogen induced cracking resistance of selected weld metals. It was mentioned that the microstructure plays an important role on the weld metal fracture behaviour and how this links to the diffusion and distribution of hydrogen in the weld. In this respect, the hydrogen traps are the key to understanding hydrogen transport and distribution.

It is known that the hydrogen traps control the distribution of hydrogen throughout the microstructure in such way that may decide whether critical levels are reached and, therefore, whether the crack is initiated or not at flaw sites. For this reason, it is useful to attempt to characterise the different microstructures with respect to their trapping capacity. The weld metal traps could be of different nature: interfaces, precipitates, NMI, dislocations and solute atoms. Knowing the relationship between trapping and microstructural features may allow the weld resistance to hydrogen cracking to be improved. As described in chapter four, the occurrence of hydrogen induced cracking needs the simultaneous interaction of four factors: hydrogen in sufficient quantity or a hydrogen critical content, the presence of stress, a susceptible microstructure and relatively low temperatures. Hydrogen traps could, in principle, be designed to redistribute the hydrogen absorbed during welding and control its concentration in places susceptible to crack initiation, provided the relationship between trapping and microstructure was known.

An electrochemical technique, described in chapters five and six, was used to study the trapping behaviour. Using this technique a trapping rate constant (k) was estimated for each of the analysed welds. This value can only be used for qualitative comparisons, at least in this investigation, due to the wide variety of traps that could occur in a typical steel weld metal and the use of a limited quantity of available samples which contains reheated regions. However, an attempt is made in this chapter to correlate the measured k values with details of the microstructure, particularly MAC content, the NMI

characteristic and weld metal resistance to hydrogen induced cold cracking as these have already been identified as important in the fracture mechanisms described in Chapter 8 but had also been isolated as key variables controlling HICC cracking in weld metals by Wildash et al [9,10].

9.1 The potentiostatic double step method and significance of the trapping constant value k

As was described in chapter 4 and 6 an electrochemical technique was used to estimate the trap capacity of selected weld metals. Basically, this method consists of introducing hydrogen in the weld metal sample by cathodic polarization charging and then, when polarisation is eliminated, permitting the egress of the absorbed hydrogen and re-oxidise it. The anodic current registered is the data to be used to estimate the trapping constant k.

During charging, hydrogen is reduced on the metallic surface. Figure 9.1 presents schematically the process of hydrogen proton reduction, adsorption, absorption and diffusion. Protons are adsorbed on the weld metal surface where they are reduced to atomic hydrogen. This atomic hydrogen could interact with others H to form molecules of H_2. If the formation of H_2 is interrupted the H atoms can be absorbed in the weld metal and diffuse into the material. The elimination of polarisation changes to zero the concentration of H on the surface and produces the absorbed H atoms to diffuse back to the surface, where they are re-oxidised.

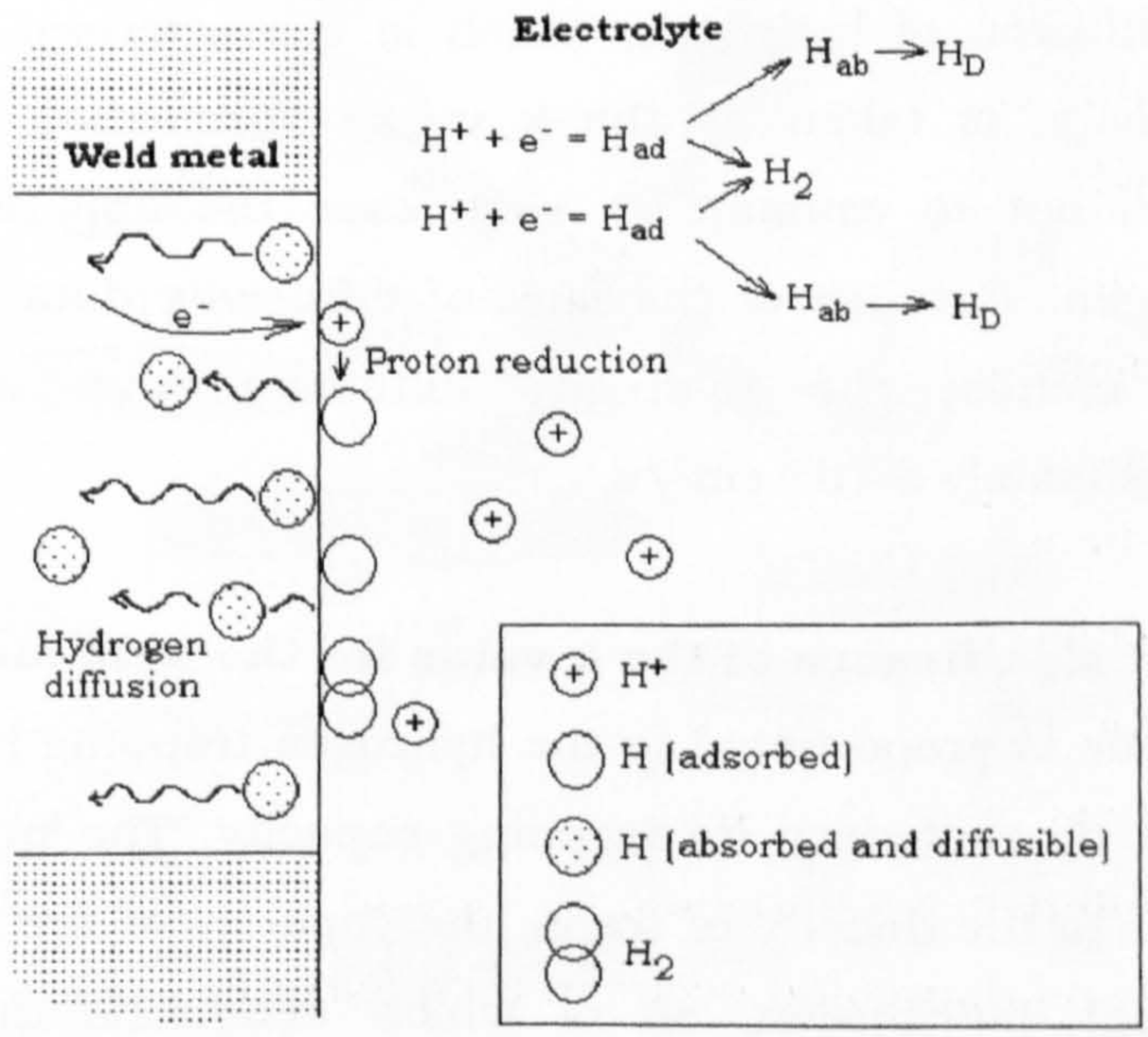

Figure 9.1 Schematic representations of the proton adsorption and reduction, hydrogen atoms adsorption, absorption and diffusion during the charging potential in the second step of the PDP test.

9.1.1 Assumptions for the diffusion model

To estimate the trapping constant for each weld metal the method shown in chapter 6, sections 6.4.6 and 6.4.7, was followed. The assumptions for the application of the model in this investigation are:

1- The hydrogen entrance is controlled by the diffusion of H into the bulk metal. This means that the transfer of H at the interface is very fast and equilibrium is reached quickly.

2- The value of C_s, the hydrogen concentration just below the surface, was considered similar in every weld metal studied. Figure 6.14 indicated that the current density peak is related strongly to the C_s value, as demonstrated in figure 6.13(a). The C_s value was estimated to be around $9.91 \cdot 10^{-9} mol/cm^3$.

3- The hydrogen traps, in contrast to the original assumption by Pound[100, 113], can be saturated. This might be the reason why in some of the weld metals the k value decreases with the charging time. However, for mathematical simplicity the k value is kept as a constant for the solution of the modified second Fick's law,

4- The hydrogen lattice diffusivity (D) has been taken as constant for all the studied weld metals. It is supposed that the effect of trapping on the diffusion of hydrogen, which is characterised by an apparent diffusivity, is taken by the k value. Permeation studies may be carried out to estimate in each case the apparent diffusivity of hydrogen. Because of the lack of diffusivity data for the different weld metals, the hydrogen diffusivity was assumed to be approximately $5\ 10^{-5}\ cm^2/s$.

9.1.2 The significance of the k value for the weld metals

The k value is proportional to the hydrogen trapping rate for a specific weld metal and characterises its trapping capacity. The precise value of k could be related to the density of traps, the capacity of the traps (size, type) and their spatial distribution, all of which determine the probability of hydrogen capture. Strong traps (high binding energy) or irreversible traps are likely to affect the k value significantly. The presence of weak or reversible traps could affect the diffusion coefficient and may only slightly influence the

value of k detected by the double pulse electrochemical test. Moreover, the k value may vary if saturation of traps occurs as charging times are increased, as the results in this investigation seem to indicate. This is discussed later.

Figure 9.2 presents the various factors that could lead to changes in the value of the trapping rate constant, k. It can be noted the complex interactions between numerous microstructural features that could affect the trapping capacity of the weld metals. Four important groups are identified: NMI, MAC constituents, microstructure and other traps (TiC, cavities, porosities, etc.). For example, the observed k value could be high for weld metals with a high number density of NMI, because the possibility of hydrogen trapping increases. Conversely, a low density of sparsely distributed NMI or similar traps could reduce the value of k. In regard to the MAC constituent, the presence of retained austenite, which is regarded as a strong trap due to its high hydrogen solubility and binding energy, would increase the k value.

The simultaneous presence of this diversity of microstructural features makes difficult the interpretation of the k value. For example, a reduction in NMI number could reduce the k value, but a simultaneous augment in proportion of MAC constituent, or the presence of retained austenite in it, could compensate the decrease in k. This indicates that all the variables have to be considered simultaneously in comparing weld metals.

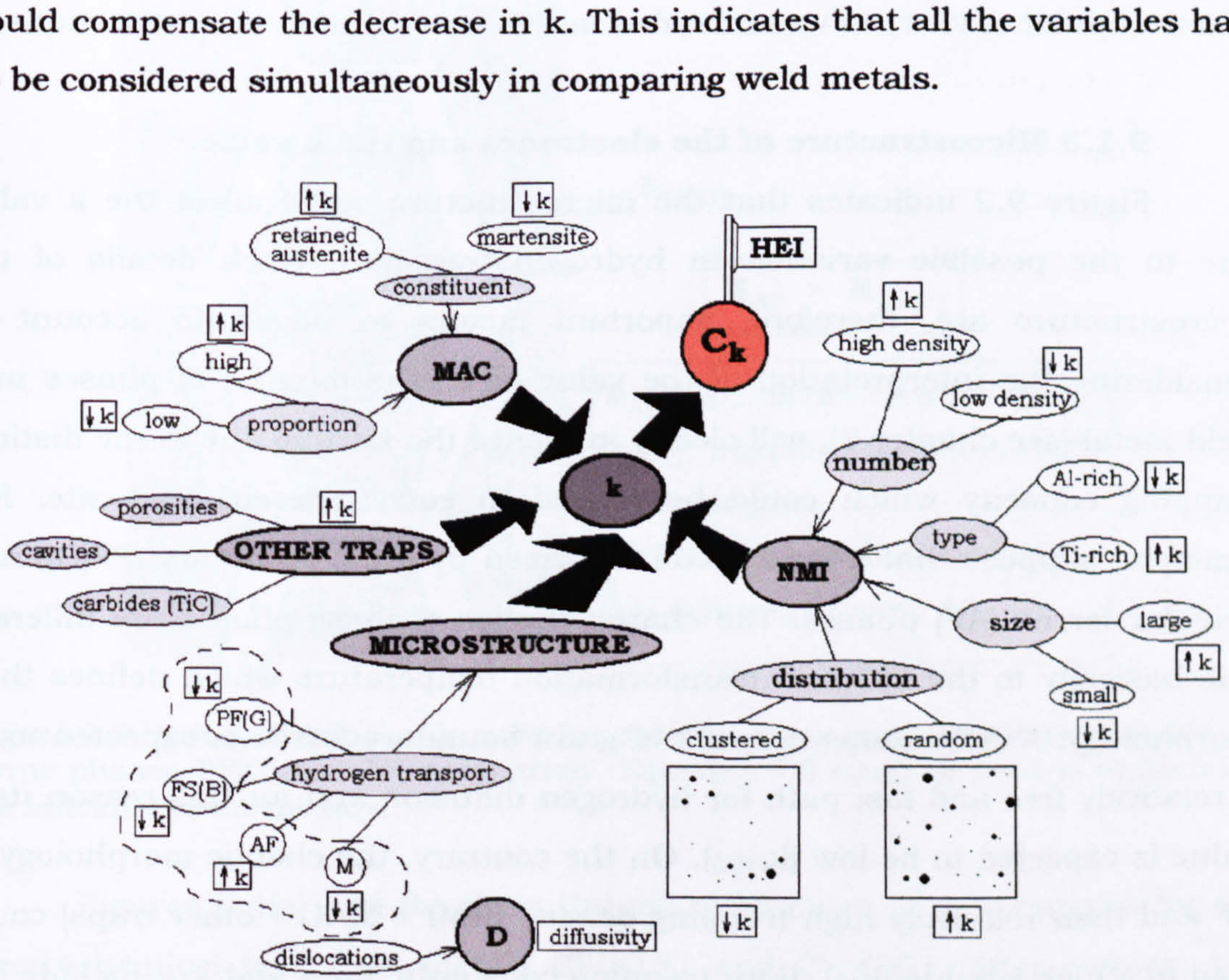

Figure 9.2 Factors influencing the value of the hydrogen trapping rate constant, k. Four groups are distinguished: NMI, microstructure, MAC and other traps. Ideally the k value could be related with the susceptibility to hydrogen cracking of the weld metals, it could be regarded as a HEI.

The k value, globally, can describe the effect of the various factors that contribute to hydrogen trapping and redistribution. Ideally, a measurement of k should relate directly to the resistance to hydrogen induced cracking of steel weld metals. Pound et. al. [100-104, 113] has proposed that the trapping rate constant value is an intrinsic hydrogen embrittlement index for different alloys. The calculation of this trapping rate constant required a complete characterisation of the alloy in terms of irreversible trapping (diameter and density of traps) and the effective hydrogen diffusion in the alloy. An equivalent and simpler approach is utilised in this investigation for the studies of high strength weld metals, where a direct interpretation of the k value (k_a, as termed in the work by Pound, the apparent rate constant) is done without further calculations: that is, a high value of k is related to a high density of traps or high capacity of trapping. This directly obtained k used here contains enough information to elucidate, in combination with other HE determinations, the resistance to hydrogen induced cracking of the weld metal. The simple determination and interpretation of k could be used to rank the weld metals in order to hydrogen induced cold cracking susceptibility. Relationships between the k value and C_k would be extremely useful from the practical point of view, as was intended in this investigation in next sections.

9.1.3 Microstructure of the electrodes and the k value.

Figure 9.2 indicates that the microstructure could affect the k value due to the possible variation in hydrogen transport. Such details of the microstructure are, therefore, important factors to take into account in considering the interpretation of the value of k. The mixture of phases in a weld metal (see chapter 7), will clearly influence the k value due to the distinct trapping capacity which could be related to each different trap site. For example, suppose that a weld metal is formed by grain boundary (PF(G)) and acicular ferrite (AF) phases. The characteristics of these phases are different due basically to the different transformation temperature which defines their morphology. A continuous network of grain boundary ferrite is expected to be a relatively free and fast path for hydrogen diffusion and for this reason its k value is expected to be low ($k_{PF(G)}$). On the contrary, the chaotic morphology of AF and their relatively high trapping density (NMI + MAC + other traps) could lead to a high k value (k_{AF}). Both trapping constants, $k_{PF(G)}$ and k_{AF}, include the presence of trap sites in each region, which is expected to be numerous in AF. Taking into account the mixture rule, the total measured k value could be:

$$k = \nu_{AF} \cdot k_{AF} + \nu_{PF(G)} \cdot k_{PF(G)} \qquad (9.1)$$

where k is the total hydrogen trapping constant and ν_{AF} and $\nu_{PF(G)}$ are the fractions of acicular and grain boundary ferrite phases, respectively.

Equation 9.1 indicates that a decrease in k value could be associated with the presence of grain boundary ferrite network and the contrary could occur when the PF(G) is reduced or the network disrupted. Figure 9.3 represents schematically the behaviour of hydrogen in a weld metal containing PF(G) and AF. A similar approach can be followed for mixtures of other microstructures and for the case of the presence of weld metal and reheated regions. For the case of a mixture of weld metal and reheated regions the approach mentioned above can be used to correct the values of k and estimate a k_{AW}, a trapping rate constant for the weld metal. The following equation could be used:

$$k = A_{AW} \cdot k_{AW} + A_{RH} \cdot k_{RH} \qquad (9.2)$$

where A_{AW} and A_{RH} are the area proportions for weld metal and reheated zone, respectively, k_{AW} and k_{RH} are their trapping rate constants.

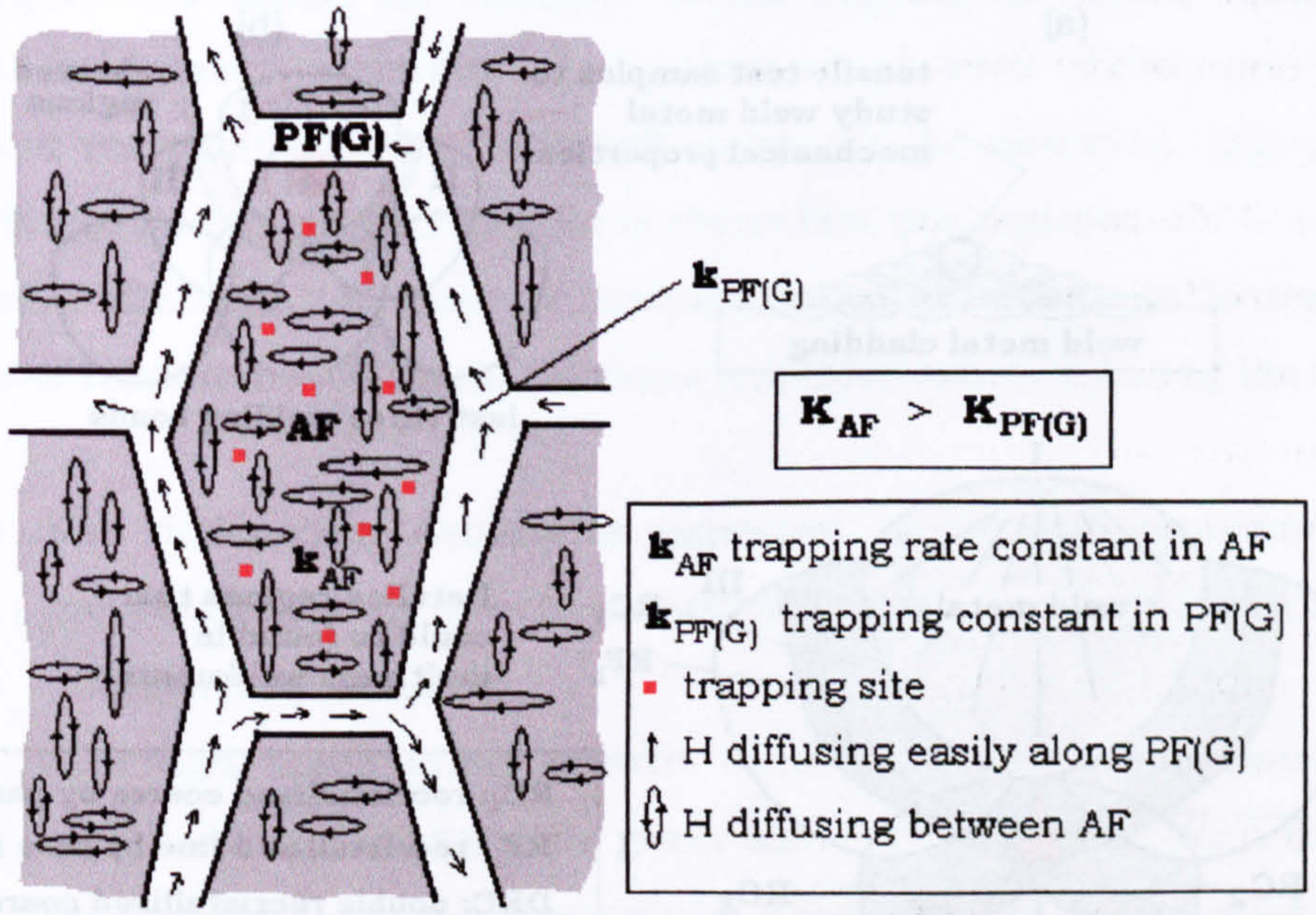

Figure 9.3 Hydrogen diffusion in a weld metal containing grain boundary and acicular ferrite phases, PF(G) and AF, respectively. Equation 9.2 could be used to understand the influence of the mixture.

Figures 9.4(a) and (b) show the microstructure of two samples for the electrochemical test: weld metals CWX181 and CWX201. After etching, two regions can be distinguished: the as welded region or weld metal and the reheated region. Figure 9.4(c) points out the effect of the reheating on the microstructure of the weld metal of previous passes and the distance from the

fusion boundary. Two sub-regions are distinguished in the reheated microstructure: a coarse and a fine recrystallised zones [188]. The coarse region is close to the fusion boundary and for this reason is reheated at higher temperatures producing a coarse recrystallised region. Away from the fusion boundary a fine recrystallised zone is found and further away partially transformed and tempered microstructure are present. These regions are schematised in figure 9.5. Most of the electrochemical test electrodes presented weld metal and recrystallised regions (coarse and fine).

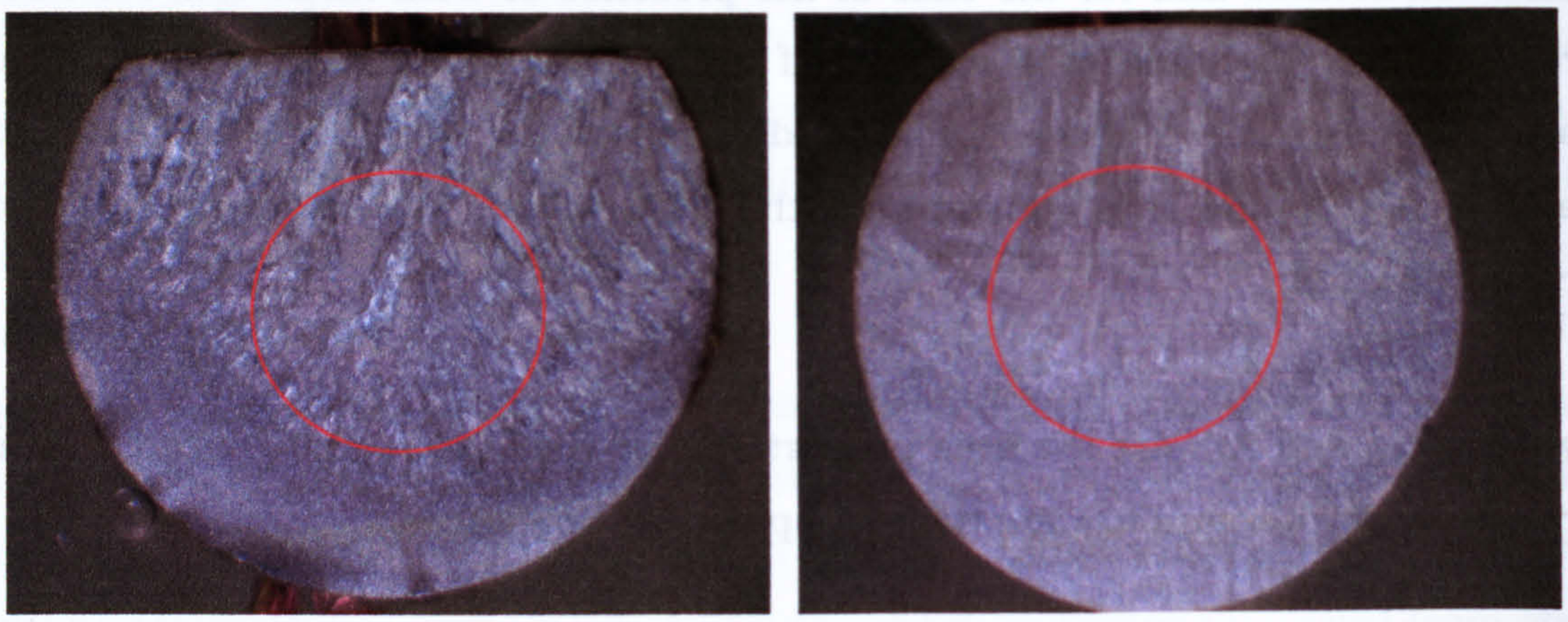

Figure 9.4 Microstructure in the electrochemical test electrodes: (a) CWX181 and (b) CWX201. (c) Schematic representation of a multi-pass weldment illustrating the different regions which suffer re-crystallisation due to reheating. The outer red circle in insert in (c) represents electrochemical samples (cut from tensile sample base) and the red circles in (a) and (b) are the targeted weld metal region for tensile test.

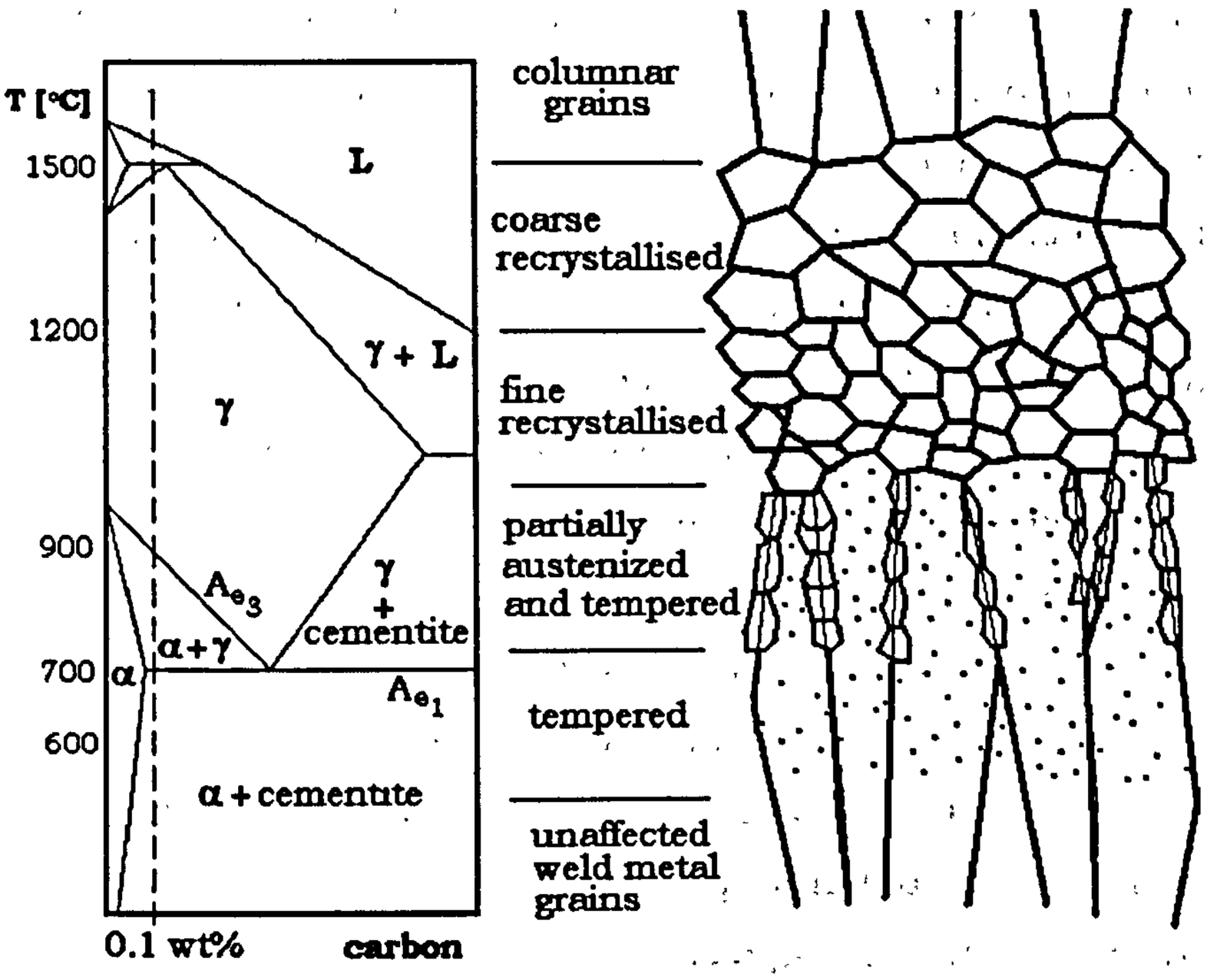

Figure 9.5 Schematic representation of the microstructural changes expected in the reheated zone of a low alloy steel weld metal. Based upon the variation of microstructure in HAZ [39, 188]

Figure 9.6 shows an example of the regions described above in the CWX181 weld metal electrode. The presence of weld metal, recrystallised coarse and recrystallised fine reheated zones can be observed, (figure 9.6(a)). Figures 9.6(b) and (c) present details of these last two regions.

From the point of view of transport and trapping of hydrogen, the presence of reheated weld metal portions will have one or more of the following effects:

1- The dislocation density is expected to decrease considerably on recrystallisation, which in turn would increase the hydrogen diffusivity appreciably.

2- Although some grain growth occurs in the coarse recrystallised region, the prior austenite grain size here is smaller than that in the weld metal. As a consequence hardenability is reduced and the proportion of polygonal ferrite will increase. This change will also accelerate hydrogen diffusion.

3- For weld metals with P_{cm} values less than 0.20, the fine recrystallised region consists mainly of fine ferrite grains between 5 and 8 μm in diameter. It is likely that precipitation of carbides occurs at the grain boundary reducing the quantity of MAC constituent compared to that present in the as cast weld metal

microstructure. This variation would also increase hydrogen diffusivity due to the reduction of dislocation density and the trapping capacity of the region.

4- For weld metals with P_{cm} values higher than 0.20, formation of bainite and or martensite would be expected depending on details of prior austenite grain size, composition and cooling rate. Combinations of these factors could promote retention of austenite and formation of MAC micro-constituents, both of which would increase hydrogen trapping.

5- Some tempering would also take place transforming the MAC constituents from martensite or bainite to ferrite and carbide, which in turn could cause reduction in trapping capacity due to a decrease in retained austenite proportion. In addition, carbides are less effective hydrogen traps compared to retained austenite.

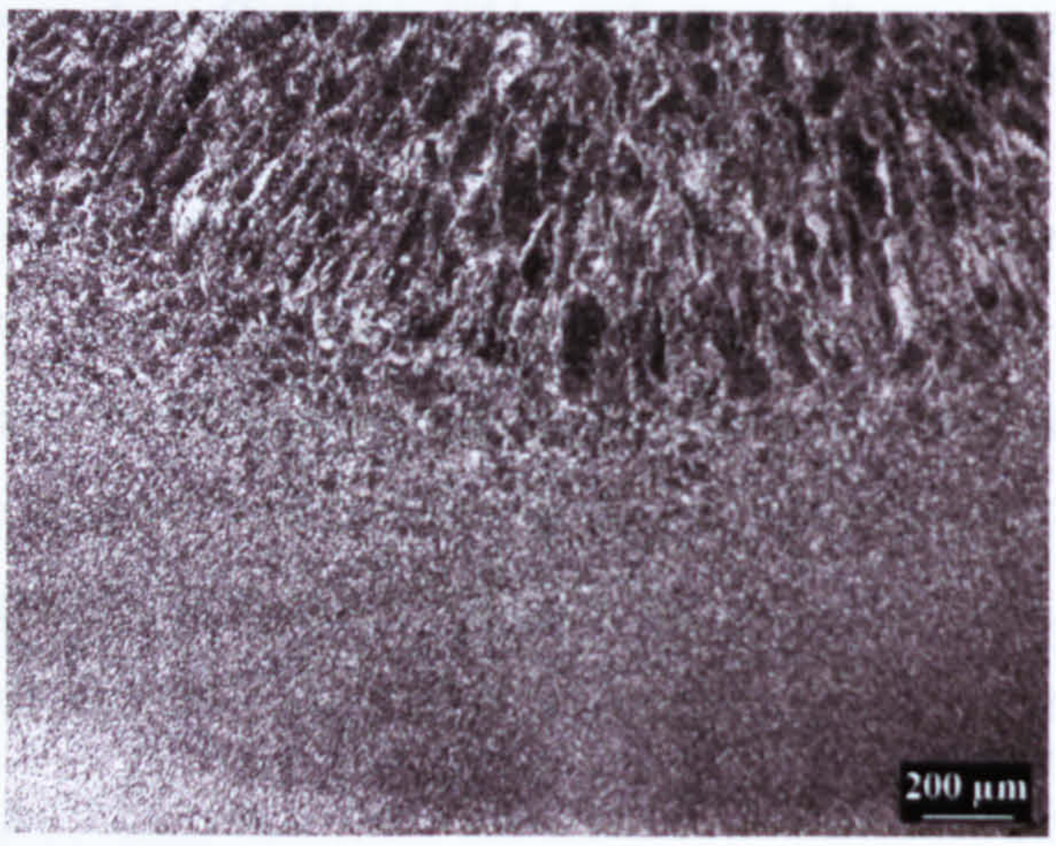

(a)

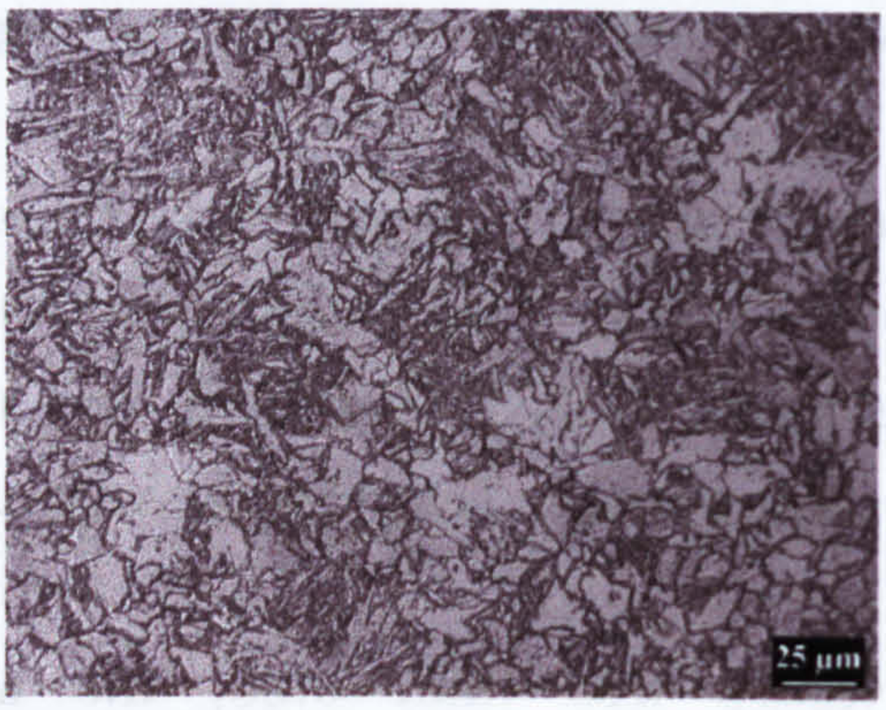

(b)

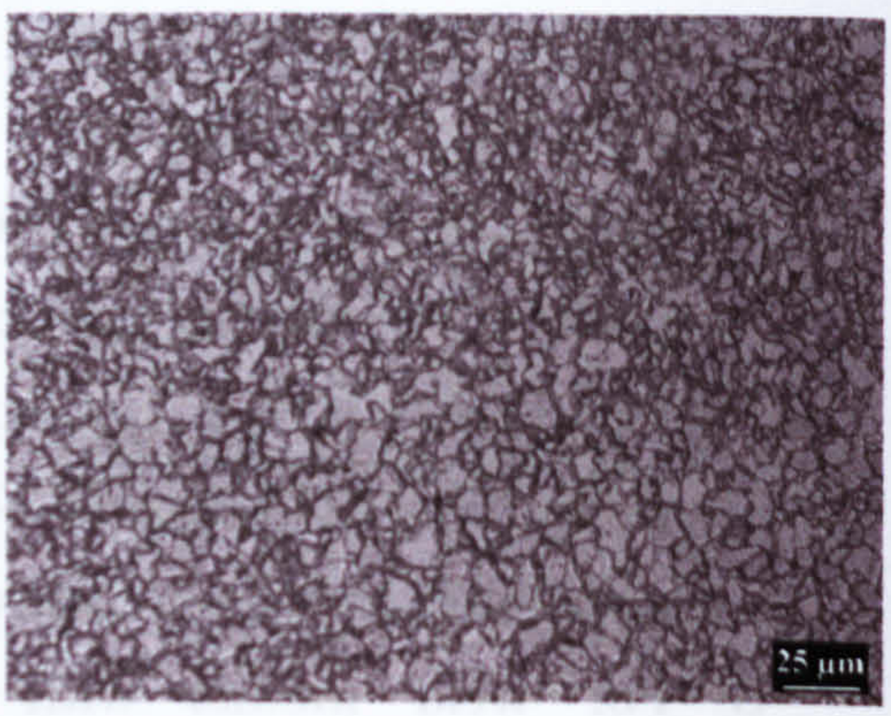

(c)

Figure 9.6 Microstructure of the CWX181 electrode containing weld metal and reheated regions. (a) general view illustrating the regions, (b) and (c) detailed recrystallised coarse and fine zones, respectively.

These observations complicate the interpretation of the electrochemical results. Some additional work is necessary to evaluate the effect of different proportions of weld metal and reheated regions on trapping rate constant (k). The hydrogen trapping test results, obtained in this investigation, include the trapping behaviour of both regions of the weldment. However, it is assumed that the errors introduced by neglecting differences in the reheated area fraction will be proportional to the area fraction exposed on the test electrode. This is because the diffusivity of hydrogen in a ferritic matrix is about an order of magnitude greater than that in a dislocated matrix typical of a martensitic or acicular ferrite matrix. This is taken into account for the discussion on weld metal k values.

9.1.4 Microstructure of the weld metal and the hydrogen diffusion.

The various different phases (AF, FS(NA), PF(G) etc.) present in each weld metal are expected to have different effective diffusion coefficients. Wang and collaborators [189], using the permeation technique, determined the effective hydrogen diffusivity (D_{eff}) for the weld metal (WM), heat affected zone (HAZ) and base metal (BM) of a TMCP weldment. They found that the lowest diffusivity was in the HAZ (4.21 $10^{-11}m^2/s$), which was predominantly bainitic in microstructure. The effective coefficients for WM (AF and PF(G)) and BM (ferrite and pearlite) were reported to be 5.21 10^{-11} and 8.51 $10^{-11}m^2/s$, respectively. These effective diffusion coefficient variations are due to the presence of different hydrogen traps in each region of the weldment. In this investigation the hydrogen diffusivity in the ferrite lattice was taken as constant and the effect of trapping is not included because this is taken into account by the trap constant, k, and no corrections are made to obtain a D_{eff} as in the work by Wang [189].

9.2 The electrochemical method and estimation of the trapping rate constant

Figures 9.7 and 9.8, present the current density variation during the different steps of the potentiostatic double-step method that was used to study hydrogen ingress and egress for the different weld metals. Three regions could be observed:

a) The initial and slightly cathodic region (at $E_A = E_{corr} - 10mV$). During this, a small cathodic current density is detected and

this is the result of the reduction of hydrogen protons on the surface, described by the reaction:

$$2H^+ + 2e^- = H_2(g) \qquad (9.3)$$

At this potential, the corrosion rate of the weld metal electrode is very low.

b) The hydrogen charging region (at $E_{ch} = E_{corr} - 150mV$). During this polarization the reduction of hydrogen protons is increased and, as the cathodic current density indicates, the reaction kinetics for equation 9.3 are increased. During this period and due to the presence of As^{3+} in solution, the formation of hydrogen molecules is perturbed. The hydrogen atoms, which are adsorbed on the electrode surface, became absorbed and hydrogen diffusion into the weld metal electrode occurs. Any other hydrogen that is not introduced into the weld metal evolves as hydrogen molecules.

c) The hydrogen re-oxidation region (at E_A). At this potential, an anodic current density due to hydrogen egress and re-oxidation is observed. Hydrogen that was introduced during the charging is induced to diffuse back to the surface, where it is desorbed and oxidised. This anodic current can be analysed to evaluate the trapping rate constant of the weld metal as is discussed below.

In figures 9.6 and 9.7, it is observed that the average charging current density was different in most cases. This varied between 10 and 35 $\mu A/cm^2$ even for the same weld metal. This charging current density might be expected to be the same for each weld metal as a consequence of the utilisation of a fixed polarisation value (150 mV below each E_{corr}). However, it is likely that the differences are due to small superficial changes in the experimental conditions that could include: small differences in microstructure of the same weld metal, proportions of weld metal and reheated zone and/or surface finish. Such differences between samples could change the hydrogen reduction (or oxidation) kinetics. As a result of this, the amount of electrical charge used for the reduction of hydrogen is, in some cases, not proportional to the charging time.

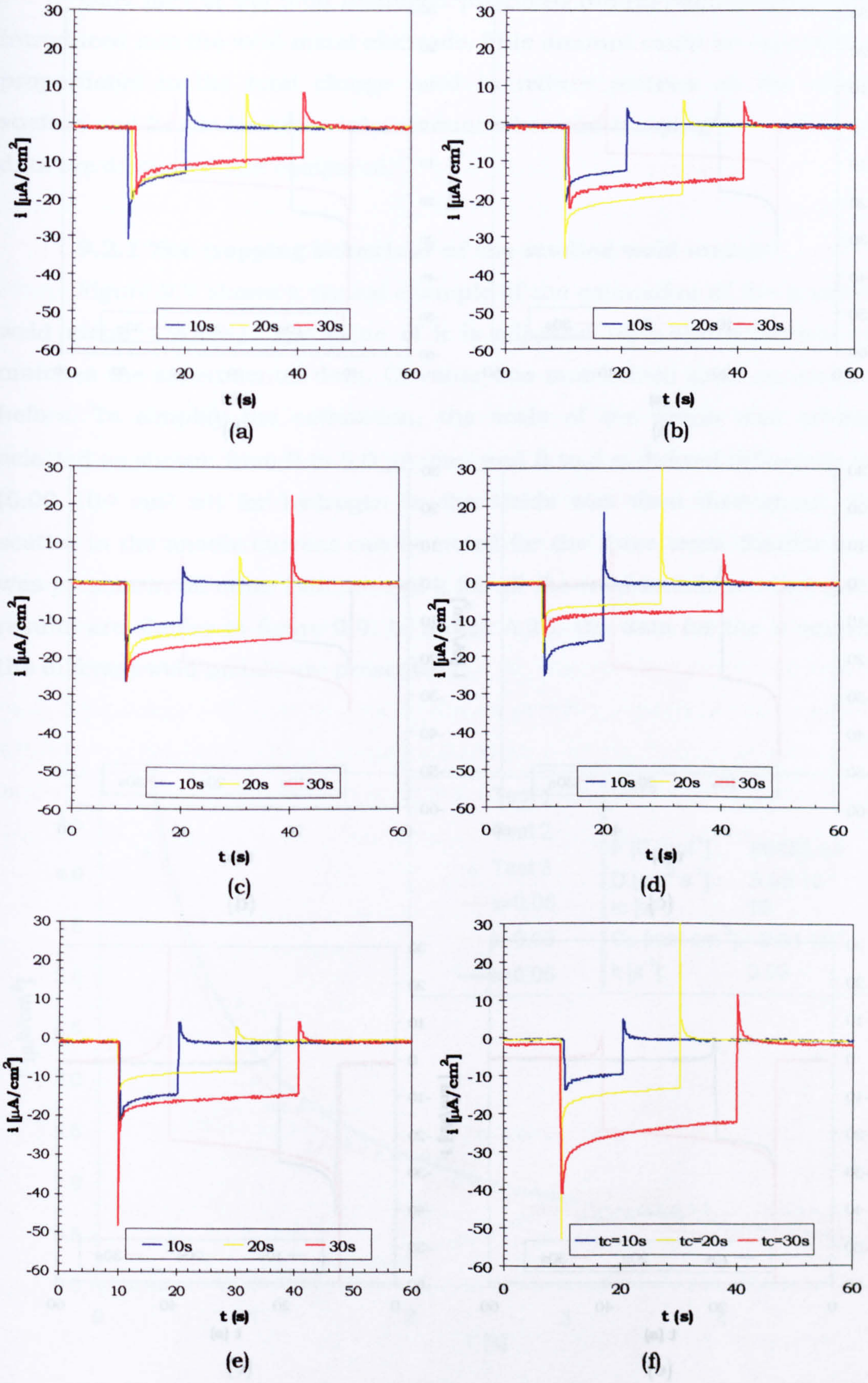

Figure 9.7 Current-time curves for the electrochemical double-step test of the weld metals: (a) CWX181, (b) CWX351, (c) 14001, (d) 15171, (e) VCX2561, (f) CWX361. In 0.87 mol/L acetic acid ($C_2H_4O_2$) and 0.5 mol/L sodium acetate ($C_2H_3NaO_2$) containing 15 ppm sodium meta-arsenite ($AsNaO_2$) as a hydrogen entry promoter at 25.0 ± 0.1°C.

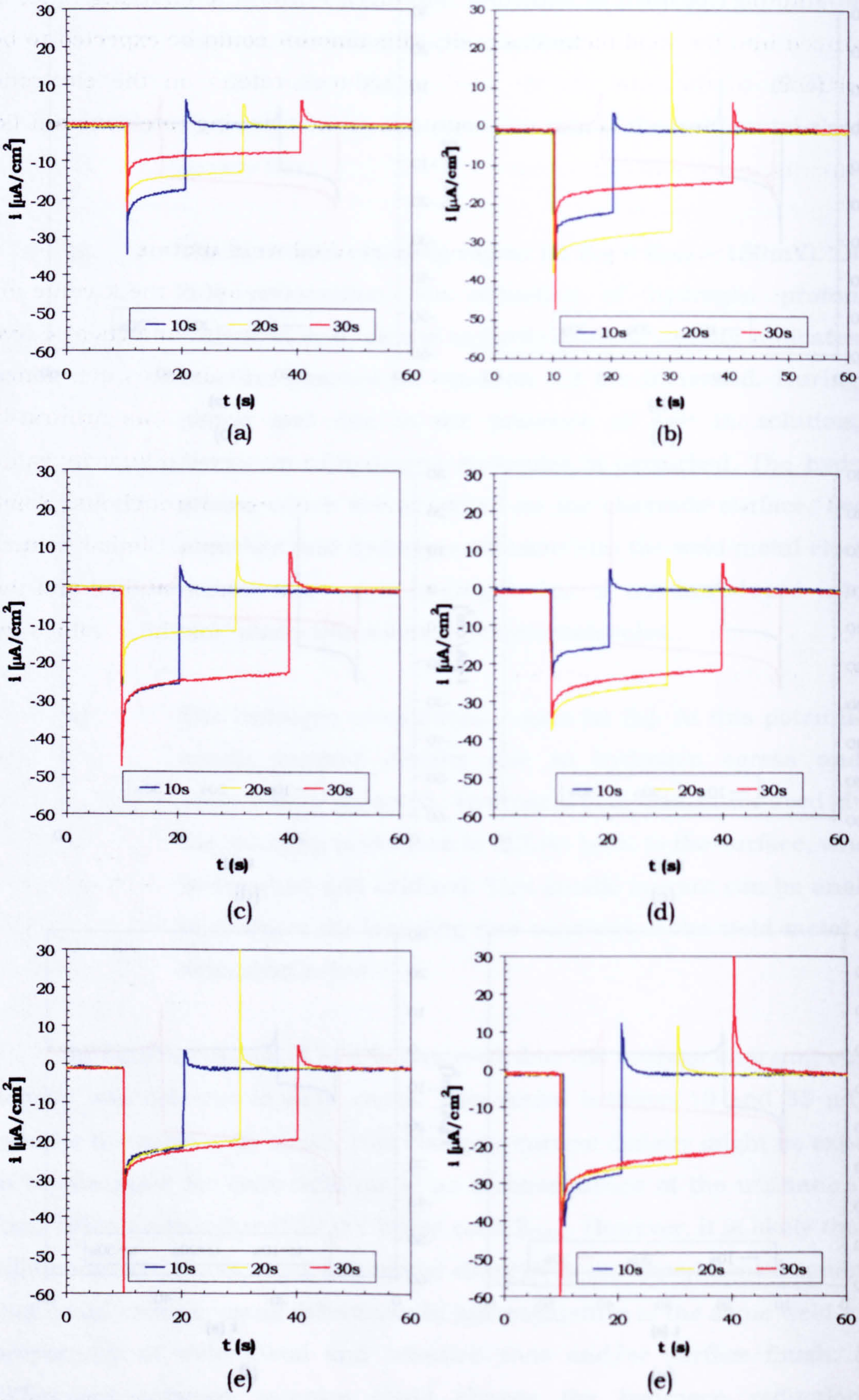

Figure 9.8 Current-time curves for the electrochemical double pulse test of the weld metals: (a) CWX201, (b) 14031, (c) CWX71, (d) CWX91, (e) CWX81 and (f) CWX331. In 0.87 mol/L acetic acid ($C_2H_4O_2$) and 0.5 mol/L sodium acetate ($C_2H_3NaO_2$) containing 15 ppm sodium meta-arsenite ($AsNaO_2$) as a hydrogen entry promoter at 25.0 ± 0.1°C.

Only part of the total hydrogen produced during the charging time, is introduced into the weld metal electrode. This amount could be expected to be proportional to the total charge used to reduce protons on the electrode surface and has to be taken into account when the trapping rate constant (k) data are discussed and compared.

9.2.1 The trapping behaviour of the studied weld metals

Figure 9.9 shows a typical example of the estimation of the k value for weld metal, CWX181. The value of k is adjusted until the analytical curve matches the experimental data. C_s value was maintained fixed as mentioned before. To simplify the estimation, the scale of the graph was arbitrarily selected as shown: from 0 to 5.0 $\mu A/cm^2$ and 0 to 5 s. A fixed diffusivity value (5.00 10^{-5} cm^2 s^{-1}) for hydrogen in the welds was used throughout. Some scatter in the anodic current can be noted for the three tests. Similar scatter was present in all other estimates of k for all the weld metals studied and the results are similar to figure 9.9. In annex A.25, the data for the k values for the different weld metals are presented.

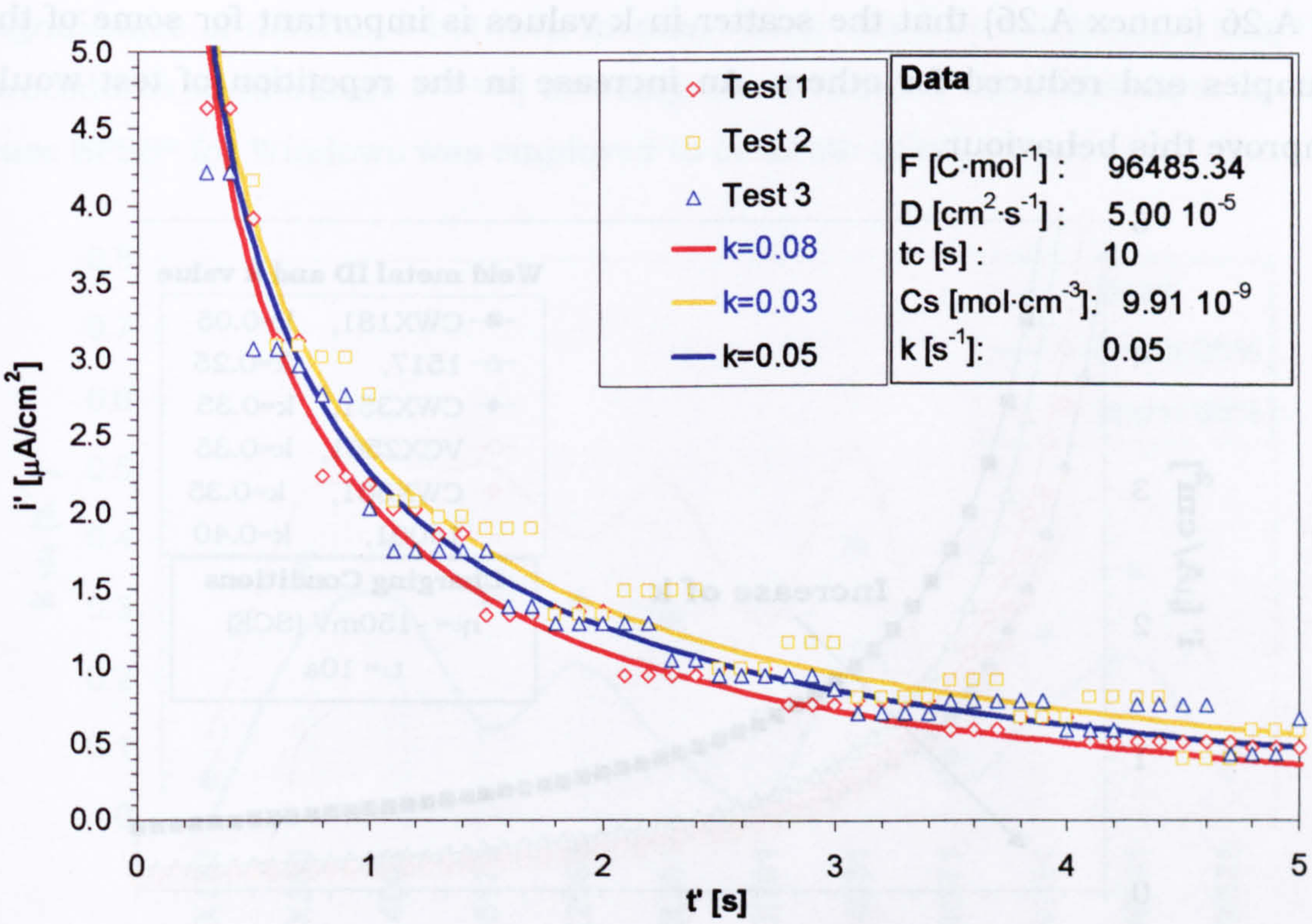

Figure 9.9 Experimental anodic current density for the re-oxidation of hydrogen for the CWX181 weld metal in 0.87 mol/L acetic acid ($C_2H_4O_2$) and 0.5 mol/L sodium acetate ($C_2H_3NaO_2$) containing 15 ppm sodium meta-arsenite ($AsNaO_2$) as a hydrogen entry promoter at 25.0 ± 0.1°C. The analytical curve was estimated graphically varying the value of k until fit experimental data.

9.2.2 Weld metals and their k value

The k value was obtained of each weld metal at three different times of hydrogen charging: 10, 20 and 30 s. Due to the small volume of samples available for the electrochemical test, each experiment was made in triplicate. Three charging times were used with the idea of obtaining as much information from each sample as possible. For this reason, a small set of data was obtained and statistical treatment is employed to analyse it safely.

Figure 9.10 presents an example of the anodic current due to the egress and re-oxidation of the hydrogen for various weld metal electrodes. For each weld metal, the curve fitted to the experimental data is shown. As can be observed, the anodic current is decreased as the k value increases. Following this approach, the k values were determined for the studied weld metals. Table 9.1 presents the k values, with their respective standard deviation, for each weld metal at different charging times. It can be noted that there exits in some cases a considerable dispersion in the data (scatter). This dispersion is below 20% for the majority of the cases (67 % of the cases in each group). To visualise this scatter a box plot is shown in annex A.26 for each weld metal tested at different charging times. It can be seen in table 9.1 and figures A.24 to A.26 (annex A.26) that the scatter in k values is important for some of the samples and reduced for others. An increase in the repetition of test would improve this behaviour.

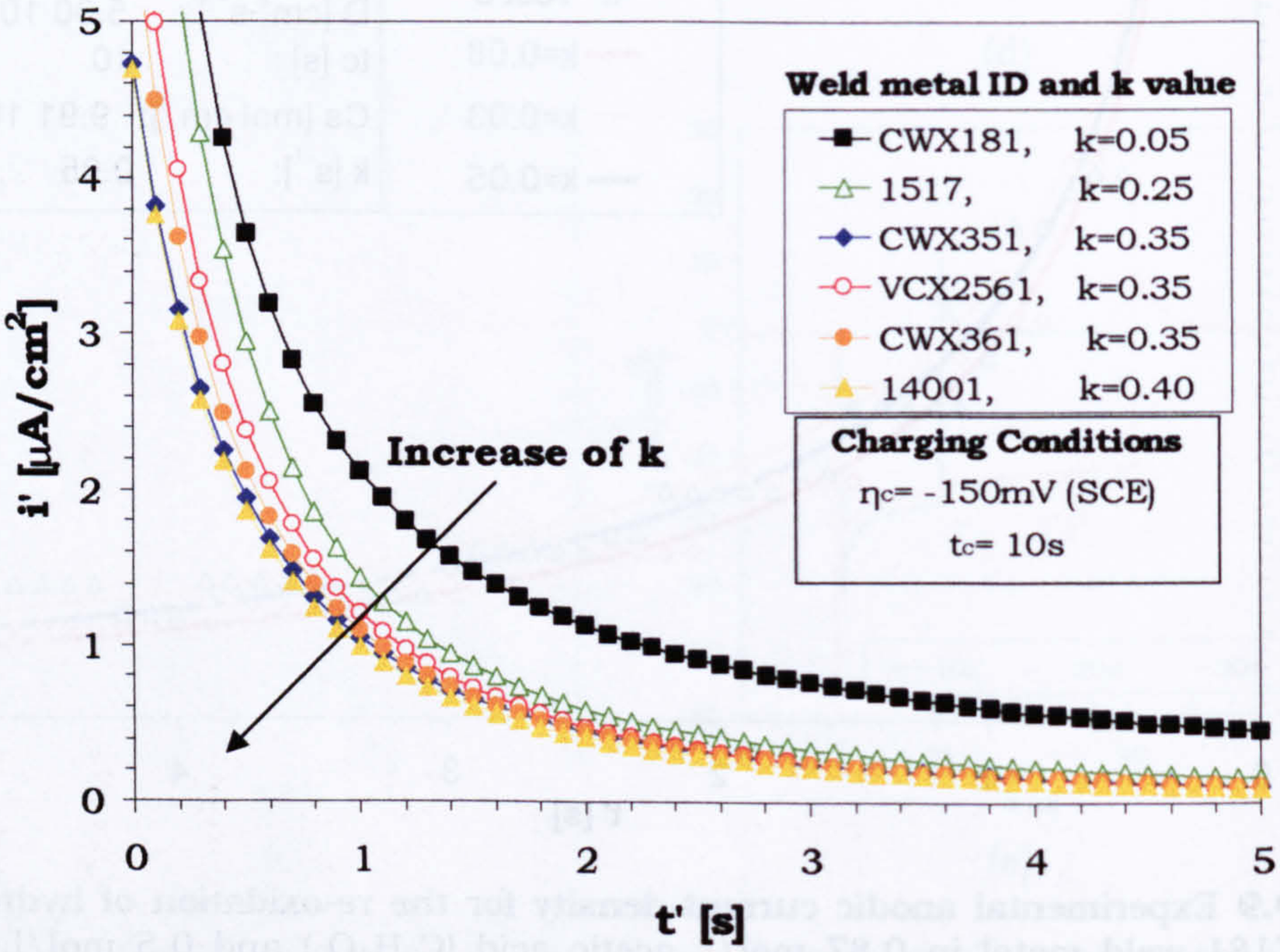

Figure 9.10 Comparison of the anodic current density for the hydrogen egress for different weld metals in 0.87 mol/L acetic acid ($C_2H_4O_2$) and 0.5 mol/L sodium acetate ($C_2H_3NaO_2$) containing 15 ppm sodium meta-arsenite ($AsNaO_2$) as a hydrogen entry promoter at 25.0 ± 0.1°C.

Table 9.1 Trapping rate constant for the different weld metals obtained by the potentiostatic double-step method

	k value ± S_x [s^{-1}]		
Weld Metal	**10s**	**20s**	**30s**
CWX181	0.053 ± 0.025	0.177 ± 0.025	0.060 ± 0.010
CWX351	0.357 ± 0.040	0.247 ± 0.025	0.170 ± 0.026
14001	0.393 ± 0.031	0.180 ± 0.020	0.150 ± 0.030
15171	0.317 ± 0.076	0.410 ± 0.036	0.273 ± 0.031
VCX2561	0.310 ± 0.036	0.550 ± 0.050	0.217 ± 0.031
CWX361	0.283 ± 0.076	0.260 ± 0.036	0.047 ± 0.006
CWX201	0.150 ± 0.050	0.400 ± 0.050	0.173 ± 0.025
14031	0.387 ± 0.055	0.127 ± 0.025	0.190 ± 0.053
CWX71	0.083 ± 0.015	0.070 ± 0.026	0.037 ± 0.015
CWX91	0.257 ± 0.040	0.033 ± 0.021	0.120 ± 0.020
CWX81	0.350 ± 0.050	0.123 ± 0.025	0.130 ± 0.020
CWX331	0.100 ± 0.020	0.097 ± 0.015	0.000 ± 0.000

In practice, to deal with a small set of data and analyse it statistically, the t-student distribution [190-196] is utilised. The estimation of confidence intervals is one of the manners to present the data to be analysed. In figures from 9.11 to 9.13, the confidence intervals (95%) around the mean k value are plotted for each weld metal for the three corresponding times of hydrogen charging. As can be observed in these figures, the comparisons between different weld metals have to be analysed considering the statistical significance of difference between means, which could be estimated using the procedures in literature [194-196] or using statistical dedicated software. In this case SPSS® for Windows was employed to facilitate calculations.

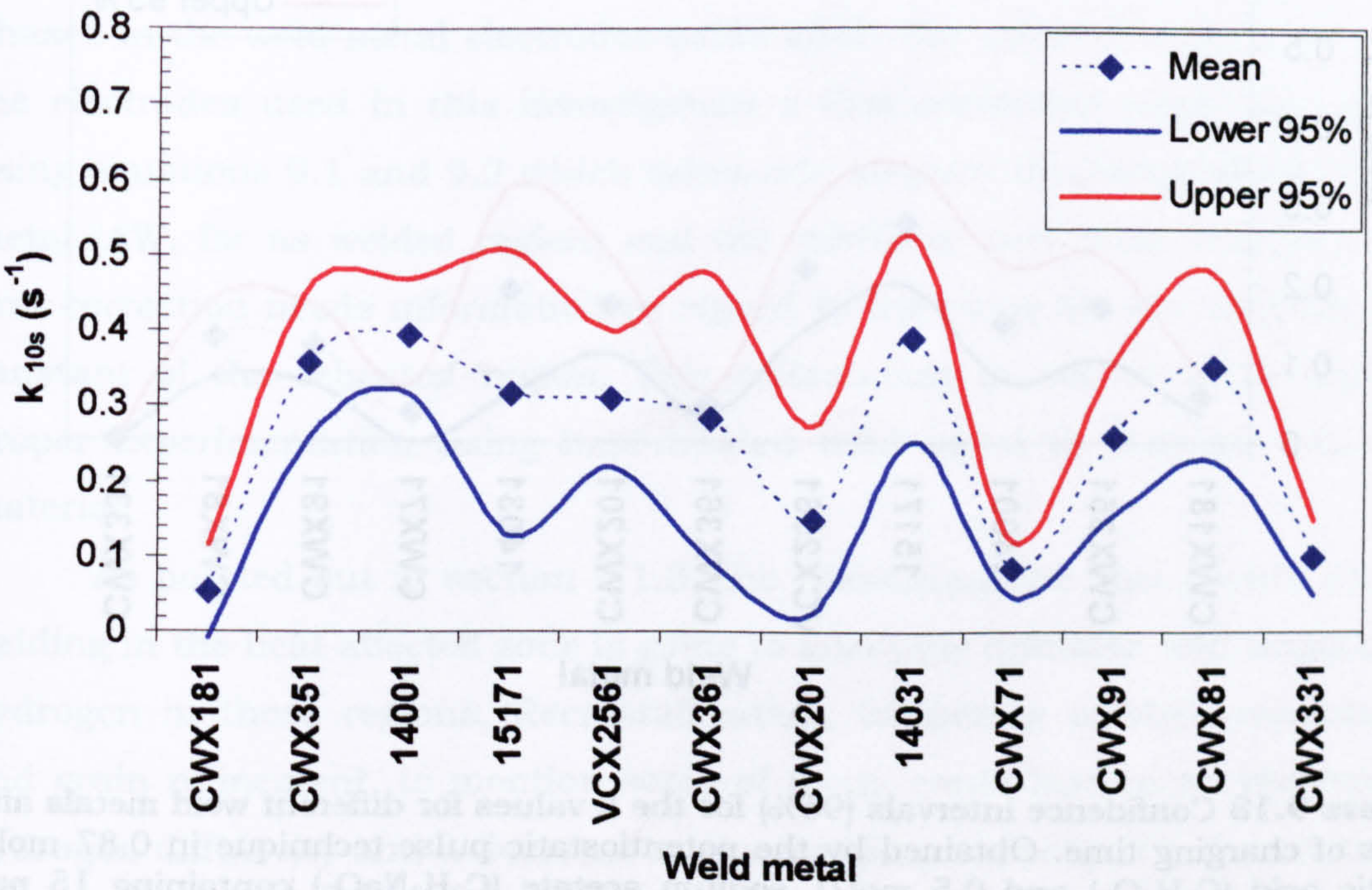

Figure 9.11 Confidence intervals (95%) for the k values for different weld metals after 10 s of charging time. Obtained by the potentiostatic pulse technique in 0.87 mol/L acetic acid ($C_2H_4O_2$) and 0.5 mol/L sodium acetate ($C_2H_3NaO_2$) containing 15 ppm sodium meta-arsenite ($AsNaO_2$) as a hydrogen entry promoter at 25.0 ± 0.1°C.

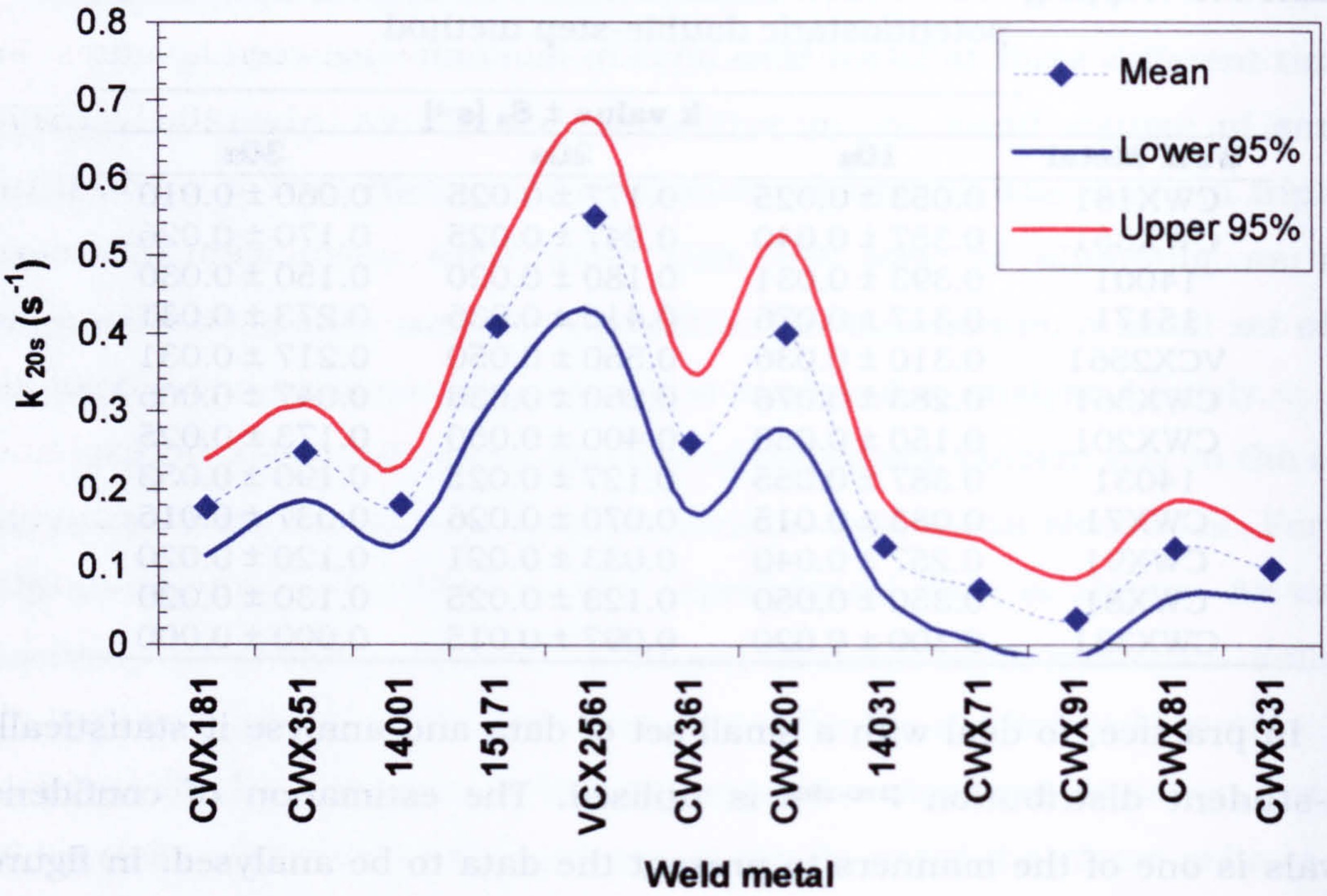

Figure 9.12 Confidence intervals (95%) for the k values for different weld metals after 20 s of charging time. Obtained by the potentiostatic pulse technique in 0.87 mol/L acetic acid ($C_2H_4O_2$) and 0.5 mol/L sodium acetate ($C_2H_3NaO_2$) containing 15 ppm sodium meta-arsenite ($AsNaO_2$) as a hydrogen entry promoter at 25.0 ± 0.1°C.

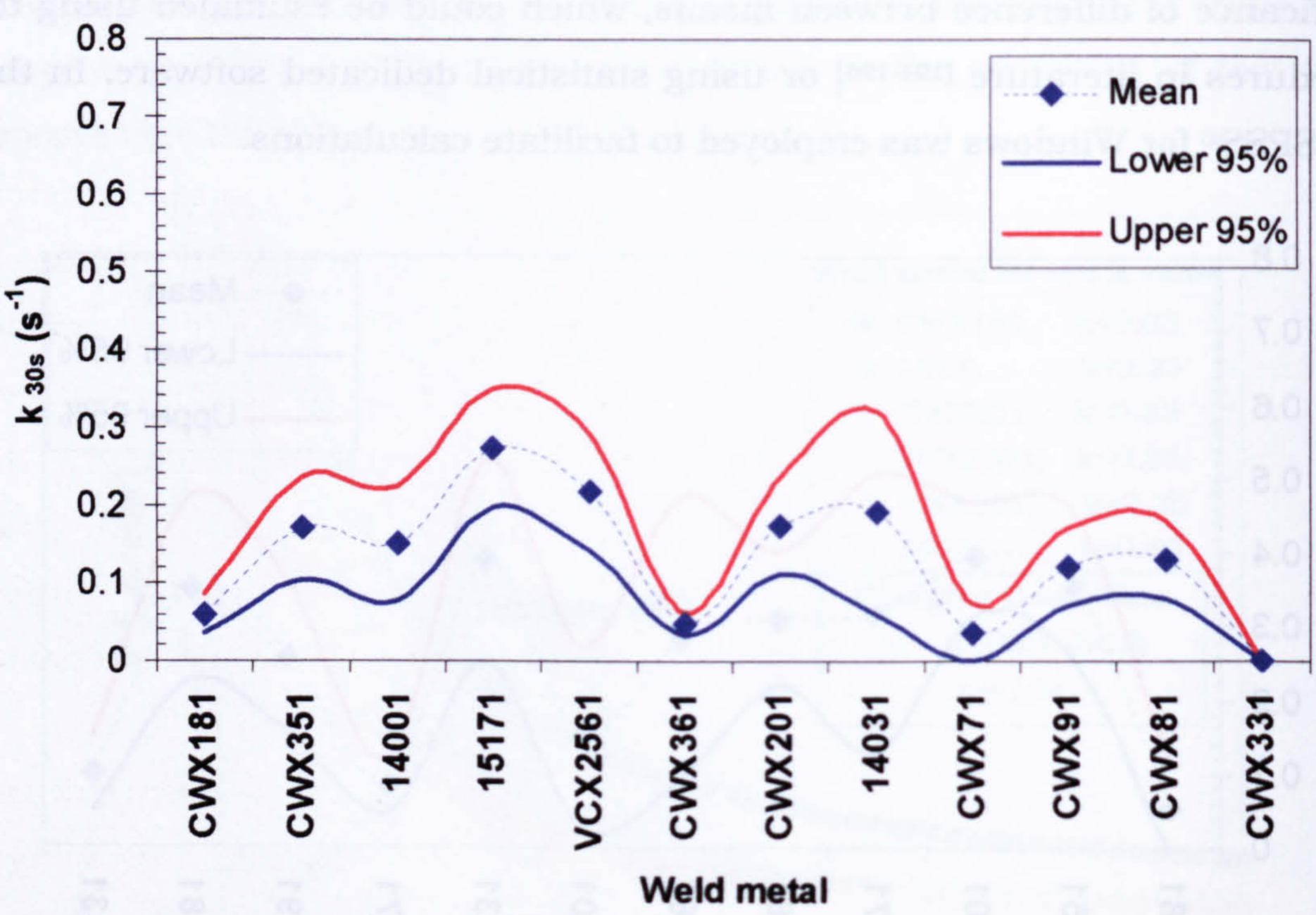

Figure 9.13 Confidence intervals (95%) for the k values for different weld metals after 30 s of charging time. Obtained by the potentiostatic pulse technique in 0.87 mol/L acetic acid ($C_2H_4O_2$) and 0.5 mol/L sodium acetate ($C_2H_3NaO_2$) containing 15 ppm sodium meta-arsenite ($AsNaO_2$) as a hydrogen entry promoter at 25.0 ± 0.1°C.

It can be noted from figures 9.11 to 9.13 that for some weld metal groups there exists no statistically significant difference between k values. For example, in figure 9.11, the group of weld metals CWX351, 14001, 15171, VCX2561 and CWX361 have no significant difference in their k value. If this group is compared with welds CWX91 and CWX81, no significant differences in k values are found and this could be associated with the several variables presented in figure 9.2. This means that the difference or equality of the trapping constant between weld metals and/or groups could be explained taking into account the similitude or inequality in microstructure characteristics: NMI density, size and distribution; MAC content and the presence of retained austenite; and the microstructure.

Comparing the figures 9.11, 9.12 and 9.13, it can be noted that the results for the k value after 20 s of hydrogen charging (figure 9.12) are better than those shows for 10 s of charging (9.11): the 95% confidence intervals are narrower for several cases. The same could be observed in the case of the results in figure 9.13 (30 s of charging). Although, all the values are going to be considered in the discussion special attention is paid in those in figure 9.12 due to their statistical quality.

9.2.3 Correction of k value due to effect of microstructure

It was mentioned in section 9.1.3 that the different proportion of ferrite phases in the weld metal electrodes could affect the value of k. In the case of the electrodes used in this investigation a first correction could be applied using equations 9.1 and 9.2 which takes into account the proportions of weld metal (AW, for as welded region) and the reheated zone (RH). However, this first correction needs information in regard to the value for the trapping rate constant of the reheated region. This information is not available without proper experimentation using heat treated weld metal to simulate reheated material.

As pointed out in section 9.1.3, the transformation that occurs during welding in the heat affected zone is going to affect the diffusion and trapping of hydrogen in these regions. Recrystallisation, tempering of MAC constituent and grain refinement, to mention some of them, could lead to an increase in hydrogen diffusivity and a decrease in the trapping capacity. On the contrary, MAC formation in high Pc_m materials due to very fast heating and cooling

cycles, the formation of carbides, between other reasons, could increase the trapping rate constant and reduce hydrogen diffusivity.

No-metallic inclusions are not expected to be affected by the reheating cycle. As a consequence, the reheated regions of the different weldments could have NMI characteristics similar to their respective weld metal. This implies that the estimation of the reheated region k value is very difficult. It has to take into account the factors that increase, decrease or maintain the intrinsic k value of the weld metal. Experimental work seems to be the correct manner to accomplish this. The supposition for the reheated region k value (k_{RH}) in this investigation has to be considered as a limitation in this investigation. It was not possible to estimate the experimental real value. Nevertheless, the correction approach is illustrated.

Table 9.2 shows, for all analysed weld metals, the factorisation of the experimentally measured k value into: k_{tcAW} and k_{RH} values, the trapping rate constant for weld metal and reheated region after the charging time t_c, respectively. It was supposed that the value for k_{RH} has a low value (0.05 s^{-1}) based on some results reported in the literature and considering that the hydrogen diffusivity is high in this region, decreasing k. As a reference, the investigation by Pound [104], reported that the trapping constant, as measured by the pulse technique, is very low for an annealed high strength steel (AerMet 100), in fact the investigator report a value of k of 0.000 ± 0.001 s^{-1}. It is difficult to suppose a value in accordance to this reference for the reheated region of the weld. The reheated region, as mentioned above, depending on the heating and cooling cycles, the composition and the NMI content of the previous weld metal, might contain certain degree of trapping capacity, which might be different for each weld. However, what is truly expected is a reduction in the k value due to recrystallisation of the reheated weld metal. Further work to establish clearly the value for k_{RH} is needed to correctly estimate the effect of this region on the overall k value and particularly the value of k_{tcAW}.

Preliminary calculations supposing a k_{RH}=0.05 s^{-1} are shown in table 9.2. The estimations seem to indicate that the correction does not change the trend indicated already for the measured k value. It seems to increase the k value for most of the weld metals and slightly change this value for few of them. Nevertheless, the qualitative comparison between the weld metals is not affected by the correction – the original behaviour is not affected by the consideration of the reheated region proportion.

Table 9.2 Corrected value of the trapping rate constant for the weld metals studied in this investigation. Correction was made using equation 9.2.

Weld metal	AW (%)	RH (%)	k_{10} (s^{-1})	k_{10AW} (s^{-1})	k_{20} (s^{-1})	k_{20AW} (s^{-1})	k_{30} (s^{-1})	k_{30AW} (s^{-1})
CWX181	69.4	30.6	0.053	0.054	0.177	0.233	0.060	0.064
CWX351	65.9	34.1	0.357	0.516	0.247	0.349	0.170	0.232
14001	55.3	44.7	0.393	0.670	0.180	0.285	0.150	0.231
15171	63.6	36.4	0.317	0.470	0.410	0.616	0.273	0.401
VCX2561	62.8	37.2	0.310	0.464	0.550	0.846	0.217	0.316
CWX361	70.9	29.1	0.283	0.379	0.260	0.346	0.047	0.046
CWX201	50.9	49.1	0.150	0.246	0.400	0.738	0.173	0.292
14031	54.1	45.9	0.387	0.673	0.127	0.192	0.190	0.309
CWX71	49.9	50.1	0.083	0.116	0.070	0.090	0.037	0.024
CWX91	60.4	39.6	0.257	0.393	0.033	0.022	0.120	0.166
CWX81	74.5	25.5	0.350	0.453	0.123	0.148	0.130	0.157
CWX331	68.9	31.1	0.100	0.123	0.097	0.118	-	-

k_{tc}: trapping rate constant for the weldment (weld metal + reheated region)
k_{RH}: trapping rate constant for the reheated region, supposed as 0.05 s^{-1}
k_{tcAW}: trapping rate constant for the weld metal as welded, tc = 10, 20 and 30 s.

The figure 9.14 presents in a graphical manner the changes in the k values after the correction and, as can be observed, the correction just amplify the value of k but keeping the differences between weld metals similar. For example, in figure 9.14(a) the k value for the CWX181 weld metal was slightly changed by the correction. On the other hand, that for the CWX351 was changed from 0.357 to 0.516, about 44.5 % increase. The difference between these two welds was increased but the behaviour is just the same as the original – the CWX351 weld metal has larger hydrogen trapping capacity than the CWX181. Although, this behaviour is repeated in several other examples in figure 9.14, it has to be taken with care due to the supposition of equal k_{RH} values for all welds, limiting the interpretation. In most of the cases, the correction maintained the differences between the original k values (see figure 9.14(b) and (c), as well). In few other cases, the correction seems to equalise the k value, as shown in figure 9.14(c) for the weld metals: CWX351-14001 and CWX81-CWX91. However, the original k values for these two pairs were similar, if it is considered their standard deviations.

The k value, as was discussed before, can be used to compare the hydrogen trapping capacities of the weld metals. The original k value contemplates the trapping rate constant for both weld metal and reheated region of weldment. On the other hand, k_{AW}, is the trapping rate constant for the weld metal alone when the k_{RH} is supposed to be similar for all the welds and a 0.05 s^{-1} value.

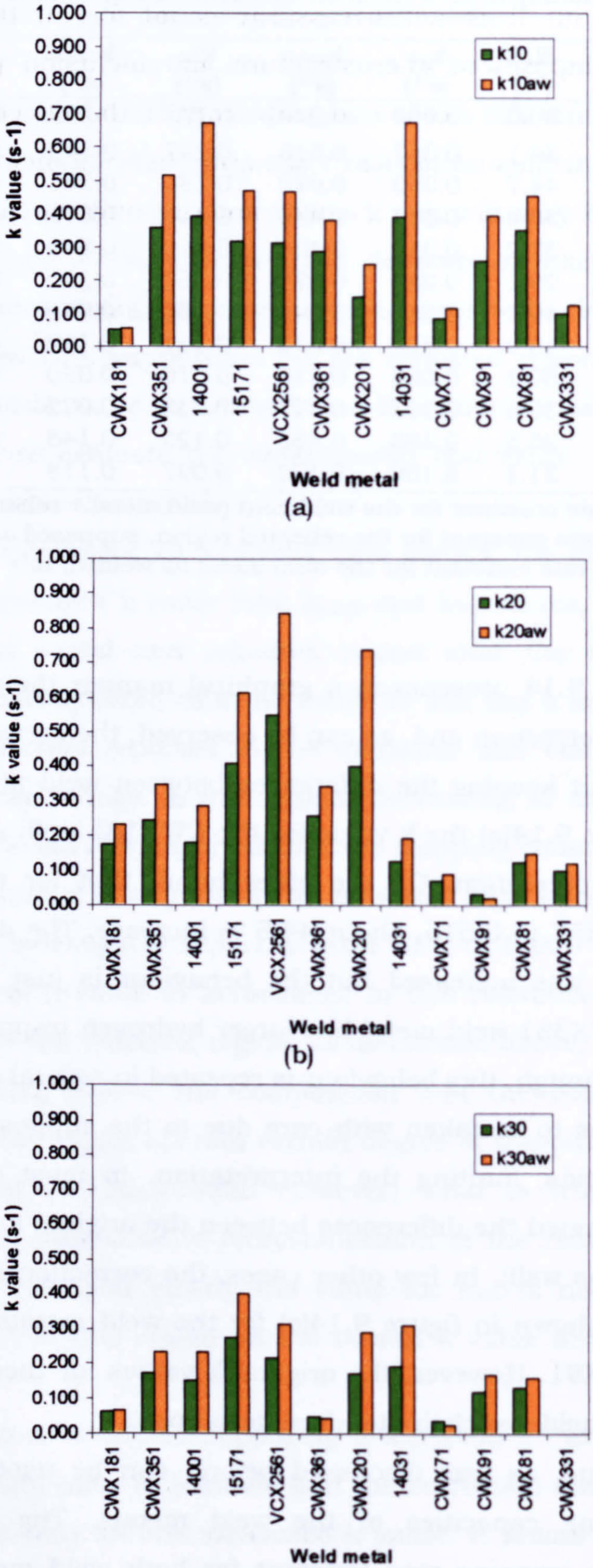

Figure 9.14 Corrected trapping rate constants (k_{10AW}, k_{20AW} and k_{30AW}) for all the weld metals. The k_{rh}, the k value for the reheated region of weldment, was supposed to be 0.05 s^{-1}. k values for times of charging (t_c): (a) 10 s, (b) 20 s and (c) 30 s. Calculation was made using equation 9.2. Table 9.2 shows the values.

This supposition may be close to the real value of the k value for the reheated region but it is not necessarily equal for all the welds due to differences in composition, microstructure and inclusion population. More detailed experiments are needed to truly correct the effect of the reheated material on the k value and to clearly separate the weld metal behaviour. This could be done by simulating reheated material and carefully studying the trapping capacity of weld metals.

For all these reasons and for simplicity, the discussion of the hydrogen trapping rate constant was based on the original k values, those who represent the trapping capacity of the weldment (weld metal + reheated region). Taking into account the k_{AW} values does not change the comparisons that are discussed in the following sections – these are qualitative comparisons.

9.2.4 Effect of hydrogen charging time on k values.

From figures from 9.11 to 9.13 it is difficult to elucidate the effect of charging time on the value of k. However, a simple inspection and comparison of figure 9.13 with the others seems to indicate that the increase in charging time (t_c) could reduce trapping capacity of the weld metal. This could be possible if the traps become saturated with hydrogen at longer times. If k values for each weld metal are plotted against charging time, taking into account their confidence intervals, it could be possible to observe the influence of charging time. Figures 9.15, 9.16 and 9.17, present three groups of weld metals. Each group behaves in a particular manner, respectively:

a- Weld metals which a k value that decrease with t_c.
b- Weld metals with a maximum k value at t_c = 20 s
c- Weld metals with a minimum k value at t_c = 20 s.

These variations in k with time of charging could be associated to different factors: hydrogen saturation of traps, size and spatial distribution of traps, heterogeneities in the weldment (defects) and variations in microstructure. Other source for k variation that can not be avoided is the proper scatter of the experiment, which is a result for using a small number of samples. Nevertheless, this does not invalidates the results if a proper statistical analysis is employed – the student distribution, for example.

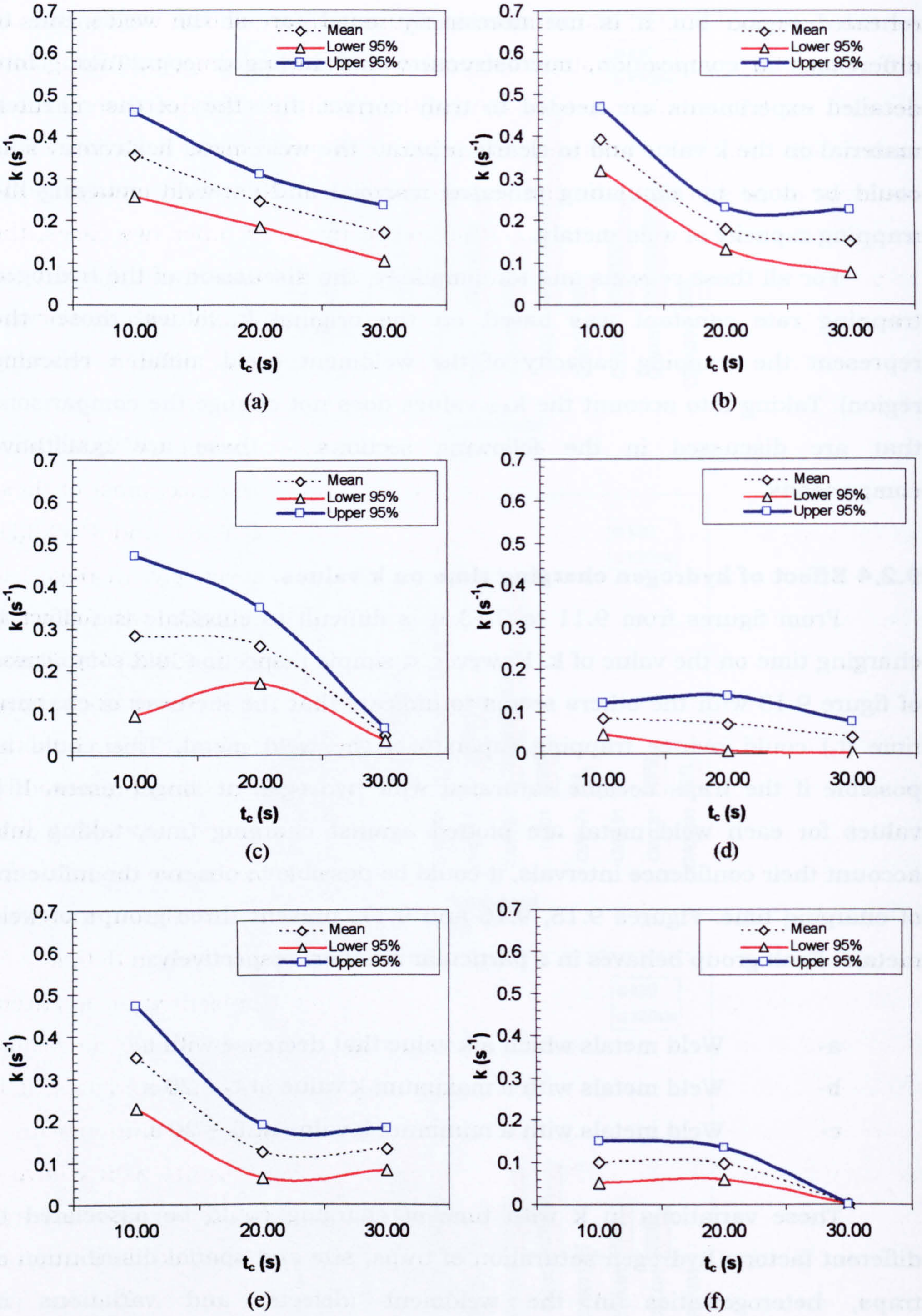

Figure 9.15 Variation of k value with the hydrogen charging time for the weld metals: (a) CWX351, (b) 14001, (c) CWX361, (d) CWX71, (e) CWX81 and (f) CWX331. The k value, for these weld metals, decreased with t_c.

Although the double-step technique supposes that hydrogen traps do not saturate with the charging times, its occurrence might be possible. This

depends on the traps capacity to accumulate hydrogen, which could depend on their size and spatial distribution. In figure 9.15 are shown weld metals of group (a), those whose k values decrease with charging time, t_c. Taking into account the 95% confidence bands, it can be noted that the decrease in the k values with time is statistically significant. In two cases, k decreases is observed at 20 s of charging and remains similar at 30 s: weld metals 14001 and CWX181, in figures 9.15(b) and (e), respectively. In other two cases, the decrease in k is observed at 30 s of charging: figures 9.15(c) and (f). Only for the weld metal CWX351, the k seems to decrease gradually with t_c. For the case of CWX71, the k value remains at the same level at the different charging times.

It was found that all the welds in figure 9.15, except CWX331, have clustered NMI distribution. With respect to NMI maximum size, most of these welds are classified as S (small): CWX361, CWX71, CWX81 and CWX331. CWX351 and 14001 are M (medium) and L (large), respectively. In regard to NMI number (see appendix A.15), these welds are classified as follow: H (CWX351, 14001, CWX71, CWX81), M (CWX361) and L (CWX331). These suggest that the size and spatial distribution of traps could contribute to their saturation with hydrogen and as a consequence a reduction in their k value. However, other microstructural features could produce the effect presented by CWX71 and CWX331. For example, the martensite content in CWX331 could increase hydrogen solubility or diffusivity, keeping k values low or inexistent trapping capacity, as in this case at 30 s. At the end of this section, the effect of size and spatial distribution of traps (NMI or MAC) are treated in detail.

Figure 9.16 present a group of weld metal that presented an apparent maximum k value at 20 s of hydrogen charging. Again, it should be related with the trap size and distribution. Comparing the NMI characteristics, it is noted that all welds in figure 9.16 have a random NMI distribution with a maximum size classified as large (L), except for weld CWX201 which have a medium size. The NMI number is from low (L) to medium (M). It could indicate, as mentioned before, that the large maximum inclusion size and their random distribution and low number (maximum frequency) are responsible for this behaviour. This is discussed latter in this section.

The presence of heterogeneities (defects) or differences in microstructure along the weld metal could cause different responses of the same weld metal. For example, some micro shrinkage was found on the fracture surface of weld metal CWX201. It is possible that the distribution of

these defects is not homogeneous and the sample tested during 20 s contains them. The presence of these cavities could trap hydrogen in large quantities giving a high k value. Nevertheless, there is no evidence to explain the behaviour of the rest of weld metals in figure 9.16. As a result, this behaviour could be attributed, in general, to differences between samples of the same weld, leaving the similarities in NMI characteristics as a more likely explanation.

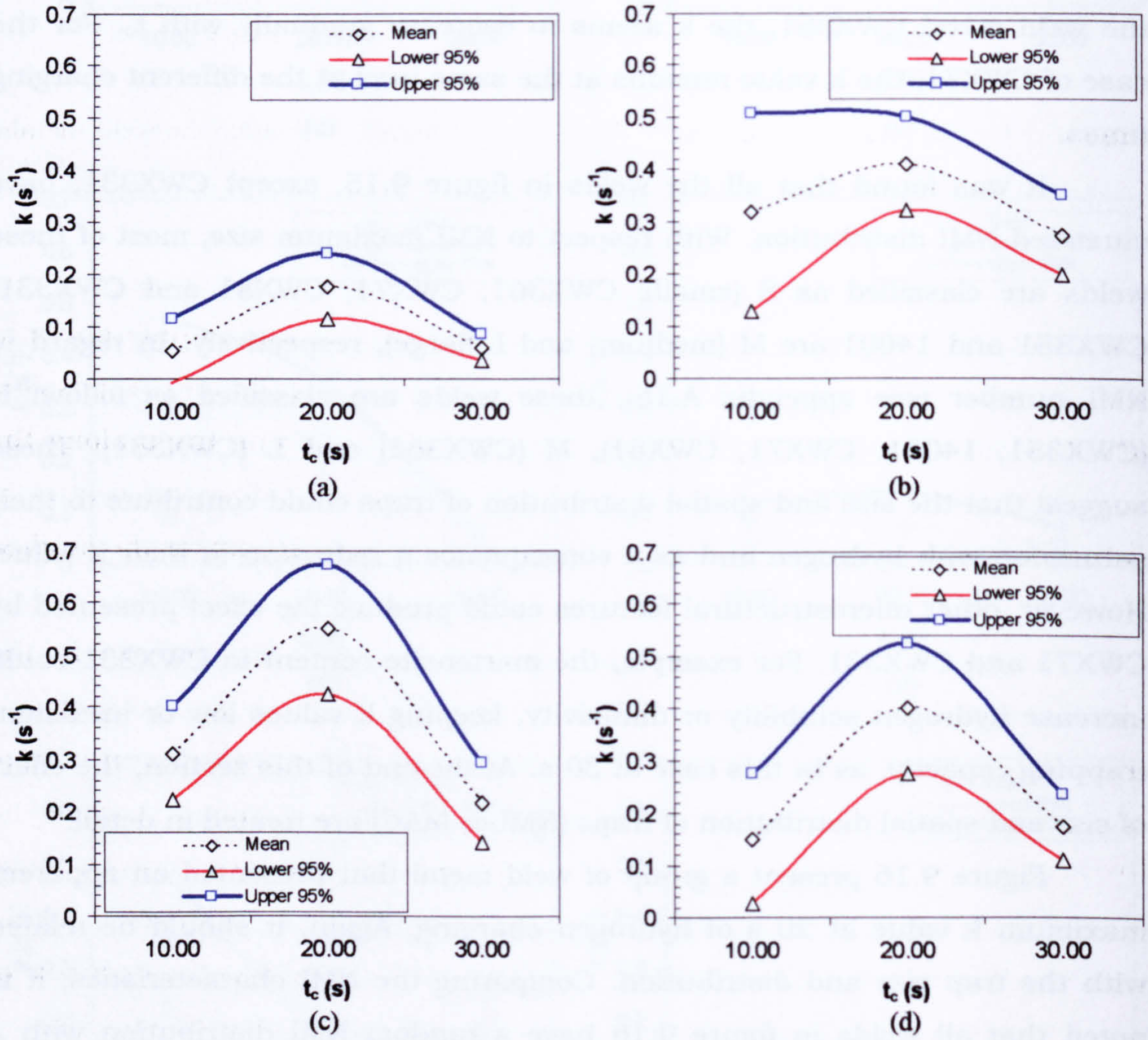

Figure 9.16 Variation of k value with the hydrogen charging time for the weld metals: (a) CWX181, (b) 15171, (c) VCX2561 y (d) CWX201. This group of weld metals presented an apparent maximum k value at 20 s of charging.

Figure 9.17 presents the remaining two weld metals. In this case, an apparent minimum k value is found. However, confidence intervals for the weld metal 14031 and CWX91 shows no statistical significance for the k values at 20 and 30 s for the first case and a similar value for the last. As a consequence, these cases could be treated as a decrease in k with t_c (group (a)). The decrease in k value could be related with the saturation of traps, which depends on size and spatial distribution as is discussed below.

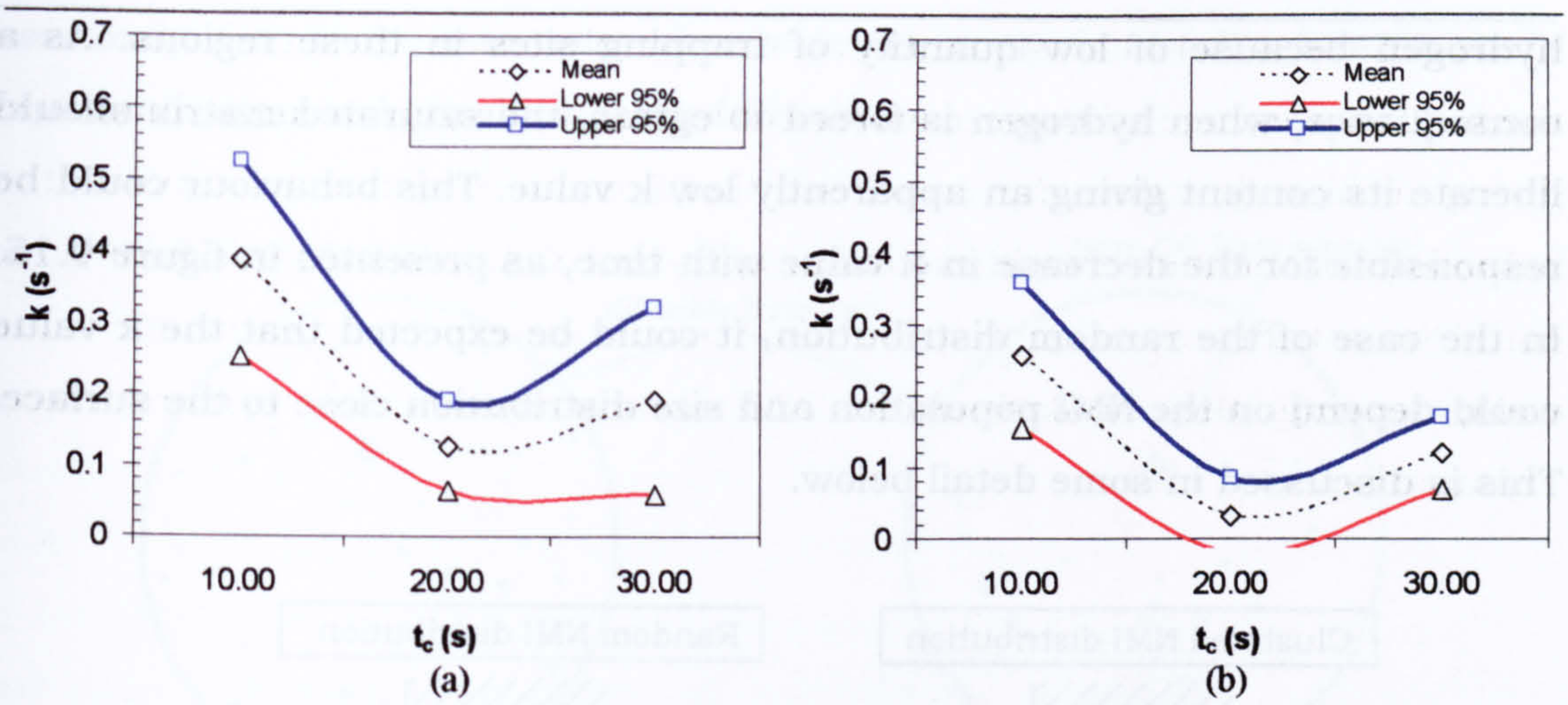

Figure 9.17 Variation of k value with the hydrogen charging time for the weld metals: (a) 14031 and (b) CWX91. These weld metals presented a minimum k value at 20 s of hydrogen charging.

In general, the k value could be affected by the hydrogen charging time and saturation of traps in the weld metal. Nonetheless, due to differences in microstructure between samples of the same weld metal, and a possible heterogeneous distribution of defects or other kind of strong traps along the weldment, the k value can suffer deviations producing the observed scatter in the experimental results. The variations in k with charging time for the studied weld metals could be summarised as follow:

1- Partial or total saturation of superficial traps. An increase in the charging time introduces more hydrogen into the weld metals samples and this could saturate the traps close to the surface of the electrode. Saturation of the traps permit the saturation of the matrix around the traps and when the hydrogen is forced to egress from the sample enough hydrogen can re-oxidise on the electrode surface giving an apparently low k value. This could explain the high k values found at short time of charging (t_c= 10 s) and the decrease of this values at longer times, as presented in figure 9.15 with few exceptions.

2- Effect of NMI clustering in the weld metals. Figure 9.18 shows schematically the effect of the NMI spatial distribution. Two distributions are presented: clustered and random. In each case the front of hydrogen diffusion is indicated for the different charging times. Suppose that both samples are charged during 10 s. The sample with clustered NMI has more probability for trap hydrogen than the individual NMI in the random distribution. The k value should indicate that more hydrogen was trapped in the first sample. An increase in charging time will introduce more hydrogen in both samples. The matrix of the sample with clustered NMI, where there are free volumes between NMI clusters for the hydrogen to diffuse, can be saturated with

hydrogen because of low quantity of trapping sites in these regions. As a consequence, when hydrogen is forced to egress, the saturated matrix should liberate its content giving an apparently low k value. This behaviour could be responsible for the decrease in k value with time, as presented in figure 9.15. In the case of the random distribution, it could be expected that the k value could depend on the NMI population and size distribution close to the surface. This is discussed in some detail below.

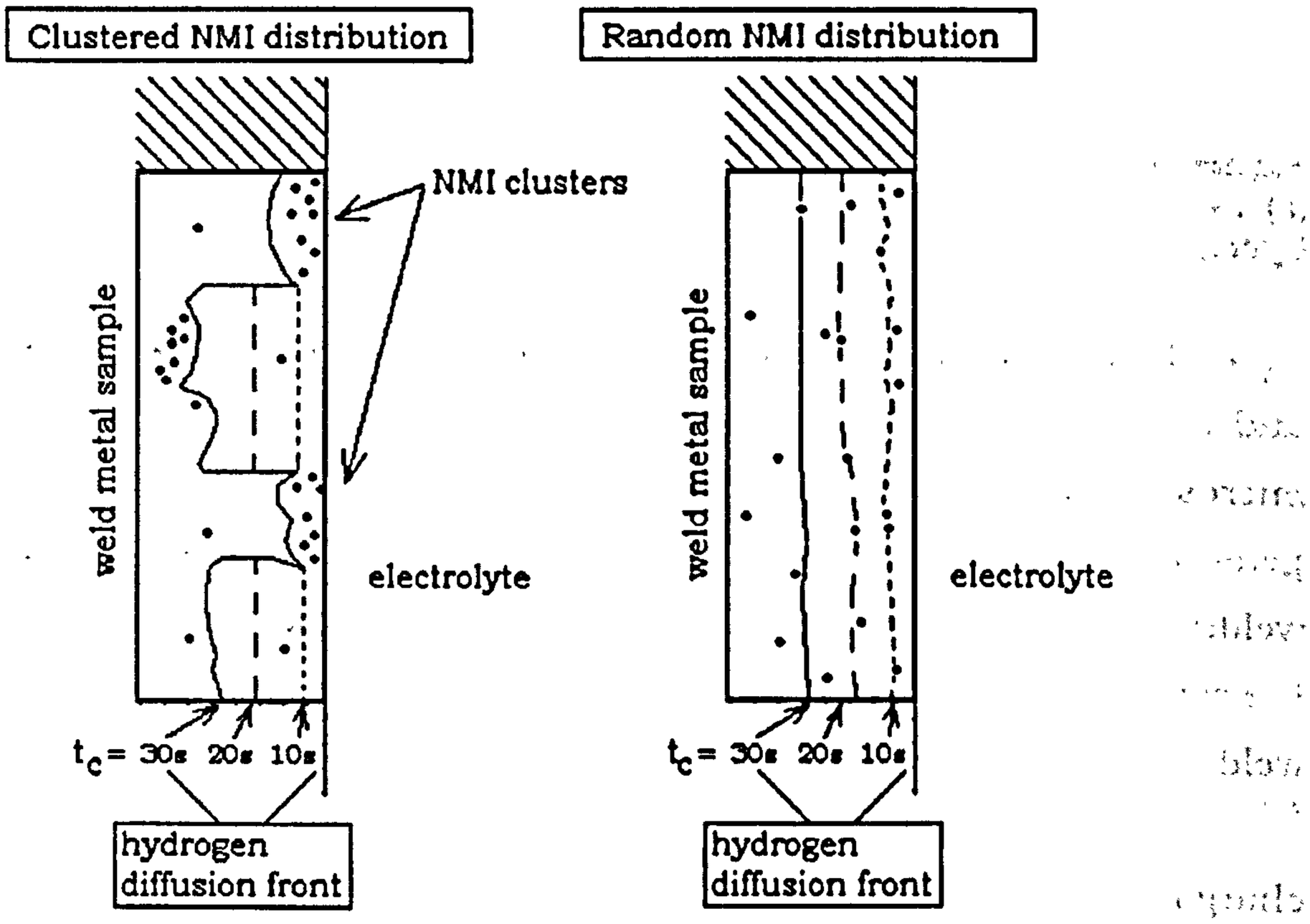

Figure 9.18 Schematic representation of the diffusion of hydrogen at different charging times for weld metals with clustered and random NMI distributions. Clustered distribution could give an apparently low k value.

The clustering of NMI in weld metals could produce the formation of large quasicleavage facets on the fracture surface, as schematically presented in figure 9.19. Basically, the effect of clustering is to permit hydrogen to have more mobility in those volumes between clusters which have low trapping density sites. Due to this, diffusible hydrogen has more chance to reach a susceptible site for crack initiation. In the figure this potential crack initiator is a large inclusion but could be another potential flaw: microcracks, voids, cavities, etc. If the critical hydrogen content for cracking is reached, then a crack is formed and its growth is assisted by the sufficient diffusible hydrogen available in the saturated matrix. In the example of the figure a large quasicleavage facet can be expected around the inclusion which initiates the crack. On the contrary, hydrogen in weld metals with a high NMI content

randomly distributed has more chance to be trapped, and the assistance to crack initiation and growth is more difficult.

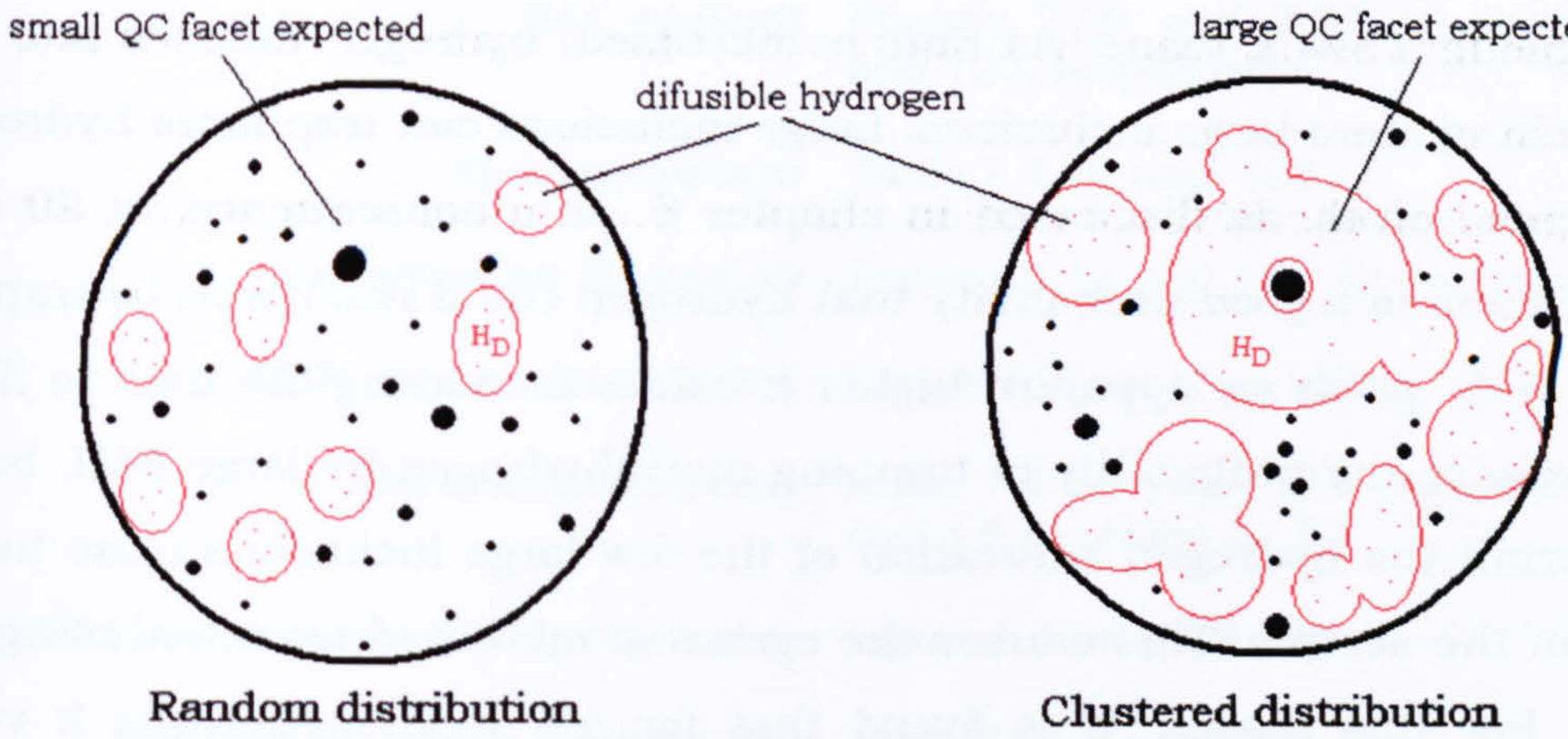

Figure 9.19 Distribution of hydrogen in the weld metal due to different NMI distributions: clustered and random.

3- Effect of trap size and distribution. Figure 9.20 shows schematically the behaviour of weld metals at different hydrogen charging times. This behaviour could be the result of the presence of large NMI in the weld.

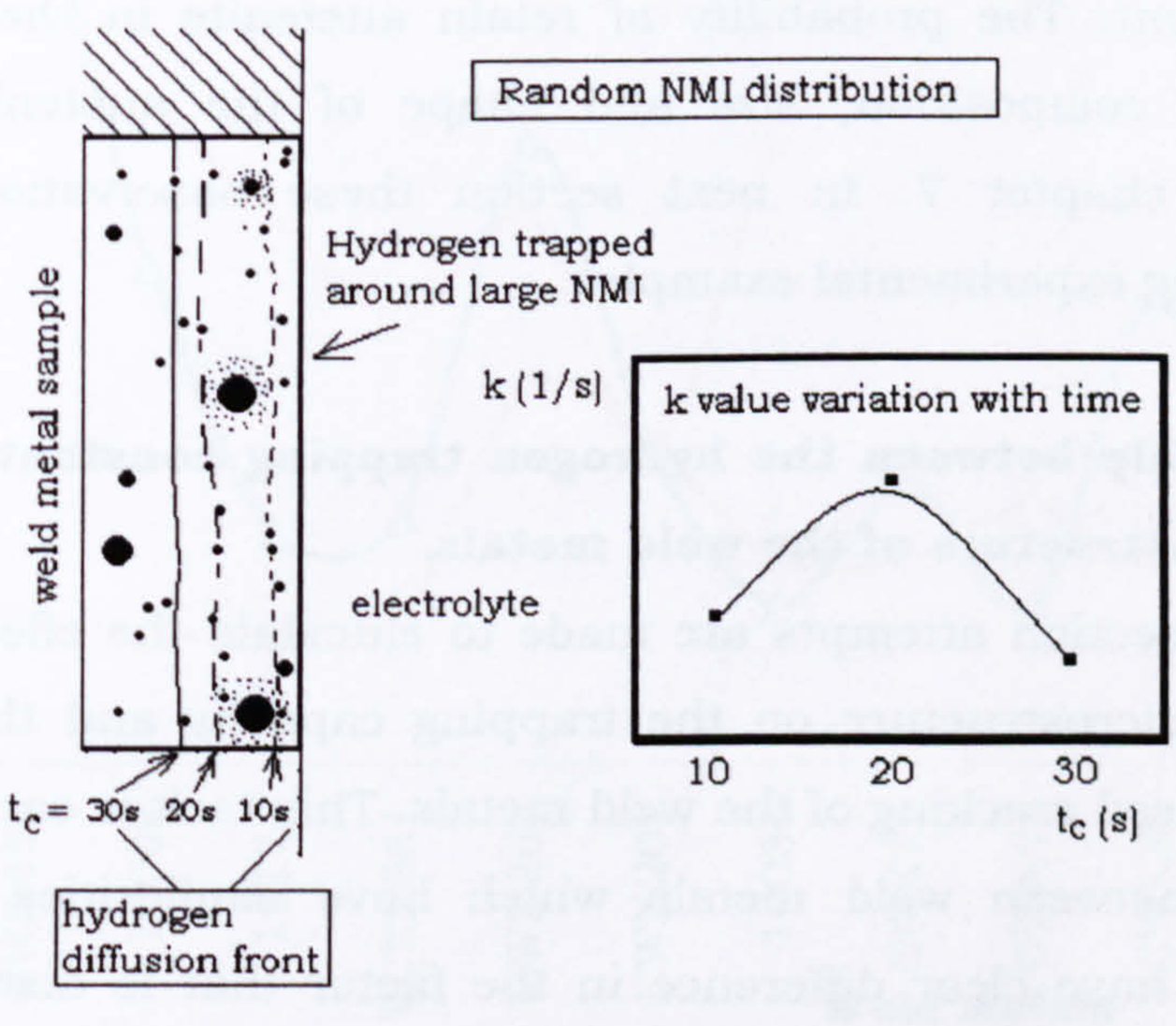

Figure 9.20 Effect of large inclusions on the variation of the k value with charging time. At short tc and apparent low k value is obtained. At medium tc, if large inclusions are presents, an apparent large k value is measured. After longer charging times and total or partial saturation of large NMI, lower k values could be registered.

In figure 9.16, four weld metals have an apparent maximum k value at 20 s of charging. These welds have a random spatial distribution of NMI, low and medium NMI number and a large maximum NMI size, as presented in figure 9.20. At short times, t_c = 10 s, hydrogen diffuses a short distance from

the surface. Between these distances large and small inclusions could be found and these should trap hydrogen in some quantity. Due to the random distribution and low population of NMI, the trapped hydrogen quantity should be low, giving a low k value. As time is increased, hydrogen diffuses into the steel reaching more large inclusions. Large inclusions can trap more hydrogen around themselves, as discussed in chapter 8. As a consequence, at 20 s of charging there is a good probability that hydrogen could reach and be trapped by large NMI, given an apparent higher k value. Increasing the time to 30 s, could increase the probability of trapping more hydrogen by large NMI, but it could permit the hydrogen saturation of the few large inclusions close to the surface of the sample. This causes the egress of more hydrogen, reducing the k value. For this reason, it is found that for few weld metals the k value present a maximum at 20 s of hydrogen charging, as shown in figure 9.16.

3- *Effect of retained austenite content.* Due to the hydrogen high solubility and binding energy of H in austenite, it is expected that an augment in retained austenite proportion can increase the k value. However, an increase in MAC content not necessarily produces an increase in the trapping constant. This could be dependent on the presence of retained austenite in the MAC constituent. The probability of retain austenite in the weld metal is influenced by composition, size and shape of the austenite particle, as discussed in chapter 7. In next section these observations are further discussed using experimental examples.

9.3 Relationship between the hydrogen trapping constant, the Ck value and the microstructure of the weld metals.

In this section attempts are made to elucidate the effect of NMI, MAC content and microstructure on the trapping capacity and the resistance to hydrogen induced cracking of the weld metals. This task is carried out making comparisons between weld metals which have similarities in a group of variables and have clear difference in the factor that is discussed. Support from previous chapters is used and to help the reader a list of key figures and tables is presented in table 9.3. Figure 9.21 collect in a visual manner part of the information which could be found in figures and tables mentioned in table 9.3. This figure shows the value of C_k, the MAC content and NMI characteristics of the weld metals studied in this investigation: number density (Nv), distribution, size and inclusion number (see annex A.15).

Table 9.3 Location of relevant information from previous chapter

Relevant information	Location
General microstructure	Figure 7.11 and table 7.2 on page 119
MAC content	Figures 7.19 and 7.20 on pages 126 and 127, respectively
M_f temperature	Table 7.3 on page 133
Size effect on M_s and M_f	Figures A.11 and A.12 in annex A.13
NMI number density (Nv)	Figure 7.27 on page 139
NMI characteristics	Table 7.4 on page 144 and tables A.5 and A.6 in annex A.14
Weld metal mechanical properties	Figure 8.1 on page 160
Critical hydrogen content (C_k)	Table 8.1 on page 166

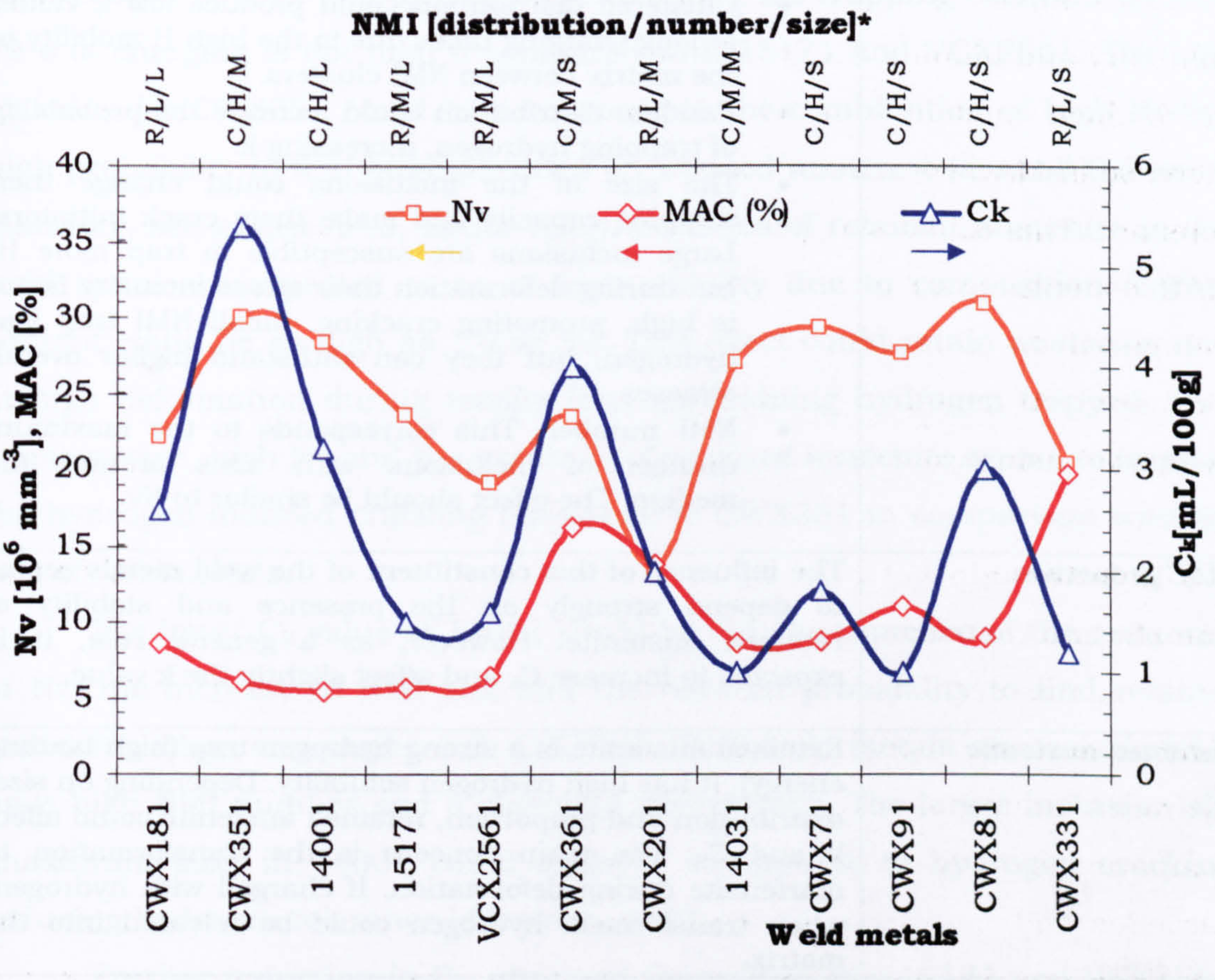

Figure 9.21 NMI true number density (Nv) and main characteristics (distribution/number/size), MAC proportion and critical hydrogen content (C_K) for the weld metals studied in this investigation. *NMI distribution: R (random) and C (clustered); number: L (low), M (medium) and H (high); size: L (large), M (medium) and S (small).

Although the visual presentation of this data has no intention of showing clearly correlation and trends of the variables and C_k, it can be observed that some C_k maximums seems to be related to MAC and N_v

maximums. This suggests that both of these variables can have a beneficial effect on the hydrogen induced cold cracking of the weld metals. This is discussed in detail in the next sections.

Table 9.4 Factors to be considered when comparing weld metals with respect to hydrogen trapping capacity (k) and hydrogen cracking resistance (C_k)

Factor	Effect on k and C_k
Microstructure	Microstructure could affect k and C_k in several ways: modifying the hydrogen transport (PF(G), AF, B, M), promoting crack formation due to the presence of susceptible features (B and M).
NMI number density, Nv	An increase in N_v could contribute to the trapping of hydrogen. The redistribution of H reduces the chance to hydrogen accumulation at susceptible sites. It is important to consider NMI size and distribution.
NMI characteristics	NMI number, size and spatial distribution could affect k and C_k in several ways: • Clustered distribution could produce low k values at long charging times due to the high H mobility in the matrix between NMI clusters. • Random distribution could increase the probability of trapping hydrogen, increasing k. • The size of the inclusions could change their trapping capacity and make them crack initiators. Large inclusions are susceptible to trap more H, but during deformation their stress intensity factor is high, promoting cracking. Small NMI trap less hydrogen, but they can withstand higher overall stresses • NMI number. This corresponds to the maximum number of inclusions with sizes around the median. The effect should be similar to Nv.
MAC proportion	The influence of this constituent of the weld metals seems to depend strongly on the presence and stability of retained austenite. However, as a general rule, it is expected to increase C_k and affect slightly the k value.
Retained austenite	Retained austenite is a strong hydrogen trap (high binding energy). It has high hydrogen solubility. Depending on size, distribution and proportion, retained austenite could affect k and C_k. The main concern is the transformation to martensite during deformation. If charged with hydrogen, when transformed, hydrogen could be released into the matrix.

Comparison between weld metals is divided into three general groups, considering similarities between each other. These groups are:

a- Weld metals with similar MAC content

b- Weld metals with similar NMI number density

c- Weld metals with combined effect: microstructure, NMI and MAC.

Each group is discussed taking into account the factors presented in table 9.4: microstructure, NMI characteristics, MAC proportion and retained austenite. The combination of these factors, as discussed before, could improve or impair the resistance to hydrogen induced cracking and the trapping capacity of the weld metals.

9.3.1 Welds with similar MAC content: effect of NMI characteristics and retained austenite presence on k and C_k.

Figure 9.22 present a group of four weld metals which have MAC contents around 6%: CWX351, 14001, 15171 and VCX2561. The first three contain a continuous network of grain boundary ferrite (PF(G)) in different proportions with acicular ferrite (AF). VCX2561 has a discontinuous PF(G) and AF. It can be noted that the weld metal CWX351 has the highest C_k value in this group: 5.4 mL / 100 g. On the other hand, the trapping constant (k) after 20 s of charging is not high if compared with 15171 and VCX2561. The high C_k value for CWX351 could be a response to the combination of high Nv and high probability to find large particles of retained austenite (around 0.6 μm in diameter, see annex A.13, figure A.11). Particles of retained austenite in this weld metal are expected to be of high stability due to composition (carbon content could be as high as 1.0 wt %). This effect could retain austenite even at high deformation during tensile test, maintaining hydrogen trapped. As a consequence, high Nv and the presence of retained austenite seems to improve the hydrogen induced cracking resistance of CWX351 in comparison with the rest of weld metals.

The lower C_k value of 14001 could be the consequence of the reduction in Nv, the increase in NMI size and the reduced probability to find retained austenite, when comparing with CWX351. Both weld metals are considered to have high NMI number and a clustered distribution. The larger inclusion size (maximum size) in 14001 could make it susceptible to hydrogen cracking, reducing hydrogen tolerance (decrease in C_k).

Further reduction in C_k, observed for weld metals 15171 and VCX2561, could be attributed to the reduction in Nv, the presence of large inclusions and, in both cases, the random distribution of them. These factors diminish the weld metal capacity to redistribute hydrogen, which could be free in the matrix to assists cracking or might be accumulated around inclusions to initiate cracking. Although it is probable to find small retained austenite particles (less than 0.1-0.2 μm), they could have less chemical stability due to

reduced carbon content (see table 7.3). That is, under deformation they can transform to martensite releasing hydrogen and, as a result, giving a low C_k to the weld metal.

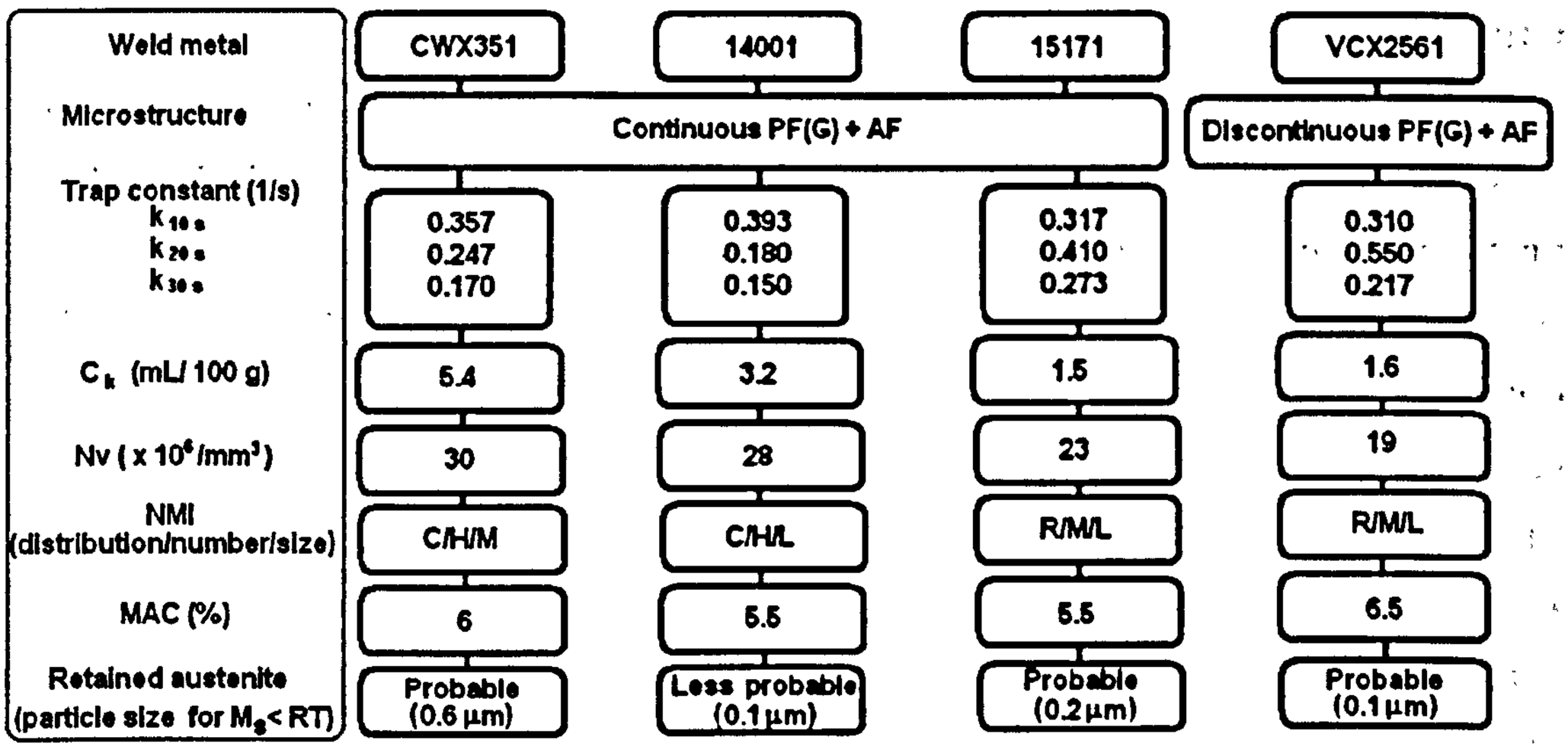

Figure 9.22 Comparison of weld metals with MAC content around 6%. It is shown the general microstructure constitution, the trapping constants (k), the critical hydrogen content (C_k), the number density of NMI (N_v) and their distribution/number/size characteristics, the MAC proportion and the probability to find retained austenite, considering the values of M_s, M_f and the effect of particle size in reducing Ms below room temperature (RT)

In regard to the variation of k value for the weld metals indicated in figure 9.22 and as discussed previously in section 9.2, it can be noted that at short charging times the apparent trapping constant is high irrespective of NMI distribution: random or clustered. However, at longer charging times a decrease in k is noted for clustered distributions. A maximum k value is reached for NMI distributed randomly after 20 s of hydrogen charging. The apparent lower k value for the clustered distribution could be attributed to the egress of hydrogen from the free volume between inclusion clusters, which is noted at longer charging times. On the other hand, the presence of a continuous network of grain boundary ferrite in large proportions could contribute in reduce the k value, as a consequence of its involvement in hydrogen transport throughout the weld metal.

Figure 9.23 shows another group of weld metals with similar MAC proportion: in this case 9 %, approximately. Weld metals 14031, CWX71 and CWX81 have similar microstructure, containing fine acicular ferrite (AF) and isolated islands of bainite (B). Their respective C_k values are: 1.0, 1.8 and 3.0 mL / 100 g. It can be observed that this increase in C_k could be related to the augment in Nv, as expected. Furthermore, the lower C_k value for 14031 could

be due to the medium size inclusions that contain, in contrast with the small in CWX71 and CWX81. This corroborates what was suggested before: there is a beneficial effect of NMI if they are small and in high numbers. The probable presence retained austenite in CWX81, together the NMI population, could contribute to its resistance to hydrogen induced cracking.

The C_k value for CWX181, which is slightly below that of CWX81, could be the consequence of the lower NMI number density and the larger inclusion size. Although this combination is detrimental to the hydrogen cracking resistance, it seems that the presence of grain boundary ferrite might have compensated this effect.

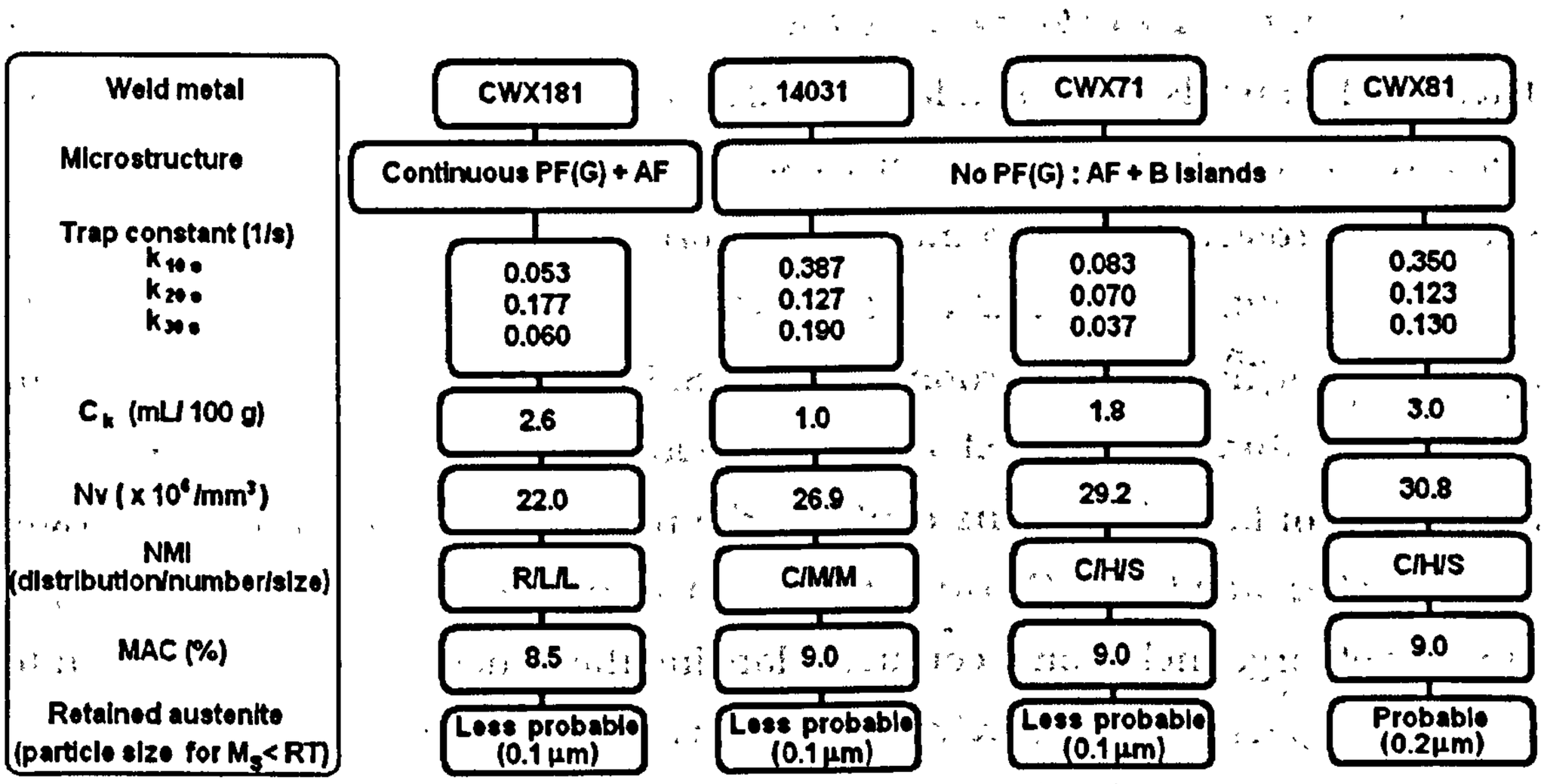

Figure 9.23 Comparison of weld metals with MAC content around 9%. See description in figure 9.20 for more detail.

With respect to the variation of the trapping constant in figure 9.23, it can be noted that the k value seems to be affected by both NMI size and the presence of retained austenite. Comparing 14031 with CWX81, it is appreciated a similar k value, although 14031 have lower Nv and larger NMI than CWX81. This suggests that the reduction in Nv is compensated by the increase in inclusion size, which could trap more hydrogen around itself. If weld metals CWX71 and CWX81 are compared, they seem to indicate that the higher k value for CWX81 is due to the combination of higher NMI number density and the probable retention of austenite. In contrast, the low k value for CWX181 could be associated with the grain boundary ferrite and the low population of large and randomly distributed inclusions. The k value is therefore seen to be sensitive to these NMI distribution and size of NMI, which could act as large volumetric traps for hydrogen in the case of clustering.

These examples illustrate the importance of the NMI population, particularly their size and distribution, on the hydrogen trapping behaviour and the hydrogen cracking resistance of the weld metals. The results suggest that for the case of weld metals with similar MAC content and nature, the NMI characteristics contribute directly to an increase in C_k. An increase in inclusion size could increase k, but affect negatively the C_k value. Finally, it is noted again the importance of the presence of retained austenite.

9.3.2 Welds with similar NMI characteristics: effect of MAC proportion and retained austenite presence on k and C_k

In figure 9.24 weld metals CWX181, 15171 and CWX361 are compared. These weld metals have similar Nv value and different MAC content. Some differences in NMI characteristics can be noted. The first two welds have similar microstructure: continuous network of PF(G) and AF. Nevertheless, they present different C_k and k values. The high C_k value for CWX181 could be related to its higher proportion of MAC (8.5%) which is expected to contain little proportion of retained austenite. The random distribution of a low population of large inclusions could be the reason for the acceptable C_k value. On the other hand, the C_k value for 15171 is the result of the slightly higher number of large inclusions, counterbalancing the benefit of retained austenite, which is expected in this weld metal. However, this beneficial effect depends on chemical and mechanical stability of retained austenite with low C content.

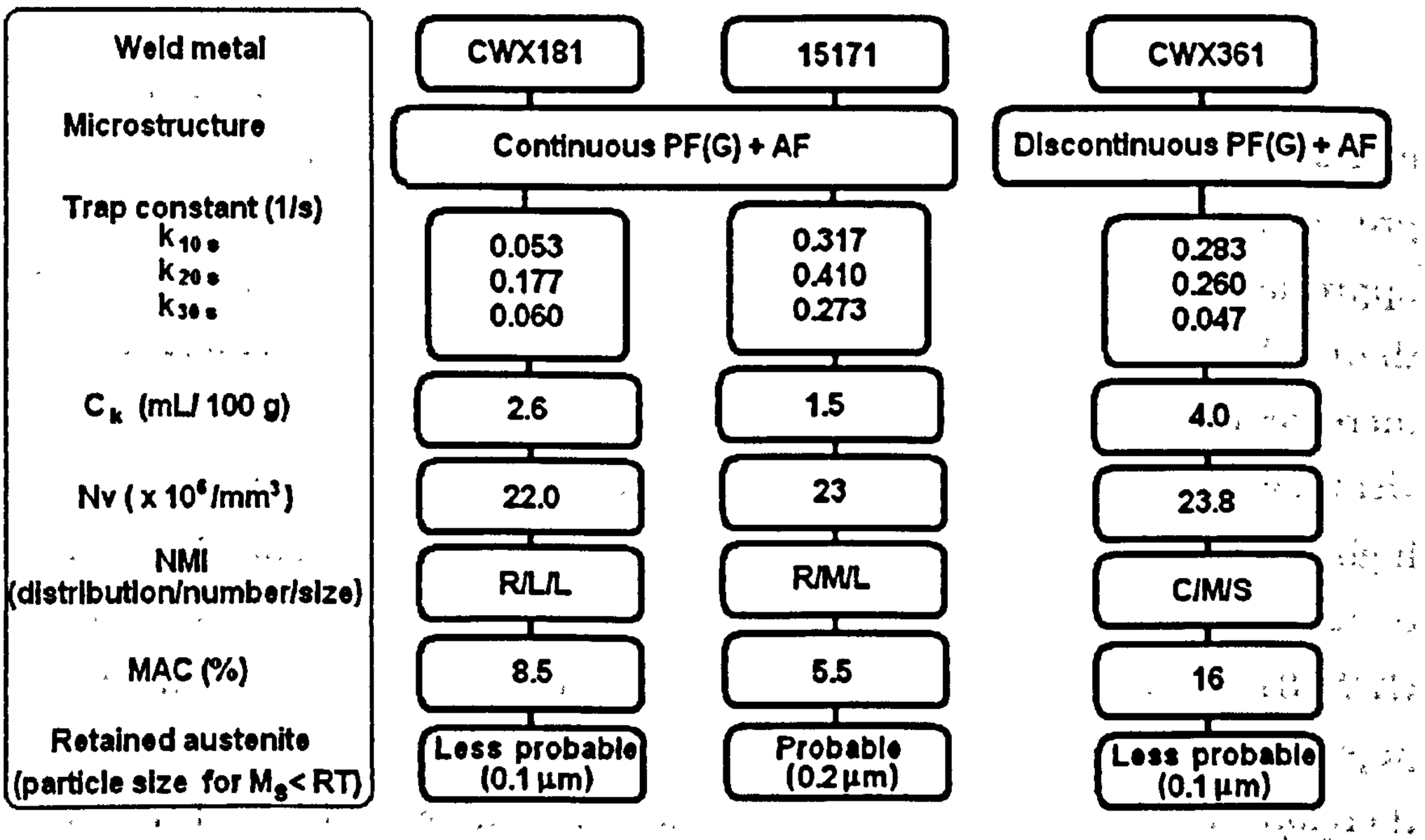

Figure 9.24 Comparison of weld metals with similar NMI number density, Nv, (between 22.0 and 23.8 10^6 mm^{-3}). See description in figure 9.20 for more detail.

The lower k value for CWX181 could be the result of the combination of the low inclusion number, though large; the presence of grain boundary ferrite and the low probability to find retained austenite. In contrast, an increase in NMI number and the probable existence of retained austenite, despite the fact that MAC has lower proportion, contribute to an increase in the trapping constant k for the 15171.

The C_k value, around 4.0 mL /100 g, for the weld metal CWX361 could be the result of the combined effect of slightly higher Nv, the clustering of inclusion of small size, and the large proportion of MAC (16 %), though it is expected low content of retained austenite in this constituent. This combined effect compensates the discontinuity of grain boundary ferrite.

In figure 9.25, there are contrasted two weld metal with similar NMI number density but very different microstructures: one containing a discontinuous network of PF(G) and AF; the other is formed by martensite (M) and bainite (B). C_k is slightly higher for the weld metal VCX2561 than for CWX331, probably due to the presence of retained austenite that is counterbalanced by the effect of larger NMI. Although the MAC proportion in CWX331 is around 20%, no apparent beneficial effect is observed. This could be the result of the little retention of austenite and its instability due to low carbon content.

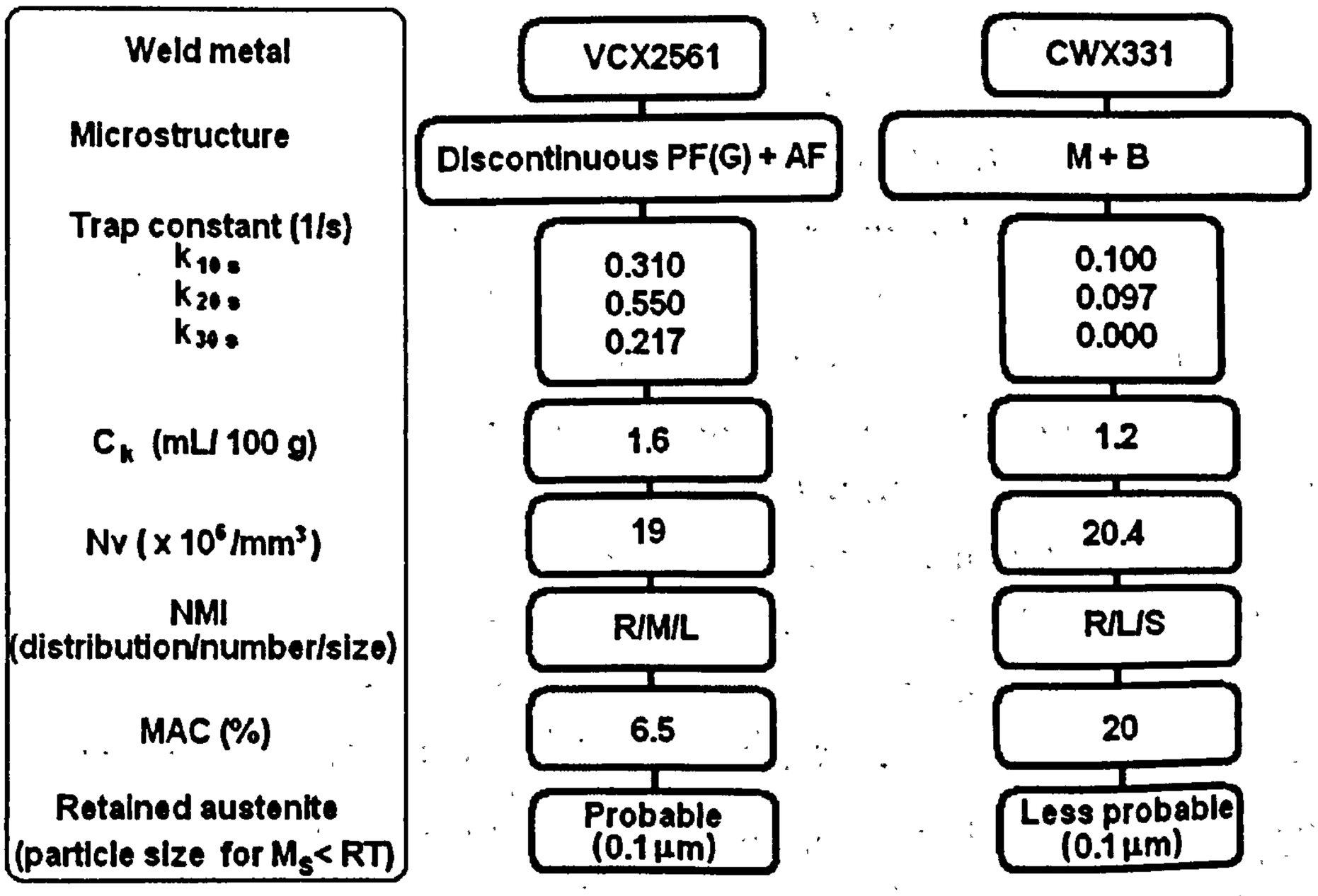

Figure 9.25 Comparison of weld metals with similar NMI number density, Nv, (around 20 10^6 mm^{-3}), but different microstructure and MAC content. See description in figure 9.20 for more detail.

The higher k value for VCX2561 could be due to the probability to find retained austenite, the presence of large inclusions and the discontinuity of the grain boundary ferrite. The smaller NMI in CWX331 limits trapping and makes the martensite susceptible to hydrogen cracking. The low C_k value for CWX331 is due to the presence of martensite, which at the same time does not have sufficient hydrogen traps to decrease hydrogen induced cracking susceptibility.

Previous examples suggest that the MAC content in a weld metal can be beneficial to increase their C_k value, especially when retained austenite exists and present high chemical and mechanical stability. However, it has been shown that microstructure plays an important role and that the combination of certain NMI characteristics with the MAC content could improve the weld resistance to hydrogen cracking. In the next section the effect of this combination is elucidated.

9.3.3 Welds metals presenting combined effects of MAC and NMI.

In figure 9.26 two weld metals that have not been compared before are presented: CWX201 and CWX91. These do not present similarities with the rest of the ten weld metals studied in this investigation and which were discussed before. Both welds contain acicular ferrite, with some bainite islands in the case of CWX91.

The C_k value for the CWX201 is twice that for the CWX91, and this seems to be contradictory due to its very low Nv. However, the MAC content in weld metal CWX201 is almost 3% higher than in CWX91 and this might contribute to the measured C_k value. The medium size and randomly distributed inclusions, although in low number, could trap hydrogen better than smaller and clustered ones, as in CWX91. Nevertheless, larger NMI could be susceptible to initiate cracks in presence of enough hydrogen quantities, limiting the hydrogen tolerance of the weld metal.

NMI number density is much higher in the weld metal CWX91, but their beneficial effect is not appreciated on the C_k value. Comparing this weld metal with CWX71 and CWX81, which have similar microstructure, higher Nv and lower MAC proportion, it can be noted that the decrease in NMI number density is responsibility of the reduction in C_k, even when the MAC is 2% above for the CWX91.

The inspection of the k values suggests that for these two anomalous cases other factors may be operating as hydrogen traps. There exists evidence that micro cavities are present in the weld metal CWX201, as shown in figures

8.16 and 8.17. These cavities are volumetric traps and can be the reason for the relative high k value. No evidence of such kind was found for the CWX91, and it could be suggested that the bainite islands may decrease the hydrogen cracking resistance for the welds that contains them.

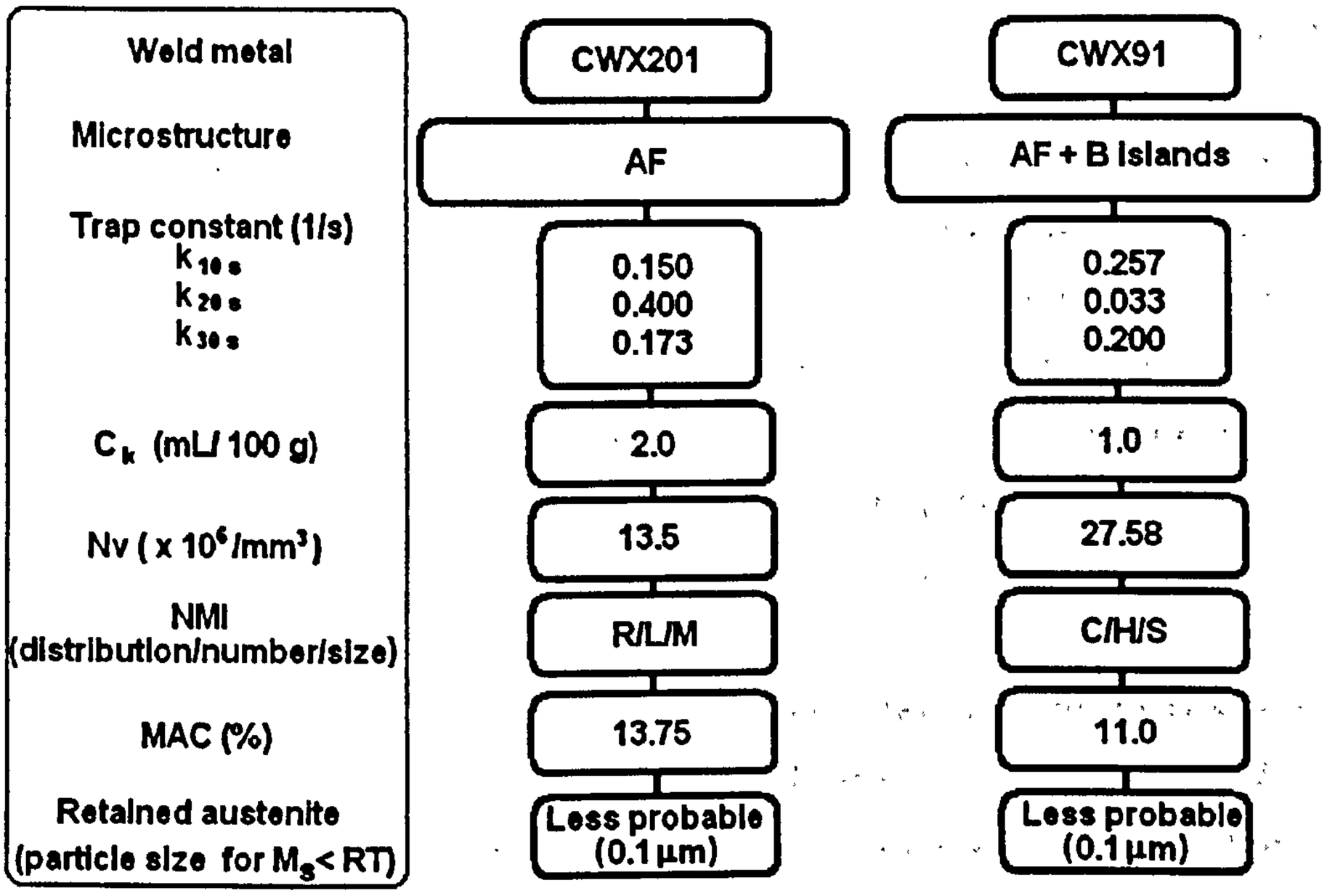

Figure 9.26 Comparison of weld metals with similar NMI number density, Nv, (around 20 10^6 mm^{-3}), but different microstructure and MAC content. See description in figure 9.20 for more detail.

Welds metals CWX201 and CWX71 have similar C_k value, as shown in figures 9.26 and 9.23. Table 9.5 presents comparatively the other characteristics.

Table 9.5 Comparison between CWX201 and CWX71

Characteristics	CWX201	CWX71
MAC (%)	13.75	8.69
Nv [10^6 mm^{-3}]	13.51	29.22
NMI characteristics	R/L/M	C/H/S

As can be noted in table 9.5, MAC and NMI have been combined to obtain the same C_k value. The effect of a low NMI population of medium size in the CWX201 on C_k, has been complemented by the large MAC content, and in the case of the weld metal CWX71, the high population of small NMI is taking control of the hydrogen that can not be trapped due to the reduction in MAC volume fraction. The result of this combination is the production of similar hydrogen resistance in these two welds. The higher MAC content and the presence of medium sized NMI of the CWX201 weld metal is detected by the

trapping constant k, which is higher than for the CWX71. This indicates the slightly better resistance to hydrogen cracking of the CWX201 weld. Similar behaviour is found when comparing other weld metals.

9.4 Summary of this chapter: The hydrogen trapping capacity of the weld metal and their resistance to hydrogen induced cold cracking.

In this chapter the results from chapter 7 and 8 converge in an attempt to establish a relationship between microstructure, properties and HICC of the HSLA steel weld metals – the title of this book. The hydrogen trapping capacity of the weld metals, characterised by the trapping constant k, is studied and analysed. Firstly, the fundamentals of the electrochemical technique to measure the trapping constant are briefly explained and the assumptions are listed. Then a revision of the k value significance is discussed. Figure 9.2 present several factors that have an influence on the k value.

The trapping constant is a measure of the hydrogen trapping capacity of the weld metal. It is known that the hydrogen traps control the distribution of hydrogen throughout the microstructure in such way that may decide whether critical levels are reached and, therefore, whether the crack is initiated or not at flaw sites. A high k value means a high capacity to trap hydrogen at specific sites and might imply a capacity of the material to tolerate higher hydrogen levels, which is distributed evenly throughout the microstructure avoiding accumulation in those crack susceptible regions. Trap sites are: interfaces, NMI, MAC, porosities, precipitates, dislocations and solute atoms.

The complexity of the k value interpretation is due to the simultaneous interaction of the different traps. Moreover, the presence of a variety of microstructural phases might influence the measurement of k. In this investigation NMI and MAC particles are considered to influence the k value and C_k, as well. The influence could be beneficial or detrimental as discussed along the chapter.

In this investigation, it was found that the k values vary with time of charging. This variation could be associated to different factors: hydrogen saturation of traps, heterogeneities in the weldment and variations in microstructure. Considering the spatial distribution of NMI a possible explanation of the k variation with time was suggested.

The effect of microstructure, MAC content and NMI on the k value and C_k could be summarised as follow:

1- *Effect of microstructure.* The k value seems to be insensible to the microstructure. Similar k values were obtained in weld metals with a continuous network of PF(G), with a discontinuous one and without grain boundary ferrite. It seems to be more dependent on MAC content and NMI inclusion characteristics. However, the presence of a continuous film of grain boundary ferrite seems to have a beneficial effect on C_k.

2- *Effect of MAC content.* The k value is sensible to the presence of particles of MAC. Nevertheless, as some evidence indicates, the important issue is not the MAC content, but the existence of retained austenite. Retained austenite is a strong hydrogen trap and hydrogen solubility in it is high. As a consequence, k value remains relatively high when there is retained austenite in the weld metal. In regard to the value of C_k, it is expected to find an increase of this value with retained austenite. However, the results of this investigation indicate that other factor can counterbalance this expected beneficial effect. Amongst this factor can be mentioned: the instability of retained austenite during deformation and the NMI characteristics. Retained austenite is an excellent hydrogen trap, but when deformed it can transform to martensite realising its hydrogen content. Chemical and mechanical stabilisation of austenite is important to be considered to improve the hydrogen induced cracking resistance of the weld metals. The effect of NMI is discussed below.

3- *Effect of NMI characteristics.* The k value is considerably affected by the NMI population, size and distribution. A random distribution of inclusions seems to favour the trapping efficiency, but it depends on their number and size. For example, a random distribution of large inclusions is expected to contribute with a high k value if they are in a medium range number. On the contrary, a random distribution of large retained austenite in lower quantities is expected to reduce the trapping capacity of the weld metal. If the NMI size is lowered, its trapping capacity is diminished. On the other hand, the clustered distribution of NMI can improve the trapping capacity, but again, the size and number is important. In regard with the C_k value, the NMI characteristic can counterbalance the beneficial effect of the

factors mentioned above. In general, large inclusions were associated with low C_k values.

As discussed in this chapter, a careful design of weld metal must consider the complex interaction observed experimentally. It has to be taken into account that a weld metal with high resistance to hydrogen induced cold cracking is the result of a combination of microstructural characteristics. Further work is needed to clarify the effect of individual factors such as retained austenite stability and the NMI characteristics.

CHAPTER TEN

CONCLUSIONS AND RECOMMENDATIONS FOR FURTHER WORK

10.1 CONCLUSIONS

10.1.1 The mixture of microstructures of the weld metals studied was classified into four principal groups which depend on weld metal composition. These groups contain: grain boundary ferrite (PF(G)), acicular ferrite (AF), ferrite with aligned second phase (FS(A)) which can be ferrite side plates (FS(SP)) and bainite FS(B), ferrite with non aligned second phase (FS(NA)) and martensite (M). The groups are shown in table 10.1.

Table 10.1 Microstructural classification of the weld metals studied

P_{cm} value	Microstructure
$P_{cm}<0.17$	$PF(G)_{continuous\ network}$ + AF + FS(A) + microphases (MAC, γ_R, NMI) *
$0.17<P_{cm}<0.20$	$PF(G)_{discontinuous\ network}$ + AF + microphases (MAC, γ_R, NMI)*
$P_{cm}\geq0.20$	AF + FS(B) + FS(NA) + microphases(MAC, γ_R, NMI)*
$P_{cm}=0.27$	M + FS(B) + microphases (MAC, γ_R, NMI)*

*Microphases: MAC (martensite-austenite-carbide islands, γ_R (retained austenite) and NMI (non metallic inclusions).

10.1.2 The spatial distribution and shape of MAC depends on the ferrite phase that forms during transformation. Elongated MAC particles are found at PF(G) boundaries and between ferrite lath in FS(A) and FS(B). Wedge shaped-MAC particles are found between AF grains. An empirical expression correlating composition and MAC content was obtained by multiple regression which shows good correspondence with experimental values. The equation is the following:

$$MAC(\%)=155\cdot C+10\cdot Mo+6.6\cdot Mn-11\cdot Cr-7\cdot Si-Ni-4 \qquad (10.1)$$

10.1.3 The probability to find retained austenite (γ_R) in MAC were carried throughout estimations of M_s and M_f temperatures for the remaining austenite. It was considered both chemical stabilisation (carbon partitioning and alloying effect) and particle size effect. Weld metals where γ_R is more probable are: CWX351, 15171, VCX2561, CWX91 (size effect) and CWX81. The small particle size necessary to stabilise austenite should be below 0.1 μm for most of the weld metals. Then, for the rest of weld metals it is less probable to find retained austenite. The weld metal CWX351 is expected to have very stable retained austenite due to high carbon content.

10.1.4 The NMI characteristics were fully assessed: number density, size and spatial distribution. Weld metals inclusions were classified based on these characteristics as random and clustered distributed; high, medium and low number; and large, medium and small size. No attempt was made to fully classify the NMI by type and composition, but some thermodynamical calculations are proposed to estimate these.

10.1.5 A method to estimate the critical hydrogen content (C_K) for hydrogen embrittlement is proposed. This consists in estimate, from experimental data, the hydrogen content that produces 50% of ductility loss.

10.1.6 The C_K value, in principle, is affected by weld metal microstructure. The presence of a continuous network of a thin film of PF(G) in combination with AF, MAC content and certain NMI characteristics, seems to be beneficial to hydrogen cracking resistance. The presence of bainite or a mixture of bainite and martensite are expected to be detrimental.

10.1.7 The C_k value is influenced by the MAC volume fraction. However, the presence of retained austenite in the MAC constituent is the important factor to increase the C_k level of the weld metals.

10.1.8 Certain NMI characteristics were identified to be beneficial for the tolerance to hydrogen. Clustered inclusions seem to be more effective than random distributed, but this effect depends on NMI size. Large inclusions were associated with low C_k values. A high number density of medium and small sized inclusions can result in an acceptable C_k.

10.1.9 The resistance to hydrogen induced cracking could be improved with the right combination of: microstructure with grain boundary ferrite, MAC particles with stabilised retained austenite, and NMI of medium to small size, in high number and clustered distributed.

10.1.10 Large NMI has been identified as the principal cracks initiators. Cavities or micro-shrinkages were observed in some weld metals to initiate large quasicleavage facets. MAC particles were not clearly related to crack initiation.

10.1.11 A phenomenological model, based on fractographic observations, is proposed. In a diagram, it is described the effect of hydrogen content, stress

intensity factor and microstructure on the occurrence of the fracture micromechanisms that can be found in hydrogen assisted cracking in weld metals: micro-void coalescence (MVC), quasicleavage (QC) and intergranular (IG) fractures.

10.1.12 An electrochemical double pulse technique was used to determine the hydrogen trapping rate constant (k) for each weld metal studied. The technique was proved to be sensitive to the microstructural differences between weld metals.

10.1.13 The trapping rate constant k is sensitive to the presence of retained austenite, changes in NMI characteristics and the time of charging of the weld metals. This value could be used as an indicator of the trapping capacity of the weld metal. However, its direct relation with C_k is difficult due to the complex interrelation between other variables: defects, NMI characteristics, MAC content and the presence of retained austenite.

10.2 RECOMMENDATIONS AND FURTHER WORK

10.2.1 To improve the statistical significance of the different results it is necessary to carry out a large quantity of experiments. Specialised equipments with high current resolution and high sampling rate for data acquisition is recommended to record the results.

10.2.2 A very detailed study using high resolution SEM is necessary to verify the presence of retained austenite in the MAC constituent. This can be carried out taking few representative samples of the weld metals and using special etching techniques to reveal the superficial morphology of the MAC particle. This method protects retained austenite from transformation, which could occur during TEM sample preparation due to the effect of low temperature or stress relief.

10.2.3 The size and spatial distribution of retained austenite could be an interesting subject to study. In combination to the NMI characteristic the role of both features can be fully understood.

10.2.4 A study about the influence of the NMI spatial distribution on the weld metal microstructure is recommended. More detailed microscopy studies to characterise the morphology of the microstructure that is formed in NMI-free regions and NMI populated regions, could be appropriate because it is possible that the clustering of inclusions favours the formation of orientated ferrite phases, such as FS(A) and FS(B), in those NMI-free regions.

10.2.5 The role of MAC on the crack initiation in hydrogen charged weld metals seems to be important. More detailed fractographic analysis is proposed using: the technique of matching fracture surfaces and chemical or electrochemical etching of the fracture surfaces to identify microstructure beneath a specific feature.

10.2.6 Using carefully designed heat treatments simulate the formation of reheated region in multipass welding. Then characterise it and estimate the k value. In this way the result in this investigation can be corrected.

10.2.7 The utilisation of a hydrogen permeation technique could corroborate the validity of the trapping constant k for the different weld metals. From these studies the diffusivity of hydrogen can be clearly estimated.

10.2.8 To fully understand the role of retained austenite on the resistance to hydrogen induced cracking and the trapping capacity of steels, it is proposed to use a TRIP-steel. This steel can be carefully heat treated to produce different proportions, particle sizes and distribution of retained austenite. This control could permit to quantify the effect of retained austenite on k and C_k. The effect of stability of retained austenite on hydrogen induced cracking can be studied after the application of deformation to samples.

10.2.9 To study the influence of MAC on the trapping of hydrogen when retained austenite is present, it is proposed to determine k for the samples with retained austenite before and after cooling it down to sub-zero temperatures to transform γ_R to martensite. Deformation to induce martensite transformation could be applied as well.

REFERENCES

1 Grong O. and Matlock D. K. Microstructural development in mild and low-alloy steel weld metals. International Metals Reviews, 1986, 31, 1, pp 27-48.

2 Etube L. S. Fatigue and Fracture Mechanics of Offshore Structures, Professional Engineering Publishing, UK, 2001, pp 1-42.

3 Wright, P. H., High-Strength Structural and High-Strength Low-Alloy Steels. In Properties and Selection: Irons, Steels, and High Performance Alloys. Metals Handbook 10th Ed., Volume 1, ASM International, USA, 1993, pp: 389-423.

4 Kuo, S. Welding Metallurgy, Second Edition, John Wiley & Sons, Inc., USA, 2003. Pp 410-417.

5 Cieslak M. J. Cracking phenomena Associated with welding. In Welding, Brazing, and Soldering, Metals Handbook 10th Ed., Volume 6, ASM International, USA, 1993, pp: 88-96.

6 Bailey N, Coe F R, Gooch T G, Hart P H, Jenkins N and Pargeter R J, Welding steels without hydrogen cracking, ASM International, Abington Publishing, UK, 1973.

7 Yurioka N. and Suzuki H. Hydrogen assisted cracking in C-Mn low alloy steels weldments. International Materials Reviews, 1990, 35, 4, pp 217-249.

8 Wildash, C, Ph.D. Thesis, Microstructural Factors Affecting Hydrogen Induced Cold Cracking in High Strength Steel Weld Metals, University of Leeds, England, UK, 1999

9 Wildash C, Cochrane R. C., Gee R. and Widgery D. J., Microstructural Factors Affecting Hydrogen Induced Cold Cracking in High Strength Steel Weld Metals, ASM International, Proceedings of the 5th International Conference on Trends in Welding Research, (1998), pp: 745-750

10 Wildash C, Cochrane R. C., Gee R. and Widgery D. J., The Influence of Hydrogen and Microstructure on the Tensile Properties of High Strength Steel Weld Metals. Institute for the Joining of Materials, Proceeding of the 9th International Conference on Joining of Materials, (1999), pp: 335-340.

11 Wildash C., Cochrane R. C., and Gee R. Simulation of hydrogen induced cold cracking using electrolytic precharging procedure, Science and Technology of Welding and Joining, 2001, Vol. 6, No. 2, pp. 73-78

12 Gladman T., The Physical Metallurgy of Microalloyed Steels, IOM, Maney Publishing, UK, 2002, pp. 19-78.

13. David S. A., and Babu S. S. Microstructure modelling in weld metal. In "Mathematical Modelling of Weld Phenomena 3". Edited by H. Cerjak. The institute of Materials, UK, 1997, pp. 151-180.

14 Babu S. S. and David S. A., Inclusion formation and microstructure evolution in low alloy steel welds, ISIJ International, 42 (2002), No 12, pp. 1344-1353.

15 Abson D. J. and R. J. Pargeter. Factors influencing as-deposited strength, microstructure, and toughness of manual metal arc welds suitable for C-Mn steel fabrications. International Metals Reviews, 1986, 31, 4, pp: 141-194.

16 Hsieh K. C., Babu S. S., Vitek J. M., and David S. A., Calculation of inclusion formation in low alloy steel welds. Materials Science and Engineering, A215, 1996, pp. 84-91.

17 Grong, O. Metallurgical Modelling of Welding. Second Edition, The Institute of Materials, UK, 1997.

18 Minkoff, I. Solidification and Cast Structure. John Wiley & Sons, UK, 1986.

19 Frost R. H., Olson D. L. and Liu S., Influence of Solidification on Inclusion Formation in Welds, Int. Trends in Welding Science and Technology, Ed. By S.A. David and J. M. Vitek, International Conference Proceedings ASM Int., 1992, pp. 205-209.

20 Kawashita, Y and Suito H, Precipitation behaviour of Al-Ti-O-N inclusions in unidirectionally solidified Fe-30mass%Ni alloy, ISIJ International, 35, (1995), No 12, pp. 1468-1476

21 Deo B. and Boom R., Fundamentals of Steelmaking Metallurgy, Prentice Hall International, UK, 1993, pp. 39-103

22 Ghosh, A., Secondary Steelmaking. Principles and Applications, CRC Press, USA, 2001, pp. 9-42.

23 Kluken A. O. and Grong Ø., Mechanisms of inclusion formation in Al-Ti-Si-Mn deoxidized steel weld metals, Metallurgical Transactions A, 20A, (1989), pp. 1335-1349.

24 Van der Eijk C., Grong Ø., and Walmsley J., Mechanisms of inclusion formation in low alloy steels deoxidized with titanium, Materials Science and Technology, 16 (2000), pp. 55-64

25 Mills A. R., Thewlis G., and Whiteman J., Nature of inclusions in steel weld metals and their influence on formation of acicular ferrite, Materials Science and Technology, 3 (1987), pp. 1051-1061.

26 Babu S. S., David S. A., Vitek J.M., Mundra K. and DebRoy T. Development of macro- and microstructures of carbon-manganese low alloy steel welds: inclusion formation, Materials Science and Technology, 11 (1995), pp. 186-199

27 Quintana M. A., McLane J., Babu S. S., and David S. A., Inclusion formation in self-shielded flux cored arc welds, Welding Journal, 80 (2001), No.4, pp. 98s-105s

28 Hsieh K. C., Babu S. S., J. M. Vitek, David S. A. Calculation of inclusion formation in low alloy steel welds, Materials Science and Engineering, A215 (1996), pp. 84-91.

29 Hong T., DebRoy T., Babu S. S., and David S. A., Modeling of inclusion growth and dissolution in the weld pool, Metallurgical and Materials Transactions B, 31B (2000), pp. 161-169.

30 Hong T. and DebRoy T., Time-temperature-transformation diagrams for the growth and dissolution of inclusions in liquid steels, Scripta mater, 44 (2001), 847-852.

31 Lehmann J., Rocabois P., and Gaye H., Kinetic model of non-metallic inclusions' precipitation during steel solidification, Journal of Non-Crystalline Solids, 282 (2001), pp. 61-71

32 Rocabois P., Lehmann J., Gaye H., and Wintz M., Kinetics of precipitation of non-metallic inclusions during solidification of steel, Journal of Crystal Growth, 198/199 (1999), pp. 838-843

33 Sanchez A., Liu S., and Olson D. L., The effect of solidification on the formation and growth of inclusions in low carbon steel welds, Materials Science and Engineering, A221 (1996) 122-133.

34 Cochrane R. C. and Keville B. R., Influence of inclusion morphology on microstructure and toughness of submerged arc weldments, Proceedings of International Conference on Steels for Line Pipes and Pipe Line Fittings. The Metal Society, London, 1981, pp. 51-60

35 Thewlis G. Transformation kinetics of ferrous weld metals, Materials Science and Technology, 10, (2), 1994, pp. 110-125.

36 Honeycombe R. W. K. and Bhadeshia H. K. D. H. "Steels. Microstructure and Properties", Edward Arnold, UK, 1995, pp. 83-150

37 Lee T., Kim H. J., Kang B. Y. and Hwang S. K. ISIJ International, 40 (2000), No. 12, pp. 1260-1268.

38 David S A and Vitek J M, Correlation between solidification parameters and weld microstructure, International Materials Reviews, 1989, 34, 5, pp: 213-245.

39 David G. J., and Garland J. G., Solidification Structures and Properties of Fusion Weld, International Metallurgical Reviews, 20, 1975, pp: 83-106.

40 Solomon H. D. Fundamentals of weld solidification. In "Welding, Brazing, and Soldering", Metals Handbook 10th Ed., Volume 6, ASM International, USA, 1993, pp: 45-54.

41 Jokl M. L., Kameda J., McMahon C. J., and Vitek V. Solute segregation and intergranular brittle fracture in steels. Metal Science, 14, 1980, pp: 375-384.

42 Vishnu R., Solid State Transformations in weldments, in "Welding, Brazing, and Soldering", Metals Handbook 10th Ed., Volume 6, ASM International, USA, 1993, pp: 70-87.

43 Cochrane R. C., Welding in the World, 1983, 21, (1/2), 16-24.

44 Choi C. L. and Hill D. C. Welding Journal, 1978, 57, 8, 232s-236s.

45 Ito Y., Nakanishi M., and Komizo Y. Effects of oxygen on low carbon steel weld metal, Met. Constr., 14, (9), 1982, pp. 472-478

46 Harrison P. L. and R. A. Farrar Application of continuous cooling transformation diagrams for welding of steels, International Materials Reviews, 1989, 34, 1, pp: 35-51.

47 Lalam, S. H. Modelling of Mechanical Properties of Ferritic Weld Metals, PhD thesis, Cambridge, October 2000.

48 Evans G. M. and Bailey N., Metallurgy of Basic weld metal, Abington Publishing, UK, 1997.

49 Sugden A. A. B. and Bhadeshia H. K. D. H, A model for the strength of the as-deposited regions of steel weld metals, Metallurgical Transactions A, 19A, 1988, pp: 1597- 1602.

50 Young C. H. and Bhadeshia, Strength of mixtures of bainite and martensite, Materials science and technology, 10, 1994, pp: 209-214.

51 Bhadeshia H. K. D. H, Modelling of steel welds, Materials Science and Technology, 8, 1992, pp: 123-133

52 Lalam S. H., Bhadeshia H. K. D. H., and MacKay D. J. C., Estimation of mechanical properties of ferritic steel welds. Part 1: Yield and tensile strength, Science and Technology of Welding and Joining, 5 (2000), No. 3, pp. 135-147

53 Lalam S. H., Bhadeshia H. K. D. H., and MacKay D. J. C., Estimation of mechanical properties of ferritic steel welds. Part 2: Elongation and Charpy toughness, Science and Technology of Welding and Joining, 5 (2000), No. 3, pp. 149-160

54 Ohkita S. and Horii Y, Recent development in controlling the microstructure and properties of low alloy steel weld metals, ISIJ International, 35 (1995), No. 10, pp. 1170-1182

55 Evans G. M. The effect of Carbon on the microstructure and properties of C-Mn all-weld metal deposits, Welding Journal, 62 (1983), No.11, pp. 313s-320s.

56 Ohkita S. and Horii Y. Recent development in controlling the microstructure and properties of low alloy steel weld metals, ISIJ International, 35, (1995), 10, pp: 1170-1182.

57 Kang B. Y., Kim H. J. and Hwang H.K., Effect of Mn and Ni on the variation of microstructure and mechanical properties of low-carbon weld metals, ISIJ International, 40 (2000), No. 12, pp. 1237-1245

58 Ventrella V. A., Alcantara N. G., dos Santos J. F., Koçak M. and Evans G.M., Microstructure of ferritic weld metals containing titanium and boron, Proceedings of OMAE99, 18th International Conference On Offshore Mechanics and Arctic Engineering, July, 1999, Canada, pp. 75-79

59 Devletian J. H. and Heine R. W., Effect of boron content on carbon steels welds, Welding Journal, 54 (1975), No. 2, pp. 45s-53s.

60 Potapov N. N., Oxygen effect on Low-alloy steel weld metal properties, Welding Journal, 72 (1993), No. 8, pp. 367s-370s.

61 Dolby R. E. The effects of V and Nb on weld metal properties, in "Steels for line pipe and pipe-line fittings", The Metals Society, London, 1983, pp. 302-312.

62 He K. and Edmonds D. V., Formation of acicular ferrite and influence of vanadium alloying, Materials Science and Technology, 18 (2002), No.3, pp. 289-296

63 Baker R. G. and Watkinson F., The effect of hydrogen on the welding of low-alloy steels. In Hydrogen in steel, Iron and Steel Institute, pp: 123-132.

64 Bailey N. Weldability of ferritic steels, Abington Publishing, UK, 1995, pp. 133-169

65 Oriani R. A., Hydrogen embrittlement of steels. Ann. Rev. Mater. Sci., 1978, 8: 327-357.

66 Hirth J. P., Effects of hydrogen on the Properties of Iron and Steel. Metallurgical Transaction A, 11A, June 1980, pp: 861-890.

67 Zapffe C. and Sims C. Trans. AIME, 1941, 145, pp: 225-261.

68 Subramanyan P. K. Electrochemical Aspects of Hydrogen in Metals. In "Comprehensive Treatise of Electrochemistry". Volume 4, Edited by Bockris J. O'M, Brian E. Conway, Ernest Yeager and Ralph E. White. Plenum Press, New York, (1981). Pp: 411-462.

69 Lawn B. R. and Wilshaw T. R. Fracture of brittle solids. Cambridge University Press, UK, 1975.

70 Garofalo F. Chou Y. T., and Ambegaokar V., Effect of Hydrogen on stability of microcracks in iron and steel, Acta Metall., 8, (8), 1960, pp: 504-512.

71 Bilby B. A. and Hewitt J., Hydrogen in steel- the stability of microcracks, Acta Metall., 10, (6), 1962, pp: 587-600.

72 Beachem C. D., A new model for hydrogen assisted cracking (hydrogen embrittlement), Met. Trans., 3, (2), 1972, pp. 437-451.

73 Lynch S. P., Mechanisms of hydrogen assisted cracking, Metals Forum, 2, (3), 1979, pp: 189-200.

74 Petch N. J. and Stables P., Nature, 1952, 169, p. 842.

75 Westwood, A. R. C. "Effects of Environment on Fracture Behaviour" in Fracture of Solids, Proceedings of an International Conference, Interscience Publishers, USA, 1963, pp: 553-605.

76 Westlake D. G. Trans ASM, 1969, vol. 62, pp. 1000-1006

77 Gahr S., Grossbeck M. L., and Birnbaum H. K., Hydrogen embrittlement of Nb. I-Macroscopic Behaviour at Low Temperatures, Acta Met., 25, 2, 1977, pp. 125-153.

78 Troiano A. R., Trans. ASM, 1959, 52, (1), pp. 54-80.

79 Lee J. A., A theory for hydrogen embrittlement of transition metals and their alloys. In "Hydrogen effects in Materials". Edited by A. W. Thompson and N. R. Moody. Proceeding of the 5th International Conference on the Effect of Hydrogen on the Behaviour of Materials (1996), pp: 569-580.

80 Bockris J. O'M. and Khan S. U. M, Surface Electrochemistry. A Molecular Level Approach. Plenum Press, USA, 1993. Pp. 811-846.

81 Messmer, R. P. and Briant, C. L. The role of chemical bonding in grain boundary embrittlement. Acta Metall., 30, 1982, pp. 457-467.

82 Eberhart M. E., Johnson K. H., and Latanision R. M., Acta Metall., 32, (6), 1984, pp. 955-959.

83 Oriani R. A., The diffusion and trapping of hydrogen in steels, Acta Metall., 18, (1), 1970, pp: 147-157.

84 Park Y. D., Landau A., Maroef I. S., Edward G. R. and Olson D. L. The role of retained austenite in the hydrogen management of high strength steel welds, ASM International, Proceedings of the 5th International Conference on Trends in Welding Research, (1998), pp: 31-36.

85 Asahi H., Hirakami D. and Yamasaki S. Hydrogen trapping behaviour in vanadium-added steel. ISIJ International, 43, 4, (2003) pp: 527-533

86 Lee H. G. and Lee J. Hydrogen trapping by TiC particles in iron. Acta Metallurgica, 32, 1, (1984), pp. 131-136

87 Maroef I., Olson D. L., Eberthart M. and Edwards G. R. Hydrogen trapping in ferritic steel weld metal. International Materials Reviews, 47, 4, (2002), pp. 191-223

88 Pressouyre, G. M. Trap theory of hydrogen embrittlement: experimental investigations. In Hydrogen in Metals, old book, 1980

89 Pressouyre, G. M. Trap theory of hydrogen embrittlement, Acta Metallurgica, 28, 1980, pp. 895-911.

90 Gibala R. and DeMiglio D. S., Hydrogen in iron and steels: interactions, traps and crack paths, in Hydrogen in Metals, old book, 1980.

91 Thompson A. W., and Bernstein I. M. Microstructure and hydrogen embrittlement. In "Hydrogen effects in Metals", Proceedings of the Third International Conference on Effect of Hydrogen on Behaviour of Materials. Edited by Thompson A. W., and Bernstein I. M., The Metallurgical Society of AIME, USA, 1980. Pp. 291-308.

92 Knott J. F. Micromechanisms of fibrous crack extension in engineering alloys. Metal Science, 14, 1980, pp. 327-336.

93 Curry D. A. Cleavage micromechanisms of crack extension in steels. Metal Science, 14, 1980, pp. 319-326.

94 Echeverría A. and Rodriguez-Ibabe J. M. Brittle fracture micromechanisms in bainitic and martensitic microstructures in a C-Mn-B steel. Scripta Materialia, 41, (2), 1999, pp. 131-136.

95 Lambert A., Garat X., Sturel T., Gourgues A. F., and Gingell A. Application of acoustic emission to the study of cleavage fracture mechanism in a HSLA steel. Scripta Materialia, 43, (2), 2000, pp. 161-166.

96 Engel L., and Klingele H. " An Atlas of Metal Damage. Surface examination by scaning electron microscope". Wolfe Publishing Ltd., Holland, 1981. Pp. 72-76.

97 McMahon C. J. Hydrogen-induced intergranular fracture of steels. Engineering Fracture Mechanics, 68, 2001, pp. 773-788.

98 Ishikawa M., Nakatani Y., and Yamada K., Mechanistic aspects of hydrogen cracking process in high strength steel, In "Hydrogen Transport & Cracking in Metals", by Trurnbull A., The Institute of Materials, UK, 1995. Pp. 95-102.

99 Smith II R. D., Landis G. P., Maroef I., Olson D. L. and Wildeman T. R. The determination of hydrogen distribution in high-strength steel weldments Part1: Laser Ablation Methods, Welding Journal 89, (5), 2001 pp: 115-121s.

100 Smith II R. D., Benson D. K., Maroef I., Olson D. L. and Wildeman T. R. The determination of hydrogen distribution in High-Strength steel weldments Part2: Opto-electronic diffusible hydrogen sensor. Welding Journal 89, (5), 2001 pp: 122s-125s.

101 McKibben R., Sharp R. M., Harrington D., Pound B. G., and Wright G. A. A potentiostatic double-step method for measuring hydrogen atom diffusion and trapping in metal electrodes- I. Theory. Acta Metall., 35, (1), 1987, pp. 253-262.

102 Pound B. G., The applications of a diffusion/trapping model for hydrogen ingress in high-strength alloys. Corrosion Science, 45, (1), 1989, pp. 18-25.

103 Pound B. G., Hydrogen trapping in work-hardened alloys. Acta Metall. Mater., 39, (9), 1991, pp. 2099-2105.

104 Pound B. G., Hydrogen trapping in precipitation-hardened alloys, Acta Metall. Mater., 38, (12), 1990, pp. 2373-2381.

105 Pound B. G., Hydrogen trapping in high-strength steels. Acta Mater., 46, (16), 1998, pp. 5733-5743.

106 Dallam, C. B. and Damkroger B. K., Characterisation of Welds, in "Welding, Brazing, and Soldering", Metals Handbook 10th Ed., Volume 6, ASM International, USA, 1993, pp: 97-106.

107 Metals Handbook, ASM Volume 8, 8th edition, Metallography, Structures and Phase diagrams, p 64.

108 Kluken A. O., Grong Ø. and Hjelen J. SEM based automatic image analysis of non-metallic inclusions in steel weld metals. Material Science and Technology, 4, 1988, pp. 649-654.

109 Russ, J. C., The Image Processing Handbook, Fourth Edition, CRC Press, USA, 2002.

110 Goodhew P. J. "Specimen preparation for transmission electron microscopy of materials". Oxford University Press, UK, 1984.

111 Thompson-Russell K. C. and Edington J. W. "Electron Microscope Specimen Preparation Techniques in Materials Science. Macmillan, UK, 1977.

112 Williams D. V. and Carter C. B. Transmission Electron Microscopy. A textbook for Materials Science. Plenum Press, USA, 1996. Pp. 157-173.

113 . Struers, Tenupol-5 Instruction Manual, UK, 2000

114 Pound B. G., Wright G. A., and Sharp R. M., A potentiostatic double-step method for measuring hydrogen atom diffusion and trapping in metal electrodes-II. Experimental., Acta Metall., 35, (1), 1987, pp. 263-270.

115 McBreen, J. and Genshaw, M.A., The electrochemical introduction of hydrogen into metals, Proceedings of Conference Fundamental Aspects of Stress Corrosion Cracking. NACE, USA, 1969, pp. 51-63.

116 Pickering, F. B.. Physical metallurgy and the design of steels. Applied Science Publishers LTD. UK, 1978. pp: 101-126.

117 Bhadeshia, H. K. D. H.. Bainite in Steels. 2nd Edition. IOM. UK, 2001. pp: 177-180, 237-275, 285-342.

118 Bhadeshia, H. K. D. H.. Thermodynamic analysis of isothermal transformation diagrams, Metal Science, 16, 1982, pp. 159-165

119 http://engm01.ms.ornl.gov/TTTCCTPlots.html (on May 2004)

120 http://engm01.ms.ornl.gov/AshbyModel.html (on May 2004)

121 Ashby, M. F. and Easterling K. E. A first report on diagrams for grain growth in welds. Acta Metall., 30, 1982, pp. 1969-1978.

122 Ion J. C., Easterling K. E. and Ashby M. F. A second report on diagrams of microstructure and hardness for heat-affected zones in welds. Acta Metall., 32, (11), 1984, pp. 1949-1962

123 Harrison P. and Farrar R. Microstructural development and toughness of C-Mn and C-Mn-Ni weld metals. Part 1: Microstructural development, Metal Construction, 19, (7), 1987, pp. 392R-399R.

124 Farrar R. and Harrison P., Microstructural development and toughness of C-Mn and C-Mn-Ni weld metals. Part 2: Toughness, Metal Construction, 19, (8), 1987, pp. 447R-450R

125 Turteltaub S. and Suiker A. S. J. Transformation induced plasticity in ferrous alloys, Journal of the Mechanics and Physics of Solids, 53, 2005, pp: 1747-1788.

126 Berrahmoune M.R., Berveiller S., Inal K., Moulin A. and Patoor E. Analysis of the martensitic transformation at various scales in TRIP steel Materials Science and Engineering A, 378, (2004), pp: 304–307

127 Jacques P., Furnémont Q., Pardoen T., and Delanna F. On the role of martensitic transformation on damage and cracking resistance in TRIP-assisted multiphase steels, Acta Mater., 49, 2000, pp: 139-152.

128 Akselsen, O. M., Solberg, J.K., and Ø. Grong. Effect of martensite-austenite (M-A) islands on intercritical heat-affected zone toughness of low carbon microalloyed steels. Scandinavian Journal of Metallurgy 17 (1988) 194-200.

129 Suh J.-Y, Byun J.-S, Shim J.-H, Oh Y.-J, Cho Y.W., Shim J.-D and Lee D. N. Acicular ferrite microstructure on titanium bearing low carbon steels, Materials Science and Technology, Vol. 16, Nov-Dic 2000, pp: 1277-1281.

130 Lancaster J. F. Metallurgy of Welding, 6th edition, Abington Publishing, UK, 1999, pp:171, 192.

131 Tutertaub, S. and Suiker, A.S.J. Transformation-induced plasticity in ferrous alloys, Journal of the Mechanics and Physics of Solids, 53, (2005), pp 1747-1788.

132 Wang S.-Ch. And Yang J.-R. Effect of chemical composition, rolling and cooling conditions on the amount of martensite/austenite (M/A) constituent formation in low carbon bainitic steels, Materials Science and Engineering, A154, (1992), pp: 43-49.

133 Balliger N. K. and Gladman T. Work hardening of dual-phase steels. Metal Science, 15, 1981, pp: 95-108

134 De Cooman, B. C. Structure-properties relationship in TRIP steels containing carbide-free bainita, Current Opinion in Solid State & Materials Science, 8, (2004), pp: 285-303.

135 Timokhina I. B., Hodgson P.D. and Pereloma E. V. Effect of Microstructure on the Stability of Retained Austenite in Transformation-Induced-Plasticity Steels, Metallurgical and Materials Transactions A, 35A, (2004), pp: 2331-2341

136 Rigsbee J. M. and VanderArend P. J. Laboratory studies of microstructures and structure-properties relationships in "dual phase" HSLA steels, HSLA Steel Proc. Symp. On Formable HSLA and Dual Phase Steels, Chicago, Il. USA, 1977, pp: 56-86.

137 Wang J. and Van der Zwaag S. Stabilization Mechanisms of Retained Austenite in Transformation-Induced Plasticity Steel, Metallurgical ans Materials Transactions A, 32A, (2001), pp: 1527-1539

138 Raghavan V. and Antia D. P. The driving force for martensitic transformations in low alloy steels, Metallurgical and Materials Transactions A, 27A, (1996), pp: 1127-1132.

139 Chang L. C. and Bhadeshia H. K. D. H. Carbon content of austenite in isothermally transformed 300M steel. Materials Science and Engineering, A184, (1994), pp: L17-L19.

140 Liu, C., Zhao Z., Northwood D. O. and Liu Y., A new empirical formula for the calculation of Ms in pure iron and super-low carbon steels, Journal of Materials Processing Technology, 113, 2001, pp: 556-562

141 Andrews, K. W. Empirical formulae for the calculation of some transformation temperatures, , 203, 1965, pp: 721-727

142 Steven W. and Haynes A. G., The temperature of formation of martensite and bainite in low-alloy steels – some effects of chemical composition, Journal of the Iron and Steel Institute, 183, 1956, pp: 349-359

143 Chen Y. T., Guo A. M., Wu X. L., Zeng J. and Li P. H. Microstructure and mechanical property development in the simulated heat affected zone of V treated HSLA steels, Acta Metall. Sinica (Engl. Lett.), 19, 1, (2006), pp: 57-67.

144 Jacques P. J. Transformation-induced plasticity for high strength formable steels, Current Opinion in Solid State & Materials Science, 8, (2004), pp: 259-265.

145 Jacques P. J., Furnémont Q., Lani F., Pardoen T. and Delannay F. Multiscale mechanics of TRIP-assisted multiphase steels: I. Characterization and mechanical testing, Acta Materialia, 55, (2007), pp: 3681-3693.

146 Lani F., Furnémont Q., T. Van Rompaey, Delannay F., Jacques P. J. and Pardoen T. Multiscale mechanics of TRIP-assisted multiphase steels: II. Micromechanical modelling, Acta Materialia, 55, (2007), pp: 3695-3705.

147 Raghavan V. and Antia D. P. The driving force for martensitic transformations in low alloy steels, Metallurgical and Materials Transactions A, 27A, (1996), pp: 1127-1132.

148 Timokhina I. B., Hodgson P. D. and Pereloma E. V. Effect of microstructure on the stability of retained austenite in transformation-induced-plasticity steels, Metallurgical and Materials Transactions A, 35A, (2004), pp: 2331-2341

149 Evans G.M., Study of inclusions and their influence on acicular ferrite nucleation, Research Report, Welding Research Institute Bratislava, 1992, pp: 1-22.

150 Dowling N. E. Mechanical Behavior of Materials. Engineering Methods for Deformation, Fracture, and Fatigue, 2nd Edition, Prentice Hall, USA, 1999.

151 Herausgeber Editors. The Appearance of Cracks and Fractures in Metallic Materials. Verlag Stahleisen mbH, Düsseldorf, Germany, 1983, pp: 5-68.

152 Hirth, J. P. Theories of hydrogen induced cracking of steels. In "Hydrogen embrittlement and stress corrosion cracking". Edited by R. Gibala and R. F. Hehemann, ASN, USA 1984, pp: 29-41

153 Birnbaum, H. K. Hydrogen related failure mechanisms in metals. Proceedings of the Symposium: Environment-sebnsitive fracture of engineering materials. The metallurgical Society of AIME, USA, 1979, pp: 326-360.

154 Sing S. K. and Sasmal B. Effect of hydrogen on toughening of a low alloy steel. ISIJ International, 44, 1, 2004, pp: 203-208

155 Tweed J. H. and J. F. Knott, Micromechanisms of failure in C-Mn weld metals, Acta Metallurgica, 35, 7, 1987, pp: 1401-1414.

156 Tong Y. and Knott J. F. Evidence for the discontinuity of hydrogen-assisted fracture in mild steel, Scripta Metallurgica et Materialia, Vol. 25, 1991, pp: 1651-1656

157 Brooksbank D. and Andrews K. W., Stress fields around inclusions and their relation to mechanical properties, JISI, 1972, 210, pp: 246-255

158 Brooksbank D. and Andrews K. W., Stress associated with duplex oxide-sulphide inclusions in steel, JISI, 1970, 208, pp: 582-586

159 Brooksbank D. and Andrews K. W., Tessellated stresses associated with some inclusions in steel, 169, 207, pp: 474-483.

160 Brooksbank D. and Andrews K. W., Thermal expansion of some inclusions found in steels and relation to tessellated stresses, JISI, 1968, 206, pp: 595-599

161 Laszló, F., Tessellated stresses – Part I, JISI, 1943, 147, No. I, pp: 173-199

162 Laszló, F., Tessellated stresses – Part II, JISI, 1943, 148, No II, pp: 137-159

163 Gerberich W. W. and Chen Y. T., Hydrogen-controlled cracking – An approach to threshold stress intensity, Metallurgical Transaction A, 6A, February, 1975, pp: 271-278

164 Gerberich, W. W., Chen Y. T., and St. John C. A short-time diffusion correlation for hydrogen-induced crack growth kinetics, Metallurgical Transaction A, 6A, August, 1975, pp: 1485-1498

165 Gerberich W. W., Livne T., Chen X. F. and Kaczorowski M., Crack growth form internal hydrogen-Temperature and Microstructural Effects in 4340 steel, Metallurgical Transactions A, 19A, 1988, pp: 1319-1334.

166 Ewalds H. L. and Wanhill R. J. H., Fracture Mechanics, Edward Arnold and DUM co-publishers, UK, 1984. pp: 28-55, 226-298.

167 Meyers, M. A. and Kumarchawla, K. K., Mechanical Behavior of Materials, Prentice Hall, Inc. USA, 1999. pp: 326-354, 381-400.

168 Dowling N. E. Mechanical Behavior of Materials. Engineering Methods for Deformation, Fracture, and Fatigue, 2nd Edition, Prentice Hall, USA, 1999. pp: 798-806.

169 Timoshenko S. and Goodier J. N., Theory of Elasticity, 2nd Edition, McGraw-Hill, USA, 1951.

170 He, X. J, Terao N. and Berghezan A., Influence of martensite morphology and its dispersion on mechanical properties and fracture mechanisms of Fe-Mn-C dual phase steels, Metal Science, 18, 1984, pp: 367-373.

171 Kim N. J. and Thomas G. Effects of morphology on the mechanical behaviour of a dual phase Fe/Si/0.1C steel, Metallurgical Transactions A, 12A, 1981, pp: 483-489

172 Lanzillotto C. A. N. and Pickering F. B. Structure-property relationships in dual-phase steels, Metal Science, 16, 1982, pp: 371-382.

173 Kim B. C., Lee S., Kim N. J. and Lee D. Y., Microstructure and local brittle zone in high-strength low-alloy steels welds, Metallurgical Transaction A, 22A, 1991, 139-149

174 Davis C. L. and King J. E. Cleavage initiation in the intercritically reheated coarse-grained heat-affected zone: Part I. Fractographic Evidence, Metallurgical and Materials Transaction A, 25A, 1994, pp: 563-573.

175 Davis C. L. and King J. E. Effect of cooling rate on the intercritically reheated microstructure and toughness in high strength low alloy steel, Materials Science and Technology, 9, 1993, pp: 8-15

176 Akselsen O. M., Grong Ø. and Solberg J. K. Structure-property relationships in intercritical heat affected zone of low-carbon microalloyed steels, Materials Science and Technology, 3, 1987, pp: 649-655

177 Choi, J-K and Pyun, S-I. A new theory describing the hydrogen-assisted intergranular cracking of high-strength steels, Journal of Materials Science, 25, 1999, pp: 246-252.

178 Pyun, S-I and Lee H-K, Effect of threshold stress intensity on fracture mode transitions for hydrogen-assisted cracking in AISI 4340 steel. Metallurgical Transactions A, 21A, September, 1990, pp: 2577-2583.

179 McMahon C. J. Hydrogen-induced intergranular fracture of steels. Engineering Fracture Mechanics, 68, 2001, pp: 773-788

180 Chattoraj I., M. Tarafder, Swapan K. and Tarafder S. Hydrogen induced brittle crack growth in Cu-strengthened HSLA-100 steels. Materials Science and Engineering, A339, 2003, pp: 136-149

181 Thompson A. W. Hydrogen assisted fracture at notches, in Fracture at Stress Concentrators, Proceedings of the 1984 International Conference in Mechanics and Physics of Fracture III, IOM, UK, 1986, pp: 61-68

182 Lufrano J. and P. Sofronis, Enhanced hydrogen concentrations ahead of rounded notches and cracks-competition between plastic strain and hydrostatic stress, Acta Materialia, 46, 5, 1998, pp: 1519-1526

183 Sofronis P. and Lufrano J., Interaction of local elastoplasticity with hydrogen: embrittlement effect, Materials Science and Engineering, A260, 1999, pp: 41-47

184 Yokobori Jr. A. T., Chinda Y., Nemoto T., Satoh K. and Yamada T., The characteristics of hydrogen difusión and concentration around a crack tip concerned with hydrogen embrittlement, Corrosion Science, 44, 2002, 407-424.

185 Taha A. and Sofronis P. A micromechanics approach to the study of hydrogen transport and embrittlement, Engineering Fracture Mechanics, 68, 2001, pp: 803-807

186 Yokobori Jr. A. T., Nemoto T., Satoh K. and Yamada T., Numerical análisis on hydrogen difusión and concentration in solid with emisión around the crack tip, Engineering Fracture Mechanics, 55, 1, 1996, pp: 47-60

187 Wang, Jian-Sheng, The thermodynamic aspects of hydrogen induced embrittlement, Engineering Fracture Mechanics, 68, 2001, pp:647-669

188 Chattoraj, I., Tarafder M., Swapan K. Das, Trafder S. Hydrogen induced brittle cracks growth in Cu-strengthened HSLA-100 steels, Materials Science and Engineering, A00, 2002, pp: 1-14

189 Easterling, K., Introduction to the Physical Metallurgy of Welding, 2nd Editon, Butterworth-Heinemann Ltd, UK, 1992.

190 Wang, S. H., Luu W. C., Ho K. F. and Wu J. K., Hydrogen permeation in a submerged arc weldment of TMCP steel, Materials Chemistry and Physics 77, 2002, pp: 447-454

191 Freund, J. E. Statistic - A first course. 2nd Edition. Prentice-Hall Inc, USA, 1970. pp: 10-55, 152-178.

192 Montgomery D. C. and Runger G. C. Probabilidad y estadística aplicada a la Ingeniería. 2da Edición, Editorial LIMUSA, S. A. México, 2006. pp: 26-48, 144-197, 294-429

193 Dowdy S. and Wearden S. Statistic for Research. 2nd Edition. John Wiley & Sons, Inc. USA, 1991. pp: 193-201, 554-555.

194 Spiegel, M. R. Statistics-crash course. Schaum's outline series. McGraw – Hill, USA 2000. pp: 11-19, 32-37, 45-68, 130-131.

195 BS2846-1: 1991. Guide to Statistical Interpretation of data– Part 1: Routine analysis of quantitative data. BSI, UK, 1999.

196 BS2846-2: 1981. Guide to Statistical Interpretation of data– Part 2: Estimation of the mean: confidence interval. BSI, UK, 1999

197 BS2846-4: 1976. Guide to Statistical Interpretation of data– Part 4: Techniques of estimation and tests relating to means and variances. BSI, UK, 1999.

198 Von Fraunhofer, J. A. and Banks, C. H. Potentiostats and its Aplications. Butterworths & Co. Publishers, Hungary, 1972, pp: 75-77.

199 Sigworth G. K. and Elliot J. F., The Thermodynamics of Liquid Dilute Iron Alloys, Metal Science, 8, pp. 298-310

200 Bodworth C. and Bell H. B., Physical Chemistry of Iron and Steel manufacture, 2nd Edition Longman 1972, pp. 485-509

201 Deo, B. and Boom, R. Fundamentals of SteelMaking Metallurgy. Prentice Hall International, UK 1993, pp. 54-55

202 Hong, T. and DebRoy, T. A computer program for the calculation of TTT diagrams for the growth and dissolution of Oxides, Nitrides and sulphides inclusions. Software's manual, 2000.

203 Dieter, G. Engineering Design – A materials and processing approach 3rd Edition. McGraw-Hill International Editions, Singapore, 2000. pp: 521-569.

ANNEXES

A.1 The equilibrium partition ratio

The equilibrium partition ratio, κ_0, controls the direction and extent of segregation. For most alloy elements in steel the partition ratio is less than 1 and the element segregates to the interdendritic liquid [19]. Table A.1 gives some approximate values of κ_0 for various alloying elements present in high strength low alloy steels.

Table A.1 Equilibrium partition ratios for different solutes in low alloy steels[19-20]

Element	κ_0
C	0.17
Si	0.8
Mn	0.7
Ni	0.85
Al	0.95
Ti	0.5
B	0.001
O	0.01
S	0.2
N	0.04

A.2 Modes of solidification depending on the temperature gradient and the constitutional super-cooling

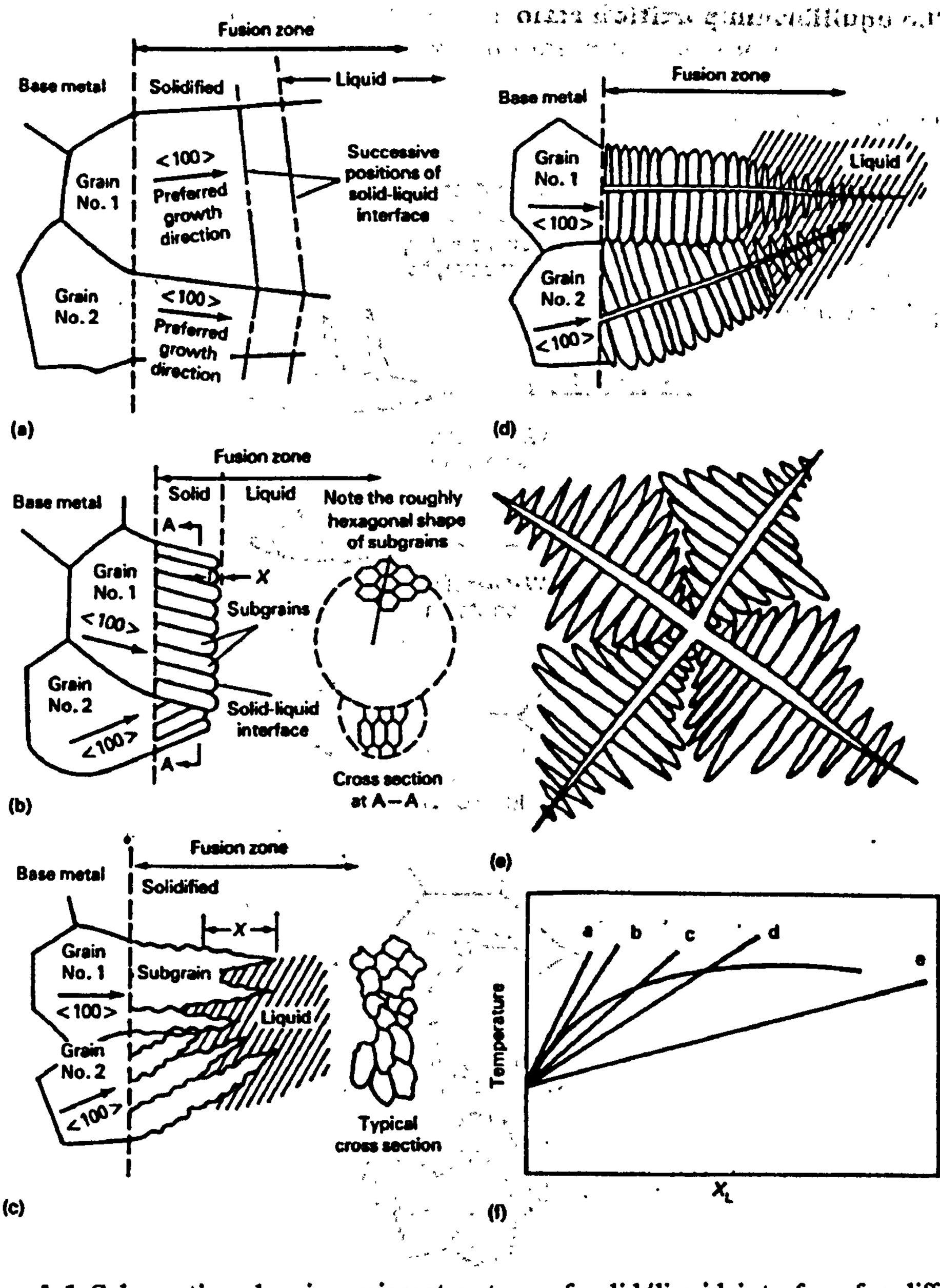

Figure A.1 Schematics showing microstructure of solid/liquid interface for different modes of solidification and the temperature gradients that generate each of the different modes. (a) Planar growth, (b) cellular growth, (c) cellular dendritic growth, (d) columnar dendritic growth, (e) equiaxed dendrite, and (e) five temperature gradient versus constitutional supercooling [40].

A.3 Dubé's classification of the ferrite morphology in steels

In the figure A.2 are shown the early classification proposed by Dubé of the morphology of the ferrite. Some of these names are still used today. The only major change to this classification is the designation of the name acicular ferrite to what Dubé called intergranular Widmanstätten ferrite.

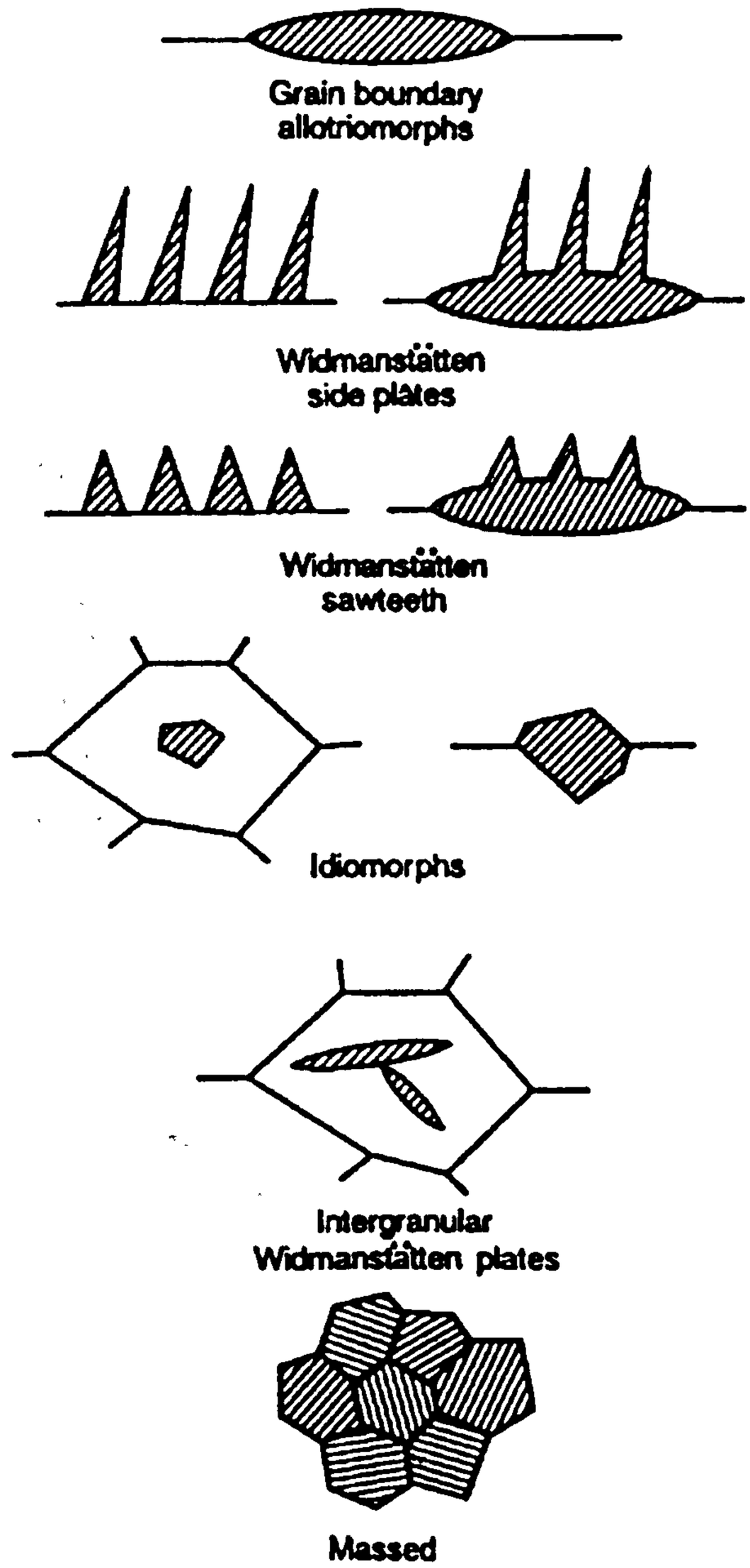

Figure A.2 Schematics showing the Dubé classification of ferrite morphologies in steels[42].

A.4 IIW algorithms for the identification of the different microstructures in low alloy steel welds

The figure A.3 shows the IIW recommended procedure to classify the different microstructural features that could be found in low alloy steel welds. This permits a systematic identification of the phases or morphologies of the steel microstructure.

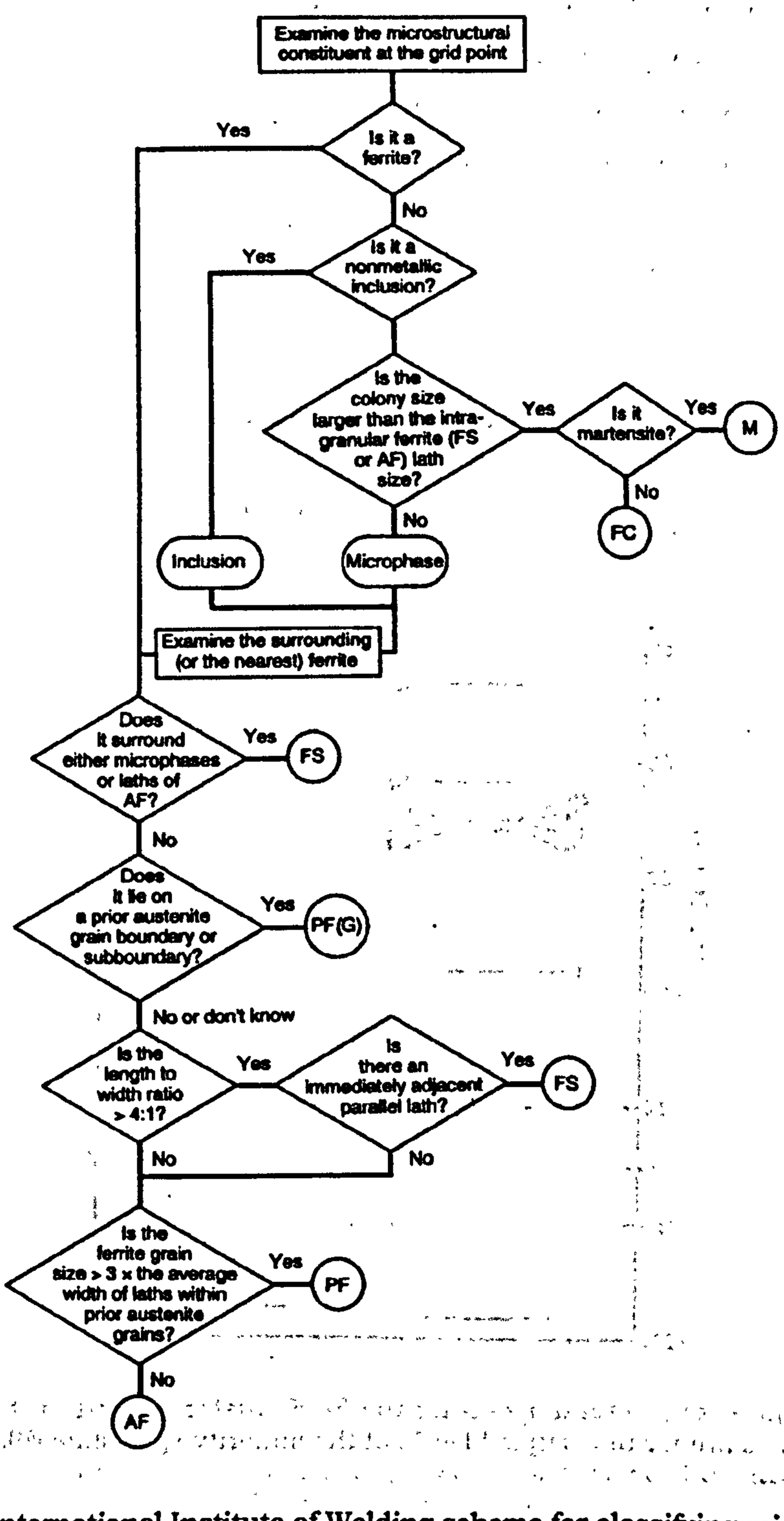

Figure A.3 International Institute of Welding scheme for classifying microstructural constituents in ferritic steel weld metals with the optical microscope [42].

A.5 Electron energy diagram for the Fe4S cluster

In these diagrams, the $1a_1$ and $1t_2$ levels are very important, because these two levels correspond to the wave functions that describe the metal-impurity interaction. The rest of the energy levels correspond to wave functions that are located either completely or almost completely on the metal atoms. For this reason, the orbital contour plots for the $1a_1$ and $1t_2$ levels are shown in the figure 4.6 (b). As could be observed in this figure for Fe_4S, the $1a_1$ orbital has practically no metal contribution and the $1t_2$ orbital also has little content on the metal atoms and are more concentrated on the impurity. Consequently, the bond has a heteropolar character [31].

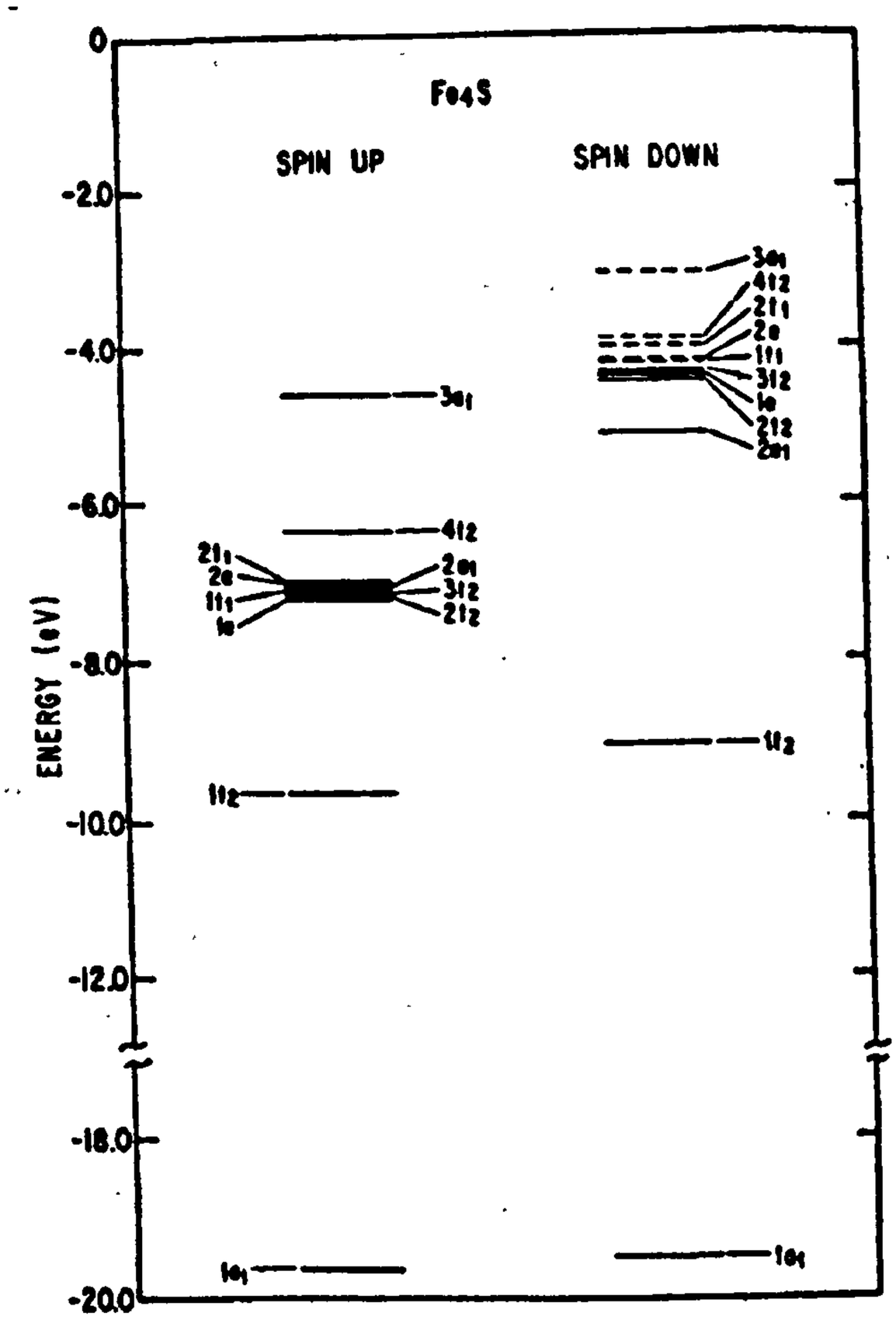

Figure A.4. The energy level diagram for the Fe_4S cluster showed in the figure 4.6(a). The dashed lines are for unoccupied levels of the minority spin-state [31].

A.6 Welding Parameters used in the production of the weld metals

The tables A.2 and A.3 present the different welding parameters used by Wildash [8] in the fabrication of the weld metal samples. The first table shows the data fro the commercial consumables and the second table for the modified consumables. The heat input (H_I) was recalculated from the original data. The weld metals studied in this investigation are those with the heat input around 1.0 kJ/mm.

Table A.2. List of commercial consumables, tubular wire 1.2 mm diameter, chosen for experimental work and welding variables used.

Consumable	CW Type	WM id	S_{YG} (MPa)	V_W (m/min)	V_{WG} (mm/min)	H_I (kJ/mm)
OK 14.00	Metal Cored	14001	460	6.5	262	1.0
OK 14.03	Metal Cored	14031	710	6.6	245	1.1
OK 15.17	Rutile	15171	560	8.7	281	1.1

Legend:
CW Type: Cored wire type
WM id: Weld metal identification
S_{YG}: Quoted yield strength
V_W: Average wire speed
V_{WG}: Average welding gun speed
H_I: Heat input.

Table A.3. List of modified consumables, tubular wire 1.2 mm diameter, chosen for experimental work and welding variables used.

WM id	CW Type	S_{YG} (MPa)	V_W (m/min)	V_{WG} (mm/min)	H_I (kJ/mm)
CWX18gb	Rutile		8.7	281	1.0
CWX201	Rutile		8.7	281	1.0
VCX256	Rutile		8.7	281	1.0
CWX35	Metal Cored		6.6	245	1.0
CWX36	Metal Cored		6.6	245	1.0
CWX33	Rutile		6.6	245	1.0
CWX18o	Metal Cored		6.6	245	1.0
CWX7	Rutile		6.6	245	1.0
CWX8	Rutile		6.6	245	1.0
CWX9	Rutile		6.6	245	1.0

Legend:
CW Type: Cored wire type
WM id: Weld metal identification
S_{YG}: Quoted yield strength
V_W: Average wire speed
V_{WG}: Average welding gun speed
H_I: Heat input.

A.7 Macros utilized for the determination of the NMI size and spatial distribution

The image analyser software utilised was the KS 400 Version 3.0 available at the Electron Microscopy Centre facilities in the University of Leeds. Some comments in parenthesis and italic letters are used to clarify some instructions. These must not be written in the macro.

A. MACRO 1. NMI size distribution and superficial density

```
imgsetpath "D:\arm\inclusions\Group2"    (location of the images in the storage disc)
# MACRO:  NMIsizedistribution
# Keywords: NMI, steel, inclusion size distribution
# BACKGROUND: Size distribution of NMI in weld metal at 1000X
# SYSTEM: KS 400 - Version 2.0 3.0
# OPTIONS:  Grey morphology
#-------------------------------------------------------------------
#Preparation of the windows
#-------------------------------------------------------------------
imgdelete "*"
if ( ISconfigured("Grey") == 0)
   MBok "Option 'Grey Morphology' is not configured !"
   stop
endif
showwindow "Display",1
Gclear 0
showwindow "Gallery",1
showwindow "Messages",1
write "@"
MSload "default"
update
#-------------------------------------------------------------------
# Getting the image
#-------------------------------------------------------------------
imgload "CWX3611.tif",1                    (name of the specific image file)
#-------------------------------------------------------------------
# Discriminate the image
#-------------------------------------------------------------------
disdyn 1,2,151,45,1
binscrap 2,3,0,1000,0
#-------------------------------------------------------------------
# binary processing
#-------------------------------------------------------------------
binnot 3,3
MSsetprop "CONDITION","FCIRCLE>0.60"
imgclear 4,0
MSlabelmask 3,1,4,1,255
distance 4,5,1
binnot 5,5
greywsheds 5,6
binnot 6,6
binand 4,6,7

#-------------------------------------------------------------------
# setup and perform measurement
#-------------------------------------------------------------------
FNAME = "CWX361"
MSsetprop "CONNECT",4
```

```
MSsetprop "REGIONFEAT","DCIRCLE"
Scale = 0.0884956  # calculated from the image micromark of 10 microns
MSsetprop "SCALEX",Scale
MSsetprop "SCALEY",Scale
MSsetprop "UNIT","micrometer"
MSsetprop "CONDITION","DCIRCLE>0"
MSmeasmask 7,1,FNAME,0,1,10
#-------------------------------------------------------------------
# measure total number per unit surface
#-------------------------------------------------------------------
MSsetprop
"FIELDFEAT","FLDCOUNT,FRAMEAREA,FLDDensity[10**6/mm2]=FLDCOUNT/FRAM
EAREA"
MSsetprop "CONDITION","DCIRCLE>0"
RGnew 7
MSmeasregion 2
MSgetvalue "FLDDensity",FLDtot
MSsetprop "CONDITION","DCIRCLE < 1"
MSmeasregion 2
MSgetvalue "FLDDensity",FLD45
MSsetprop "CONDITION","DCIRCLE > 1"
MSmeasregion 2
MSgetvalue "FLDDensity",FLD10
swrite S1,"              Total : $1/6.2F ",FLDtot * 1000
swrite S2,"Diameter   <1: $/6.2F ",FLD45 * 1000
swrite S3,"Diameter >1: $1/6.2F ",FLD10 * 1000
Gclear
Gstring 10,10,"Surface density of particles (in thousand/mm2):",11,"SWV___18"
Gstring 10,50,S1,11,"SWV___18",0
Gstring 10,80,S2,11,"SWV___18",0
Gstring 10,110,S3,11,"SWV___18",0
#-------------------------------------------------------------------
# show results
#-------------------------------------------------------------------
datahisto FNAME,"DCIRCLE",0,20,0.0,5.0,100.0, "CWX361"("ID" related with sample)
Gmerge 1,255
Gclear
imgdisplay 1
write "Done."
stop
```

B. MACRO 2. NMI spatial distribution

```
imgsetpath "C:\arm\inclusions\Group5"
# MACRO:  NMIspacialdistribution
# Keywords: NMI, steel, inclusion spacial distribution
# BACKGROUND: The image is processed to obtain a bynary representation of the inclusions.
The eucledean distance map is utilised to define regions around the inclusion. The boundaries
produced after skeletonizasion represent the maximun distance from the matrix and the
inclusion. The distribution of areas will show the spacial distribution of the inclusion: random,
uniform or clustered.
# SYSTEM: KS 400 - Version 2.0 3.0
# OPTIONS:  Grey morphology
#-------------------------------------------------------------------
#Preparation of the windows
#-------------------------------------------------------------------
imgdelete "*"
if ( ISconfigured("Grey") == 0)
   MBok "Option 'Grey Morphology' is not configured !"
   stop
endif
showwindow "Display",1
Gclear 0
showwindow "Gallery",1
```

```
showwindow "Messages",1
write "@"
MSload "default"
update
#-------------------------------------------------------------------------
# Getting the image
#-------------------------------------------------------------------------
imgload "CWX9112.tif",1
#-------------------------------------------------------------------------
# Discriminate the image
#-------------------------------------------------------------------------
disdyn 1,2,151,45,1
binscrap 2,3,0,1000,0
#-------------------------------------------------------------------------
# binary processing
#-------------------------------------------------------------------------
binnot 3,3
MSsetprop "CONDITION","FCIRCLE>0.60"
imgclear 4,0
MSlabelmask 3,1,4,1,255
distance 4,5,1
binnot 5,5
greywsheds 5,6
binnot 6,6
binand 4,6,7
#-------------------------------------------------------------------------
# setup and perform measurement
#-------------------------------------------------------------------------
FNAME = "CWX91nd"
MSsetprop "CONNECT",4
MSsetprop "REGIONFEAT","AREA"
Scale = 0.0884956  # calculated from the image micromark of 10 microns
MSsetprop "SCALEX",Scale
MSsetprop "SCALEY",Scale
MSsetprop "UNIT","micrometer"
MSsetprop "CONDITION","AREA>0"
#  Spacial distribution calculation
binnot 7,8
distmapeuclid 8,9
greywsheds 9,10
binnot 10,11
MSsetframe
MSmeasmask 11,1,FNAME,1,1,10
#-------------------------------------------------------------------------
# show results
#-------------------------------------------------------------------------
datahisto FNAME,"AREA",0,40,0.0,250.0,250.0, "CWX91"
Gmerge 1,255
Gclear
imgdisplay 1
write "Done."
Stop
```

A.8 Instrumentation Amplifier circuit and Stable potential pulse generator circuit

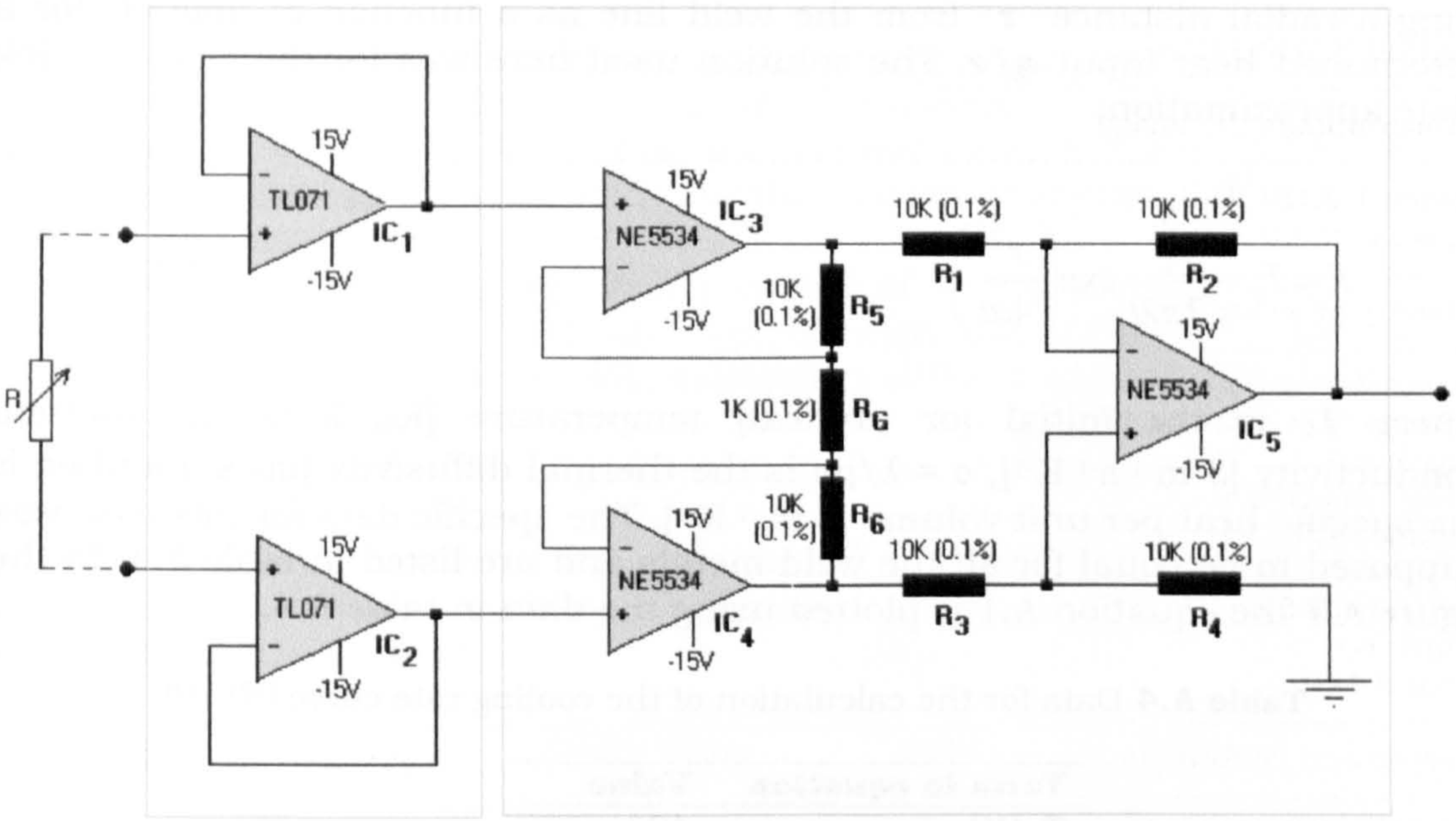

Figure A.5 Instrumentation amplifier unit

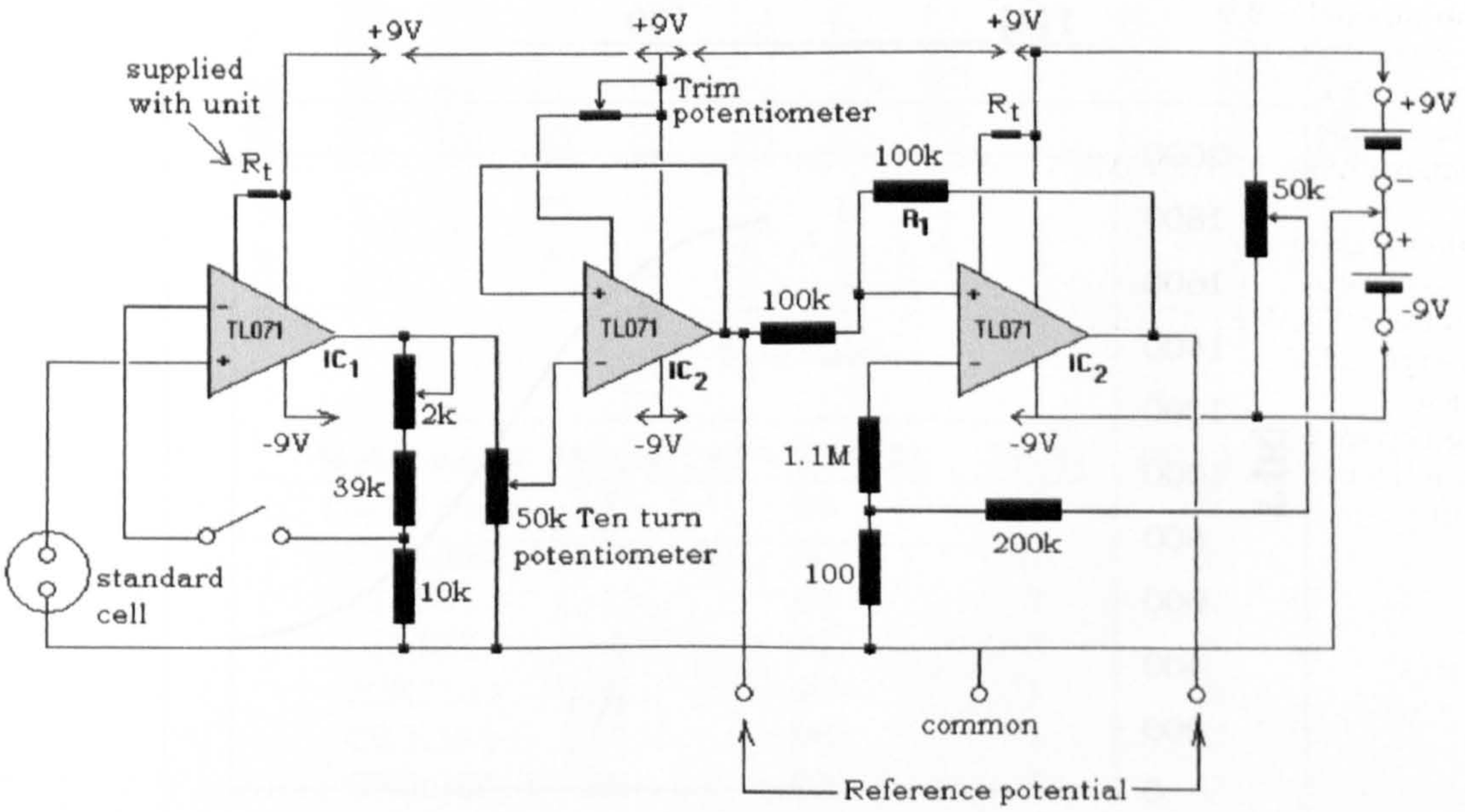

Figure A.6 Dual polarity reference potential unit [197]

A.9 Calculation of the cooling rate for the weld metal

The temperature/time profiles in the weld metal were calculated form the equations of Rosenthal. The equation A.1 give the temperature **T** at a point lying a radial distance **r** from the weld line as a function of time **t**, for a determined heat input **q/v**. The solution used here was for the case of thick plate approximation.

$$T = T_0 + \frac{\frac{q}{v}}{2\pi\lambda t}\exp\left(\frac{r^2}{4at}\right) \qquad (A.1)$$

where T_0 is the initial (or preheat) temperature [K], λ is the thermal conductivity [J m^{-1} s^{-1} K^{-1}], $a = \lambda/\rho c$ is the thermal diffusivity [m^2 s^{-1}] and ρc is the specific heat per unit volume [J m^{-3} K^{-1}]. The specific data for this case was supposed to be equal for all the weld metals and are listed in table A.4. In the figure A.7 the equation A.1 is plotted using the data in table A.4.

Table A.4 Data for the calculation of the cooling rate curve [121-122]

Term in equation	Value
T_0 [K]	423
ρc [J m^{-3} K^{-1}]	4500000
a [m^2 s^{-1}]	9.1 10^{-6}
λ [J m^{-1} s^{-1} K^{-1}]	41
η [none]	0.85
H=q/v [J m^{-1}]	1000000
r [m]	0.005
v [m/s]	0.0041
U [V]	28
I [A]	190

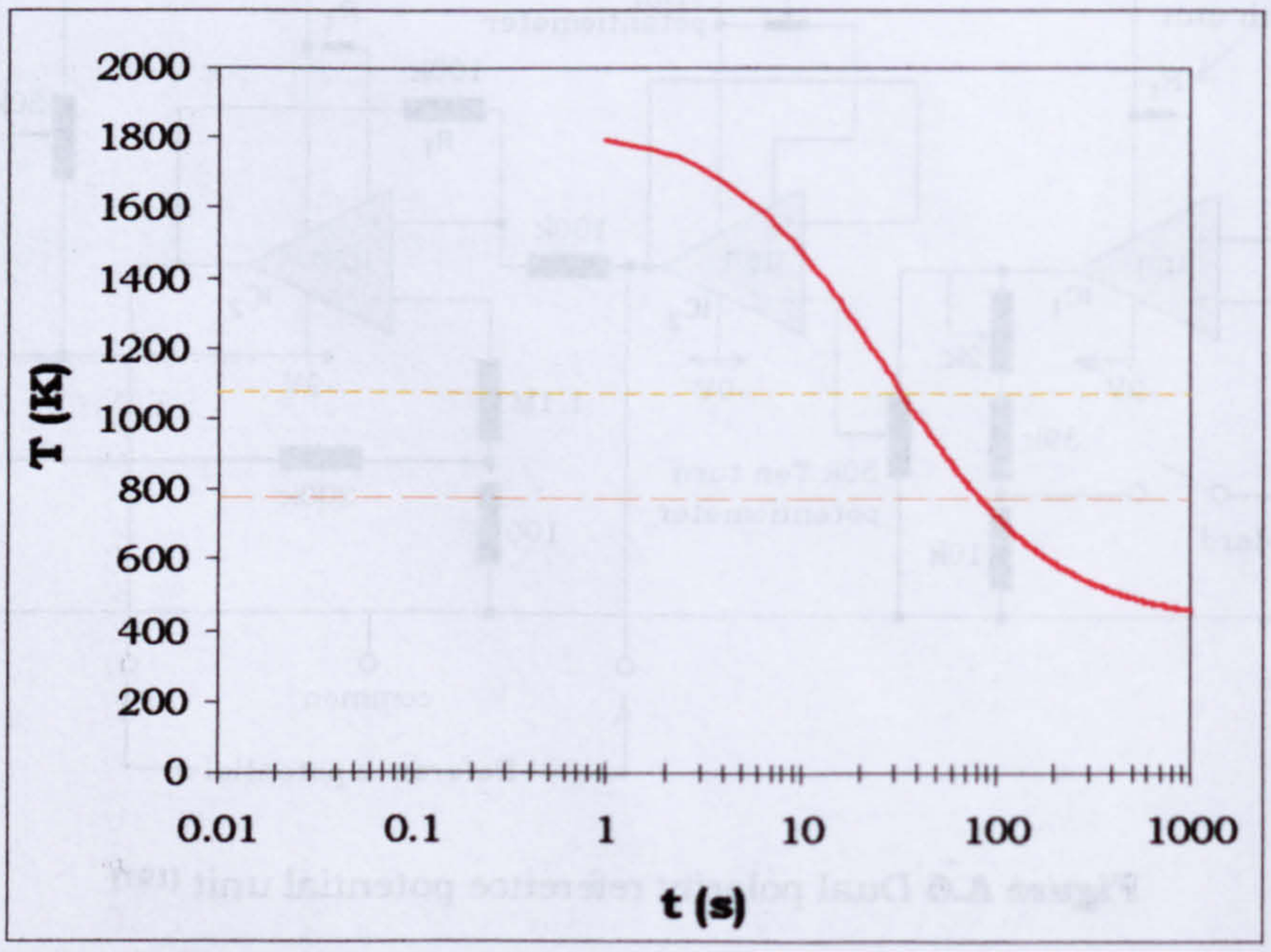

Figure A.7 Cooling rate curve for the different weld metals calculated at a distance of 5mm from the welding line

A.10 Phase proportion of the weld metal microstructures

Figure A.8 presents the phase proportion in each weld metal. These proportions are based partially on the Wildash[8-11] work and on detailed observations during this investigation. The huge effort to determine the phase proportion by Wildash[8-11] was corroborated with new metallographic observation and some corrections were included. These corrections include: the observation of isolated island of bainite, the presence of a very fine acicular ferrite, the identification of martensite. In some cases the identification was clear. In others, on the contrary, the separation of the different features was very difficult. For this reason, it is proposed to group the microstructures as follow:

1- AF + FS(NA): group that consists of a chaotic microstructure as acicular ferrite (AF) and ferrite with non-aligned second phase (FS(NA)) – a very fine microstructure without spatial orientation.
2- M: martensite.
3- FS(A): ferrite with aligned second phase, that is, bainite.

A more detailed revision of the weld metal microstructure could permit a complete characterisation of it. Different techniques can be used: X-ray diffraction, MEB, TEM, etc.

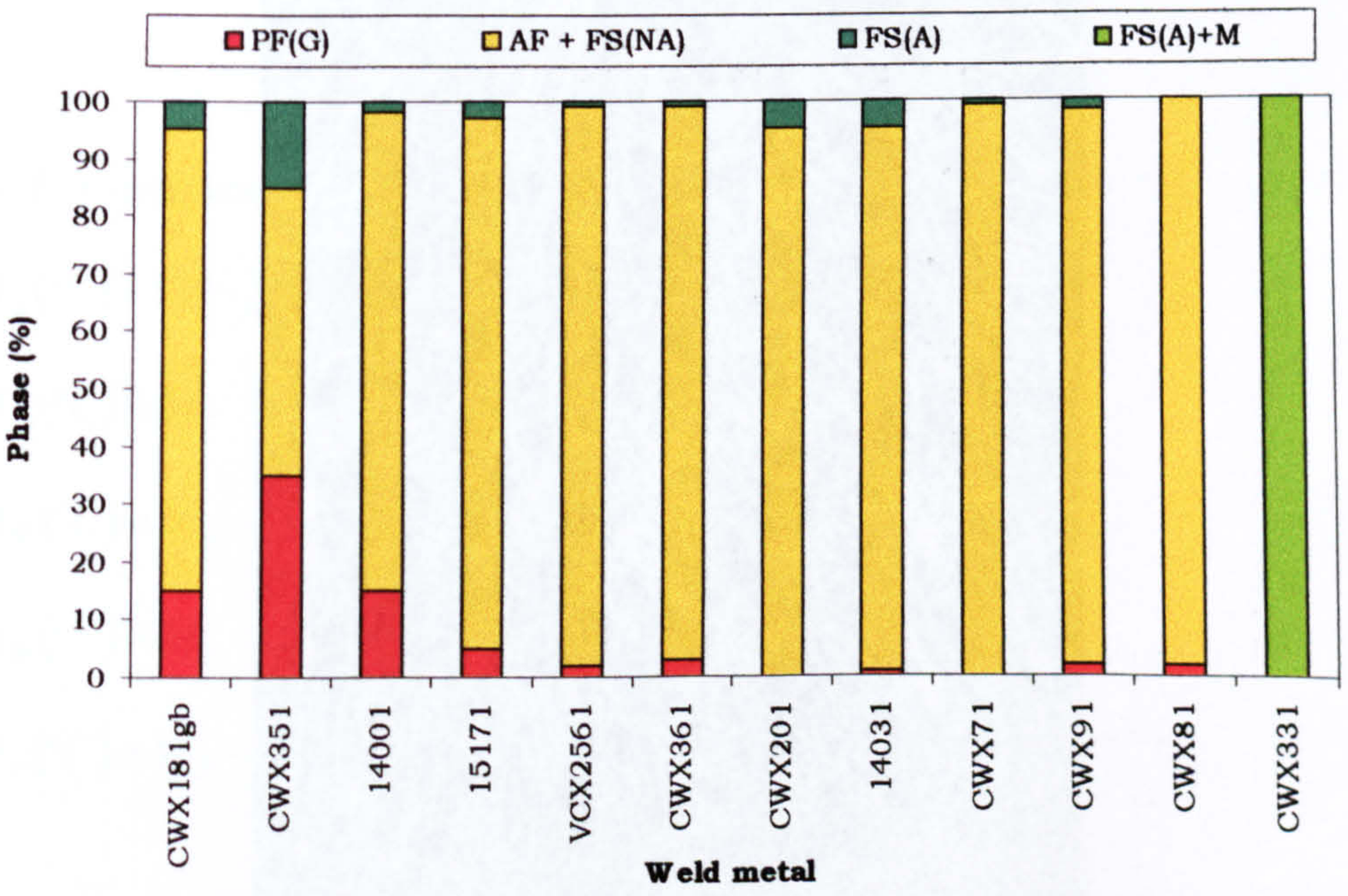

Weld metal	PF(G)	AF + FS(NA)	FS(A)	FS(A)+M
CWX181gb	15	80	5	0
CWX351	35	50	15	0
14001	15	83	2	0
15171	5	92	3	0
VCX2561	2	97	1	0
CWX361	3	96	1	0
CWX201	0	95	5	0
14031	1	94	5	0
CWX71	0	99	1	0
CWX91	2	96	2	0
CWX81	2	98	0	0
CWX331	0	0	0	100

Figure A.8. Phase proportion of the weld metals.

A.11 Complete microstructure of a weld metal: CWX181

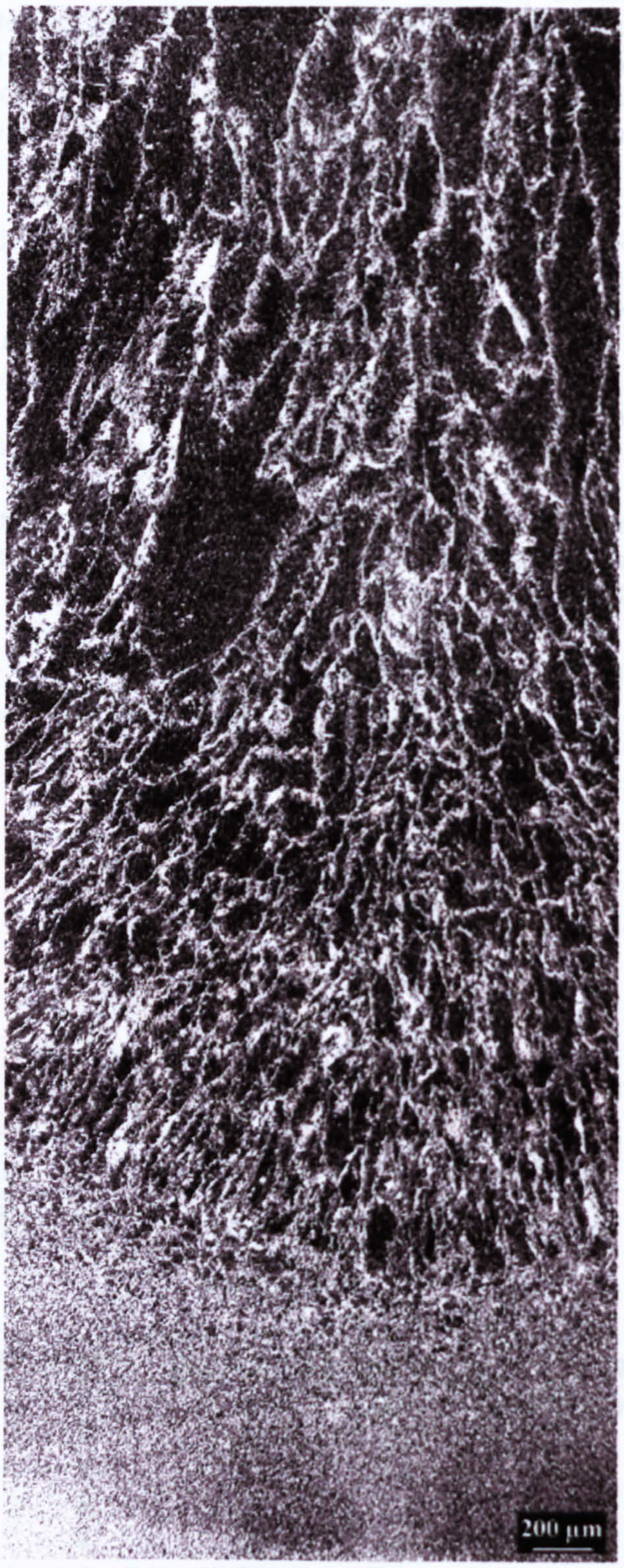

Figure A.9 Microstructure of the CWX181 weld metal presenting the different prior austenitic grain sizes: small grains near the fusion line and large grains close to the centre. It is shown the reheated zone, which is the region with small ferritic grains at the bottom of the figure.

A.12 Bainite and martensite transformation temperatures.

Equations used to estimate B_s, B_{50}, B_f, M_s, M_{10}, M_{50}, M_{90} and M_f were found in Liu et. al [140], Andrews [141] and Steven and Haynes[142]. The following equations were used:

A- For bainite transformation[142]:

$$B_s(°C) = 830 - 270C - 90Mn - 37Ni - 70Cr - 83Mo \quad \text{A.2}$$

$$B_{50}(°C) = B_s - 60 \quad \text{A.3}$$

$$B_f(°C) = B_s - 120 \quad \text{A.4}$$

B- For martensite transformation[141, 142]:

$$M_s(°C) = 539 - 423C - 30.4Mn - 17.7Ni - 12.1Cr - 7.5Mo \quad \text{A.5}$$

$$M_{10}(°C) = M_s - 10 \quad \text{A.6}$$

$$M_{50}(°C) = M_s - 47 \quad \text{A.7}$$

$$M_{90}(°C) = M_s - 103 \quad \text{A.8}$$

$$M_f(°C) = M_s - 215 \quad \text{A.9}$$

Several more equation could be found in Liu[140], specially for the very low carbon and alloy steels. In this investigation were used the equations from A.2 to A.9.

A.13 Effect of austenite particle size on Ms

The change in Gibbs free energy due to the austenite to martensite transformation ($\Delta G_m^{\gamma\to\alpha'}$) could be written as:

$$\Delta G_m^{\gamma\to\alpha'} = \Delta G_{Ch}^m - E_m^{extra} + E_m^{barrier} \qquad (A.10)$$

where ΔG_{Ch}^m, E_m^{extra} and $E_m^{barrier}$ are the chemical driving force, the reduction in energy due to other factors (Zener ordering of C (E_m^{η}) and stacking fault energy (E_m^D)) and the energies opposing the nucleation of martensite (elastic strain (E_m^e), internal defect energy ($E_\perp^{\alpha'}$) and interfacial energy(E_m)), respectively. Substituting all these terms equation A.10 becomes:

$$\Delta G_m^{\gamma\to\alpha'} = \left(G_m^{\gamma} - G_m^{\alpha}\right) - \left(E_m^{\eta} + E_m^{D}\right) + \left(E_m^{e} + E_\perp^{\alpha'} + E_m\right) \qquad (A.11)$$

Of particular interest is the term E_m, the interfacial energy between austenite and martensite, because this could be important due to the reduction in austenite particle size. Wang et. al. propose a treatment to estimate the value of this energy and found a way to elucidate the effect of the austenite particle size on M_s temperature. Figure A.9 presents the important variables to consider in the estimation of E_m using equation A.12.

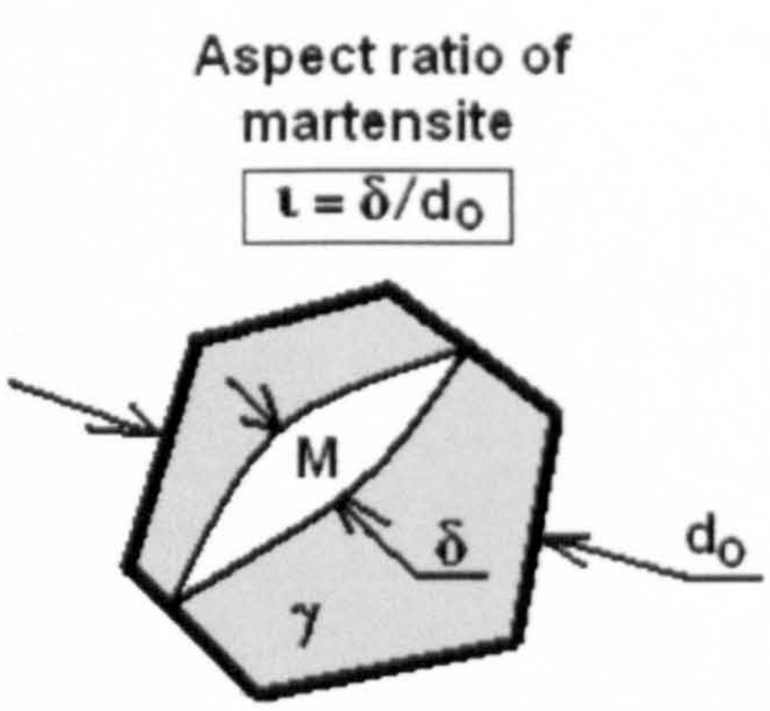

Figure A.10 Schematic representation of an austenite particle of diameter (d_o), and an internal martensite plate of thickness (δ). The aspect ratio is ι which is assumed to have a value around 0.05 for convenience and simplification of the interpretation.

$$E_m = \frac{2 \cdot V_m^{\alpha'} \cdot \gamma_{\alpha'/\gamma}}{\iota \cdot d_o} \qquad (A.12)$$

where $V_m^{\alpha'}$ is the martensite molar volume, $\gamma_{\alpha'/\gamma}$ is the specific surface energy of the martensite/austenite interface and the rest were defined in figure A.19. A reduction in (d_o) is going to produce an increase of E_m which opposes the formation of martensite. As a consequence the driving force should increase to permit the formation of martensite and this means that M_s have to be decreased. At Ms-temperature equation A.11 becomes:

$$\left(G_m^{\gamma}-G_m^{\alpha}\right)^{*}-\left(E_{\eta}^{*}+E_{D}^{*}\right)+\left(E_{e}^{*}+E_{\perp}^{*}+E_{m}^{*}\right)+W_f^{*}=0 \qquad \text{(A.13)}$$

where W_f^{*} represents all other types of energies that may exist but cannot be considered in an explicit manner. Following Wang [137] approach, the predictable items are grouped on the right hand side of equation A.13 and assuming that the remaining part is a function of Ms, this equation changes to:

$$W_f^{*}-E_D^{*}=-\left(G_m^{\gamma}-G_m^{\alpha}\right)^{*}+E_{\eta}^{*}-\left(E_{e}^{*}+E_{\perp}^{*}\right)-E_m^{*} \qquad \text{(A.14)}$$

$$g(M_s)-E_m^{*}=f(M_s) \qquad \text{(A.15)}$$

where $f(M_s)$ could be obtained experimentally. Wang et. al. [137] reported an equation for $f(M_s)$ as A.16 which was obtained for a Fe-0.6C-1.5Mn-1.5Si TRIP-steel. Raghavan et. al.[147] reported a similar equation for 1152 steel compositions yielding the linear equation A.17. This equation is valid for steels with the following range in compositions: 0.1 to 0.6C, 0 to 1.4Cr, 0.3 to 0.9Mn, 0 to 0.32Mo, 0 to 2.2Ni and a fixed 0.25Si, all in wt%. These compositional ranges cover approximately the weld metals which were studied in this investigation. The accuracy of this equation was estimated to be ± 25 J/mol.

$$E_{net}(J/mol)=f(M_s)=A+B\cdot M_s=3931-6.761\cdot M_s(K) \qquad \text{(A.16)}$$

$$\Delta G(J/mol)=1975-1.234\cdot M_s(^{\circ}C)=2311.9-1.234\cdot M_s(K) \qquad \text{(A.17)}$$

Combining A.15 with A.16 or A.17 (equation to be used with the weld metals) and neglecting the g(T) dependence, an expression for the decrease in Ms temperature due to grain size effect can be obtained:

$$\Delta M_s=\left|\frac{E_m^{*}}{B}\right| \qquad \text{(A.18)}$$

Then, considering the decrease in the martensite transformation temperature as M_s-ΔM_s, it is possible to estimate the combined effect of composition and size on the appearance of retained austenite. The effect of C on the molar volume of martensite was taken into account using the equations A.19 and A.20 [36] to estimate the volume of the bct cell:

$$\frac{c}{a}=1+0.045\cdot C(wt\%) \qquad \text{(A.19)}$$

$$c=2.86+0.1143\cdot C(wt\%) \qquad \text{(A.20)}$$

Figures A.10 and A.11 present the results of the above approach for all the weld metals which were studied in this investigation. These results are taken in a qualitative manner.

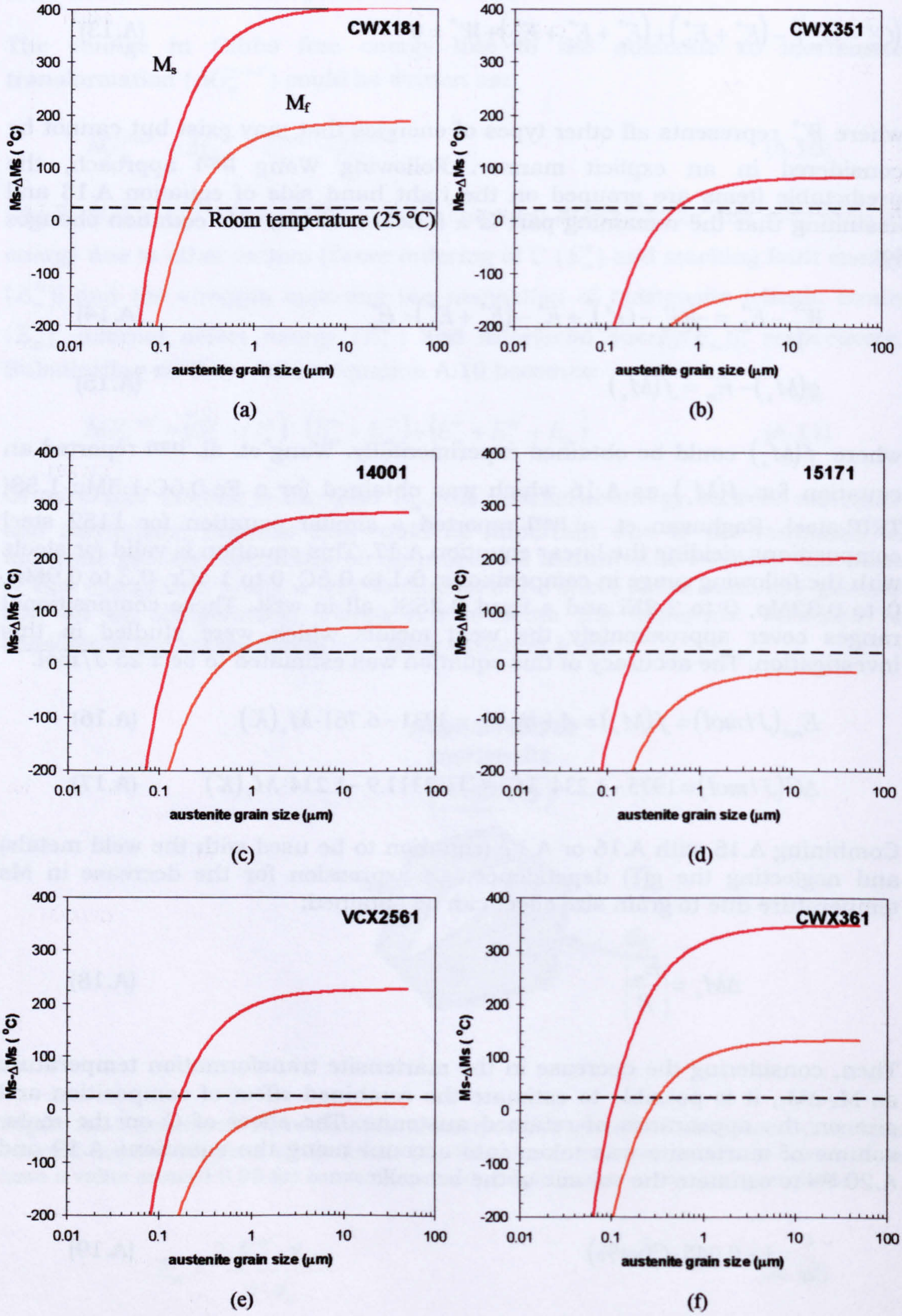

Figure A.11 Effect of the austenite particle size on M_s and M_f for the weld metals: (a) CWX181, (b) CWX351, (c) 14001, (d) 15171, (e) VCX2561 and (f) CWX361. It was assumed for the calculations ι=0.05, B=1.234 and the carbon concentration as the corresponding $C\gamma$ in table 7.3.

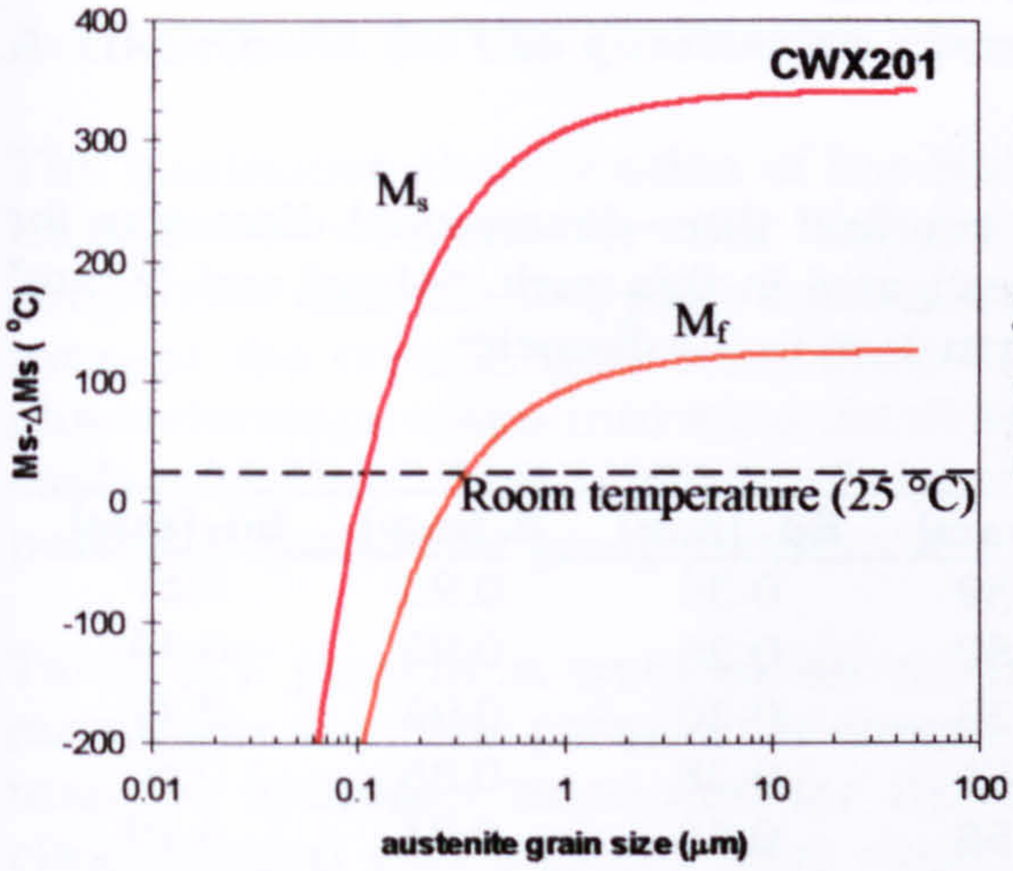

(a)

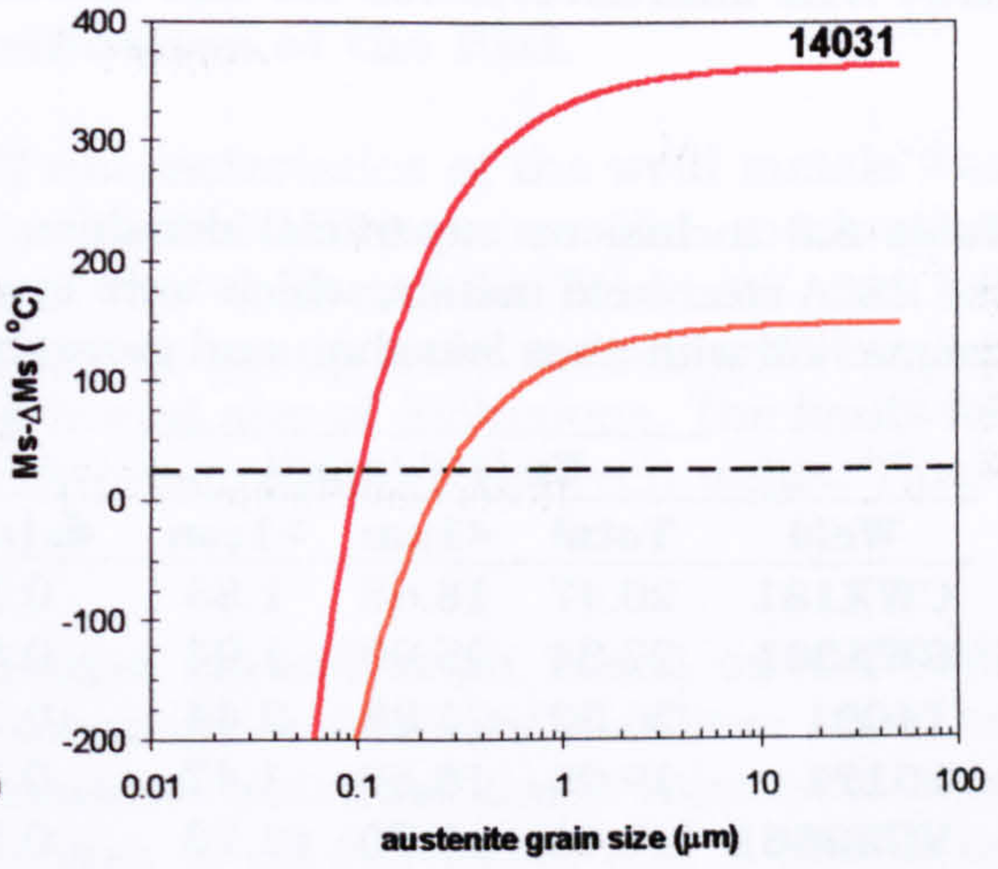

(b)

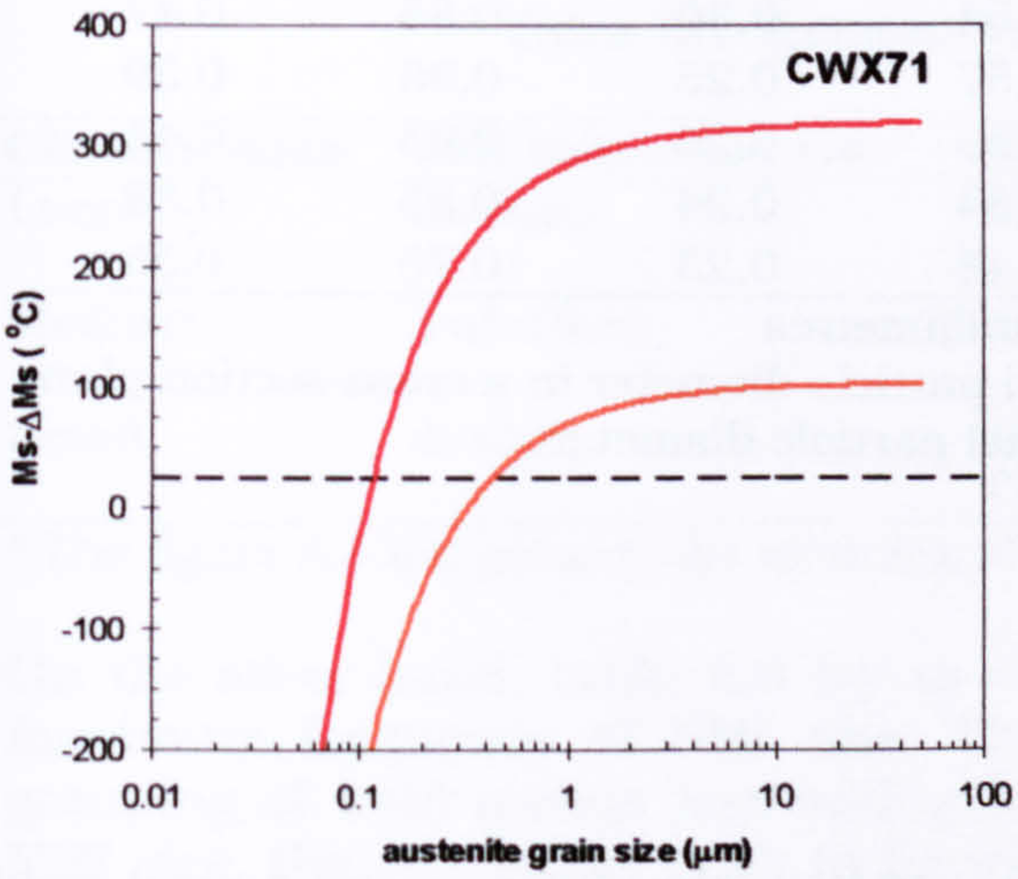

(c)

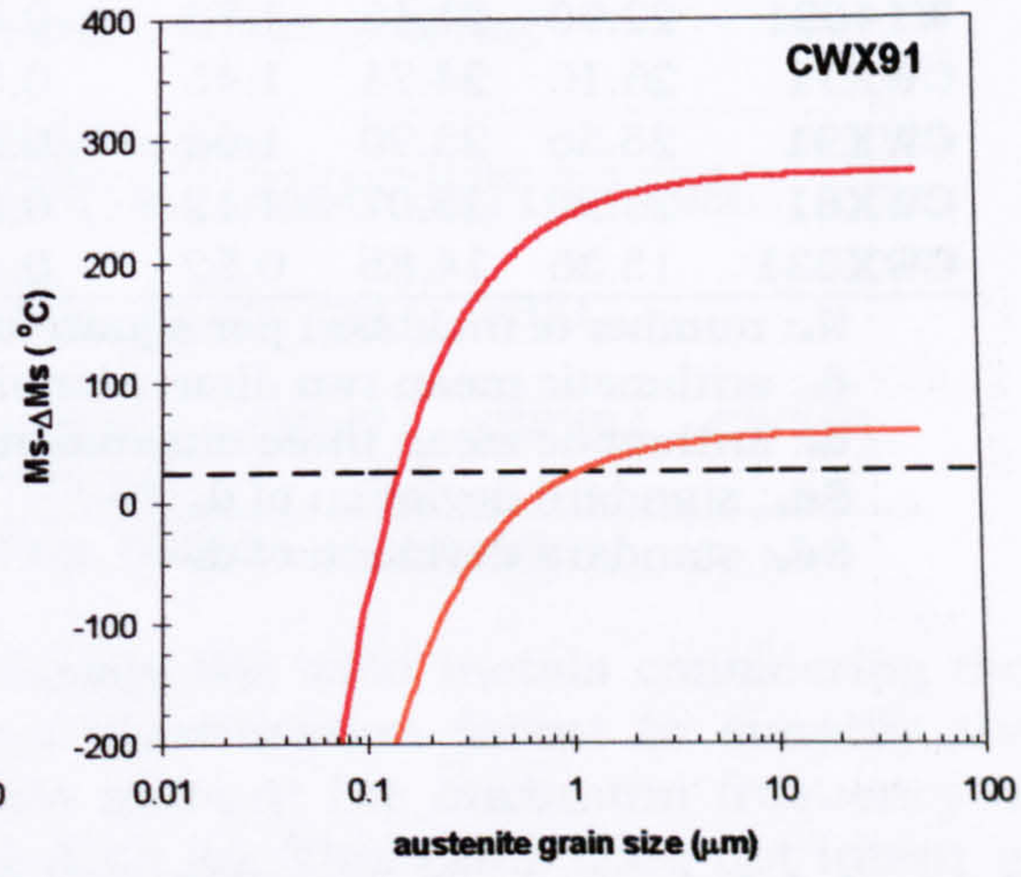

(d)

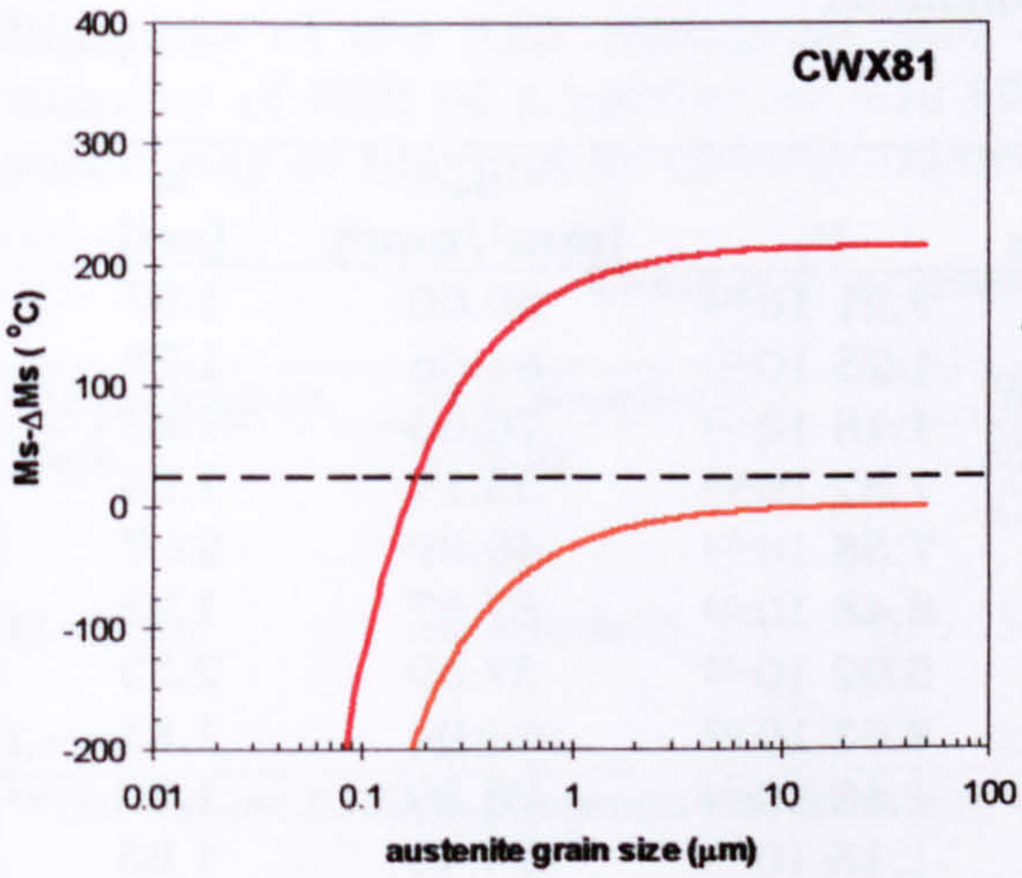

(e)

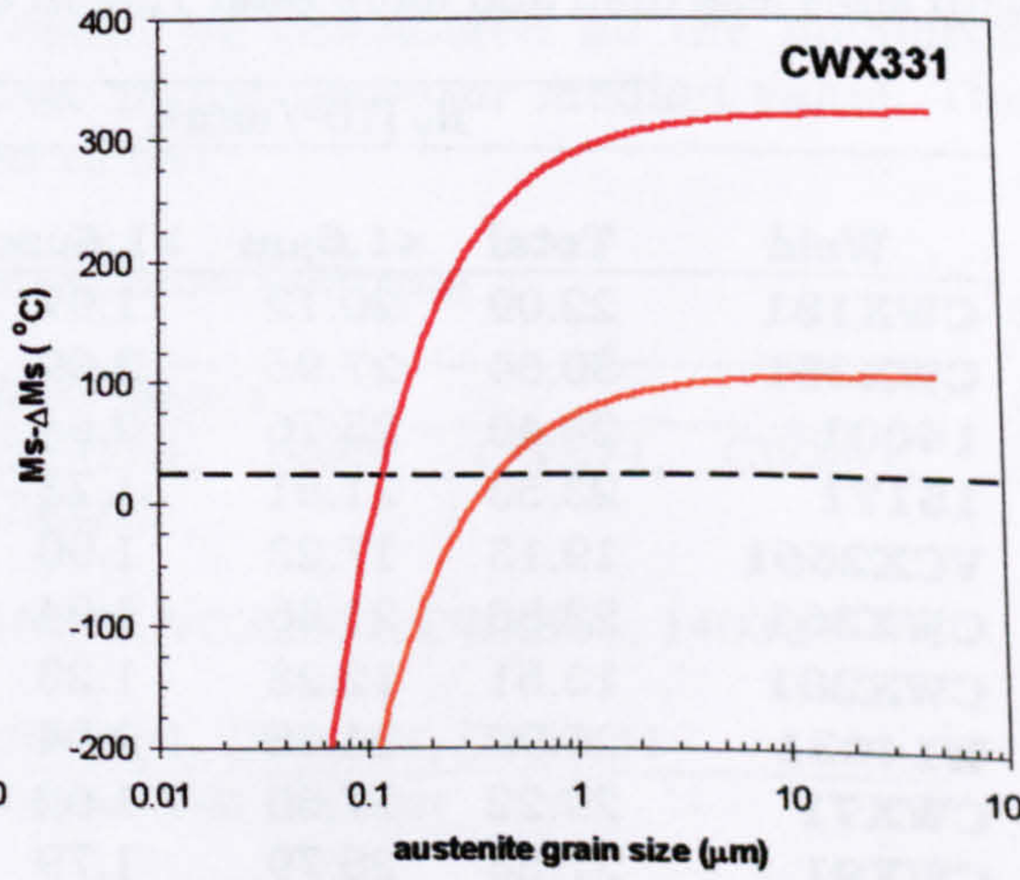

(f)

Figure A.12 Effect of the austenite particle size on M_s and M_f for the weld metals: (a) CWX201, (b) 14031, (c) CWX71, (d) CWX91, (e) CWX81 and (f) CWX331. It was assumed for the calculations ι=0.05, B=1.234 and the carbon concentration as the corresponding $C\gamma$ in table 7.3.

A.14 NMI characteristics for the different HSLA steel weld metals

Table A.5 Inclusions superficial densities, two and three-dimensional diameters for the HSLA steel weld metals, which were investigated in this work. "<1μm" and ">1μm" denote NMI with sizes less than and more than 1μm in 2D-diameter.

	Na [10^3/mm^2]						
Weld	**Total**	**<1μm**	**>1μm**	**d_a [mm]**	**Sd_a [mm]**	**d_v [mm]**	**Sd_v [mm]**
CWX181	20.47	18.65	1.83	0.59	0.36	0.93	0.57
CWX351	27.84	25.90	1.94	0.59	0.28	0.93	0.44
14001	26.32	23.88	2.44	0.59	0.30	0.93	0.47
15171	19.96	18.50	1.47	0.54	0.38	0.85	0.60
VCX2561	17.43	15.70	1.73	0.58	0.50	0.91	0.79
CWX361	20.94	19.23	1.71	0.56	0.24	0.88	0.38
CWX201	12.73	11.57	1.16	0.60	0.30	0.94	0.47
W14031	22.90	21.16	1.73	0.54	0.30	0.85	0.47
CWX71	26.16	24.71	1.45	0.57	0.25	0.90	0.39
CWX91	25.56	23.90	1.66	0.59	0.26	0.93	0.41
CWX81	26.20	25.07	1.12	0.54	0.24	0.85	0.38
CWX331	15.36	14.85	0.52	0.48	0.23	0.75	0.36

N_a: number of inclusion per square millimetres
d_a: arithmetic mean two dimensional particle diameter in a cross-section plane
d_v: arithmetic mean three dimensional particle diameter
Sd_a: standard deviation of d_a
Sd_v: standard deviation of d_v

Table A.6 Volumetric characteristics of the NMI in the different HSLA steel weld metals which were studied in this investigation. "<1.6μm" and ">1.6μm" denote NMI with sizes less than and more than 1μm in diameter.

	N_v [10^6/mm^3]					
Weld	**Total**	**<1.6μm**	**>1.6μm**	**V_v**	**S_v [mm^2/mm^3]**	**λ_v [μm]**
CWX181	22.09	20.12	1.97	$9.21\ 10^{-03}$	59.60	1.97
CWX351	30.04	27.95	2.09	$1.25\ 10^{-02}$	81.06	1.78
14001	28.40	25.76	2.64	$1.18\ 10^{-02}$	76.63	1.82
15171	23.53	21.81	1.73	$7.52\ 10^{-03}$	53.19	1.93
VCX2561	19.13	17.23	1.90	$7.58\ 10^{-03}$	49.89	2.07
CWX361	23.80	21.86	1.94	$8.48\ 10^{-03}$	57.87	1.93
CWX201	13.51	12.28	1.23	$5.92\ 10^{-03}$	37.69	2.33
W14031	26.99	24.95	2.04	$8.63\ 10^{-03}$	61.01	1.85
CWX71	29.22	27.60	1.62	$1.10\ 10^{-02}$	73.59	1.80
CWX91	27.58	25.79	1.79	$1.15\ 10^{-02}$	74.41	1.83
CWX81	30.88	29.56	1.33	$9.87\ 10^{-03}$	69.80	1.77
CWX331	20.38	19.69	0.69	$4.57\ 10^{-03}$	36.39	2.03

N_v: number of inclusion per cubic millimetres
V_v: inclusion volume fraction
S_v: total particle surface area per unit volume
λ_v: mean particle centre to centre volume spacing

A.15 Criteria for the qualitative classification of the NMI.

The qualitative classification of the NMI characteristics of the weld metals was considered relevant for the influence that NMI has on the mechanical properties and the trapping behaviour of the weld metals. Table A.7 and A.8 present the criteria that were used to try to group weld metals with similar characteristics taken into account density and size of inclusions. The limits for each parameter were selected after careful comparisons between welds. These permit a qualitative grouping of welds.

Table A.7 present a weld metal qualitative classification based on the NMI maximum size. The presence of large inclusions is detrimental. These could be massive hydrogen traps and for this reasons potential crack initiators. This classification was selected after comparison of all the welds and it has to be considered as qualitative.

Table A.7 Inclusion maximum size grouping

Classification	NMI maximum size*	Weld metals
Large	dv>5μm	CWX181, 14001, 15171, VCX2561
Medium	3<dv≤5μm	CWX351, CWX201, 14031
Small	dv≤3μm	CWX361, CWX71, CWX81, CWX91, CWX331

* The figure A.13(a) present the meaning of the NMI maximum size.

On the other hand, table A.8 try to classify the weld metals considering the maximum frequency of NMI size. This classification intent to simplify the grouping of weld metals just taking into account the maximum frequency of NMI size, the size of the peak in figure A.13 (a). This value does not intent to substitute the NMI number density (Nv) in table A.6, which is taken into account in the trap discussion. NMI number is a simple way to describe the highness of the NMI histogram and could be considered as the maximum number of NMI of a particular size close to the mean or median value. This value may or may not be directly related to Nv.

Table A.8 Inclusion number grouping

Classification	NMI number**	Weld metals
High	N>800	CWX351, 14001, CWX71, CWX91, CWX81
Medium	600≤N≤800	15171, VCX2561, CWX361, 14031
Low	N≤600	CWX181, CWX201, CWX331

**The figure A.13(a) presents the meaning of the NMI number

With respect to the NMI spatial distribution, it was found an indirect way to characterise it: measuring the area around each inclusion which is free of other NMI, at least on the surface plane. In figure 6.4 could be observed that the spatial distribution of the NMI can be classified based on the histograms shape. Figure A.13 (b) shows to possible ways to take it into account: the median value and the ratio r. Both indicators, presented in table A.9, could be used to qualitatively describe the spatial distribution of inclusions: random, clustered or normal.

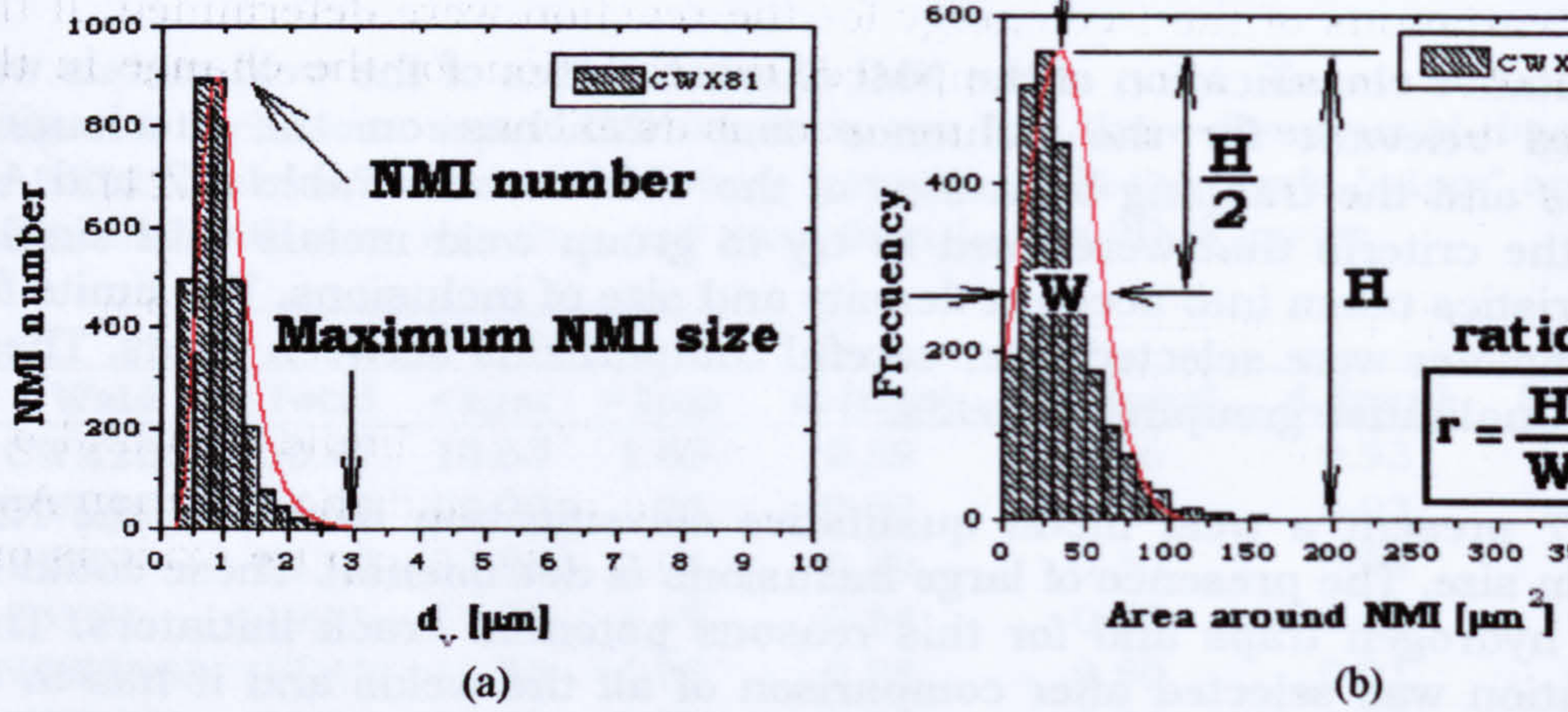

(a) (b)

Figure A.13 Measurement of the parameter for classification of NMI characteristics for the weld metals (a) NMI number and maximum size, (b) median value and ratio H/W.

It seems that the ratio r value is a simple manner to describe the spatial distribution of NMI in the weld metals. To calculate this ratio H (cm) and W (cm) are defined in figure A.13 (b). From the values of r the NMI spatial distribution was as follow:

1- Random spatial distribution: weld metals with $H/W < 3$
2- Clustered spatial distribution: weld metals with $H/W \geq 3$
3- Normal spatial distribution: symmetrical distribution around the median value. None of the weld metal presented this kind of spatial distribution.

Taking onto account the median value of the area around the inclusions, it could be suggested that weld metals with random spatial distribution of NMI have large median value. On the contrary, the clustered distribution is characterised by lower median values. The limit value, considering the classification that was made using H/W, seems to be 40 μm^2.

Table A.9 Parameters for the classification of the NMI weld metal characteristic. Inside parenthesis are some values from table A.5 and A.6. The spatial distribution qualification was made using the r value (H/W) (cm/cm) taken on figures of equal size.

Weld ID	Size (µm)	NMI Number ($10^6/mm^3$)	Median (μm^2)*	Ratio* (H/W)	NMI Distribution
CWX181	6 (0.93)	600 (22.09)	43.6	2.1	Random
CWX351	4 (0.93)	1000 (30.04)	32.7	6.8	Clustered
14001	5 (0.93)	900 (28.40)	36.3	6.0	Clustered
15171	6 (0.85)	700 (23.53)	43.6	1.7	Random
VCX2561	10 (0.91)	625 (19.13)	50.9	1.7	Random
CWX361	3 (0.88)	750 (23.80)	40.0	4.1	Clustered
CWX201	4 (0.94)	400 (13.51)	72.7	0.6	Random
14031	4 (0.85)	700 (26.99)	40.0	3.6	Clustered
CWX71	3 (0.90)	950 (29.22)	36.3	5.3	Clustered
CWX91	3 (0.93)	900 (27.58)	36.3	5.3	Clustered
CWX81	3 (0.85)	900 (30.88)	32.7	4.9	Clustered
CWX331	2.5 (0.75)	600 (20.38)	58.2	1.1	Random

*The figure A.13(b) presents the meaning of the NMI media value and ratio (r=H/W)

A.16 Thermodynamical calculation of NMI stability diagrams

For the calculation of the stability of inclusions in the liquid iron of the weld pool, the variations of the free energy for the reaction were determined. If the formation of the oxide M_xO_y is supposed, the equation for the change in the free energy due to the formation of the oxide is as follow:

$$x\underline{M} + y\underline{O} = M_xO_y \tag{A.21}$$

$$\Delta G = \Delta G^0 + RT\ln\left(\frac{a_{M_xO_y}}{a_{\underline{M}}^x a_{\underline{O}}^y}\right) \tag{A.22}$$

where M and O denotes diluted metal and oxygen in the liquid iron and **a** is the activity of the diluted species. At equilibrium $\Delta G=0$ and the equation A.22 is further simplified if it is supposed that the activity of the pure oxide is one ($a_{M_xO_y}=1$):

$$\Delta G^0 = -RT\ln\left(\frac{1}{a_{\underline{M}}^x a_{\underline{O}}^y}\right) = RT\ln\left(a_{\underline{M}}^x a_{\underline{O}}^y\right) \tag{A.23}$$

To estimate the activity of any of the involved species, M and O, the following expressions were used:

$$\log(a_{\underline{M}}) = \left[\log(h_{\underline{M}})\right] = \log(f_{\underline{M}}(wt\%)_{\underline{M}}) = \log(wt\%)_{\underline{M}} + \log(f_{\underline{M}}) \tag{A.24}$$

$$\log(f_{\underline{M}}) = \sum_{j=1}^{n} e_{\underline{M}}^{j} \cdot (wt\%)_j \tag{A.25}$$

where $e_{\underline{M}}^{j}$ is the first order interaction coefficient that describes the effect of solutes j on the activity of M, $(wt\%)_j$ is the quantity of the j alloying element in weight percent, and $f_{\underline{M}}$ is the activity coefficient of M. The same is applied to the activity of oxygen. Selected data for the first order interaction coefficient are shown in the tables A.10. The equations to calculate the standard free energy for the formation of some oxides or nitrides are shown in table A.11. The following example for Al_2O_3 describes the equations used to calculate the stability diagram for this oxide:

$$\frac{\Delta G^0}{2.303 \cdot R \cdot T} = 2\log(a_{\underline{Al}}) + 3\log(a_{\underline{O}}) \tag{A.26}$$

$$\begin{aligned} 2\log(a_{\underline{Al}}) + 3\log(a_{\underline{O}}) = {} & 2\log(wt\%)_{\underline{Al}} + \left(2e_{\underline{Al}}^{Al} + 3e_{\underline{O}}^{Al}\right)(wt\%)_{\underline{Al}} + \\ & + 3\log(wt\%)_O + \left(3e_O^O + 2e_{Al}^O\right)(wt\%)_O + \\ & + 2\sum_{x=i}^{j} e_{Al}^x (wt\%)_x + 3\sum_{x=i}^{j} e_O^x (wt\%)_x \end{aligned} \tag{A.27}$$

The equality in equation A.26 was obtained varying $(wt\%)_{Al}$ and iterating for $(wt\%)_O$ at low and high values for each value of $(wt\%)_{Al}$.

Thermodynamic information in the following tables was collected from references 199 to 202.

Table A.10 The first order interaction coefficient e_i^j in liquid iron at 1873K

j→ / i↓	Al	B	C	Csat	Ce	Cr	H	La	Mn	Mo	N	Nb
Al	0.043		0.091	-0.019		0.03	0.24		0.035		-0.58	
B		0.038	0.22	0.009			0.49				0.074	
C	0.042	0.24	0.14			-0.024	0.67		-0.012	-0.0083	0.11	-0.06
Csat	0.0069	0.021				-0.015			-0.007	-0.007	0.13	-0.018
Ce					-0.003		-0.6					
Cr	0.054		-0.0118	-0.139		0.0129	-0.33		0.004	0.002	-0.19	
H	0.013	0.058	0.06		0	-0.0022	0	-0.027	-0.0014	0.002		-0.0023
La							-4.3					
Mn	0.07	-0.024	-0.07	-0.108		0.004	-0.31		-0.003	0.005	-0.091	
Mo			-0.097	-0.192		-0.0003	-0.2		0.005	0.0121	-0.1	
N	-0.028	0.094	0.13	0.18		-0.047			-0.02	-0.011	0	-0.06
Nb			-0.49	0.276			-0.61				-0.42	0.006
Ni	0.008		0.042	-0.018		-0.0003	-0.25		-0.008		0.028	
O	-2.81	-0.31	-0.35	-0.44	-0.57	-0.037	-3.1	-0.57	-0.03	0.0035	0.057	-0.12
P	0.13	0.015	0.13	-0.005		0.03	0.21		0.094	0.001	0.094	
S	0.035	0.134	0.113	0.003		0.011	0.12		-0.025	0.003	0.01	-0.013
Si	0.058	0.2	0.18	0.177		0.0003	0.64		0.033	2.36	0.092	
Ta			-0.37	-0.363			-4.4				-0.47	
Ti	0.12		-0.3	-0.229		0.055	-1.1		-0.043		-2.06	
U												
V	0.1		-0.34	-0.181		0.012	-0.72		0.006		-0.35	
Zr											-4.1	

Table A.10 (cont.) The first order interaction coefficient e_i^j in liquid iron at 1873K

j→ / i↓	Ni	O	P	S	Si	Ta	Ti	U	V	Zr
Al		-4.77		0.03	0.056			0.011	0.06	
B		-0.21		0.047	0.078					
C	0.012	-0.26	0.051	0.045	0.08	-0.02			-0.077	
Csat	0.012	-0.22	0.013				-0.039			
Ce		-5								
Cr	0.0002	-0.12	-0.053	-0.02	-0.004		0.06			
H		-0.19	0.011	0.008	0.026	-0.02	-0.02		-0.007	
La		-5								
Mn		-0.1	-0.0035	-0.048	0.06					
Mo		-0.0007		-0.0005	0.048					
N	0.01	0.05	0.045	0.007	0.045	-0.032	-0.53		-0.093	-0.63
Nb		-0.7		-0.046						
Ni	0.0009	0.01	-0.0035	-0.004	0.006					
O	0.006	-0.23	0.07	-0.133	-0.14	-0.11	-0.42	-0.44	-0.3	-3.41
P	0.0002	0.13	0.062	0.028	0.12					
S	0	-0.27	0.29	-0.028	0.065		-0.072		-0.016	-0.053
Si	0.005	-0.25	0.11	0.056	0.11				0.16	
Ta		-1.3		-0.02		0.002				
Ti	-1.1	-1.27	-0.11	-0.11	2.1		0.056			
U		-6.6						0.01		
V		-0.97	-0.008	-0.028	0.27				0.015	
Zr		-19.5		-0.16						0.023
		-4.77		0.03	0.056			0.011	0.06	

Table A.11 Standard free energy expressions for various reactions in the form of $\Delta G^0 = A + B \cdot T$, and the values at 1873K

Precipitation Reaction	A (Cal/mol)	B (Cal/mol)	A (J/mol)	B (J/mol)	ΔG°_{1873K} (cal/mol)	ΔG°_{1873K} (J/mol)
2[Al]+3[O]=Al_2O_3	-289060	93.52	-1209427	391.2877	-113883.012	-476486.522
3[Ti]+5[O]=Ti_3O_5	-419680	136.5	-1755941	571.116	-163995.025	-686155.185
2[Ti]+3[O]=Ti_2O_3	-260120	85.25	-1088342	356.686	-100433.963	-420215.699
[Ti]+2[O]=TiO_2	-161460	55.95	-675549	234.0948	-56657.258	-237053.965
[Ti]+[O]=TiO	-87560	29.14	-366351	121.9218	-32976.409	-137973.295
[Si]+2[O]=SiO_2	-140950	54.62	-589735	228.5301	-38638.547	-161663.681
[Mn]+[O]=MnO	-68816	29.95	-287926	125.3108	-12715.158	-53200.219
[Al]+[N]=AlN	-63890	28.54	-267316	119.4114	-10430.299	-43640.371
3[Si]+4[N]=Si_3N_4	-203000	75.3	-849352	315.0552	-61951.805	-259206.352
[Ti]+[N]=TiN	-80380	24.29	-336310	101.6294	-34881.187	-145942.884
[Fe]+[S]=FeS	-111370	57	-465972	238.488	-4600.450	-19248.283
[Mn]+[S]=MnS	-39500	17	-165268	71.128	-7656.450	-32034.587
[Mn]+2[Al]+4[O]=$MnO.Al_2O_3$	-369376	125.22	-1545469	523.9205	-134820.157	-564087.537
[Si]+2[Al]+5[O]=$SiO_2.Al_2O_3$	-319875	97.32	-1338357	407.1869	-137580.042	-575634.896
[Fe]+2[Al]+4[O]=$FeO.Al_2O_3$	-330180	108.4	-1381473	453.5456	-127130.540	-531914.179
[Mn]+[Si]+3[O]=$MnO.SiO_2$	-200466	75	-838750	313.8	-59979.750	-250955.274

A.17 The equilibrium ratio Q/K_{eq}

For a general reaction the variation of the free energy is:

$$x\underline{M} + y\underline{N} + z\underline{O} = M_xN_yO_z \tag{A.28}$$

$$\Delta G = \Delta G^o + RT\ln\left(\frac{a_{M_xN_yO_z}}{a_{\underline{M}}^x a_{\underline{N}}^y a_{\underline{O}}^z}\right) = \Delta G^o - RT\ln\left(a_{\underline{M}}^x a_{\underline{N}}^y a_{\underline{O}}^z\right) = \Delta G^o - RT\ln(Q) \tag{A.29}$$

The parameters in the equation A.10 have the usual meaning. At equilibrium, where ΔG=0 the equation A.10 *is simplified* and K_{eq}, the equilibrium constant, is presented:

$$\Delta G^o = -RT\ln\left(\frac{a_{M_xN_yO_z}}{a_{\underline{M}}^x a_{\underline{N}}^y a_{\underline{O}}^z}\right)_{eq} = RT\ln\left(a_{\underline{M}}^x a_{\underline{N}}^y a_{\underline{O}}^z\right) = RT\ln\left(K_{eq}\right) \tag{A.30}$$

The formation of MxNyOz occurs spontaneously if. Then, simplifying the equation A.10 the equilibrium ratio is obtained:

$$\Delta G = RT\ln\left(K_{eq}\right) - RT\ln(Q) = RT\ln\left(\frac{K_{eq}}{Q}\right) \tag{A.31}$$

It is necessary that $\ln\left(\frac{K_{eq}}{Q}\right) < 0$ to produce a ΔG<0, which means that:

$$\left(\frac{Q}{K_{eq}}\right) > 1 \tag{A.32}$$

Inclusion formation is possible when the concentration of oxygen, nitrogen or sulphur and the alloying elements for deoxidation, denitrogenation and desulphuration exceed the equilibrium values for a particular compound. That is, the equation A.13 is satisfied. The effect of segregation was estimated using the partition coefficients from table A.1, at the beginning of this chapter and the Scheil equation:

$$C_L = C_0 f_L^{\kappa_0 - 1} = C_0\left(1 - f_S\right)^{\kappa_0 - 1} \tag{A.33}$$

In the equation, C_0 is the bulk concentration in the weld pool, C_L is the concentration in the liquid at the interface, f_L and f_S are the liquid fraction and the solid fraction, respectively; and κ_0 is the equilibrium partition ratio [18-20].

A.18 Variability in Weld Metal Properties.

The weld metal properties S_y, S_m and S_f, as measured by Wildash[8], were not reported with their respective scatter. No standard deviation was considered in that previous work. These values are of importance to consider small variation in data from sample to sample under slightly different conditions, in this case, the hydrogen content.
Although not all the mechanical properties are normally distributed, a normal distribution is a good first approximation that usually results in a conservative value. Dieter[203] propose that when statistical data are not available, the standard deviation can be estimated by assuming that the upper x_u and the lower x_L values of a sample are three standard deviations from the mean. In figure A.13, and equation A.34, this is presented.

$$(x_u - x_L) = 6 \cdot \sigma \qquad \sigma = \frac{(x_u - x_L)}{6} \tag{A.34}$$

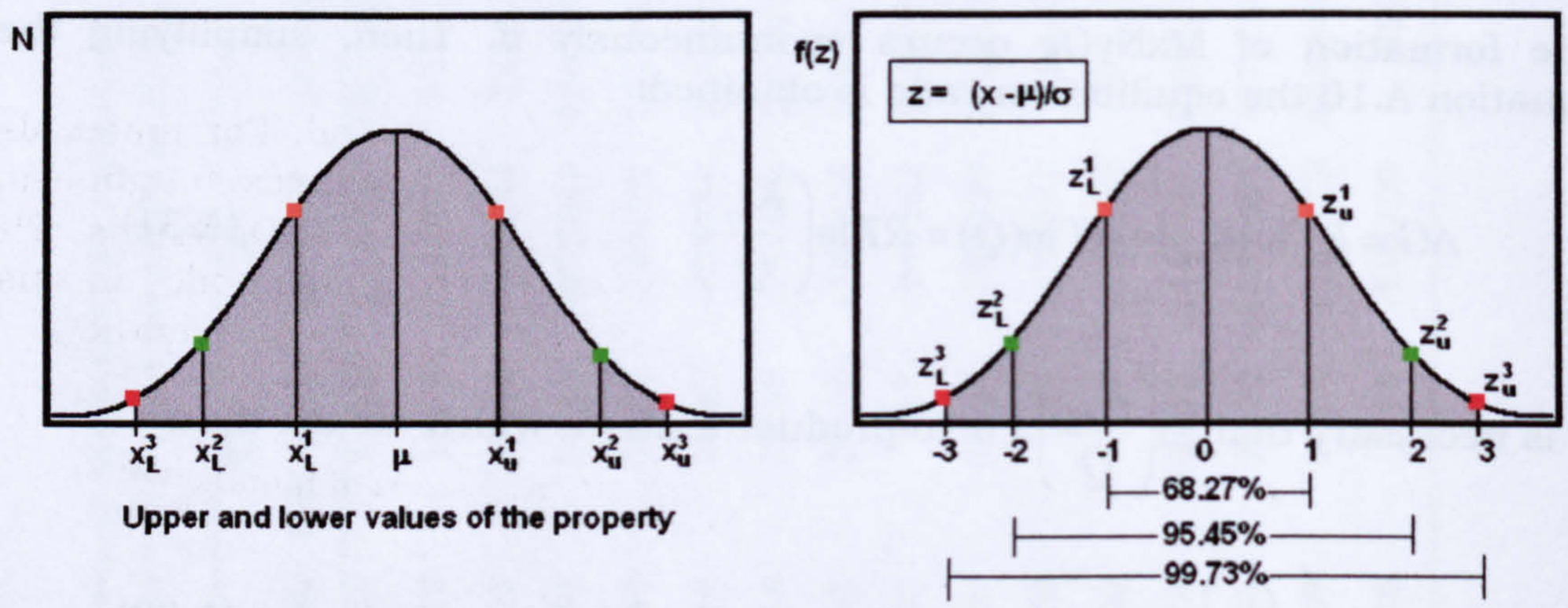

Figure A.14 Schematic representation of the normal distribution for a material property. Several possibilities are shown for $(x_u - x_L)$: 2σ, 4σ and 6σ. As suggested in Dieter [203] $(x_u - x_L) = 6\sigma$ could be used to estimate standard deviation.

It can be observed from figures that considering x_u and x_L apart by 6σ will give a lower estimated standard deviation value than considering 4σ, which give several possibilities:

a. $x_u = \mu + 1\sigma$ and $x_L = \mu - 3\sigma$ that covers 84.00 % of probability
b. $x_u = \mu + 2\sigma$ and $x_L = \mu - 2\sigma$ that covers 95.45 % of probability
c. $x_u = \mu + 3\sigma$ and $x_L = \mu - 1\sigma$ that covers 84.00 % of probability

Whichever the case (a, b or c), supposing that the values of S_{fu} and S_{fL} are 4σ apart, give a good chance to guess the position of these values with respect to μ. As a consequence, it becomes feasible to estimate an approximated value for σ by considering a pair of values measured under similar conditions, for example, without hydrogen charging or with similar hydrogen content. This approach will be used to estimate the potential scatter of the Wildash[8] original data for S_f. Using 4σ instead to 6σ gives a more conservative guessing. However, these values have to be taken with care.
From figures in annex 18 a pair of values were selected and a σ value estimated. In table A.12 can be observed the values obtained for each case.

Table A.12 Values extracted from figures A.14 to A.17 to estimate σ, supposing that the values are 4σ apart.

Weld metal ID	S_{fu} (MPa)	S_{fL} (MPa)	S_{fu}-S_{fL} (MPa)	± σ (MPa)
CWX181	1400	900	500	125
CWX351	1150	1050	100	25
14001	Close values found for a pair under similar conditions			
15171	1400	1300	100	25
VCX2561	1200	1100	100	25
CWX361	1400	1200	200	50
CWX201	1100	1000	100	25
14031	900	950	50	12.5
CWX71	1000	900	100	25
CWX91	950	850	100	25
CWX81	1400	1200	200	50
CWX331	1500	1200	300	75

It could be observed from table A.12 that the estimated standard deviations are in order of repetition as: 25 (50% of all cases), 50 (16.6%), 75 (8.3%), 125 (8.3%), 12.5 (8.3%) and a small value (8.3%). The average value is 42.0 MPa, approximately. The potential scatter in the measurement of S_f is presented in the corresponding figure as ± 3 σ, taking σ as 25 MPa.

In the case of S_y and S_m, other recommendation was followed. For materials property data, such as yield strength, hardness, and fractures toughness, coefficients of variation δ_x are generally in the range 0.05 to 0.20, that is, 5% to 20%. In table A.13 some values are presented which could be applied in this case to estimate the potential scatter of the weld metal properties: S_y and S_m.

Table A.13 Coefficients of variation (δ_x) for some properties of metals [168]

Value x	δ_x, %
Yield strength of metals	7
Ultimate strength of metals	5
Modulus of elasticity of metals	5
Fracture toughness of metals	15
Tensile strength of welds	10

A.19 Presentation of the results about the effect of hydrogen on the mechanical properties of weld metals studied in this investigation.

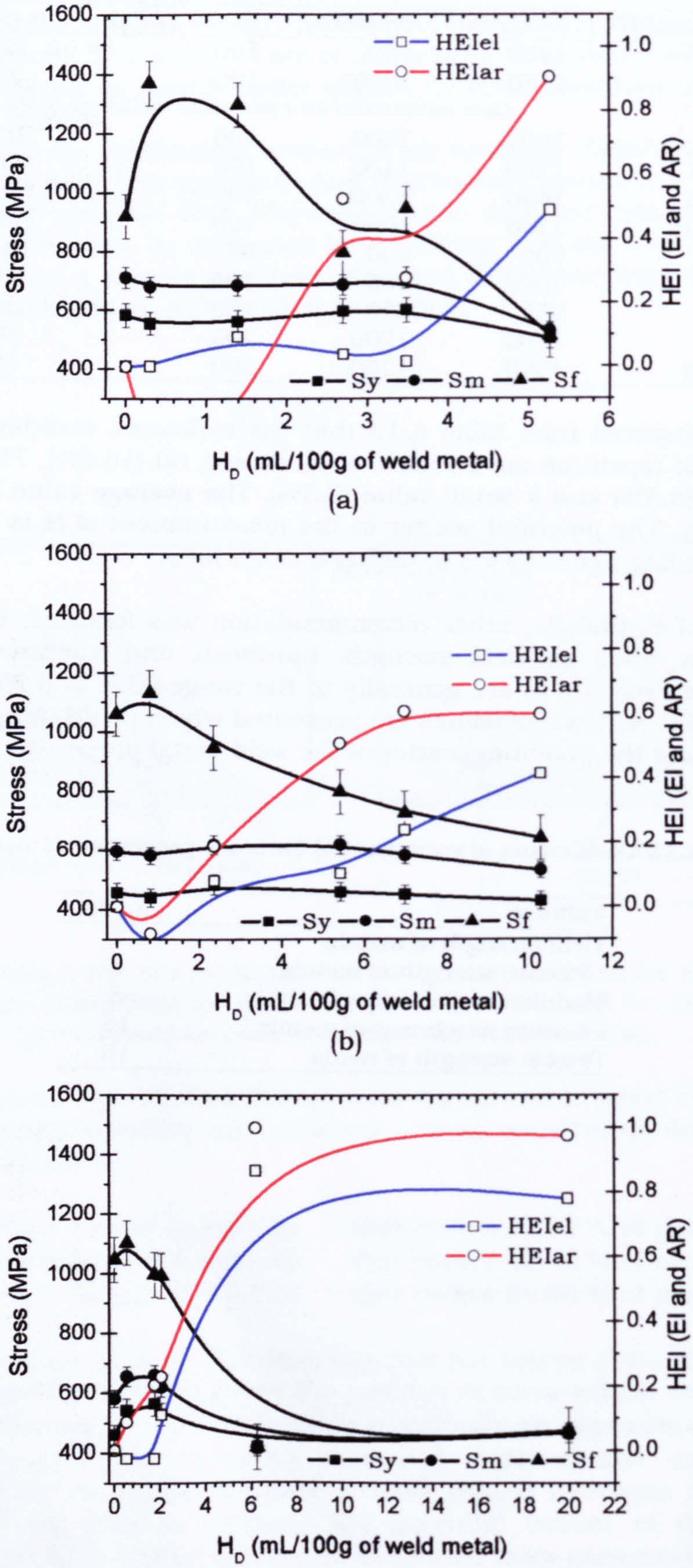

Figure A.15 Effect of diffusible hydrogen content (HD) on the strength and ductility of the weld metals: (a) CWX181gb and (b) CWX351 and (c) 14001. Figures are based on data obtained by C. Wildash [8].

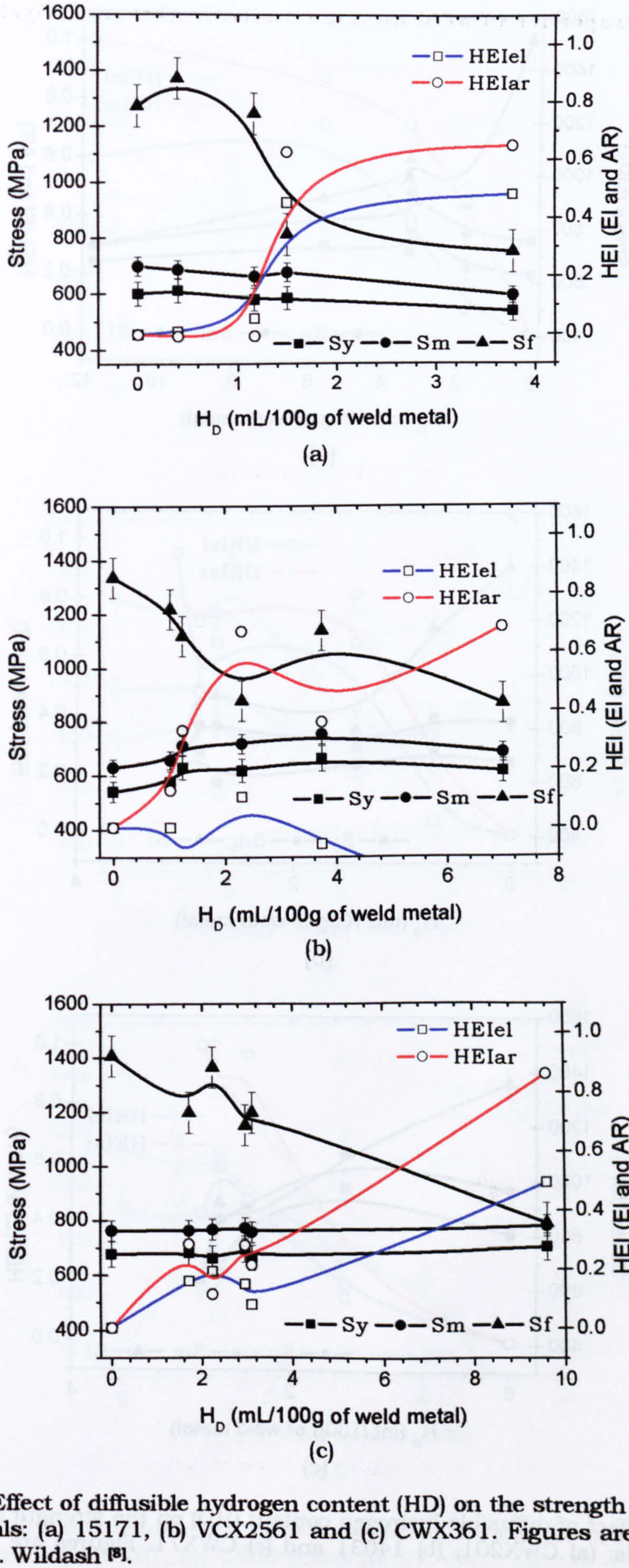

Figure A.16 Effect of diffusible hydrogen content (HD) on the strength and ductility of the weld metals: (a) 15171, (b) VCX2561 and (c) CWX361. Figures are based on data obtained by C. Wildash [8].

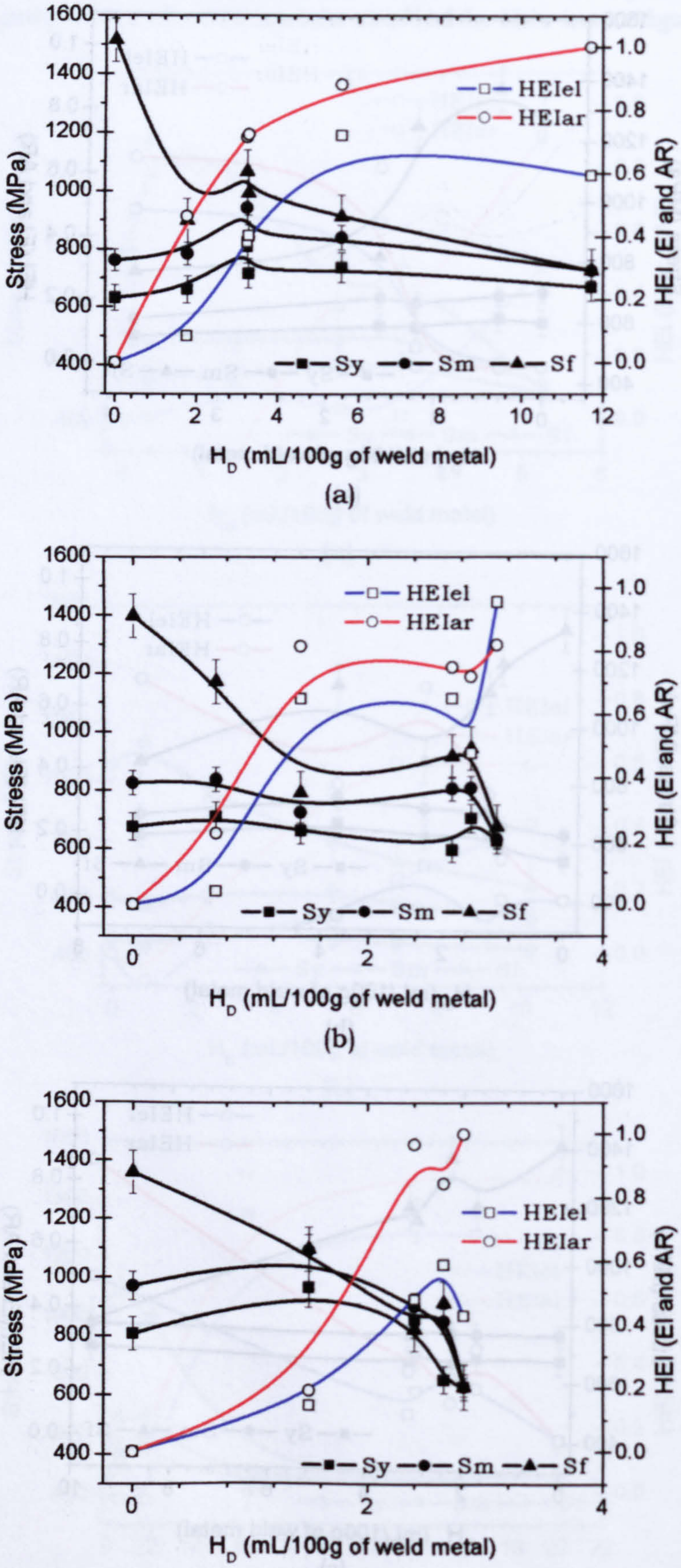

Figure A.17 Effect of diffusible hydrogen content (HD) on the strength and ductility of the weld metals: (a) CWX201, (b) 14031 and (c) CWX71. Figures are based on data obtained by C. Wildash [8].

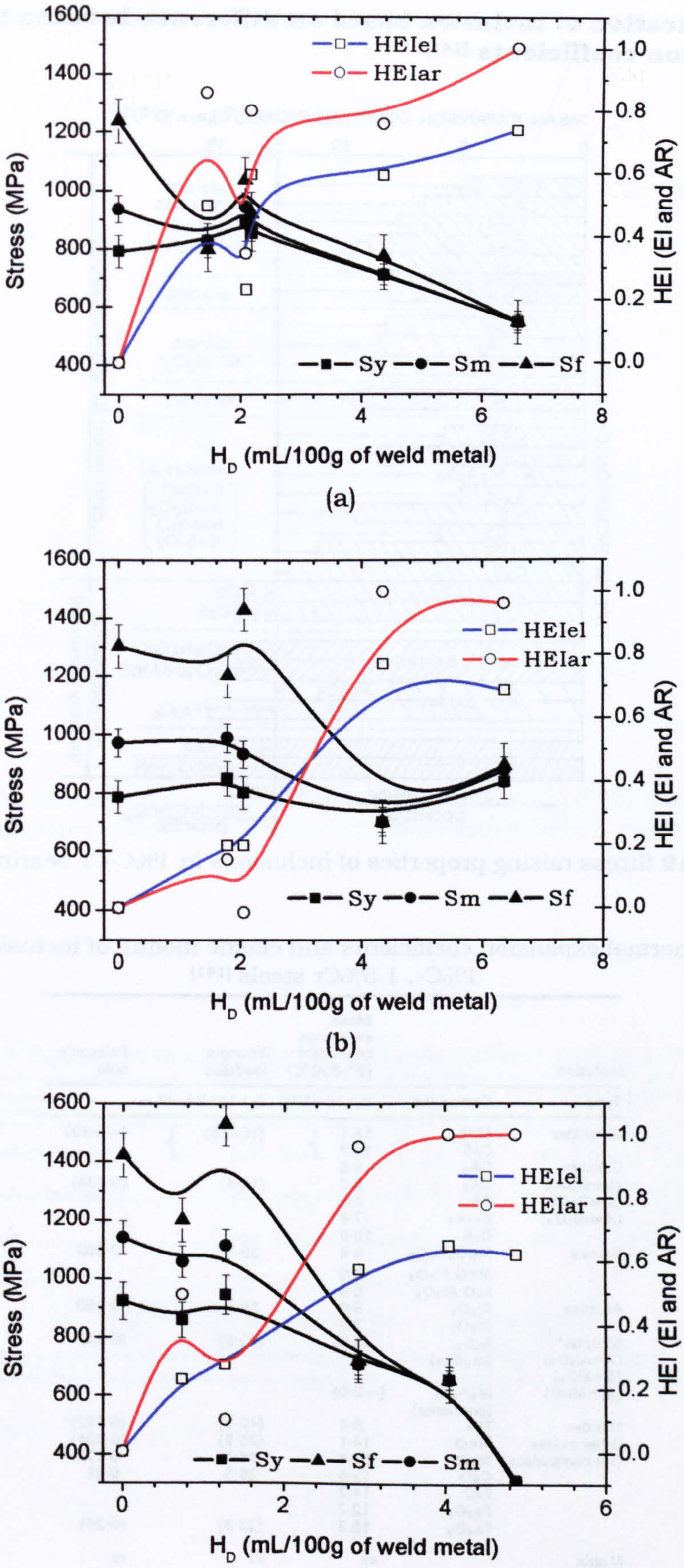

Figure A.18 Effect of diffusible hydrogen content (HD) on the strength and ductility of the weld metals: (a) CWX91, (b) CWX81 and (c) CWX331. Figures are based on data obtained by C. Wildash [8].

A.20 Classification of inclusion based on difference between the steel and NMI expansion coefficients [141]

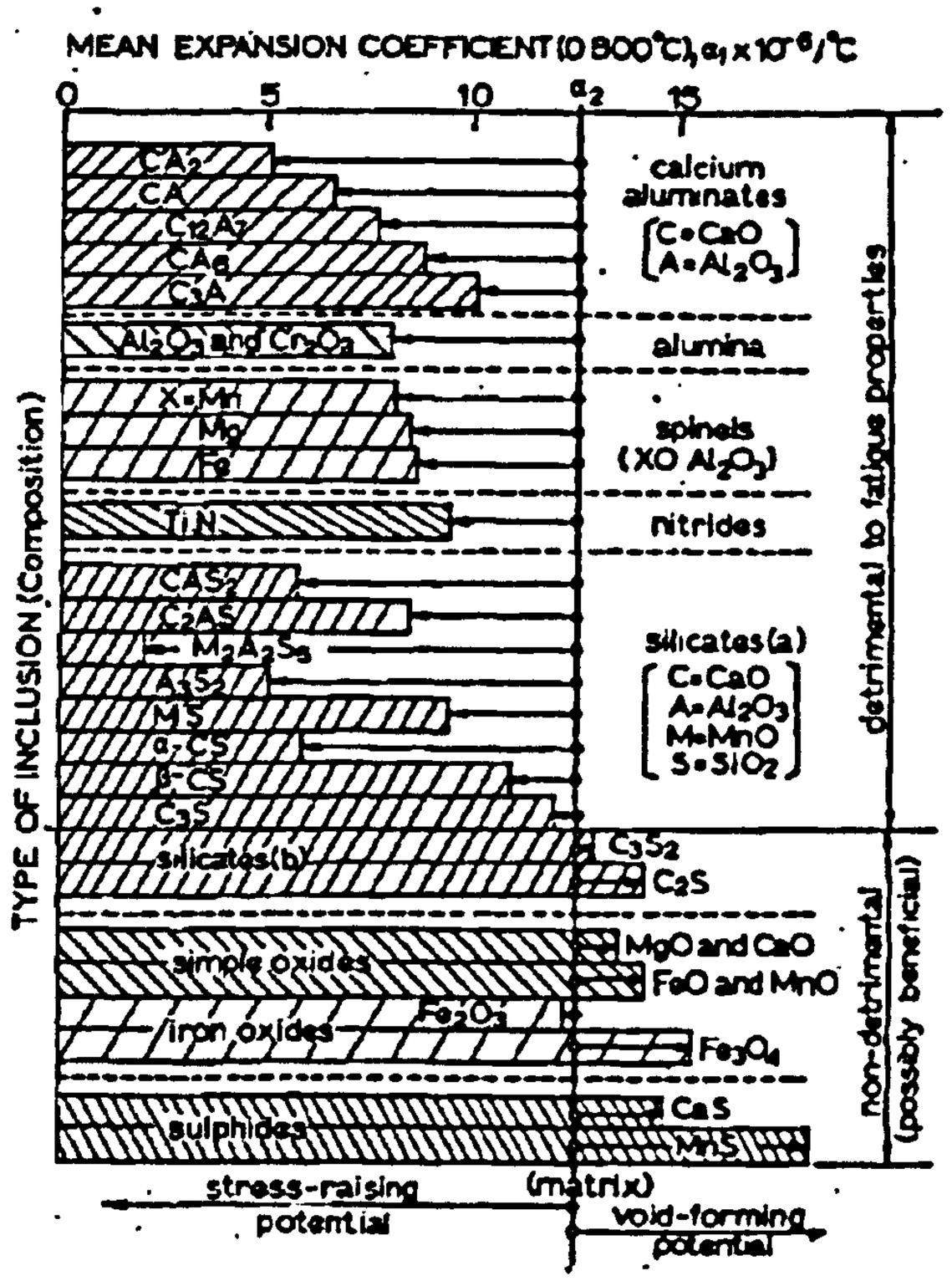

Figure A.19 Stress raising properties of inclusions in 1%C-Cr bearing steels [141]

Table A.14 Thermal expansion coefficients and elastic moduli of inclusion materials in 1%C-, 1.5%Cr steels [141]

Inclusion		Mean expansion coefficient (0°–800°C)	Young's modulus	Poisson's ratio
Type	Compound	$\alpha_1 \times 10^{-6}$/°C	$E_1 \times 10^6$ lbf/in²	ν_1
Sulphides	MnS	18·1	(10–20)	(~0·30)
	CaS	14·7		
Calcium aluminates (C=CaO) (A=Al₂O₃)	CA_6	8·8		
	CA_2	5·0	(16·4)	(0·234)
	CA	6·5		
	$C_{12}A_7$	7·6		
	C_3A	10·0		
Spinels	$MgO.Al_2O_3$	8·4	39·3	0·260
	$MnO.Al_2O_3$	8·0		
	$FeO.Al_2O_3$	8·6		
Alumina	Al_2O_3	8·0	58·4	0·250
	Cr_2O_3	7·8		
Silicates* (A=Al₂O₃) (S=SiO₂) (M=MnO)	A_3S_2 (mullite)	(5·0)	(20·8)	(0·24)
	$M_2A_2S_5$ (cordierite)	(~2·0)		
Nitrides	TiN	9·4	(46·0)	(0·182)
Other oxides (for comparison)	MnO	14·1	(25·8)	(0·308)
	MgO	13·5	44·4	0·178
	CaO	13·5	26·5	0·21
	FeO	14·2		
	Fe_2O_3	12·2		
	Fe_3O_4	15·3	(33·8)	(0·26)
Matrix		α_s	E_s	ν_s
En31 steel (1%C, 1·5%Cr)	Austenite (γ) (850°→M_s)	(23·0)		
	Martensite (α′) (M_f→R.T.)	(10·0)		
Average	γ→α′ (850→R.T.)	12·8	30·2	0·290

A.21 Calculation of tessellated stress around the inclusion, taking into account plastic deformation of matrix (steel)

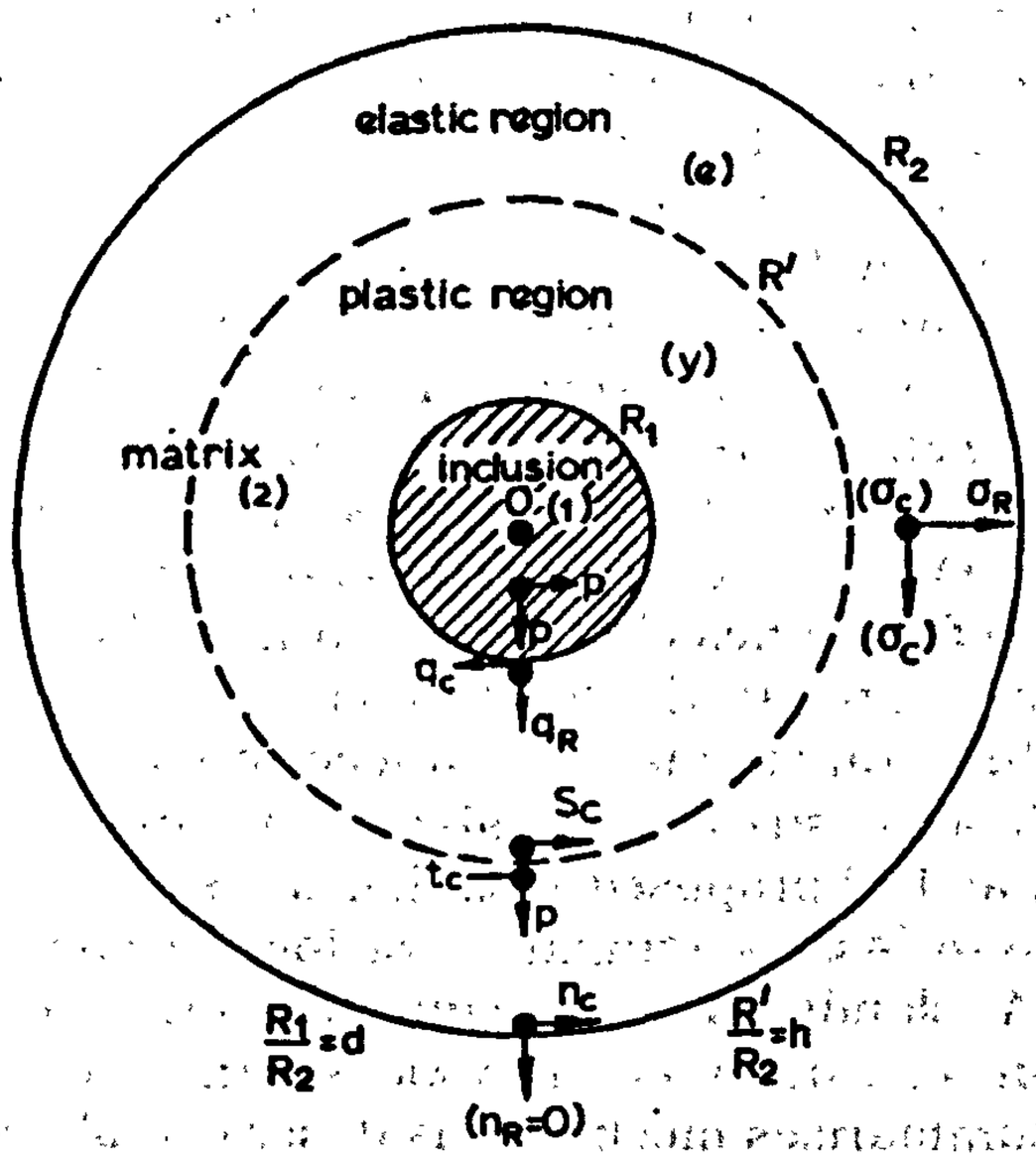

Figure A.20 Schematic representation of the regions around the inclusion and significance of notation used in the equations of table A.13 [141-144]

Table A.15 Equations to calculate the different stresses around a NMI [141-144]

Type of stress	Inclusion (1) $(0 \leqslant R \leqslant R_1)$	Plastic zone (matrix) (2y) $(R_1 \leqslant R \leqslant R')$	Plastic zone (matrix) (2e) $(R' \leqslant R \leqslant R_2)$
Radial	$(\sigma_R)_1 = p$ (constant) ..... (1d)	$(\sigma_R)_{2y} = -2Y_2\left\{\ln\frac{R'}{R} + \frac{1}{3}(1-h^3)\right\}$ .... (4d)	$(\sigma_R)_{2e} = -\frac{2}{3}Y_2\left\{\left(\frac{R'}{R}\right)^3 - h^3\right\}$ ..... (7d)
Circumferential	$(\sigma_C)_1 = p$ (constant) ..... (2d)	$(\sigma_C)_{2y} = Y_2 - 2Y_2\left\{\ln\frac{R'}{R} + \frac{1}{3}(1-h^3)\right\}$ .. (5d)	$(\sigma_C)_{2e} = +\frac{2}{3}Y_2\left\{\frac{1}{2}\left(\frac{R'}{R}\right)^3 + h^3\right\}$ ..... (8d)
Reduced shear	$F_1 = 0$ ..... (3d)	$(F_2)_{2y} = Y_2$ (by definition) ..... (6d)	$(F_2)_{2e} = Y_2\left(\frac{R'}{R}\right)^3$ ..... (9d)

where $p = -2Y_2\left\{\ln\frac{R'}{R_1} + \frac{1}{3}(1-h^3)\right\}$ ..... (10d) and R' and Y_2 are related by:

$$\left(\frac{1-2\nu_2}{E_2} - \frac{1-2\nu_1}{E_1}\right)\cdot\left[3\ln\frac{R'}{R_1} + (1-h^3)\cdot\right] = \frac{3}{2}\left[(\varepsilon_2 - \varepsilon_1)\frac{Y}{Y_2} + \left(\frac{1-\nu_2}{E_2}\right)\cdot\left(\frac{R'}{R_1}\right)^3\right] \quad \text{..... (11d)}$$

stresses at the boundaries (q_1, q_c, p', t_c, s_c, n_1, n_c) are obtained by substituting the appropriate value of R into the above equations

A.22 Observations about the influence of MAC constituent on the toughness of HSLA steels weldments.

Kim and collaborators [171] found that when ductile or brittle fractures are dominant the initiation of the cracks occurs by void formation at the elongated-MA/ferrite interface. Cracks grow by microvoids coalescence (ductile) or cleavage (brittle). The cleavage propagates catastrophically until the prior austenite grain boundary is reached. This mechanism is schematically represented in figure A.20. Davis and King[175] pointed out that the embrittlement of the intercritical zone is associated with the presence of a connected grain boundary network of blocky MA phase ("necklace" appearance), which debond readily producing sufficient stress raising to promote local cleavage. Isolated MA particles did not have such detrimental effect on toughness. Other mechanisms proposed by Davis and King [174] is that the impairment of toughness by the network of blocky MA particles is the combination of the interfacial decohesion mentioned above and the overlapping of residual transformation induced stress in the regions between them, creating high local stresses capable of produce cleavage of the steel matrix. Alkensel et. al. [176] proposed a similar stress overlapping mechanisms to explain the subzero loss of toughness of low carbon microalloyed steels. They considered MA islands as stress concentrators due to the effect of the transformation strain and difference in yield strength with the matrix. Figure 8.20, in chapter 8 summarises mechanisms described above

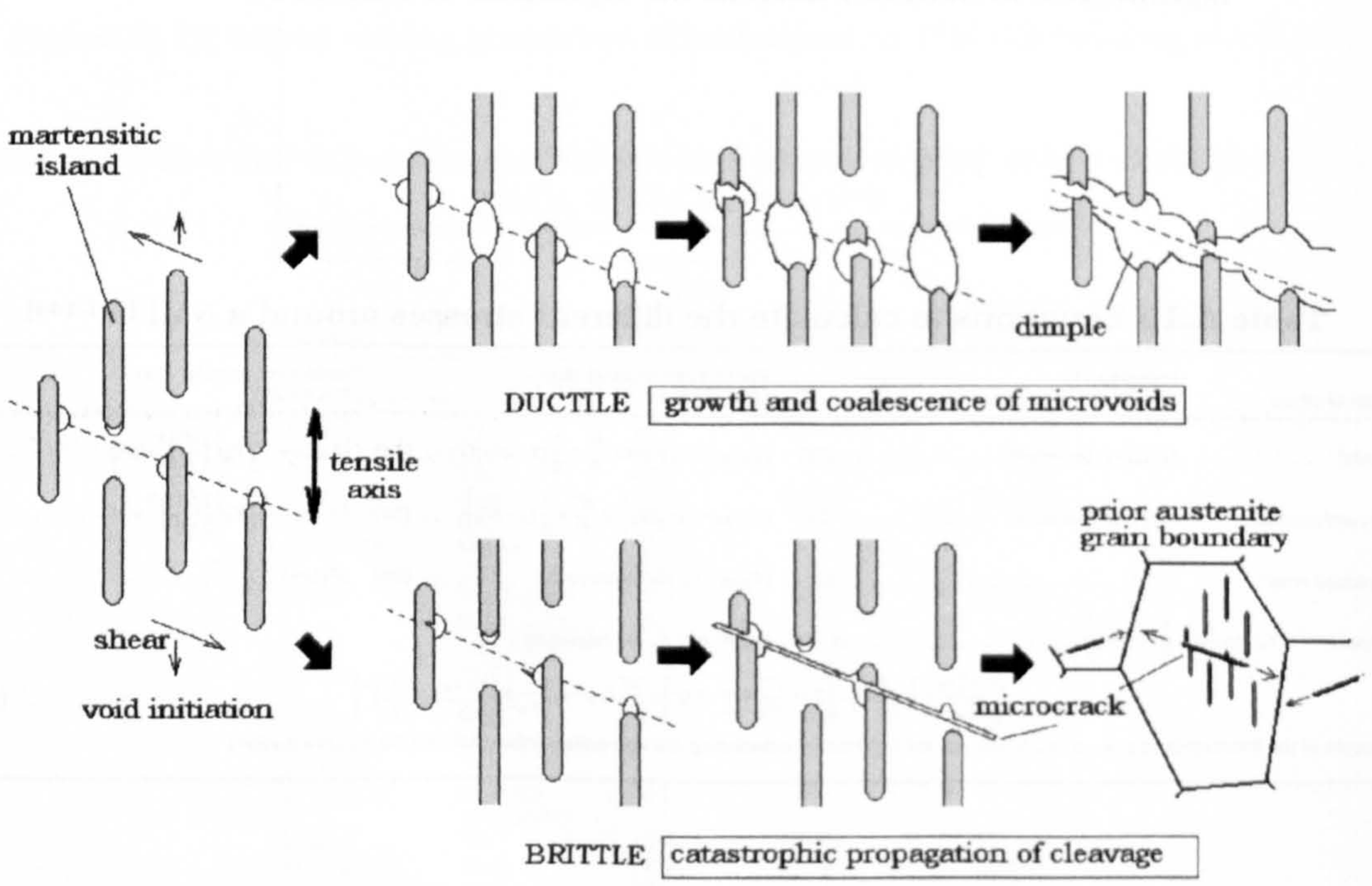

Figure A.21 Mechanism for ductile or brittle fracture involving elongated MAC constituents. Adapted from Kim et. al. [174, 175]

A.23 Theoretical model for the intergranular fracture of high strength steel charged with hydrogen.

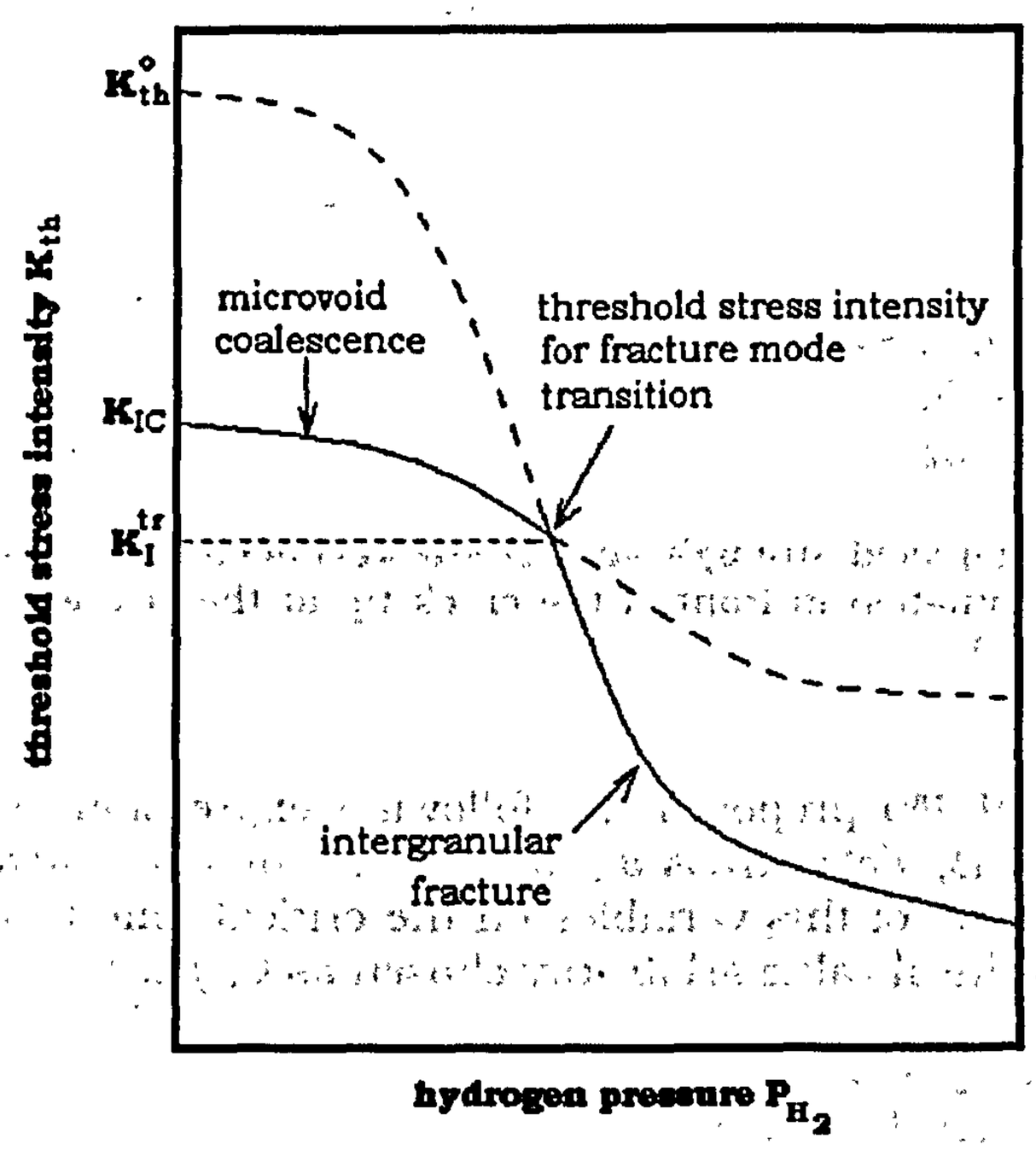

Figure A.22 Schematic representation of fracture mode transition for hydrogen assisted cracking as related to the relationship K_{th} against hydrogen pressure [177, 178]

A.24 Hydrogen diffusion and accumulation in the crack tip: the effect of yield strength (σ_{ys}) and stress concentration factor (K)

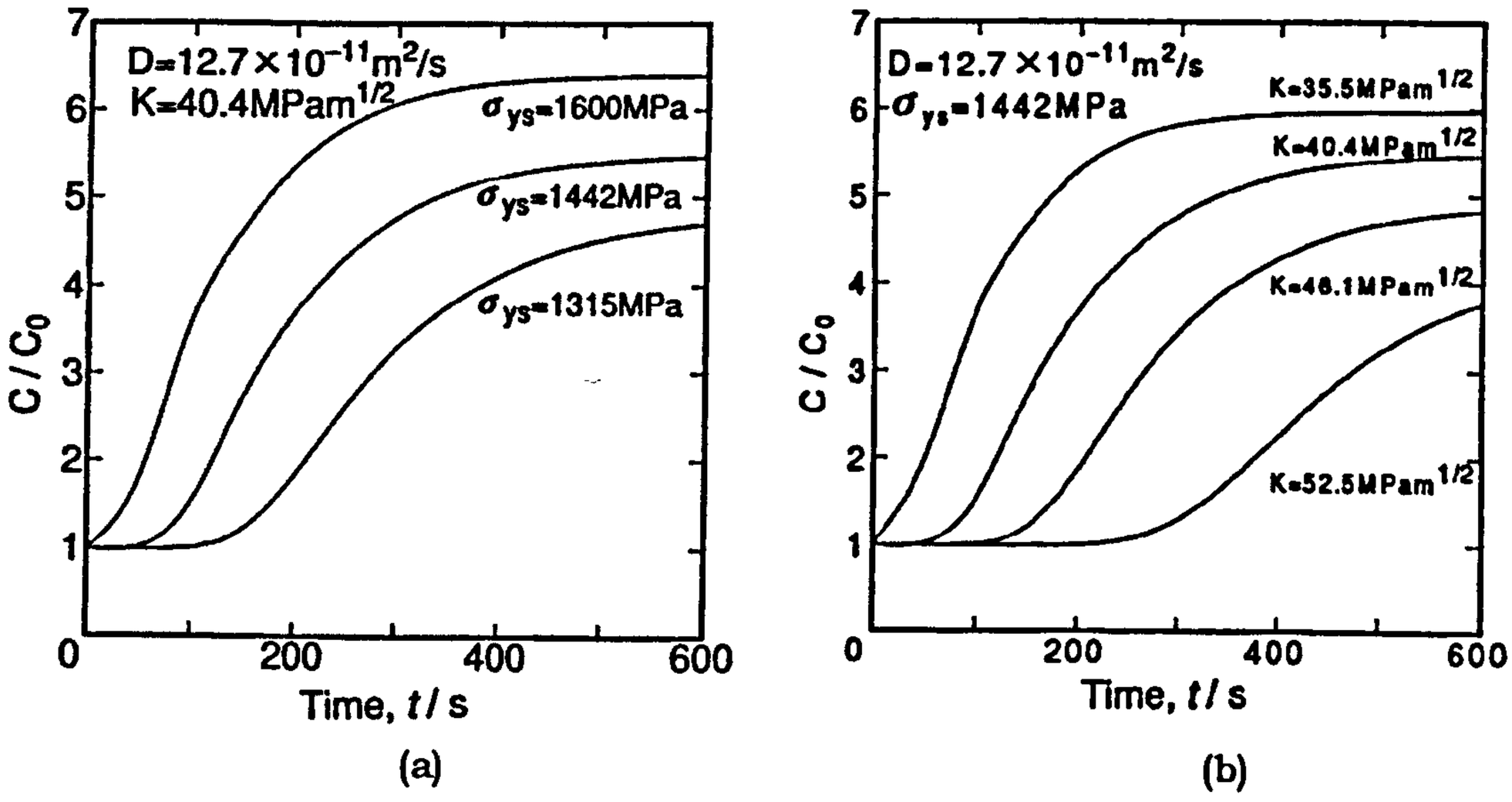

Figure A.23 Effect (a) yield strength and (b) stress concentration factor on hydrogen diffusion and accumulation in front of the crack tip at the elastic-plastic boundary , from Yokobori [184, 186]

Yokobori et. al [184, 186] proposed the following expressions with relates the diffusion constant D, yield stress σ_{ys}, and stress intensity factor, K. Equation A.15 shows the effect of this variables on the critical time t_{cr} which hydrogen takes to reach a critical value arbitrarily chosen as $C_{cr}/C_0=3$.

$$\frac{1}{t_{cr}} = A\left(\frac{D}{b^2}\right)\left(\frac{\sigma_{ys}}{E}\right)^6\left(\frac{K}{E\sqrt{b}}\right)^{-4.5} \qquad \text{(A.35)}$$

where b is the Burger's vector and E is the Young's modulus. A is a constant that depends on plate thickness (A=2.10 10^{-6} s^{-1} for thick and 1.49 10^{6} s^{-1} for thin plates). The author's final proposal is an embrittlement index which is shown in the following equation:

$$HE = \left(\frac{D}{b^2}\right)\left(\frac{\sigma_{ys}}{E}\right)^6\left(\frac{K}{E\sqrt{b}}\right)^{-4.5} \qquad \text{(A.36)}$$

A.25 Experimental data for the trapping constant k estimation

Tables from A.16 to A.18 present the estimated values for k. Three values for each weld metal where obtained (M_1, M_2 and M_3). It is shown the mean and the standard deviation (S_x). This data is presented in different ways in the main text. Statistical analysis of the data using t-distribution was employed to estimate the confident intervals at a 95%.

Table A.16 Estimated values for k (s^{-1}) for the weld metals charged during 10 s

Weld	M_1 (s^{-1})	M_2 (s^{-1})	M_3 (s^{-1})	Mean (s^{-1})	S_x (s^{-1})
CWX181	0.08	0.03	0.05	0.053	0.025
CWX351	0.40	0.32	0.35	0.357	0.040
14001	0.42	0.36	0.40	0.393	0.031
15171	0.30	0.40	0.25	0.317	0.076
VCX2561	0.28	0.30	0.35	0.310	0.036
CWX361	0.20	0.30	0.35	0.283	0.076
CWX201	0.20	0.10	0.15	0.150	0.050
14031	0.45	0.36	0.35	0.387	0.055
CWX71	0.08	0.07	0.10	0.083	0.015
CWX91	0.25	0.22	0.30	0.257	0.040
CWX81	0.40	0.35	0.30	0.350	0.050
CWX331	0.12	0.08	0.10	0.100	0.020

Table A.17 Estimated values for k (s^{-1}) for the weld metals charged during 20 s

Weld	M_1 (s^{-1})	M_2 (s^{-1})	M_3 (s^{-1})	Mean (s^{-1})	S_x (s^{-1})
CWX181	0.15	0.18	0.20	0.177	0.025
CWX351	0.27	0.22	0.25	0.247	0.025
14001	0.18	0.16	0.20	0.180	0.020
15171	0.45	0.38	0.40	0.410	0.036
VCX2561	0.60	0.50	0.55	0.550	0.050
CWX361	0.30	0.23	0.25	0.260	0.036
CWX201	0.45	0.35	0.40	0.400	0.050
14031	0.10	0.13	0.15	0.127	0.025
CWX71	0.06	0.05	0.10	0.070	0.026
CWX91	0.04	0.01	0.05	0.033	0.021
CWX81	0.10	0.12	0.15	0.123	0.025
CWX331	0.11	0.10	0.08	0.097	0.015

Table A.18 Estimated values for k (s^{-1}) for the weld metals charged during 30 s

Weld	M_1 (s^{-1})	M_2 (s^{-1})	M_3 (s^{-1})	Mean (s^{-1})	S_x (s^{-1})
CWX181	0.07	0.06	0.05	0.060	0.010
CWX351	0.16	0.20	0.15	0.170	0.026
14001	0.12	0.18	0.15	0.150	0.030
15171	0.28	0.24	0.30	0.273	0.031
VCX2561	0.19	0.21	0.25	0.217	0.031
CWX361	0.05	0.04	0.05	0.047	0.006
CWX201	0.17	0.15	0.20	0.173	0.025
14031	0.15	0.17	0.25	0.190	0.053
CWX71	0.04	0.02	0.05	0.037	0.015
CWX91	0.12	0.14	0.10	0.120	0.020
CWX81	0.13	0.11	0.15	0.130	0.020
CWX331	0.00	0.00	0.00	-	-

Table A.19. Table to construct figure 9.21

Weld metal	N_v (10^6 mm^{-3})	MAC (%)	C_k (mL/100g)	NMI Character
CWX181	22.09	8.58	2.6	R/L/L
CWX351	30.04	6.08	5.4	C/H/M
14001	28.4	5.40	3.2	C/H/L
15171	23.53	5.65	1.5	R/M/L
VCX2561	19.13	6.50	1.6	R/M/L
CWX361	23.39	16.26	4.0	C/M/S
CWX201	13.51	13.75	2.0	R/L/M
14031	26.99	8.64	1.0	C/M/M
CWX71	29.22	8.69	1.8	C/H/S
CWX91	27.58	10.95	1.0	C/H/S
CWX81	30.88	8.96	3.0	C/H/S
CWX331	20.38	19.71	1.2	R/L/S

Nv: NMI 3-D density, MAC: martensite-austenite-carbide content, Ck: critical hydrogen content to produce 50% of ductility reduction, NMI Character: NMI characteristics (spatial distribution/NMI number/NMI maximum size)

A.26 Box plot to visualise the scatter in the k data value.

In figures A.23 to A.25 are presented the measured k values in a box plot. Each box shows the median, quartiles, and extreme k values for each weld metal sample.

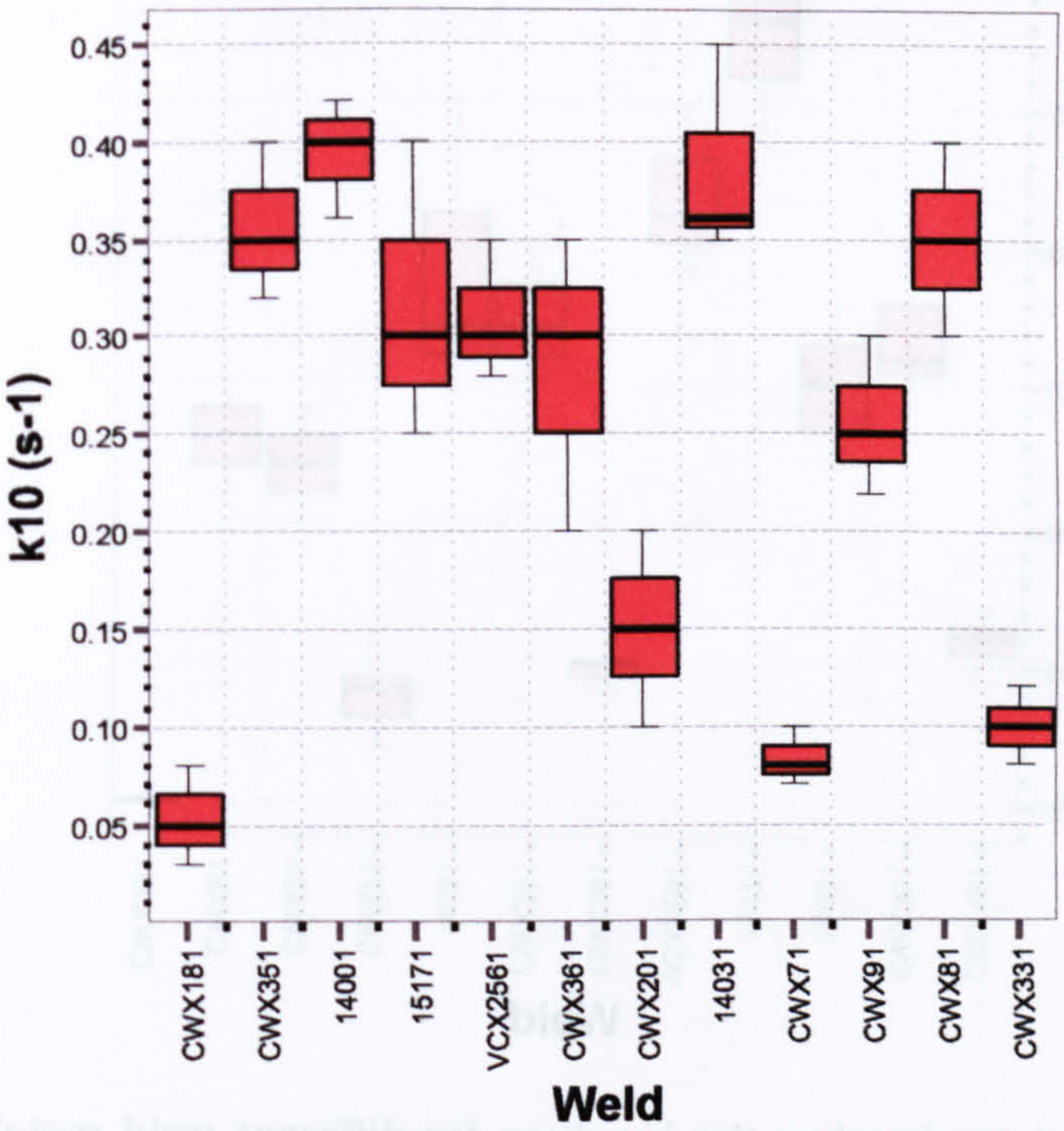

Figure A.24 Box plot to visualise the k values for different weld metals after 10 s of charging time. Obtained by the potentiostatic pulse technique in 0.87 mol/L acetic acid ($C_2H_4O_2$) and 0.5 mol/L sodium acetate ($C_2H_3NaO_2$) containing 15 ppm sodium meta-arsenite ($AsNaO_2$) as a hydrogen entry promoter at 25.0 ± 0.1°C.

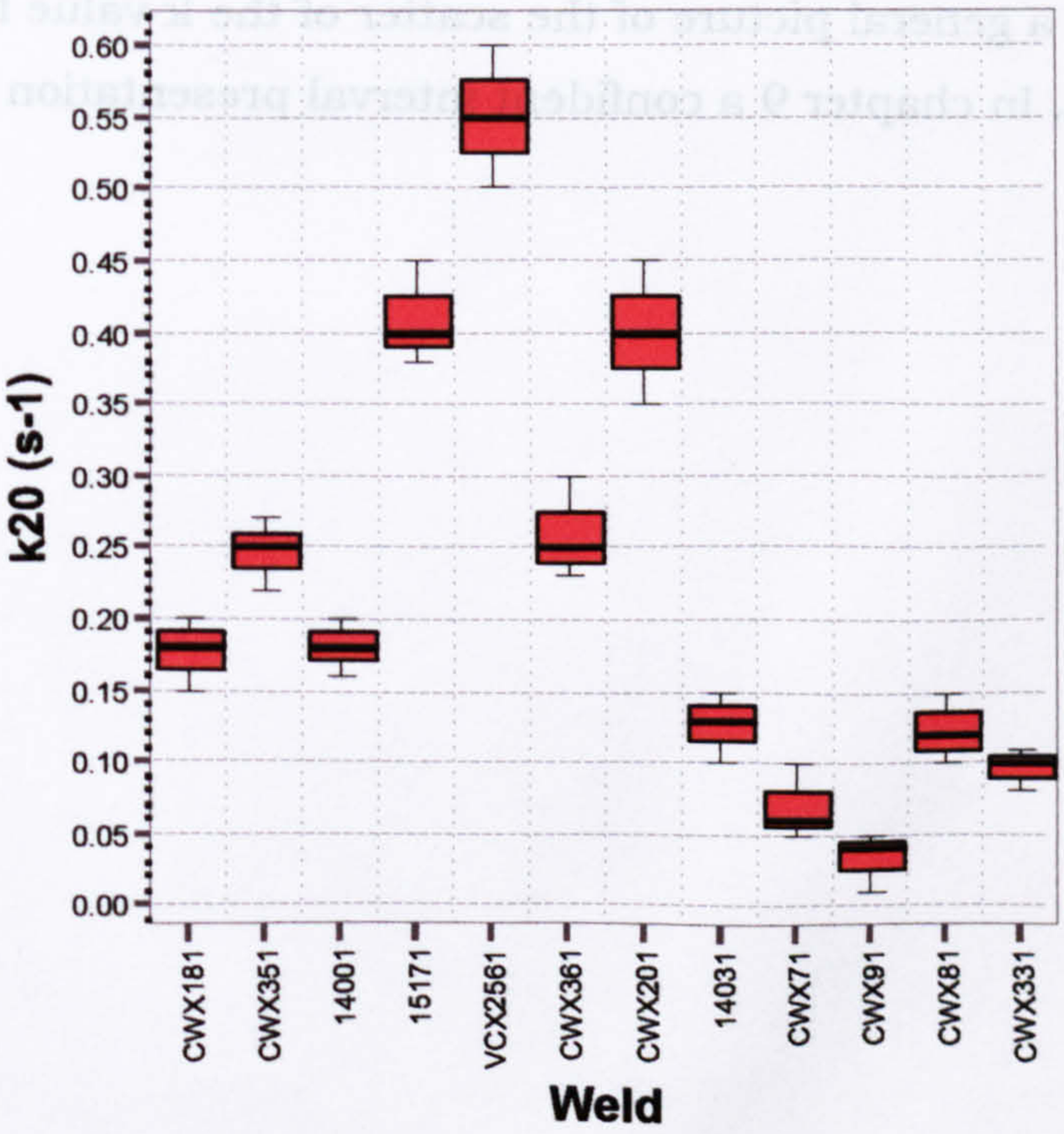

FigureA.25 Box plot to visualise the k values for different weld metals after 20 s of charging time. Obtained by the potentiostatic pulse technique in 0.87 mol/L acetic acid ($C_2H_4O_2$) and 0.5 mol/L sodium acetate ($C_2H_3NaO_2$) containing 15 ppm sodium meta-arsenite ($AsNaO_2$) as a hydrogen entry promoter at 25.0 ± 0.1°C.

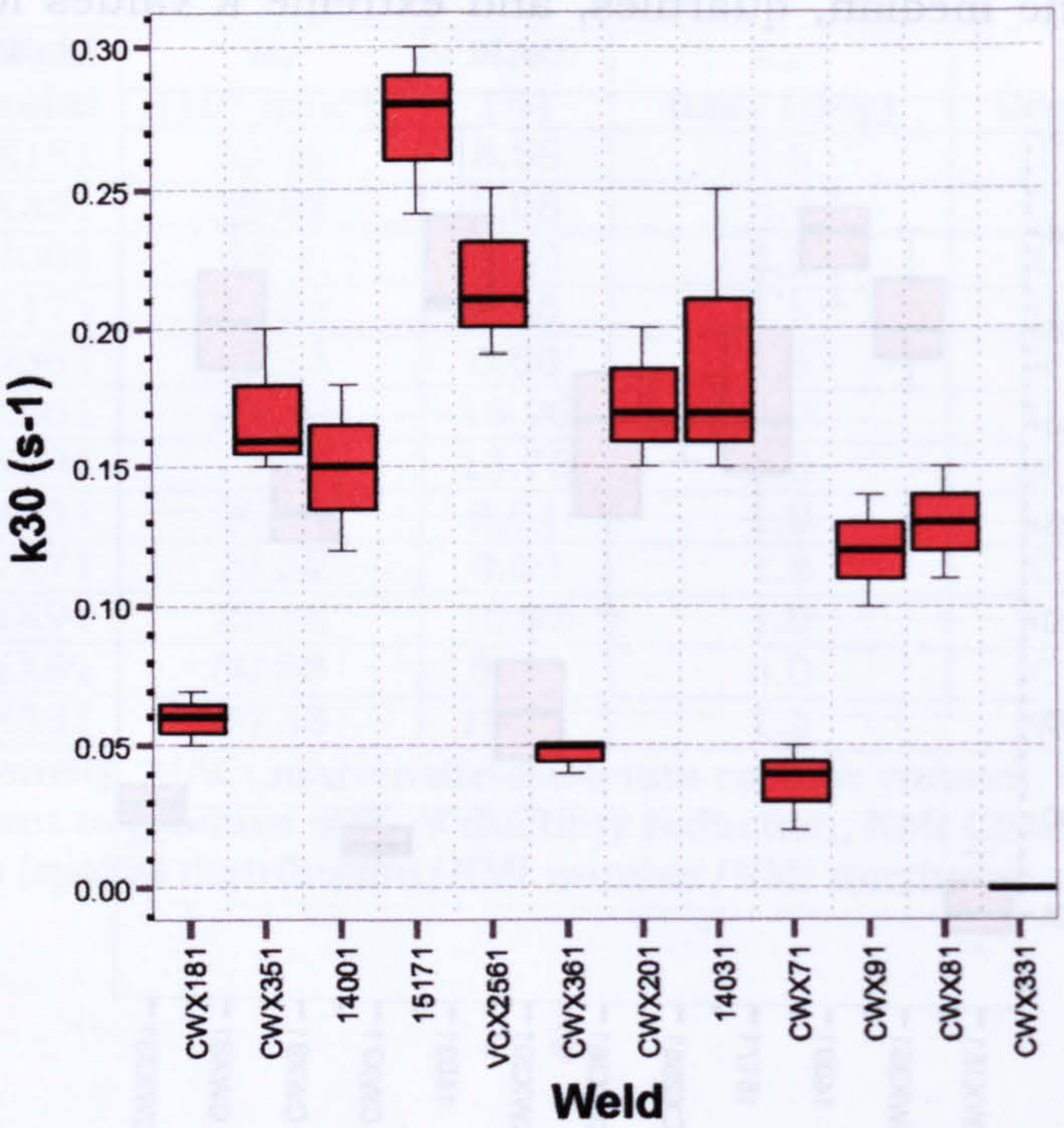

Figure A.26 Box plot to visualise the k values for different weld metals after 30 s of charging time. Obtained by the potentiostatic pulse technique in 0.87 mol/L acetic acid ($C_2H_4O_2$) and 0.5 mol/L sodium acetate ($C_2H_3NaO_2$) containing 15 ppm sodium meta-arsenite ($AsNaO_2$) as a hydrogen entry promoter at 25.0 ± 0.1°C.

These figures give a general picture of the scatter of the k value for the totality of the weld metals. In chapter 9 a confident interval presentation was used.